THE UNIVERSITY *of* EDINBURGH

Experimental Study on Local Heat Transfer Coefficients and the Effect of Aspect Ratio on Flow Boiling in a Microchannel

Sofia Korniliou

A thesis submitted for the degree of Doctor of Philosophy.
The University of Edinburgh.

October 2017

Lay summary

Flow boiling in microchannels is a promising technology for cooling of small-scale devices such as electronic chips, power rectifiers, radar arrays, chemical microreactors that require dissipating heat fluxes of several MW m^{-2} while maintaining constant temperature at the surface. Although flow boiling in macroscale provides higher performance than single-phase or pool boiling heat transfer, the advantages in microscale have not been yet completely justified. This study aims to assist in the better understanding of some outstanding issues regarding flow instabilities, two-phase heat transfer mechanisms and early dryout that occur in microchannels while increasing their aspect ratios (a). Fully integrated and instrumented silicon multi-microchannel heat sinks of width-to-height aspect ratios from 0.3 to 3 and hydraulic diameters D_h from 50 to 150 μm were developed in order to fully characterise their local heat transfer performance during flow boiling. Local wall temperature measurements were obtained from five thin nickel film temperature sensors with simultaneous pressure measurements and flow visualisation from the top. Uniform heating was achieved with a thin aluminium heater integrated at the back of the microchannels. The effect of a, mass flux, inlet subcooling temperature and bubble dynamics on two-phase flow boiling local heat transfer coefficient and pressure drop were investigated for constant heat fluxes. Severe pressure and temperature fluctuations in excess of 250 °C were measured at high a microchannels. The heat sinks with microchannels of a = 1.5 and D_h = 120 μm, achieved the maximum heat transfer performance. High spatial and temporal resolution wall temperature maps were obtained with advanced thermography technique, synchronised with simultaneous high-speed imaging and pressure measurements from integrated miniature piezoresistive pressure sensors inside a high aspect ratio ($a = 22$) transparent Polydimethylsiloxane (PDMS)-based microchannel of D_h =192 μm. The aim was to produce accurate two-dimensional (2D) high spatial and temporal resolution two-phase heat transfer coefficient maps across the full domain of a single microchannel using FC-72 dielectric liquid. The novel PDMS based microchannel provided measurements in the vicinity of the wall due to the transparency of PDMS to midwave infrared radiation. Synchronised flow visualisation images were related with liquid-vapour distribution of the channel base and were correlated with the two-phase heat transfer coefficient maps in order to elucidate flow boiling instabilities, film thinning during bubble confinement and wetting / rewetting phenomena during annular flow pattern.

Résumé

L'ébullition en micros canaux est une technique de refroidissement très prometteuse pour les composants en microélectronique. Ces derneirs, de plus en plus miniaturisés, nécessitent souvent la dissipation de densités de flux importantes, pouvant atteindre quelques MW m-2 pour maintenir des températures acceptables. L'objet de cette étude est de mieux comprendre les instabilités des écoulements, le transfert thermique par changement de phase tout comme l'effet des rapports de forme (a) sur l'apparition de sites de nucléation à la surface de micro canaux. L'analyse des échanges convectifs locaux lors de l'ébullition a été réalisée dans le cas de micro canaux de rapport de forme allant de 0.3 à 3 et de diamètres hydrauliques allant de 50 à 150 μm. Le banc d'essai a été instrumenté de manière à pourvoir mesurer simultanément les températures de surface à l'aide capteurs en film mince de nickel, de capteurs de pressions instantanées et de caméra rapide pour la visualisation du phénomène d'ébullition. Le chauffage du fluide a été réalisé à l'aide du dépôt en couche mince d'un film résistif en aluminium directement appliqué à la surface des micro canaux. L'étude expérimentale a permis d'analyser les phénomènes de changement de phase par ébullition, du transfert thermique local ainsi que la chute de pression de l'écoulement. En particulier, le travail expérimental a permis de mettre en évidence les effets sur le transfert, du rapport de forma a, de la température de sous refroidissement du fluide à l'entrée des canaux et de la dynamique de formation et de grossissement des bulles. Des fluctuations importantes de pression et de températures ont été enregistrées pour des températures de surfaces avoisinant les 250°C. Les micro canaux avec a= 1.5 et Dh=120mm, correspondent à la configuration la plus performante. Les mesures par thermographie infrarouge (IR) combinées à la visualisation par caméra rapide et aux mesures des fluctuations de pressions par capteurs piézoresitifs, ont été réalisées dans le cas de canaux en Polydimethylsiloxane (PDMS) de grand rapport de forme (a=22) et de diamètre hydraulique Dh =192 μm. L'objectif était d'identifier des cartographies bidimensionnelles et instationnaires de coefficients d'échanges convectifs dans le cas d'un micro canal utilisant un fluide diélectrique le FC72. La double visualisation par thermographie infrarouge et par caméra CCD rapide a permis de corréler la dynamique de l'ébullition, et notamment le grossissement des bulles, l'asséchement et ou le mouillage des parois, aux coefficients d'échanges convectifs locaux.

Declaration

"I declare that this Thesis has been composed by me (i.e. Sofia Korniliou), the work is my own, and it has not been submitted for any other degree or professional qualification except as specified."

Abstract

Flow boiling in integrated microchannel systems is a cooling technology that has received significant attention in recent years as an effective option for high heat flux microelectronic devices as it provides high heat transfer and small variations in surface temperature. However, there are still a number of issues to be addressed before this technology is used for commercial applications. Amongst the issues that require further investigation are the two-phase heat transfer enhancement mechanisms, the effect of channel geometry on heat transfer characteristics, two-phase flow instabilities, critical heat flux and interfacial liquid-vapour heat transfer in the vicinity of the wall. This work is an experimental study on two-phase flow boiling in multi- and single-rectangular microchannels. Experimental research was performed on the effect of the channel aspect ratio and hydraulic diameter, particularly for parallel multi-microchannel systems in order to provide design guidelines. Flow boiling experiments were performed using deionised water in silicon microchannel heat sinks with width-to-depth aspect ratios (α) from 0.33 to 3 and hydraulic diameters from 50 μm to 150 μm. The effect of aspect ratio on two-phase flow boiling local heat transfer coefficient and two-phase pressure drop was investigated as well as the two-phase heat transfer coefficients trends with mass flux for the constant heat fluxes of 151 kW m^{-2}, 183 kW m^{-2}, 271 kW m^{-2} and 363 kW m^{-2}. Wall temperature measurements were obtained from five integrated thin nickel film temperature sensors. An integrated thin aluminium heater enabled uniform heating with a small thermal resistance between the heater and the channels. The microfabricated temperature sensors were used with simultaneous high-speed imaging and pressure measurements in order to obtain a better insight related to temperature and pressure fluctuations caused by two-phase flow instabilities under uniform heating in parallel microchannels. The results demonstrated that the aspect ratio of the microchannels affects flow boiling heat transfer coefficients. However, there is not clear trend of the aspect ratio on the heat transfer coefficient. Pressure drop was found to increase with increasing aspect ratio. Wide microchannels but not very shallow, with α = 1.5 and D_h = 120 μm, have shown good heat transfer performance, by producing modest two-phase pressure drop of maximum 200 mbar for the highest heat flux and heat transfer coefficients of 200 kW m^{-2} during two-phase flow boiling conditions. For the high aspect ratio, values of 2 and 3 two-phase flow boiling heat transfer coefficients were measured to be lower compared to aspect ratio of 1.5. Microchannels with aspect ratios higher than 1.5 produced severe wall temperature fluctuations for high heat fluxes that periodically reached extreme wall temperature values in excess of 250 ˚C. The consequences of these severe wall temperature and pressure fluctuations at high aspect ratios of 2 and 3 resulted in non-uniform flow distribution and temporal dryout. Abrupt increase in two-phase pressure drop

occurred for a > 1.5. The effect of the inlet subcooling was found to be significant on both heat transfer coefficient and pressure drop. Furthermore, the effects of bubble growth on flow instabilities and heat transfer coefficients have been investigated. Although the thin film nickel sensors provide the advantage of much faster response time and smaller thermal resistance compared to classic thermocouples, they do not allow for full two-dimensional wall temperature mapping of the heated surface. An advanced experimental method was devised in order to produce accurate two-dimensional heat transfer coefficient data as a function of time. Infrared (IR) thermography was synchronised with simultaneous high-speed imaging and pressure measurements from integrated miniature pressure sensors inside the microchannel, in order to produce two-dimensional (2D) high spatial and temporal resolution two-phase heat transfer coefficient maps across the full domain of a polydimethylsiloxane (PDMS) microchannel. The microchannel was characterised by a high aspect ratio (a = 22) and a hydraulic diameter of 192 μm. The PDMS microchannel was bonded on a transparent indium tin oxide (ITO) thin film coated glass. The transparent thin film ITO heater allowed the recording of high quality synchronised high - speed images of the liquid-vapour distribution. This work presents a better insight into the two-phase heat transfer coefficient spatial variation during flow instabilities with two-dimensional heat transfer coefficient plots as a function of time during the cycles of liquid-vapour alternations for different mass flux and heat flux conditions. High spatial and temporal resolution wall temperature measurements and pressure data were obtained for a range of mass fluxes from 7.37 to 298 kg m^{-2} s^{-1} and heat fluxes from 13.64 to 179.2 kW m^{-2} using FC-72 as a dielectric liquid. 3D plots of spatially averaged two-phase heat transfer coefficients at the inlet, middle and outlet of the microchannel are presented with time. The optical images were correlated, with simultaneous thermal images. The results demonstrate that bubble growth in microchannels differs from macroscale channels and the confinement effects influence the local two-phase heat transfer coefficient distribution. Bubble nucleation and axial growth as well as wetting and rewetting in the channel were found to significantly affect the local heat transfer physical mechanisms. Bubble level heat transfer coefficient measurements are important as previous researchers have experimentally investigated local temperature and high speed visualisation in bubbles during pool boiling conditions and not flow boiling. The effect of the confined bubble axial growth to the two-phase heat transfer coefficient distribution at the channel entrance was investigated at low mass fluxes and low heat fluxes. The 3D plots of the 2D two-phase heat transfer coefficient with time across the microchannel domain were correlated with liquid-vapour dynamics and liquid film thinning from the contrast of the optical images, which caused suspected dryout. The 3D plots of heat transfer coefficients with time provided fine details of local variations during bubble nucleation, confinement, elongated bubble, slug flow and

annular flow patterns. The correlation between the synchronised high-resolution thermal and optical images assisted in a better understanding of the heat transfer mechanisms and critical heat flux during two-phase flow boiling in microchannels.

Acknowledgements

I gratefully acknowledge the financial support of the UK Engineering and Physical Sciences Research Council through the grant EP/K00963X/1.

I would like to express my sincere gratitude to my supervisor, Professor Khellil Sefiane for giving me the opportunity to work in his group, supporting me and leading me through my PhD. I would like to thank Professor Khellil Sefiane for all his understanding, patience, his support and kindness. It has been a great pleasure to work with him, in supportive and encouraging environment of his research group.

I am also thankful to Professor Anthony J. Walton and his research group at the Scottish Microelectronic Centre. Particularly, I would like to acknowledge Dr. Yifan Li for fabricating and Dr. Coinneach MacKenzie Dover for fabricating the test devices I used in my research.

My sincere thanks goes to Professor Souad Harmand in the Université de Valenciennes et du Hainaut-Cambrésis (UVHC) who provided me the opportunity to use the laboratory facilities. It has been a pleasure collaborating with her group in France. The experimental setup for the synchronised infrared thermography and high-speed flow visualisation experiments was built in UVHC.

I am thankful to Dr. Coinneach MacKenzie Dover, Dr. John Christy and Dr. George Serghiou for their assistance during the writing of my thesis.

I would also like to thank the technicians at both universities particularly Mr Douglas Carmichael (University of Edinburgh) and Mr Jesse Schiffler (UVHC) for their assistance and patience.

I would like to acknowledge my friends and Ph.D. students from the Institute of Materials and Processes (IMP). I would like to give special thanks to Charithea, Rohan, James, Dimitrios, Nelly and Dr. Patrick Schmidt for their friendship and support during my PhD. I am also thankful to all my colleagues Alessio, Nick, Mengyu, Steven , Davide, Dr. Dimitris Mamalis, Dr. Alex Harisson, Dr. Alex Askounis, Dr. Ares Gomez, Dr. Pedro Saenz, Dr. Eleni Shiko and all the rest for the nice moments we spent in the group and their support and encouragement throughout the entire PhD experience. I would also like to give special thanks my colleague and friend Maryam Parsa from for LAMIH laboratory in UVHC for her assistance and support during the months I spent in France.

Finally, I would like to thank my family and my friends for their love, encouragement and support that contributed to the achievement of this work.

Table of contents

List of tables

List of figures

Chapter 1

Chapter2

Chapter 3

Chapter 4

Chapter 6

Nomenclature

A	aspect ratio (W_{ch} / H_{ch})
A	heated area of the channel, m^2
A_{cr}	cross sectional area of the channel
Bo	boiling number
Bi	Biot number
Co	confinement number
c_p	specific heat of the liquid, J K^{-1} kg^{-1}
D	tube diameter, m
D_h	hydraulic diameter, m
Eo	Eotvos number
f	frequency
f_D	friction factor
F'_M	force that acts in on the vapour bubble due to momentum change, N
F'_S	force that acts on the vapour bubble due to surface tension, N
g	acceleration of gravity, m s^{-2}
G	mass flux, kg m^{-2} s^{-1}
h_z	local heat transfer coefficient, W m^{-2} K^{-1}
$h\ (x,y)$	two-dimensional heat transfer coefficients as a function of channel length (x axis) and channel width (y axis), W m^{-2} K^{-1}
h_{fg}	latent heat of evaporation, J kg^{-1}
H_{ch}	height of the microchannel
h_f	enthalpy of fluid, J kg^{-1}
h_l	enthalpy of saturated liquid, J kg^{-1}
h_g	enthalpy of saturated vapour, J kg^{-1}
h_{fg}	latent heat of vaporization, J kg^{-1}
$h_{tp,in}\ (x,y)$	two-dimensional interfacial heat transfer coefficients as a function of channel length (x axis) and channel width (y axis), W m^{-2} K^{-1}

I	electrical current, A
I_O	initial radiation intensity received by the sample material
I_R	radiation intensity transmitted by the material sample
k	thermal conductivity, W m^{-1} K^{-1}
K	loss coefficient
L	channel length [m]
La	Laplace number
L_{sat}	saturation length [m]
L_{sub}	subcooling length [m]
m	fin parameter
$\dot{m}$	mass flow rate, kg s^{-1}
N	total number of microchannels
P	pressure, bar
P_h	heated perimeter, m
ΔP	pressure drop, mbar
Q	wall heat flux, kW m^{-2}
q_c	critical heat flux, kW m^{-2}
q_{co}	saturated critical heat flux, kW m^{-2}
Q	Input power to the heater, W
Q_{eff}	effective heating power, W
Q_{loss}	heat loss, W
r_b	radius of bubble during nucleation, m
r_c	cavity mouth radius, m
$r_{c,crit}$	critical cavity radius, m
$r_{c,min}$	minimum radius of the nucleating cavity, m
$r_{c,max}$	maximum radius of the nucleating cavity, m
Re	Reynolds number
t	time, s

t_c	critical time, s
T	temperature, °C
T_{inlet}	liquid temperature at the inlet of the microchannel, °C
T_s	local temperature measured by the sensor at distance of 112 μm underneath the microchannel, C
Tw	wall temperature, °C
Tw, in	inner wall temperature, °C
TC	temperature measurement from thermocouple, °C
U	velocity, m s^{-1}
V	voltage, V
W	width of the channel assembly
W_{ch}	channel width, m
X	distance from the microchannel entrance, m
x_e	exit mass vapour quality
Y	distance from one side of the channel cross section, m
y_s	distance of the stagnation location from the heated wall, m
z	stream-wise distance from the channel inlet
z_{sat}	distance required for the liquid to reach T_{sat}

greek letters

γ	surface tension, N m^{-1}
ΔHi	inlet
ΔP	pressure drop, bar
ΔT	temperature difference, ˚C
ΔT_{sat}	wall superheat necessary to cause nucleation, ˚C
ΔT_{sub}	degree of subcooling, ˚C
δ	thermal liquid boundary layer thickness, m
ε	surface emissivity
ε_{paint}	surface emissivity of the black paint

ε_{ITO}	measured emissivity of the at the glass - ITO interface
η	fin efficiency
θ	bubble interface angle, rad
k	monochromatic absorption coefficient, m^{-1}
λ	characteristic penetration length, m
μ	dynamics viscosity
ν	kinematic viscosity, $m^2 s^{-1}$
σ	surface tension, $N m^{-1}$
ρ	liquid density, $kg m^{-3}$
τ	transmittance
φ	portion of the total power transferred to the liquid
ω	Stefan-Boltzmann constant, $W m^{-2} K^{-4}$
δ_{max}	maximum superheated thermal layer

subscripts

amb	ambient
avg	averaged
b	bubble
bulk	bulk liquid
ch	channel
CHF	critical heat flux
crit	critical
conv	convective
DNB	departure from nucleate boiling
eff	effective
f	fluid
FD	fully developed
fg	latent quantity, difference between vapour and liquid

HTC_{max}	maximum heat transfer coefficient
IR	Infrared
in	inlet
im	Inner manifold
om	Outlet manifold
max	maximum
min	minimum
ONB	onset of nucleate boiling
out	outlet
l	liquid
rad	radiative
ref	reference temperature
s1	sensor 1 at the channel inlet
s2	sensor 2 at the channel outlet
sd1	sidewall 1 of the microchannel
sd2	sidewall 2 is the opposite to sd1 wall of the microchannel
tp	two-phase
sat	saturation
sub	subcooled
sp	single-phase
v	vapour
w	wall

Chapter 1 Introduction and objectives

1.1 Introduction

Boiling heat transfer in microchannels is a cooling technology that emerged from the urgency of high heat flux dissipation in miniaturized electronic components. The rapid growing trends in packing density and the increasing speed of computer processors predicted by Moore's law, require replacing convectional air-cooling with liquid cooling technology. The International Technology Roadmap of Semiconductors (ITRS 2011) [1] reported that the power dissipation from a microprocessor chip will exceed 800 W by 2026. This implies that the average heat flux in computer chips is expected to reach 2 MW m^{-2} for high performance computers and 4.5 MW m^{-2} in desktop computers by 2026. Local hotspots are very common in electronic chips and they can reach 6-10 times the chip average power. Based on that, local hotspots can be as high as 12-45 MW m^{-2} by 2016 while in high power semiconductor devices [2]. At the same time, the maximum chip temperature should be typically 85 °C in order to guarantee the reliable performance of the system. Liquid cooling offers higher heat transfer coefficients due to better liquid thermophysical properties compared to air. Therefore, is possible to replace convective air cooling providing heat flux dissipation greater than 1 MW m^{-2} [3].

During last decades, flow boiling in small diameter channels has been recognised by the research community as a promising heat transfer technology for effective heat flux dissipation [4]. Two-phase flow boiling in microchannels can be used for cooling of electronic components of computers (CPUs, GPUs, memory cards, data storage services), cooling of high power semiconductor devices (IGBT inverters and switch-mode power supplies), cooling of laser diode arrays, medical X-ray equipment, cooling of proton exchange membrane fuel cells and fusion reactor and evaporators/condensers in miniature vapour compression refrigerators. Other applications of microchannels include inkjet printers, air conditioning units in automotive industry, and applications where evaporators use small diameter passages with plate-fin heat exchangers. Two-phase flow boiling in microchannels could be efficient in the case of cooling of small modules due to the capability of reducing the hot spots inside the chip.

An example of an overheated insulated-gate bipolar transitor (IGBT) chip module is presented in Figure 1.1. An IGBT chip is a three-terminal power semiconductor device developed to be used for fast switching. Figure 1.1a presents a schematic drawing of a typical

IGBT chip module with a size of 150 × 160 mm^2. This module dissipates 6.52 kW and requires a maximum temperature at the chip-solder interface (junction temperature) of 175 °C and maximum case temperature of 125 °C. The junction to case thermal resistance was 23 K kW^{-1} for the IGBT chip. Taking into account that the maximum allowed temperature difference between the junction and the case is 50 K, the power dissipated from the IGBT was estimated as 2.17 kW.

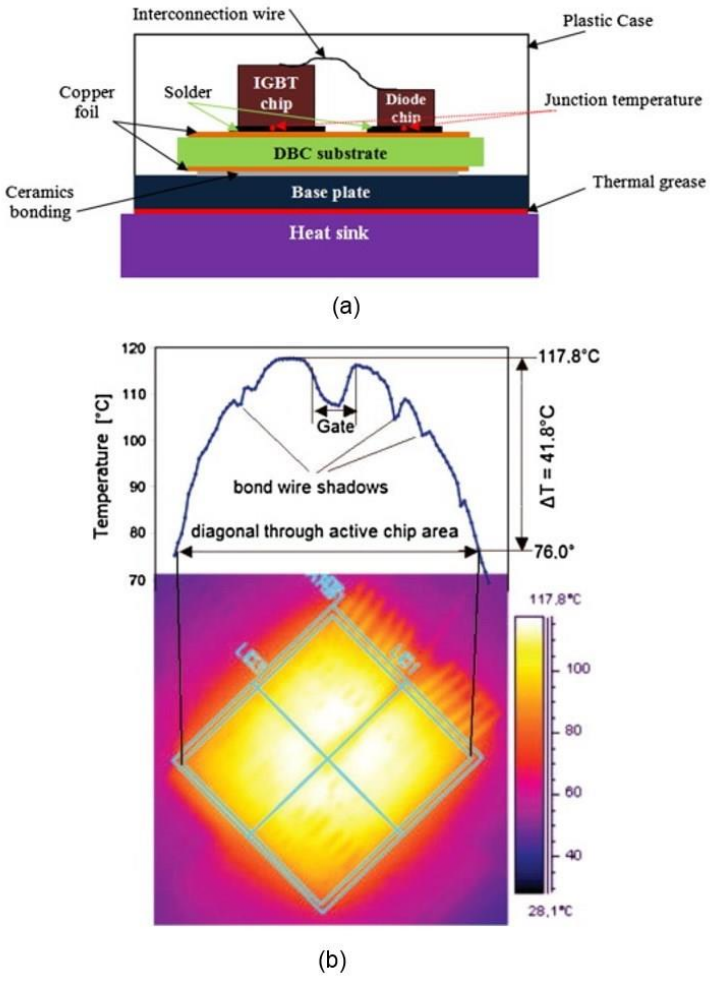

Figure 1. 1 *(a) Schematic drawing of typical IGMT module produced by Mitsubishi Electronic Corporation in 2015 and (b) temperature distribution across the diagonal of an IGMT chip.*

According to the literature [2], the die size of IGBT chips ranges from 6.5 6.6 mm^2 to 14.3 mm^2. Using the above die sizes and the estimated power dissipation rate from each chip, the heat flux at the chip base could be as high as 10 – 50 MW m^{-2} for the IGBT chip [2]. These values are very high compared to the average heat fluxes of 0.26 MW m^{-2}. This shows that the

local heat fluxes are not uniformly distributed inside the module. Figure 1.1b shows that the local temperature difference between the edges of the chip can reach the value of 41.8 K, inducing local hotspots.

Liquid cooling can be achieved inside multiple parallel channels formed in a high conductivity substrate or inside single microchannels or of a certain geometry. Single-phase liquid cooling has been extensively explored [5]–[7]. However, during single-phase flows in microchannel heat sinks, high heat flux applications producing high-pressure drop and large temperature gradient at the direction of fluid flow.

Tuckerman and Pease [6] were the first to use microchannels heat sinks for the investigation of flow boiling. They produced large aspect ratio heat sinks with channel width in the order of 50 μm on the back of integrated circuit (IC) chips, which achieved up to 790 W cm^{-2} heat dissipation using water while maintaining the chip temperature below 71 °C. This innovative cooling technique attracted great attention and extensive theoretical and experimental studies have since been conducted by various researchers. Two-phase microchannel heat sinks provide better axial temperature uniformity and higher heat transfer coefficients compared to single phase, by utilizing the coolant's latent heat [8]. Additionally, lower coolant flow rate is required to dissipate the same amount of heat compared to that of a single-phase heat sink. This results in lower energy consumption of the pump and the entire cooling system. Recent iNEMI roadmap 2016 shows that flow boiling using dielectric liquids and water can provide heat transfer coefficients greater than 1,000 W m^{-2} K^{-1} for systems that require dissipation of more than 10,000 W [9]. Dielectric liquids are ideal for electronics because they protect the electrical parts in case of leakage.

During last decades, many studies have been carried out regarding flow boiling in microchannels [2], [10]–[13]. There are many parameters that can affect convective heat transfer in microchannels, such as channel size, surface roughness, axial heat conduction, surface geometry and different working liquids [14]. Circular cross section tubes are usually used in macroscale size channels. For microscale studies, the most commonly used cross sections are rectangular, due to ease of fabrication and this results in non-applicability of the current correlations. Additionally, heat transfer mechanisms, pressure drop and flow patterns in microchannels have been found to differ from those in macroscale flows, due to a different scaling of various forces during microscale phenomena. An implication for the future application of this cooling technology is the insufficient knowledge, particularly in the fundamental phenomena that take place during liquid evaporation in microscale. Large discrepancies that exist in correlations of heat transfer at the microscale are induced due to the different forces that play important role in this microscale. For example, surface tension and

viscosity are more important in microchannels. Therefore, detailed experimental data are required to obtain a better understanding of the complex two-phase flow phenomena and improve existing predictive methods.

It is necessary to provide design guidelines for microchannels heat sinks for their stable operation and high performance if they are going to be used in commercial applications for cooling. The effect of the different cross sectional aspect ratios and sizes on the heat transfer characteristics of microchannel heat sinks are still unknown and it is important to understand their behaviour in order to exploit their high cooling potential. Because of the lack of databases for predictive tools for high aspect ratio microchannels, it is therefore important to carry out experiments in order to validate the performance for increasing aspect ratio microchannels. It is necessary to ensure the operating stability of the microchannels heat sinks at high heat flux conditions. At high heat fluxes, flow instabilities flow boiling instabilities that are induced on the microchannel surface result in reverse flow and dryout. Flow reversal occurs when the bubble diameter approaches the channel diameter during two-phase flow in microchannels and the bubble grows in axial direction at both upstream and downstream direction. It is important to understand the effect of wall temperature and pressure oscillations on the interfacial heat transfer coefficient, pressure drop, critical heat flux and the flow stability during flow boiling. The causes of temperature fluctuations and the locations of temperature hot spots must be well understood in order to be able to use two-phase flow boiling in microchannels as a reliable CPU cooling method.

In order to bridge this literature gap, we propose to undertake an experimental investigation using microchannels heat sinks with different channel aspect ratios. One of the present study objectives is to address the limited understanding in literature on the effects of channel cross section aspect ratio and mass flux on the heat transfer coefficients, pressure drop, and flow boiling instabilities and boiling flow patterns in microchannels. The hydraulic diameters ranged between 50 and 150 μm, dimensions (D_h< 200 μm) where bubbles are confined and interfacial forces are significant according to Kandlikar [15]. The effect of aspect ratio ($a = W_{ch}/H_{ch}$) increase on two- phase pressure drop and consequently the two-phase heat transfer coefficient profile along the flowstream direction in the microchannels heat sinks.

Previous researchers determined the heat transfer coefficients from wall temperature measurements obtained using embedded thermocouples [16], [17] below the surface of microchannels and temperature sensors integrated at the bottom surface [18]–[23]. These measurements provided heat transfer coefficients at fixed positions along or across the heater base or area-averaged and did not enable mapping of the whole channel base. The majority of studies focus on temperature measurements, and hence the heat transfer coefficients, along a

single line of the flow, rather mapping the completely heated surface [24]–[28]. Also in many studies the heat transfer coefficients were calculated using pressure measured outside the microchannel, [18], [19], [22], [24], [29]. This leads to potential errors in the estimation of local heat transfer coefficients.

In order to minimize the inconsistencies in microchannels pressure drop data, it is recommended to obtain pressure measurement from inside the microchannel [30], in order to accurately estimate the local saturation temperature used for the calculation of the heat transfer coefficient. Only one study has been identified that used integrated pressure sensors for accurate two-phase heat transfer measurements in microchannels [26]. Kohl *et* al. [30] developed a microchannel experimental platform that enables measurements of pressure inside the microchannel. They utilised bulk etched silicon components that integrated pressure-sensing membranes with the microchannel test section.

Although there is extensive literature on the parameters that affect flow boiling heat transfer in microchannels, there is still need for more spatially and temporally resolved temperature data. Knowledge of hydrodynamics near the wall is important in order to interpret the local heat transfer coefficient maps. Therefore, infrared (IR) thermography should be always combined with flow visualisation in order to capture the mechanisms (local dryout, rewetting) and transition between flow regimes that provide in depth description of the phenomenon. Ong and Thome [31] found that flow boiling heat transfer coefficients are a function of the flow pattern type. Therefore, the details of the local heat transfer coefficient (HTC) variation could be better elucidated with high-resolution infrared thermography technique, which minimizes the accuracy problems of standard sensors, as it is non-invasive.

One of the main fundamental challenges of two-phase boiling in microscale is to carry out heat transfer measurements with high sensitivity in order to measure the transient heat transfer from the inner side of the wall. The liquid-solid contact angle or the heated surface wettability plays an important role in the formation of a liquid microlayer on the vapour bubbles base. Previous methods that have been used to characterise the temperature at the interface such as laser induced fluorescence and thermochromic liquid crystal thermography [32] are intrusive. Also, do not always imply optical accessibility in the channel to allow the visualisation of the dryout or liquid.

A summary of some fundamental issues of flow boiling in microchannels [2] so far is :

1. Lack of general definition of mini channel or microchannel.
2. Difficulties on triggering boiling because of the large superheats that are required.
3. Lack of generally accepted prediction methods for flow patterns, heat transfer and pressure drop.

4. Early dryout (low critical heat flux) and the unclear understanding on its dependence on the operating parameters.
5. Flow reversal and instabilities
6. Unclear dominant heat transfer mechanism (s)
7. Non-circular channel effects not well understood and as well as high aspect ratio effect on heat transfer.

In the present work, an experimental method is devised to measure accurately the wall temperature distribution together with simultaneous synchronised flow visualisation with a midwave range (2-5μm) infrared camera in an optically transparent Polydimethylsiloxane (PDMS) high aspect ratio microchannel (D_h= 192 μm). A thin glass slide coated with indium tin oxide (ITO) metallic semi-conductive transparent film of 200 nm thickness was used for heating on the bottom side. A high frame rate of 200 Hz was utilized to obtain the temperature across the microchannel surface or interface. Flow boiling experiments were carried out with FC-72 in order to calculate the local heat transfer coefficient distributions using local pressure obtained from the integrated pressure sensors at the inlet and outlet and the inner wall temperature measurements. The novelty of this method is that allows measurement of accurate heat transfer distribution on the inner interface (solid-liquid) of the microchannel wall (thickness ≈ 0.17 mm) because of the PDMS transparency to infrared radiation. Additionally, the correlation between simultaneous flow visualisation from the channel base and interfacial heat transfer coefficients will provide a better understanding of the physical mechanisms of flow boiling in microscale. The obtained temperature data were used for the calculation of the interfacial heat transfer coefficients during flow boiling flow instabilities along the whole microchannel domain and single bubble level. This investigation will help to uncover the relation of heat transfer mechanism to bubble dynamics detailed measurement on single bubble level.

The mechanisms affecting the two-phase nature of the heat transfer and the critical heat flux are complex and higher resolution simultaneous measurement across the full domain are expected to elucidate in detail, important boiling phenomena in microchannels. The conditions of the maximum heat transfer coefficient (HTC_{max}) and critical heat flux (CHF) near the outlet of the microchannel are investigated for different conditions. In contrast to other studies using infrared thermography to study multiphase flows, this study uses high frame rates of up to 200 Hz and high spatial resolution of 15.39 μm / pixel. Due to the high surface to volume ratio (α = 22) of the microchannel, high heat transfer coefficients are expected at very low flow rates. Therefore, very low mass fluxes were used. This is an important advantage of two-phase flow boiling in microchannel cooling devices because it requires less pumping energy consumption

compared to single-phase. The high aspect ratio rectangular microchannel is ideal in order to reveal the characteristics of confined convective boiling in terms of pressure drop, flow patterns, critical heat flux and heat flux. Indium tin oxide (ITO) film was used as a heater because of its good optical properties: the ITO is optically accessible to both infrared (IR) and visual wavelengths, allowing temperature measurements of the ITO/glass and observations of bubbles in the flow. The effect of heat flux on local temperature variation, flow boiling heat transfer coefficient distribution and two-phase pressure drop was studied. The vapour quality with increasing heat flux was also determined and is presented together with the local two-phase heat transfer coefficients. As the bubble occupies the microchannels cross section, the heat transfer mechanisms are not only affected by the fluid thermal properties but also from the bubble contact angles with the channel wall and the confined bubble could be a limiting factor of the heat transfer at certain conditions. Interfacial heat transfer measurements at the solid wall-liquid interface are expected to provide details of the bubble growth cycles.

The main novelty of this study compared to the previous studies of Barber *et* al. [24] and Wang *et* al. [33] is the high spatial and temporal resolution wall temperature measurements acquired at the inner side of the channel wall. These measurements were used to obtain high spatial and temporal resolution two-dimensional heat transfer coefficients maps across the whole microchannel domain. This was achieved with the use of a novel PDMS-based microchannel, which is transparent to midwave infrared radiation and at the same time to optical wavelength. In the previous studies of Barber *et* al. [24] and Wang *et* al. [33], the channels were fabricated from borosilicate glass, which is not transparent to infrared radiation. Therefore, the measurements were less sensitive and accurate because they were acquired from the outer side of the wall using the IR camera. They assumed negligible diffusion by thermal conduction in the channel wall. Additionally they used rectangular cross section channels with hydraulic diameters greater than 571 μm, which are considered as minichannels by many authors. In this study, microchannels were used with hydraulic diameters from 50 to 192 μm. Additionally, this study provides high quality optical images from the channel base due to the thin film of indium tin oxide, which is transparent to optical wavelength. Barber *et* al. [24] and Wang *et* al. [33] used a coating layer of tantalum on the outer surfaces, which is thicker and requires higher power inputs. Another novelty is the integration of piezoresistive pressure sensors near the inlet and the outlet of the microchannel. In all the previous studies [24], [33], [34] the researchers used pressure transducers before and after the microchannels. Finally, a range of silicon microchannels was used with different aspect ratios from 0.3 to 3 compared to only one channel size of hydraulic diameter of 192 μm and aspect ratio of 0.75 used in the previous study of Bogojevic [34].

1.2 Objectives

The main objectives achieved by this experimental work are summarised below:

1. Development of fully integrated and instrumented microchannels of different aspect ratios for fully characterising flow boiling heat transfer coefficients and pressure drop.
2. Advanced and detail experiments to generate new data on pressure fluctuations, local temperature and liquid-vapour dynamics that will help elucidate the fundamental mechanisms.
3. Interfacial wall temperature measurements of high spatial and temporal resolution across the whole microchannel domain using a microchannel transparent to infrared radiation.
4. Integration of pressure sensing of miniature size in the channel for accurate saturation temperature determination.
5. Synchronised infrared thermography and high-speed imaging for the investigation of bubble confinement and local dryout during annular flow. Correlation of optical images with the heat transfer coefficient maps.
6. Bubble dynamics.

1.3 Summary

This chapter outlines the background of research on flow boiling in microchannels and states the applications of two-phase flow boiling technology in microelectronics. Following this, challenges that need to be addressed in order to apply this technology in the thermal management of electronics were highlighted. Finally, the objectives of this research work were summarised.

1.4 Outline of the thesis

The outline of the following chapters is given below:

- ***Chapter 1*** *presents an introduction on flow boiling in microchannels, the fundamental issues, the objectives of the study and the outline of the thesis.*
- ***Chapter 2*** *presents literature review on macroscale flow boiling and microscale flow boiling heat transfer.*
- ***Chapter 3*** *describes the experimental facilities, including flow loops, test devices, microfabrication and measurement uncertainties.*

- ***Chapter 4*** *presents results of the pressure drop and the heat transfer coefficients of silicon parallel microchannels heat sinks with different aspect ratios.*
- ***Chapter 5*** *presents the results obtained using a PDMS microchannel with synchronised IR thermography from the ITO / glass base and simultaneous high-speed visualization.*
- ***Chapter 6*** *presents investigation of interfacial heat transfer using a dual temperature mapping method with synchronised flow visualisations and local pressure measurements and the effect of bubble dynamics on flow instabilities and heat transfer coefficient.*
- ***Chapter 7*** *presents general conclusions and future work.*

Chapter 2 Literature review

2.1 Introduction

This chapter reviews well-established theory on flow boiling in macroscale channels and theory on mini-/microscale channels. Then, presents previous experimental studies on two-phase flow boiling in mini-/ microchannels. The literature review provides a summary on the criteria used to determine the transition from macro- to microscale flows and on results from experimental investigations on liquid-vapour phase change in mini- and microchannels. Experimental results are presented on the effect of two-phase flow boiling heat transfer characteristics, microchannel geometry and cross section in mini- /microchannels as a function of mass flux, heat flux, flow boiling instabilities and critical heat flux. The existing experimental approaches are discussed with emphasis on the accuracy and resolution of the obtained temperature, pressure and heat transfer coefficient data. Some latest reviews on flow boiling heat transfer in microchannels presented by Karayiannis and Mahmoud [2], Thome [13], Cheng *et* al. [36], Tibiriçá [37] state the numerous issues that still need to be addressed and need to be resolved in order to use flow boiling in microchannels for cooling of microelectronics within specified conditions. Amongst these outstanding issues are the lack of established transition criteria from macro- to microscale flows, unclear dominant heat transfer mechanism(s) and flow boiling instabilities including flow reversal and early dryout. These issues need to be better understood in order to enhance flow boiling heat transfer and use it for future high heat flux dissipation.

Flow boiling in mini- and microchannels requires further investigation as it can be significantly different from the well-established conventional flow boiling heat transfer. The dominant forces that govern microscale differ from macroscale. Kandlikar [38] reported that in microchannels, the gravitational force is small compared to the forces due to inertia and momentum change The forces produced due to rapid evaporation become significant for microchannels, as the growing bubbles interact with the channel walls [38]. At high heat fluxes, bubble grows rapidly resulting in abrupt expansion and quickly occupies the channel with a vapour slug. Therefore, interface interactions are important during flow boiling in microchannels. Other forces acting on the interface are due to the inertia of the flow and the

surface tension in the contact line region which is plays an important role in microscale as reported by Thome [39]. Two-phase pressure drop imposes a restriction on the lower limit of cross-sectional dimension of ~50 μm due to limited pumping power. Therefore, the optimisation of channel dimension for different heat dissipation requirements is becoming increasingly necessary.

2.2 The criteria for transition from macro- to micro-channels

Recent reviews [2], [37], [40] on flow boiling in microchannels show that there is not clear definition of the term microchannel. There is a confusion regarding the use of the term "micro scale". Researchers use this term widely when they want to describe any significant change compared to macroscale behaviour despite the fact that these channels have diameters in the millimetres range (small/minichannels). According to Tibiriçá and Ribatski [40] the absence of firm classification criteria can be attributed to not considering heat transfer and pressure drop characteristics. Kandlikar and Grande [41] classified flow boiling in three channel size regimes, namely conventionally sized channels (D > 3 mm), minichannels (D = 0.2 – 3 mm) and microchannels (D = 0.01– 0.2 mm). Recently, Tibiriçá and Ribatski [40] proposed two criteria based on different models for the transition from macro- to microscale flow based on a review of flow boiling experiments with various fluids for tubes with diameters of between 1.00 mm and 2.32 mm. The criteria were established after analysis of the flow pattern differences between macroscale and microscale channel behaviour. The first criterion was based on a mechanistic model for plug flow in a circular channel and the transition was assumed to occur when stratified flow no longer exists, which is a typical flow characteristic in microchannels. In this model, assuming an equilibrium between the hydrostatic pressure force and surface tension forces, the transition from macro- to microscale was found to occur when the tube diameter is smaller than the equilibrium diameter:

$$\mathrm{D} = \mathrm{La}\sqrt{8\cos\theta} \tag{2.1}$$

where La is the Laplace number and θ is the interface angle described in Figure 2.1. They ignored the effects of inertia, which according to them was a reasonable assumption for the conditions of stratified flow. The effects of contact angle are considered significant.

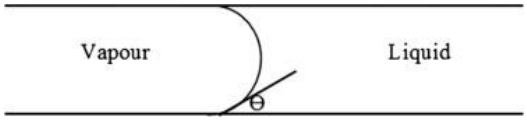

Figure 2. 1 *Schematic drawing for the definition of the contact angle used in the model proposed by Tibiriçá and Ribatski [40]*

The second criterion is based on uniformity of the liquid film thickness in annular flow, which is the other typical flow characteristic in microchannels, which pinpoints the macro- to micro transition at:

$$\mathrm{D} = \mathrm{La}\sqrt{\frac{1}{20}} \tag{2.2}$$

where La is the Laplace constant described in eq.2.4.

A number of studies used a non-dimensional criterion for the transition from macro- to microscale flow [31], [42]–[45]. In particular, the confinement number was used as an indicator of the two-phase macro- to microscale transition. The transition is defined at the point where the channel dimension changes flow behaviour. In macroscale flow, bubbles slide along the top wall due to buoyancy. As the channel diameter decreases, the importance of the surface tension increases and at some point the bubble, surrounded by a thin liquid film, "fills" the cross-section of the channel. Ong and Thome [46] found that the liquid film surrounding a bubble is symmetric for the confinement number of Co ($\frac{1}{D}\sqrt{\frac{\sigma}{g\,(\rho_l-\rho_v}}$) > 1. From the results obtained from image processing, it was observed that gravity forces were supressed and overcomed by surface tension forces at Co = 1, where gravity force was found to be a weak force as compared to surface tension. According to the authors, this occurred when top and bottom liquid film thickness had similar magnitude. The transition to macroscale then occurs when the channel diameter is increased and the buoyancy effect becomes more important, until Co < 0.3, where gravity clearly dominates surface tension. The authors proposed that the macro- to microscale transition becomes gradually between the values of 0.3 < Co < 1. Kew and Cornwell [47] proposed criteria for macro- to microscale transitions in two-phase flows, based on the confinement number :

$$\mathrm{Co} = \frac{\mathrm{La}^{0.5}}{\mathrm{D}} \tag{2.3}$$

where La is the Laplace constant, defined as:

$$\mathrm{La} = \sqrt{\frac{\sigma}{\mathrm{g}(\rho_{\mathrm{l}}-\rho_{\mathrm{v}})}} \tag{2.4}$$

They suggested that confinement effects are significant for channels with hydraulic diameters whose confinement numbers are greater than 0.5. Brauner *et* al. [45] included the Eotvos number criterion of $Eo \sim 0.2$ for microchannel flows where Eo is defined as:

$$\text{Eö} = \frac{g\,(\rho_l - \rho_v)\,{d_{in}}^2}{8\sigma} \tag{2.5}$$

The Bond number criterion ($Bd^{0.3} \leqslant 0.3$) was used by Suo and Griffith [42] where the *Bd* number is defined as:

$$\text{Bd} = \frac{(\rho_l - \rho_v)\,D^2}{\sigma} = \frac{{D}^2}{\text{La}} = \text{Co}^{-2} \tag{2.6}$$

Another proposed classification criterion from macro- to microscale flow was recently considered by Harrirchian and Garimella [11]. They classified the flow regimes into confined and unconfined flows. Confined flow was considered to occur for microscale flow and they found that the transition depends on the channel cross section and flow inertia. The proposed macro- to micro transition criterion is based on the following product:

$$\text{Bo}^{0.5} \times \text{Re} = \frac{1}{\mu_l}\left(g\,\frac{\rho_l - \rho_v}{\sigma}\right)^{0.5} GD^2 \tag{2.7}$$

where $Bo^{0.5} \times Re$ is the convective confinement number. If $Bo^{0.5} \times Re \leq 160$ the vapour bubbles are confined and the channel is considered microchannel. The Reynolds number for the liquid (Re_L) is defined as:

$$\text{Re}_L = \frac{\rho_L U_l D_h}{\mu_l} \tag{2.8}$$

2.3 Macroscale flow boiling two-phase heat transfer

A schematic drawing of the flow patterns and corresponding heat transfer regions during flow boiling in a vertical tube is presented in Figure 2.2. Qualitative profiles of the heat transfer coefficient and the temperature are also presented as a function of the length of the heated tube. Boiling occurs at a zero vapour quality on the walls of the channel and the flow patterns change due to vapour production as the flow moves downstream in the channel. This is an important difference between pool boiling and flow boiling; i.e. that the forced flow of flow boiling causes flow pattern transitions at given wall heat fluxes, as the integral power provided to the fluid

increases along the channel. The flow mechanisms of nucleate boiling and convective boiling can coexist during flow boiling. At low heat fluxes, convective boiling is significant. Forced convection mechanism dominates where an increase in the heat transfer coefficient occurs with increasing flow. In annular flows, when the liquid film at the wall becomes very thin, nucleate boiling is restrained and heat removal is by evaporation of the thin liquid film. The critical heat flux (CHF) occurs when the thin liquid film dries out, also known as the dryout condition. CHF condition can also occur when the vapour removal rate from the heater surface is smaller than the vapour generation rate, i.e. when liquid at the heater surface is not replaced fast enough to compensate for that lost due to evaporation.

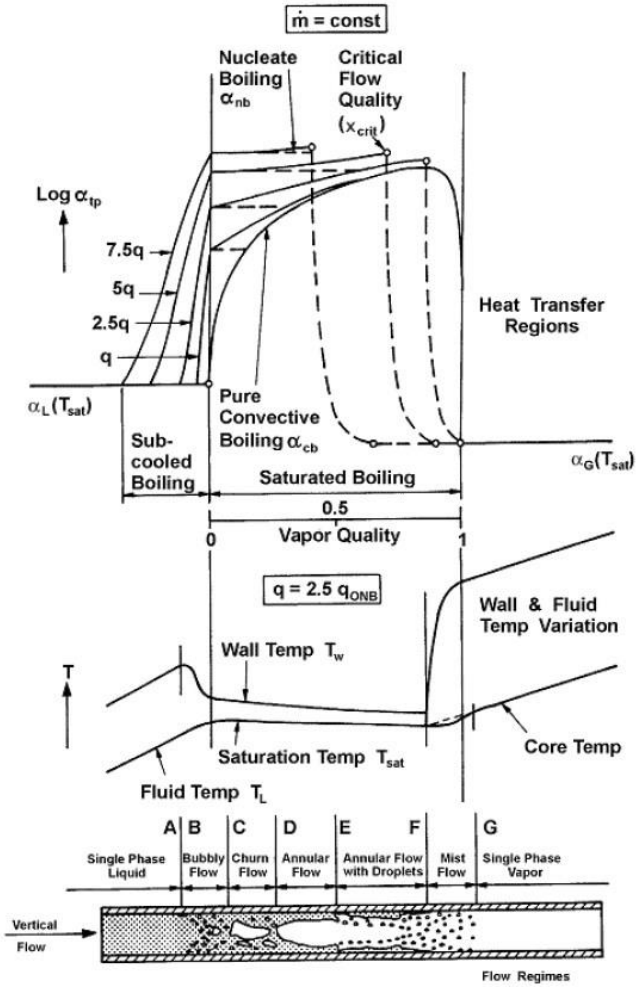

Figure 2. 2 *Illustration of forced convective boiling with qualitative temperature profile and heat transfer coefficient profile for a uniform heat flux boundary condition at a vertical tube used by Steiner and Taborek [48].*

2.4 Microscale flow boiling two-phase heat transfer

Lee and Mudawar [49] summarised in the schematic in Figure 2.3 the overall performance of small diameter ($50 < D_h < 1000$ μm) channels during two-phase flow boiling. Figure 2.3

illustrates the effect of mass flux and subcooling on pressure drop, heat transfer coefficient and CHF. Increasing mass flux increases both the convective heat transfer coefficient and CHF. Increasing the inlet subcooling can increase the convective heat transfer coefficient. However, these advantages occur with the penalty of high-pressure drop. Operation at low subcooling is unreliable because of low CHF. The highest CHF can be achieved by increasing both mass flux and inlet subcooling. Figure 2.3 also points out the differences between macro- and microscale flow on flow patterns and flow instabilities. Lee and Mudawar [49]considered microchannel flow behaviour when high vapour qualities occur at a given diameter at low mass fluxes and low subcooling temperature.

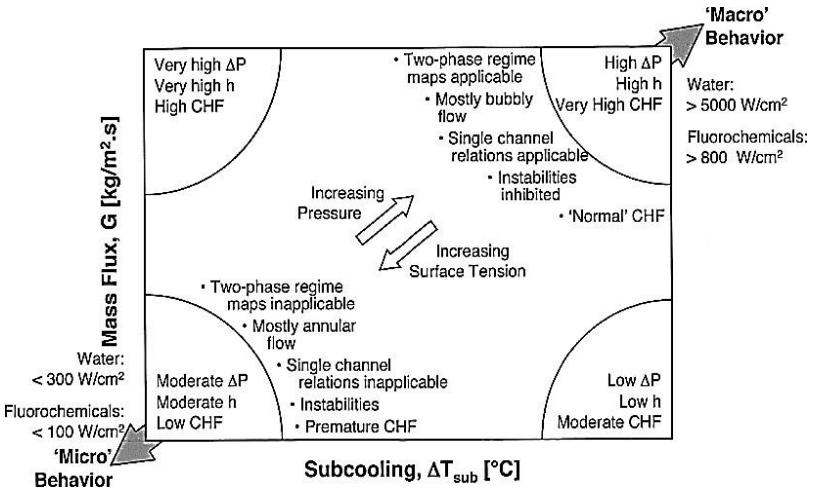

Figure 2. 3 *Overall performance trends of small diameter (50 µm < D_h < 1000 µm) two-phase microchannel heat sinks, produced by Lee and Mudawar [49].*

Despite the extensive experimental studies in the field of two-phase flow boiling in microchannels, there is still disagreement regarding the dominant heat transfer mechanism (nucleate boiling, convective boiling and thin film evaporation). A summary of the outcomes of a number of different studies on the heat transfer mechanisms is provided by Ong and Thome [31]. Different research groups support different heat transfer mechanisms, which are eventually divided between four group categories: (i) nucleate boiling, (ii) convective boiling, (iii) nucleate and convective boiling and (iv) thin film evaporation.

The most reported trend in mini- / microchannels is that of the two-phase heat transfer coefficient increasing with heat flux up to a point, as reviewed by Tiribica and Ribatski [37] and Thome [13]. Beyond this point, the two-phase heat transfer coefficient declines as the vapour quality increases to such a level (x_e > 0.9), that partial dryout of the wall can occur [17]. Cheng *et* al. [36] found that the local boiling heat transfer coefficient in microchannels peaks at low

vapour quality ($0 < x_e < 0.2$) and then decreases due to partial dryout of the wall. Agostini *et* al. [50] investigated the influence of heat flux, mass flux and vapour quality on the heat transfer coefficient during two-phase flow boiling in silicon microchannels of D_h = 336 µm using R245a (N = 67, W_{ch} = 223 µm, H_{ch} = 680 µm, α = 0.33). Figures 2.4a and b show the heat transfer coefficient as function of vapour quality for heat fluxes from 3.6 to 189 W cm^{-2} at constant mass fluxes.

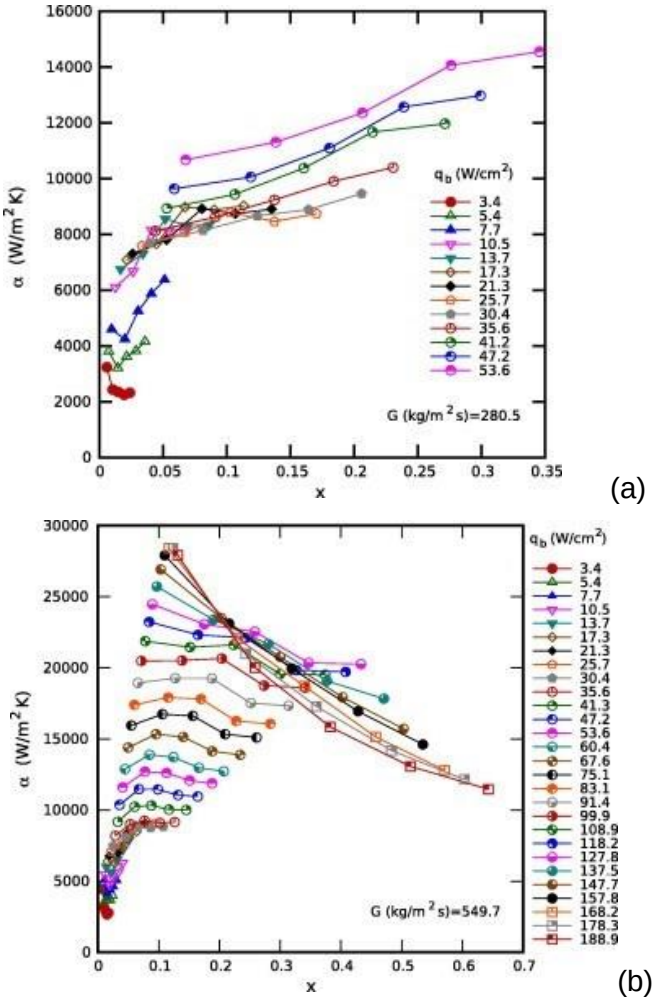

Figure 2. 4 *(a) Local flow boiling heat transfer coefficient versus local vapour quality for increasing base heat fluxes for G = 280.5 kg m^{-2}s^{-1} and (b) local flow boiling heat transfer coefficient versus local vapour quality for increasing base heat fluxes for G = 549.7 kg m^{-2}s^{-1}[50].*

Figure 2.4a shows the increasing trend of the heat transfer coefficient with vapour quality for the mass flux (G) of 280.5 kg m^{-2}s^{-1}. Figure 2.4b presents the heat transfer coefficient as a function of the vapour quality at higher G = 549.7 kg m^{-2}s^{-1}. The heat transfer coefficient appears

to decrease with increasing vapour quality for G = 549.7 kg m^{-2}s^{-1}. Figure 2.5 shows the flow boiling heat transfer coefficient versus wall heat flux at low vapour quality for mass fluxes from 275 kg m^{-2}s^{-1} to 1,503 kg m^{-2}s^{-1}. Heat transfer coefficient appears to increase with increasing heat fluxes greater than 100 W cm^{-2}.

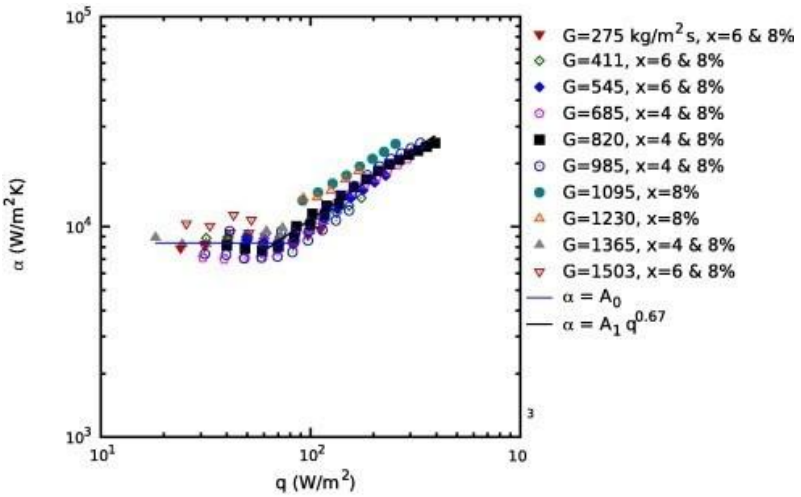

Figure 2. 5 *Flow boiling heat transfer coefficient versus channel wall heat flux at low vapour quality with R245fa [50].*

2.4.1 Effect of flow pattern on flow boiling two-phase heat transfer

Ong and Thome [46] presented two dependences of HTC with mass flux: (i) HTC is almost independent of vapour quality and (ii) for vapour qualities higher than certain values the heat transfer coefficient increases linearly with increasing vapour quality. They also found that the effect of heat flux on the heat transfer coefficient was gradually suppressed by decreasing diameter of the channels using R245fa for a D = 1.03 mm channel with Co = 0.99 and a D = 2.20 mm channel with Co = 0.46.

The flow patterns usually observed in small diameter channels are churn, slug, elongated bubbles, plug, slug-annular and annular flow. Vapour phase takes the form of nucleating bubbles, dispersed bubbles, elongated bubbles and an annular core. Liquid phase exist as bulk liquid, slugs, thin film on the heated wall, or dispersed droplets. Figure 2.6 shows schematics of flow regimes, and variation of heat transfer coefficient in mini-/ microchannels with uniform circumferential heat flux for (a) nucleate boiling dominant heat transfer and (b) convective boiling dominant heat transfer [51]. In Figure 2.6a, the heat transfer coefficient decreases monotonically along the channel due to gradual suppression of nucleate boiling. Nucleate boiling is the main flow regime and bubbly and slug flow regimes occupy a significant fraction of the channel length.

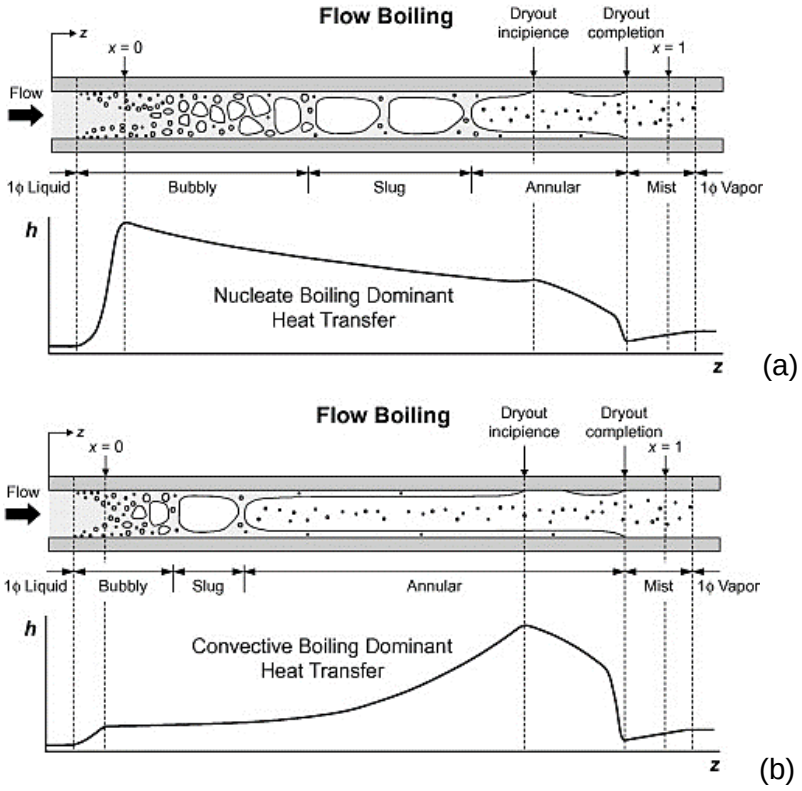

Figure 2. 6 *Schematics of flow regimes, with local variation of heat transfer coefficient in mini/microchannels with uniform circumferential heat flux for (a) nucleate boiling dominant heat transfer and (b) convective boiling dominant heat transfer [51].*

In contrast, Figure 2.6b depicts the convective boiling dominant heat transfer regime, where annular flow mainly established in the channel, and the heat transfer coefficient increases along the channel due to gradual thinning of the annular liquid film. For both heat transfer regimes, the heat transfer coefficient begins to decrease appreciably where dry patches begin to form at the location of dryout incipience (*i.e.*, onset of dryout, or partial dryout). Complete dryout or CHF, eventually occurs at a location further downstream, where the liquid films fully evaporated.

Ong and Thome [46] studied flow boiling heat transfer and CHF for R134A, R236fa and R245fa in single horizontal channels of 1.03, 2.20 and 3.04 mm diameters. They showed that the flow pattern influence on the heat transfer coefficient is significant. From flow visualisations, it was observed that flow pattern transitions occurred earlier at higher mass fluxes and lower vapour qualities. This occurred because of the suppression of isolated bubbles and coalescence bubbles flow regimes and the expansion of annular flow. Annular flow pattern was associated with the heat transfer coefficient-increasing trend with vapour quality and the early domination of forced convection mechanism in the channel and mostly observed for low heat

fluxes. However, the magnitude of the heat transfer coefficient increased sharply when the transition from coalescing bubbles to annular flow is complete. This again indicates a significant flow pattern influence on the heat transfer coefficients and the same trend was observed for all the fluids and channels tested.

2.4.2 Effect of bubble confinement on flow boiling two-phase heat transfer

Two-phase flow boiling heat transfer in microchannels linked to the liquid-vapour phase distribution on the channel base [52]. The increase of the heat transfer coefficient at low vapour qualities in microchannels attributed to confinement effects [32], [46].Confined bubble growth that occurs in microchannels can alter the heat transfer behaviour. The bubble growth in a microchannel has been recently studied numerically by Gedupudi *et* al. [53] and Zu *et* al [54]. The forces acting on an evaporating interface under flow boiling conditions in a microchannel are analysed by Kandlikar [38] and shown in Figure 2.7. Figure 2.7a presents the evaporation momentum force acting on the evaporating interface of a growing bubble during pool boiling and Figure 2.7b the forces due to evaporation momentum and surface tension acting on a liquid-vapour interface of a bubble filling the microchannel cross-section. The net force due to the evaporation momentum change acts in the direction opposite to the flow. At lower heat fluxes, the surface tension and inertial forces are large enough to prevent a reverse flow. However, at higher heat fluxes, the evaporation momentum forces overcomes the two opposing forces and causes reverse flow. The surface tension and evaporation momentum forces are dominant in small-diameter channels operating under high heat flux conditions. Most of the thin film evaporation occurs at the tip of the confined bubble [2].

Geisler and Bar-Cohen [55] found that confinement effects during bubble growth in channels lead to the enhancement of two-phase heat transfer at the low heat flux region of the nucleate boiling curve under the heat transfer mechanism of thin film evaporation around elongated bubbles. Blomquist *et* al. [56] performed simulations of a growing bubble in a microchannel and found that the wall heat transfer improved with an increase in wall superheat and bubble growth rates. They confirmed the existence of an entrapped thermal boundary layer located under the bubble. They found that for bubbles with low contact angles the entrapped thermal boundary layer located under the bubble upstream meniscus moves upward resulting in deformation of the upstream liquid-vapour interface. Mukherjee *et* al. [57] numerically simulated the bubbles during flow boiling in microchannels. They found that the bubble with the lowest contact angle resulted in the highest heat transfer.

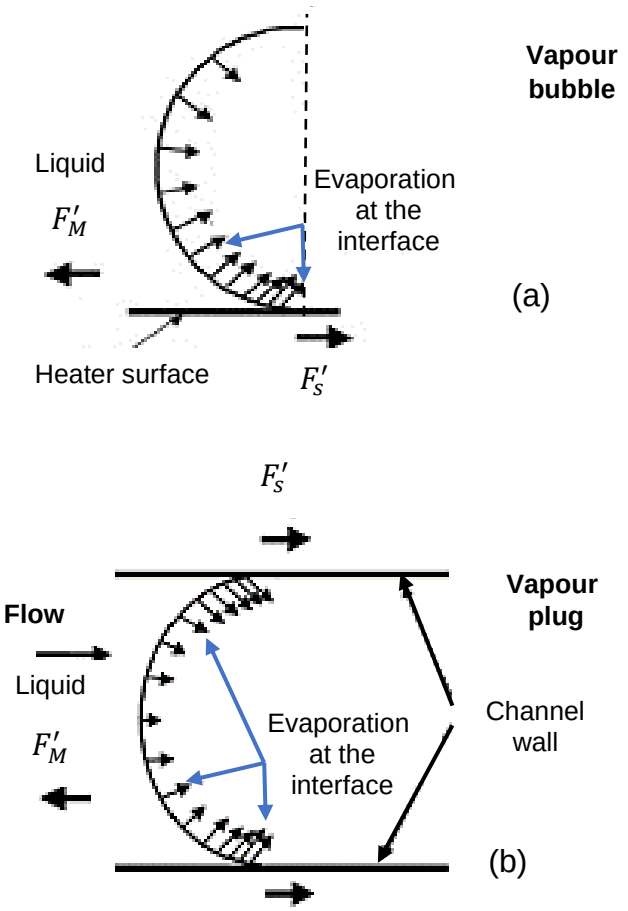

Figure 2. 7 *(a) Evaporation momentum force acting on the evaporating interface of a growing bubble and (b) forces due to evaporation momentum and surface tension acting on a liquid-vapour interface of a bubble filling the microchannel cross-section [38].*

2.4.3 Effect of channel shape, hydraulic diameter and cross-sectional area on flow boiling two-phase heat transfer

The understanding of the effects of the channel cross sectional characteristics on pressure drop and heat transfer coefficients during two-phase flow boiling conditions is required in order to provide guidelines for the design of future high performance microchannel heat sinks. A variety of parameters have been investigates, such as the channel geometry, working liquid, saturation pressure and applied heat flux. The trends two-phase heat transfer coefficients and pressure drop are still controversial for mini and microchannels. The disagreement amongst experimental studies is due to effects including axial heat conduction within the tube wall, heat losses and entrance effects not taken into account [37]. Because of these controversies there are no clear conclusions concerning the effects of channel cross sectional dimensions and particularly aspect ratio on boiling regimes in rectangular microchannels [58], [59]. For

rectangular microchannel cross-sections, the cross-sectional characteristics refer to the channel geometry, size and aspect ratio.

One of the parameters that significantly affects pressure drop and heat transfer during flow boiling in microchannels is the channel hydraulic diameter. There has been extensive investigation with different channel diameters from many authors [23], [33], [44], [60], [61]. Decreasing the microchannel hydraulic diameters results in higher heat transfer coefficient but higher-pressure drop values.

The shape and dimensions of the microchannel cross section are very important as well for the enhancement of the heat transfer performance during flow boiling since the channels are directly related to the vapour-liquid interface interactions, the heat transfer surface and bubble growth. The geometry of the channel cross-section has been reported that strongly affects the flow boiling patterns and heat transfer characteristics. Circular microtubes were of interest for simulations more than rectangular cross section channels or channel shapes because they have to take into account the corner effects. Therefore, there is an important research gap in slug formation during flow boiling in non-circular microchannels and specifically high aspect ratio channels [62].

Figure 2.8 shows the effect of channel shape (square, rectangular, triangle and circle), as well as the effect of the channel orientation (horizontal, vertical) on the mean heat transfer coefficient. The heat transfer coefficients are presented as a function of length at a constant mass flux of 500 kg $m^{-2}s^{-1}$ using R134a refrigerant. According to Lee *et* al. [63] the channel shape affects the evolving flow patterns due to convective flow boiling that takes place in microchannels. They used a nearly rectangular microchannel with a high aspect ratio of 8.57 and D_h = 24 μm. The height of the microchannels was 14 μm and the width, 120 μm. They compared their results for the nearly rectangular shallow cross section microchannels to similar work by Jiang *et* al. [20] for triangular cross section microchannels of D_h = 26 μm using deionised water. The comparison was carried out based on the force balance across the vapour–liquid interface. Annular flow regime in nearly shallow rectangular microchannels was found to be less stable as compared to triangular microchannels. According to the authors, the stable flow in triangular microchannels was related to the development of a size and shape dependent restoring force, which was damping out the forming perturbations. In contrast, for shallow rectangular microchannels within the annular flow pattern regime the restoring force could not develop thus resulting in the merging of two liquid films on either side of a vapour core. They reported that both the merging of the liquid films and disconnecting of the vapour core can be identified as the mechanisms responsible for the: (i) bubble departure, (ii) instability of annular

flow and (iii) development of intermittent flow downstream of the transition region in shallow rectangular microchannels.

Tran *et* al. [64] and Yen *et* al. [65] examined flow boiling heat transfer in minichannels with different cross sectional geometries. Tran *et* al. [64] compared boiling experiments of a small circular channel of D = 2.46 mm with a small rectangular channel of D_h= 2.40 mm with refrigerant R12. Yen *et* al. [66] compared a circular microtube of D = 210 μm inner diameter with a square Pyrex glass microchannel of D_h = 214 μm. The results from both studies showed that heat transfer increased in square channels as compared with the circular ones because the corners of square channels served as nucleation sites.

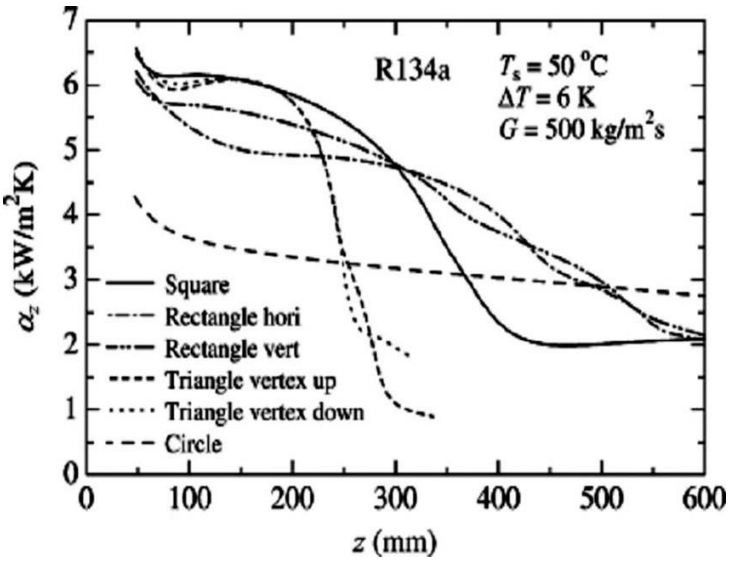

Figure 2. 8 *Variation in mean heat transfer coefficients along microchannels of different shapes [67] .*

The effects of microchannel dimensions on mass flux, the flow patterns and heat transfer characteristics have been summarised in the review of Harrirchian and Garimella [11]. Lin *et* al. [68] and Saitoh *et* al. [60] studied the effect of mass flux and channel diameter on flow boiling heat transfer coefficients of small diameter channels. Saitoh *et* al. [60] experimentally investigated the boiling heat transfer of R-134a flow in three horizontal tubes of diameter 0.51, 1.12, and 3.1 mm and mass fluxes ranging from 150 to 450 kg $m^{-2}s^{-1}$. The local heat transfer coefficient increased with increasing mass flux in larger tubes but was not significantly affected by mass flux in smaller tubes. The heat transfer coefficient increased with increasing heat flux in all three tubes. They found that the contribution of forced convective evaporation to the boiling heat transfer decreased with decreasing tube diameter. Lin *et* al. [68] showed that the transition from nucleate to convective boiling at high heat fluxes occurred at higher qualities in

the smaller diameter tubes. In the absence of dryout in the saturation-boiling region, they found that the mean heat transfer coefficient varied only slightly with the tube diameter and was mainly a function of heat flux. Lee and Mudawar [63] studied the effects of hydraulic diameter, mass velocity and subcooling on boiling flow patterns with HFE-7100. Zhang *et* al. [22] investigated the effects of hydraulic diameter of microchannels in the range of 27-171 μm and surface roughness on two-phase flow patterns using deionised water. They studied bubble nucleation, flow patterns and transient pressure fluctuations. They showed that in channels with D_h smaller than 50 μm, the bubble nucleation mechanism was eruption boiling and mist flow, which was developed almost right after single-phase flow because of the large amount of wall superheat. The boiling mechanism was determined by the wall surface conditions rather than the channel dimensions. Betch *et* al. [69] and Chen and Garimella [70] studied the effect of mass flux on boiling in microchannels using FC-77. Harrirchian and Garimella [44], [71] studied the effect of channel size, mass flux and heat flux on flow boiling heat transfer coefficients but only for rectangular microchannel heat sinks of $D_h \geq 100$ μm. In their first study [44] they tested seven different test pieces made from silicon and consisting of parallel microchannels of a constant nominal height of 400 μm and changing widths ranging from 100 to 5,850 μm (α = 0.25 to 14.63 and D_h from 160 to 749 μm). They performed experiments for mass fluxes ranging from 250 to 1,600 kg $m^{-2}s^{-1}$. They measured local temperatures and heat transfer coefficients using an array of temperature sensors located under the substrate. They showed that for microchannels of W_{ch}= 400 μm and greater than this width, the heat transfer coefficients corresponding to a fixed wall heat flux were independent of channel size. In addition, the heat transfer coefficients and boiling curves were independent of mass flux in the nucleate boiling region for a fixed channel size, but were affected by mass flux as convective boiling dominated. They indicated that for a fixed value of the wall heat flux, pressure drop increased with decreasing channel width. A later study by Harrirchian and Garimella [71] suggested that channel dimension was not individually a determining factor on the heat transfer characteristics in microchannels but the channel cross sectional area plays a more determining role. The authors came to these conclusions after studying the effect of channel dimensions for flow boiling of FC-77 in microchannels with W_{ch} ranging from 100 to 1,000 μm and H_{ch} from 100 to 250 μm with various channel numbers from 2 to 61. For the microchannels with a cross-sectional area of 0.089 mm^2 (D_h = 291 μm, W_{ch}= 250 μm, H_{ch} = 400 μm, N = 35, α = 0.625) and larger, the heat transfer coefficient was found to be independent of the microchannel size. Figure 2.9 shows the effects of microchannel width on boiling (a) heat transfer coefficient of FC-72 and (b) pressure drop versus wall heat flux at G = 700 kg m^{-2} s^{-1} [22]. For microchannels smaller cross-sectional areas where bubble

confinement was visually observed, the heat transfer coefficient behaviour was higher at the lower heat fluxes.

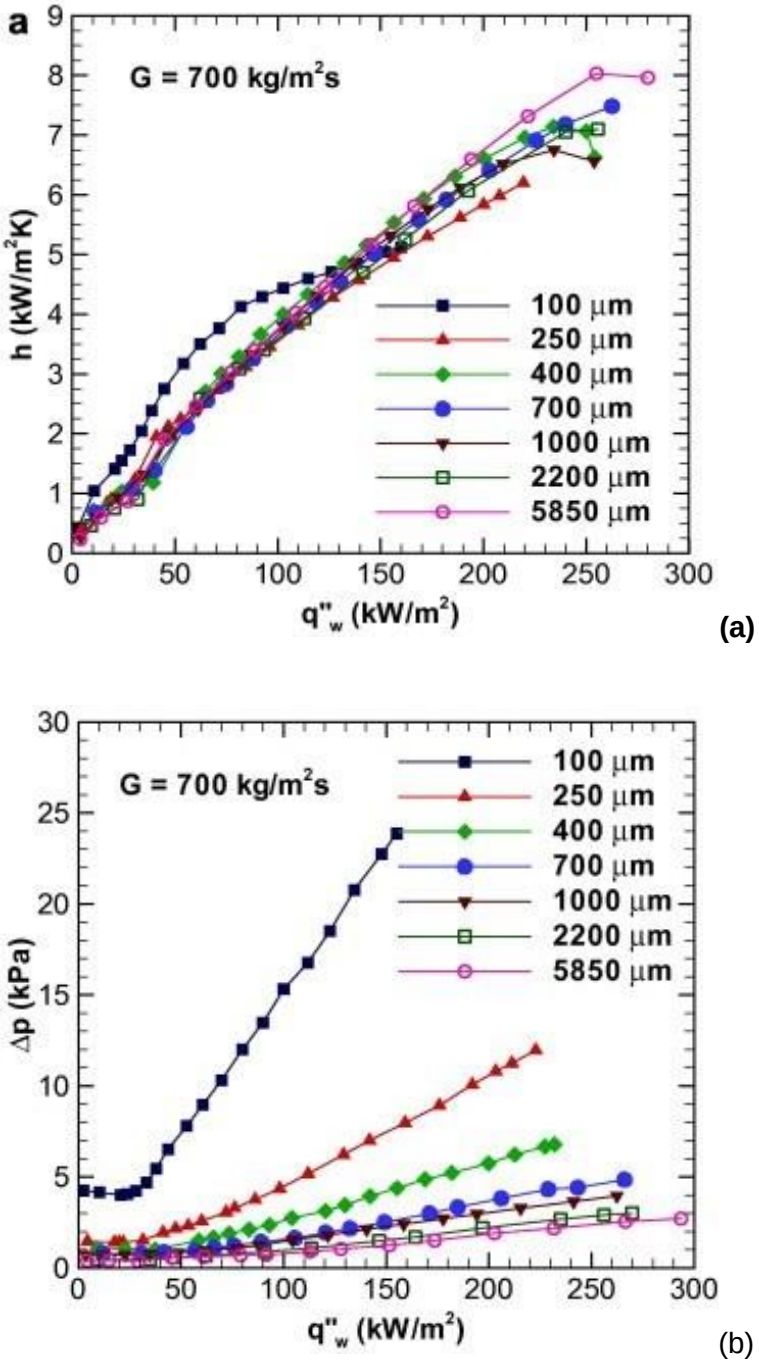

Figure 2. 9 *Effect of microchannel width on boiling (a) heat transfer coefficient of FC-72 and (b) pressure drop versus wall heat flux at $G = 700$ kg m $^{-2}$ s^{-1} [22].*

By increasing the heat flux, the curves crossed over, resulting in lower values of heat transfer coefficient. The largest heat transfer coefficient was measured for the 100 × 220 µm

microchannels (h = 5 kW m^{-2} K^{-1} at q = 160 kW m^{-2} and G = 630 kg m^{-2}s^{-1}), with a cross sectional area of 0.021 mm^2, before the occurrence of partial dryout. For the 100 × 100 μm microchannels, the heat transfer coefficient was relatively lower at low heat fluxes compared to the other tested channel sizes since partial dryout occurred even at very low heat fluxes. The larger values of the heat transfer coefficients in the smaller microchannels were attributed to the confinement effects caused by bubbles occupying the entire cross-section of the microchannels due to the small cross-sectional area relative to the bubble diameter at departure. Flow visualisations revealed that in all of the microchannels with a cross sectional area smaller than 0.089 mm^2, slug flow commenced soon after the onset of boiling and flow entered the churn–annular flow regime at relatively low heat fluxes [20], [22]. As a result, bubble nucleation at the walls was not the only heat transfer mechanism, and the evaporation of the thin liquid film at the walls in the slug and annular flows contributed to the heat transfer. Therefore, the value of heat transfer coefficient was higher for these smaller microchannels at lower heat fluxes. The early establishment of annular flow in microchannels of very small diameter was reported in other studies. At high heat fluxes for small channel diameter, a decrease in heat transfer coefficient was detected, which occurred due to an early partial dryout at the wall. In microchannels with larger cross-sectional areas, nucleate boiling was the dominant flow regime, and hence, the heat transfer coefficient was independent of channel size. It is important to mention that these trends of the heat transfer coefficient has also been reported in a confined pool boiling study on plate spacing in parallel-plate configurations, performed by Geisler and Bar-Cohen [55]. By reducing the plate spacing below the bubble departure diameter, the heat transfer enhanced in the low heat flux region due to confinement effects. As the spacing decreased further, the heat transfer coefficient increased until it reached a maximum, after which it deteriorated with decreasing channel spacing.

Dupont and Thome [72] studied the transition from macro- to microchannel evaporation using a three-zone flow boiling model based on evaporation of elongated bubbles in microchannels presented in Figure 2.10. The model predicted an increase in heat transfer coefficient with a decrease in diameter of the channel, for low values of vapour quality and a decrease in heat transfer coefficient for large vapour qualities.

Figure 2.11 shows the cyclic variation in boiling heat transfer coefficient with time as calculated by Revellin and Thome [73] for a channel with D_h. = 1.95 mm at $G = 446$ kg m^{-2}s^{-1} and q = 67 kW m^{-2} at x_e = 0.05 using R11. The increase occurred at the beginning of the elongated bubble before liquid film dryout occurred. The heat transfer coefficient reached the maximum value of 2.5 × 10^5 W m^{-2}K^{-1} at the position where the liquid film was minimum before the dry zone. Man *et* al. [61] has studied the effect of microchannel height on nucleation-site

activity and bubble dynamics using water, methanol, and ethanol. The heat sink consisted of 10 parallel microchannels fabricated in a silicon wafer, with a width ranging from 150 to 9,000 μm and height ranging from 5 μm to 500 μm. They found that the bubble nucleation activity was dependent on channel height for all fluids tested.

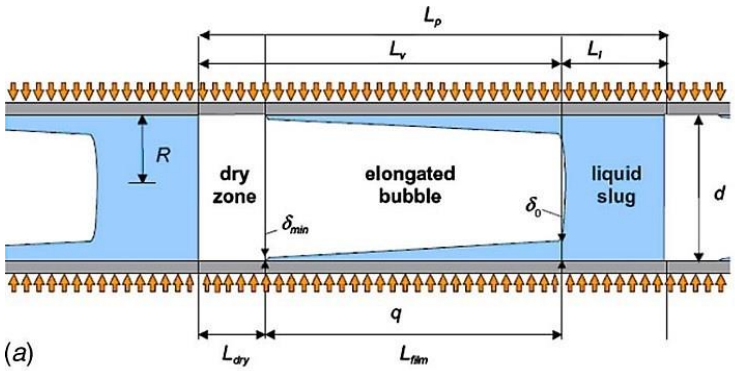

Figure 2. 10 Three-zone model for elongated bubble flow, from the study of Revellin and Thome [73].

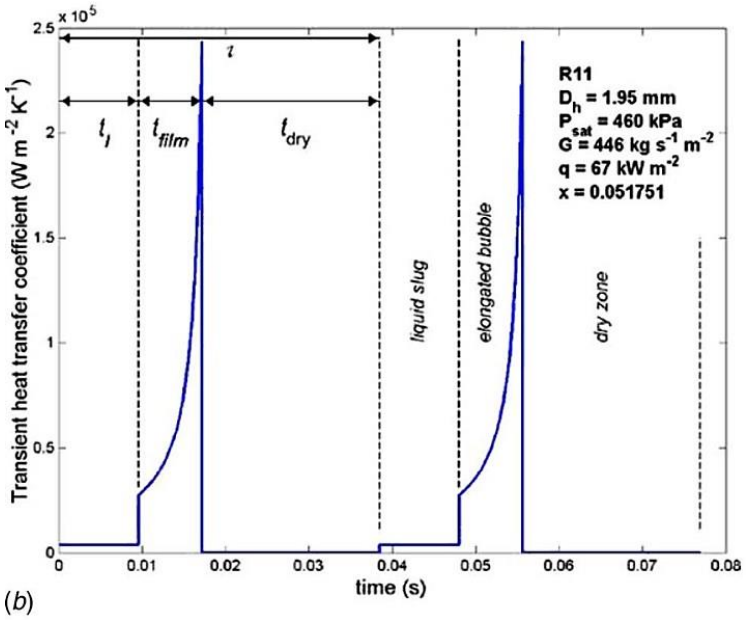

Figure 2. 11 *Cyclic variation in boiling heat transfer coefficient from the study of Revellin and Thome [73].*

2.4.4 Effect of cross-sectional aspect ratio on flow boiling two-phase heat transfer

Another important parameter that can affect flow boiling heat transfer and pressure drop

and is not extensively investigated for parallel microchannel configurations is the aspect ratio. High aspect ratio microchannels ($\alpha = W_{ch} / H_{ch}$) are considered shallow and wide for $\alpha > 1$. A channel with this geometry can provide many advantages for the cooling of small-scale devices. High aspect ratio microchannels ae expected to have good heat transfer characteristics [74]. Firstly, their large surface-to cross-sectional area ratio can reduce the working liquid consumption while providing a large cooling area. Secondly, the high aspect ratio channels can potentially reduce vapour side pressure drop and increase vapour side heat transfer as reported by Morkrani *et* al. [75]. Thome [13] reported that using microchannel heat sinks with microchannels with 10 times the wetted perimeter relative to that of their footprint could increase CHF. Despite their potential, there are only a few studies in the literature that study the flow boiling in high aspect ratio microchannels.

Soupremanien *et* al. [76] investigated the effect of aspect ratio change at constant hydraulic diameter minichannels and concluded that aspect ratio plays a substantial role in flow boiling in single rectangular minichannels. The effect of α on two-phase flow heat transfer in microchannels is strong, especially on pressure drop [77] due to the increase of friction factor that increases with α as the width of the channel increases. Surface tension appears to be an important factor. In addition, the period character of flow boiling adds extra complexity as the channels usually interact with each other in parallel channel configurations. There are only a few studies that have investigated the effect of aspect ratio on flow boiling heat transfer coefficients, pressure drop and flow regimes in microchannel heat sinks. Singh *et* al. [78] firstly investigated the effect of α on two-phase flow in microchannels. They studied the effect of aspect ratio on pressure drop during flow boiling of water in silicon microchannel heat sinks of 142 µm constant hydraulic diameter of and length of 20 mm. Seven microchannels with constant hydraulic diameter but different aspect ratios that ranged from 1.23 to 3.75 were tested for three constant heat fluxes in the range of 29.0 to 36.6 W cm^{-2} and mass fluxes from 82.4 to 126.2 kg $m^{-2} s^{-1}$. Figure 2.12 shows that for a given mass flow rate and heat flux value, the pressure drop first decreases with an increase in aspect ratio, and then increases with a further increase in aspect ratio. This trend also occurs for increasing heat flux. The minimum pressure drop recorded experimentally, corresponding to α = 1.56 was about 1/6 of that of pressure drop for α = 1.23 and about 1/4 of pressure drop for α = 3.75. The minimum pressure drop was measured experimentally at α = 1.56 for all four cases of heat fluxes and mass flow rates that were investigated. However, they stated that since experimental aspect ratio values are discrete in nature, a pressure drop minimum is observed over a range rather than a single point. The minimum of the pressure drop was explained to occur because of the opposing trends of frictional and acceleration pressure drops with respect to the aspect ratio. Also two-phase pressure drop was found to be lower than that for single-phase flow at constant heat flux and

varying mass flux. The pressure drop minimum was identified but further investigation was required with different fluids and channel geometries.

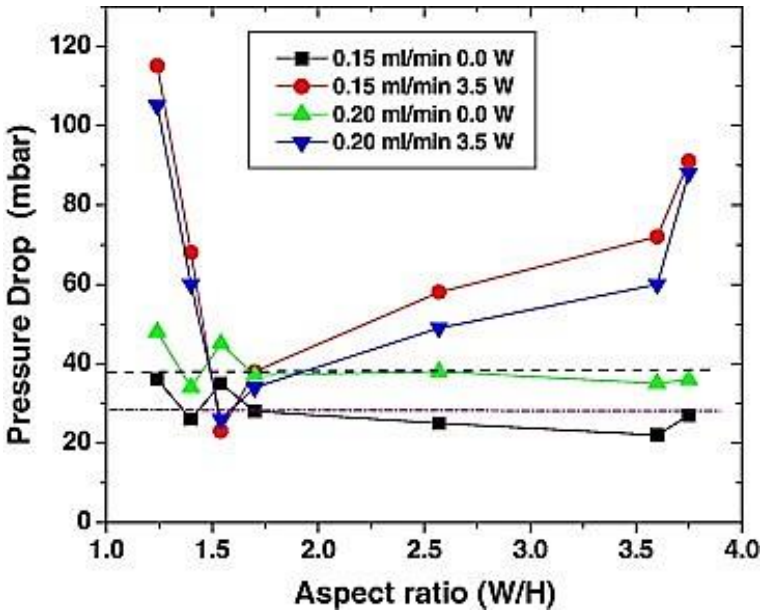

Figure 2. 12 *Experimentally determined pressure drop across the microchannel versus aspect ratio (α), at the power of 3.5 W from the study of Singh et al.* [78]. *The theoretical single-phase pressure drop values are shown by dash-dot and dashed lines for the mass flow rates of 0.15 and 0.20 ml min^{-1} respectively* [78].

The first systematic study of aspect ratio effect on flow boiling heat transfer and pressure drop in parallel multi-microchannel heat sinks was performed by Markal *et* al. [79]. They investigated the effect of aspect ratio on both flow boiling heat transfer and pressure drop. They examined the effect of aspect ratio on flow boiling in rectangular parallel silicon microchannels at a constant hydraulic diameter of 100 μm using deionised water. The six silicon microchannel heat sinks consisted of 29 silicon parallel rectangular microchannels with aspect ratio values of 0.37, 0.82, 1.22, 2.71, 3.54 and 5.00. They heated up the test section by using four cartridge heaters and they used thermocouples embedded in the copper block under microchannel base for local wall temperature measurements. Flow boiling experiments were conducted for mass fluxes of 151, 195, 238, 281 and 324 kg m^{-2}s^{-1}and for the heat fluxes of 71–131 kW m^{-2}. The inlet temperature of deionized water was kept constant at 50 ± 1˚ C throughout the tests. Flow visualisations were obtained with temperature and pressure measurements. The effect of mass flux was studied too. The heat transfer coefficient was obtained only at the location of the ninth thermocouple, 41.5 mm from the channel inlet. The calculated heat transfer coefficient increased with increasing aspect ratio up to the value of α = 3.54 and then decreased with further increase

of the aspect ratio. The microchannels with α = 1.22 achieved the maximum heat transfer coefficient performance and thee lowest pressure drop values between 100 and 200 mbar. No regular relationship was identified between the aspect ratio and the total pressure drop. The total pressure drop appeared to have similar trends for all the heat fluxes. It attained minima with decreasing mass flux for a constant heat flux and then increased again with increasing mass flux. For a constant value of the mass flux, the pressure drop increased with an increase in the heat flux. From flow visualisation, quasi-periodic rewetting and drying phenomena were observed as well as rapid bubble growth and elongation towards both upstream and downstream of the channels, reverse flow and strong interactions between neighbouring microchannels.

2.5 Design parameters for plate-fin heat sink configuration

Plate-fin heat sinks consist of microchannels, parallel to each other that have the same shape and size. This configuration is very efficient for heat transfer because it provides high surface to volume ratio. The thermal efficiency of the heat sink during single-phase and two-phase flow boiling conditions depends on the uniformity of the flow distribution between the parallel channels. Flow uniformity in branched channels is strongly affected by the shape of the device that affects the residence time distribution [80]. Non-uniform distribution between the channels can lead to individual blockage and hotspots that can lead to irreversible damage of the microchannel heat sink. The shape of the inlet /outlet manifold, the position and the size of the inlet / outlet holes are among the main parameters that can affect the pressure drop of the heat sink. An optimal design of the microchannels heat sink will provide equal distribution of the fluid into each channel for high thermal performance.

The development of the optimal design requires first simulation using CFD-based optimisation approaches. These simulations use simplified models in order to reduce the computational time. Generally, the three approaches used to design microchannel configurations in order to ensure even distribution between the channels are analytical, computational fluid dynamics (CFD) modelling and experimental. Tonomura *et* al. [80] simulated an approximate design with a new microdevice that equalises the flow pattern around the inlet of each branched channel and creates uniform flow distribution within the channels. Bogojevic [34] used an approximate model based on the one developed by Amador *et* al. [77], in order to design the inlet distributor and the outlet collector of a silicon parallel microchannels heat sink. The results obtained by the aforementioned model were compared with the results of 3D simulations with a CFD-based optimisation method proposed by Tonomura *et* al. [73]. Bogojevic [34] performed simulations to obtain velocity and pressure field in microchannel heat sinks. The influence of the manifold shape and the position of manifold holes was studied for different inlet flow rates.

In addition, experiments for single and two-phase flow boiling conditions were carried out in order to validate the temperature uniformity of the microchannels. Based on the approximate model developed by Bogojevic [34], a consecutive Z-type structure with non-constant, linear cross section manifolds achieved uniform flow distribution between the channels, as shown in Figure 2.13. Figure 2.13 presents simulation results and the respective microchannel configurations as obtained from the study of Bogojevic [34]. The graph presents the normalised flow rate between 40 parallel channels for the non-constant (a) and constant (b) linear cross section manifolds. The plot in Figure 2.13 shows that non–linear cross section yielded a better flow distribution amongst channels. The flow rate in each channel is worked out by a numerical analysis method presented in the study of Bogojevic [34]. The approximate model design (a) shown in Figure 2.13 was also used for the purposes of this study. The inlet and outlet holes were placed inside the manifolds to enable better flow distribution within channels and to minimize the manifold area. The latter also enabled more devices on one silicon wafer during the microfabrication process.

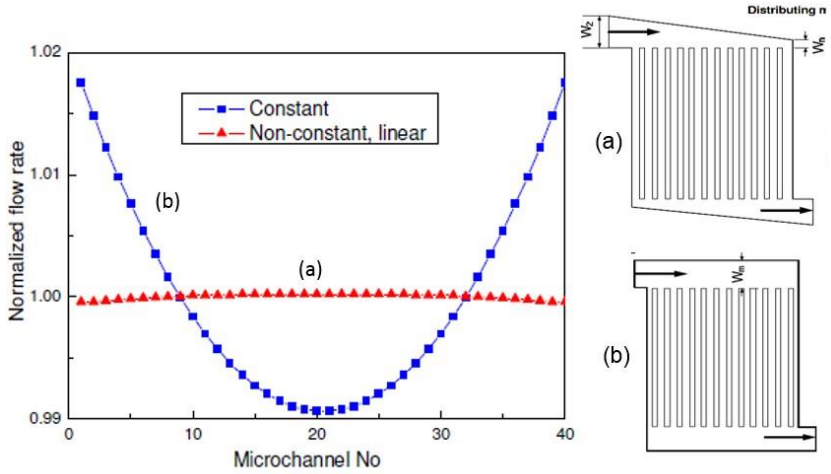

Figure 2. 13 *Flow distributions with 40 parallel rectangular channels for two manifolds structures, with (a) non-constant cross section and (b) with constant linear cross section manifold [34].*

2.6 Two-phase flow patterns in macroscale

The flow patterns shown in Figure 2.1 are defined as follows:

- *Bubbly flow.* The gas bubbles are dispersed in the liquid phase; in horizontal tubes, these bubbles tend to congregate in the upper half of the tube because of the buoyancy force.

At higher mass flow rates, when shear forces are dominant, the bubbles tend to disperse uniformly in the tube.

- *Plug flow*. Here, the small bubbles coalesce to from elongated bubbles separated by the liquid plugs. The elongated bubbles are smaller than the tube. The bubbles tend to move to the upper half of the tube.
- *Slug flow*. In this flow regime, a higher vapour velocity causes an increase in the bubbles diameters, which become similar in size to the channel height.
- *Stratified-wavy flow*. Stratified flow exists at low liquid and vapour velocities, when complete separation between vapour and liquid phase occurs. The liquid flows at the bottom of the tube and the vapour along the top part the tube, separated by undisturbed horizontal interface. At higher vapour velocity, waves are formed on the interface and travel in the direction of flow, giving the stratified-wavy or wavy flow regime.
- *Annular flow*. In this flow regime, the liquid phase flows as a film on the tube wall, and the vapour phase flows in the centre forming vapour core. The liquid film is thicker at the bottom than the top due to the effect of gravity. Usually, there is presence of the liquid droplets in the vapour core.
- *Mist flow*. This flow regime occurs at very high vapour velocities when only continuous vapour phase exists inside the tube.

2.7 Two-phase flow patterns in microscale

Revelin and Thome [81] found that there are three stable flow regimes in microchannels, bubbly flow, slug flow and annular flow, separated by a transition zone of bubbly-slug flow and slug annular flow. The flow is characterised as intermittent when the geometry of the flow has a periodic character. Ong and Thome's [46] flow pattern maps shown in Figure 2.14a show which flow regime is present with increasing vapour quality. The bubbly and slug flow regimes are renamed respectively isolated and coalescing bubble flow. Dispersed flows usually include small bubbles in the liquid or the liquid is detached from the wall and flows as small droplets within the vapour core (mist flow). Figure 2.14b shows results obtained from flow visualisations from the study of Wang *et* al. [74]. The flow patterns show that decreasing the diameter of the channel results in more confined flows. Figure 2.14b shows that during flow boiling of FC-72 in a high aspect ratio rectangular channel with D_h = 1454 μm at G = 22.4 kg m^{-2}s^{-1} and q = 8.13 kW m^{-2}, bubble nucleation occurs at the channel sidewalls and slug-annular flow occurs rapidly in the channel due to channel confinement effect. Liquid droplets are entrained in the fast-moving vapour core and wispy-annular flow with film evaporation is attained.

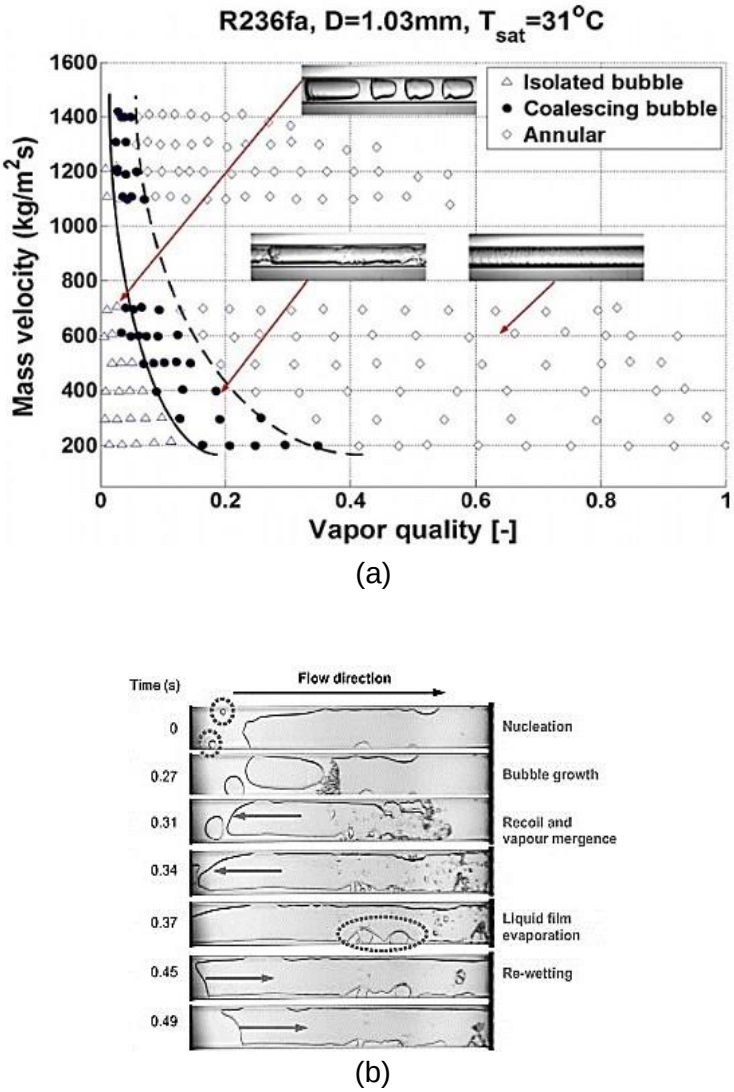

Figure 2. 14 *(a) Flow pattern map by Ong and Thome [46] and (b) flow patterns recorded during FC-72 boiling in a high aspect ratio rectangular channel with D_h = 1454 μm, G = 22.4 kg $m^{-2}s^{-1}$ and q = 8.13 kW m^{-2} from the study of Wang et al.* [74].

2.8 Nucleate boiling

The heat transfer from the channel wall to the liquid was found to be affected by the bubble growth and wall nucleation in microchannels [55, 80]. The nucleation of the bubbles on the heater surface requires a certain amount of wall superheat and presence of cavities on the heated wall. The cavity size that is activated first with increasing wall temperature is called the critical cavity size [83]. Most researchers have proposed the nucleation criteria for the onset of nucleation during flow boiling based on a comparison between the liquid temperatures on the

vapour bubble interface at the top location and the wall and the saturation temperature inside the bubble. For the initial assumptions, some researchers used a bubble contact angle of 53.1° [84], others [85] used a hemispherical bubble shape (90° contact angle), and the rest [80] left the contact angle as a variable. Kandlikar *et* al. [86] performed numerical simulations of the flow over a bubble attached to a channel wall at a given contact angle. The authors noted that for nucleation in the presence of liquid flow, flow stagnation occurred at $y_s = 1.1 \cdot r_b$ with y_s representing the distance of the stagnation location from the heated wall, and r_b the radius of the bubble at nucleation. They modified the bubble nucleation model of Hsu [9] by using the liquid temperature at the stagnation point for the temperature of liquid at the bubble top and derived the following equation for the range of active nucleation cavities:

$$\left(r_{c,min} - r_{c,max}\right) = \frac{\delta_t \sin\vartheta_r}{2.2}\left(\frac{\Delta T_{sat}}{\Delta T_{sat} - \Delta T_{sub}}\right)\left[1 \mp \sqrt{\frac{8.8\sigma(\Delta T_{sat} + \Delta T_{sub})}{\rho_g h_{lg} \delta_i {\Delta T_{sat}}^2}}\right] \tag{2.9}$$

where $r_{c,min}$ and $r_{c,max}$ are the minimum and maximum radius of the nucleating cavities.

The critical cavity radius $r_{c,crit}$ that will nucleate first is given by:

$$r_{c,crit} = \frac{\delta_t \sin\vartheta_r}{2.2}\left(\frac{\Delta T_{sat}}{\Delta T_{sat} - \Delta T_{sub}}\right) \tag{2.10}$$

The corresponding local superheat is:

$$\Delta T_{sat,ONB} = \sqrt{\frac{8.8\sigma T_{sat} q)}{\rho_g h_{lg} k_l}} \tag{2.11}$$

in addition, the local liquid subcooling is obtained by using the single-phase heat transfer equation prior to nucleation, defined as :

$$\Delta T_{sub,ONB} = \frac{q}{h} - \Delta T_{sat,ONB} \tag{2.12}$$

The different heat transfer mechanisms during boiling according to Kandlikar *et* al. [83], are the following: transient conduction (when the bubble departs is then replaced by bulk liquid), micro-convection (when the rapid movement of the bubble interface induces liquid motion, this heat transfer contribution increases as the interface velocity increases) and microlayer evaporation (which results from the evaporation of the thin film layer underneath a bubble).

The contact line at the base of the bubble in nucleate boiling can be divided into nano-, micro- and macro-regions depicted in Figure 2.15a and b, [87]. Figure 2.15b shows the non-evaporating thin-film region (a) where liquid is adsorbed on the heater surface and forms a non-evaporating layer with molecular forces having controlling influence (nano-region). Then (b) is the evaporating thin-film region where maximum evaporation and heat transfer occurs in this region and the liquid is fed from the bulk liquid through the intrinsic meniscus region (micro-region). Then, (c) is the intrinsic meniscus region where fluid mechanics in this region is governed by the conventional equation of capillarity (macro-region). There is a region between the non-evaporating thin film region and the evaporating thin film region over which the film varies in thickness and curvature to accommodate the transition between the two regions. This is called the interline region and is the thinnest portion of the meniscus over which vaporisation can occur. Since at this location he film has a very low thickness, it provides the highest evaporation rate...

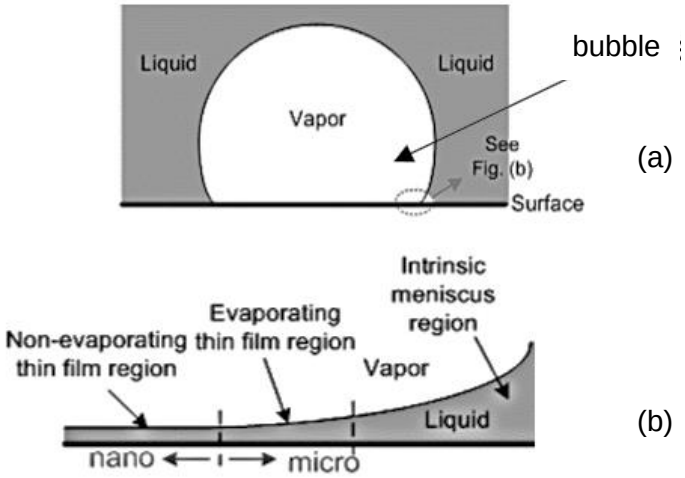

Figure 2. 15 *Schematic of bubble growth at the wall, (a) overall picture at macro-scale (shaded region depicts the area covered by non-evaporating thin film) and (b) zoomed in nano- and micro-scale regions at the three-phase contact line [87].*

Sharp [88] was the first to capture experimentally the liquid microlayer during bubble nucleation on a glass surface. The results showed that the heated surface wall temperature fluctuates, explained by the theory of microlayer, first developed by Snyder and Edward [89] and Moore and Mesler [90]. They explained the existence of a microlayer because of the liquid and surface-wetting action as the liquid adjacent to the heated surface could not be displaced. The thickness of this layer was calculated based on how much heat is removed from the heated surface and was found to approximately from 2 to 2.3 μm.

2.9 Entrainment mass transfer in annular flow regime

Droplet entrainment mass transfer occurs through the mechanisms of roll waves (1), undercutting waves crest by the flowing vapour (2), bursting of bubbles at the interface (3) and impingement of existing droplets of vapour core to the surface of liquid film (4).These mechanisms are illustrated in Figure 2.16.

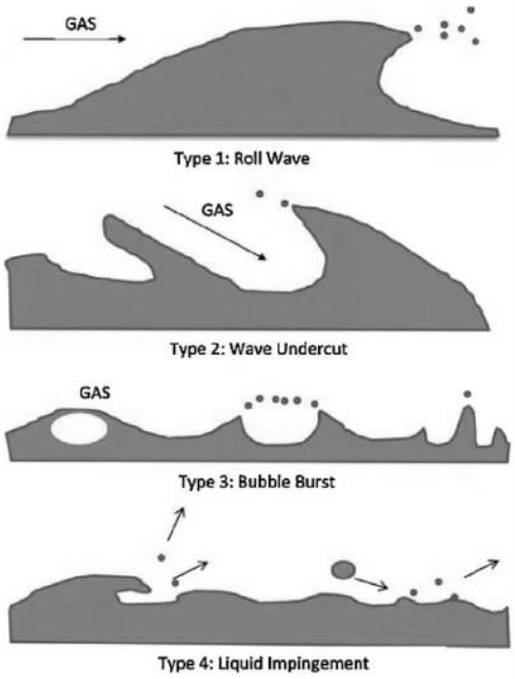

Figure 2. 16 *Different droplet entrainment mechanisms [91].*

Entrainment mass transfer can affect heat transfer and fluid flow behaviour as has been identified through experimental studies using fluids like water and a limited number of refrigerants [92]–[94]. During the bubble burst mechanism, the bubble bursts in the vapour core resulting in droplets that remain in the vapour and consequently evaporate as the vapour film goes back to its initial position. Periodic movement of the liquid-vapour interface is attributed to the bubble nucleation at the channel sidewall, which is wetted by the liquid. As the liquid is drained from the film, it eventually ruptures in several places resulting in entrained fine droplets. According to Ishii and Grolmes [91] much larger drops can be formed on the bursting of bubbles by the motion of the surrounding liquid film filling on the crater left by the bubble. A spike-like filament rises at the centre of the crater, which then disintegrates, into droplets. During the annular flow regime, entrainment mass transfer occurs due to the effects of interfacial waves

formed between liquid film and vapour core. In other words, as the interfacial stress exceeds the retentive force of surface tension, liquid droplets start to transfer into the vapour core in the annular flow regime. It was found that lower values of entrainment result in lower probability of dryout occurrence [95]. Entrainment contribution of mass transfer is similar and in some situations higher order than the evaporation contribution[91].

2.10 Two-phase flow boiling instabilities

Flow boiling instabilities are a critical issue that need to be taken under consideration during the design of microchannel heat sinks. Instabilities can effect dramatically the overall system performance of the microchannel heat sinks. Particularly the flow becomes in the system when pressure and temperature oscillate with large amplitudes. These amplitudes can be as high as 36 K for the wall temperature, as found by Wang *et* al.[96] and 992.4 kg $m^{-2}s^{-1}$ and 60 Pa for mass flux and pressure drop, respectively found by Fu *et* al. [97]. Wang *et* al. [96] and Bogojevic *et* al. [98] classified these instabilities into stable and unstable regimes, depending on the heat to mass flux ratio. Two types of unstable oscillations were reported, one with long-period oscillations and another with short-period oscillations in temperature and pressure. According to Bogojevic *et* al. [98] the stable flow regime for the multi-microchannels exists for q/G < 2.62 kJ/kg for T_{inlet} = 25°C and q/G < 0.99 kJ/kg for T_{inlet} = 71 °C including single-phase flow and incipient flow boiling. Incipient flow boiling exists when isolated bubbles grow inside microchannels which are then flushed downstream by the bulk flow. The pressure fluctuations are considered very low amplitude for the stable flow. This implies that the flow stability depends on the q/G ratio as well as inlet subcooling condition. Asymmetrical flow distribution within microchannels during flow boiling under constant heat flux might lead to the occurrence of LAHF instabilities at higher value of mass flux than is the case with uniform flow distribution within microchannels under the same heat flux. There are several possible reasons for the asymmetrical flow distribution during flow boiling inside the present heat sink with microchannels such as the shape and geometry of the inlet/outlet manifolds, the position of the inlet/outlet holes and uneven depth of the microchannels. Instabilities occur after the incipience of boiling inside the 194 μm hydraulic diameter channels, when increasing heat flux at a constant mass flux or decreasing mass flux with a constant heat flux. HALF instabilities existed for q/G ranging between 2.62 and 3.44 kJ/kg at inlet water temperature of 25 °C and q/G values from 0.99 to 1.55 kJ/kg with an inlet water temperature of 71 °C. Figure 2.17 shows simultaneous temperature and pressure fluctuations for the two types (HALF, LAHF) of instabilities for 40 parallel rectangular silicon microchannels of D_h =192 μm from as produced from the study of Bogojevic *et* al. [34]. Figure 2.17(a) shows HALF (high amplitude low

frequency) instabilities at q = 210 kW $m^{-2}$and Figure 2.17(b) shows LAHF (low amplitude – high frequency) instabilities at q = 376 kW m^{-2} .Mass flux was 208 kg $m^{-2}s^{-1}$ and inlet temperature was 71 °C for both graphs.

During simultaneous pressure and temperature instabilities as shown in Figure 2.17 flow reversals occurred because inlet pressure exceeded outlet pressure and from flow visualisations, alternation between liquid, two-phase and vapour flows occurred. Uncorrelated disturbances developed in individual channels, introduced more modes of oscillation that depend on the transverse stiffness within the manifolds. This resulted in significantly shorter periods of multiphase alternations with increasing heat flux. This, in turn, led to a higher frequency of pressure and temperature oscillations for higher heat fluxes.

Some of the main reasons that cause flow instabilities have been summarised [2] as :

1. Rapid bubble growth and expansion on the upstream and downstream sides of the channels. It was observed that the bubble remains steady with some small axial oscillations. Evaporation of the thin film layer beneath the bubble during the period a dirty patch is formed under the bubbles which results in temperature increases. When the bubble departs, fresh liquid replaces the nucleation site and wall temperature drop again.
2. Accumulation of bubbles at the outlet plenum that cause a large vapour patch which can temporary block the flow and lead to a larger pressure drop as a result of the vapour quality increase.
3. Inlet compressibility effects. High pressure drop due to compressibility and flashing in multi-microchannel heat sinks, or even two-phase choking [99]. Severe flow instabilities and oscillations in multichannel heat sinks can occur at high heat fluxes and induce premature critical heat flux (CHF) [63], [98], [100].
4. Nucleation near the inlet. Kandlikar [15] reports that the location of nucleation affects flow reversal. Bubble nucleation at the inlet causes flow reversal, resulting in unstable flow conditions. In contrast, when the nucleation occurs at the channel exit, no flow reversal occurs [86].

Therefore, it is important to understand the causes of flow instabilities induced by temperature and pressure fluctuations in microchannels. Understanding the reasons for instabilities may assist in heat transfer enhancement.

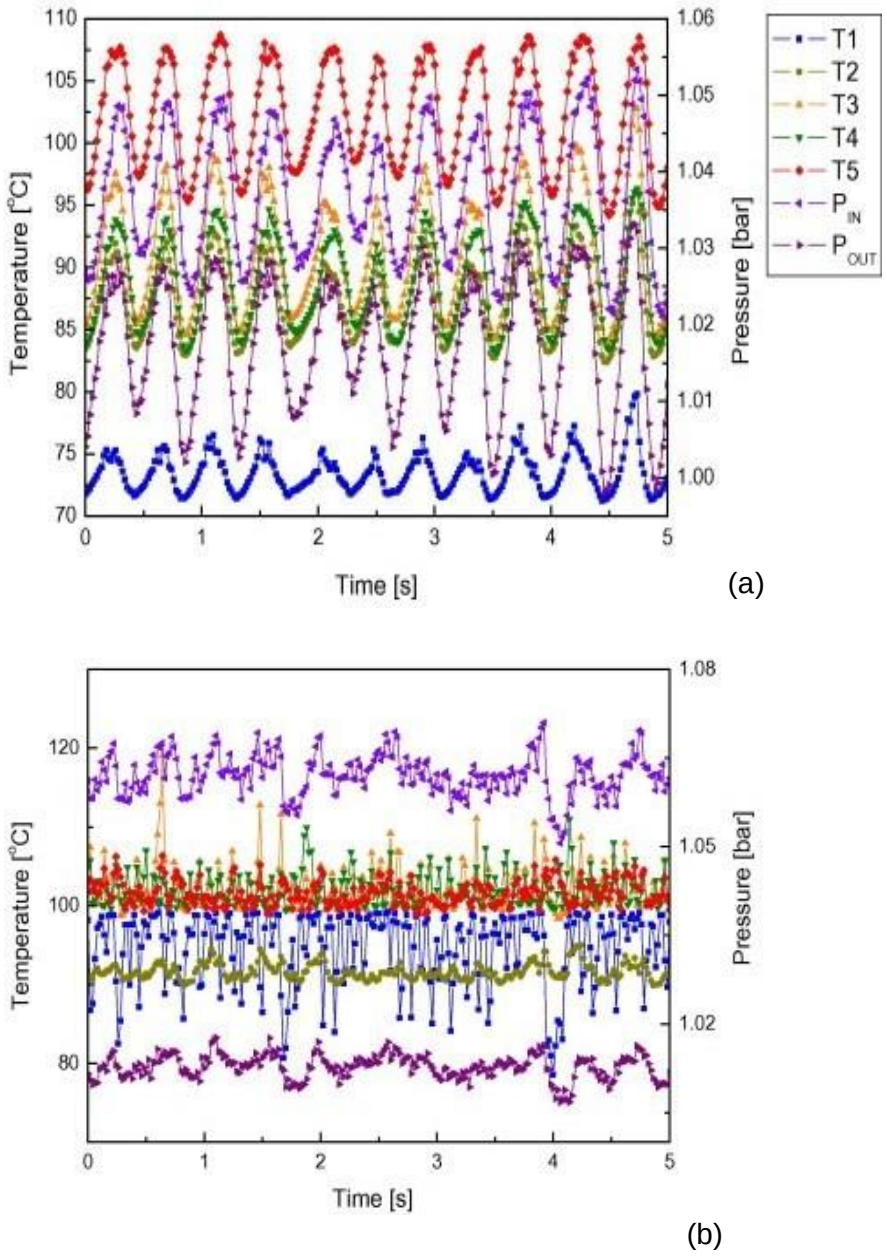

Figure 2. 17 *Simultaneous temperature and pressure fluctuations for two types of instabilities HALF (high amplitude low frequency) and LAHF (low amplitude –high frequency) for the same mass flux of 208 kg $m^{-2}s^{-1}$, at the inlet temperature of 71 °C for the 40 parallel rectangular silicon microchannels of D_h =192 µm from the study of Bogojevic et al. [34] for (a) q = 210 kW $m^{-2}$and (b) q = 376 kW m^{-2}.*

It has been confirmed by many studies that fluctuations of wall temperature at the inlet and outlet pressure occur because of bubble nucleation and growth under confinement. As a result, the local time averaged heat transfer coefficient may be strongly influenced by these fluctuations. Understanding the reasons for instabilities may help find solution to this issue. The effect of instabilities on heat transfer rate is not necessarily significant. In other words, unstable flow may not always give lower heat transfer rates compared to stable flow.

2.11 Critical heat flux (CHF) and dryout

Understanding the triggering conditions of CHF and maximum HTC is important for the design of enhanced heat transfer performance microchannel cooling equipment. CHF was first studied by Bowers and Mudawar [99], who suggested that the small-size (D_h = 2,510 μm, L = 1 cm) of microchannel heat sinks significantly contributes to delaying CHF by conducting heat away from the downstream region (undergoing partial or total dryout) to the boiling region of the channel. They concluded that CHF increased with mass flux for microchannels.

Fu *et* al. [101] experimentally studied convective boiling heat transfer and the critical heat flux (CHF) of ethanol–water mixtures in a diverging microchannel with artificial cavities. The tests were carried out in silicon microchannels with a divergence angle of 1° and 24 laser-drilled cavities (with a uniform spacing of 1 mm) distributed along the bottom wall. The inlet width of the microchannels was 215 μm and the outlet width was 1,085 mm. The average hydraulic diameter was 147 μm. Flow visualisation was performed using a high-speed digital camera. The typical frame rate and exposure time were set at 5,000 fps and 50 μs, respectively. For a mass flux of 175 kg $m^{-2}s^{-1}$ the heat fluxes were in the range of 15.3 - 1,105 kW m^{-2}. The results showed that the boiling heat transfer and the CHF were affected by the molar fraction (x_m) as well as the mass flux. After boiling incipience, the two-phase heat transfer coefficient was much higher than that of single-phase convection. The two-phase heat transfer coefficient reached a maximum in the region of bubbly-elongated slug flow and decreased with a further increase in the wall superheat until it approached a condition of CHF, indicating that the heat transfer was mainly dominated by convective boiling. The thin annular liquid film was responsible for achieving high heat transfer coefficients in this regime [102]. Two other important influences were turbulence and waviness in the liquid film [58].

Wang and Sefiane [33] calculated the local flow boiling heat transfer coefficients for three single high aspect ratio (α = 20, 20 and 10) microchannels (D_h = 571, 762 and 1454 μm) using FC-72 for three different mass fluxes (G = 11.2, 22.4 and 44.8 kg m^{-2} s^{-1}) and heat fluxes ranging from 1 to 18 kW m^{-2}. Figure 2.18 shows the heat transfer coefficient, time averaged as a function of heat flux for three mass fluxes of 11.22, 22.4 and 44.8 kg $m^{-2}s^{-1}$ tested with FC-72 in a high aspect ratio microchannel with round corners and D_h = 550 μm. For all the tested mass fluxes, the time averaged two-phase heat transfer coefficients increased with heat flux to a peak (HTC_{max}) shortly after the onset of boiling and then reduced with further heat flux increase because of partial dryout. HTC_{max} occurred mainly in the bubbly-slug flow regime. The partial dryout was caused by reduced liquid film thickness downstream. CHF was found to increase with mass flux from 12 to 20 kW m^{-2}.

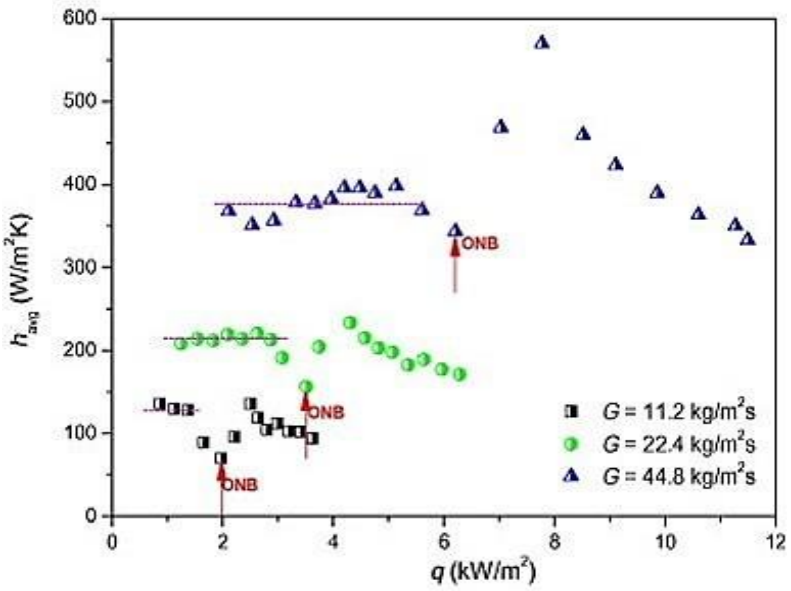

Figure 2. 18 *Heat transfer coefficient, time averaged as a function of heat flux for three mass fluxes of 11.22, 22.4 and 44.8 kg $m^{-2}s^{-1}$ tested with FC-72 in a high aspect ratio microchannel with round corners and D_h = 550 µm [33].*

Chen and Garimella [19] analysed experimental data from heat sinks of 60 silicon parallel microchannels (100 µm in width and 380 µm depth, D_h= 158 µm) using FC-77 fluorinert for high mass fluxes of between 253.7 and 1015.0 kg m^{-2} s^{-1}. They found that the time averaged heat transfer coefficient, which was determined prior to the exit of the microchannels, decreased with heat flux shortly after the onset of nucleate boiling (ONB) because of partial dryout near the channel exit, Figure 2.19. The decreasing trends of the heat transfer coefficient at high vapour qualities were further discussed by Alam *et* al. [10] and Harrirchian and Garimella [11] for a wide range of mass fluxes. Cornwell and Kew [47] reported that the two-phase heat transfer coefficient decreased with heat flux as soon as the entire channel cross-section was occupied by an elongated bubble. They concluded that thin film evaporation around the bubble was the possible controlling mechanism that triggers the CHF. This was also reported by Theofanous *et* al. [100, 101]. Recent work by Borhani and Thome [105] investigated the dryout mechanism of annular flows. They performed high-speed visualisation in rectangular silicon multichannels (D_h = 336 µm , W_{ch} = 223 µm and H_{ch} = 680 µm) and they proposed that the intermittent dryout of the evaporating thin film (referred to as metastable liquid film) is responsible for the contradictory heat transfer coefficient trends observed with changes in vapour quality in the microchannels.

Katto and Ohno [106] correlation is one of the most widely used empirical methods developed for predicting saturated CHF in a single channel. For no liquid subcooling, the correlation is the following:

$$\frac{q_{co}}{Gh_{fg}} = C\left(\frac{\rho_v}{\rho_l}\right)^{0.133}\left(\frac{\sigma\rho_l}{G^2 l}\right)^{1/3}\left\{1/\left[1+const.\left(\frac{\rho_l}{\rho_v}\right)^{m}\left(a\frac{\rho_l}{G^2 l}\right)^{n}\frac{l}{d}\right]\right\} \tag{2.13}$$

For most regimes, they found a linear rise in CHF as a function of increasing liquid subcooling. Based on thermohydraulic consideration and world data, Katto [107] proposed characteristic regimes of CHF, i.e. L (low mass velocity); H (high mass velocity), N (non-linear) and HP (high-pressure) regimes. CHF (q_c) is related to q_{co} by:

$$\mathrm{q_c = q_{co}\left(1 + K\frac{\Delta H_i}{H_{fg}}\right)} \tag{2.14}$$

where q_c is the CHF for subcooled conditions, q_{co} is the saturated CHF, ΔH_{in} is the inlet enthalpy of subcooling with respect to saturation and LK is an empirical inlet subcooling parameter. The linear relationship of q_c - ΔH_i exists only in L, H, HP regimes.

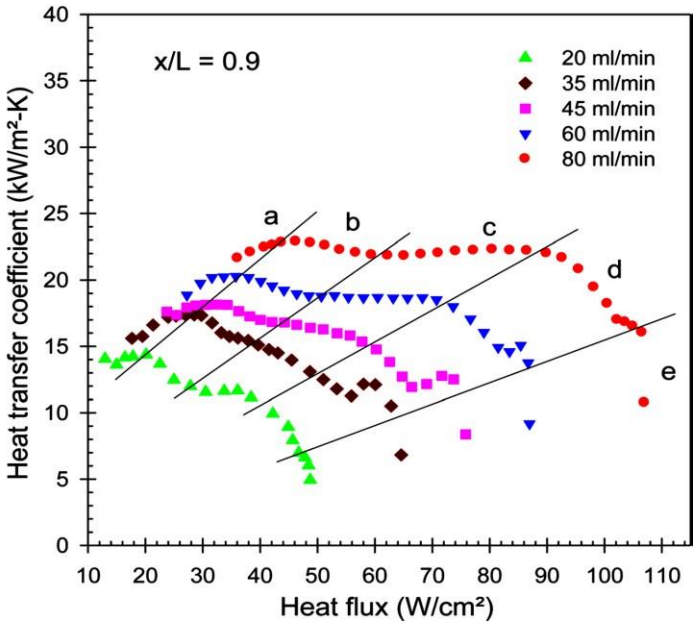

Figure 2. 19 *Heat transfer coefficients, obtained just prior to the exit of the microchannels for the five flow rates considered in this study of Chen and Garimella [19].*

2.11.1 Dryout

CHF mechanisms found in mini- /microchannel heat sinks with parallel microchannels are shown in Figure 2.20. Dryout is generally associated with saturated inlet conditions or low inlet subcooling, low mass velocities, and large length-to-diameter ratios [51]. This form of CHF occurs in the annular regime as the liquid film is fully consumed by gradual evaporation, exposing the wall directly to the vapour core. A precursor to this form of CHF is dryout incipience, where local portions of the liquid film begin to dryout. Dryout in parallel microchannels is presented in Figure 2.20b during flow boiling of R134a in a heat sink containing rectangular microchannels [108].

Premature CHF occurrence is the other important limitation of two-phase microchannel heat sinks, which is associated with significant flow instabilities and oscillations. Figure 2.20c illustrates premature CHF in the upstream region of a microchannel heat sink using HFE-7100 as working fluid [63]. Because of low mass velocity and a large volume of vapour produced inside the microchannels, the momentum of incoming liquid in the inlet plenum is momentarily too weak to overcome the pressure drop between the inlet and outlet plenums. This causes vapour from the microchannels to flow backwards into the inlet plenum, blocking any incoming liquid from entering the microchannels, and eventually resulting in dryout and temperature rise in the microchannels. Lee and Mudawar [63] concluded that there are two effective means to overcoming premature CHF, by increasing mass velocity, to prevent vapour backflow and by increasing inlet subcooling, to reduce bubble growth and coalescence in the inlet plenum.

As has already been mentioned, dryout incipience causes CHF and can result in heat transfer deterioration. Figure 2.21 shows possible causes of local dryout incipience. Figure 2.21a shows the formation of a hot spot under a growing bubble (microlayer of liquid under the bubble evaporates). In this dry zone, the wall temperature rises due to the deterioration in heat transfer. Figure 2.21b shows the near-wall bubble crowding and inhibition of vapour release, where the boundary layer becomes too crowded with bubbles, vapour escape is impossible and the surface becomes dry and overheated, giving rise to burnout. Figure 2.21d shows the possibility of dryout occurrence under a slug. In plug or slug flow, the thin film surrounding the large bubble may dryout giving rise to localized overheating and hence burnout. Film dryout in annular flow is presented in Figure 2.21d. The liquid film locally can dryout due to evaporation and due to the partial entrainment of the liquid in the form of droplets in the vapour core.

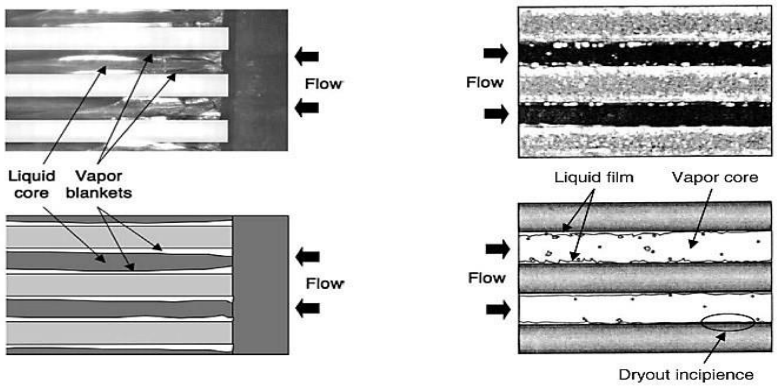

(a) (b)

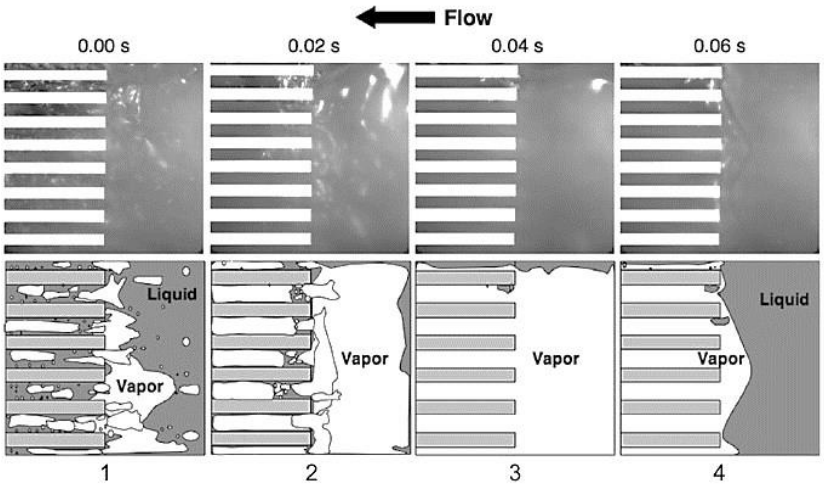

(c)

Figure 2. 20 *CHF mechanisms in mini- /microchannel heat sinks. (a) DNB for HFE-7100 in heat sink with D_h =334.1 μm for G= 341 kg $m^{-2}s^{-1}$ and q =325.8 W cm^{-2} [63], (b) Dryout incipience for R134a in a heat sink with D_h =348.9 μm for G= 128 kg $m^{-2}s^{-1}$ and q = 31.6 W cm^{-2} (adapted from [16]) and (c) Premature CHF and flow oscillations for HFE-7100 in heat sink with D_h = 415.9 μm for G = 670 kg $m^{-2}s^{-1}$ and q =250.0 W cm^{-2}: (1) initial vapour pocket build up in upstream plenum, (2) growth of vapour mass, (3) complete blockage of inlet.*

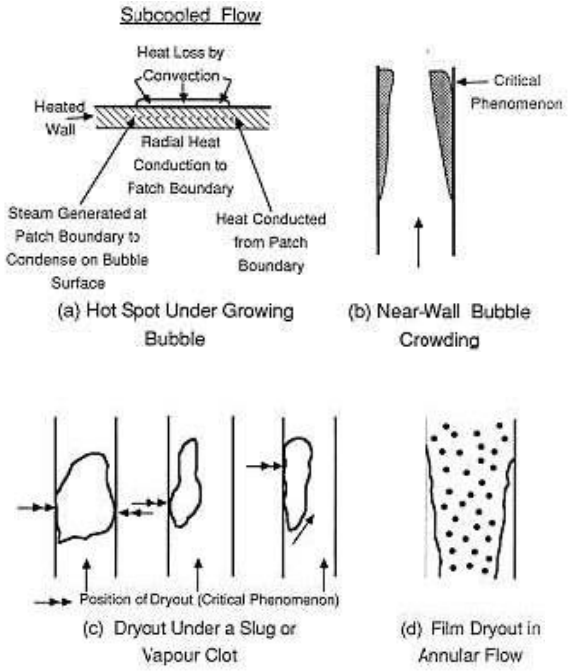

Figure 2. 21 *Dryout incipience caused by (a) the formation of a hotspot under a growing bubble, (b) near wall bubble crowding that reduces liquid film, (c) dryout under a slug and (d) liquid film dryout during annular flow at the outlet of the channel.*

2.12 Experimental approaches

A great number of studies focuses on improving the current experimental techniques in order to be able to achieve better agreement with experimental results as the disagreement between results has been attributed to the superficial characteristics, thermal instabilities and experimental errors [37], [39], [40]. More precise equipment and experimental techniques have been developed recently to accurately measure the wall temperature. Kanizawa [109] pointed out that the difficulties when measuring temperature using probes, such as thermocouple junctions, are caused because the size of the probes is the same size with the tested channels.

It is important to be able to map the channel surface and to acquire the wall temperature patterns with simultaneous optical images because the liquid distribution on the heater surface is affected by the local flow patterns, as shown in Figure 2.22, schematic from the study of Yao and Chang [110]. Numerous experimental studies have been performed using infrared (IR) thermography technique to obtain a better insight into the flow boiling heat transfer mechanisms in microchannels, but only a few of them were used for bubble level characterisation during flow boiling. Important recent approaches in microchannels used with IR thermography techniques are: (a) heating channel from borosilicate glass or silicon, coated with IR –opaque material (b) IR opaque heating film (titanium, indium tin oxide, chromium based layers,) deposited on an IR-transparent substrate (sapphire, soda lime glass, CaF_{2}- calcium fluoride).

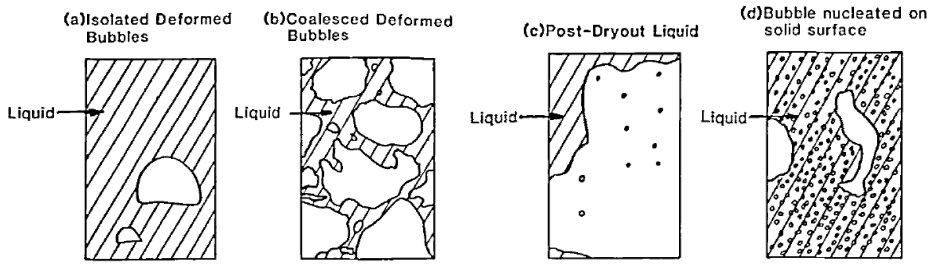

Figure 2. 22 *Boiling phenomena in confined spaces* [110].

Kim *et* al. [111] developed a new technique for the measurement of heat transfer coefficient distributions using an infrared camera to determine the temperature distribution in the wall of a channel of an opaque silicon substrate (Figure 2.23b). The disadvantage of silicon is that it is not optically transparent, although transparent to IR. Wang *et* al. [74] and Barber *et* al. [25] used metallic coating shown in Figure 2.23a deposited on glass to provide transparent heating and measured heat transfer by neglecting thermal diffusion phenomena within the channel wall (Bi << 1). Both studies were limited, the former because optical accessibility and the latter because of high thermal resistance of the wall, which resulted in measurement of the outer wall temperature. Wang *et* al. [74] used borosilicate glass minichannels coated with tantalum deposit for transparent heating to study flow boiling phenomena of FC-72 in three high aspect ratio channels with D_h= 571 µm, 762 µm and 1,254 µm for the mass fluxes of 11.2 kg $m^{-2}s^{-1}$, 22.4 $kgm^{-2}s^{-1}$ and 44.8 kg $m^{-2}s^{-1}$ respectively. The results showed that T_w fluctuated chaotically with channel axial direction and they observed using high-speed visualisation that the main flow regimes were bubble nucleation, confined bubble flow, slug flow, and wispy-annular flow. The studies of Barber *et* al. [25] and Wang *et* al. [74] used microchannels with tantalum coating on borosilicate glass, with IR thermography and high-speed visualisation.

Liu *et* al. [112] measured the fluid temperature of ethanol through a transparent germanium window during two-phase flow using infrared thermography. The wall temperature was measured with thermocouples. The heater design is depicted in Figure 2.24. The IR camera obtained the results though a transparent to IR sapphire window.

Kenning [113] captured wall temperature in the vicinity of the wall during pool boiling using liquid crystal thermography. Photographs of the liquid crystals were taken at intervals of 10 s. The centre of the cold spots and the rings was assumed that is related to nucleation sites. The black regions observed in the figures indicated heating of the liquid crystal beyond its colour play limit of 132 °C. The spatial resolution was 0.2 mm. The low response time of measurements and the possibility of interference of the crystal with the flow and the low-resolution of the data does not make this method desirable for high-resolution data during flow boiling.

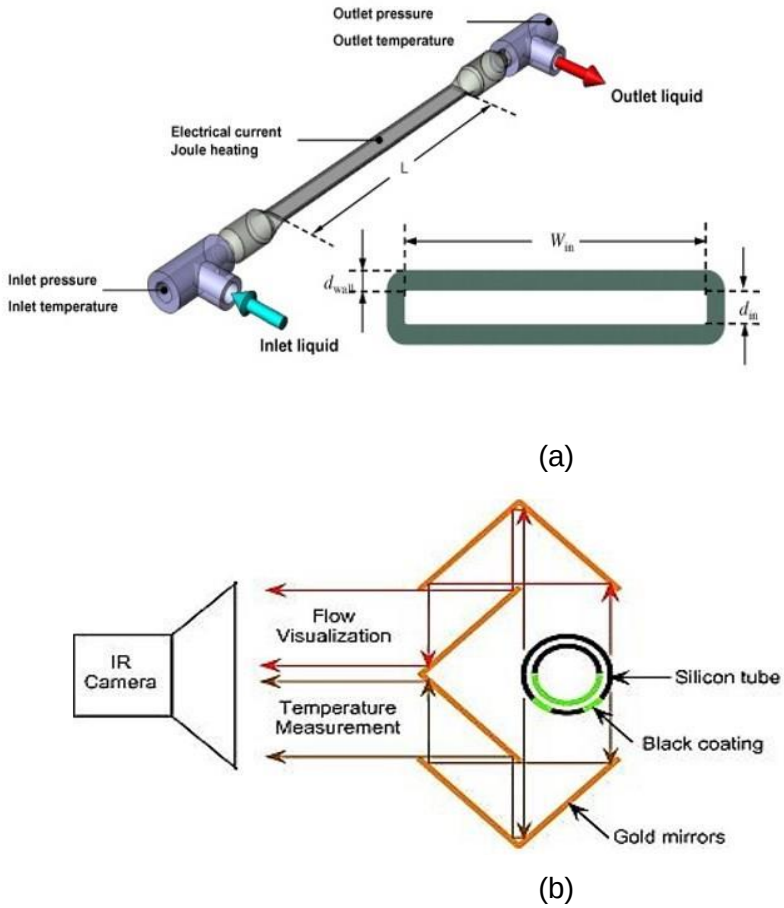

Figure 2. 23 *(a) Tantalum deposition on borosilicate glass* [74] *and (b) silicon tube* [111] *used with infrared thermography technique.*

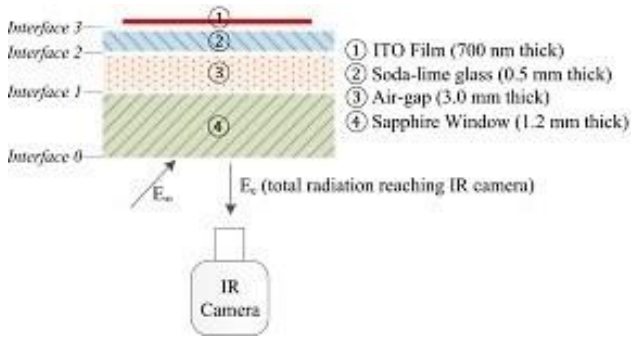

Figure 2. 24 *Heater wall design used with IR thermography experiments by Yoo et al.* [114].

Jinliang *et* al. [115] carried out flow boiling experiments in 10 silicon parallel microchannels of D_h = 155.4 μm using acetone as the working liquid. IR thermography technique was used to measure the thin Pt film temperature on the back of the silicon wafer with a typical resolution of 320 × 240 pixels with 50 Hz frequency. The IR results were synchronised with optical visualizations. The pressure drop over the microchannels were around 30 kPa, and

the mass fluxes varied from 63.3 kg $m^{-2}s^{-1}$ to 133.3 kg m^{-2} s^{-1}. The wall temperature was found to increase with increasing heat flux. The maximum chip surface temperature was still 89.4 °C, even though the heat flux was high up to 288.65 kW m^{-2}, and the mass flux only 110 kg m^{-2} s^{-1}, demonstrating the large two-phase cooling capabilities in microchannels. The produced two dimensional chip temperature and heat transfer coefficient distributions of the thin film heating area (16 mm × 4.2 mm) are illustrated in Figure 2.25. It was concluded from Figure 2.25 that the chip temperatures are indeed non-uniform. The temperature differences in the heated area are about 6 °C, with the lower temperatures in the inlet, outlet and the four margin regions the lower, smooth but increased temperatures in the entrance region are caused by the greater possibility of the channel entrance to be immersed in the liquid. The chip temperatures in the majority of the chip heating area display spatial variation behaviour, which may be caused by the transient flow patterns. Liquid or vapour phase alternated in the channel. The lower temperatures at the margins are caused by the thermal conduction of the silicon wall at the interface between the heated area and the unheated area. They subdivided a full cycle into three sub stages of liquid refilling, bubble nucleation, growth and coalescence stage and transient liquid film evaporation stage. Four characteristic flow patterns where periodically repeated in a timescale of milliseconds. The cycles of fluctuations were divided in the liquid refilling stage, bubble nucleation, growth and coalescence stage and transient annular flow stage. During these periodic fluctuations, it was found that the pressure and temperature of the fluid was stable while the chip presented spatial variation of the wall temperature. The temperature variation occurred due to liquid-vapour alternations at the majority of the heating area. For example, for an inlet liquid temperature of 30.8 ˚C, at G = 110.1 kg $m^{-2}s^{-1}$ and q = 141.92 kW m^{-2} the time averaged pressure drop was 30.41 kPa and the wall temperature spatially variated from 62 to 74 ˚C. The heat transfer coefficient was found to increase from 1,000 to 25,000 W m^{-2} K^{-1} after a small distance from the inlet. They observed that paired or triplet bubbles nucleated simultaneously in or very close to the channel corner at the same cross section. Then a single liquid plug appeared after the bubble nucleation, which was later separated in two parts that were pushed out of the flow field. During the transient annular flow stage the liquid at the channel corners was observed to decrease in time and after partial or full dryout occurred at the end of each cycle, the microchannels were partially or totally dried out and then liquid refilling was initiated.

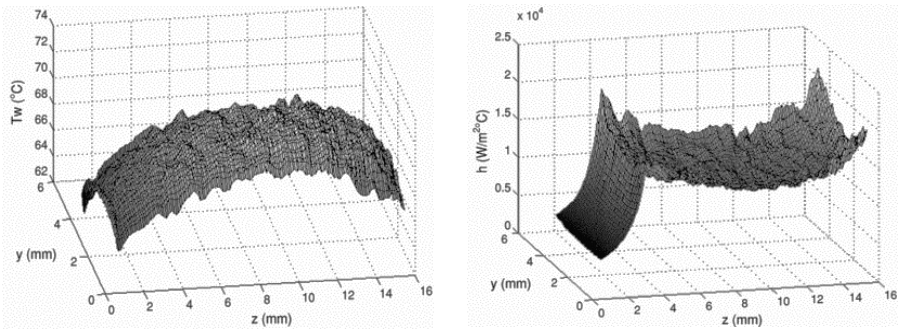

Figure 2. 25 *Chip wall temperature and heat transfer coefficient distributions (T_{in}=30.8 °C, ΔP =30.41 kPa, G = 110.1 kg m^{-2}s^{-1}, q =141.92 kW m^{-2}, x_e = 0.5268, Re = 65.2). Results from the study of Jinliang et al. [115]..*

The infrared and optical images low spatial and temporal resolution did not allow to identify details in the images. The camera resolution was 320 × 240 pixels for the focus heating area of 16.0 × 4.2 mm^{-2}. Although there was simultaneous, optical and thermal visualisations the optical images were not clear enough and the resolution of the IR images was poor. In addition, there was no correlation of the optical images with the heat transfer coefficients.

Amongst the infrared (IR) thermography studies on flow boiling heat transfer in microchannels [24], [25], [111], [112], [116]–[119], only that of Krebs *et* al. [119] provided high spatial resolution (10 µm /pixel) wall temperature measurements at high temporal resolution (120 frames per second). The other studies used lower spatial resolution (≥ 50 µm /pixel). Hetsroni *et* al. [114, 115] used IR thermography to investigate the relation between the thermal patterns and the flow regimes and to measure the surface temperature of the microchannel heat sink. They measured wide variations of wall temperature (up to 20 K) on the surface for time intervals of 0.04 s (i.e. at 25 fps) and low resolution of 246 pixels per line. Liu and Pan [112] calculated local two-phase heat transfer coefficients in the stream-wise and axial direction from outer wall temperature measurements that were obtained with thermocouples. Infrared thermography was used to capture the fluid temperature. Barber *et* al. [24], used n-Pentane (T_{sat} = 35.5 °C) to perform flow boiling experiments using a single rectangular microchannel having rounded corners with D_h = 771 µm (α = 20, D_h = 8,000 µm, H_{ch} = 400 µm and L_{ch} =70 mm) with infrared thermography. They obtained local temperature measurements from the outer wall of the microchannel with a spatial resolution of 100 µm / pixel and a frame rate of 50 Hz. For G = 3.52 kg m^{-2} s^{-1} and q = 2.33 kW m^{-2} the spatially averaged heat transfer coefficient at the inlet of the microchannel where bubble nucleation occurred, was observed to vary rapidly between 200 and 1,600 W m^{-2} K^{-1}. Liu and Pan [112] used IR thermography to

study heat transfer during flow boiling in a microchannel fabricated from aluminium plate. They measured the wall temperature with five thermocouples and the fluid temperature with IR thermography technique. The microchannel was fabricated from aluminium with a length of 28 mm long, a depth of 250 μm and a width of 1 mm (α = 4, D_h = 400 μm). In order to measure the wall temperature that was used for the calculation of the heat transfer coefficient, two thermocouples were embedded 2 mm beneath the channel surface at the intervals of 6.5 mm in the flow direction. Flow boiling experiments were carried out at a mass flux of 20.3 kg $m^{-2}s^{-1}$and at the heat flux range of 3.1 - 244.1 kW m^{-2}. The two-phase flow patterns based on IR images were obtained at 0.1 s intervals. Bubble formation and bubbly-slug flow were the flow patterns observed from the IR visualisation for the heat flux of 81.8 kW m^{-2}. When the heat flux was increased at 199.44 kW m^{-2}, long slug flow appeared because of the merging between bubbles. The bubble production rate was found to increase with increasing heat flux. At higher heat flux of 244.1 kW m^{-2} they observed a thin film on the sidewalls from IR visualisation and some intermittent liquid in the centre of the microchannel. The measured high wall superheat of 2.2 K, resulted in the deterioration of heat transfer under high heat flux conditions. They plotted the local heat transfer coefficients at the five locations of the thermocouples with the axial location from the channel entrance and they concluded effective heat transfer for heat fluxes less than 199.44 kW m^{-2}. For heat fluxes less than 199.44 kW m^{-2} the local heat transfer coefficient increased with increasing heat flux and was generally constant in the flow direction. However, at heat fluxes higher than 199.44 kW m^{-2} the flow pattern changed to long slug flow and resulted in a decrease of the heat transfer coefficient with increasing heat flux and axial location. The cause of the decrease of the heat transfer coefficient was the possible dryout appearance during annular flow. This study revealed the temperature distribution of the microchannel but the images were not high quality images and only the fluid temperature was measured using IR technique.

Piasecka *et* al. [120] used IR thermography together with liquid crystal thermography to study flow boiling heat transfer in vertical minichannels of 1 mm depth using FC-72. Liquid crystal thermography was used to measure the temperature of the liquid close to the solid wall surface, which was achieved by attaching a foil on the inner side of the glass that would be in contact with the fluid. This setup allowed the detection of the temperature changes on foil. The IR thermography technique was used to measure the outer wall temperature of the glass, but in a different channel. The temperature measurements were used for the validation of the existing models for 1D and 2D heat transfer coefficients. The comparison between the 1D and 2D heat transfer models revealed that there were similar values and distributions of the heat transfer coefficient. The results show that the heat transfer coefficient decreased with developing boiling length. The 1D model was more sensitive to measurements errors. The heat transfer coefficients at the outlet ranged from 1,000 to 71,000 W

$m^{-2}K^{-1}$. Although the temperature measurements were obtained at the fluid-solid interface, the results were not accurate enough, as this method was intrusive to the flow. In addition, the experiments were not carried out simultaneously at the same channel but at different channels.

The aforementioned studies on flow boiling in microchannels indicate that there are still many challenges the need to be addressed in flow boiling in microchannels field. It is crucial to understand the nature and behaviour of flow boiling instabilities, heat transfer mechanism(s) for modelling of heat transfer in microchannels. There is a need to develop reliable models. Flow boiling heat transfer investigation requires synchronised high spatial and temporal resolution two-dimensional local measurements with synchronised high-speed imaging for high accuracy results.

For the purposes of this work, Polydimethylsiloxane (PDMS) is used for the channel microfabrication, as it is transparent to midwave infrared (IR) radiation and optically accessible and allows for simultaneous flow visualisation and thermal image acquisition. Synchronised measurements at the channel interface with flow visualisation for flow boiling in microchannels has not yet been reported in the literature. Lu *et* al. [121] used a PDMS microchannel of $D_h = 120$ μm and 280-220 μm depth and a length of 7-10 mm. The heater was a fine platinum wire. The temperature was measured from thermocouples emended at the base of the channel. They found that the bubbles stemmed from the PDMS walls instead of the heater wire. Micro droplets were found in the bubbles due to condensation at the channel walls.

2.13 Material selection for optically accessible and transparent to infrared microchannels

The selection of the right material to be used with IR thermography technique is crucial in microchannel two-phase flow boiling experiments as the emissivity of the material defines the interface of the wall temperature measurements. In addition, application of simultaneous high-speed visualisation with IR thermography requires materials with unique optical properties. Yoo *et* al. [114] summarised the techniques used by researchers for pool boiling experiments with IR thermography: (1) Heating channel coated with IR opaque material, (2). thin metal foil heater and (3) a heating film deposited on IR-transparent substrate. Polydimethylsiloxane (PDMS) is one of the most used silicon-based organic polymers. It is optically clear, inert, nontoxic, non-flammable and is commonly used in many microfluidic applications [15], [108]. It is widely used to many different applications in microfluidics because of its low cost, easy fabrication, flexibility, and transparency to visible and mid-IR spectrum. For this study, PDMS was used to fabricate microchannels because of its transparency to mid-IR spectrum, which can allow for inner wall temperature measurements and optical visualisation. Indium tin oxide (ITO) is one

of the most widely used transparent conducting oxides because of its good electrical conductivity and optical transparency, as well as the ease with which it can be deposited as a thin film. ITO film deposited at room temperature has a fully amorphous structure. ITO It needs to be annealed at a higher temperature (250 ºC) in order to crystallize [122]. This results in a lower electrical resistivity and a higher transparency'. The annealing will help to crystallise ITO films at about to gain low resistivity and high transparency. Tuna *et* al. [123] measured optical transmission of above 85 % in the visible region for an ITO film with thickness of 70 nm. Wettability is a property of the solid-liquid interface defined by the contact angle. The chemical composition and the geometrical nanostructuring of PDMS are important parameters that can affect its wettability. Wetting and the surface forces that control wetting are also responsible for other effects, including capillary effects. The surface topography of the PDMS microchannel can affect their wetting properties. In this study, the channel base is from glass which is uniformly and stably hydrophilic and is a major advantage. In contrast, Polydimethylsiloxane (PDMS) is hydrophobic and it has a water contact angle of 110 °C. But, this hydrophobicity is variable in time and space [*Murakami et al*.[124]]. This is a major disadvantage. It is known that plasma treatments can modify surface wettability, as a result of both chemical and morphological modification of the surface [125].Wetting characteristics can be measured in many ways and in defining the static contact angle; the static advancing contact angle is most commonly used due to its stability.

2.14 Absorption coefficient

The effective transmissivity of liquid decreases with increasing film thickness and the system becomes opaque at large thicknesses as the *Beer –Lambert Law implies:*

$$I_R(z) = I_o \cdot e^{-k z} \tag{2.8}$$

where I is the radiation intensity after it passes through the sample and Io is the initial intensity and z is the penetration length and k is the monochromatic absorption coefficient. From eq.2.8 absorption increases for increasing film thickness.·· The transmittance is related to the optical depth and is defined as follows:

$$\tau = \frac{I_R}{I_o} = e^{-k z} \tag{2.9}$$

The surface emissivity is related to the transmittance as follows:

$$\varepsilon = 1 - \tau \tag{2.10}$$

The characteristic penetration depth s is defined as follows:

$$\lambda = \frac{1}{k} \tag{2.11}$$

where k is the monochromatic absorption coefficient.

2.15 Scope of research

The present experimental work is divided in two parts. The first part focuses on the investigation of flow boiling heat transfer in nine-silicon microchannel heat sink with parallel, rectangular microchannels of hydraulic diameters in the range of 50 to 150 μm and aspect ratios from 0.33 to three. The objective is to obtain two-phase flow regimes using temperature and pressure measurements in order to investigate flow boiling instabilities, bubble dynamics and heat transfer mechanisms of microchannel heat sinks with increasing aspect ratios. The experimental setup consists of a test module with an integrated heater and the experiments were carried out for uniform heating using integrated temperature sensors that allow for local temperature measurement with a high response time. The second part investigates two-dimensional interfacial heat transfer coefficient maps by using a novel technique to measure interfacial wall temperature. A transparent microchannel device was fabricated with a transparent to infrared radiation wall from Polydimethylsiloxane (PDMS) and an optically transparent heater of ITO thin film coated glass.

2.16 Summary

This chapter reviews well-established theory on flow boiling in macroscale channels and theory on mini- / microscale channels. The literature review provides a summary on the criteria used to determine the transition from macro- to microscale flows and on results from experimental investigations on liquid-vapour phase change in mini- and microchannels. Then heat transfer mechanisms of nucleate boiling and convective boiling were described for flow boiling heat transfer in macroscale and microscale. The importance of the flow patterns on two-phase flow boiling heat transfer mechanisms was discussed, as well as the effect of bubble confinement on heat transfer. Experimental results were presented on the effect of two-phase flow boiling heat transfer characteristics, microchannel geometry and cross section in mini-/microchannels as a function of mass flux, heat flux, flow boiling instabilities and critical heat flux. The importance of the design parameters such as inlet and outlet manifolds of the microchannel heat sink in order to achieve uniform flow distribution between the channels was discussed. The existing the different experimental approaches that have been used to measure wall temperature on microchannel were discussed. The accuracy and resolution of the existing

measurements from other experimental studies on temperature, pressure and heat transfer coefficient data was compared. Finally, the issues that need to be resolved in order to use flow boiling in microchannels for cooling of microelectronics within specified conditions were highlighted. Amongst these outstanding issues are the lack of established transition criteria from macro- to microscale flows, unclear dominant heat transfer mechanism(s) and flow boiling instabilities including flow reversal and early dryout.

Chapter 3 Experimental Facility and Methodology

3.1 Introduction

This chapter describes the equipment used to carry out the experiments as well as microfabrication techniques used to manufacture the microchannels. Two experimental systems were designed and built for the investigation of liquid-vapour phase change, flow boiling and heat transfer in multi- and single microchannels. Each experimental facility employed a different technique to obtain wall temperature measurements from the microchannel(s). Particularly, five thin film Ni sensors were placed at five different locations at the bottom of the silicon microchannels which obtained local temperature measurements. An infrared thermography technique was used with the transparent Polydimethylsiloxane (PDMS) microchannel device which was used to obtain two-dimensional temperature distributions from the microchannel wall. The loop facility built at the University of Edinburgh, referred to as loop 1, was used to examine heat sinks comprising multiple, parallel microchannels and the arrangement at the University of Valenciennes (loop 2) was utilised for the study of a single, high aspect microchannel.

The effect of aspect ratio on characteristics of heat transfer (heat transfer coefficients, pressure drop) during flow boiling were studied in order to identify the optimum dimensions for most efficient heat transfer. The experimental system in this case consisted of a test flow loop and a test module. Local wall temperature measurements were obtained using nickel (Ni) temperature sensors integrated into the backside of the microchannels. The setup allowed for simultaneous acquisition of pressure and local wall temperature as well as high-speed imaging through the transparent top of the silicon microchannels. Flow visualisation was achieved with a high-speed camera mounted on a microscope. Local heat transfer coefficient profiles were obtained along the heat sink central flowstream direction.

The facility built at University of Valenciennes and Hainut Cambresis, used simultaneous infrared thermography and high-speed optical to visualise a flow of FC-72 dielectric coolant through a novel transparent polydimethylsiloxane (PDMS) microchannel device with integrated pressure sensors. The wall temperature maps and pressure measurements were used to calculate two-dimensional heat transfer coefficients across the lateral dimension of the channel as a function of time. The innovative synchronisation of highly spatiotemporally resolved optical and

thermal data allows for an unusually detailed examination of heat transfer phenomena in microchannels. A further novelty is the ability to obtain interfacial wall temperature measurements because of the inherent transparency of PDMS to mid-wave infrared radiation. Accurate quantification of transient heat transfer coefficients during flow boiling was achieved by using data from integrated pressure sensors near the inlet and the outlet of the channel. Local pressure measurements were used to determine the local saturation temperature along the channel. Accurate quantification of transient heat transfer coefficients during flow boiling was achieved by using data from integrated pressure sensors near the inlet and the outlet of the channel. The local pressure measurements were used to determine the local saturation temperature along the channel.

3.2 Design, microfabrication process and facility used for silicon microchannel heat sinks

3.2.1 Design of the silicon microchannels heat sinks

The thermal efficiency of the heat sinks depends on how flow is distributed between the channels. Non-uniform distribution of liquid between the channels can lead to individual blockage and hotspots that can cause irreversible damage. The shape of the inlet and outlet manifold, the positions and the size of the inlet and outlet holes are important parameters as can affect the pressure drop level in the heat sink. The parameters taken into account in order to obtain uniform flow distribution in parallel microchannels heat sink designs have been discussed in chapter 2. Based on the approximate model results [34], a consecutive Z-type structure with non-constant, linear cross section manifolds was selected to achieve uniform flow distribution between the channels and is shown in Figure 2.13 of chapter 2. The inlet and outlet holes are placed inside the manifolds to enable better flow distribution within channels and to minimize the manifold area. This also allowed more devices to be placed on one silicon wafer during the microfabrication process. In this study, the approximate model was used to design the microchannel heat sinks in order to achieve optimum flow distribution between the microchannels.

The geometry of the heat sink with silicon microchannels is presented in Figure 3.1a. Figure 3.1b shows the depth of the inlet and outlet manifold of the silicon microchannel heat sinks used for the flow boiling experiments. The depth of the manifolds is the same as the depth of the microchannels. A 500 μm thick Pyrex glass cover plate was anodically bonded to the silicon wafer to seal the channels and permit visualisation of boiling within channels. The silicon heat sink was sandwiched between the top and the bottom frames as shown in Figure 3.1b. The

schematic drawings of the case are provided in Figure A.1, Appendix A. The water was supplied through external stainless tubes, connected to the top frame and the inlet and the outlet holes formed in the Pyrex glass cover plate using the technique of powder blasting. Two small O-rings were used to seal the connections between the holes on the top frame and those drilled in the Pyrex glass in order to prevent any leaks from the heat sink.

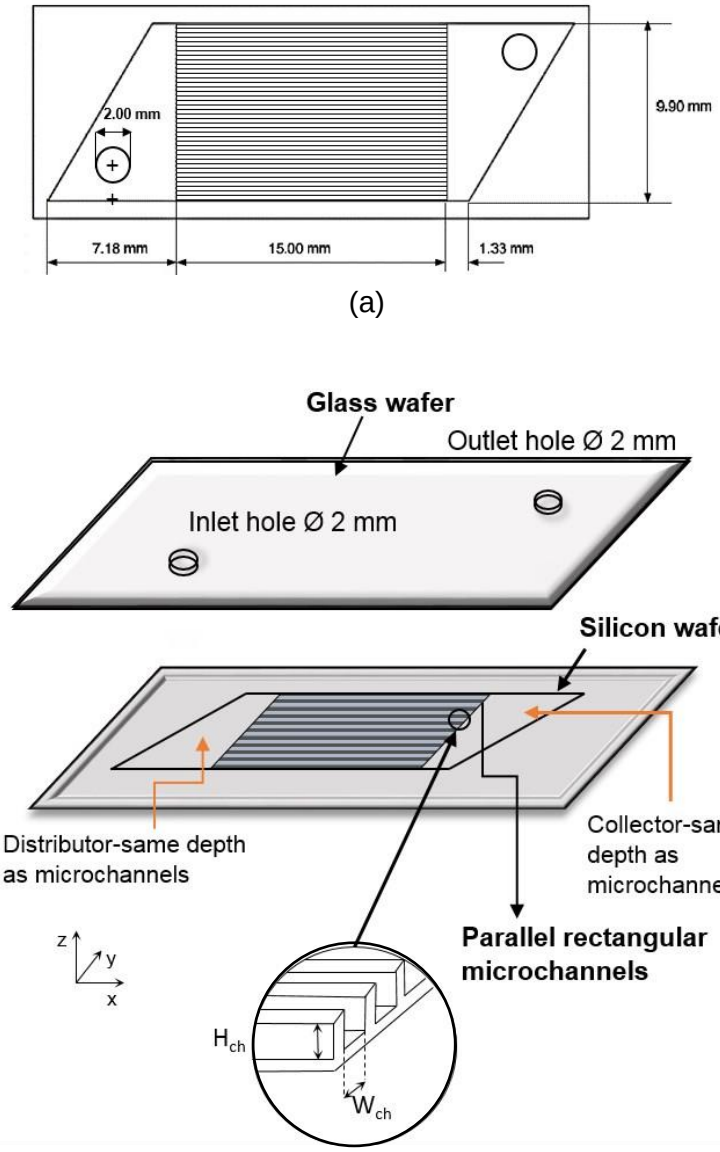

Figure 3. 1 *(a) Geometry of the inlet and outlet manifold and (b) split view of the microchannel heat sink device.*

Three different designs (designated A, B, C) were carried forward for production and their specifications are catalogued in Table 3.1. Design A consists of microchannels with constant

height of 50 μm, design B with constant height of 100 μm and design C with constant height of 150 μm. For each design, the microchannel widths take the values of 50, 100 and 150 μm. The hydraulic diameters range from 50 μm to 150 μm with aspect ratios that range from 0.33 to 3. The channel cross sections are represented schematically in Figure 3.2.

Table 3. 1*Characteristics of the silicon microchannels heat sinks.*

Design	W_{ch} [μm]	H_{ch} [μm]	a	D_h [μm]	A_{cr} [mm^2]	N	P_h [μm]
1A	150	50	3	75	0.0075	40	350
2A	100	50	2	66.7	0.005	66	300
3A	50	50	1	50	0.0025	100	150
1B	150	100	1.5	120	0.015	40	350
2B	100	100	1	100	0.01	66	300
3B	50	100	0.5	66.7	0.005	100	250
1C	150	150	1	150	0.0225	40	450
2C	100	150	0.67	120	0.015	66	400
3C	50	150	0.33	75	0.0075	100	350

Abbreviations: W_{ch}: width of the microchannel, H_{ch}: height of the microchannel, a: width-to height aspect ratio of the microchannel cross section, D_h: hydraulic diameter of the microchannel, A_{cr}: cross sectional area of the microchannel, N: number of microchannels, P_h: heated perimeter ($2*H_{ch} + W_{ch}$)..

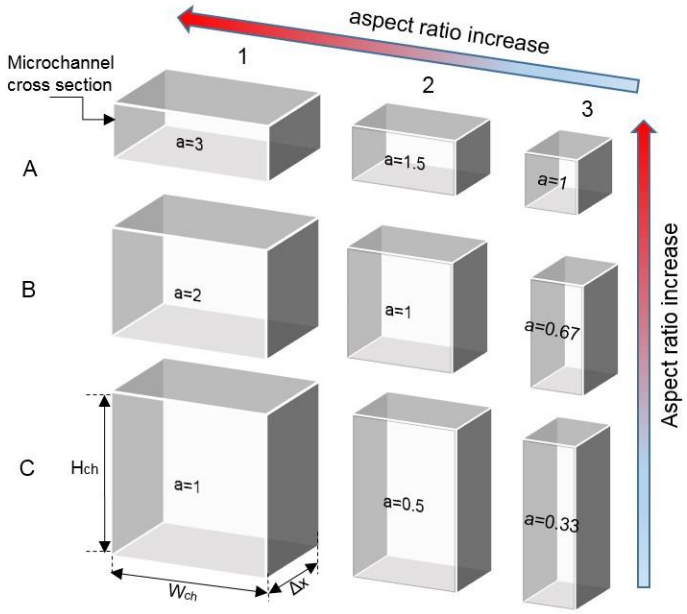

Figure 3. 2 *Schematic drawing with the microchannel cross sections of the different heat sink designs presented in table 3.1.*

3.2.2 Microfabrication of silicon microchannel heat sinks

The silicon microchannels were fabricated using an inductively coupled plasma (ICP) dry etch in conjunction with photolithographic techniques where a layer of light sensitive material (photoresist) is applied to a Si surface and exposed to light through a mask. Selective etching can then be carried out as some areas of the wafer are exposed and others are protected from the plasma by the layer of photoresist. Figure 3.3 shows the layout of masks used for the deep silicon etch process.

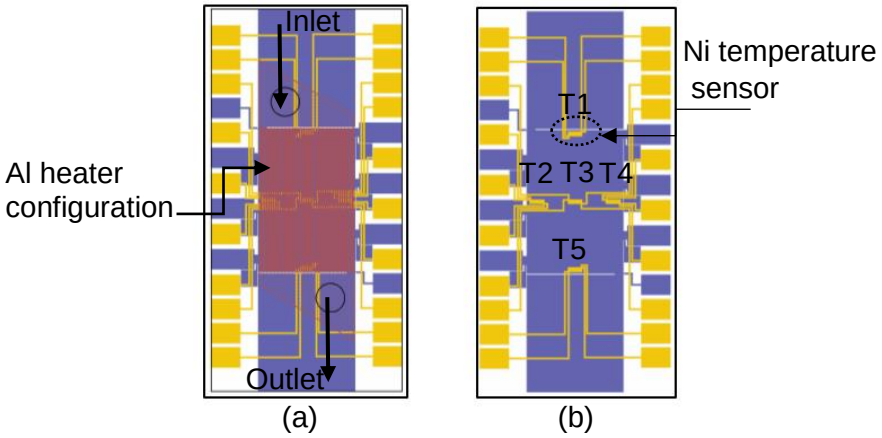

Figure 3. 3 *Layout of masks used in microfabrication of silicon microchannel heat sinks. (a) Mask for the heater and (b) mask for the temperature sensors.*

A thermal silicon dioxide layer of 250 nm was grown on both sides of a 3-inch double-side polished n-type (100) single crystalline silicon wafer to electrically isolate the temperature sensors from the silicon substrate on the back-side of the wafer as well as to help insulate against physical damage during processing (Figure 3.4a). A lift-off process was then used to form temperature sensors on the backside of the wafers; A negative photoresist (AZ5214E) was used with spin coating method to define sensor tracks and the patterned photoresist formed a shadow mask for the subsequent Ti / Ni deposition, shown in Figure 3.4b. A combination of 20 nm Ti followed by 250 nm Ni was then deposited using magnetron sputtering. In this case, the titanium acts to allow strong adhesion of Ni to the oxide surface, significantly reducing the probability of the failure of the temperature sensors during processing or in practical application (Figure 3.4c and d). The wafers were then immersed in acetone during an ultrasonic cleaning cycle. The photoresist was dissolved in the acetone and the metal coating the photoresist, is shaken off the wafer by the agitation provided by the ultrasonic cleaner, Figure 3.4e. The lift-off process is finished with a deionised water rinse (15 minutes) and wafer drying. A 3 μm layer of silicon oxide was deposited on the surface containing the temperature sensors via plasma-enhanced chemical vapour deposition (PECVD), Figures 3.4f and g. The PECVD oxide surface was then planarised using chemical mechanical polishing (CMP). Manually applied paint SPR 220-7 photoresist at the alignment mark areas, Figure 3.4h. Heaters were fabricated on top of the planarised oxide layer, electronically isolated from the temperature sensors; a 1 μm film of aluminium was deposited using magnetron sputtering, followed by a lithography step to define the lateral dimensions of the heaters by protecting areas of the Al film during the subsequent reactive-ion etching (RIE) step, Figures 3.4i and j. PECVD HFSIO etching for pad opening followed in Figure 3.3m. The heater was then covered by PECVD oxide and the top surface planarised, again using CMP, Figure 3.4k. The silicon dioxide layer on the front side of the wafer was then dry etched using RIE, Figure 3.4g. The microchannels were defined using a thick photoresist SPR220-7 (7.0 μm), and the channels were etched using ICP, Figures 3.4n and o. After removing, the photoresist from its front side, the wafer was anodic ally bonded to a glass wafer.

The diagram in Figure 3.5a shows the position of the five thin Ni film temperature sensors located at the back of the microchannels. Each of the sensors has serpentine configuration with 13 turns and total width of 435 μm and length of 1500 μm. The sensors are located 112 μm underneath the channel bottom wall. Figure 3.5b shows an optical image of the thin Ni film temperature sensors configuration. Each sensor has four pads for electrical connections, two for current supply and another two for voltage measurements. The “four points” resistivity measurements circuit is presented in Figure 3.5c. The heater also has a serpentine configuration

with 17 turns covering an area of 10.15 × 15.00 mm^2 and is powered via two large pads for uniform heating.

Figure 3.6 shows photographs of the processed wafer prior to dicing into individual devices. Figure 3.6a shows the silicon wafer from the front side comprising three different microchannel test devices. The height of the microchannels are the same for the whole wafer while the channel widths are different for each microchannel test device. The channel widths are 50 μm (1), 100 μm (3) and 150 μm (2), constant for each test device. Figure 3.6b shows the backside of the three different silicon microchannel heat sinks with the sensor pads and the heater pads for the electrical connections indicated. Heat sinks, 1 and 2 in the figure, have the same configuration of sensor pads and heater pads at their backside. In contrast, the heat sink labelled as 3 has a sensor configuration that is a mirror image of the arrangement found in devices 1 and 2. The different configuration of the sensor pads of device 3 does not have any effect on the results of the experiments. However, the different configuration of the sensor pads affected the interface connections with the flow loop1 and the electronic connections with the power supply system and the data acquisition device. For this reason, a specific PCB board was fabricated for the easy plug in of the cables as will be further discussed in section 3.6.1.1.

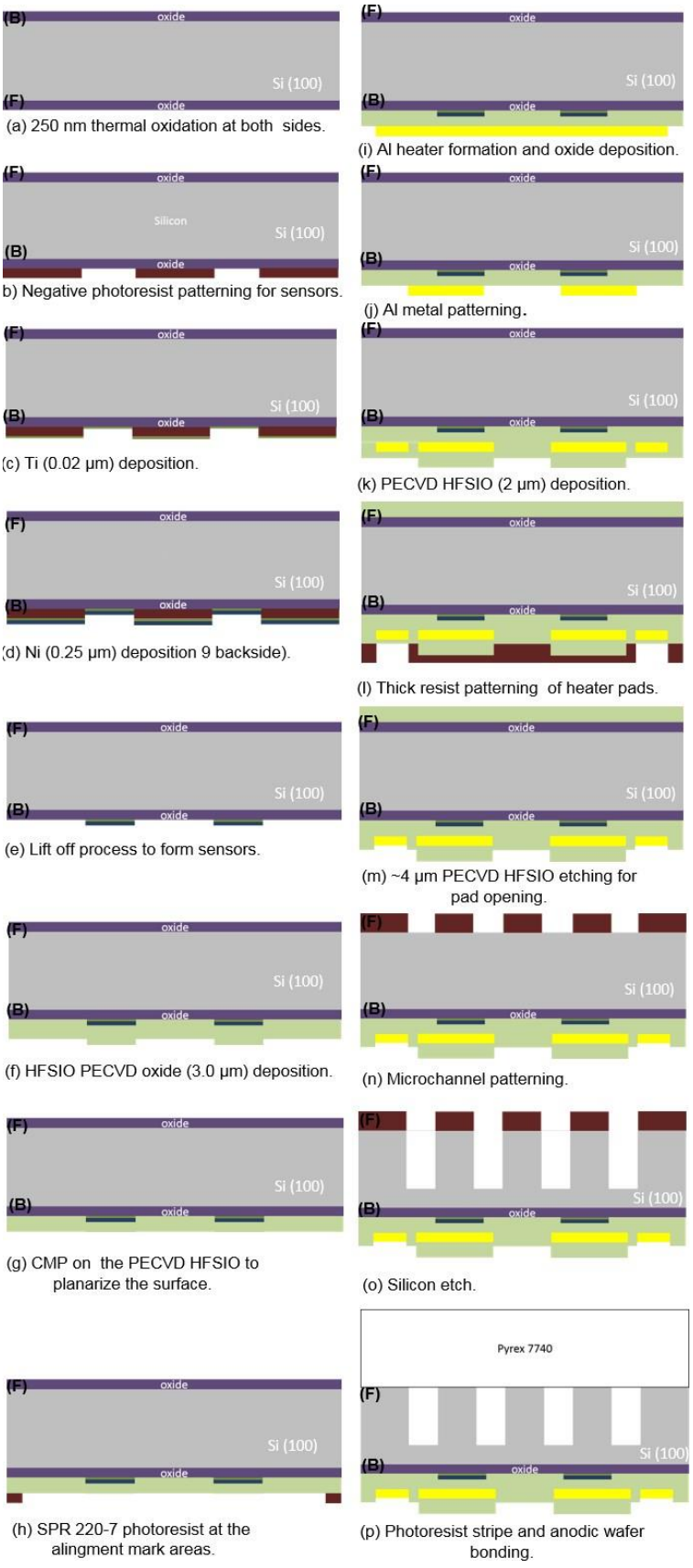

Figure 3. 4 *Microfabrication steps of silicon microchannels heat sink.*

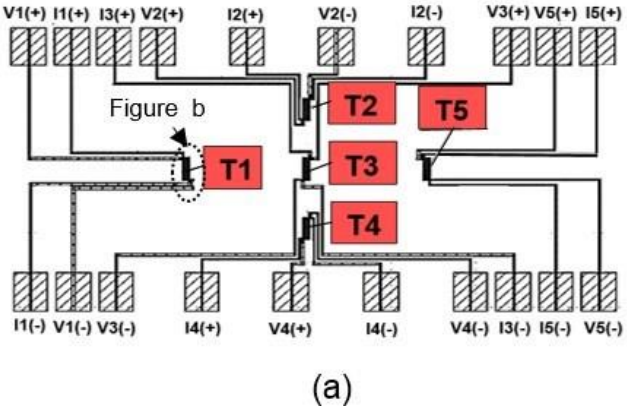

Figure 3. 5 *(a) Diagram of the temperature sensors from the backside of the microchannels, (b) position of temperature sensors from the front side of the microchannels heat sink and (c) schematic diagram of the four-point resistivity measurement by the temperature sensor.*

Figure 3.7a shows pads for the sensors and the heater that allow for the electrical connections. Figure 3.7b shows the top-down view of the microchannels. The heater was designed to enable either uniform or non-uniform heating, the latter being achieved by the independent operation of the upstream, middle or downstream heating elements. For this study,

only uniform heating was used and therefore only the two heating pads shown in Figure 3.7a were used in order to make electrical contact. The characteristics of all the silicon microchannels heat sinks are presented in Table 3.1. Both width and depth of the microchannels changes from 50 to 150 μm. The two holes at the inlet and outlet manifold were formed using powder blasting (Heriot Watt University). In previous study of Cummins [126] , drilling was the method used to form holes at the Pyrex glass [34] inlet and outlet manifold. Powder blasting proved to be the superior method of engineering holes to permit liquid flow into the channels as it was shown to cause significantly less damage to the glass than drilling.

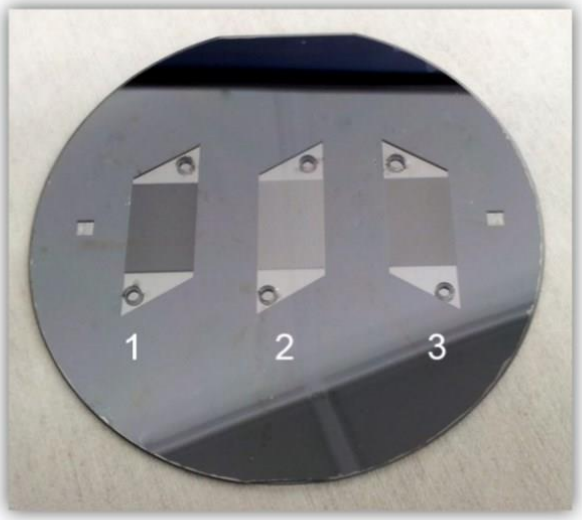

(a)

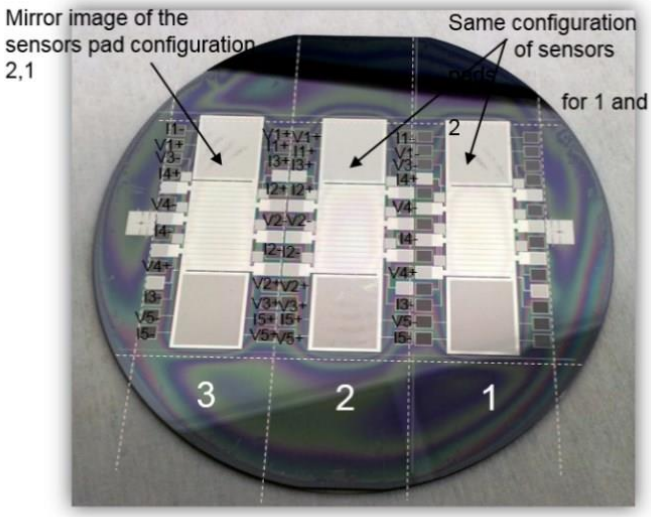

(b)

Figure 3. 6 *Silicon wafer with microchannel heat sinks devices, from the front side (a) and the backside (b). The numbers 1, 2, 3 are used to distinguish the test devices with different microchannel widths of 150 μm (2), 100 μm (3) and 50 μm (1).*

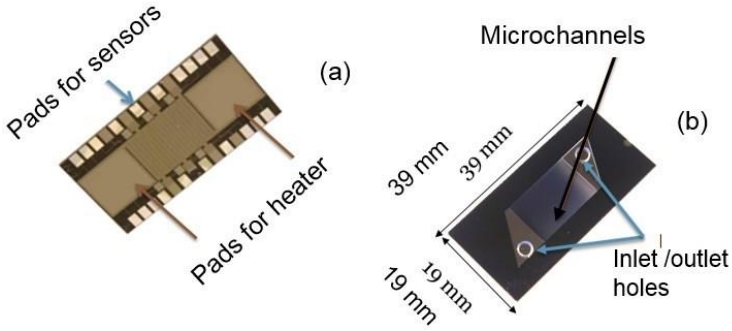

Figure 3. 7 (*a) Backview and (b) top view of one silicon microchannels heat sink.*

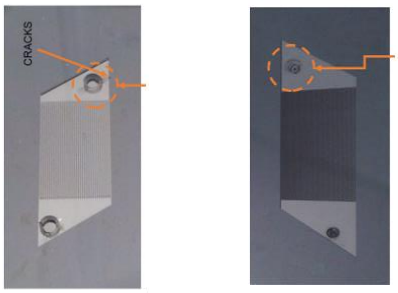

Figure 3. 8 *Holes in the inlet and outlet manifolds of the silicon microchannel heat sinks using a (a) drilling technique (b) powder blasting technique.*

The powder blasting setup is shown in Figure 3.9. Powder blasting is a recently invented technology, in which small particles are accelerated by an air jet and are directed towards a brittle target for mechanical material removal.

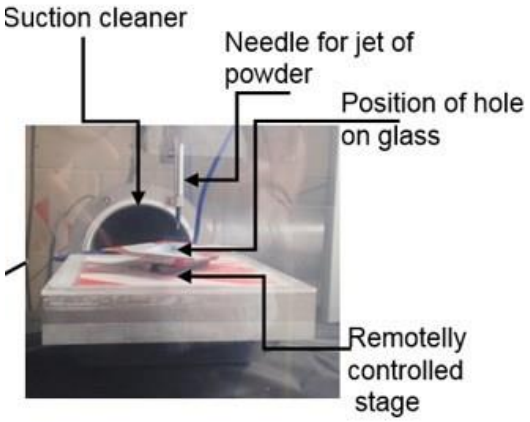

Figure 3. 9 *Test section for local injection of powder with the needle during powder blasting technique for micromachining small size holes on Pyrex glass, located at Heriot-Watt University.*

3.2.3 Housing for the silicon microchannel heat sinks

Connecting microfluidic devices to macro-scale systems presents many challenges. Particular interfaces were used to enable easy fluidic and electrical connections between the microchannel test devices and the flow loops. The silicon microchannels heat sinks were sandwiched between the top cover plate and the bottom frame shown in Figure 3.10a and b. A drawing with dimensions of the top and the bottom frames is shown in Figure 1.A of Appendix A. The bottom frame was fabricated from polyether ether ketone (PEEK plastic) which has a good thermal insulation. PEEK has a thermal conductivity of 0.25 W m^{-1} K^{-1} and a maximum service temperature of 260 °C. The top frame is a transparent acrylic glass with a thermal conductivity of 0.19 Wm K^{-1} and a maximum service temperature of 120 °C.

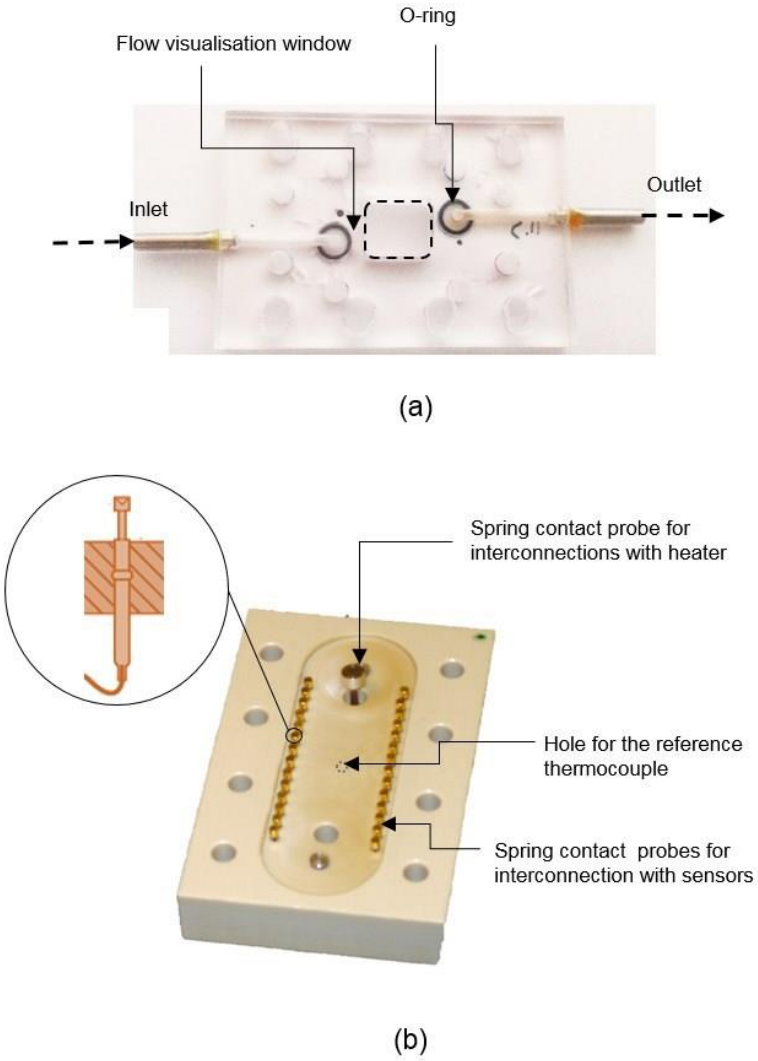

Figure 3. 10 *(a) Transparent cover plate from Plexiglas and (b) bottom frame from polycarbonate block used for the electrical connections.*

These properties ensure that the water flow absorbed most of the heat with a minimal heat dissipated due to conduction. In the top frame, holes for external stainless steel tubes and a square window for visualisation inside microchannels were machined. Water was supplied through external stainless steel tubes, connected to the top frame and the inlet and outlet holes drilled in the Pyrex glass cover plate. Two small O-rings were used to seal the connections between the holes in the top frame and those drilled in the Pyrex glass and prevent any leaks from the heat sink. Electrical connections for the heater and the sensors were made via aluminium pads deposited on the backside of the device and spring probes inserted inside the holes drilled in the bottom frame, Figure 3.10b. The spring probes were connected to data acquisition device (DAQ).

3.2.4 Experimental facility for flow boiling in silicon microchannel heat sinks

The experimental flow loop used for experiments with silicon microchannel heat sinks was originally designed by Bogojevic [98] and was used as a template for the new facility, including a number of changes. The experimental facility is located at the University of Edinburgh. The setup was used for flow boiling experiments with heat sinks of different silicon microchannels aspect ratios and hydraulic diameters. The flow loop was designed to control the liquid mass flow rate, inlet subcooling and saturation pressure. Flow visualisation was also performed simultaneously with pressure and temperature measurements. A test module was also designed to facilitate the silicon microchannels heat sink and allow for the interconnections with macroscale. A schematic of the test flow loop is shown in Figure 3.11. The flow loop is used in order to supply deionised water to the microchannels at the desired subcooling conditions, flow rates and system pressures. Photographs of the experimental facility and the test flow loop are presented in Figure 3.12. A reservoir served as a degassing and condensation chamber during flow boiling experiments. Three immersion heaters with total power of 1500 W were installed inside the reservoir to preheat and degas the water. The heaters were controlled using a PI controller with a K-type thermocouple. The water level inside the reservoir was monitored through a glass tube. Previously, a magnet was used to turn one a series of LED lights by touching the resistors located along the length of the stainless steel tube by floating at the liquid surface. This setup was found to be problematic and unreliable because the magnet was found not to always move on the right location to turn on the LED. Therefore, the stainless steel tube was replaced by a transparent glass tube with specific fittings that fit in the flow loop and to allow for direct visualisation into the water level of the reservoir. A copper coil with a cooling water supply, positioned inside the reservoir, served both as a condenser for vapour generated in the test module and as a regulator of pressure of the flow loop. The desired pressure was obtained by controlling the flow rate of water through the copper coil. A magnetically coupled gear pump (Micropump

GA-T23PFSB) was used to pump the water from the liquid reservoir and circulate it through the flow loop. The pump is capable of generating flow rates from 4.6 to 460 ml min^{-1} of water at a maximum differential pressure of 5.2 bar. A plate heat exchanger with water as a coolant was installed between the reservoir and the pump to prevent pump cavitations. The pump's exit was monitored by a pressure gauge situated immediately downstream from the pump. A 15-µm filter was used to prevent any solid particles from entering the test section. Flow rates were measured by a thermal mass flow meter (Bronkhorst L30 Series) calibrated for the range from 1 to 50 g min^{-1} using water. Subcooling conditions for water were maintained using negative feedback control on a low flow liquid circulation heater (Omega AHPF-122) with a total power of 1200 W. The flow rate through the test section area was regulated using a bypass valve and a fine needle valve located upstream of the microchannel test section area.

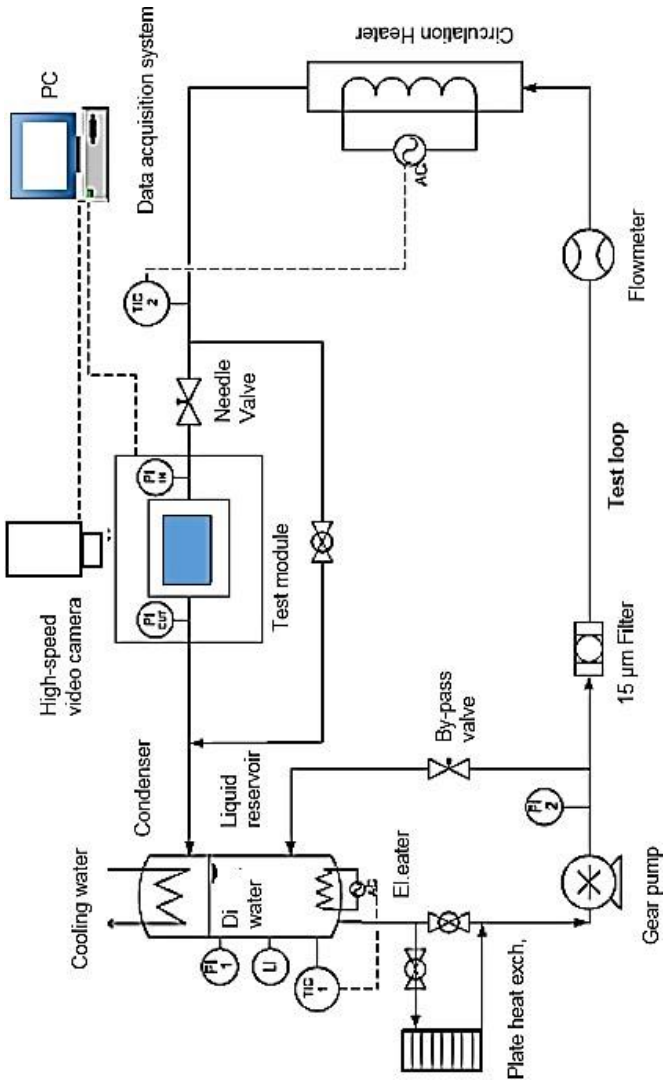

Figure 3. 11 Schematic of the test flow loop1.

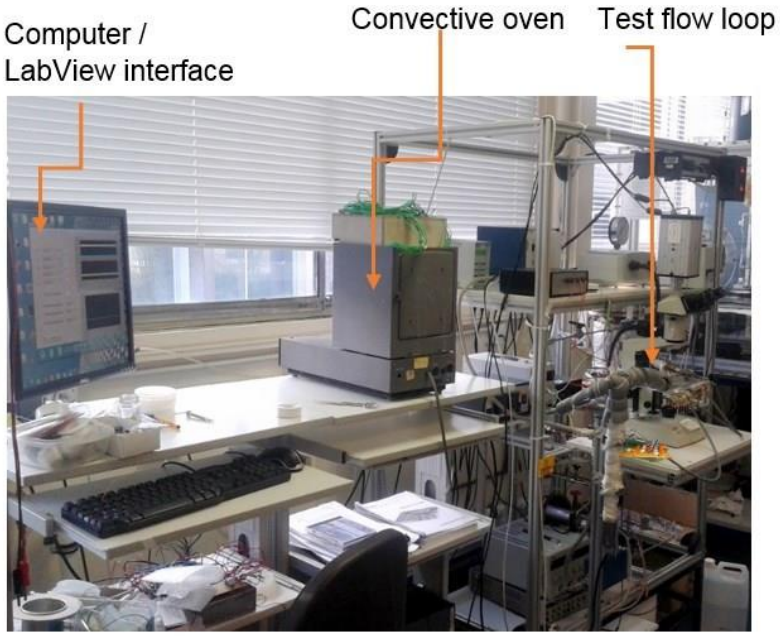

(a)

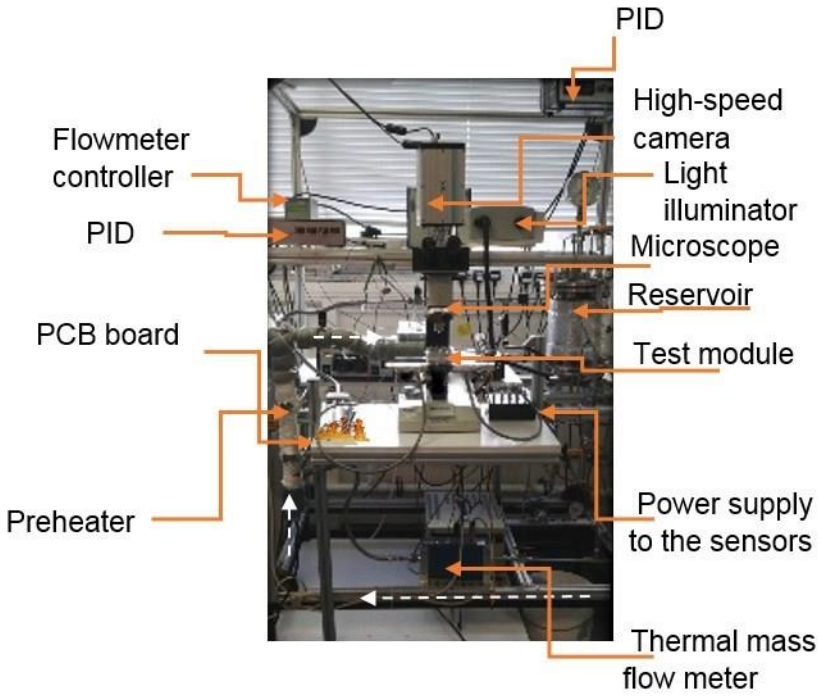

(b)

Figure 3. 12 *Photograph of the (a) experimental facility (b) test flow loop 1 with nomenclature of some of the main devices.*

Flow visualisation of the boiling process within the channels was performed using a high-speed camera (Nano Sense MkII X-Stream™ XS-4), mounted on a microscope with a 5´ magnification objective and axial illumination, as shown in Figure 3.13. Pressure measurements

were acquired simultaneously with fluid temperature measurements at the inlet and outlet of the microchannels and the reference temperature from the microchip base. LabVIEW software used for the acquisition of the results and the interface is provided in Figures A.6 and A.9 of Appendix A. The camera's maximum frame rate is 5,130 fps at full resolution of 1280 × 1024 pixels. The minimum exposure time of the camera was 1 μs. Flow boiling experiments are conducted in order to investigate the effect of aspect ratio on flow boiling heat transfer for varying mass flux from 29.2 to 1600 kg $m^{-2}s^{-1}$ and constant heat fluxes of 151, 183, 271 and 363 kW m^{-2} at the inlet temperature of 25 ˚C and 81 ˚C.

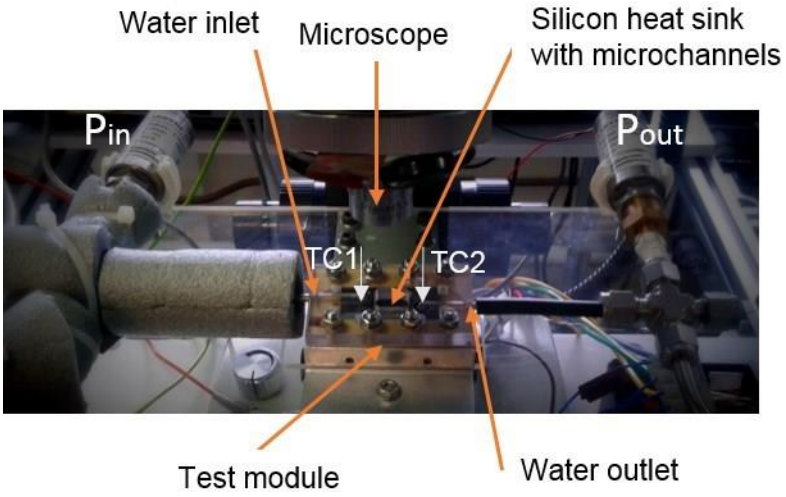

Figure 3. 13 *Test module, fluid thermocouples and pressure transducers located before the test module (, TC1) and after the outlet of the test module (P_{out}, TC2).*

3.2.5 Data acquisition system and measurement uncertainties

The voltage-temperature relationship of each Ni sensor was calibrated before each experiment in order to obtain the relationship between them. The calibration was achieved by placing the assembled device, consisting of the microchannels device sandwiched between the cover plate and the bottom frame, into the convective oven shown in Figure 3.14. Schematic drawings of the cover plate and the bottom frame are shown in Figure A.5 of Appendix A. Both cover plate and the bottom frame are fabricated from Plexiglas which has a thermal conductivity of 0.20 W m K^{-1}. The top frame has a service temperature of 160 ˚C and is transparent. The top cover plate was fabricated from transparent Plexiglas and was screwed down to the bottom case to enable good electrical contact between the temperature sensor pads with the spring probes, as shown in Figure 3.15. Calibration with the convective oven was also used in a study of flow boiling conducted by Chen and Garimella [118]. Three T-type thermocouples (TC1, TC_{ref} and TC2) were used to obtain temperature measurements at the top and bottom surface of the silicon

microchannel heat sink respectively. The thermocouples were first calibrated using a thermocouple calibrator of accuracy of ± 0.01 °C at the full range from 25 ˚C to 150 ˚C. The thin Ni film temperature sensors were calibrated using a reference T-type thermocouple to characterise the temperature-resistance relationship. The accuracy related to the thermocouples measurements was ± 0.5 ˚C. Figure 3.15 shows that one of the thermocouples was used to measure the temperature inside the oven (TC1) and the other two thermocouples were used to measure the temperature on the top-surface (TC_{ref}) and the underside of the chip (TC2). The T-type thermocouples were connected to the data acquisition system (USB-2523) and the temperature values were logged in using the LabVIEW software. Two pads from each sensor were used for an independent current source providing 0.5 mA constant current and another two pads were utilized for the measurements of the voltage across the sensor using a DAQ system.

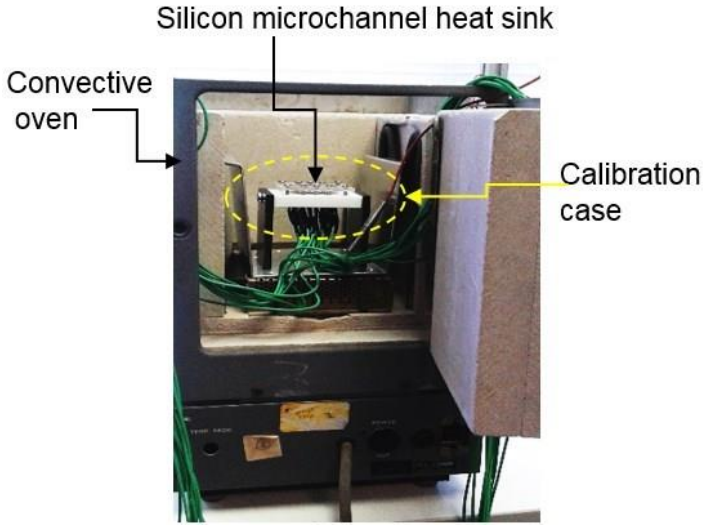

Figure 3. 14 *Convective oven used for the calibration of the thin film Ni temperature sensors integrated into the microchannels heat sink.*

Once a stable temperature was achieved in the oven by maintaining constant temperature, the resistance of each sensor was recorded as a function of the temperature (TC_{ref}) from the top surface of the silicon microchip, while TC1 and TC2 were used in order to examine the temperature uniformity of the oven and the heat sink. The recorded temperatures of all the five temperature microsensors for one of the microchannels heat sinks are plotted as a function of resistance in Figure 3.16. The accuracy of the temperature measurements was within ± 0.23 ˚C. The resistance was determined from the measurements of the voltage and constant current and converted to corresponding temperature using the temperature vs electrical resistance function

obtained from calibration. The liquid temperature at the inlet of the microchannel heat sink was maintained within ± 1 °C.

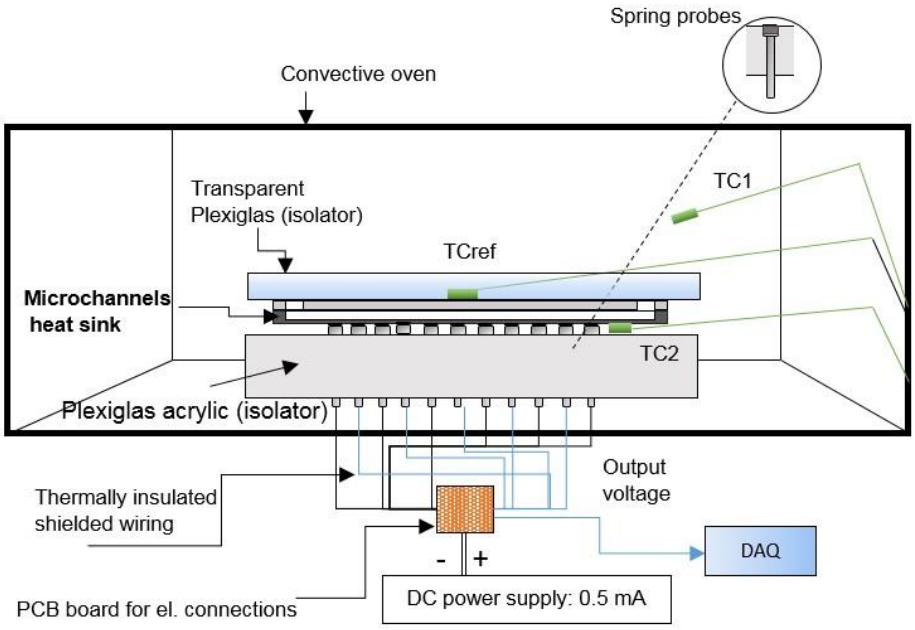

Figure 3. 15 *Side view of the calibration assembled device. The microchannels heat sink is mounted between two Plexiglas frames and the sensor pads are connected to the power supply and the data acquisition device. TC1, TC_{ref}, TC2 are the three K-type thermocouples.*

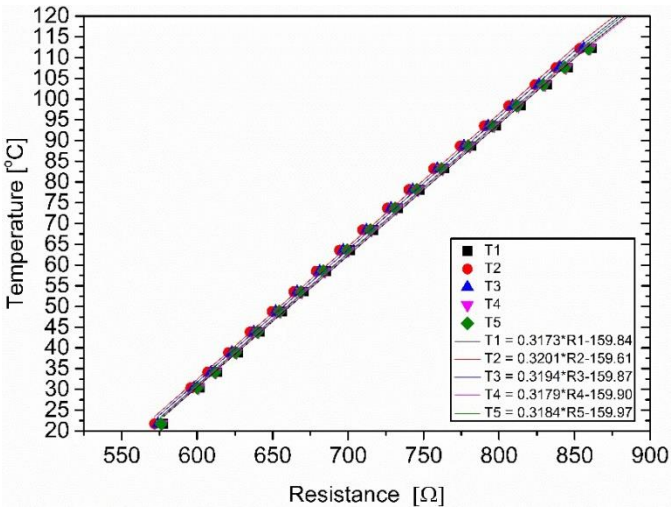

Figure 3. 16 *Calibration curve of temperature sensors*.

All the temperature sensors were found to have on average, a typical sensitivity of 3 ± 0.25 mV/°C. The temperature measurements accuracy was ± 0.25 °C, using the employed acquisition system. The thermal time constant associated with the Ni film temperature sensors was 1.6 $\times 10^{-4}$ s. The temperature measurements and pressures were recorded at 500 and 250 Hz.

Figure 3.17 presents a diagram the electrical connections of the five temperature sensors and thermocouples with the power supply and the data acquisition system. A constant DC current of 0.5 mA is supplied to each of the temperature sensors using independent 9V batteries. The temperature sensor can therefore be considered as ungrounded (floating) differential signal with a voltage output from 0–1 V. It is important that the input impedance of the DAQ device is much higher relative to the output impedance of the selected transducer. Impendence is a combination of resistance, inductance and capacitance across the input or output terminals of the circuit. In general, the higher the input impedance of the DAQ device the less the measured signal will be disturbed by the DAQ device. It is also important to select a sensor with as low output impedance as possible to achieve the most accurate analogy input (AI) readings by the DAQ device. The output of the sensor is directly connected to the DAQ where the signals are recorded and monitored. In order to minimize electrical interference, shielded cables were used for the electrical connections. In particular, the output signal is converted to temperature using equations 3.1 to 3.5 shown in Figure 3.17 which are extracted during the calibration process.

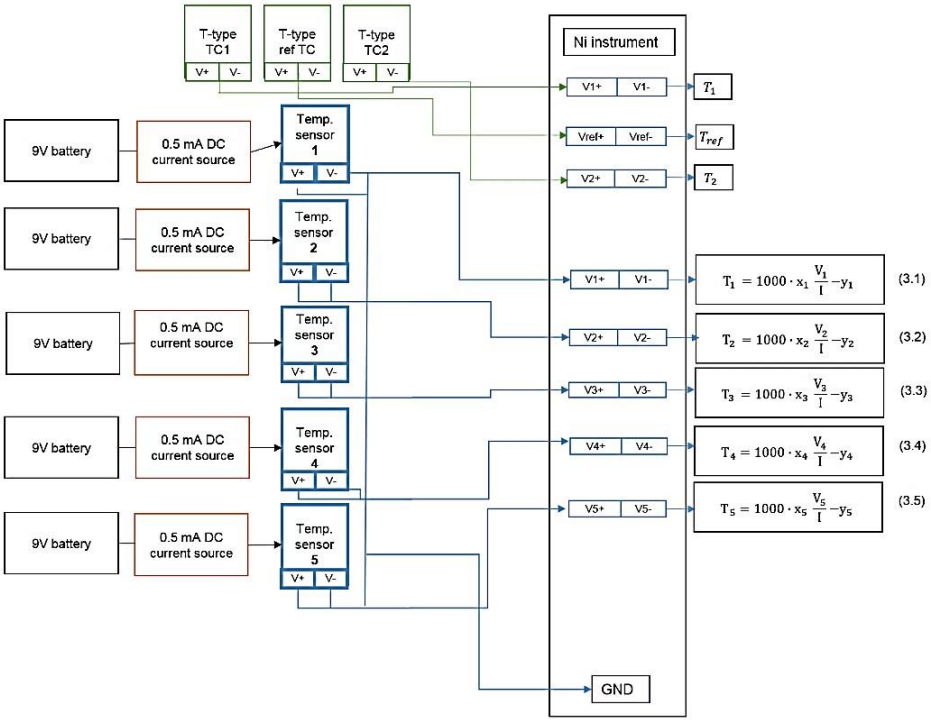

Figure 3. 17 *Diagram of electrical connections to the temperature sensors. The power supply connections appear on the left side and the connections to the data acquisition device on the right side.*

Figure 3.18 is a photograph of the printed circuit board (PCB) interface designed to facilitate the electrical connections of the temperature sensors. The PCB board was fabricated in order to simplify the procedure of plugging in the cables. The PCB board ensures the minima

losses and provides a good shield from noise. The PCB board was fabricated in order to make the plug in of cables easier. Table 3.2 provides the measurement uncertainties of the devices used in the experiments.

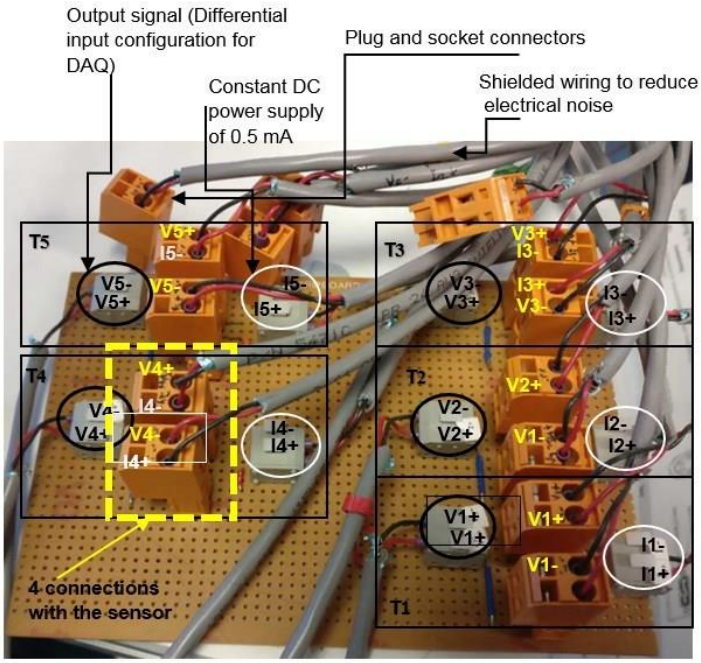

Figure 3. 18 *Photograph of the printed circuit board (PCB) for electrical connections of the temperature sensors and the acquisition of their output response.*

Table 3. 2 *Measurement uncertainties.*

Measurements	Device	Units	Uncertainty
P	Pressure transducer	bar	0.25 %
TC_1 liquid	Thermocouple	^{o}C	± 0.5 ^{o}C
TC_2 liquid	Thermocouple	^{o}C	± 0.5 ^{o}C
TC_{ref}	Thermocouple	^{o}C	± 0.5 ^{o}C
T_w at position1,2,3,4,5 on the bottom of the channels	Thin nickel integrated sensors (calibrated for each chip)	^{o}C	± 0.5 ^{o}C
Q	Thermal mass flow meter	g min^{-1}	±0.5
Flow Rate (Pump)	Micropump	ml min^{-1}	±0.2
Input Power	Multimeter	W	0.9 %

3.3 Polymethylsiloxane (PDMS)-based microchannel device, microfabrication and experimental facility

3.3.1 Design of a single Polymethylsiloxane (PDMS)-based microchannel device

A high aspect-ratio ($a = \frac{W_{ch}}{H_{ch}} > 20$), rectangular cross-section (width (W_{ch}) = 2.26 mm, height (H_{ch}) = 100 µm and length (L_{ch}) = 20 mm) polydimethylsiloxane (PDMS)-based microchannel, with a hydraulic diameter (D_h) of 192 µm, was designed. A photograph of the PDMS microchannel device is displayed in Figure 3.19. Figure 3.19 shows the transparent high aspect ratio PDMS microchannel device with the dimensions of the channel used for the flow boiling experiments. The bottom surface is the ITO/glass and the top surface is the PDMS. The microchannel has a high confinement number of $Co \approx 4.38$ that allows to investigate the confinement effects during flow boiling in a microchannel. The backside of the 0.17 mm thick microscope glass slide (22 × 50 mm^2) was coated with a 200 nm conductive, transparent thin film of indium tin oxide (ITO), deposited using magnetron sputtering, to facilitate the heating of fluid in the channel. Table 3.3 summarises the dimensions of the different parts that comprise the PDMS microchannel device.

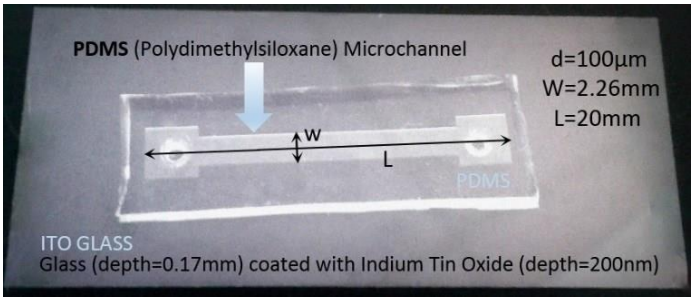

Figure 3. 19 *PDMS microchannel, bonded to ITO coated glass.*

Table 3. 3 *Characteristic dimensions of the different components of the microchannel device.*

	H_{ch} [µm]	W_{ch} [mm]	L_{ch} [mm]
Microchannel	100	2.26	20
ITO layer	200 ×10^{-6}	22	50
Glass	0.17	22	50
PDMS substrate	1-2	8	40

3.3.2 Microfabrication of Polydimethylsiloxane (PDMS) microchannel

For the purpose of this work, polymethylsiloxane was used to fabricate single microchannels with a high aspect ratio rectangular cross section. PDMS is the most commonly used polymer in recent years for rapid prototyping and microfluidic applications. It is easy to use for fabrication of microfluidic devices with casting and curing procedures. It is an inexpensive material, which is transparent to both the mid-infrared spectrum and the visible spectrum. The transparency to infrared radiation of the PDMS wall allows for synchronous inner wall temperature measurements and optical visualisation.

Two miniature piezoresistive pressure sensors were integrated close to the inlet and outlet of the microchannel in order to measure the local pressure drop in the microchannel during flow boiling conditions. Two types of pressure sensors were utilized for the study of flow boiling. Piezoresistive NPP-301 series pressure sensors were for the flow boiling experiments discussed in chapter 5. New higher sensitivity pressure sensors were integrated in the microchannel and used for the experiments carried out in chapter 6. Table 3.3 below presents the basic specifications for the NPP-301 Series pressure sensors.

Table 3. 3 *Basics specifications for NP-301 series pressure sensors.*

Parameter	**Value**	**Units**
Pressure range	100, 200, 700	kPa
Maximum pressure	3 × rated pressure	kPa
Excitation	3	V
Input impedance	5,000 ± 20%	Ω
Output impedance	5,000 ± 20%	Ω
Electrostatic damage (ESD)	Class 1	
Operating temperature	-40 to 125	^{o}C
Weight	0.1	G
Offset	10	mV/V
Full scale output	60 ± 20	mV
Linearity	± 0.2	% FSO
Hysteresis &Repeatability	0.1	% FSO
Thermal coefficient of resistance	0.3	% / ^{o}C
Thermal coefficient of Sensitivity	-0.2	% FSO/ ^{o}C
Thermal hysteresis of zero	0.1	% FSO
Long term stability of FSO	0.2	% FSO

The size of the pressure sensor hole is 2.03 mm in diameter. The width of the chip is 4.1 mm and the length is 5.1 mm without the legs for the cable attachment. Figure A.3 of Appendix A provides analytical schematic drawing of the pressure sensor with dimensions. Figure 3.18 shows the PDMS microchannel with the two integrated pressure sensors and the location of the pressure sensors at the inlet and outlet.

Figure 3.20 presents the diagram of the circuit of the piezoresistive pressure sensor. In resistive sensors, pressure changes the resistance by mechanically deforming the sensors, enabling the resistor in the bridge circuit to detect pressure as a function of differential voltage across the bridge. Piezoresistive pressure sensors also operate with the aforementioned resistive principle. The resistance change in monocrystalline silicon semiconductor is higher than in standard strain gauges, where the resistance changes with geometrical changes in the structure. The advantage of using doped semiconductors is their high sensitivity, which results from their ability to detect extremely small mechanical deformation because of compression or stretching of the crystal grid.

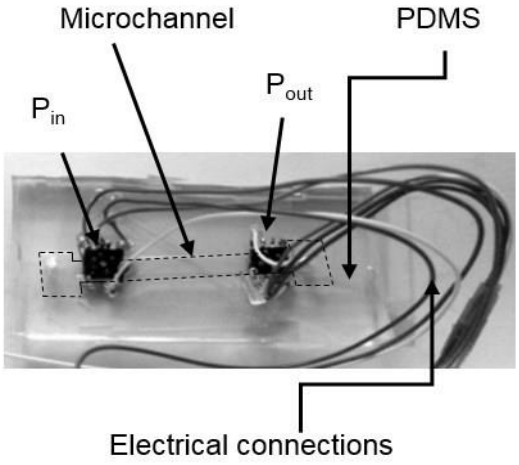

Figure 3. 20 Photograph of a PDMS microchannel with the two integrated NNP-301 series piezoresistive pressure sensors at the inlet and outlet.

Figure 3.21 shows the piezoresistive pressure sensor during trial tests with the connections of the PCB circuit. The pressure sensors (NPP-301 series) were coated with Parylene before the integration into the channel. Parylene was used a as a passivation layer in order to protect part of the chip in contact with the liquid as these sensors were not recommended for use with liquids. The next step was soldering special thin flexible cables to the legs of the sensors. Each sensor consisted of one positive and one negative voltage input, connected to the power supply and two outputs connected to the data acquisition system in order to obtain measurements. The sensors were also connected with a ceramic capacitor of 100 μF. Two 3V batteries were used to supply

DC current to each pressure sensor. The output signal of the sensors was measured in the range of 20 to 100 µV.

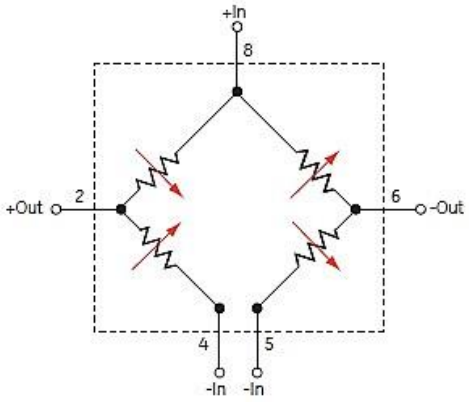

Figure 3. 21 *Schematic diagram of the circuit, of NPP-301 series pressure sensor.*

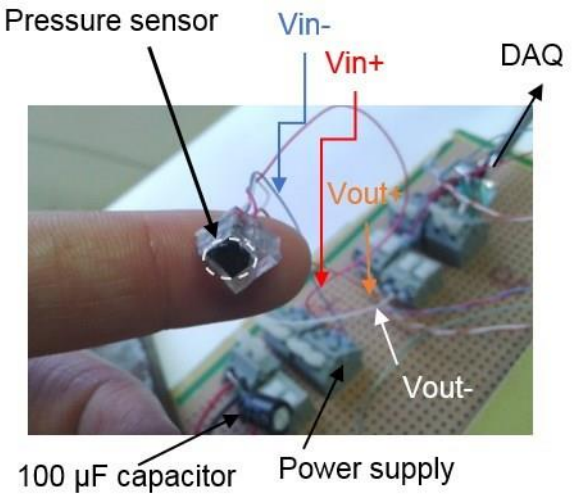

Figure 3. 22 *Pressure sensor and electrical connections.*

For the next set of experiments, the NPP-301 series sensors were replaced with Honeywell Trustabilty pressure sensors. These sensors have a measurement range of 0-1 bar and were capable of making higher resolution measurements when integrated into the channel. These pressure sensors where highly compatible with non-corrosive liquids, as opposed to the previous sensors that were not recommended for use with liquids. The Trustability sensor is displayed in Figure 3.23. Two pressure sensors were again integrated near the inlet and outlet of the channel. 3.3 VDC was supplied to the sensors using four batteries. The typical response time of the pressure sensors is 1 ms. The accuracy of the sensors is ± 0.25 % FSS (Full-scale span). Full-scale span is the algebraic difference between the output signal measured at the maximum

pressure (P_{max}) and minimum (P_{min}) limits of the pressure range. The circuit board (PCB) for electrical connections is presented in Figure 3.24 and it was used to facilitate electrical connections for both pressure sensors.

Figure 3. 23 *Honeywell pressure sensor HSC Series True Stability.*

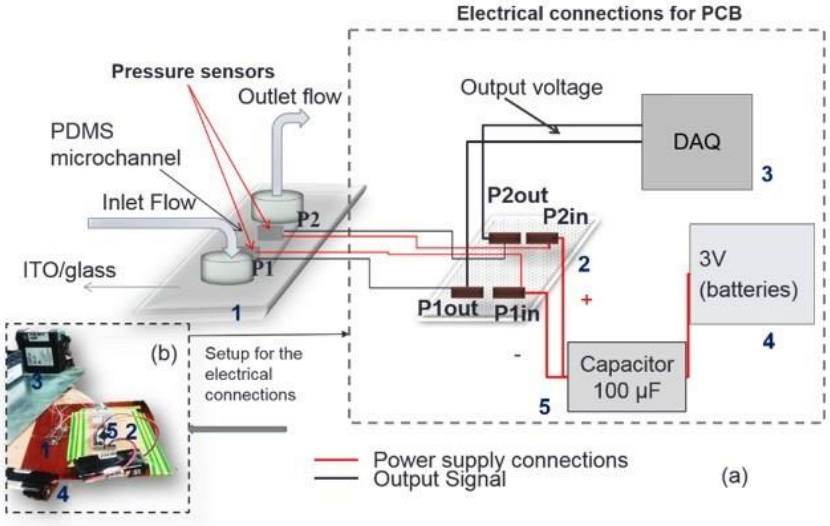

Figure 3. 24 *Analytical graph of the electrical connections of the pressure sensors with the circuit board.*

The following is a brief discussion of the microfabrication steps of single PDMS microchannel with integrated pressure sensors in the inlet and outlet. Figure 3.25 shows the steps of channel microfabrication and integration of the pressure sensors A mould of the rectangular single-microchannel is fabricated by spin coating 100 µm of SU-8 photoresist on a Si wafer (Figure 3.25a) and the resist is exposed through a photomask resist (Figure 3.25b). The parts of SU-8 that are exposed to UV light stay in negative The resulting SU-8/Si mould has microscale resolution and therefore a channel can be produced that closely mimics the shape of one etched in Si. PDMS used for the devices is a 10:1 mix of Sylgard 184 silicone elastomer and cure (Dow Corning). The mixture was poured over the SU-8 mould (Figure 3.25c) and a pair of dummy sensors are placed in the wet PDMS (Figure 3.25d). These dummy sensors are used to create a cavity in which to put working sensors. The dummy sensors are then removed (Figure 3.25e) and

when the PDMS has cured they are replaced with the working sensors (Figure 3.23f), which each have 3 attached wires for connecting to the power supply and a data acquisition system. A second layer of PDMS is poured (Figure 3.25g) and cured, to create an airtight seal. After curing, the PDMS was peeled off carefully from the mould (Figure 3.25h). Inlet and outlet holes of 2 mm diameter were punched into the reservoirs using biopsy puncher to define the inlet and outlet for fluids. Then, the bottom of the channel was plasma treated [126] following oxygen plasma activation and bonded to a glass slide that is coated in indium tin oxide (ITO) and serves as the heater (Figure 3.25i). Plasma activation causes the PDMS surface to reorder so that it has -OH groups oriented at the surface and these can bond easily to glass to create a tight seal. Analytical steps of the fabrication are detailed in Table 3.4.

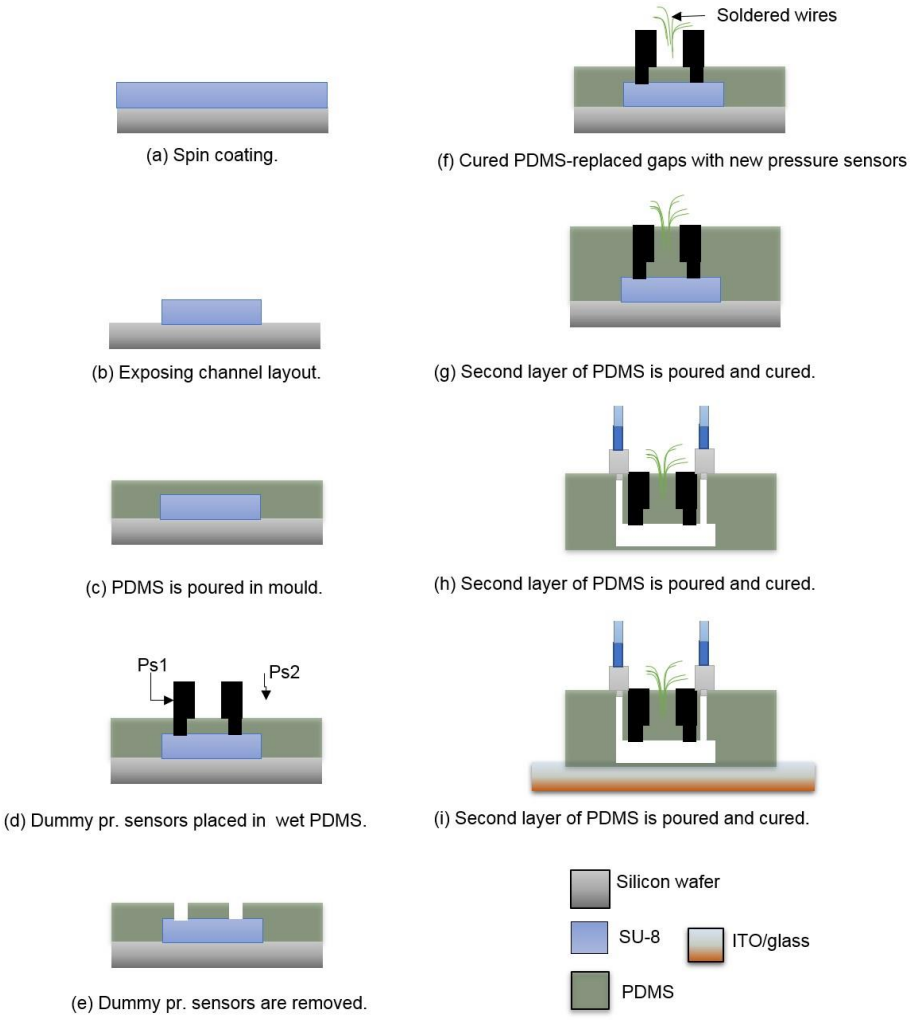

Figure 3. 25 *Schematic view of integration steps of the piezoresistive pressure sensors in the PDMS microchannel near the inlet (P_{s1}) and the outlet (P_{s2}).*

Table 3. 4 *Analytical steps for PDMS cross-linking process.*

Step	Description	Recipe- Parameters
1	Mix PDMS with curer	Sylgard 184 elastomer with Curing agent, 10:1 ratio
2	PDMS outgassing	1 hour
3	Moulding	Pour into SU-8
4	PDMS out gassing 2nd time	1 hour
5	Curing	overnight at 60 ˚C
6	Peel off	

3.3.3 Indium tin oxide (ITO) film characteristics

The optical transmittance of ITO films can be affected by surface roughness and optical inhomogeneity in the direction normal to the film surface. Annealing results in near single crystal ITO with uniform grain size, which leads to increased conductivity. The thermal conductivity of ITO films ranges from 11 to 12 W $m^{-1}K^{-1}$ [127]. The resistivity of ITO decreases with annealing at temperatures in excess of 100 ºC. This is advantageous to reduce the resistance as the power required to produce a desired heating effect is reduced relatively. Pre-annealed ITO coated glass with sheet resistance of 115 Ω sq^{-1} was compared with post-annealed ITO coated glass of resistance of 26 Ω sq^{-1}. Annealing reduced the sheet resistance of the thin films used in these devices from 115 Ω sq^{-1} to 26 Ω sq^{-1} because it requires less power to resistively heat to a given temperature. The emissivity of the indium oxide films is found to increase with the sheet resistance [128].

Wall temperature measurements with an infrared camera were carried out across the whole microchannel in order to evaluate the ITO/glass heating uniformity. The IR camera measured the two-dimensional wall temperature map with increasing power without any liquid in the microchannel. Input power was increased from 0.1 to 1.62 W. A linear relationship was established between the input power and spatially averaged wall temperature measurements using infrared thermography, shown in Figure 3.26. Figure 3.27 shows the wall temperature measurements obtained by infrared camera for both 1 mm and 0.17 mm thick glass as function of

input power. At 1 mm thickness it was found that higher input power was required to generate a given wall temperature, relative to 0.17 mm.

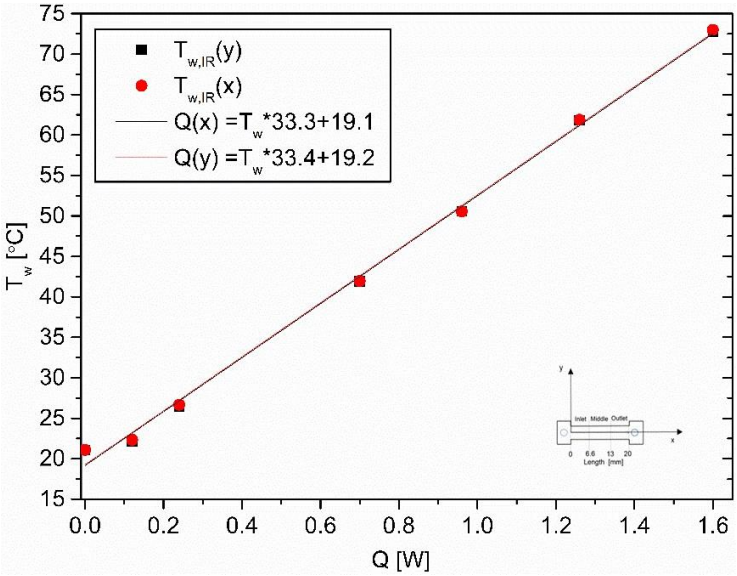

Figure 3. 26 *Channel wall temperature measured with IR as a function of input power without liquid in the microchannels.*

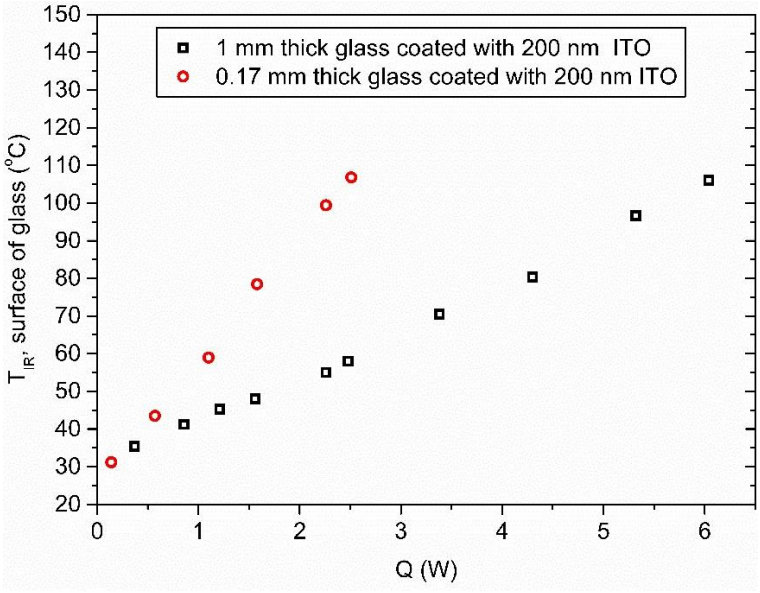

Figure 3. 27 *Glass wall temperature measured with IR camera for both 1 mm and 0.17 mm thickness glass as function of input power to ITO film of 200 nm thickness.*

3.3.4 Surface emissivity measurements of ITO coated glass and PDMS for infrared thermography

In order to measure the temperature of the surface of a grey object by infrared thermography, it is necessary to know the surface emissivity of the examined object. The total energy emitted by a grey body (ε = 0.80) is equal to the energy emitted by a black body at the same temperature multiplied by the emissivity. The emissivity of ITO/glass (annealed or non-annealed) as well as PDMS was measured following the calibration method followed by Madding [129]. Figure 3.28a shows the calibration setup for the emissivity measurements. High emissivity ($\varepsilon_{paint} = 0.95$) black paint is applied to a copper block (8 mm × 4 mm × 1 mm) to be used as blackbody radiator.

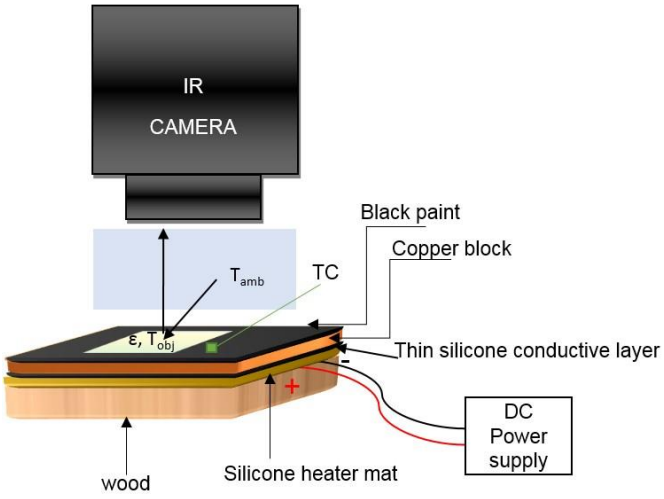

(a)

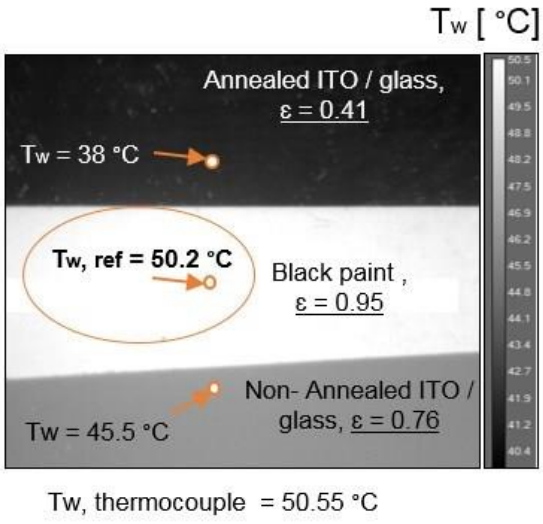

(b)

Figure 3. 28 *(a) Setup for calibration of surface emissivity and (b) thermal image from the IR used to measure the emissivity of ITO coated glass and annealed ITO coated glass in reference to the emissivity of the black paint.*

The copper block then was attached to a silicon heater mat (8 mm × 4 mm) via a very thin electrically conductive silicone sheet (8 mm× 4 mm × 1.6 mm). The silicon heater mat was then attached on a wooden block (8 mm × 4 mm × 2 mm). The conductive thin layer of the silicone sheet ensured a good electrical contact. The sample was placed onto the painted copper block using thermal adhesive tape. Then the IR camera lens should be adjusted to a distance of 30 ± 1 cm from the surface of the black paint in order to be able to measure the temperature on this surface. The silicon heater was connected with a DC power supply and as the power was increased, temperature measurements were made by capturing thermal images with the IR camera. A K-type thermocouple was attached to the sample surface in order to validate the temperature measurements obtained from the IR camera. The maximum difference between the thermocouple and the measurement from the IR camera was 0.25 ºC. Figure 3.26b shows the thermal image used to obtain emissivity measurements for a constant power. The thermal image shows the differences between wall temperature of annealed ITO/glass, black paint and non-annealed ITO/glass. For this specific power, the temperature of the black paint, $T_{w,\,\mathrm{IR}}$ = 50.2 ˚C was used as a reference for calibration because black paint has the highest emissivity and the value is similar (± 0.2 ˚C) with measurement obtained from the thermocouple. The emissivity of the other two materials was corrected until their temperature values were equal to $T_{w,\,\mathrm{IR}}$ = 50.2 ˚C. The calibration was achieved using the IR Research software. The two ITO/glass slides were placed on the black paint. The temperature for the annealed ITO/glass was 38 ˚C and for the non-annealed, 45.5 ˚C. The temperature values from the ITO coated glass surfaces were lower than the temperature from the black paint. This occurs because the radiation received by the IR camera is less than the one from the blackbody at the same temperature and so the surface will appear colder than it is unless the IR camera reading is adjusted to take into account the material surface emissivity. The surface emissivity measurements for the annealed ITO/glass and non-annealed ITO/glass were found to be 0.46 and 0.76 respectively after the calibration to the reference temperature. The same process was repeated for increasing power input at higher surface temperatures.

Figure 3.29 shows the emissivity measurements as a function of surface temperature for the temperature range of 38-75 °C for the annealed ITO coated glass, non- annealed ITO coated glass and PDMS. The measured emissivity for the annealed ITO/glass was lower than the emissivity of the non-annealed ITO/glass (Figure 3.29).The emissivity value of non-annealed ITO/glass was roughly constant with temperature. From the experimental results, the estimated average emissivity of value over temperature for the non-annealed ITO/glass is 0.76 (Figure 3.29).This means that 76 % of the ITO/glass surface behaves as a blackbody. The transparency of the substrate was calculated to be 0.80 ($\varepsilon_{ITO}/_{paint}$). The emissivity error is 0.1 for every degree of

temperature increase. PDMS averaged emissivity was calibrated with the same procedure and it was measured to be 0.88, averaged value among the values obtained at different power levels, as shown in Figure 3.29.

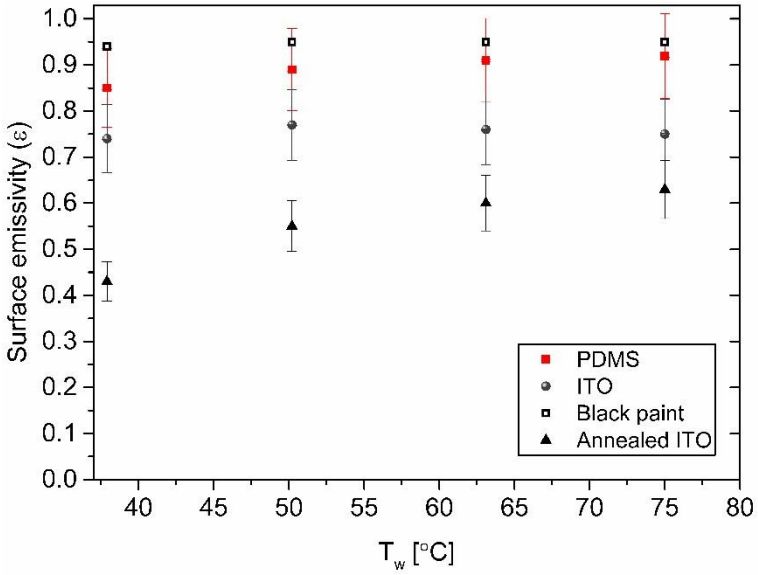

Figure 3. 29 *Averaged surface emissivity of non-annealed ITO glass.*

3.3.6 Determination of the "penetration depth" for interfacial wall temperature measurements

Light that is transmitted through the PDMS is attenuated as it passes through. The rate of absorption is proportional to the intensity for a given wavelength. "Penetration depth" describes the decay of electromagnetic waves inside of the material. It is important to know the value of the absorption coefficient of FC-72 in the tested IR midwave range in order to understand if the temperature measurements from the PDMS side are near the side of the wall in contact with the fluid (wall interface) or the bulk fluid temperature. For example, water is characterized by a high absorption coefficient, which means that using low liquid thickness from 4 to 40 μm it is feasible to obtain the bulk fluid temperature. On the contrary, FC-72 liquid film is required to have higher thickness, in the range of ~ 150 - 1000 μm in order to allow for measurements in the liquid because it has a low absorption coefficient [111].

Figure 3.30 shows interfacial wall temperature measurements obtained at the liquid-solid interface from the PDMS side, which is transparent to IR midwave range. The measurements were obtained at the vicinity of the wall and they were assumed to be averaged across the channel depth, as it is only 100 μm. The effective transmissivity of liquid decreases with increasing film thickness and the system becomes opaque at large thicknesses (see eq. 2.28). From the Beer

Lambert law (eq. 2.28) increasing film thickness results in increasing absorption. In our case, 100 μm (channel depth) was the maximum liquid film thickness of FC-72 at single-phase, therefore the liquid was considered as semi-transparent (< 5 mm liquid thickness [104]). The liquid layer from the literature is considered 'optically thick' when it exceeds 5 mm. FC-72 is semi-transparent to the infrared wavelength of 3 - 5 μm. Because of the thin heating wall of glass, the axial conduction is restricted therefore; the heat losses are not high.

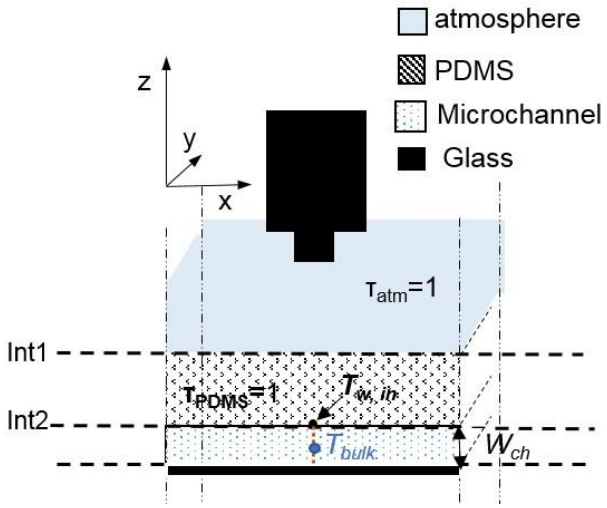

Figure 3. 30 *Schematic of the interfacial wall temperature measurement obtained from the PDMS side using an infrared camera.*

The transmittance is related to the optical depth. The monochromatic absorption coefficient of FC-72, at the midwave spectral range of 3-5 μm was found to be k =1.98 mm^{-1} at 25 ^{o}C [130]. k was calculated using the known global emissivity ε= 0.18 of FC-72 (using eq.2.10 and 2.11) of FC-72, experimentally measured by Brutin *et* al. [121], at the optical thickness of 0.1 mm using the Beer-Lambert Law for the emissivity (Figure A.2, Appendix A). Brutin *et* al. [121] measured the global emissivity of FC-72 as a function of the fluid optical in a wavelength of 3-5 μm. The results were experimentally obtained at T_{amb} = 25 ^{o}C and with fluid optical thickness uncertainty of 40 μm. The characteristic penetration depth was then calculated to be 0.52 mm as measured from eq. 2.11. These results in the conclusion that the penetration length magnitude is lower than the desired value, therefore the measurement that is obtained is from the channel inner wall and not the liquid bulk temperature. During evaporative cooling applications the bulk liquid temperature is higher than the interfacial temperature ($T_{w,}$) because surface evaporation occurs and $T_{bu} > T_{w,in}$. If the working liquid is transparent to IR radiation, then the IR camera will capture the fluid $T_{bulk.}$ It is assumed that the interfacial wall temperature is averaged along the channel depth, as the temperature change along the z -axis cannot be measured.

3.3.7 Interface connections and housing for the PDMS-based microchannel

Common systems to connect microfluidics devices with other equipment typically use commercial connectors, which are not always compatible with the dimensions of the device. For the purpose of this study, customised male adapters were used, as shown in Figure 3.31.

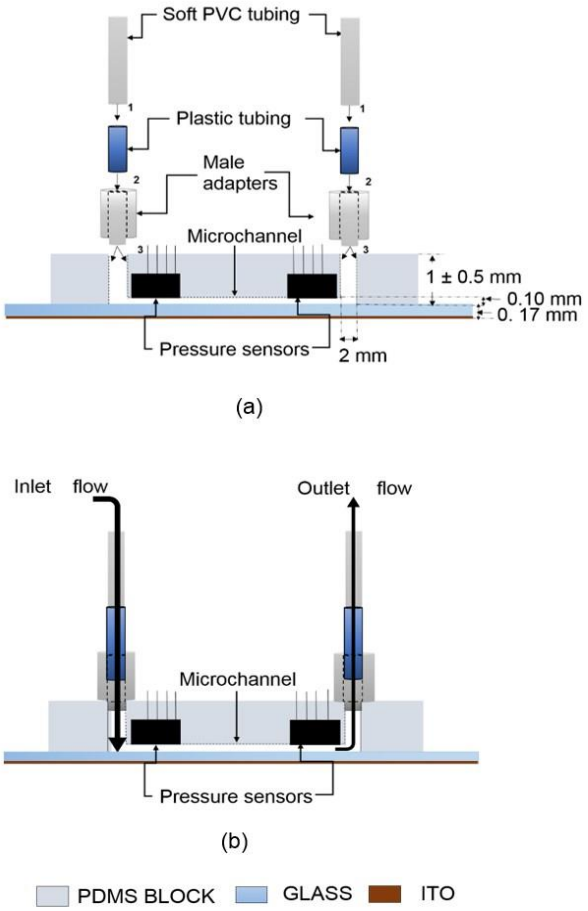

Figure 3. 31 *PDMS device (a) before the microfluidic connections and (b) after the microfluidic connections have been done.*

The adapters were fabricated from transparent Plexiglas in order to fit in the inlet and outlet 2 mm holes located in the centre of the inlet and outlet reservoirs of the PDMS microchannel. Strong bonding between the adapters and the PDMS was achieved by using a Loctite type super glue. Plastic tubes were inserted in the connectors and rubber tubing was then connected to the stainless steel connectors used in the flow loop system. The maximum liquid flow rate that was tried using deionised water was 5 ml min^{-1}, beyond this limit it is possible for the PDMS/glass bond to fail. The effective area of the ITO/glass was 2.26 × 20 mm^2. The single sided copper board depicted in Figure 3.29a served only to hold the device and to provide the electrical contacts to the ITO heater. It had a cut-away section underneath the channel. The liquid in the channel was

heated by passing a DC current through the ITO film via contacts with two copper tracks. During heating of the liquid in the channel, a spatial map of the wall-temperature is recorded from the glass side of the device using a FLIR X6580 SC high-speed infrared camera of 20 mK thermal sensitivity at a high resolution of 640 × 512 pixel (representing 15.39 µm/pixel) and a high frame rate of 200 Hz. The spectral range of the camera was 1.5 to 5.1 µm and the detector pixel pitch was 15 µm. The housing of the transparent PDMS microchannel device consisted of an acrylic transparent cover that holds the device in place. Then the ITO/glass side is attached on the copper surface of the PCB support .A schematic view of the microchannel heat sink section is presented in Figure 3.32a. There is a window that allows for flow visualisation through the microchannel underside.

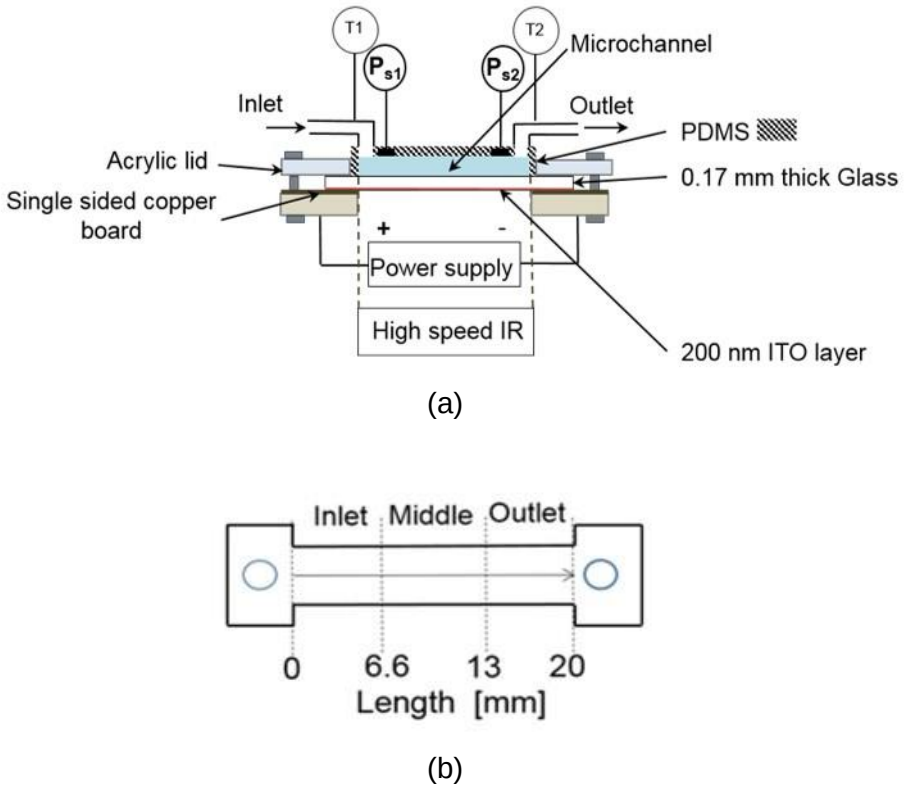

Figure 3. 32 *Schematic drawing of (a) housing with the PDMS microchannel which consists of a microchannel with integrated pressure sensors (P_{s1},P_{s2}) and its support (b) the three measurement sections along the microchannel.*

Fluid temperatures were measured using two K-type thermocouples (TC1, TC2) and recordings synchronised with pressure measurements were recorded at both the inlet and outlet of the microchannel. The field of view of the IR camera could not capture the whole microchannel surface and therefore the microchannel was divided into three measurement sections, that were examined separately as shown in Figure 3.32b. FC-72 was circulated at the desired subcooling

conditions, flow rates and system pressures. A syringe pump was required to deliver the liquid to the channel. Figure 3.33 shows a top view of the PCB board used to power the heater.

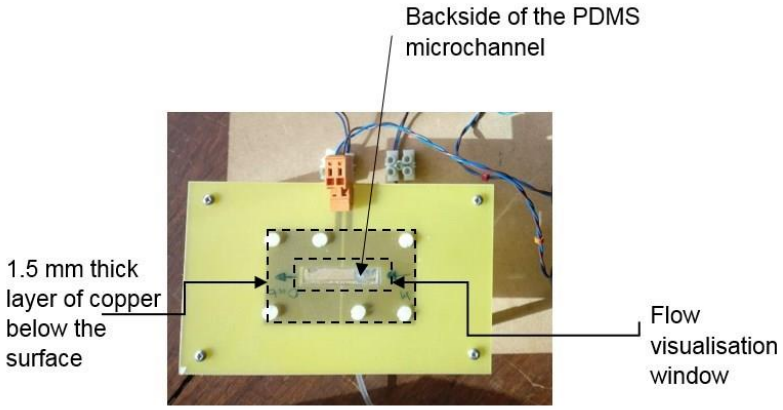

Figure 3. 33 *Top view of PCB board base for electrical connections to the heater. The flow visualisation window has optical access to the ITO / glass base of the microchannel.*

Figure 3.34 indicates the interface (dotted line) at which wall temperature measurements were recorded for both the case of the where IR measurements were carried out from the heater side and the case where the IR camera recorded the wall temperature from the PDMS side. From the ITO coated glass microchannel base, two-dimensional high spatial and temporal resolution 15 µm/pixel and 200 fps temperature measurements were achieved from the channel wall.

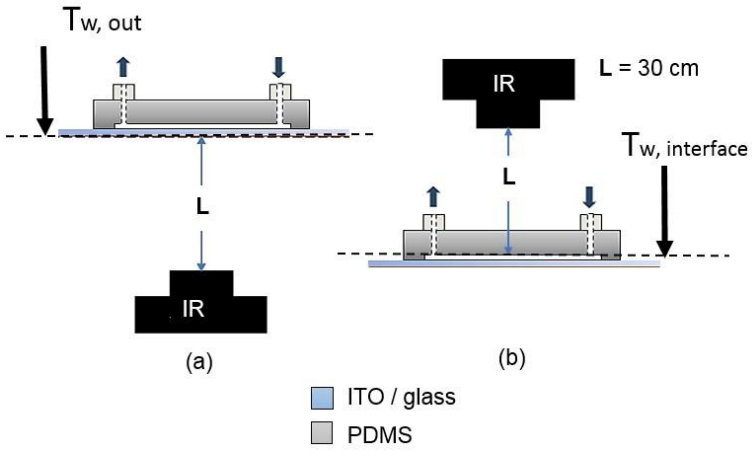

Figure 3. 34 *Two different types of temperature measurements using infrared thermography technique used in this study, where the camera examines the wall temperature (a) from ITO/glass side (channel base) and (b) from PDMS side, interfacial wall temperature measurements.*

3.3.8 Experimental facility for transparent PDMS –based microchannel device

An experimental stand (flow loop2) was built in order to facilitate infrared (IR) thermography experiment with simultaneous flow visualisation. High spatially and temporally resolved local temperature distributions from the inner and outer wall of the transparent microchannel were obtained using IR thermography technique.

The flow loop arrangement presented in Figure 3.35a consists of the test section, the cooling water bath (Julabo EH, F 25), a copper coil, the reservoir, the preheater, the micropump (GAT23-PFS-B)., the pressure gauge, a plate heat exchanger, a filter, the power supply and an infrared camera (FLIR X6580s) and the high-speed camera. Fluorinert FC-72 (T_{sat} = 56 ^{o}C at P = 1 atm) was circulated at a constant flow rate through the microchannel. The liquid temperature prior to entry to the channel via the inlet was maintained at 21 ± 1 ^{o}C. A copper coil with cooling water supply, positioned inside the reservoir, served both as a condenser for vapour generated in the test module and a regulator of pressure in the flow loop. The desired pressure was maintained in the system by controlling the flow rate of FC-72 through the copper coil. A plate heat exchanger with water as a coolant was installed between the reservoir and the pump to prevent any pump cavitations. The pump's exit was monitored by a pressure gauge situated immediately downstream from the pump. A 15-µm filter was used to prevent any solid particles from entering the test section. Flow rates were measured by a digital mass flow meter (Bronkhorst Mini-CoriFlow series) with a controller that was calibrated for FC-72. Subcooling conditions were maintained by using negative feedback control on a low flow liquid circulation heater with a total power of 1200 W. The flow rate through the test module was regulated using a bypass valve and a fine needle valve located upstream of the test module. The reservoir served as both a degassing and condensation chamber during flow boiling experiments. Immersion heaters were installed inside the reservoir to preheat and degas the liquid. The heaters were connected with a PI controller to control the temperature. The fluid temperature was measured at the inlet and outlet of the microchannel using two K-type thermocouples. The flow loop connections were made of stainless steel tubes (1/4 in diameter). Two data acquisition devices were used for voltage acquisition (NI 9205) and temperature acquisition from the thermocouples (NI 9213). The high-speed camera was synchronised with the IR high-speed camera to 250 Hz to calibrate them temporally. Two power supplies were used to power the pressure transducers and the ITO heater power supply. The IR camera has a thermal sensitivity of 20 mK, an accuracy of ± 1 °C, a resolution of 640 x 512 pixel and image frame rate of 200 Hz. The high-speed camera (VW-600C high-speed colour Keyence) was used with a microscope (RR, Microscope) with an integrated light and lens ((VH-Z20) at a working distance of 25.5 mm. The resolution of the camera was

640 ×480 pixels. The images were visualised through the monitor of the microscope (VW-9000 High -speed Microscope).

Dual flow boiling experiments in chapter 6 were performed using a slightly improved flow loop presented in Figure 3.35b and a photograph of the setup is shown in Figure 3.36. The experiments examine the transparent device from both sides (through PDMS or ITO/glass). The loop comprises a boiling and degassing chamber for FC-72 (1), a degassing chamber for FC-72 (2), a gear pump (3) a 15 μm filer (4), a flowmeter (5), the test section area (7), a water cooling bath (8) and a condenser (9).

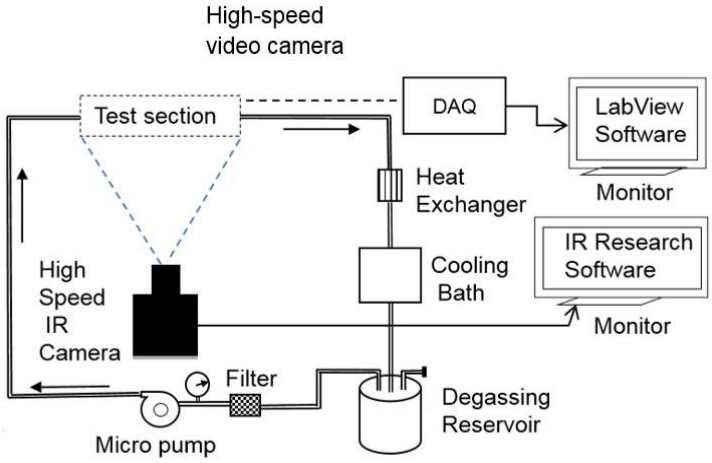

(a)

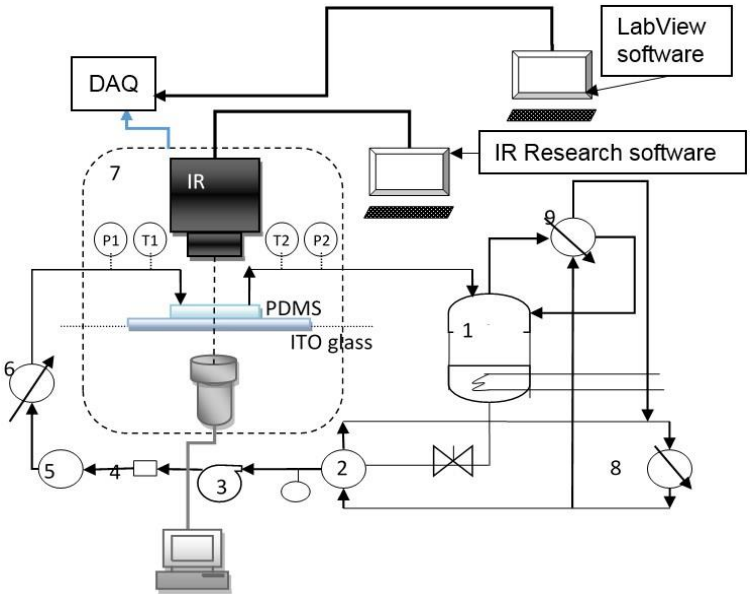

(b)

Figure 3. 35 *Schematic drawing of (a) the wall temperature measurements from the ITO/glass base and (b) the flow loop used to facilitate wall temperature measurements PDMS side.*

When working alongside electronics, water has obvious risks whilst refrigerants on the other hand are inherently dielectric fluids, meaning that even with a leak, the electronics will be safe from damage. FC-72 has a low boiling point of 56 ˚C, allowing lower superheat values between the heated surface and the liquid than water. The properties of FC-72 cooling liquid are presented in Table 3.5.

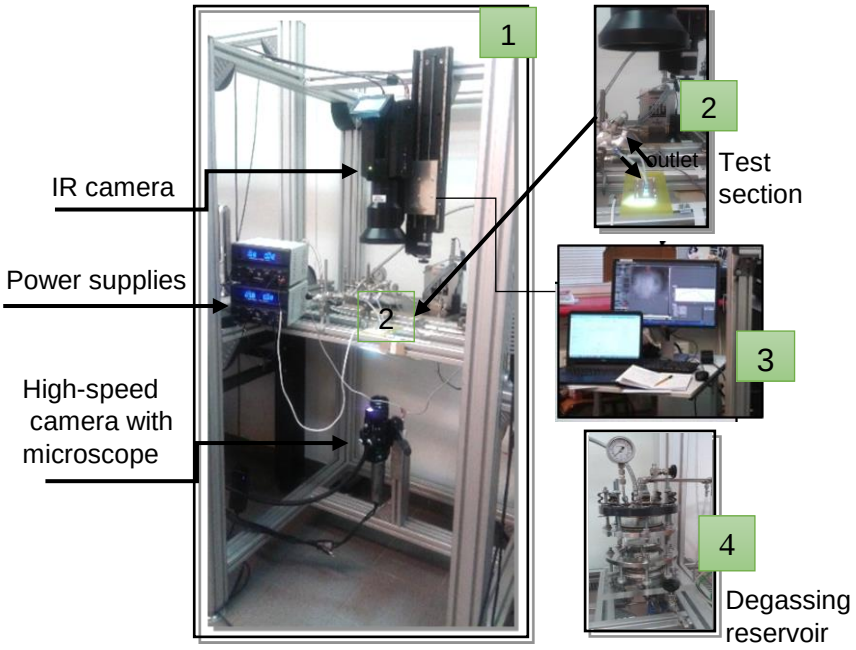

Figure 3. 36 *Photograph of the flow loop2 (1) used for synchronised IR thermography from PDMS top of the channel and high-speed imaging from the ITO/glass base. Photographs of the test section (1), the IR research software and LabVIEW interface (2) and the degassing reservoir for FC-72 (4) are also presented.*

Table 3. 5 *Properties of FC-72.*

Properties	**FC-72**
Boiling Point(^{o}C)	56
Vapour Pressure (Pa)	30.9×10^{3}
Latent Heat of Vaporisation (Jg^{-1})	88
Liquid Density (kg m^{-3})	1680
Liquid Specific Heat (J kg^{-1} ˚C $^{-1}$)	1100
Liquid Thermal Conductivity(W m^{-1} $^{o}C^{-1}$)	0.057
Surface Tension (dynes cm^{-1})	10
Ozone Depletion Potential	0
Dielectric Constant	1.75

3.3.9 Data acquisition system and measurements uncertainty

The miniature pressure sensors were calibrated using two company calibrated Omega pressure transducers that operate in the range from 1 to 2.5 bar and have 0.25 % accuracy. The pressure transducers were calibrated using the static pressure calibration setup presented in Figure 3.37. The end of the tube after the location of pressure transducer P_{out}, was blocked. This occurred in order to allow for stable, uniform pressure across the whole test section, from the syringe pump to the blocked output. A known pressure FC-72 was applied to the calibration system via a syringe pump and the pressure on the system was increased by adding fluid. The voltage response to pressure plot is shown in Figure 3.38. The deviation from the average output voltage of only ± 2 mV, indicated that there were no leaks in the microchannel.

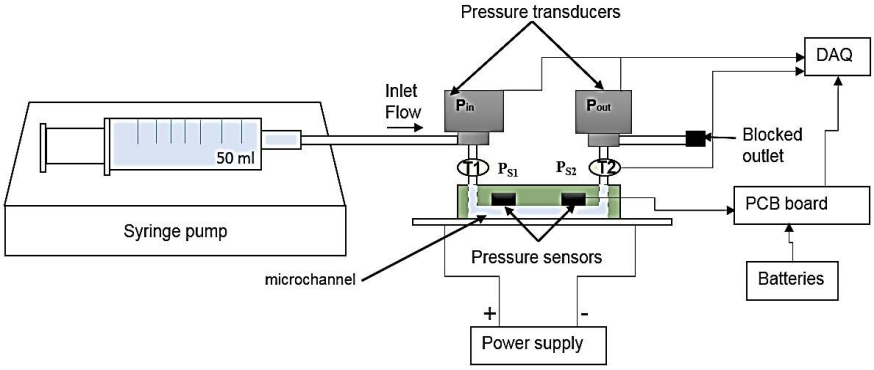

Figure 3. 37 *Schematic drawing of the calibration setup.*

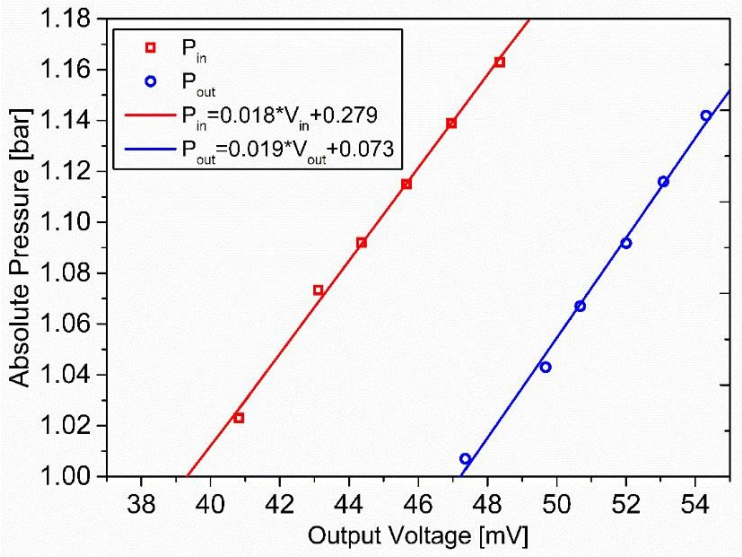

Figure 3. 38. *Calibration curves for the two pressure sensors HSC Series True Stability. The pressure was obtained as a function of the output voltage of the pressure sensors.*

Table 3. 6 *Summary of measurements uncertainties.*

Parameter	**Maximum Uncertainty**
Standard K-type thermocouple	±0.5 °C
Pressure sensors	0.20 %
DC power supply	±1 % of reading
IR camera measured temperature	±1 ˚C (from 20 ˚C to 120 °C)
Pump volumetric velocity	0.5 %
Mass flux	9%
Heat flux	6 %
Heat transfer coefficient	11%
Vapour quality	3.2 %

3.4 Summary

This chapter presented the two different facilities and the methodology. The design and the microfabrication process for the silicon microchannels were analytically described as well as the experimental facility used for the flow boiling experiments using the silicon microchannels. Then, the polydimethylsiloxane (PDMS)-based microchannel microfabrication technique was described as well as the experimental facility for the simultaneous IR thermography and high speed imaging visualisation. The novelties for each setup where highlighted and the microfabrication techniques for the silicon microchannel and PDMS microchannels heat sinks were experimentally discussed. The methodology that was used to perform in site emissivity measurements of the microchannel was described. The calibration of the miniature pressure sensors was explained and measurement uncertainties were displayed analytically.

Chapter 4 Effect of aspect ratio on two-phase flow boiling heat transfer in silicon rectangular microchannels

4.1 Introduction

High aspect ratio microchannels are characterised by shallow and wide cross section, which is believed to provide many advantages. Firstly, their large surface-to cross-sectional area ratio can reduce the working liquid consumption while providing large cooling area. Secondly, the high aspect ratio channels can potentially reduce vapour side pressure drop and increase vapour side heat transfer as reported by Morkrani *et* al. [75]. Thome [13] also reported possible increase in CHF. Despite their potential, few studies in literature study the effect of aspect ratio on multimicrochannels two-phase heat transfer and pressure drop. Pressure drop can be severely increased during two-phase flow conditions because of parallel channel instabilities or vapour compressibility in the outlet of the channels that results in flow reversal and dryout. The understanding of the effect of the channel cross sectional aspect ratio and cross section dimensions on pressure drop and heat transfer coefficients during flow boiling in parallel microchannels heat sinks is required in order to provide guidelines for the design of future high performance devices. In order to fill this literature gaps, flow boiling experiments are performed using deionised water in microchannel heat sinks with aspect ratios (α) of 0.33, 0.5, 0.67, 1, 1.5, 2, and 3. The hydraulic diameters (D_h) of the silicon microchannels range from 50 to 150 μm.

4.2 Experimental setup and procedure

The experimental system described in section 3.2.4 is utilized to investigate two-phase flow boiling heat transfer and pressure drop of deionised water in the different rectangular silicon microchannels heat sinks. Three sets of microchannel designs (A, B, C) were used, with aspect ratios of 0.33, 0.5, 0.67, 1, 1.5, 2, and 3 with hydraulic diameters that range from 50 to 150 μm. The detailed characteristics of each microchannel design are presented in Table 3.1. Prior to carrying out the experiments, deionised water was boiled for one hour and degassed in the reservoir. The degassed liquid was circulated in the flow loop and was set to specific inlet liquid temperature conditions. Then the desired heat flux was applied in the test section. The experiments started with single-phase flow conditions at a low heat flux and high mass flux then

by decreasing the mass flux or increasing the heat flux two-phase flow boiling conditions were imposed in the channels. The experimental data were recorded after 20 minutes were stable conditions were established in the microchannels. The local temperatures from the five thin Ni film temperature sensors were recorded simultaneously with pressure measurements from two pressure transducers and with simultaneous high-speed flow visualisations from the microchannels top view. The effect of aspect ratio on two-phase flow boiling pressure drop and heat transfer was studied for the constant heat fluxes (q) of 151, 183, 271 and 363 kW m^{-2}. These specific values of heat flux values were dependent with the maximum voltage limit of the DC power supply and the resistance of the Al heater. The maximum electric power that was applied on the microchip was 60 W which in terms of the heat flux was found to be ~363 kW m^{-2}. Using a higher voltage power supply to the system result in very high temperatures and damage of the whole test section. Single-phase flow experiments were initially carried out for the constant heat flux and a high mass flux and then the mass flux the effect of mass flux was studies was decreased in order to study two-phase flow. The experiments were stopped before critical heat flux conditions. The sharp temperature increase during critical conditions can damage the microchip device. Two inlet liquid temperatures were tested, first 25 °C and then 81 °C in order to study the inlet subcooling effect on the heat transfer performance ego the heat sinks. The effect of channel cross sectional aspect ratio and cross section dimensions on pressure drop, local heat transfer coefficient and flow patterns are discussed.

4.3 Data reduction

The heat flux transferred to the water was calculated from the measured input voltage, V and the current, I across the film heater:

$$q = \frac{\varphi\, VI}{A} \tag{4.1}$$

where A is the area of the heated microchannels region (10.15 × 15.00 mm^2), and the portion of the total power transferred to the water. The method of calculating the portion of the total power transferred to the water is explained in chapter 3. It was found to vary in a range from 82 to 92 % for all the microchannel heat sink designs of the input power was transferred to water for the range of conditions considered in this study.

The local heat transfer coefficient, h_z is calculated from:

$$h_z = \frac{q_w}{T_w - T_f} \tag{4.2}$$

in which q_w is the wall heat flux, T_w is the local channel bottom wall temperature and T_f is the local fluid temperature. The local heat transfer coefficients were calculated along microchannels where integrated temperature sensors T1, T3 and T5 were located. The wall heat flux was calculated using fin analysis method:

$$q_w = \frac{q(W_w - W_{ch})}{W_{ch} + 2nD_h} \tag{4.3}$$

Assuming the uniform heat transfer coefficient, averaged along the entire heated perimeter of the microchannel. The fin efficiency is defined as:

$$n = \frac{tanh(mD_h)}{W_{ch} + 2nD_h} \tag{4.4}$$

where is the fin parameter:

$$m = \sqrt{\frac{h_z}{k_{si}W_w}} \tag{4.5}$$

Eq. (6.2) – (6.5) require an iterative procedure and an initial guess of the heat transfer coefficient was obtained assuming the wall heat flux being equal to the effective heat flux for the first step of the iterative procedure.

The local channel bottom wall temperature, T_w in Eq. (6.2) was calculated assuming one-dimensional heat conduction through silicon substrate:

$$\mathrm{T_w} = \mathrm{T_s} - \frac{\mathrm{q} \cdot \mathrm{d}}{\mathrm{k_{so}}} \tag{4.6}$$

where T_s is the local temperature measured by the sensor located at a distance d = 112 μm underneath the channel bottom wall.

The local fluid temperature T_f was determined depending on the region along the length of microchannels. Cooling water was supplied into microchannels in a subcooled condition (T_{inlet} = 81 °C) and a subcooling boiling region extended over a certain distance from the microchannels inlet along microchannels length. Therefore, the length of the microchannel can be divided into the subcooled liquid region and saturated region with respect to thermodynamic equilibrium quality. The separating point between the two regions is the location of zero

thermodynamic quality. The thermodynamic equilibrium quality for the subcooled liquid region is negative and for the saturated region is positive. The subcooled region can be evaluated by an energy balance as follows:

$$L_{sub}\frac{\dot{m}c_p(T_{sat}-T_{inlet})}{qW} \tag{4.7}$$

where T_{sat} is the saturation temperature at the position of zero thermodynamic quality. T_{sat} was evaluated using the measured inlet pressure, assuming the pressure drop over the subcooled liquid region in microchannels is negligible. The length of the saturated region L_{sat} was calculated as follows:

$$L_{sat} = L - L_{sub} \tag{4.8}$$

The local fluid temperature T_f for subcooled liquid region at a distance l from the channels inlet was calculated using an energy balance:

$$T_f = T_{inlet} + \frac{qWl}{\dot{m}c_p} \tag{4.9}$$

The local fluid temperatures were calculated at locations of sensors T1, T3 and T5 axially positioned at 0.367, 7.500 and 14.632 mm respectively from the channels inlet. The uncertainties in the reported two-phase heat transfer coefficients obtained using standard error analysis were in the range of 2.1 – 25 %. The larger uncertainties occurred for the subcooled liquid region and at the lower mass fluxes. The uncertainties in the measurements are given in chapter 3. The saturation temperature was evaluated based on the pressure drop. The inlet pressure was assumed to decrease linearly with the outlet pressure.

The vapour quality at the exit was calculated knowing the mass flow rate, $\dot{m}$ and the net input power, Q as:

$$x_e = \frac{Q - \dot{m}c_p(T_{sat}-T_{in})}{\dot{m}h_{fg}} \tag{4.10}$$

where T_{sat} is saturation temperature corresponding to the outlet pressure.

For the two-phase region the subcooling pressure drop was extracted from the total pressure drop so that the initial value for pressure was that calculated at $x_e = 0$ where T_{sat} (x_e=0) was also calculated. Knowing the pressure at x = 0 the pressure at each sensor position was calculated

and local saturation temperature consequently. Fourier analysis was performed in chapter 4 and 6 using discrete Fourier Transform (DFT) to perform the signal analysis of the pressure from fluctuations. The algorithm used for computing the DFT is Fast Fourier Transform (FFT). FFT transforms the time dependent pressure domain data into frequency domain data.

For the multichannel configuration, the flow enters the channels through an inlet manifold and leaves the channels through a manifold, which is depicted in Figure 3.1. Thus the pressure loss term ΔP_{loss} in Eq. (4.11) is given by:

$$\Delta P_{loss} = \Delta P_{im} + \Delta P_c + \Delta P_e + \Delta P_{om} \tag{4.11}$$

where ΔP_{im} and ΔP_{om} are the pressure losses across the inlet and outlet manifolds, respectively. These losses are given by the following equations, see Ref.[131] .

$$\Delta P_{im} = [1 - \sigma^2 + K_{im}] \times \frac{1}{2} G v^2 \tag{4.12}$$

$$\Delta P_{om} = [-\frac{1}{\sigma^2} - 1 + K_{om}] \times \frac{1}{2} G v^2 \tag{4.13}$$

The loss coefficients K_{im} and K_{om} are summarised in Ref. [131] in a table form as a function of *fRe* and *a*. ($a = W_{ch}/ H_{ch}$). The values are 0.134 for K_{im} and 0.11 for K_{om} for our design. In the above equations σ is the small to large cross sectional area ratio. The sudden contraction and enlargement in Eq. (3.4, 3.5) are given by the following equations, see Ref.[131]:

$$\Delta P_e = -[\frac{1}{\sigma^2} - 1 + (1 - \sigma)^2] \times \frac{1}{2} G v_f^2 \tag{4.14}$$

$$\Delta P_{im} = [1 - \sigma^2 + 0.5(1 - \sigma)] \times \frac{1}{2} G v^2 \tag{4.15}$$

The Fanning friction factor can then be calculated using Eq. (4.16) for multichannels as:

$$f = \frac{\Delta P_{ch} D_h}{2 L_{ch} \rho_f V_{ch}^2} \tag{4.16}$$

The Reynolds number is defined as:

$$Re = \frac{\rho_f V_{ch} D_h}{\mu_f} \tag{4.17}$$

The above experimental values were correlated with theoretical values of pressure drop. Friction factor was calculated from equation for fully developed laminar flow from Shah and London [132] :

.

$$f_{FD} = \{24\,[1 - (1.3553\,a) + (1.9467a^2) - (1.7012a^3) + (0.9564\,a^4) - (0.2537a^5)]\}/Re \tag{4.18}$$

The predicted numerical friction factor results in Figures 4.1, 4.2, and 4.3 were verified using current experimental data and the Shah and London [132] correlation for developed laminar flow. Figures 4.1, 4.2 and 4.3 depict experimental friction factor produced from Eq.4.16 for each microchannel heat sink configuration as well as the theoritical friction factor produced from Eq.4.18. It indicates that correlation underpredicts the experimental values by about 10 % only.

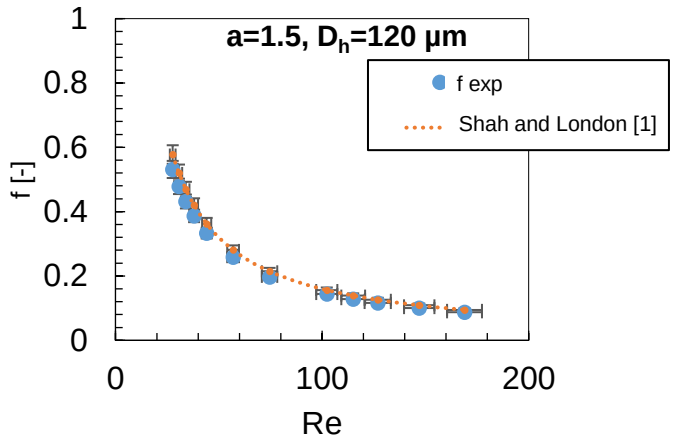

(a)

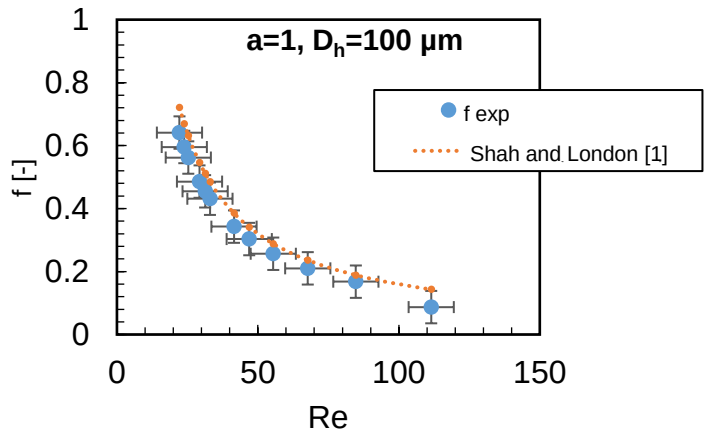

(b)

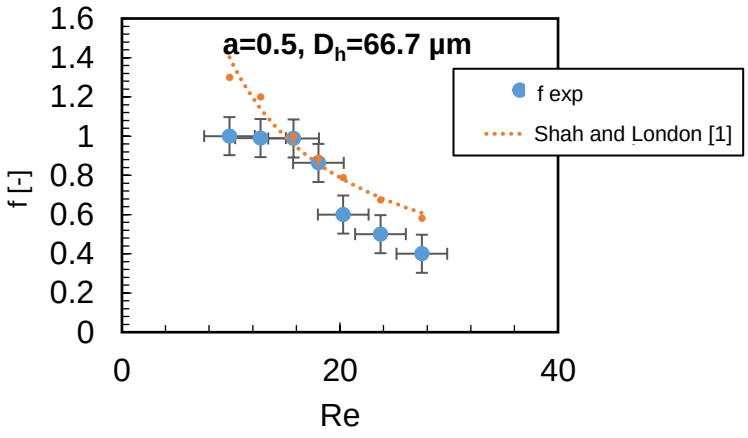

(c)

Figure 4. 1 . *Comparison of predicted friction factor with existing experimental results and existing correlation.*

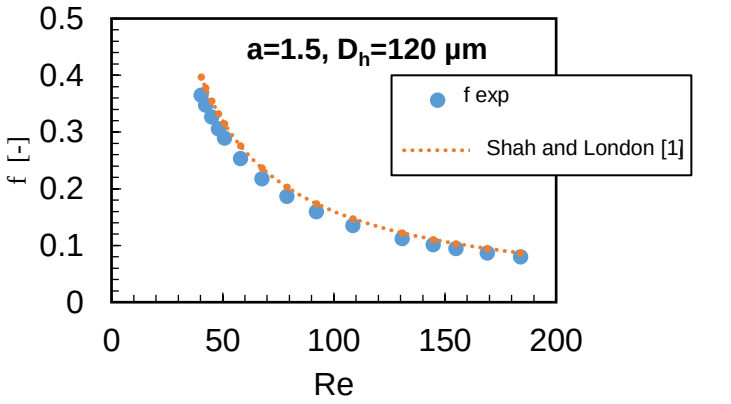

(d)

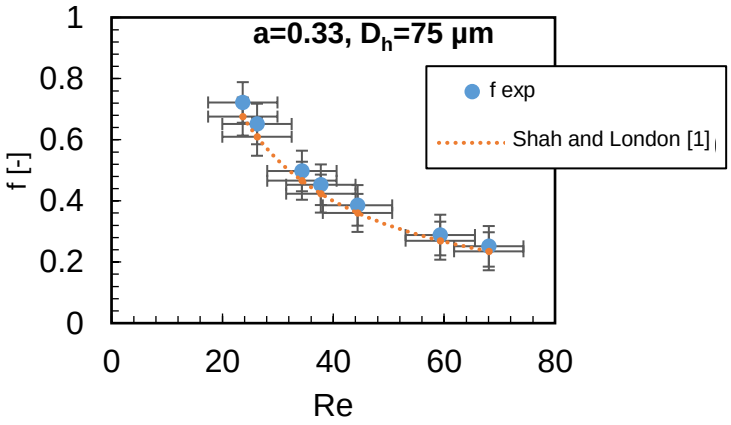

(e)

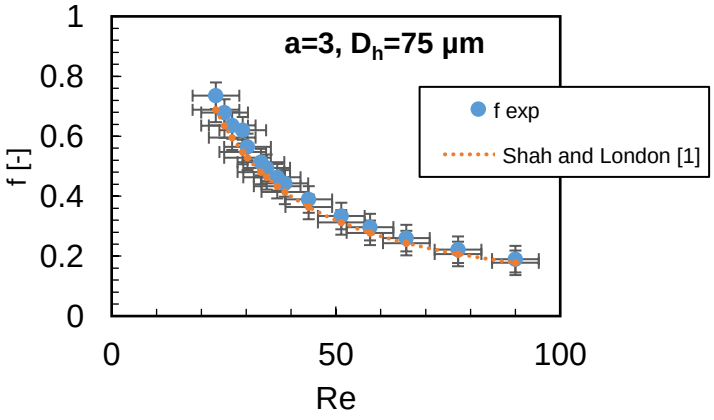

(f)

Figure 4. 2 *Comparison of predicted friction factor with existing experimental results and existing correlation.*

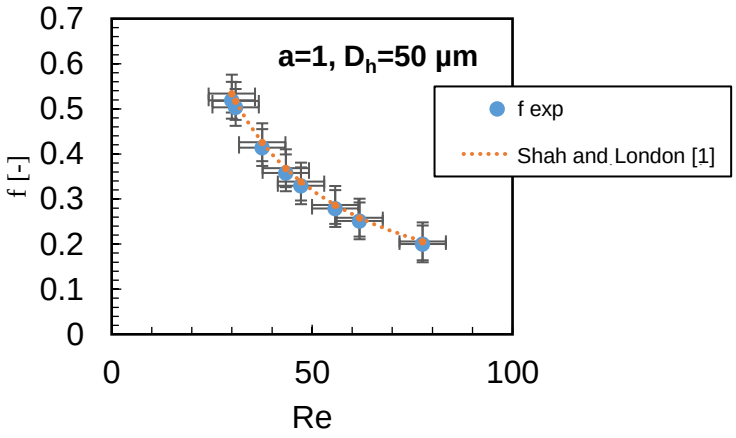

(g)

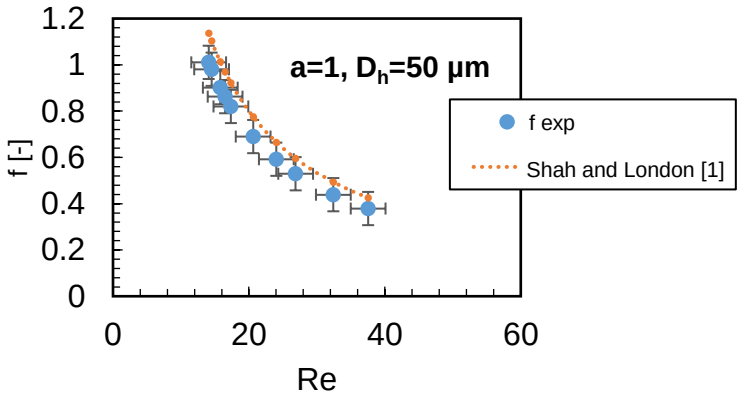

(h)

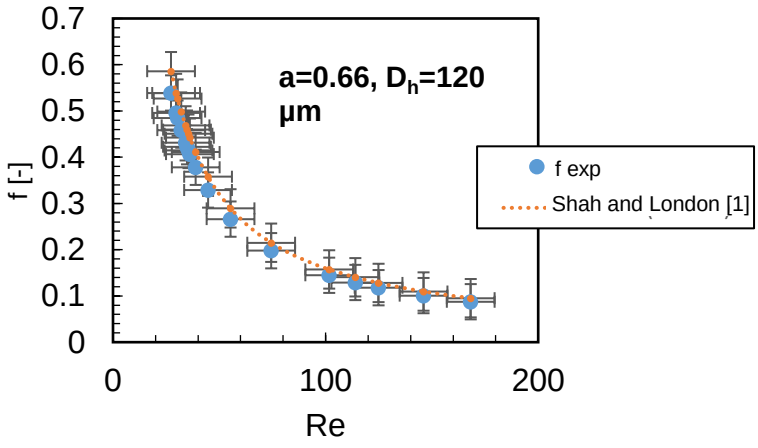

(i)

Figure 4. 3 *Comparison of predicted friction factor with existing experimental results and existing correlation.*

4.4 Results and discussion

4.4.1 Effect of different microchannel cross section size and aspect ratio on pressure drop

Figure 4.4a presents time averaged pressure drop data as a function of mass flux for q = 151 kW m^{-2}, Figure 4.4 for q = 271 kW m^{-2} and Figure 4.5 for q = 363 kW m^{-2}**.** The characteristics of the microchannel heat sink designs are presented in Table 3.1. The inlet temperature is 25 ºC ± 1 ºC. Figures 4.1 and 4.2 show time averaged pressure drop data over 60 s as a function of mass flux for both two-phase and single-phase flow conditions for all microchannel heat. The inlet liquid temperature was maintained at 25 ºC ± 1 ºC. Each point on the graphs is an average value from one experimental data set. The total averaged pressure drop appears to have similar trend for all heat fluxes and devices tested. Pressure drop reaches minima (at G_{cr}) with decreasing mass flux, for a constant heat flux. The gradient of pressure drop curve increases in the two-phase region for mass fluxes lower than G_{cr}. At high aspect ratio microchannels, the pressure drop versus mass flux gradient presents a sharp increase for $G < G_{cr}$ which was attributed to the partial dryout observed to occur at the outlet of the microchannels, from flow visualisations, which will be later discussed. The two-phase pressure drop reached the value of 800 mbar for the high aspect ratio microchannels of α = 2 (D_h = 66.7 μm) and α = 3 (D_h = 75 μm). The effect of aspect ratio was found to be important on the two-phase pressure drop as the hydraulic diameter for these two high aspect ratio configurations could be assumed constant considering that the difference from 66.7 μm to 75 μm is only 8.3 μm. The gradient of the two-phase pressure drop curve at G < G_{cr} and vale of of G_{cr} that pressure drop minima occurs (low or high mass flux range) was found to depend on the microchannel aspect ratio, considering that 75 μm and 66.7 μm are almost equal. In general, it can be concluded from Figures 4.4 and 4.5 that the pressure drop values in both single-phase and two-phase region increase with increasing heat flux conditions. The lowest pressure drop values were measured for the microchannel design of α = 1.5 (W_{ch} = 150 μ m and D_h = 120 μm) which was found to variate between the values of 5 to 200 mbar for all the three four fluxes and both single-phase and two-phase conditions. The channels with H_{ch} = 100 μm and 150 μm the pressure drop is lower because of the lower mass flux range, between 40 and 1600 kg m^{-2}s^{-1}. Figure 4.6a shows that microchannels of smaller hydraulic diameters 50 μm height, pressure drop is higher as they demand higher mass fluxes. Single-phase pressure drop is expected to increase linearly with increasing mass flux. Deviations of the pressure data from the linearity during the single-phase regions result from measurements errors, defined on the graph.

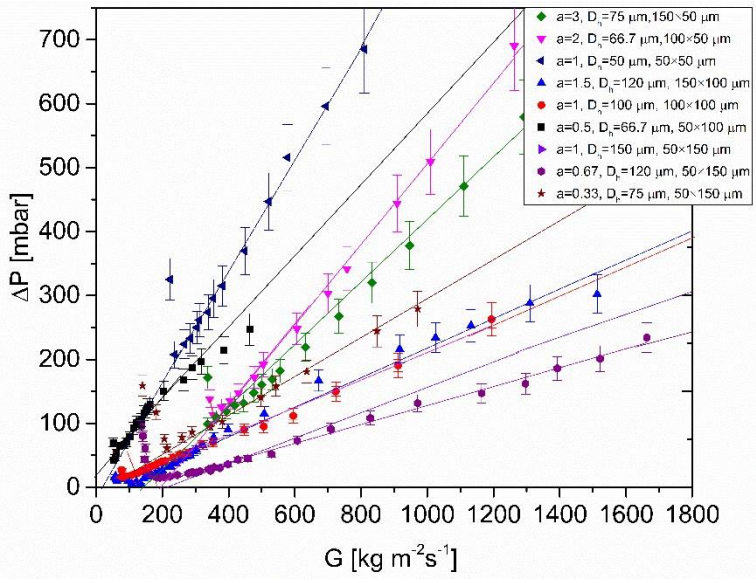

(a)

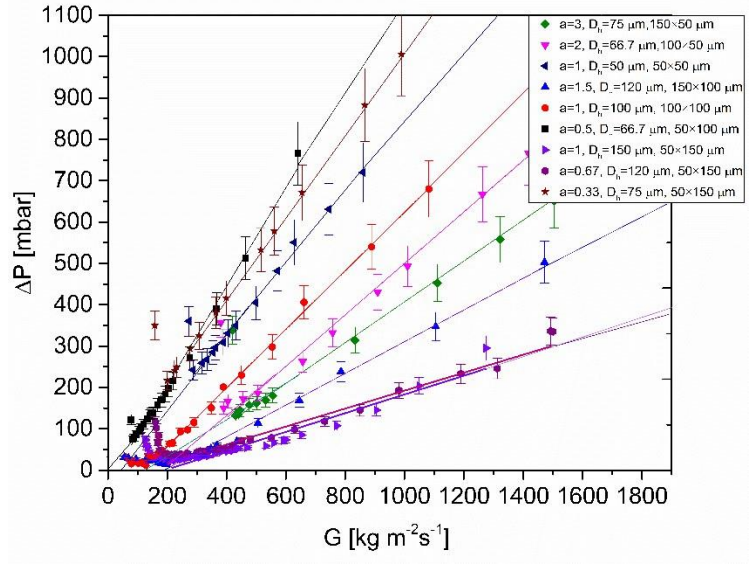

(b)

Figure 4. 4 *Pressure drop averaged over time as a function of mass flux at the constant heat fluxes of (a) q = 151 kW m^{-2} and (b) 185 kW m^{-2} for both two-phase and single-phase flow conditions for all nine microchannel heats sinks.*

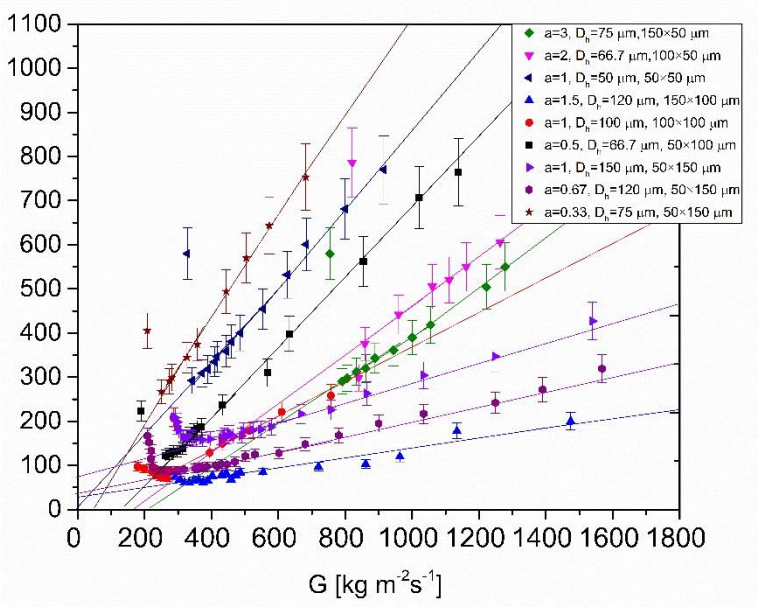

Figure 4. 5 *Pressure drop averaged over time as a function of mass flux at the constant heat flux of 271 kW m^{-2} for both two-phase and single-phase flow conditions for all nine microchannel heat sink designs with characteristics presented in Table 3.1 of chapter 3. The inlet temperature is 25 ºC ± 1 ºC.*

Figure 4.6a shows the effect of increasing aspect ratios of 1, 2, and 3 (D_h = 50 µm, 66.7 and 75 µm) at widthwise direction on pressure drop for constant height. Figure 4.3b examines the effect of increasing aspect ratios of 0.5, 1, 1.5 (D_h = 66.7 µm, 100 and 150 µm) at channel widthwise direction on pressure drop for constant height. The effect of increasing aspect ratios of 0.33, 0.66, 1 (D_h = 50 µm, 100 and 150 µm) at widthwise direction on pressure drop for constant height was examined and the results are shown in Figure 4.6c. According to Figures 4.6a, b and c, the pressure drop results are classified in low mass fluxes and high mass fluxes. Low mass fluxes from 1600 kg m^{-2}s^{-1} to 40 kg m^{-2}s^{-1}.were the limits of the low mass flux regions. For aspect ratios lower than 1.5 (Figures 4.6a and 4.6b) with D_h between 66.7 and 150 µm, the mass flux limits remained in the low mass flux region. For the aspect ratios higher than 1.5, a =1, 2 and 3 between mass flux limits were increased from 200 and 1,800 kg m^{-2}s^{-1}.All the three graphs in Figure 4.6 provided results of pressure drop at the same heat flux conditions, of q = 151 kW m^{-2}.

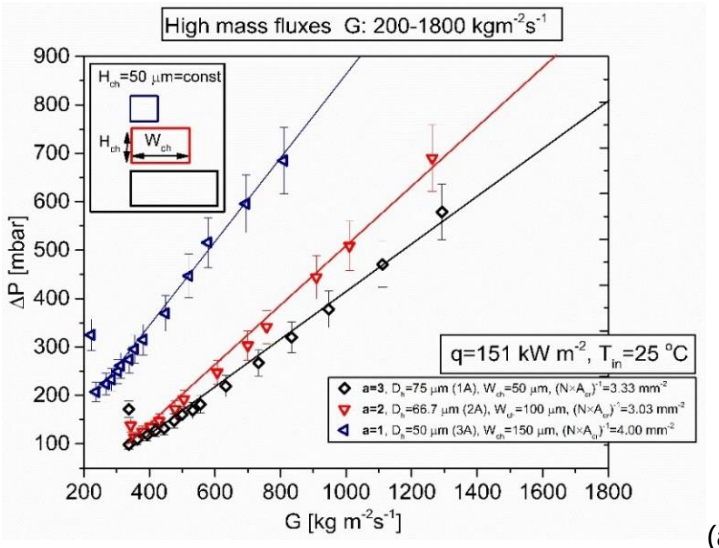

(a)

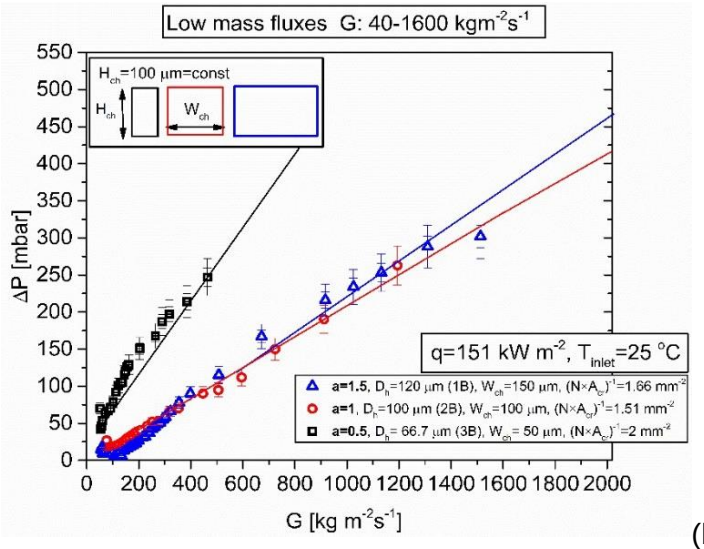

(b)

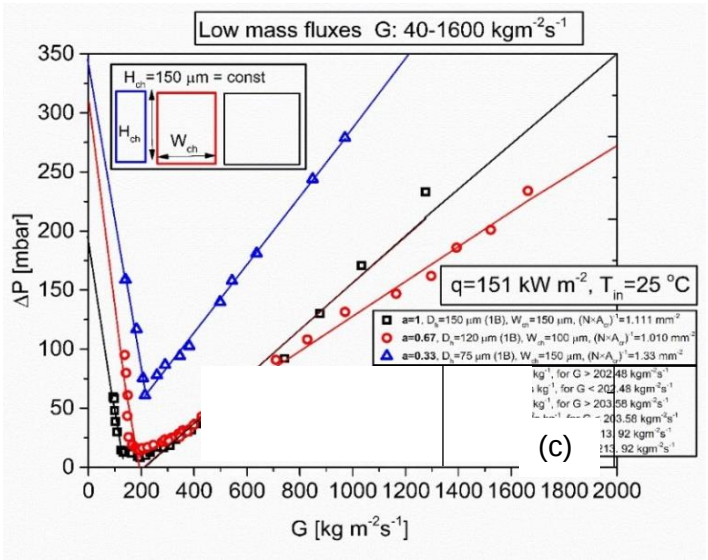

(c)

Figure 4. 6 *Pressure drop averaged over time as a function of mass flux at the constant heat flux of q = 151 kW m^{-2} for (a) constant height of 50 μm and increasing widths of 50, 100 and*

150 μm constant and $a \geq 1$ (b) constant height of 100 μm and increasing widths of 50, 100 and 150 μm and $0.5 \leq a \leq 1.5$ and (c) constant height of 150μm and increasing widths of 50, 100 and 150 μm for two-phase and single-phase flow conditions and $a \leq 1$. The inlet liquid temperature is 25 ºC ± 1 ºC.

Figure 4.7 presents $\Delta P/\Delta G$ values with increasing channel widths of 50 μm, 100 μm and 150 μm for a constant H_{ch}= 50 μm (Figure 4.7a), H_{ch} = 100 μm (Figure 4.7b) and H_{ch} = 150 μm (Figure 4.7c). $\Delta P/\Delta G$ was calculated for the case of $G > G_{cr}$, where r_{cr} is the value where $\Delta P/\Delta G$ slope changes. Increasing the aspect ratio by decreasing the height of the microchannels for a constant width resulted in pressure drop increase.

At low mass fluxes high amplitude pressure drop and temperature oscillations are induced deteriorating the flow boiling heat transfer coefficients. In contrast, wide microchannels but not very shallow (a = 1.5, $W_{ch} > 1.5H_{ch}$) show good performance for heat transfer, producing modest pressure drop. Smaller width channels result in parallel microchannel instabilities because of increase of the microchannels number. Elongated bubbles are proved to be a limited factor for the heat transfer coefficients (Kandlikar *et* al. [15] D_h. < 200 μm) inducing flow reversal and uniform dryout. At low mass fluxes the pressure drop curve presents a minimum and then increases again. Wide microchannels but not very shallow produce modest pressure drop *(a* =1.5). For a constant height and a constant channel width, the effect of increasing heat flux on pressure drop is stronger because the slope increases with heat flux. There is no important effect of increasing channel width on pressure drop after partial dryout. Particularly, for H_{ch} = 100 μm and $\Delta P/\Delta G$ slope remains almost constant with increasing channel aspect ratio for the same heat fluxes at width direction. There is a slight increase of $\Delta P/\Delta G$ at the lowest Wch at H_{ch} =100 μm and $\Delta P/\Delta G$. For the shallowest channels (H_{ch} = 50 μm and a = 1, 2, 3) ΔG was the highest in the two-phase region for $G < G_{cr}$. $\Delta P/\Delta G$.

Figures 4.7 a, b and c show that $\Delta P/\Delta G$ decreases with increasing aspect ratio by increasing the$\Delta P/\Delta G$channel width for a constant height for G > Gcr. Increasing the heat flux at a constant channel width and height resulted in alternating slopes with higher difference between them from the shallow (H_{ch} = 50 μm) to the deep (H_{ch} = 150 μm) channels.

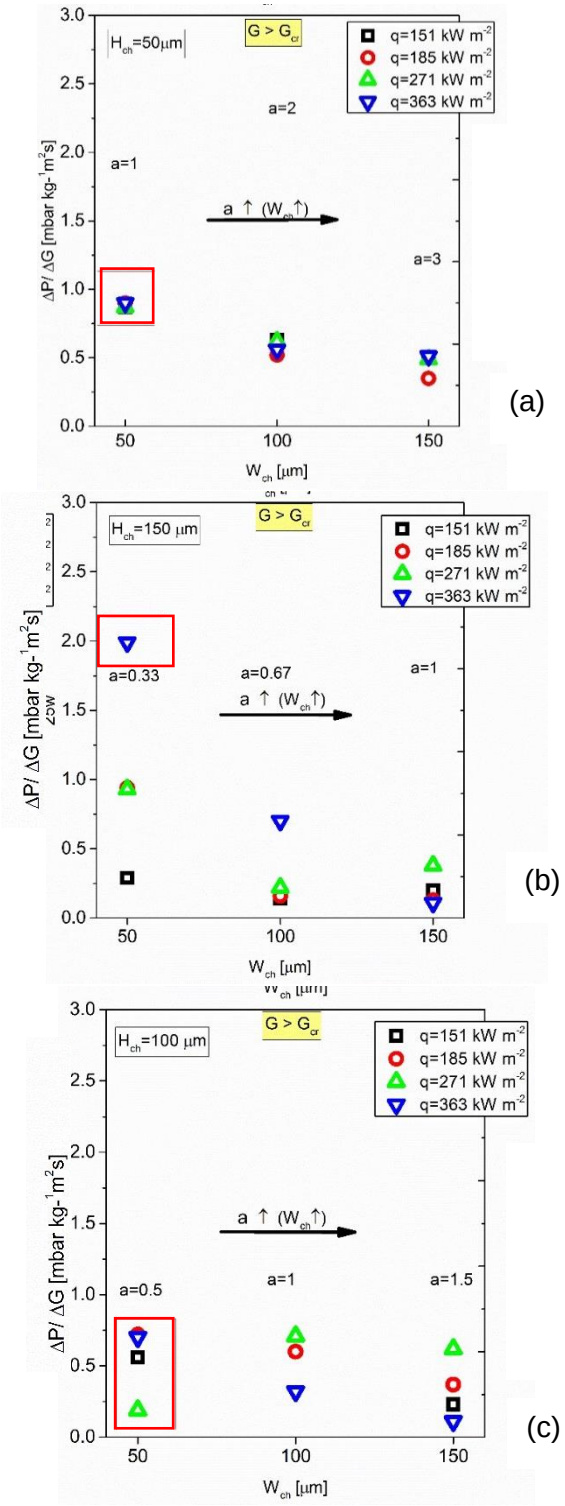

Figure 4. 7 *Effect of increasing width for three constant heights of (a) H_{ch} = 50 µm (a=1, 2, 3 and D_h = 50 µm, 66.7 µm and 75 µm) (b) H_{ch}=100 µm (α = 1.5, 1, 0.5) and D_h = 120 µm, 100 µm and 66.7µm) and (c) H_{ch} = 150 µm (α =1, 0.67, 0.33 and D_h = 150 µm, 120 µm and 75µm.*

The highest $\Delta P/\Delta G$ = 2.6 mbar kg^{-1}m^{2}s was measured as shown in Figure 4.8c for the 3C design (H_{ch} =150 μm and W_{ch} = 50 μm) which consisted of microchannels with the highest depth and smallest width cross section (D_h. =75 μm, A_{cr} = 0.0.075 mm^2, N = 100). The lowest $\Delta P/\Delta G$ was measured between 0.28 and 1.99 for all heat fluxes at the highest width of 150 μm (highest aspect ratio for a constant height). Figures 4.5a, b and c show that the increasing heat flux for a constant channel height and width does not imply increase at the value of the slope of the pressure drop vs mass flux curve. Harrirchian and Garimella [44] found that for a fixed q, pressure drop increases with decreasing channel width. The channel widths were in the range of 100 to 5,820 μm and the channel height was constant at 400 μm. The conclusion is that increasing the aspect ratio of the microchannels by the direction of the channel width, reduces the pressure drop for G < G_{cr} as it results in increase of the hydraulic diameter of the microchannel. Table 4.1 shows the variables of the experiments.

Figures 4.8a,b and c show that increasing the aspect ratio by decreasing the channel height results in slightly higher pressure drop values for G < G_{cr}. Both previous Figures show that for the two-phase region of G < G_{cr}, the results are also correlated with the number of $1/N\ A_{cr}$, and D_h. All the results for all cases were correlated also with the number $1/N\ A_{cr}$. As this number was not constant. $1/N\ A_{cr}$ ranged from 1.010 to 4. Figure 4.9 shows the relation of $1/N\ A_{cr}$ with the channel aspect ratio and the hydraulic diameter.

Table 4. 1 *Constants and variables of the experiments.*

Constants	Variables
D_h, A_{cr}, G	W_{ch} (↑ with ↑ a) L_{ch}, H_ch, P_h (↓with ↑ a)

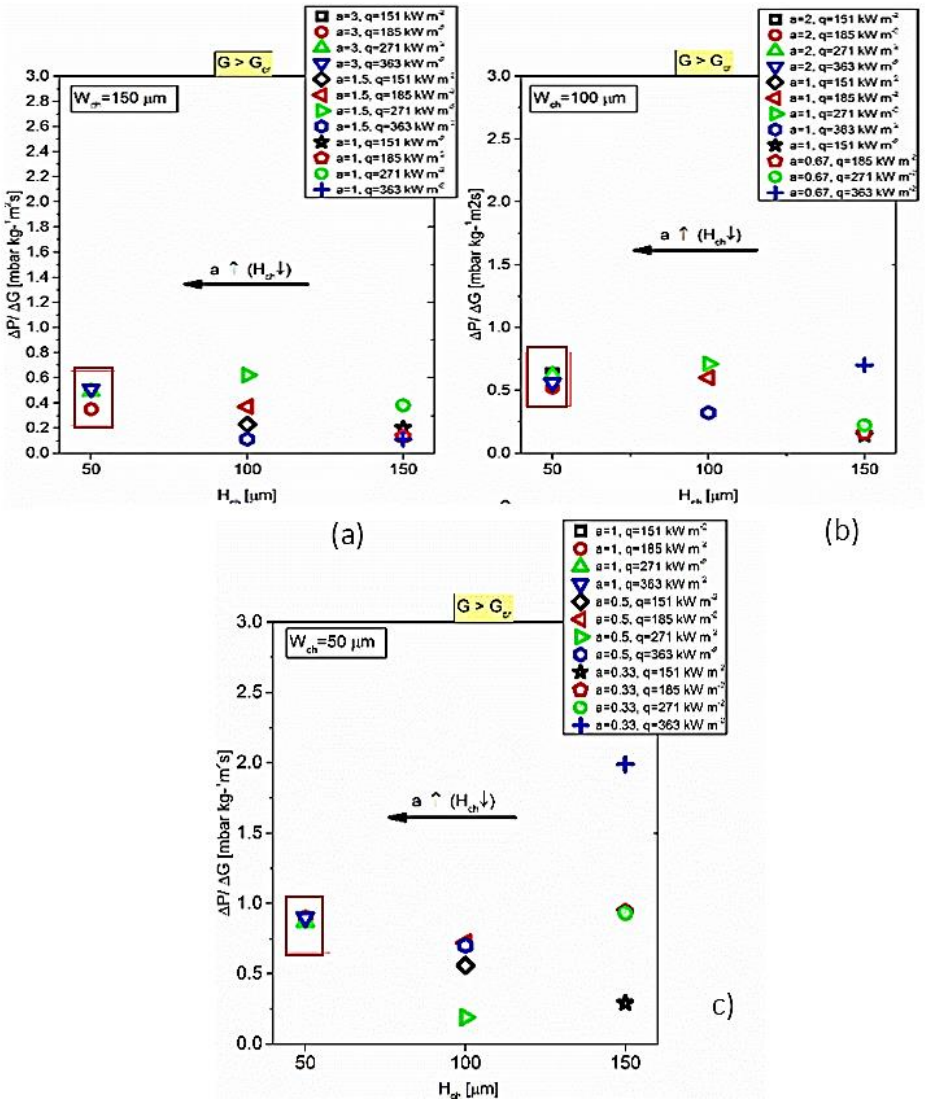

Figure 4. 8 *Channel height as a function of* $\Delta P/\Delta G$ *for the three constant widths of (a)* W_{ch} *=150 µm (b) 100 µm, (c) 50 µm. for the case of* $G < G_{cr}$*, where* G_{cr} *is the value where the* $\Delta P/\Delta G$ *slope changes.*

Figure 4.10 shows that for the low mass flux where G < G_{cr}, $_{\Delta G}$ takes its maximum value after the occurrence of partial dryout at the outlet of the microchannels heat sink with $1/N\ A_{cr}$ > 3.0. $N\ A_{cr}$ is the product of the number of the microchannels and the cross sectional area of the channels. As both number of channels and cross sectional area changes, the number N A_{cr} was used to compare the pressure drop effect. The microchannel heat sinks with $N\ A_{cr}$ > 3.0 were those with the lowest microchannel height of 50 µm and $D_h \leq$ 75µm (a = 1, 2, 3). The microchannel heat sinks with the lowest pressure drop during two-phase conditions was a =1.5 and a = 1 for D_h = 120 µm and D_h = 100 µm. In the case of changing channel height and channel

width the question about narrow or shallow microchannel cross sections choice on the effect of pressure drop can be possibly answered. During two-phase flow the highest pressure drop values were measured.

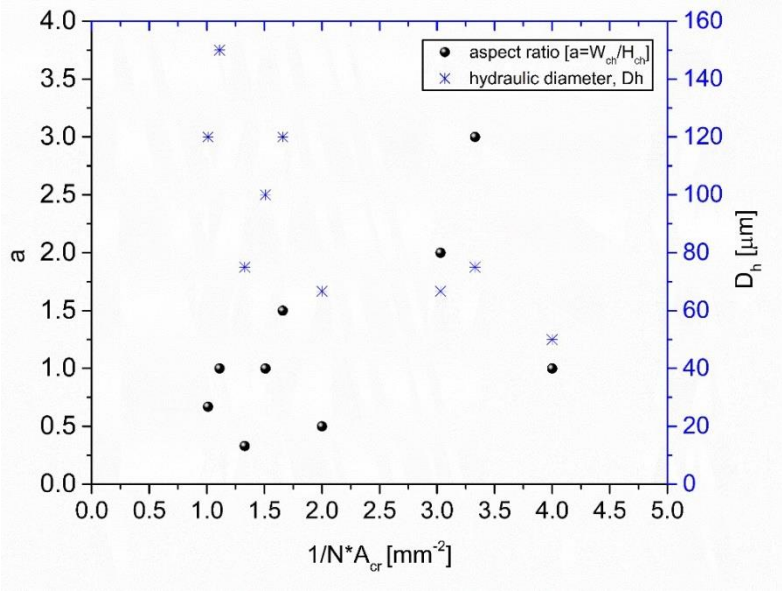

Figure 4. 9 *Aspect ratio of the channel as a function of $1/N A_{cr}$ and D_h.*

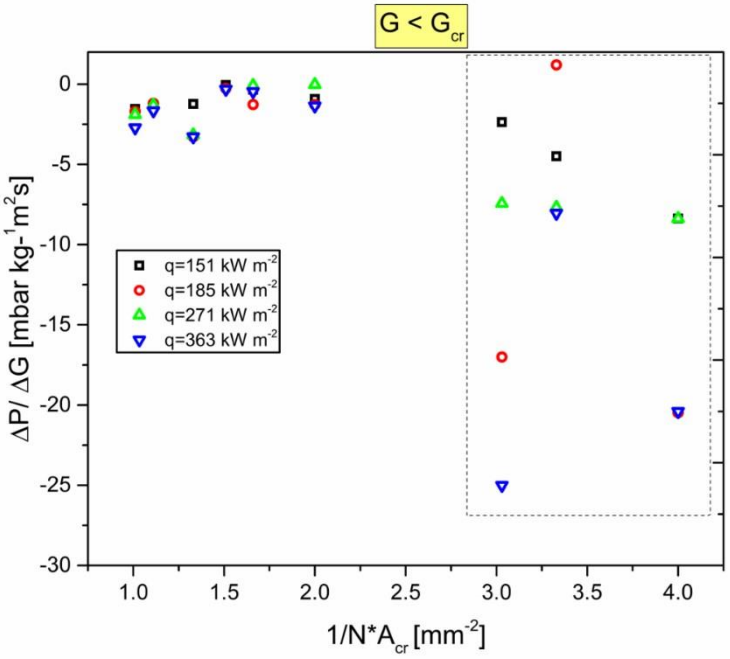

Figure 4. 10 *$\Delta P/\Delta G$ was plotted as a function of $1/N A_{cr}$ where $N A_{cr}$ is the product of the number of the microchannels N and r_{cr} the cross sectional area of the channels.*

4.4.2 Effect of aspect ratio on pressure drop for constant D_h

The comparison of pressure drop was carried out for a range of parameters. The selected W_{ch} and H_{ch} dimensions were in the same range, from 50 µm to 150 µm. This can assist the designer better for the fabrication of the optimum design for low pressure drop performance during boiling in microchannels of 66.7 µm ≤ D_h. ≤ 120 µm and 0.33 ≤ α ≤ 3. Figure 4.11 shows that the comparison was carried out only for these three hydraulic diameters because for the minimum D_h. = 50 µm and the maximum D_h. = 150 µm there was no second set of results to compare aspect ratios, only for α = 1. Table 4.2 shows the constants and variables during these tests. The pressure drop results were produced for both T_{inlet} = 25 ˚C and T_{inlet} = 81 ˚C ± 1˚C. The parameters are given in detail in Table 4.2 of chapter 3. The effect of aspect ratio increase on theD_h. The values of 66.7 µm, 75 µm and 120 µm, were studied. When the microchannel aspect ratio is more than 1 implies that the width of the channel is greater than the height and the microchannels are wider for a constant height. Therefore, the microchannels heat sinks with a > 1 were considered high aspect ratio microchannels. Table 4.3 shows the constants and variables of the experiments. Figure 4.9 presents the $\Delta P/\Delta G$ two-phase slopes for $G < G_{cr}$ and D_h for the two-phase region as a function of the aspect ratio of the microchannel cross section for q = 151 kWm^{-2} (Figure 4.12a) q = 271 kW m^{-2} (Figure 4.9a) and q = 363 kW m^{-2}(Figure 4.12c). Microchannels heat sinks with the same D_h are presented in Figure 4.13 with the same colour. The inlet temperature of the liquid is 25 ºC. Figure 4.10a shows the effect of mass flux on pressure drop for q = 151 kW m^2 and Figure 4.13d shows the results for q =363 kW m^{-2}. For D_h = 66.77 µm the aspect ratios were a = 0.5 and a = 2, for D_h = 75 µm aspect ratios values were 3 and 0.33 and for the D_h = 120 µm the aspect ratios were α = 0.67 and α = 1.5. The increase of aspect ratio resulted in higher-pressure drop values for all designs and heat fluxes except for α =1.5 at q =363 kW m^{-2} which was measured to be lower at the highest heat flux. For constant hydraulic diameter, increasing the aspect ratio resulted in shallower and wider microchannels. The constant highest pressure drop was measured at the lowest aspect ratio and not the highest aspect ratio. Narrow and deeper microchannels resulted in higher-pressure drop values. The pressure drop was also found to increase with decreasing hydraulic diameter. The lowest pressure drop values were found for α = 1.5. The effect of aspect ratio increase on pressure drop is more pronounced for shallower and wider microchannels were both D_h determine the pressure drop effect. For D_h ≤ 100 µm and α >1 which means that W_{ch}>H_{ch}.

Table 4. 2 *Constants and variables of the experiments.*

Constants	Variables
D_h, A_{cr}, G	W_{ch} (↑ with ↑ a) L_{ch}, H_{ch}, P_h (↓with ↑ a)

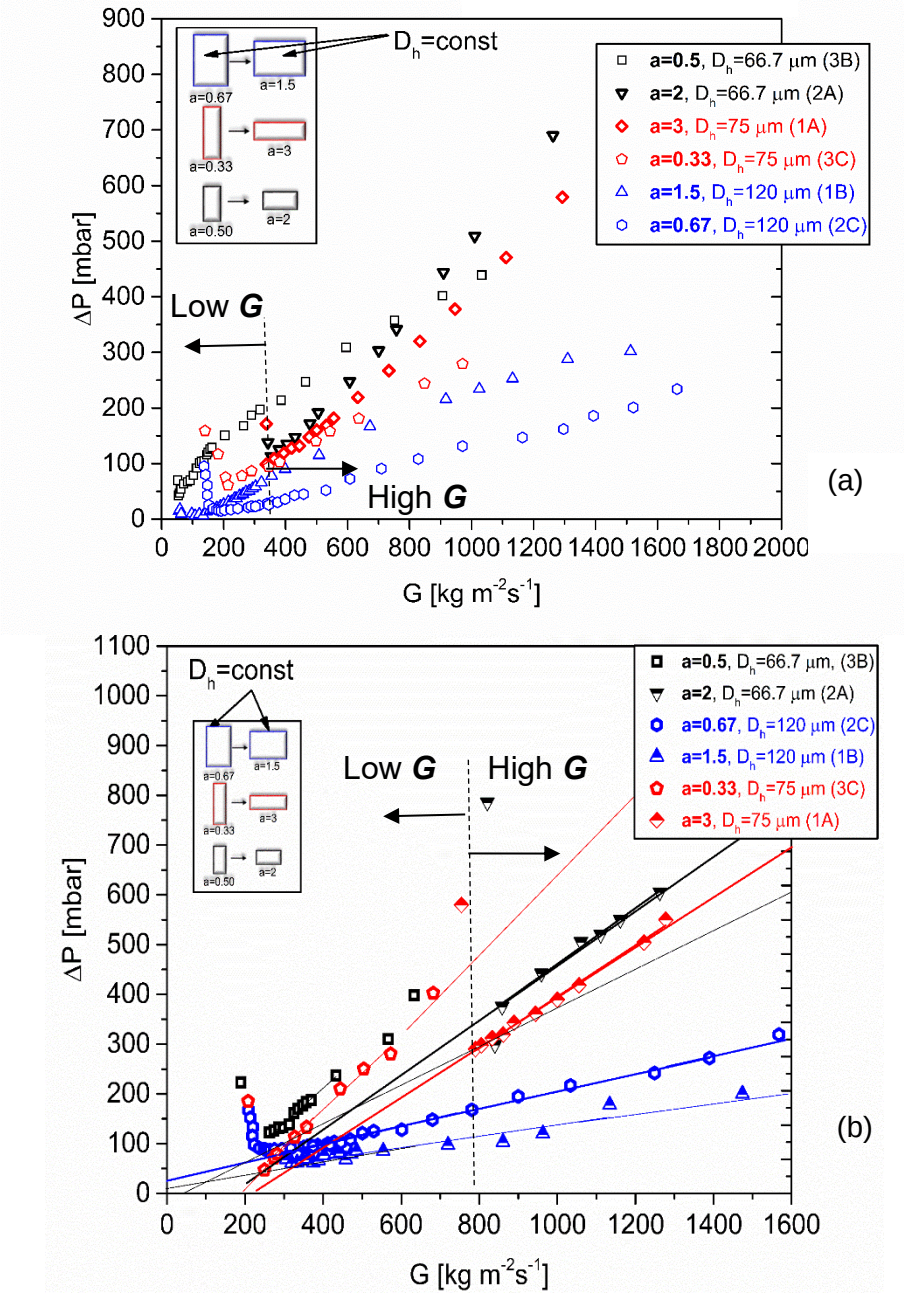

Figure 4. 11 *Effect of mass flux on pressure drop values for single-phase and two-phase pressure drop for six microchannels heat sinks of different aspect ratios but constant D_h. The D_h was kept constant at 66.7, 75 and 120 μm. For D_h =66.7 μm a = 0.5 and a = 2, for D_h = 75 μm constant the aspect ratios were 3 and 0.33 and for the D_h =120μm the aspect ratios were a = 0.67 and a = 1.5 (a) for q=151 kW m^{-2} and (b) for q =363 kW m^{-2} at T_{inlet} =25 ˚C.*

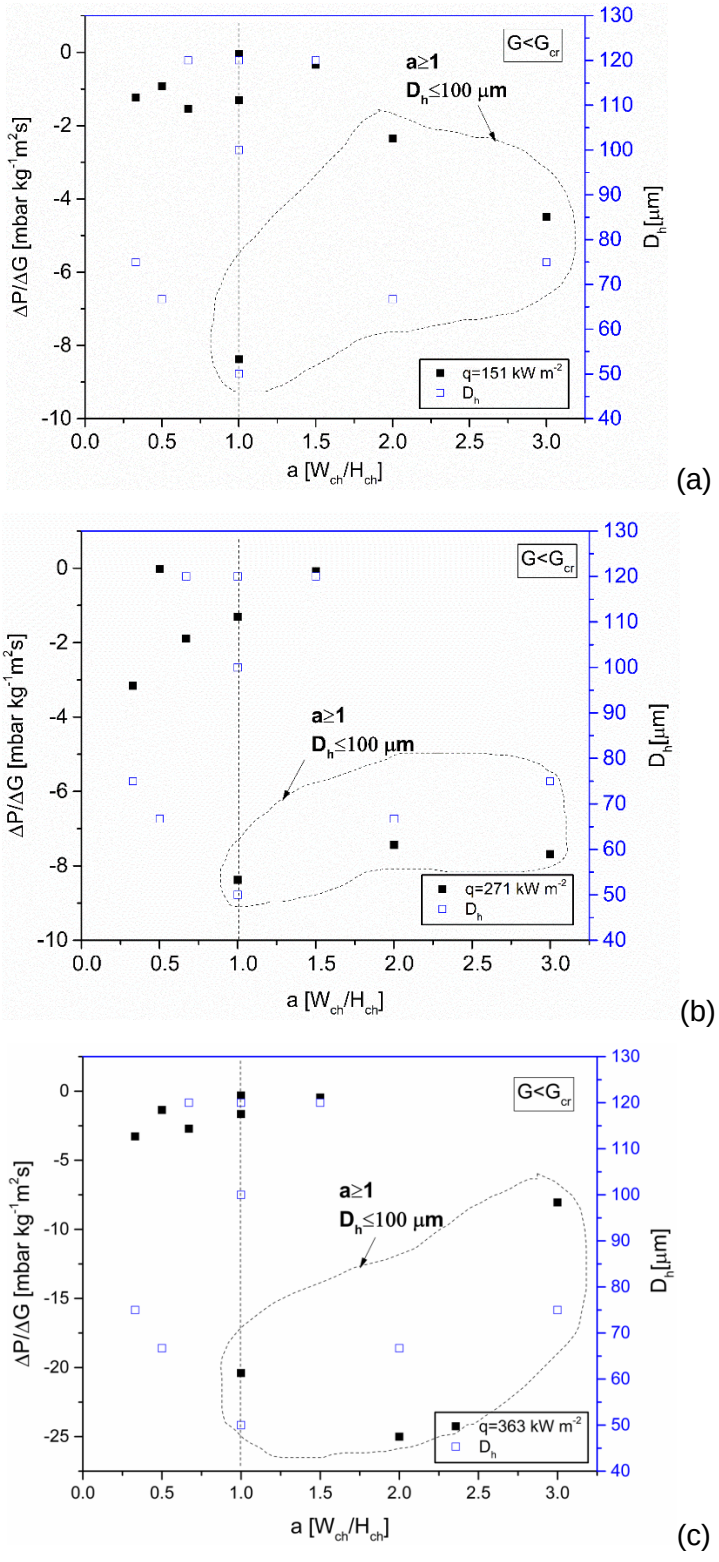

Figure 4. 12 *$\Delta P/\Delta G$ slope and D_h for the two-phase region as a function of the aspect ratio of the microchannel cross section for (a) $q = 151$ kW m^{-2} (b) $q = 271$ kW m^{-2} and (c) $q = 363$ kW m^{-2}.*

Figures 4.13 and 4.14 show the pressure drop versus mass flux only for the two-phase region for a constant heat fluxes. The effect of aspect ratio increase on pressure drop is more intense for shallower and wider microchannels. For $D_h \leq 100$ µm and a which means that $W_{ch} > H_{ch}$.

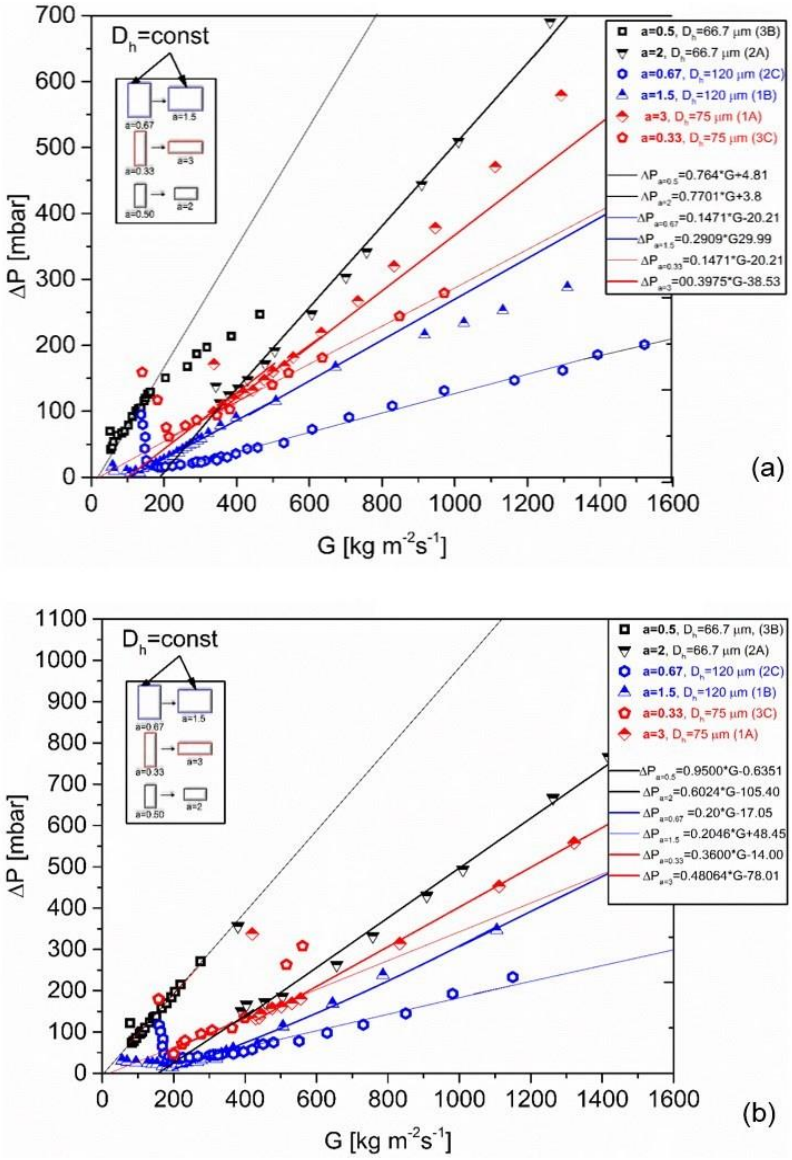

Figure 4. 13 *Pressure drop for single and two-phase flow conditions for a constant hydraulic diameter and changing aspect ratio as a function of mass flux for the heat fluxes of (a) q = 151 kW m^{-2} and (b) q =183 kW m^{-2} for T_{in} = 25 ˚C.*

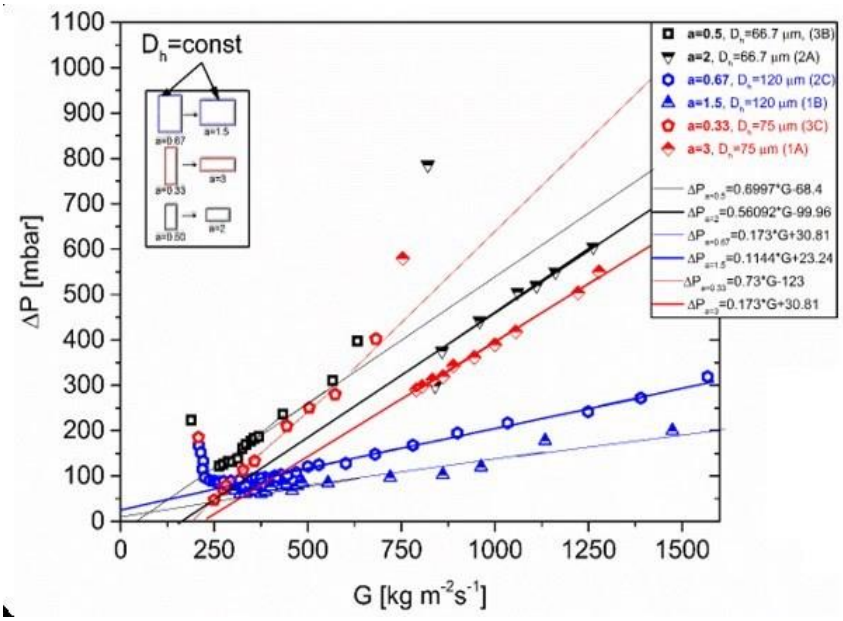

Figure 4. 14 *Pressure drop for single and two-phase flow conditions for a constant hydraulic diameter and changing aspect ratio as a function of mass flux for the heat flux of q = 363 kW m^{-2}, the inlet temperature of T_{inlet} = 25 ºC.*

Figure 4.15 presents pressure drop data for single and two-phase flow conditions for a constant hydraulic diameter and changing aspect ratio as a function of mass flux for the heat fluxes of (a) q = 151 kW m^{-2} and (b) q = 183 kW m^{-2} at T_{inlet} = 81 ºC. Figure 4.16 shows pressure drop data for inlet subcooling of 81 ˚C for single and two-phase flow conditions for a constant hydraulic diameter and changing aspect ratio as a function of mass flux. For the heat fluxes of (a) q = 271 kW m^{-2} and (b) q = 363 kW m^{-2} at T_{in} =81 ºC.

For T_{inlet} = 81˚C dryout results in a sharp increase of the curve after the pressure drop minima. All the values of pressure drop were measured in a higher range compared to 25 ˚C. Figure 4.19 shows the effect of aspect ratio on the product of number of channels with the channel cross section on pressure drop.

Figure 4.17 shows the two-phase time averaged pressure drop as a function of the increasing mass flux for the heat fluxes of 151 kW m^{-2}, 175 kW m^{-2}, 271 kW m^{-2} and 363 kW m^{-2} and the α= 2 and D_h = 66.7 μm at T_{inlet} = 81ºC. The product was used because the hydraulic diameters as well as the aspect ratio of the channels were both changing.

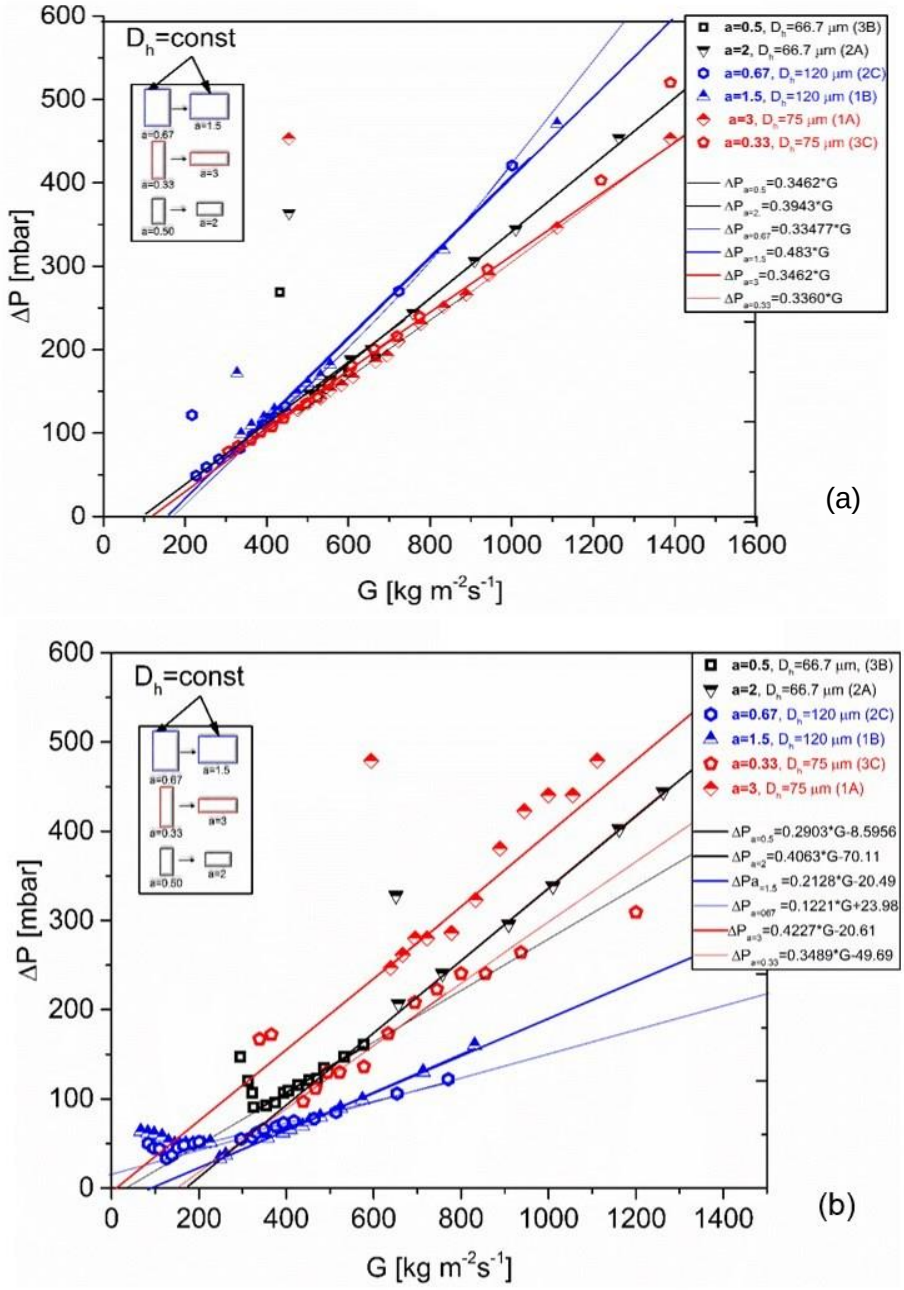

Figure 4. 15 *Pressure drop data for single and two-phase flow conditions for a constant hydraulic diameter and changing aspect ratio as a function of mass flux. For the heat fluxes of (a) q = 151 kW m^{-2} and (b) q = 183 kW m^{-2} at T_{inlet} = 81 ºC.*

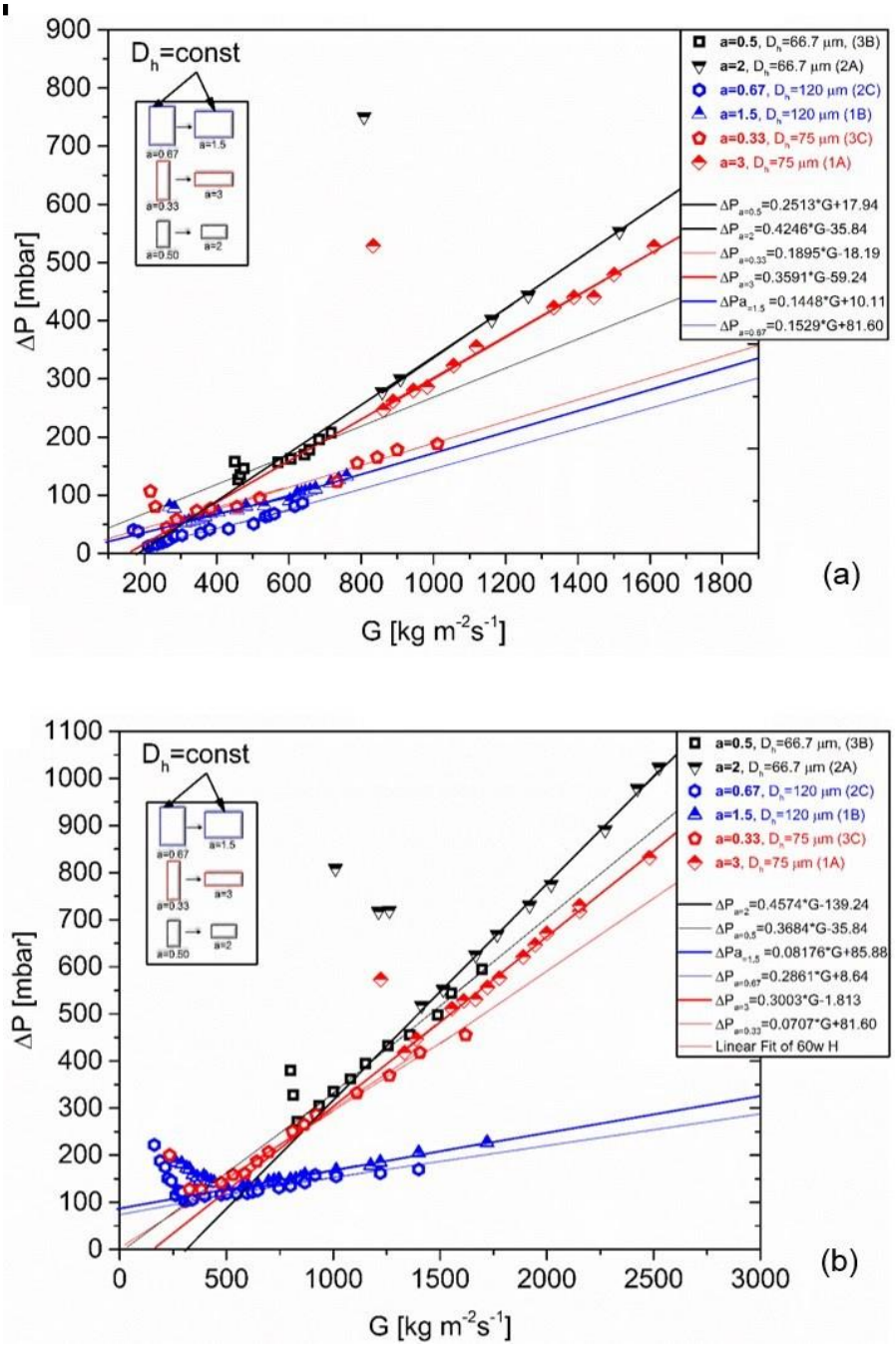

Figure 4. 16 *Pressure drop data for single and two-phase flow conditions for a constant hydraulic diameter and changing aspect ratio as a function of mass flux. For the heat fluxes of (a) q = 271 kW m^{-2}and (b) q = 363 kW m^{-2} at T_{inlet} = 81 ºC.*

Markal *et* al. [72] investigated too the effect of aspect ratio on both flow boiling pressure drop. They examined the effect of aspect ratio on flow boiling in rectangular parallel silicon microchannels at a constant hydraulic diameter of 100 μm using deionised water. The six silicon microchannel heat sinks consisted of 29 silicon parallel rectangular microchannels with aspect

ratio values of 0.37, 0.82, 1.22, 2.71, 3.54 and 5.00.. Flow boiling experiments were conducted for mass fluxes of 151, 195, 238, 281 and 324 kg $m^{-2}s^{-1}$and for the heat fluxes of 71–131 kW m^2. Microchannels with a = 1.22 achieved lowest pressure drop values between 100 and 200 mbar. It was found that there is no regular relationship between the aspect ratio and the total pressure drop. The total pressure drop appeared to have similar trends for all the heat fluxes. It attained minima with decreasing mass flux for a constant heat flux and then increased again with increasing mass flux.

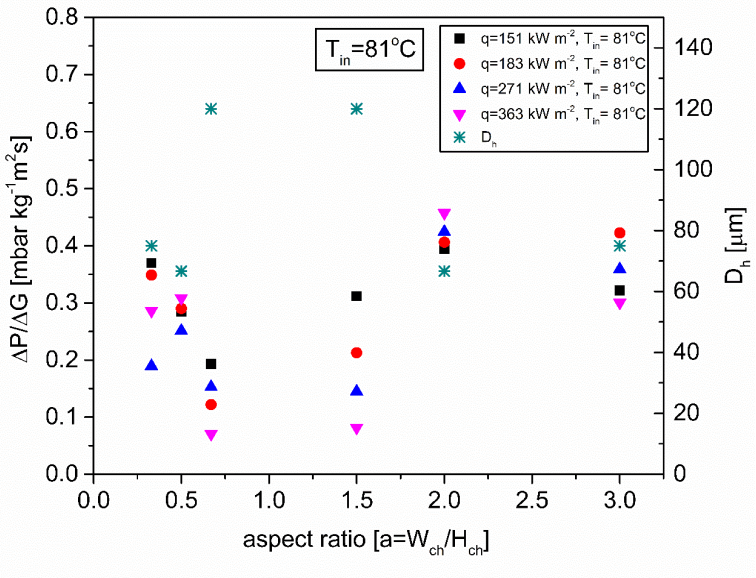

Figure 4. 17 *$\Delta P/\Delta G$ as a function of aspect ratio and D_h for all heat fluxes for (a) T_{inlet} = 25ºC and (b) T_{inlet} = 81 ºC.*

4.4.3 Effect of mass flux on pressure drop of high aspect ratio microchannels of a = 2, a = 3

Figure 4.18 shows the two-phase pressure drop averaged over time as a function of mass flux for the heat fluxes of 141.74 kW m^{-2}, 175.85 kW m^{-2}, 266.34 kW m^{-2}, 364.95 kW m^{-2} for the design 2A, characterised by the aspect ratio of a = 2 and D_h = 66.7 µm at the inlet conditions of T_{inlet} = 81 ºC. Figure 4.19 provides two-phase pressure drop averaged over time as a function of mass flux for the constant heat fluxes of 145.31 kW m^{-2}, 178.16 kW m^{-2}, 273.97 kW m^{-2} and 384.77 kW m^{-2} for the same design at lower inlet temperature of T_{inlet} = 25 ºC. For T_{inlet} = 81 ºC there is requirement for higher flow rates at the same heat fluxes used for lower inlet temperature of 25 ºC.

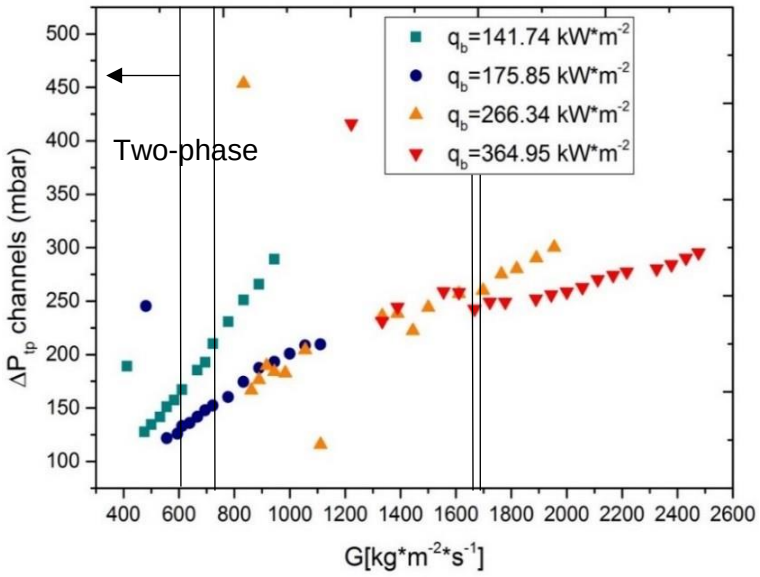

Figure 4. 18 *Two-phase pressure drop averaged over a time interval of 5 min as a function of mass flux for the heat fluxes of 141.74 kW m^{-2}, 175.85 kW m^{-2}, 266.34 kW m^{-2} and 364.95 kW m^{-2} measured for the design 2A with α = 2 at T_{inlet}= 81 ºC.*

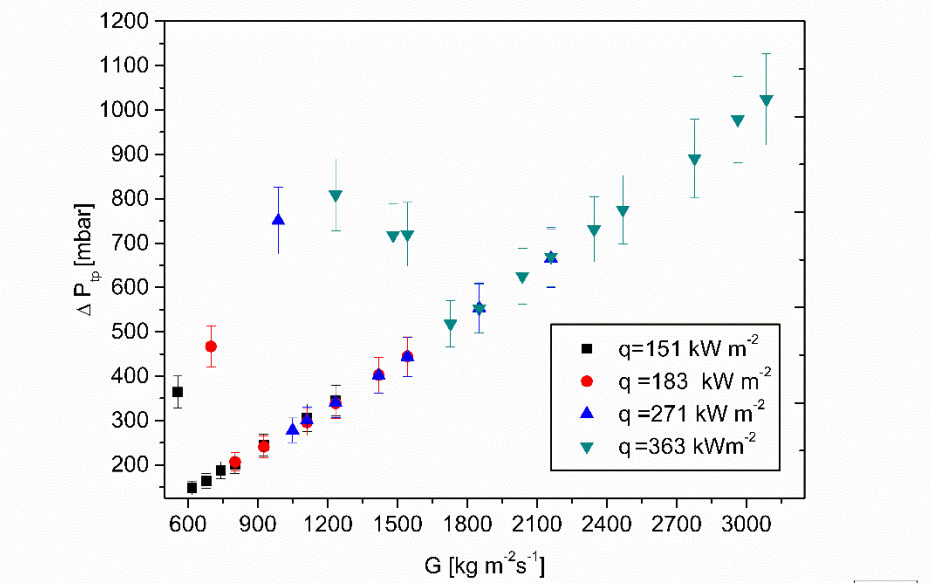

Figure 4. 19 *Two-phase pressure drop averaged over the time interval of 5 min as a function of mass flux for the heat fluxes of 145.31 kW m^{-2}, 178.16 kW m^{-2}, 273.97 kW m^{-2} and 384.77 kW m^{-2} for the design 2A with α = 2 at T_{inlet} =25 ºC.*

4.4.4 Two-phase pressure drop as a function of wall temperature for microchannels with a > 1

Figure 4.20 shows time averaged two-phase pressure drop data as a function of wall temperature at position T5 for the heat fluxes of 151 kW m^{-2}, 183 kW m^{-2}, 271 kW m^{-2} and 363 kW m^{-2} near the exit of a = 2, D_h = 66.7 µm microchannels.

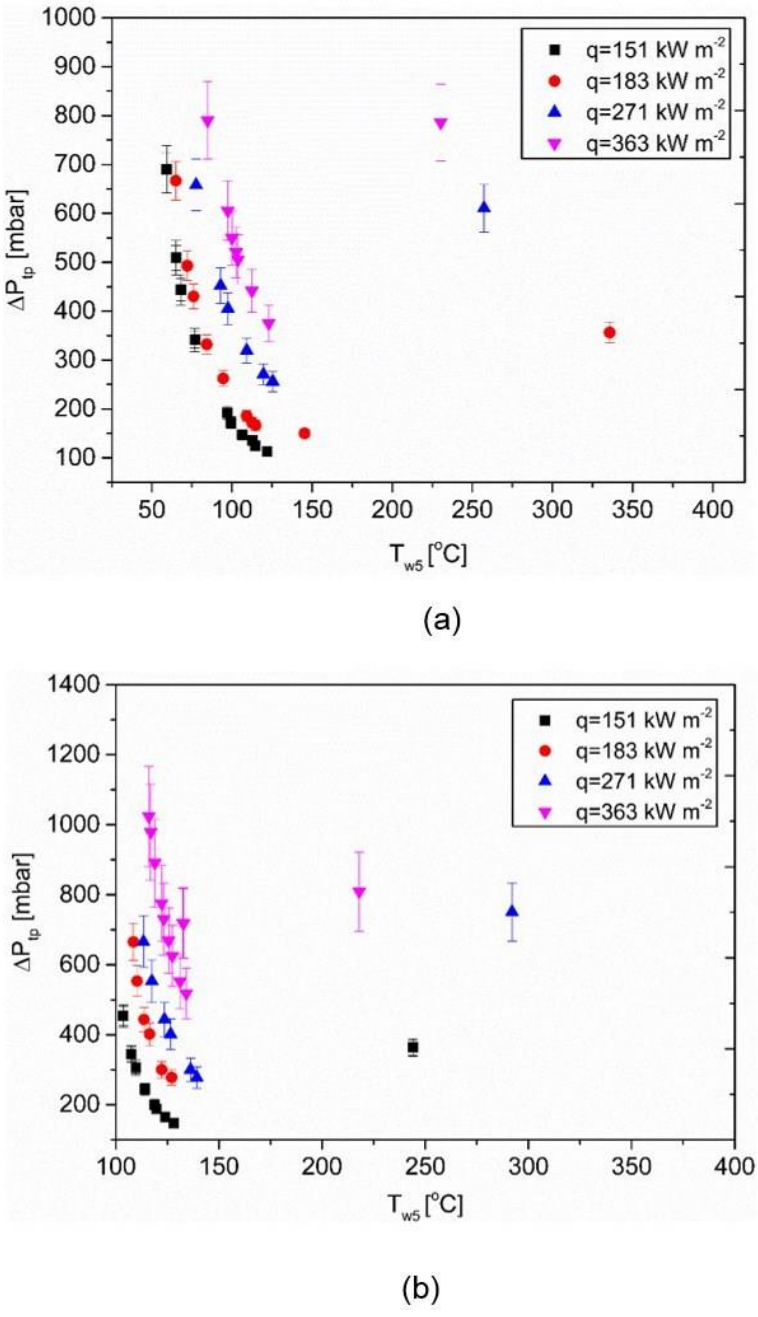

Figure 4. 20 *Time averaged two-phase pressure drop as a function of wall temperature at T5 for the heat fluxes of 151 kW m^{-2}, 183 kW m^{-2}, 271 kW m^{-2} and 363 kW m^{-2} for a = 2 and D_h = 66.7µm for (a) T_{inlet} =25 ºC and (b) T_{inlet} = 81ºC .*

Figure 4.21 shows time averaged two-phase pressure drop as a function of wall temperature at position 5 for the heat fluxes of 151 kW m^{-2}, 183 kW m^{-2}, 271 kW m^{-2} and 363 kW m^{-2} for high aspect ratio channels of α = 3 with D_h = = 66.7 µm (a) and α = 2 (b) with D_h = 75 µm at T_{inlet} = 25 ºC.

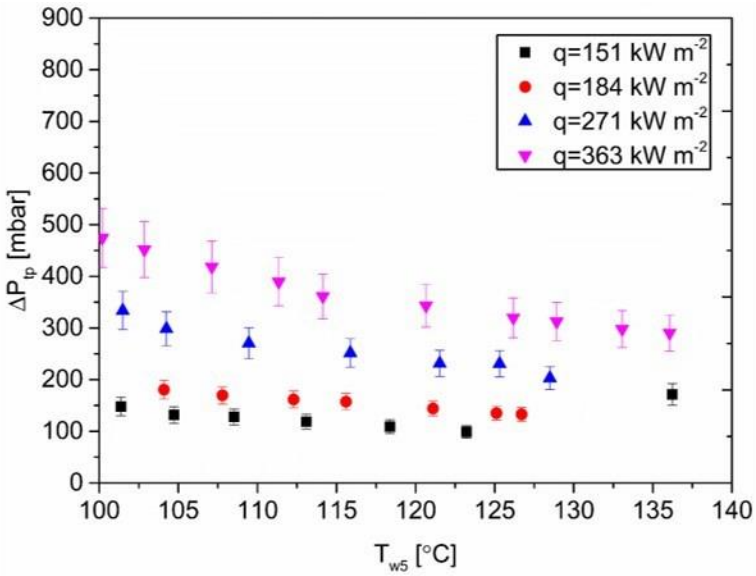

(a)

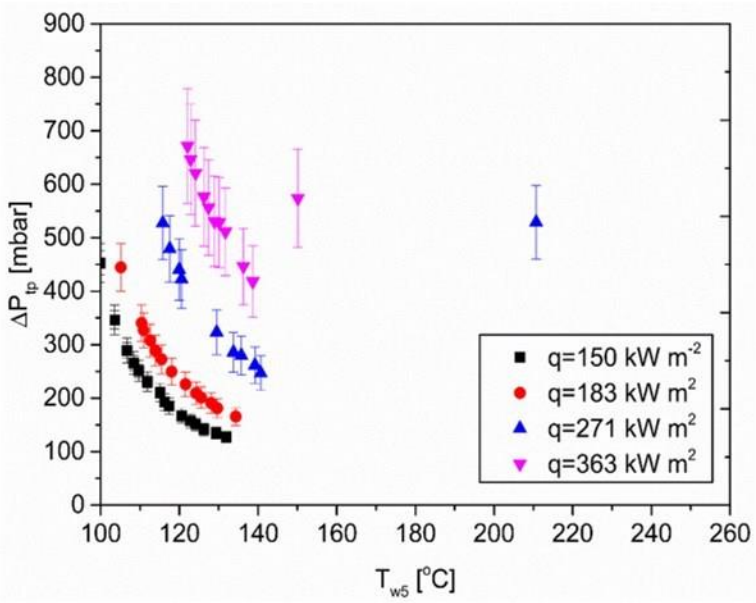

(b)

Figure 4. 21Averaged over time two-phase pressure drop as a function of wall temperature at *T5 for the heat fluxes of 151 kW m^{-2}, 183 kW m^{-2}, 271 kW m^{-2} and 363 kW m^{-2} near the exit (location of T5) of (a) α = 3, D_h = 75 µm and (b) α = 2, D_h = 66.7µm at T_{inlet} =25 ºC.*

The averaged pressure drop ranged from 100 to 500 mbar for all the test heat fluxes for the high aspect ratio microchannels of α = 3 and from 100 to 700 mbar for the aspect ratio of α = 2 for the same heat fluxes. For the medium aspect ratio microchannels, the pressure drop values were found to range only from 5 to 86 mbar for the same inlet conditions used for the α = 2 and α = 3 microchannels. The lower pressure drop values were found in both single-phase and two-phase conditions for the medium aspect ratio of 1.5.

Figure 4.22 shows time averaged two-phase pressure drop as a function of wall temperature at position 5 for the heat fluxes of 151 kW m^{-2}, 183 kW m^{-2}, 271 kW m^{-2} and 363 kW m^{-2} for medium aspect ratio channels of α = 1.5 $_h$ = 120 µm at T_{inlet} = 25 ºC.

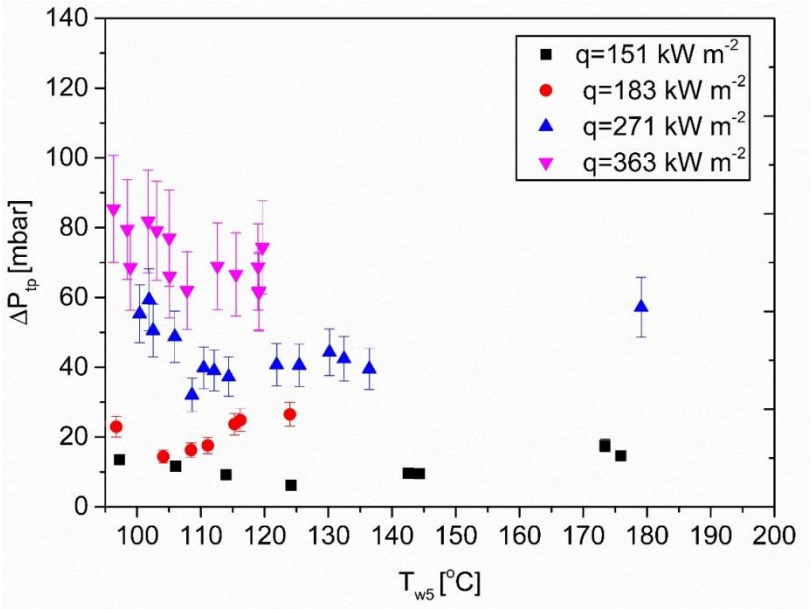

Figure 4. 22. *Averaged over time two-phase pressure drop as a function of wall temperature at position 5 for the heat fluxes of 151 kW m^{-2}, 183 kW m^{-2}, 271 kW m^{-2} and 363 kW m^{-2} near the exit of α =1.5, D_h =120 µm microchannels at T_{inlet}=25 ºC.*

4.4.5 Two-phase pressure drop as a function of the vapour quality

Figure 4.23a shows the averaged (over time) two-phase pressure drop as a function of vapour quality at position 5 for the heat fluxes of 151 kW m^{-2}, 183 kW m^{-2}, 271 kW m^{-2} and 363 kW m-2 near the exit. Figure 4.23a shows two-phase pressure drop results for the highest aspect ratio microchannels of a = 3 and D_h = 75 µm. For the lowest heat flux of 150.43 kW m^{-2}, two-phase pressure drop ranges from 100 to 250 mbar. By increasing the heat flux pressure drop increases from 250 to 450 mbar. For the low heat fluxes, the vapour quality remained in the range between 0 and 0.045. For high heat fluxes of 271.85 kW m^{-2} and 362.69 kW m^{-2} pressure drop increases with increasing vapour quality. For the heat flux value of 271.85 kW m^{-2} pressure drop increased sharply to x_e = 0.15. Increasing the heat flux to 362.69 kW m^{-2} resulted

in sharp increase of the pressure drop. The increase of pressure drop did not happen slowly but rapidly. This could be explained from the flow visualisations. Rapid expansion of vapour occurred simultaneously at all the parallel rectangular microchannels. For the highest aspect ratio (α = 3) microchannels the pressure drop ranged from 100 to 700 mbar for all the heat fluxes. Figure 4.23b shows the pressure drop as a function of vapour quality for the microchannels of aspect ratio of 1.5 and a hydraulic diameter of 120 µm at T_{inlet} = 25 °C. Pressure drop ranges from 5 to 75 mbar for the same heat fluxes as in Figure 4.20a.

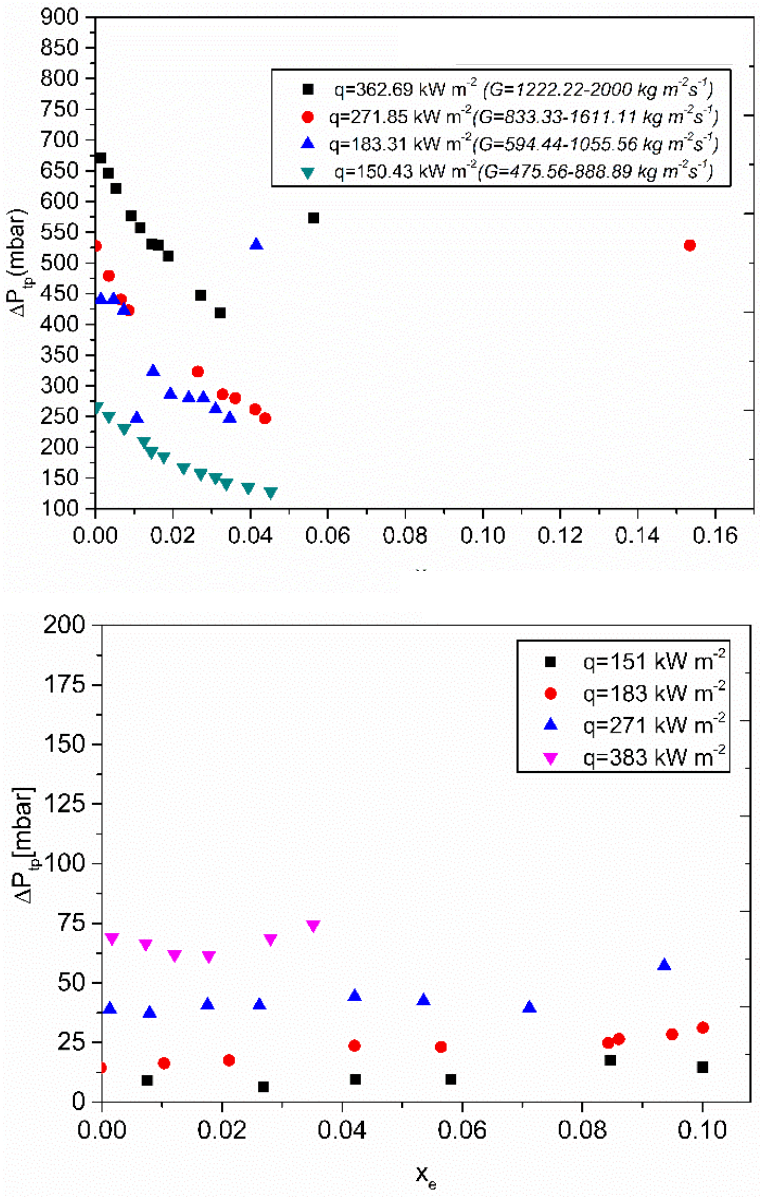

Figure 4. 23. *Averaged over time two-phase pressure drop as a function of vapour quality at T5 for the heat fluxes of 151 kW m^{-2}, 183 kW m^{-2}, 271 kW m^{-2} and 363 kW m^{-2} near the exit of (a) α = 3, D_h = 75 µm, T_{inlet} = 81 ºC (b) α =1.5, D_h = 120 µm microchannels at T_{inlet}=25 ºC.*

4.4.6. Two-phase heat transfer coefficients and flow visualisations

The highest values of heat transfer coefficient with modest pressure drop were obtained during two-phase flow mode for silicon microchannels heat sink of α = 1.5 and hydraulic diameter of 120 µm. Figure 4.24 shows the local heat transfer coefficient h_{1tp} calculated at location of *T1* during two-phase flow boiling at T_{inlet} = 81 ºC and q = 271 kW m^{-2} as a function of mass flow rate ($\dot{m}$). The silicon microchannel heat sinks are characterised by aspect ratios of α = 3, 2, 1, 1.5, 1, 0.5 and D_h = 75 µm, 66.7 µm, 120 µm, 100 µm, 66.7 µm, respectively. The points of the graph are spatially averaged values at location of sensor T1 over t = 5 min. The microchannels cross section shape for each case is shown in Figure 4.24 in a schematic next to the graph. The colour of the cross section represents the colour of the points. Figure 4. shows that the microchannel heat sinks with aspect ratios of 0.5,1 ,1.5 and D_h = 66.7, 100, 120 µm, respectively, require less liquid mass flow rate compared to the other two shallow rectangular cross sections of α = 3, 2 with D_h = 75, 66.7 µm. The results show that the highest $h_{1.tp}$ values are achieved for α= 1.5 and D_h = 120 µm and they range from 25 to 176 kW m^{-2}K^{-1}.

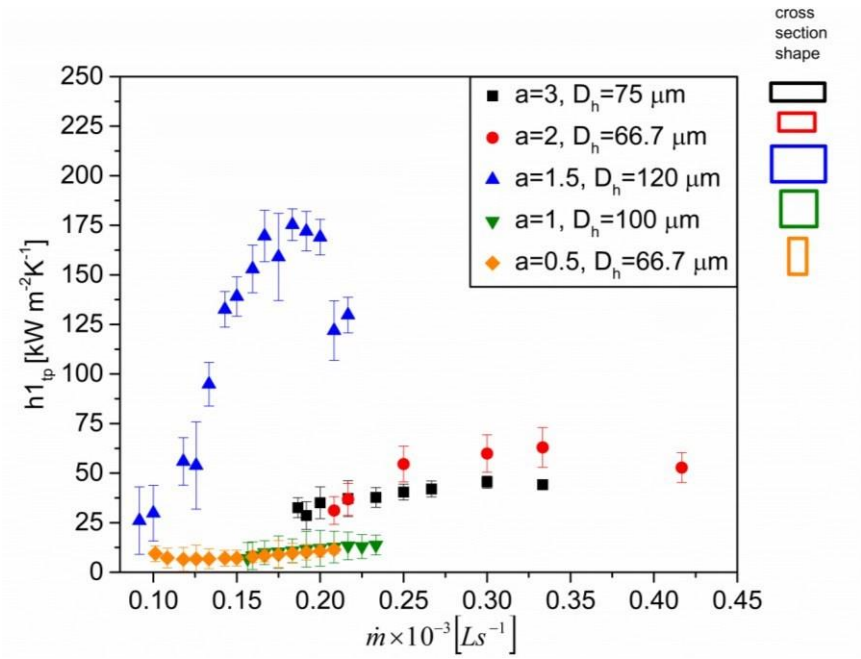

Figure 4. 24 *Local time averaged heat transfer coefficient calculated at location of sensor T1 as a function of mass flow rate at T_{inlet}= 81 ºC, at q = 271 kW m^{-2} for the designs with α = 3, 2, 1.5, 1 and 0.5 and D_h = 75, 66, 120, 100, 66.7 µm.*

Markal *et* al. [72] examined the effect of aspect ratio on flow boiling in rectangular parallel silicon microchannels at a constant hydraulic diameter of 100 µm using deionised water. The six silicon microchannel heat sinks consisted of 29 silicon parallel rectangular microchannels

with aspect ratio values of 0.37, 0.82, 1.22, 2.71, 3.54 and 5.00. They heated up the test section by using four cartridge heaters and they used thermocouples embedded in the copper block under microchannel base for local wall temperature measurements. Flow boiling experiments were conducted for mass fluxes of 151, 195, 238, 281 and 324 kg $m^{-2}s^{-1}$and for the heat fluxes of 71– 131 kW m^{-2}. The inlet temperature of deionized water was kept constant at 50 ± 1˚ C throughout the tests. The heat transfer coefficient was obtained only at the location of the ninth thermocouple, 41.5 mm from the channel inlet. The microchannels with a = 1.22 achieved the maximum heat transfer coefficient performance and the lowest pressure drop values between 100 and 200 mbar.

It was found that there is no regular relationship between the aspect ratio and the total pressure drop. The value of $h_{1,}$ is higher for a = 2 compared to a = 3. For the microchannel heat sinks with shallow rectangular cross sections of a = 3, 2 (D_h = 75, 66.7 μm) the mass flow rate requirement is higher because of the smaller D_h. The lowest heat transfer coefficients $h_{1,}$ is measured for the =1, 0.5 at D_h = 100 and 66.7 μm.

Figure 4.25 shows the annular flow regime optically recorded with the high-speed camera at 1000 Hz for $\dot{m} = 0.084\ 10^{-3}\ Ls^{-1}$ and q = 271 kWm^{-2} during two-phase flow at T_{inlet} =81 ºC for the designs with microchannel cross sections of a = 1.5, 1, 0.5. For all three cases the microchannel height is constant at 100 μm and the aspect ratio increases by increasing the channel width from 50 (a = 0.5) to 150 μm (a = 1.5).

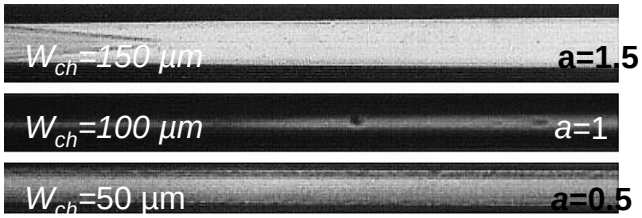

Figure 4. 25 *Annular flow regime recorded with the high-speed camera at 1000 Hz for $\dot{m} = 0.084 \times 10^{-3}$ kg s^{-1} and q = 271 kW m^{-2} during two-phase flow at T_{inlet}= 81 ºC for the designs with microchannel cross sections of a =1.5, 1, 0.5 at a constant channel height of 100 μm and increasing channel width.*

4.4.7 Two-phase heat transfer coefficients for α = 3 and D_h= 75 μm microchannels

Figure 4.26a shows the local heat transfer coefficient as a function of vapour quality at the location of sensor *T1* for α = 3 at constant heat fluxes for α = 3, D_h = 75μm and Figure 4.26b the local heat transfer coefficient at T5 as a function of mass flux at constant heat fluxes of 151 kW $m^{-2}K^{-1}$, 174 kW $m^{-2}K^{-1}$, 271 kW $m^{-2}K^{-1}$ and 364 kW $m^{-2}K^{-1}$ for α = 3 and D_h = 75μm.

Figure 4.27 shows images from flow visualisations obtained with high-speed camera at 1000 Hz that show evaporation at the inlet of the channels at G = 337.22 kg m^{-2} s^{-1}, q =151 kWm^{-2} for the design of α = 3, D_h = 75 μm at location of sensor T5. The images were cropped to show the evolution of the regime in time for one microchannel.

Figure 4.28a shows uniform liquid film evaporation from both channel sidewalls, as well as Figure 4.28b. Non-uniform film evaporation at the inlet of the channels at G = 337.22 kg m^{-2} s^{-1}, q = 151 kW m^{-2} at 1000 Hz high aspect ratio in direction of the width of the microchannels of α = 3, D_h = 75μm at location of sensor T5. The images are cropped to show the evolution of the regime in time for one microchannel. Bubble nucleation was found to occur at the sidewalls during annular flow regime in the high aspect ratio microchannels, Figure 4.b.

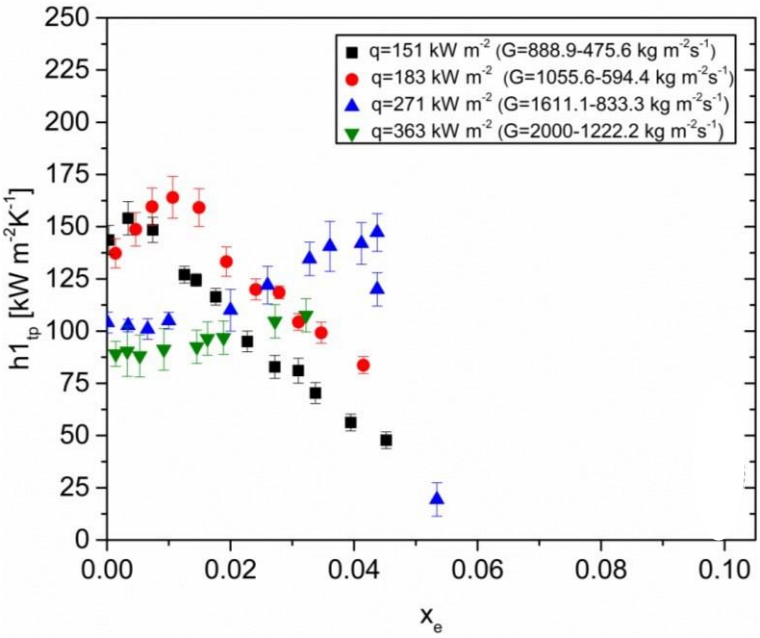

(a)

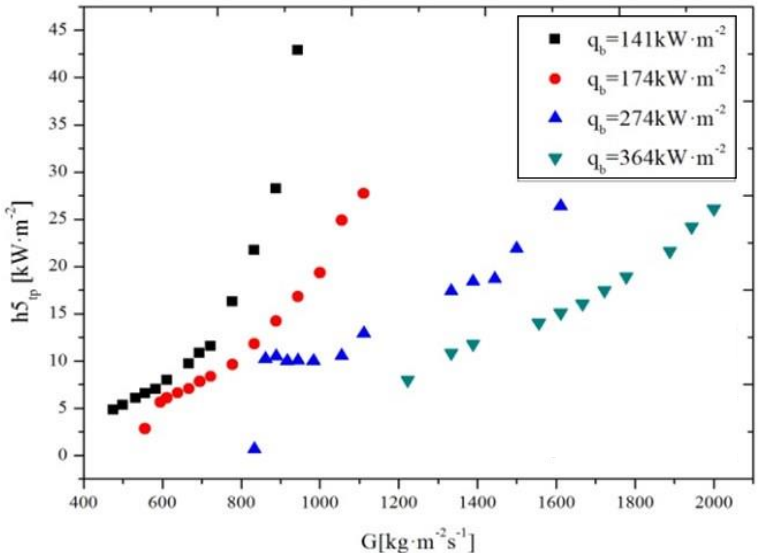

(b)

Figure 4. 26 *Local heat transfer coefficient as a function of vapour quality (a) at T1 and (b) at T5 as a function of mass flux at constant heat fluxes of 151 kW m^{-2}K^{-1}, 174 kW m^{-2}K^{-1}, 271 kW m^{-2}K^{-1} and 364 kW m^{-2}K^{-1} for α = 3 and D_h = 75 µm microchannels.*

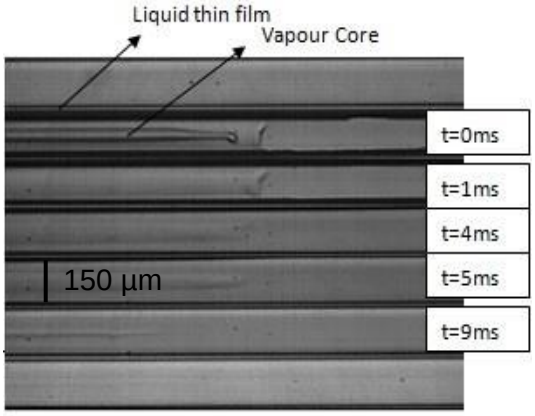

Flow visualisation obtained with high-speed camera at 1000 Hz that shows evaporation at the inlet of the channels at G = 337.22 kg m^{-2} s^{-1} and q = 151 kWm^{-2} for the design of α = 3, D_h = 75µm at location of sensor T5.

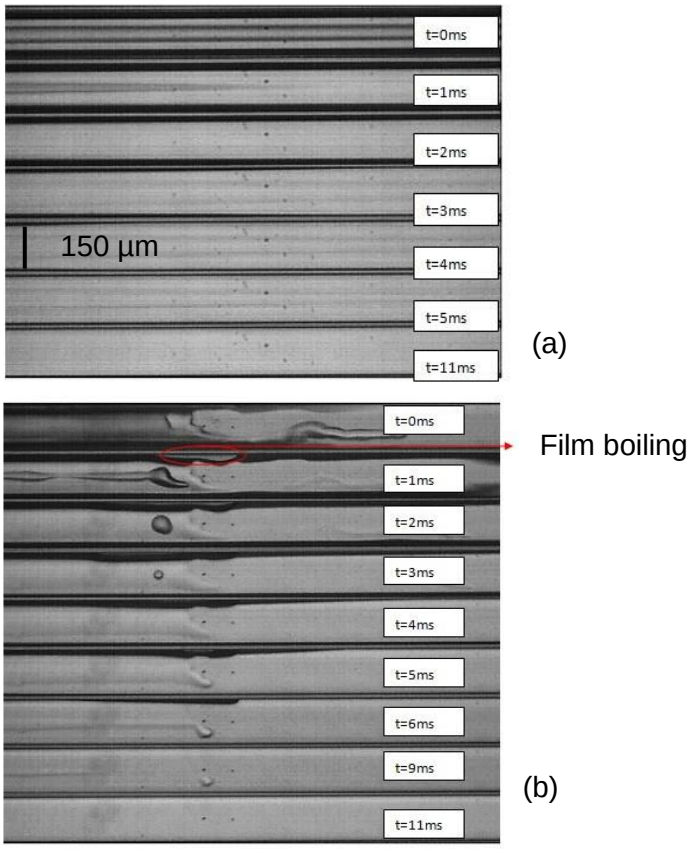

Figure 4. 27*(a) Uniform thin film evaporation and (b) non uniform film evaporation at the inlet of the channels for G = 337.22 kg m^{-2} s^{-1} and q =151 kWm^{-2} at 1000 Hz with α = 3, D_h = 75µm at location of sensor T5.*

Figure 4.2 illustrates with image sequence the rewetting and wetting periodic cycles for α = 3 with D_h = 75 µm, at the heat flux of 271 kW m^{-2}, T_{inlet} = 25 ˚C. The periodic cycles were

characterised by the flow pattern of plug flow, annular flow the observed flow patterns were recorded at 5130 Hz.

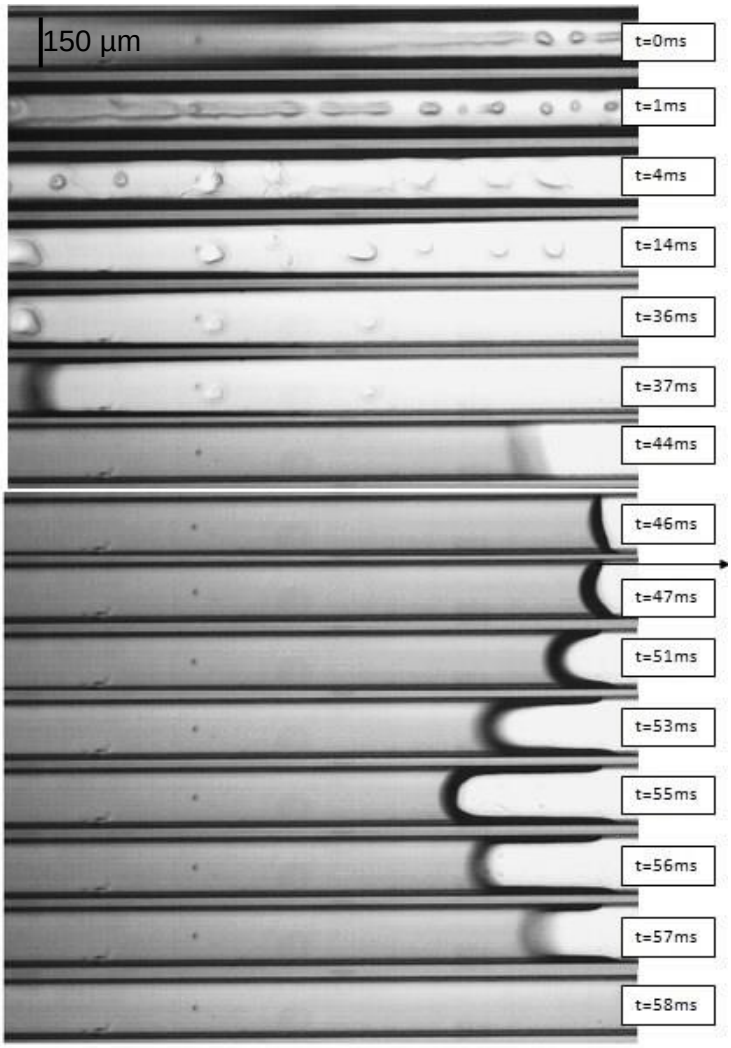

Figure 4. 28. *Image sequence of periodic cycles of instabilities for α = 3, D_h = 75µm, at the heat flux of 271 kW m^{-2}, T_{inlet} = 25 ˚C. The observed flow patterns were annular flow, mist flow and plug flow and were recorded at 5130 Hz. The width of the microchannels is 150 µm.*

Figure 4. 29 shows measurements of the width of the liquid which was observed to exist at high aspect ratio (α = 3) microchannel meniscus and was captured using the high–speed camera. The width of the liquid attached to the two sidewalls (sd1 and sd2) was also measured using ImageJ software. The liquid width was measured for the microchannel of 150 µm for each frame presented in previous Figure .4.28.

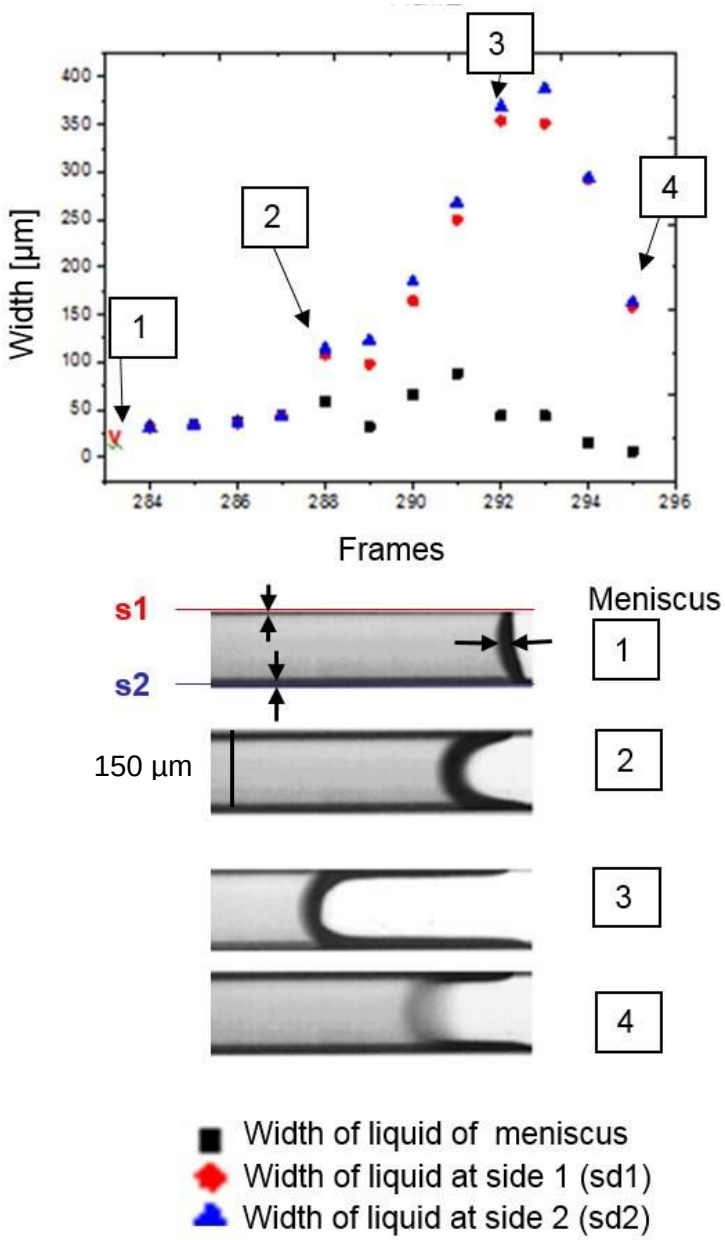

Figure 4. 29 *Measurements of length from high-speed visualisation images for high aspect ratio of α = 3 using Image J.*

4.4.8 Two-phase heat transfer coefficients for α = 2

Figure 4. 30 shows the local heat transfer coefficients (a) T1 (b) T2 (c) T3 (d) T4 averaged over time as a function of mass flux for T_{in} = 81 ºC for design 2A, α = 2.

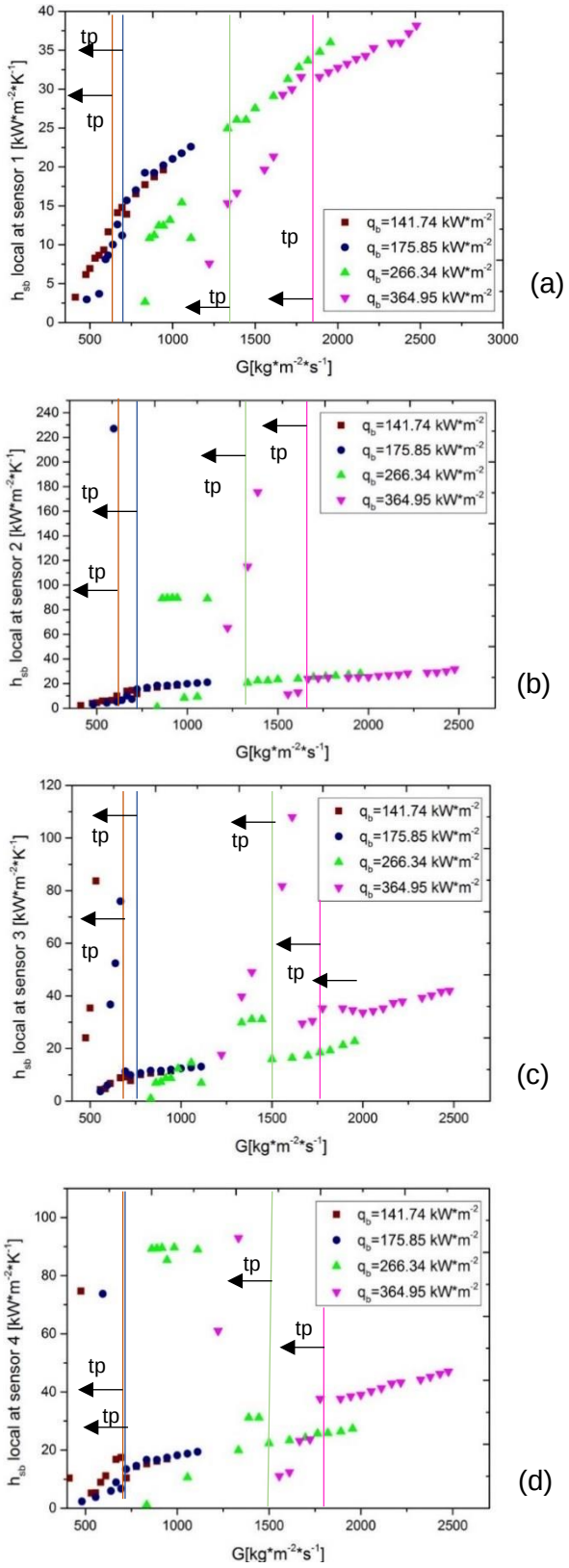

Figure 4. 30 *Local heat transfer coefficients at locations of (a) T1 (b) T2 (c)T3 (d) T4 averaged over time as a function of mass flux for T_{inlet}= 81 ºC for design 2A, α = 2.*

For α = 3 (D_h = 75 μm), eruption boiling occurred directly after single- phase, flow there is annular and mist flow at low mass flux because of large superheat. Figure 4.31 shows the existence of different flow regimes at parallel microchannels (t = 5 ms, 10 ms and 15 ms). Of α = 2, D_h = 66.7 μm, using × 5 magnification, at 5000 Hz, q = 363 kW m^{-2}, G = 1263 kg m^{-2}s^{-1}, location of T1. Figure 4.30 shows the flow patterns with × 10 magnification for α = 2, D_h = 66.7 μm, at 5000 Hz, q = 363 kW m^{-2}, T_{in} = 81 °C at the location of T1. Figure 4.31 shows a sequence of optical images that show the different flow regimes in the parallel microchannels of α = 2, D_h = 66.7 μm. Flow visualisations were obtained at the position of T4 (x_e = 0.0494). The optical images were obtained at q = 363 kW m^{-2} and G = 1,263 kg m^{-2}s^{-1} at T_{inlet} = 81 ºC. The recording rate was 5000 Hz and × 5 magnification.

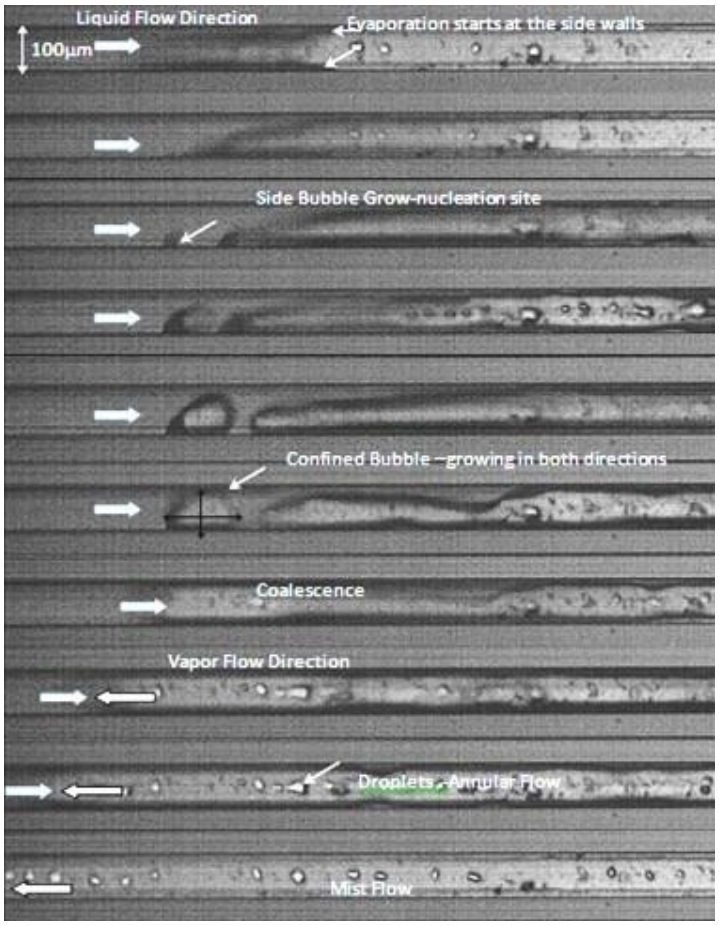

Figure 4. 31 *A sequence of optical images of one selected microchannel that shows how bubble nucleation, confinement and flow reversal results in suspected dryout conditions along a microchannel of α = 2, D_h = 66.7 μm. Flow visualisations were obtained at the position of T4 (x_e = 0.0494). The optical images were recorded at q = 363 kW m^{-2} and G = 1,263 kg m^{-2}s^{-1} at high inlet temperature of T_{inlet} = 81 ºC. The recording rate was 5000 Hz with × 5 magnification.*

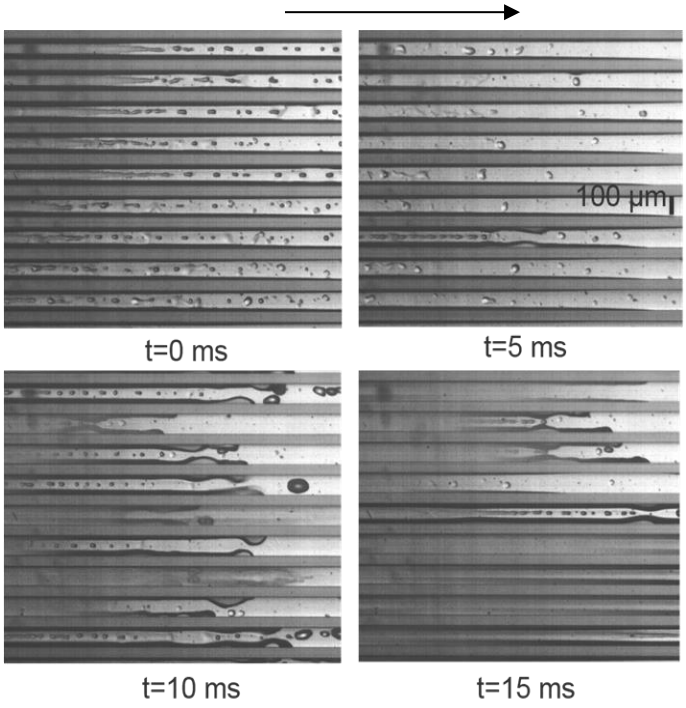

Figure 4. 32 *Flow visualisations presented with a sequence of optical images obtained at location of T1 that reveal the existence of different flow regimes at parallel microchannels (t = 5 ms, 10 ms and 15 ms).* $\alpha = 2$, $D_h = 66.7\ \mu m$, × 5 magnification, 5000 Hz, $q = 363\ kW\ m^{-2}$, $G = 1263\ kg\ m^{-2}s^{-1}$, *location of T1. Arrow shows the bulk flow direction.*

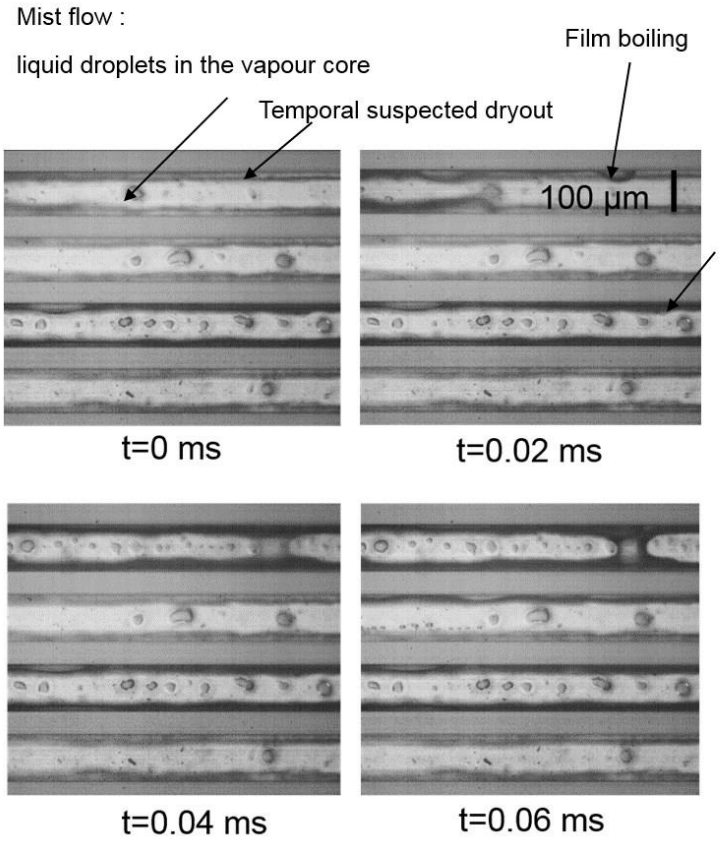

Figure 4. 33 *Details of the flow regimes in parallel microchannels are shown using ×10 magnification for α = 2, D_h = 66.7 µm, at 5000 Hz, q = 363 kW m^{-2}, T_{inlet}= 81 °C, location of sensor T1.*

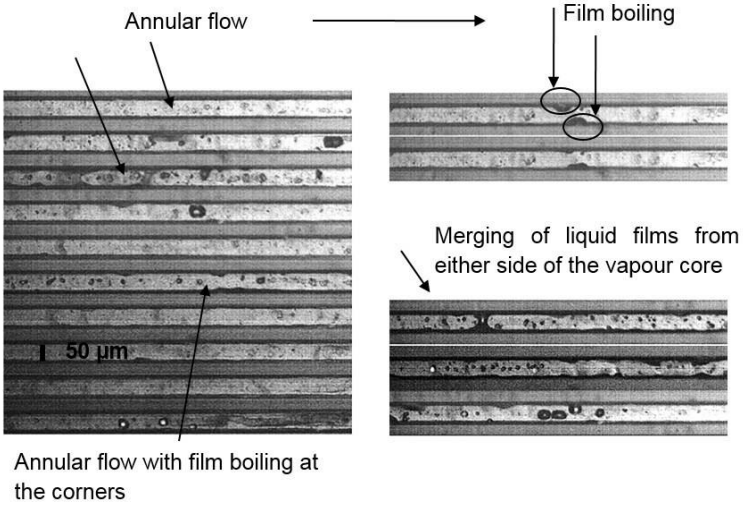

Figure 4. 34 *A sequence of optical images that show the different flow regimes in the parallel microchannels of α = 2, D_h = 66.7 µm. Flow visualizations occurred at the location of T4 (x_e = 0.0494). The optical images were obtained at q = 383 kW m^{-2} and G = 1263 kg m^{-2}s^{-1} at high inlet temperature of T_{inlet} = 81 ºC. The recording rate was 5000 Hz and × 5 magnification. Arrow on top of figure shows bulk flow direction.*

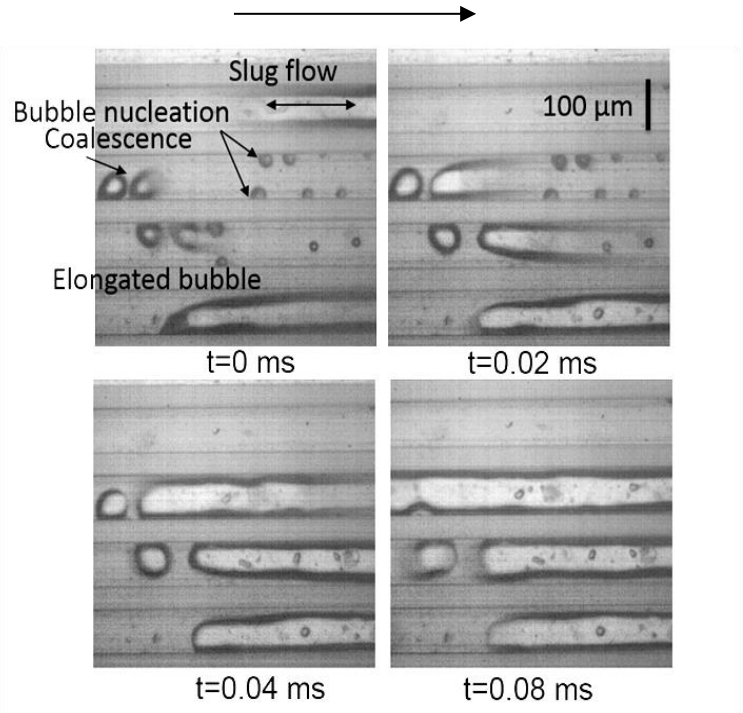

Figure 4. 35 *A sequence of optical images that show the increase of nucleation sites at higher mass flux, along a microchannel of a = 2, D_h = 66.7 µm. Images sequence captured at the location of T4 (x_e = 0.0494). The optical images were obtained at q = 440 kW m^{-2} and G = 1263 kg m^{-2}s^{-1} at high inlet temperature of T_{inlet} = 81 ºC. The recording rate was 5000 Hz and × 10 magnification was used. Arrow on top of figure shows the bulk flow direction.*

Figure 4.34 shows the local heat transfer coefficient as a function of vapour quality at T5 for constant heat fluxes for a = 2. The exit vapour quality is in the range of 0 to 0.55. The local heat transfer coefficient decreases with vapour quality. At q = 271 kW m^{-2} the microchannel wall temperature are presented in the graphs with decreasing mass flux. There is a sharp increase of the wall temperature because of the parallel channel instabilities. The temperature reached 350 ºC at the location of T3 for the mass flux of 802.47 kg m^{-2}s^{-1}. Figure 4.35 shows the local heat transfer coefficients at positions 1, 3, 5 as a function of vapour quality at a constant mass flux of 1234.5 kg m^{-2}s^{-1} for a = 2. At constant mass flux of 1234.5 kg m^{-2}s^{-1} the local heat transfer coefficients show a strong dependence with increasing heat flux. At constant mass flux of 1234.5 kg m^{-2}s^{-1} the local heat transfer coefficients show a strong dependence with increasing heat flux. At vapour quality higher than 0.05 the heat transfer coefficient is very low because of the dryout in the channels as the temperature locally at positions 2, 3, 4 and 5 is higher than 135 ºC with a maximum at position 5 of 187.85 ºC averaged.

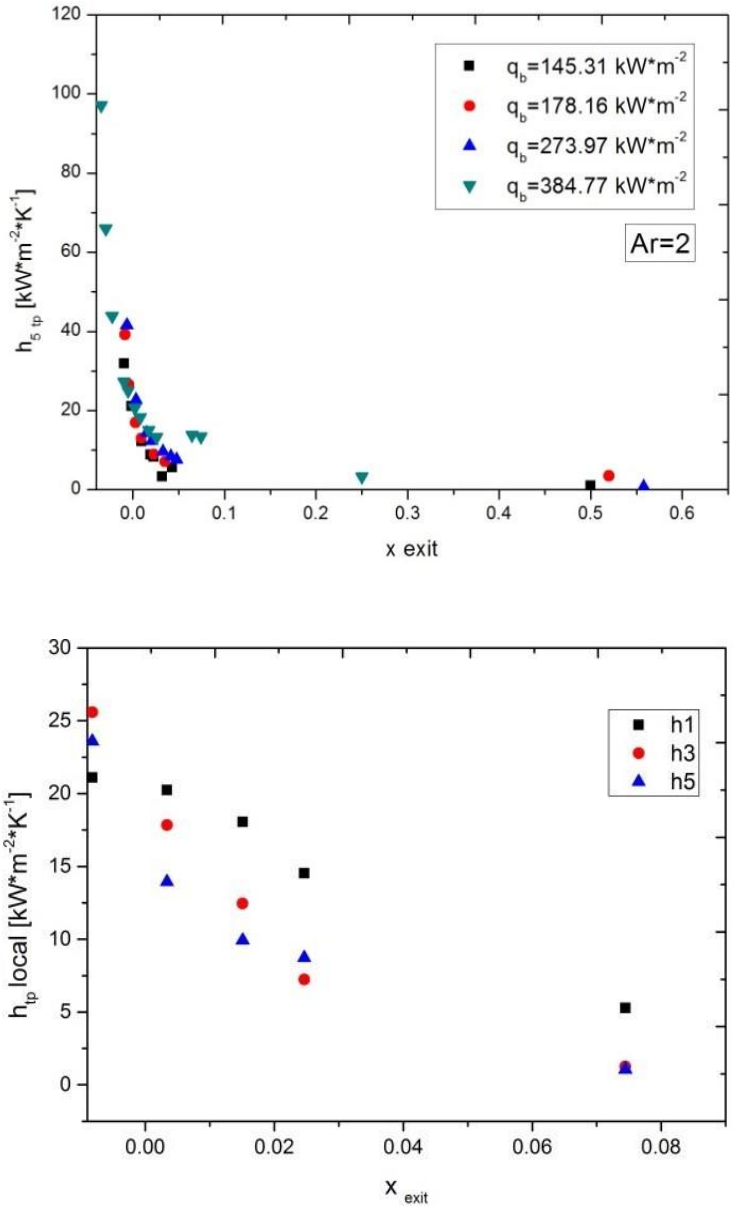

Figure 4. 36 *(a)Local heat transfer coefficient as a function of vapour quality at location of T5 for constant heat fluxes of 145.31 kW m^{-2}, 178.16 kW m^{-2}, 273.97 16 kW m^{-2}, 384.77 16 kW m^{-2}, for the microchannels with α = 2. (b) Local heat transfer coefficients at T1,T 3 and T5 plotted as a function of vapour quality for the constant mass flux of 1234.57 kg m^{-2}s^{-1} for α = 2.*

Figures 4.37 and 4.38 show image sequences obtained at 100 Hz at the location of T3 and T1 respectively for α = 2 and q = 271 kW m^{-2}, x_e > 0.05. Arrow on top of figure shows the bulk flow direction.

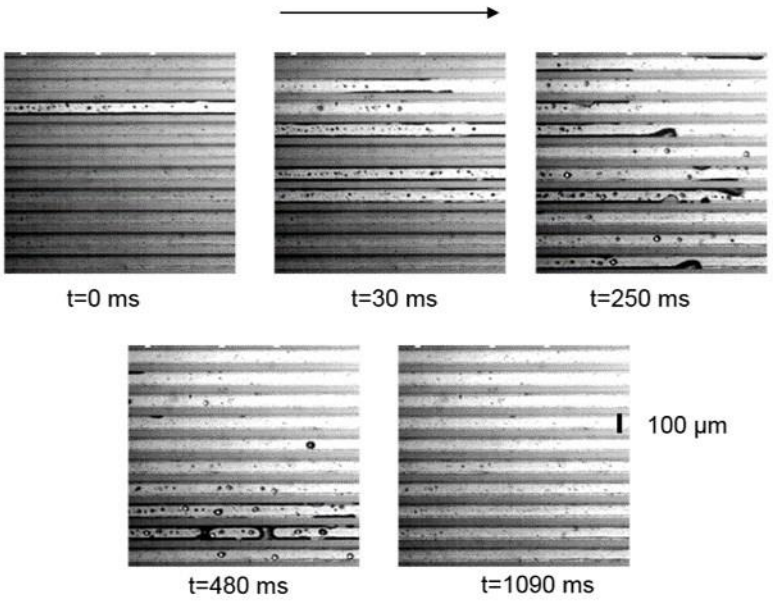

Figure 4. 37 *Image sequences obtained at 100 Hz at the location of T3 for α = 2 and q =271 kW m^{-2}, α = 2, where x_e = 0.05. Arrow on top of figure shows the bulk flow direction.*

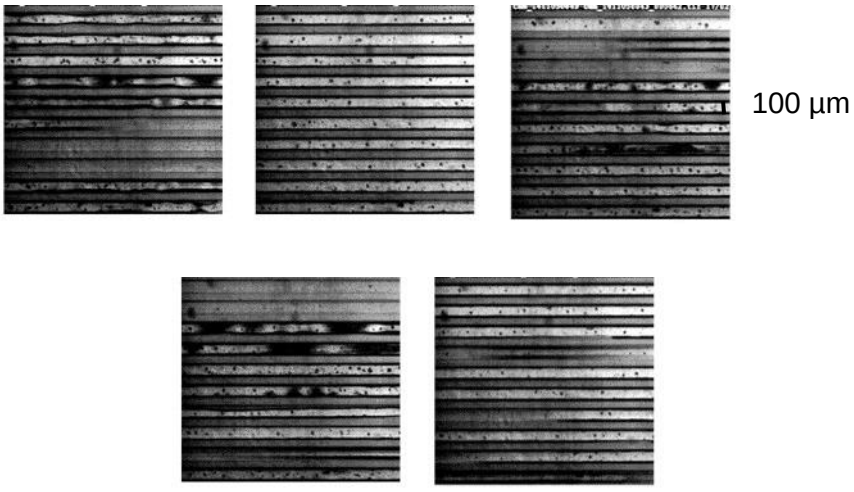

Figure 4. 38 *Image sequence, captured at location of T1, at 100 Hz, q = 271 kW m^{-2}, α = 2 where x_e = 0.05.*

4.4.9 Two-phase heat transfer coefficients for α = 1.5

Figure 4.38 shows the two-phase heat transfer coefficients as a function of exit vapour quality for two different heat fluxes of 183 kW m^{-2} and 271 kWm^{-2} for the design 1B, D_h = 120 µm, a = 1.5 at T_{inlet} = 25 ºC.

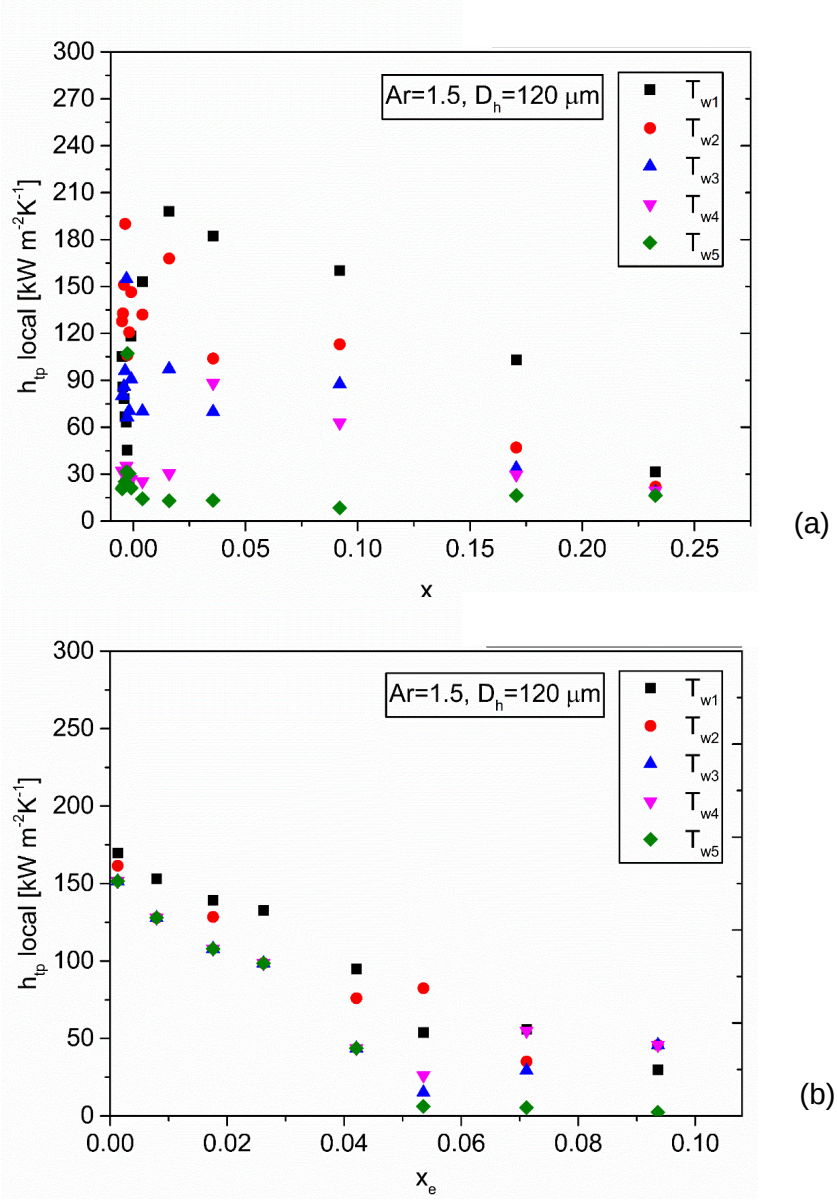

Figure 4. 39 *Local to-phase heat transfer coefficients as a function of exit vapour quality for two different heat fluxes for design 1B, D_h = 120 μm, a =1.5.*

Figure 4.40 shows the uniformity of flow regimes across the microchannels of α = 1.5 and D_h = 120 µm where the maximum two-phase heat transfer coefficients where calculated at G = 88.8 kg $m^{-2}s^{-1}$ T_{inlet}= 25 ºC, 1000 Hz, at location of T2.

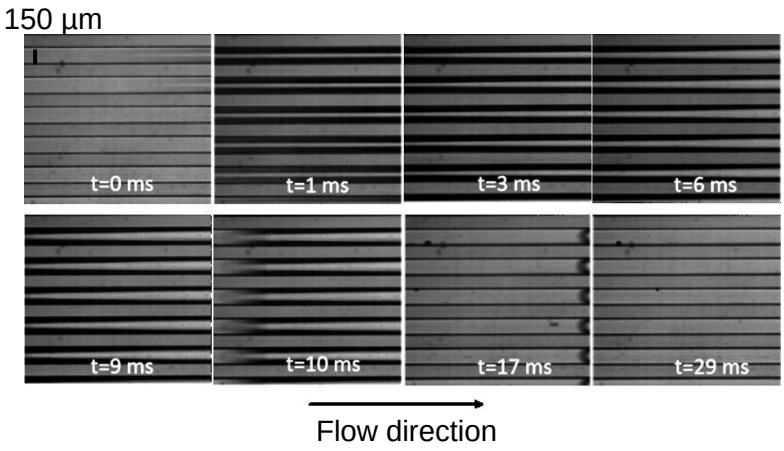

Figure 4. 40 *Image sequence of parallel rectangular cross section microchannels at location of sensor T2. The images were recorded at 1000 Hz and show uniform flow distribution with occurrence of simultaneous flow regimes at all the microchannels of α = 1.5 and D_h =120 µm, G = 88.8 kg $m^{-2}s^{-1}$. T_{in} = 25 ºC, 1000 Hz, location of T2. The highest heat transfer coefficient values were obtained during these conditions.*

Figure 4.41 shows the local heat transfer coefficient at T5 as a function of mass flux for four heat fluxes and T_{inlet} = 25 ºC for design with a = 1.5 and D_h = 120 µm.

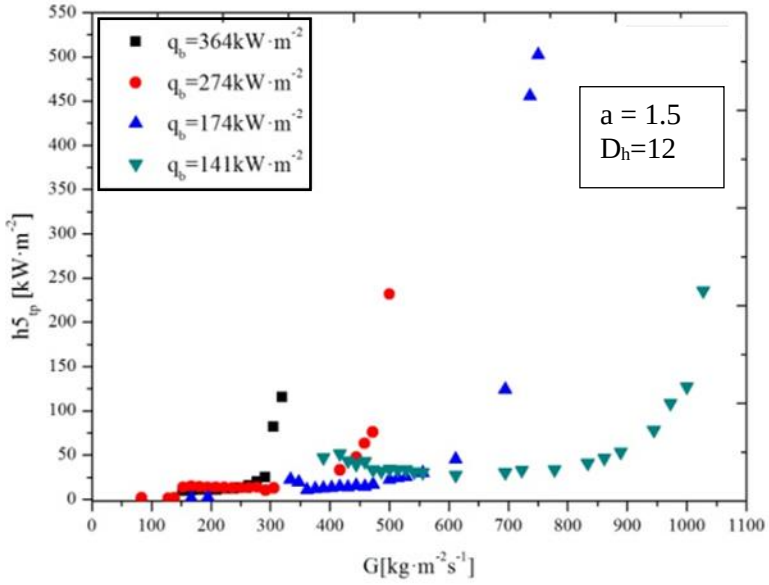

Figure 4. 41 Local heat transfer coefficient at position T5 close to the microchannel exit as a function of mass flux for four heat fluxes and T_{inlet} = 25 ºC for design with α = 1.5 and D_h = 120µm.

Figure 4.42a shows local heat transfer coefficients as a function of vapour quality for the design 2B with a = 1 and D_h = 100 µm. Figure 4.41b shows the bubble evolution with time for one channel at sensor T2. Confinement effect is important in microchannels heat sinks of D_h = 120 µm, a = 1.

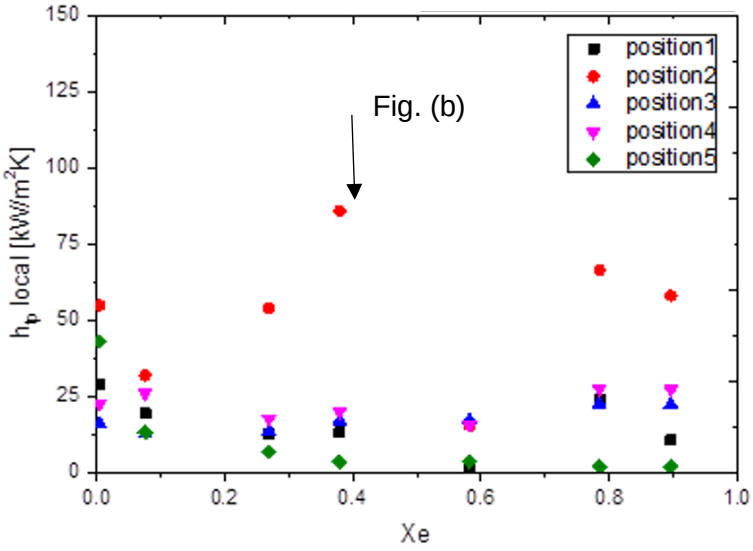

(a)

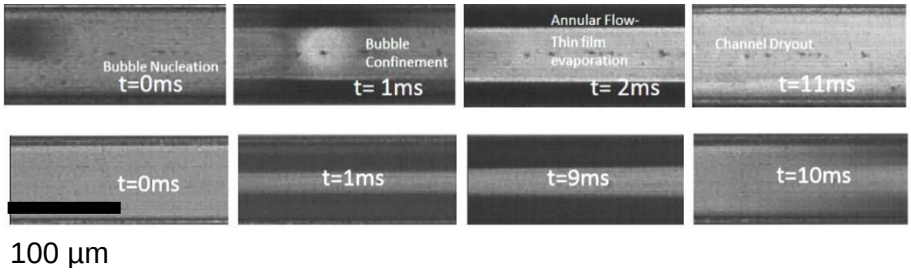

(b)

Figure 4. 42 *(a) Local heat transfer coefficients as a function with vapour quality for the design 2B with a = 1 and D_h = 100 µm and (b) bubble evolution with time for one microchannel at sensor T2. Confinement effect is important in microchannels heat sinks of D_h = 120 µm, a =1.5.*

Figure 4.43 presents image sequences f the two-phase flow patterns at the location of sensor T2 where the highest averaged h_{tp} was obtained for a = 1.5 and D_h = 120 µm microchannels heat sink at G = 88 kg $m^{-2}s^{-1}$ q = 151 kW m^{-2} and T_{inlet} = 25 °C. The arrow on top of Figure 4.42 shows direction of bulk flow. The images were obtained at 1000 Hz and show uniform annular flow regime to occur simultaneously in all the microchannels.

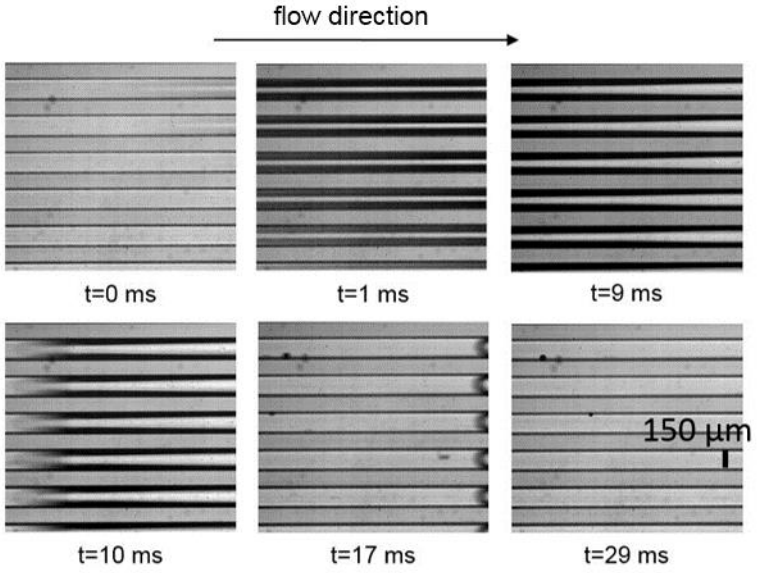

Figure 4. 43 *Image sequence that show the two-phase flow regime at the location of T2 where the highest averaged h_{tp} was obtained for α = 1.5 and D_h = 120 µm microchannels heat sink at G = 88 kg $m^{-2}s^{-1}$ q = 151 kW $m^{-2}$and T_{inlet}= 25 °C. Arrow on top of figure shows direction of bulk flow. The images were obtained at 1000 Hz and show uniform flow simultaneously at all the microchannels. The main flow pattern observed was annular flow regime.*

4.4.10 Effect of inlet subcooling on local heat transfer coefficients

Figure 4.44a and b show the local heat transfer coefficient as a function of mass flux for inlet temperature of T_{inlet}= 25 ºC at position *T1* and *T5* respectively, for design 1A, α = 3. Figure 4.44c and d show the local heat transfer coefficient as a function of mass flux for inlet temperature of T_{inlet}= 81 ºC at position T1 and T5 respectively for design 1A, α = 3. Local heat transfer coefficients at T_{inlet}= 81 ºC achieved higher values.

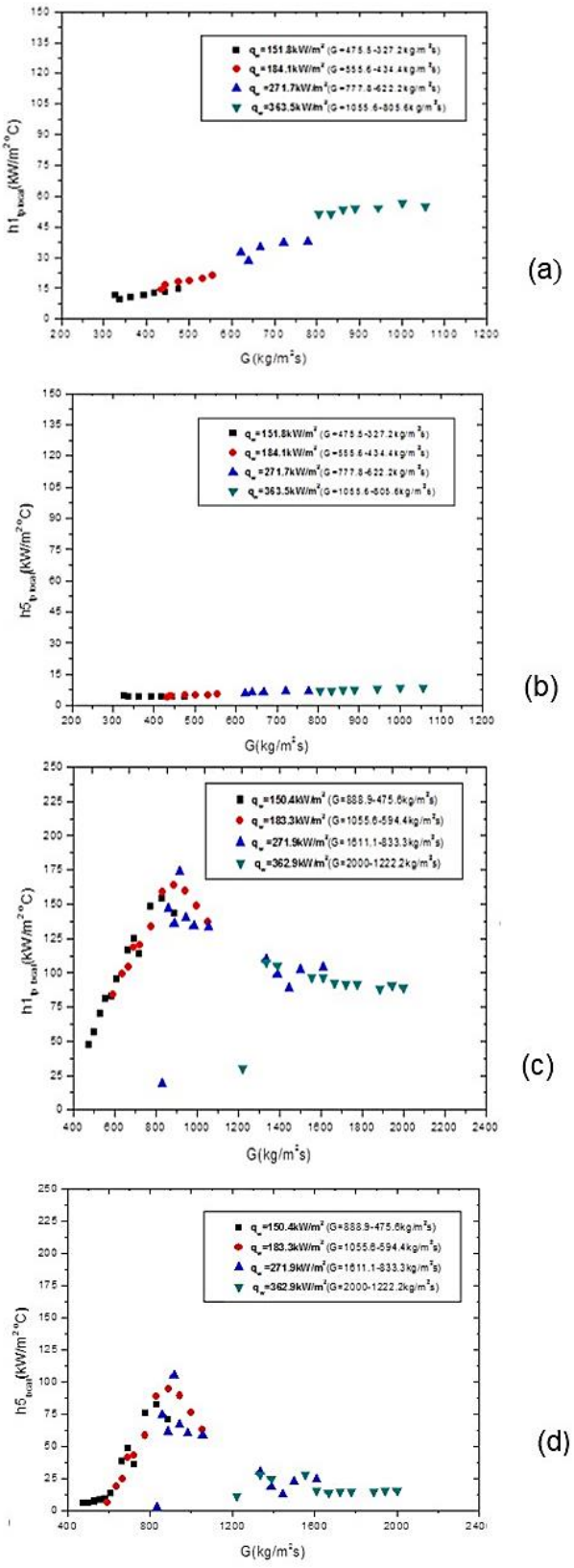

Figure 4. 44 *Local heat transfer coefficient as a function of mass flux for inlet temperature of T_{inlet} =25 ºC (a), (b) and inlet liquid temperature of T_{inlet} =81 ºC for the design with α = 3 shown in (c) and (d).*

4.4.11 Influence of increasing aspect ratio on flow instabilities

Two-phase flow instabilities are categorized into severe pressure drop oscillations and mild parallel channels instabilities according Mudawar [9]. At the lowest mass flux, severe pressure oscillations were found to occur because of the increase in upstream pressure. The mild parallel instability is a result of the density wave oscillation within each channel and feedback interaction between channels. The occurrence of the mild instabilities is not expected to change the cooling performance of the heat sink. [9]. Figure 4.45 shows wall temperature fluctuations with simultaneous pressure measurements for G = 88.82 kg m^{-2}s^{-1}, q = 151 kW m^{-2} and T_{inlet}= 25 ºC for a = 1.5, design 1B.

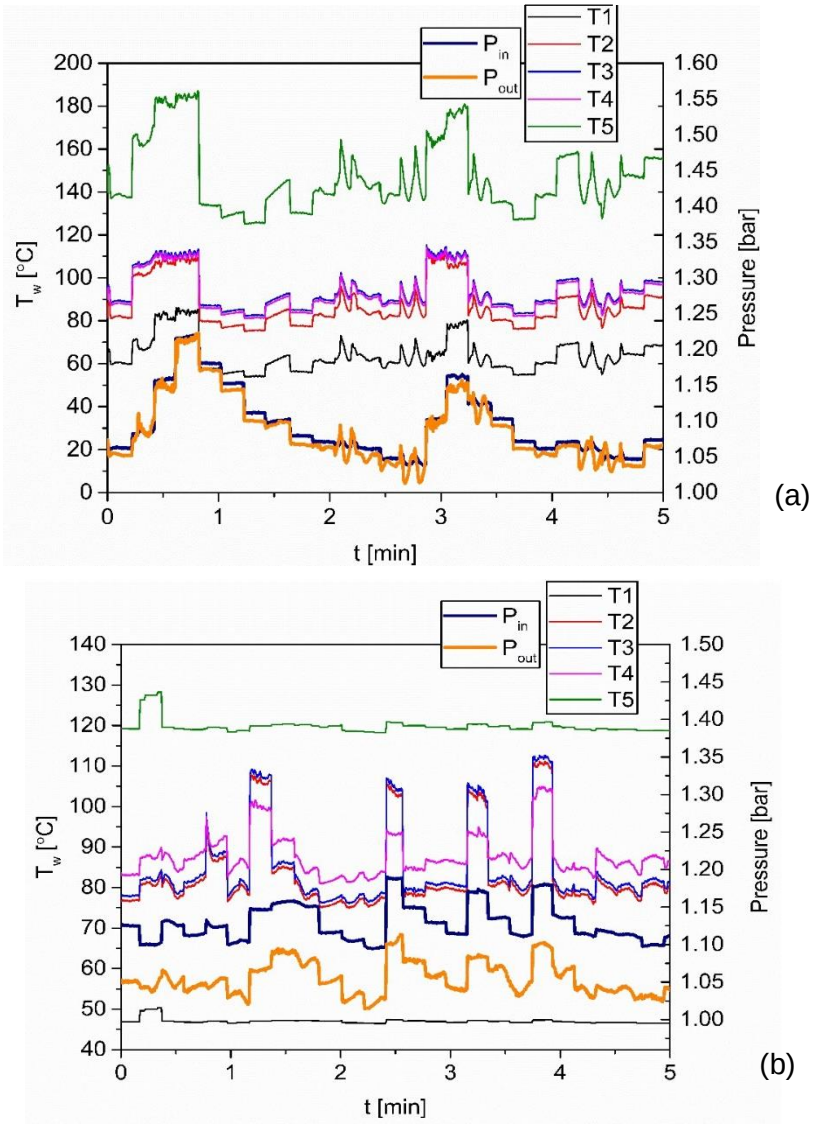

Figure 4. 45 *Wall temperature fluctuations correlated with simultaneous pressure fluctuations for (a) G = 88.82 kg m^{-2}s^{-1}, q = 151 kW m^{-2} and (b) G = 247 kg m^{-2}s^{-1}, q = 363 kW m^{-2} for T_{inlet} = 25 ºC for design 1B with a =1.5 and D_h = 120 μm.*

Small width channels result in instabilities because they consist of higher number of microchannels.

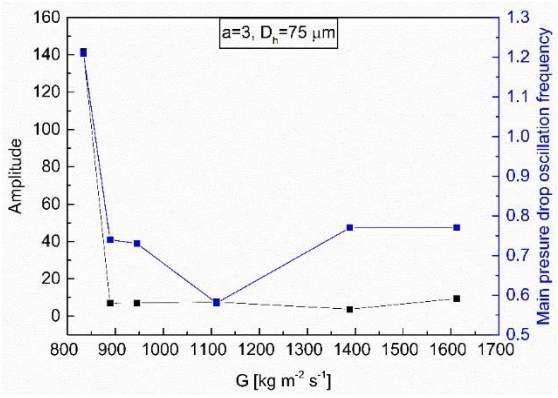

(a)

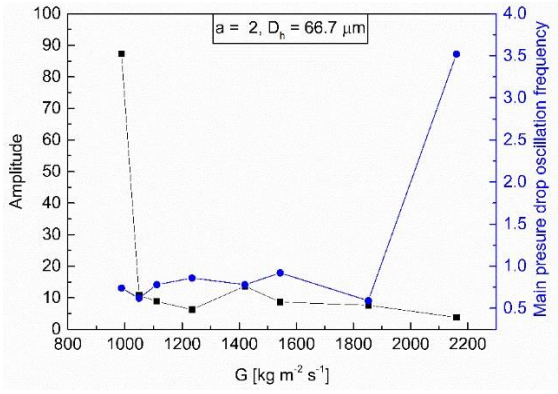

(b)

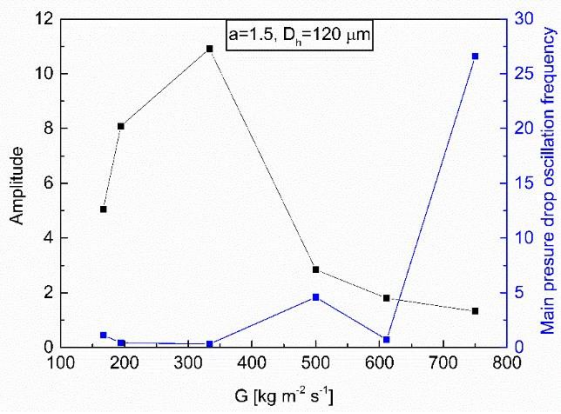

(c)

Figure 4. 46 *Results for pressure drop amplitude and main frequency of two-phase pressure oscillations, produced using FFT, T_{inlet}= 81 ºC, q = 271 kW m^{-2}, for (a) design 1A with α = 3 and (b) for the design 2A with α = 2 and (c) design1B with α = 1.5.*

Figure 4.46a shows the two-phase pressure drop amplitude and main frequency of two-phase pressure oscillations, produced using FFT processing method for T_{inlet} = 81 ºC, q = 271 kW m$^{-2,}$ for design 1A, α = 3. Figure 4.46b shows two-phase pressure drop amplitude and main

frequency of two-phase pressure oscillations, produced using FFT processing method for a = 2 and Figure 4.46c for the design 1B, a = 1.5. Figure 4.46 shows the wall temperature fluctuations at the 5 locations for T_{inlet}= 81 ºC and q = 271 kW m^{-2}, a = 3. Figure 4.47 shows the flow instabilities, recorded with high- speed-camera at T1 within a period of 36.37 s at 100 Hz for a = 3, T_{inlet}= 81 ºC and q = 271 kW m^{-2}.

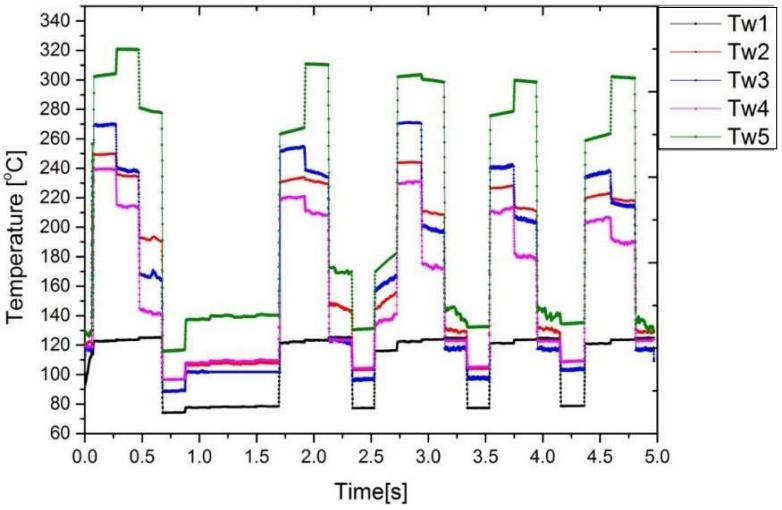

Figure 4. 47 *Wall temperature fluctuations at T1, T2, T3, T4 and T5 for the high aspect ratio microchannels of a = 3 at T_{inlet}= 81 ºC and q = 271 kW m^{-2}.*

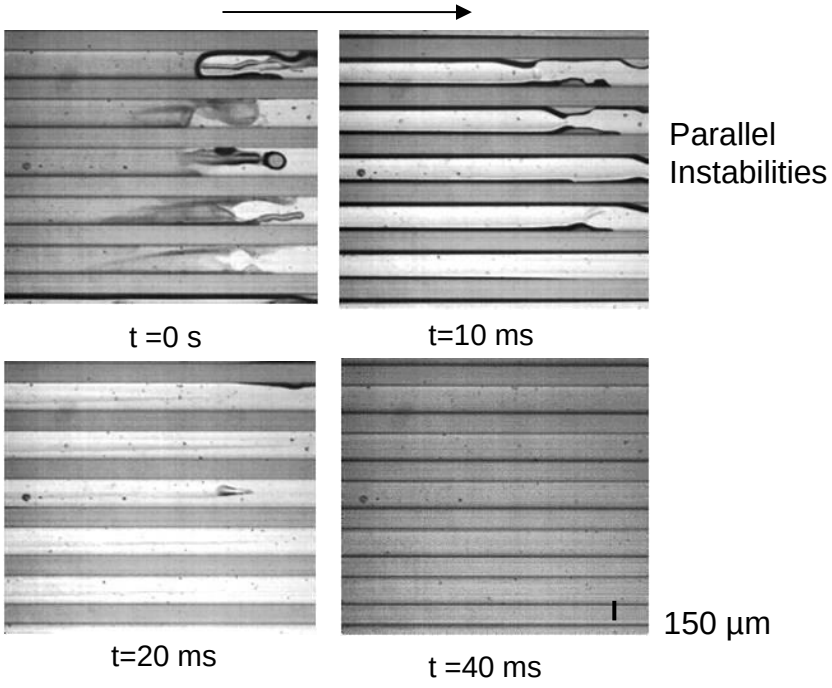

Figure 4. 48 *Image sequence that shows flow instabilities during flow boiling in microchannels of D_h=1.5 as recorded with high speed camera at the location of T1 within a period of 36.37 s at 100 Hz for a = 3, T_{inlet} = 81 ºC and q = 271 kW m^{-2}.*

The flow patterns shown in Figure 4.48 reveal that during the high wall temperature fluctuations shown in Figure 4.47, channel flow instabilities occur at this location of sensor T1. These instabilities occur almost simultaneously in all channels at this location and they are characterised by a periodic cycle of wetting, film evaporation, dryout and rewetting phenomena. At t = 0 s inlet rewetting occurs, however the channels are already occupied by vapour that forces the liquid into opposite direction of flow direction simultaneously. In all the microchannels. The meniscus shape is non uniform, as shown in Figure 4.48 as the vapour pushes the liquid with high velocity. At t = 0.01 s backflow occurred simultaneously in all microchannels. At t = 0.01s film boiling occurs at the channel corners of the sidewalls. Probably bubble nucleation occurs in the channel corners and the bubbles grow as a result of superheated liquid at these locations. Film boiling occurs at either sides of the vapour core resulting in the merging of the two liquid films. At t = 0.02 s possible local dryout occurs at the inlet manifold because of complete flow reversal and at t = 0.04 s, inlet rewetting of the channels occurs and the instability cycle starts again.

Figure 4.49 and 4.50 shows a sequence of images captured a high frequency of 5130 Hz for G = 833.33 kg m^{-2}s^{-1}, T_{in}= 81 ºC and q = 271 kW m^{-2} at location $T1$. At a frame rate of 5130 Hz the flow patterns are clear and bubbles can be identified at the inlet of the microchannels. The bubbles grow near the sidewalls with a non-spherical shape. The bubble grows in both directions and then flow regime changes to slug flow**.** The slugs are moving in the opposite direction resulting in dryout. The temporary dryout lasts for 11 ms.

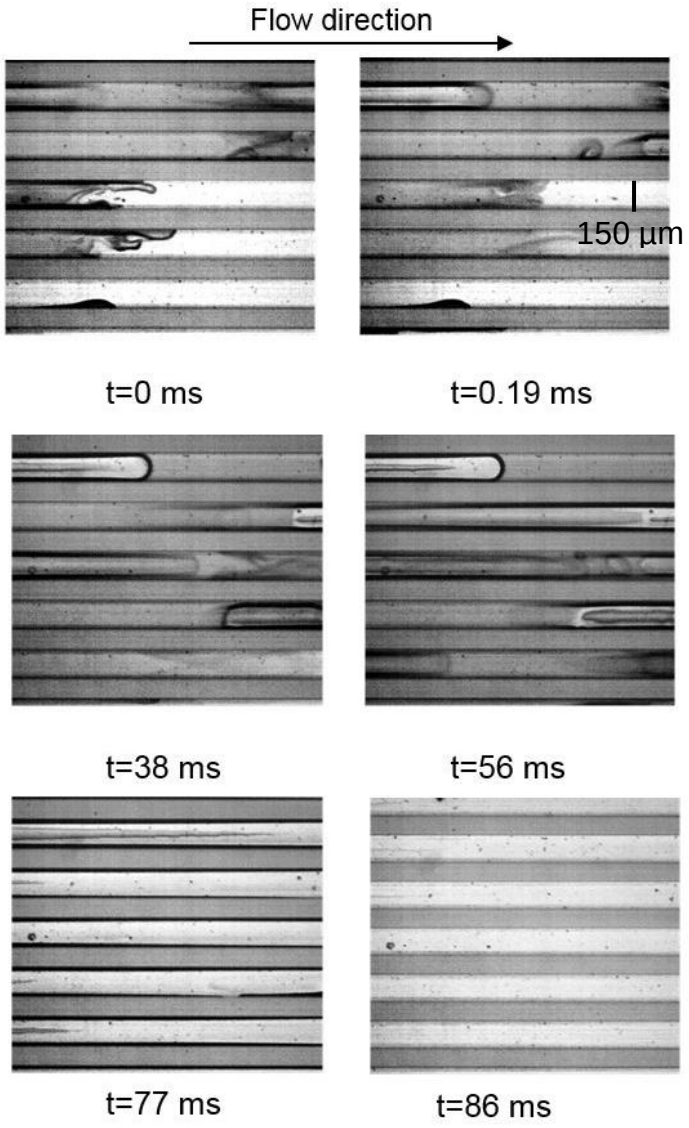

Figure 4. 49 *Image sequence that shows the flow instabilities, recorded with high-speed camera at T1 at 5130 Hz for a = 3 at* T_{inlet} *= 81 ºC and q = 271 kW* m^{-2}*.Arrow on top of figure shows the flow direction.*

After the bubble grows and expands, there is backflow and pressure increases in the inlet as the vapour flows backward also, the flow pattern is annular flow with the thin film evaporation at the inlet of the microchannels being dominant. Temporary dryout occurs at all the microchannels simultaneously.

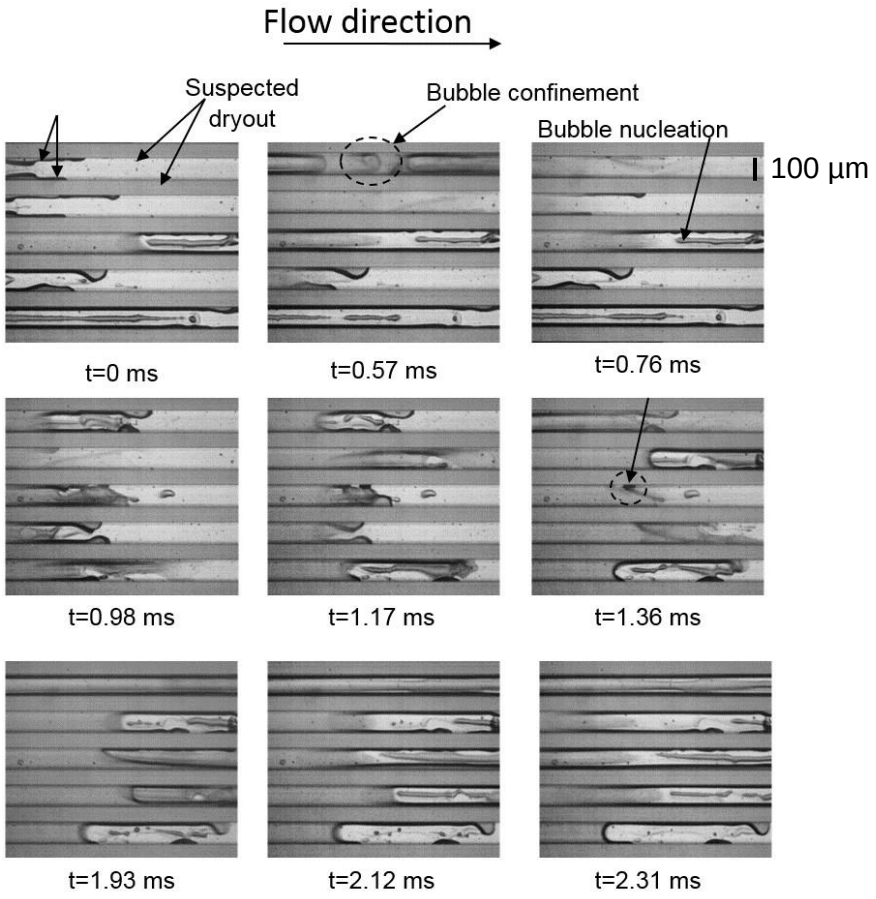

Figure 4. 50 *Image sequence captured at the high frequency of 5130 Hz for* $G = 833.33$ *kg* m^{-2} s^{-1}, $T_{inlet} = 81\ ^{o}C$ *and* $q = 271$ *kW* m^{-2} *at location of T1, for the design 1A with microchannels of* $\alpha = 3$ *and* $D_h = 75\mu m$.

Figure 4.51a shows the wall temperature fluctuations for all sensors simultaneously at q = 363 kW m^{-2}, G = 1222.22 kg $m^{-2}s^{-1}$ for design 1A, α = 3. Figure 4.51b shows the inlet and outlet pressure fluctuations with time at q = 363 kW m^{-2} G = 1222.22 kg $m^{-2}s^{-1}$ for design 1A, α = 3. The upstream pressure is fluctuating with time with peaks reaching the maximum of 2.1 bar. This increase can be attributed to the increased compressible volume since boiling started in the heat sink, which creates increased flow resistance. At some point, the pressure will decrease again allowing the vapour to leave the channels, which are again filled with liquid until a next period of oscillations is initiated. These instabilities are known as severe pressure oscillations and are undesirable as the amplitude of the oscillations is very high and premature CHF can be caused. These instabilities can be eliminated with the use of throttling valve upstream the test section.

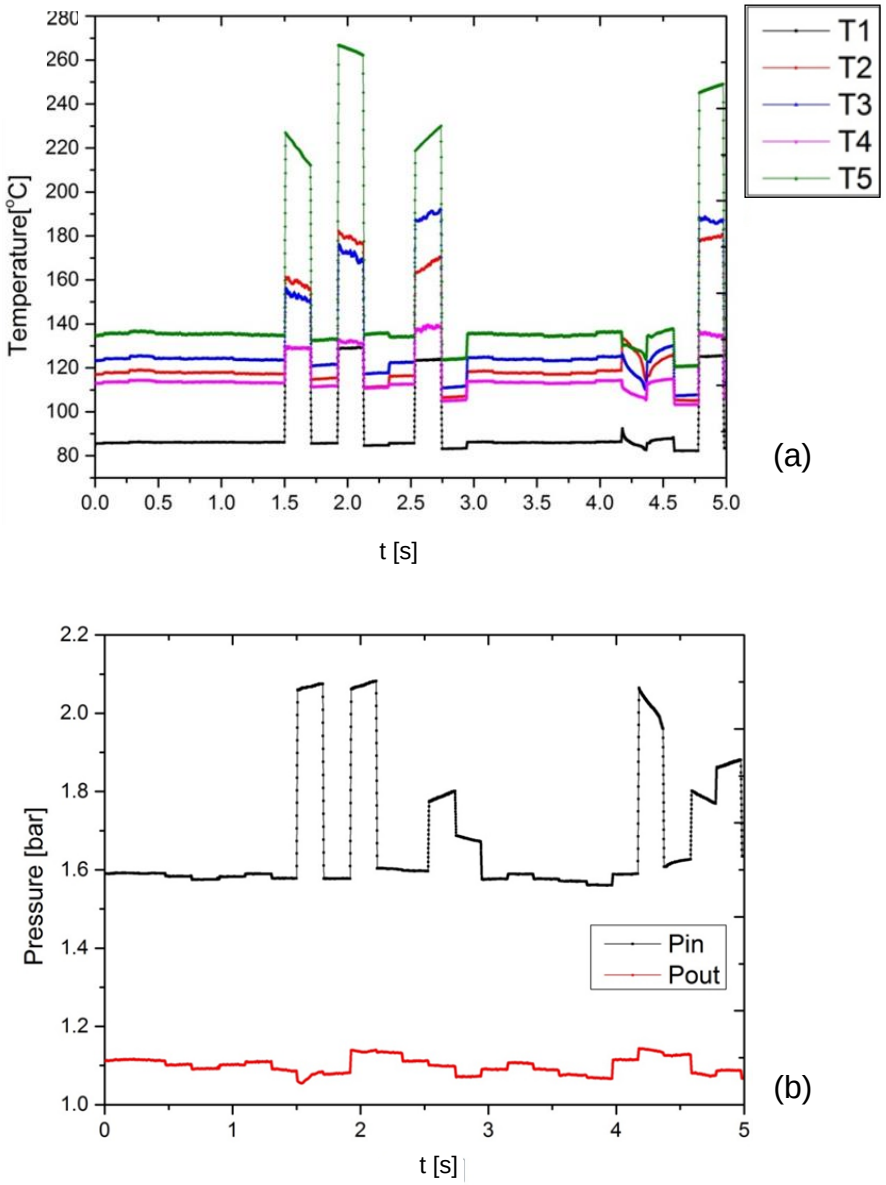

Figure 4. 51 *Wall temperature fluctuations for all sensors simultaneously at q = 363 kW m^{-2} and G = 1222.22 kg m^{-2}s^{-1} for design 1A with α= 3. T_{inlet}= 81 ºC (b) inlet and outlet pressure fluctuations with time for α = 3.*

Figure 4.52 shows the local temporal dryout occurrence at a high frequency of 5130 Hz at location of sensor $T3$ for q = 363 kW m^{-2} G = 1222.22 kg m^{-2}s^{-1} for design 1A, α = 3.

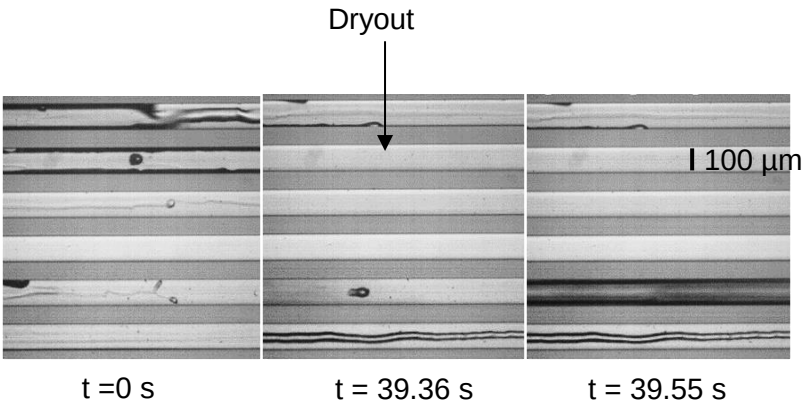

Figure 4. 52 *The images were captured a high frequency of 5130 Hz at location of sensor T3 for q = 363 kW m^{-2}, G = 1222.22 kg $m^{-2}s^{-1}$ for design 1A, at T_{inlet} = 81 ºC, α = 3 and they show the temporal dryout.*

The amplitude of temperature and pressure fluctuations is strongly increasing with higher aspect ratio microchannels. The main frequency of the fluctuations is small however, the amplitude is high enough. Figure 4.53 shows the amplitude as a function for the frequency of wall temperature and pressure drop oscillations produced from FFT analysis for 2 designs of constant D_h = 66.7 µm and different aspect ratios of (a) 0.5 and (b) 2 for T_{inlet} = 81 ºC at the same heat flux. The period of fluctuations from thin film evaporation to dryout was measured from the frames as f = 0.917 Hz (T = 1.09 s) which almost agrees with the FFT results from the pressure drop fluctuations where the main frequency was identified as 1.0 Hz with a very high amplitude of 132.13 mbar. In addition, other two peaks were identified close to the maximum peak, at 0.40 Hz and the other at 1.41 Hz.

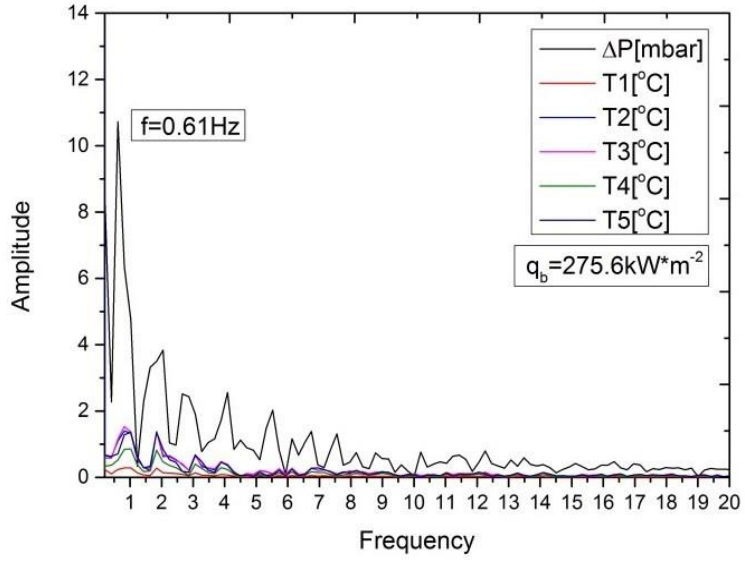

(a)

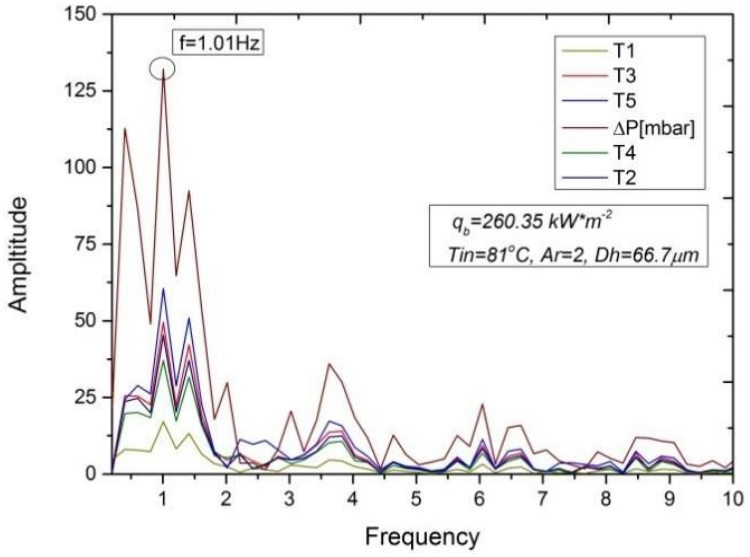

(b)

Figure 4. 53 *Amplitude as a function of the frequency of wall temperature and pressure drop oscillations produced from FFT analysis for two designs of constant* D_h *= 66.7 μm and different aspect ratios of (a) 0.5 and (b) 2 for* T_{inlet} *= 81 ºC at the same heat flux.*

Figure 4.54 compares the liquid Reynolds number (*Re*) as a function of the heat flux for a = 2 and a = 3 microchannel heat sinks with the same D_h = 66.7 μm at the same mass flow rate.

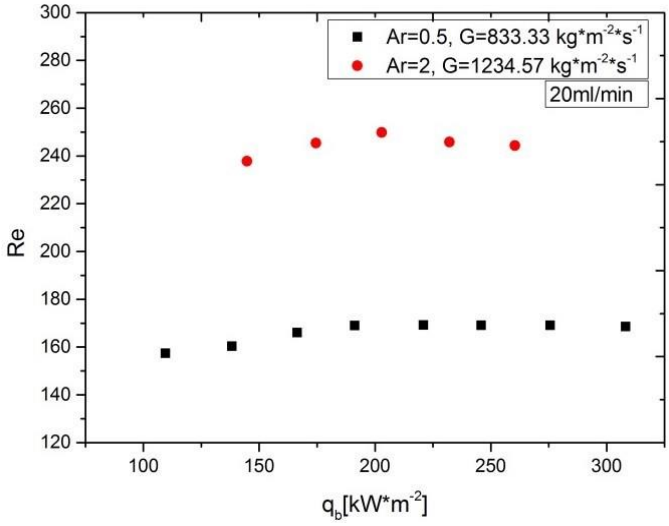

Figure 4. 54 *Reynolds number (Re) as a function of the heat flux for $\alpha = 2$ and $\alpha = 3$ microchannel heat sinks with the same D_h= 66.7 µm at the same mass flow rate.*

4.4.12 3D plots of heat transfer coefficients distribution along the flowstream line of the heat sink

Figure 4.55 shows a schematic diagram with the locations of temperature sensors along the flow stream line of the microchannels heat sinks. The wall temperature measurements from these locations were used to obtain 2D plots of h_{tp} vs G.

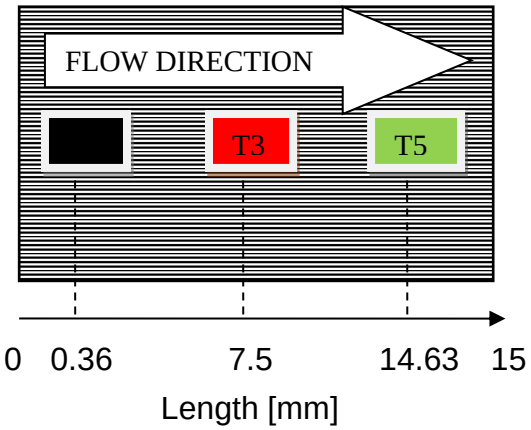

Figure 4. 55 *Location of temperature sensors along the flowstream line of the silicon microchannels heat sink.*

Figure 4.56a shows that h_{tp} at *T5* decreases with decreasing G and at *T3* decreases with decreasing G but when boiling starts h_{tp} decreases for G = 1700 kg m^{-2}s^{-1}. Figure 4.55b shows h_{tp} calculated for higher D_h but lower a microchannels. h_{tp} at both *T3* and *T5* decreases with decreasing G and then increases for G > 700 kg m^{-2}s^{-1}.

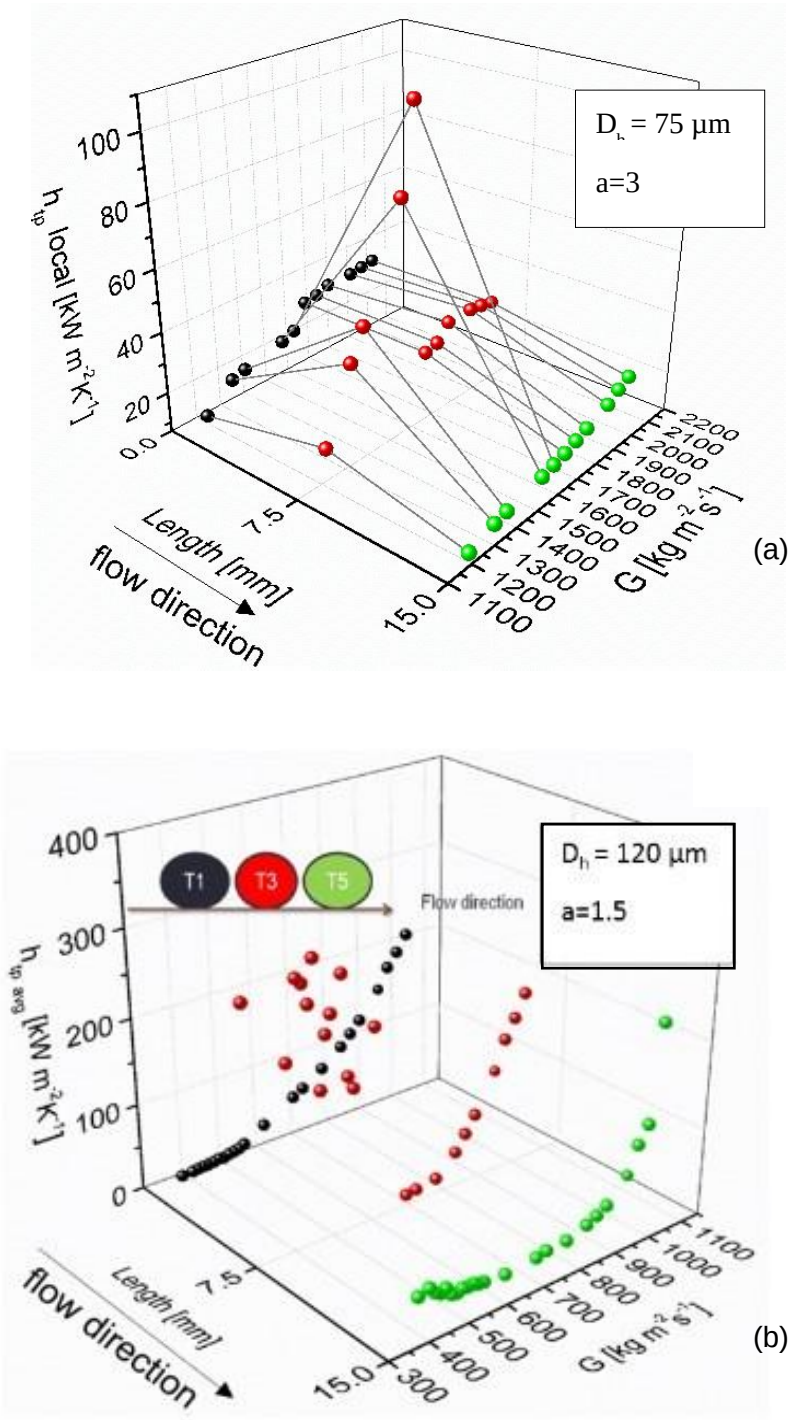

Figure 4. 56 *Two-phase local heat transfer coefficients h_{tp} at T1, T3, T5 along the channel flowstream line as a function of the channel length and the mass flux for a = 3, D_h = 75 µm and (b) for a = 1, D_h = 120 µm microchannels (T_{inlet}= 81 °C) for constant q = 363 kW m^{-2}. The data points are averaged over time and the connecting lines show the trends along the flowstream as a function of the length.*

Figure 4.57 shows 2D plot of the two-phase local heat transfer coefficients ($h_{z,tp}$) at the location of T1, T3, T5 as function of mass flux for design 3A at T_{inlet} = 81 ºC and q = 271 kW m^{-2}.The points are averages over time. The heat transfer coefficient distribution in the microchannels heat sink changes significantly in time.

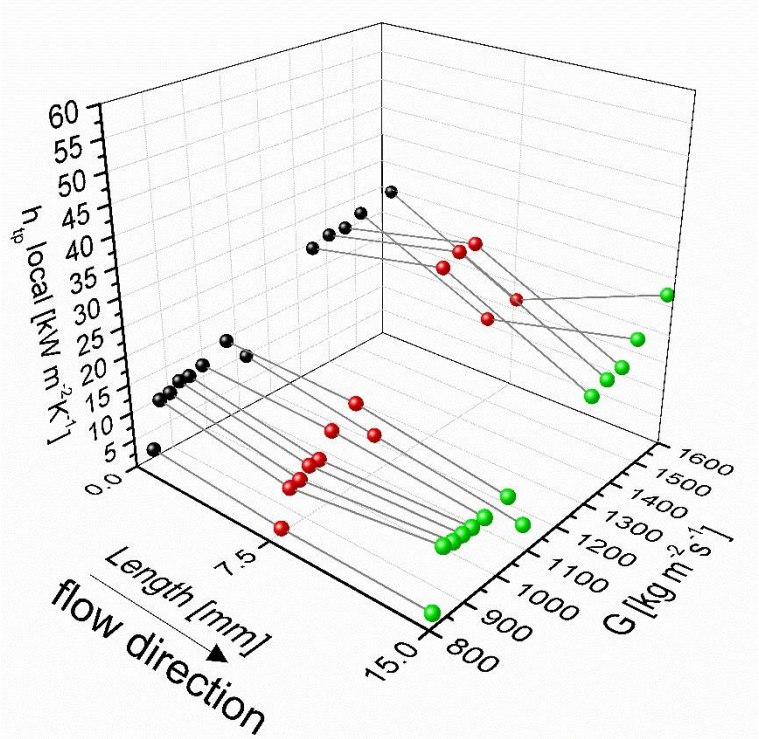

Figure 4. 57 *3D plot of the local heat transfer coefficient calculated at T1, T3, T5 as function of mass flux G and position for design 1A and T_{inlet} = 81 ºC and q = 271 kW m^{-2} ,for the design 1A with microchannels of a = 3. The points are averaged over time values. The heat transfer coefficient distribution at the microchannels heat sink changes significantly with G.*

Figure 4.58 shows the local wall temperature fluctuations at q = 363 kW m^{-2}, design 1A, a = 1.5, D_h = 120 µm. Flow reversal occurred when bubbles grow at the inlet of the microchannels. The oscillation amplitude increased after a specific value for each sensor for decreasing mass fluxes. The maximum temperature was 125 °C measured at sensor T5. These wall temperature fluctuations were measured at the design with the maximum heat transfer coefficient at the two-phase region. Figure 4.58 shows the local (T1, T3, T5) wall temperature fluctuations for the design 1A (a = 3, D_h = 75 µm) with simultaneous pressure drop oscillations for constant heat flux of q = 363 kW m^{-2} and varying G.

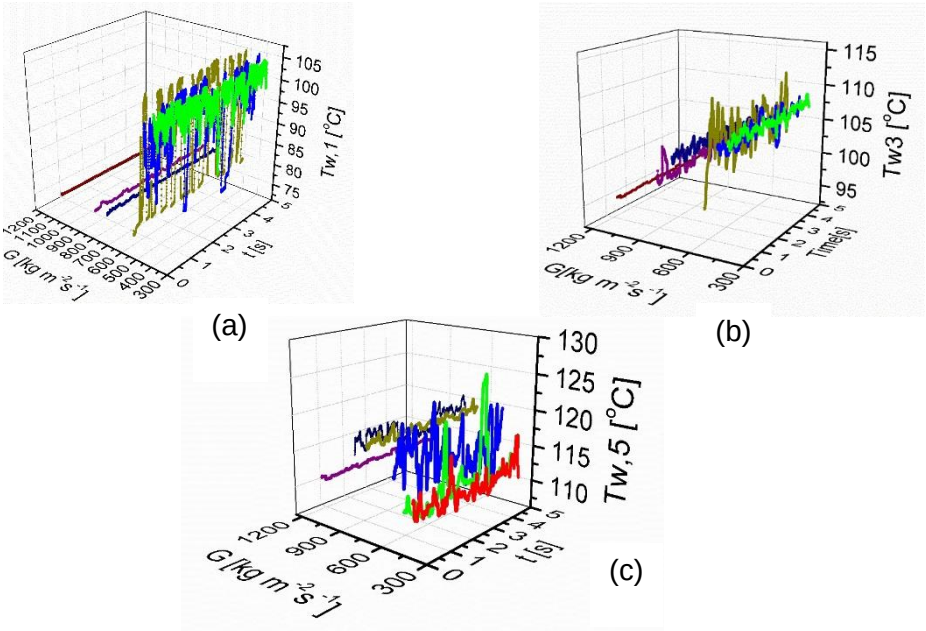

Figure 4. 58 *Local wall temperature fluctuations as a function of mass flux at locations of (a)T1, (b) T3 and (c) T5 for q = 362 kW m^{-2} , design 1B (a = 1.5, D_h = 120 μm) at T_{inlet} = 81 ˚C.*

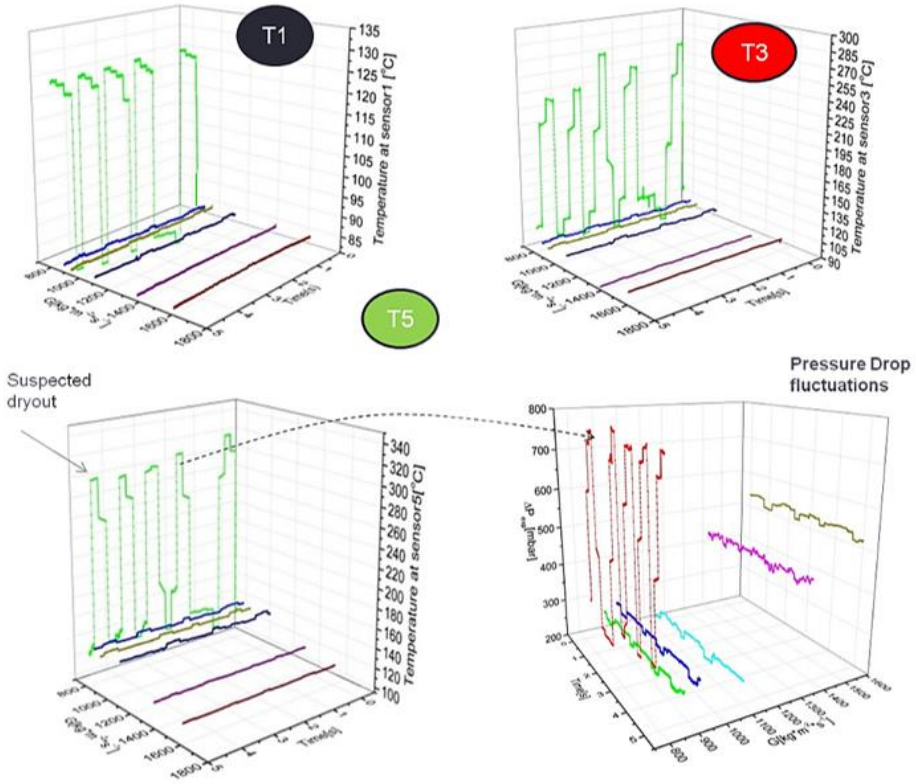

Figure 4. 59 *Local wall temperature fluctuations at T1(a), T3(b), T5(c) for the highest aspect ratio of α = 3, D_h = 75μm design 1A with (d) simultaneous pressure drop oscillations for the constant heat flux of 363 kW m^{-2} and varying G from 833.3 to 1611.1 kg·m^{-2}·s^{-1}.*

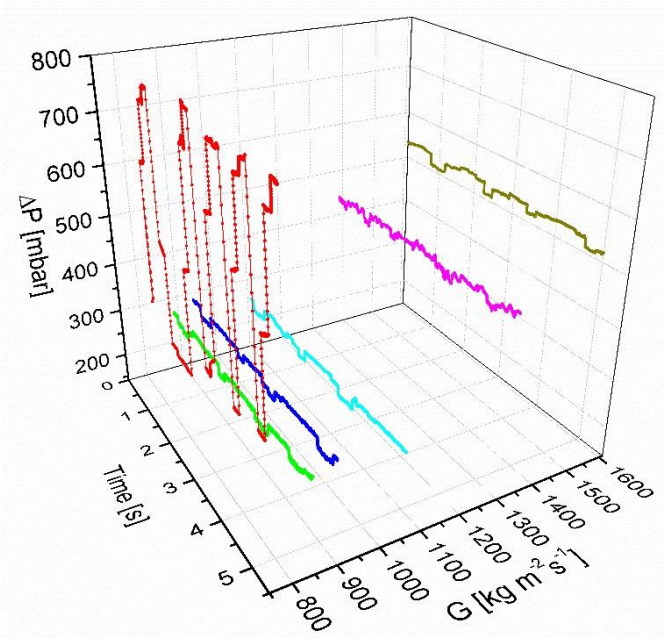

Figure 4. 60 *Pressure drop oscillations for constant q = 363 kW m^{-2} and varying G from 833.3 to 1611.1 kg·m^{-2}·s^{-1}.*

Figure 4.60 shows the dryout that occurs during the parallel instability in microchannels of high aspect ratio α = 3 and D_h = 75 μm at location of T3. Temporary dryout occurs due to non-uniformity of flow in microchannels of high aspect ratio α = 3 and D_h = 75 μm at *T3*.

.

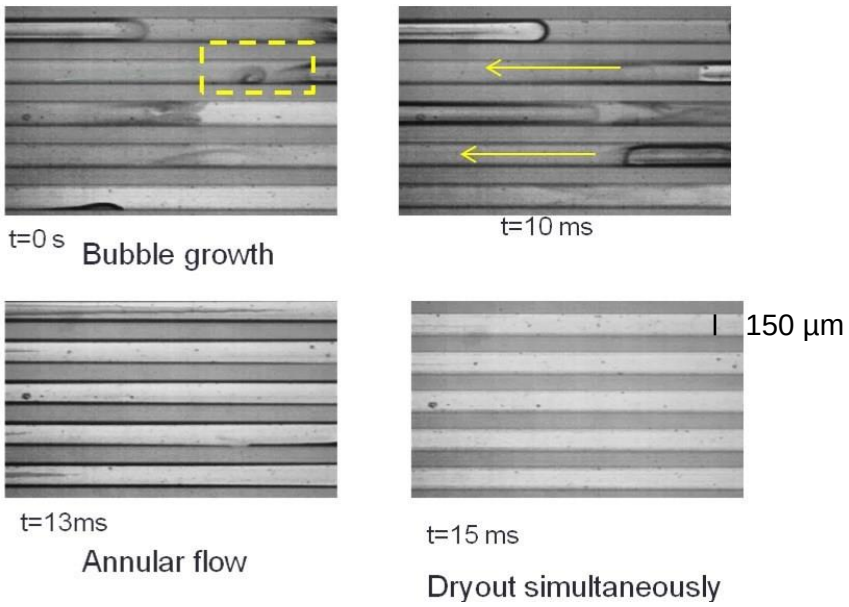

Figure 4. 61 *Dryout parallel instability in microchannels of high aspect ratio α = 3 and D_h= 75 μm at T3. Parallel channel instabilities were observed to occur, resulting in flow reversal and temporal dryout (high amplitude oscillations) in the heat sink for G = 833.3 kg·m^{-2}·s^{-1} and q = 363 kW m^{-2}.*

Parallel channel instabilities resulting in flow reversal and temporary uniform dryout (high amplitude oscillations) in the heat sink for G = 833.3 to kg·m^{-2}·s^{-1}and q = 363 kW m^{-2}. Parallel channel instabilities result in flow reversal and temporal dryout (high amplitude oscillations) in the heat sink for G = 833.3 to kg·m^{-2}·s^{-1}and q = 363 kW m^{-2}. Figure 4.62 shows that the local wall temperature fluctuations reached locally values of 340 ºC at the channel outlet. Sudden pressure drop increase at low mass flux due to increase of P_{in} (flow reversal) and high superheat. Figure 4.62 shows the local wall temperature fluctuations at the locations of sensors T1, T3, T5 for aspect ratio of a = 2, design 2A (D_h = 66.7 μm) at T_{inlet} = 81 ºC with simultaneous pressure drop oscillations for constant heat flux of 271 kW m^{-2} and varying G.

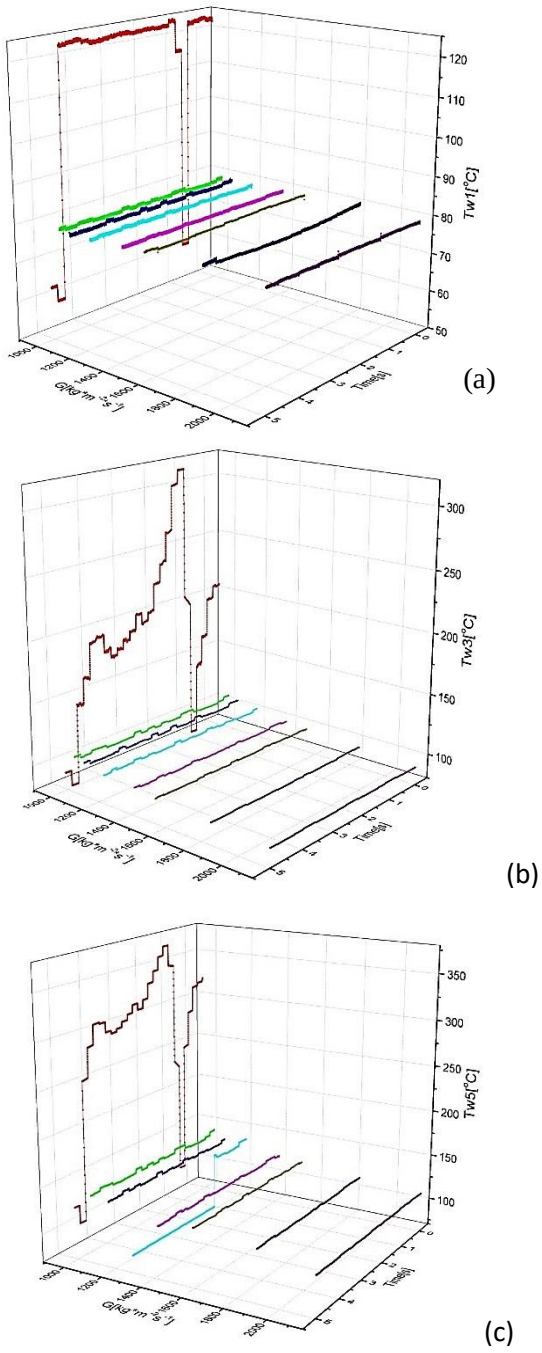

Figure 4. 62 *Local (T1, T3, T5) wall temperature fluctuations for aspect ratio of α = 2, design 2A (D_h = 66.7 µm) at T_{inlet} = 81 ºC with simultaneous pressure drop oscillations for constant q = 271 kW m^{-2} and varying G.*

Figure 4.63 shows the 3D plot of the local heat transfer coefficient calculated at T1, T3 and T5 as a function of mass flux (G) for the design 2A , at T_{inlet} = 81 ºC and q = 363 kW m^{-2}. The data points in Figure 4.63 are averaged over time and the lines that connect the points show the trends along the flowstream line of the microchannels heat sink. The heat transfer coefficient distribution in the microchannels heat sink changes significantly with decrease in G.

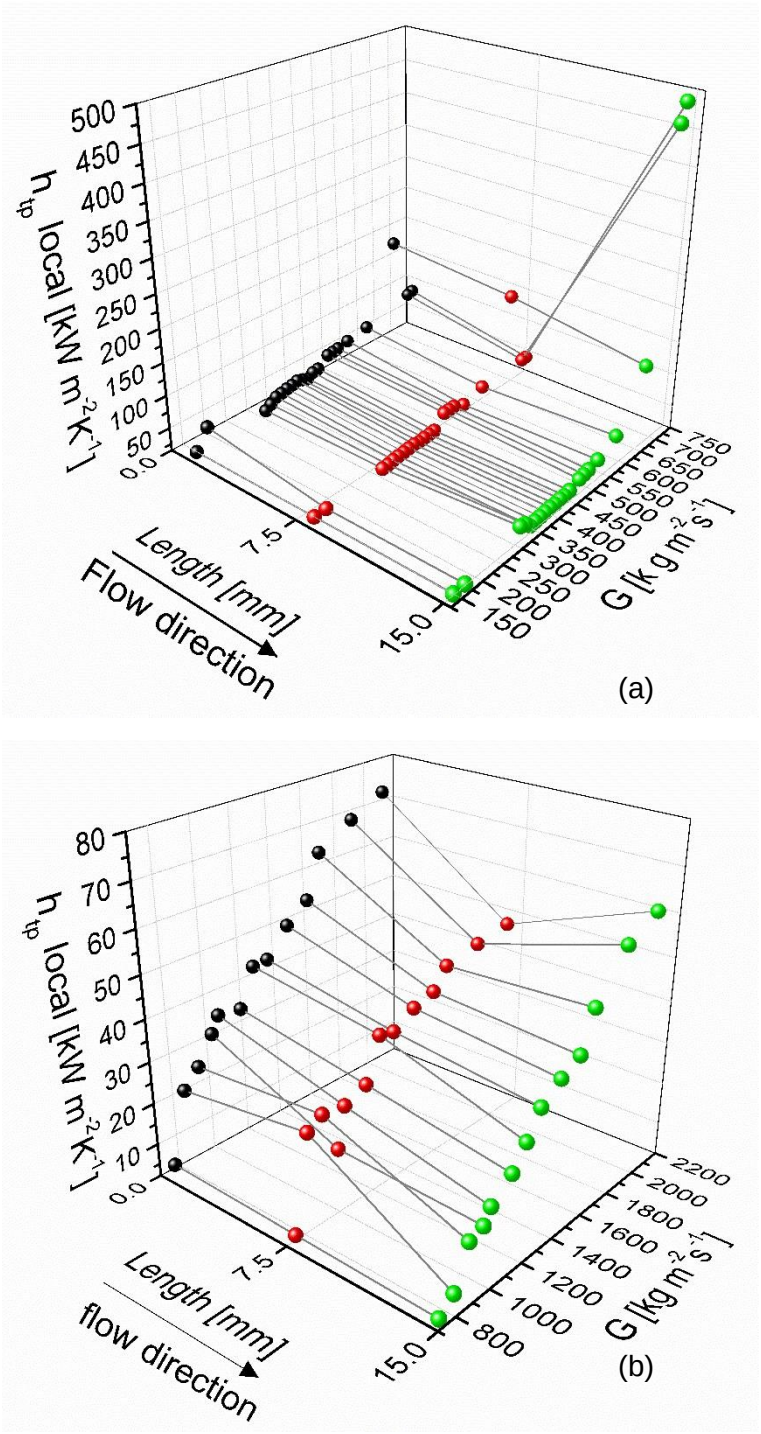

Figure 4. 63 *3D plot of the local heat transfer coefficient calculated at locations of T1, T3, T5 as function of mass flux G for T_{inlet} = 81 ºC and q = 363 kW m^{-2} for (a) the design of 1B (a =1.5) and (b) the design of 3B. The points are averaged values over time and the grey connecting lines show the trends along the flowstream line of the microchannels head sink. The heat transfer coefficient distribution at the microchannels heat sink changes significantly with G.*

Figure 4.64 shows a sequence of high speed images recorded at 5000 Hz at location of T3 for the design of 2A, α = 2, D_h = 66.7 µm, the heat flux of 363 kW m^{-2} at T_{iinlet} = 81 ºC. At *t*

= 0 ms the bubble diameter is D_b = 48.66 μm and H_b = 37.4 μm, at t = 0.2 ms d = 63.260 μm and H_{ch} = 48.18 μm, at t = 0.4 ms the bubble gets confined D_b =122.409 μm and H_{ch} = 100 μm, elongated bubble at t = 0.8 ms D_b = 122.14 μm and H_{ch} = 100 μm. As the bubble grows, it is confined from the microchannels width, grows axially, and connects with the rest of the vapour creating big slugs. The flow patterns for this design seem to have liquid droplets in the middle of the vapour core and different flow patterns are happening at the same time in different microchannels.

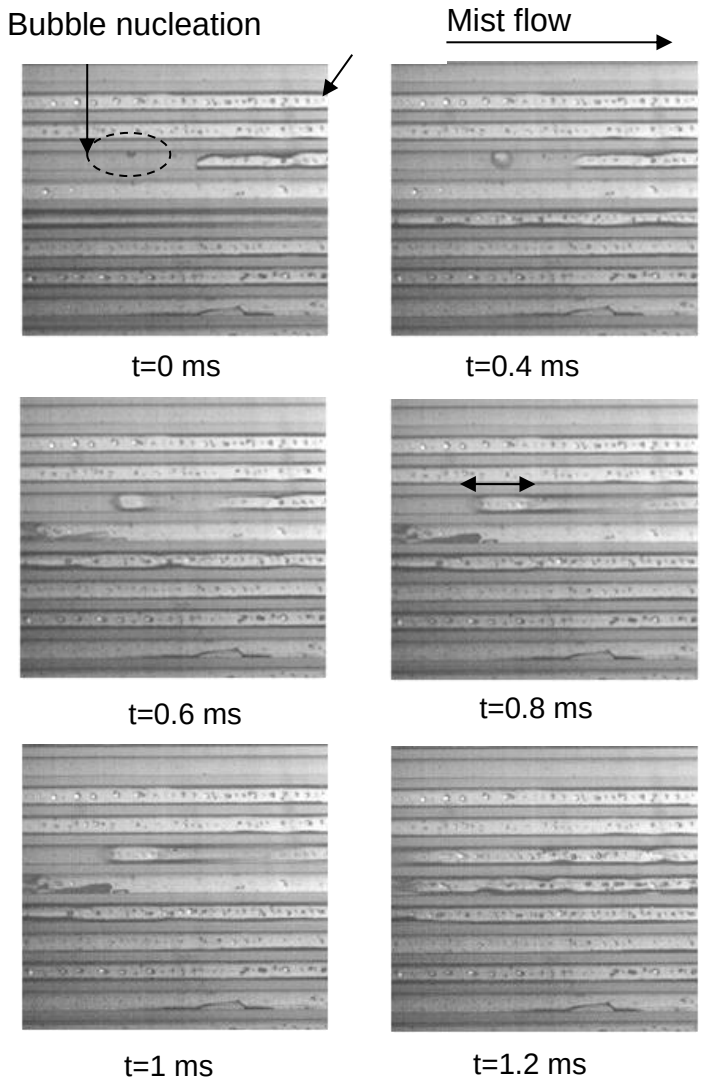

Figure 4. 64 Sequence of high-speed images recorded at 5000 Hz at location of T3 for the design of 2A, α = 2, D_h = 66.7 μm, the heat flux of 363 kW m^{-2} and T_{inlet} = 81 ºC.

Figure 4.65 shows the 3D plot of the two-phase local heat transfer coefficient at the locations of T1, T3 and T5 as function of mass flux G and channel position, for the design 3B (α = 0.5, D_h = 66.7 μm) at T_{inlet} =81 ºC and q = 363 kW m^{-2}. The points are averaged over time

and connecting lines between the points show the trends along the flowstream line of the microchannels heat sink. The heat transfer coefficient distribution in the microchannels heat sink changes significantly with G.

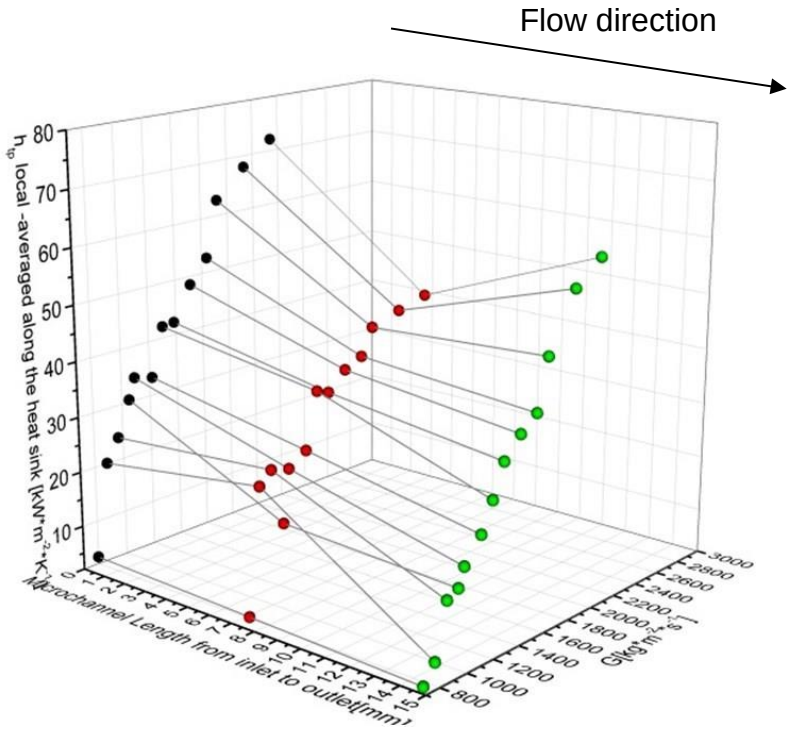

Figure 4. 65 *3D plot of the local heat transfer coefficient at T1, T3, T5 as a function of mass flux for the design 3B (a = 0.5, D_h = 66.7μm) at T_{inlet} = 81 ºC and for q = 363 kW m^{-2}. The points are averaged over time and the lines that connect the punts show the trends along the flowstream line of the microchannels heat sink. The heat transfer coefficient distribution in the microchannels heat sink changes significantly with G.*

4.4.13 Bubble growth

Bubble growth characteristics in the present study are for bubbles observed in the six channels located in the middle of the microchannel assembly above sensor T3. Bubbles nucleation in the observed microchannels was present by boiling in the outlet zone of the microchannels with intensive flow instabilities and reversed slug-vapour flow. The wall superheat for boiling onset measured at the location of sensor T5 situated immediately before channels exit was in the range from 3.3 to 8.6 °C depending on the mass flow rate of water. The observed bubbles were classified into bottom wall bubbles and sidewall bubbles. Figure 4.66 presents bubble nucleation that occurs at the sidewall of a microchannel with D_h =150 μm and a =1.5.

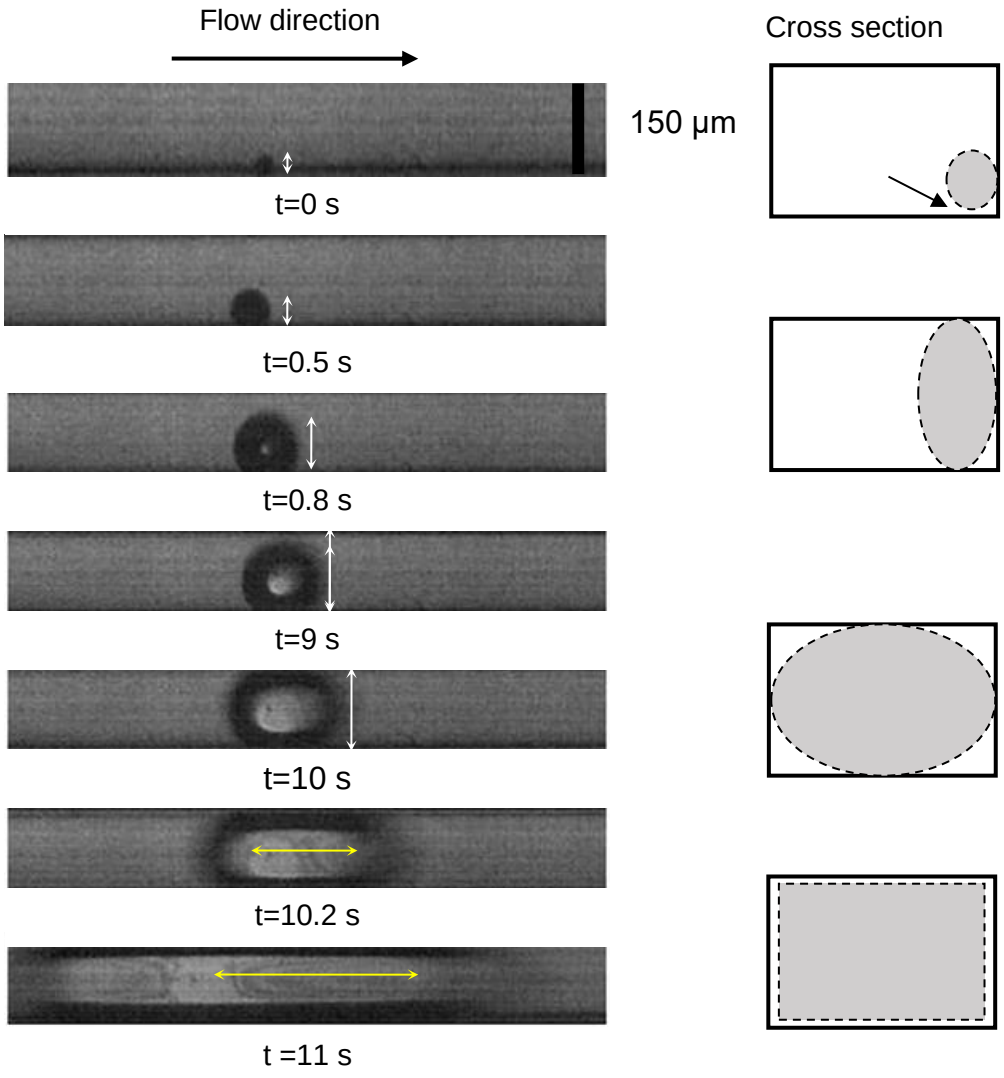

Figure 4. 66 *Sequential images of sidewall bubble growing during flow boiling for D_h = 120 µm and α = 1.5, square cross section microchannel. White arrows show height of bubble and the yellow arrows show the axial growth of the elongated bubble. Arrow on top shows bulk flow direction.*

Figure 4.67a shows the bubble height as a function of time for α = 1.5 microchannels at q = 151 kW m^{-2} andT_{inlet}= 25 ºC. Figure 4.66b shows the bubble diameter as function of time for the same conditions.

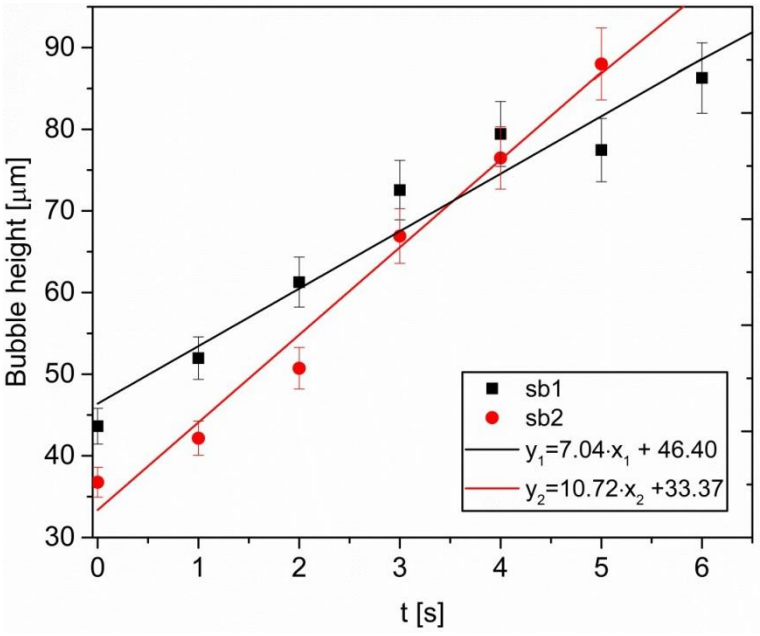

(a)

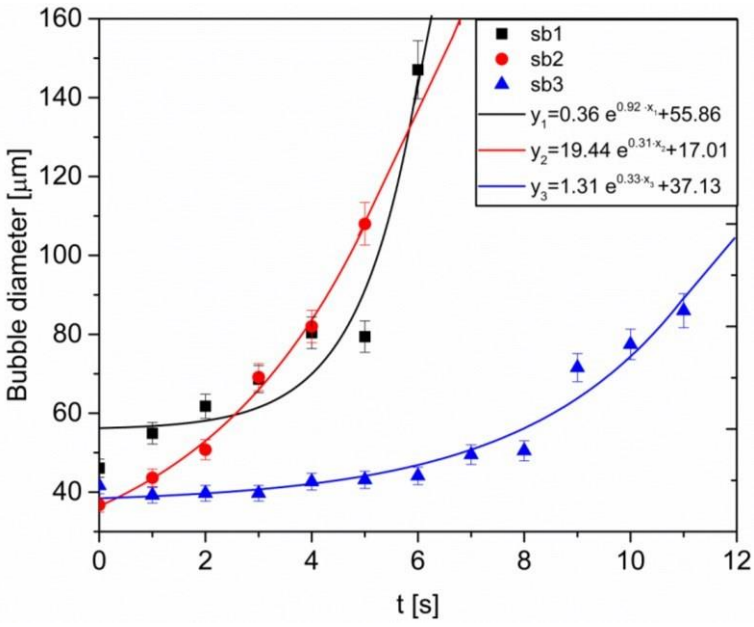

(b)

Figure 4. 67 *(a) Bubble height and (b) bubble diameter as a function of time for* a *= 1.5 microchannels at* q *= 151 kW m*$^{-2}$ *and* T_{inlet} *= 25 ºC.*

Figure 4.68 shows the trends of bubble height and bubble diameter as a function of normalised time for a = 1.5 microchannels at q = 151 kW m^{-2} and T_{inlet} = 25 ºC.

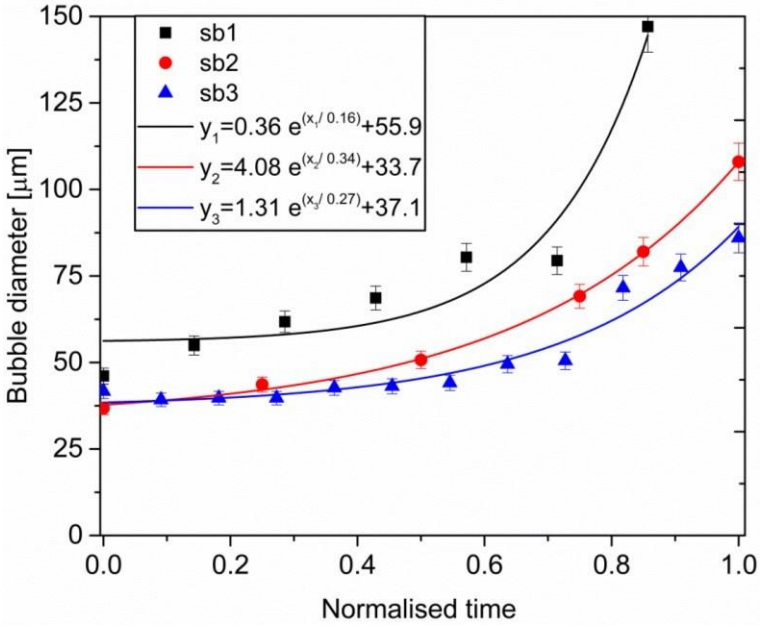

(a)

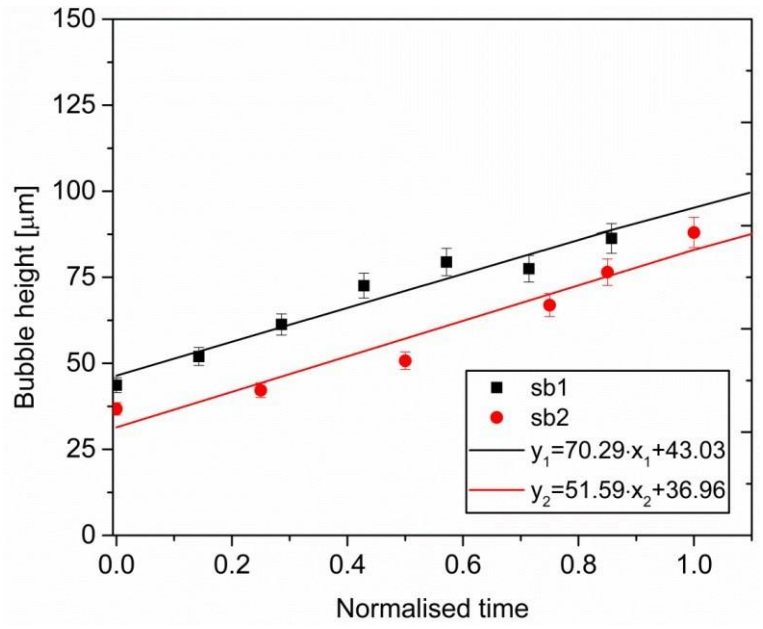

(b)

Figure 4. 68 *(a) Bubble height and (b) bubble diameter as a function of normalised time for* a *= 1.5 microchannels at* q *= 151 kW m*$^{-2}$ *and* T_{inlet} *= 25 ºC.*

4.5 Conclusions

For high aspect ratio microchannels (α = 3) bubbles were observed to grow at sidewall at the inlet (T1) of the microchannels heat sink inducing parallel instabilities that result in temporary measured dryout simultaneously in all parallel microchannels (high amplitude instabilities). Highest wall temperature values and temperature fluctuations were measured at the microchannels heat sink of α = 3 and D_h = 75 μm. Elongated bubbles have been proved to be a limited factor for heat transfer in microchannels .They result in pressure drop increase and flow reversal, inducing parallel channel instabilities. The highest h_{tp} occurred for the heat sink design1B with α = 1.5, wide microchannels but not shallow compared to the other cross sections and D_h = 120 μm with averaged modest pressure drop .

Two-phase periodic pressure drop increase significantly affects the heat transfer coefficient in microchannels. The amplitude of the pressure fluctuations increases with heat flux and aspect ratio and is significantly affects the heat transfer coefficients at low mass fluxes. Increasing the width of the microchannels for a constant depth, results in a decrease of pressure drop. In contrast, the use of small width channels results in parallel microchannel instabilities because of increase of the microchannels number and can induce temperature oscillations and dryout.
The general trend identified in all the cases for the saturated region at position 5 downstream is that the local heat transfer coefficient decreased with mass flux. For heat, transfer coefficients calculated in the middle the heat sink at T3 the heat transfer coefficient initially increased with decreasing mass flux, then reached a maximum and then decreased with decreasing mass flux. The heat transfer coefficient was found to be highest at the inlet and then it decreased sharply in the high vapour quality region, corresponding to localized dryout and superheated flow ($x_e >$ 0.1) where the heat is removed mostly from the vapour [10]. The heat flux at which a surface undergoes transition from nucleate boiling to film boiling is termed the critical heat flux [10]. Velocity and subcooling of the fluid increase CHF.

After comparing the microchannel heat sinks at constant W_{ch} of 150 μm and changing height from 50 μm (D_h = 75 μm, α = 3, A_{cr} = 7,500 μm^2) to 100 μm (D_h = 120 μm, α = 1.5, A_{cr} = 15,000 μm^2), we can conclude that the heat transfer coefficients in the higher height microchannels were higher and the pressure drop was lower. There is an important effect of the microchannel height on the heat transfer and pressure drop and bubble nucleation and growth in the microchannels. For the highest height microchannel heat sinks, the average pressure drop values for changing mass flux were the lowest from all the heat sinks that were tested.

After boiling ensues, the pressure drop increases significantly with increasing heat flux for the high aspect ratio microchannels. As the hydraulic diameter decreased, the magnitude of the

pressure drop increased, which agrees with the theory. The frictional pressure drop for the single-bubble in the rectangular microchannel is related to the liquid film thickness that surrounds the bubble. The pressure drop in a single elongated bubble decreased with the aspect ratio of the channels.

The identification of the flow regimes and their transitions are necessary to develop reliable tools for the prediction of pressure drop and heat transfer in two-phase microchannel heat sinks.

The microchannel size has an effect on the flow regime development. For all the cases at higher quality region, the main flow pattern was annular flow, which indicates that the main heat transfer mechanism is thin film evaporation. At low mass fluxes and high heat fluxes nucleation was observed in the thin liquid film on the sides of the channels.

For microchannels with α = 1.5, bubble nucleation was observed at low mass fluxes. The bubble grows very fast and occupies the whole channel length. The vapour slug elongated at the upstream and downstream end of the microchannels resulting in flow reversal and temporary dryout. Is was observed that when this the rest of the microchannels are affected by the excess flow as the microchannel is blocked and causes parallel channel instabilities [1]. Periodic wetting and rewetting phenomena were observed. Since the heated length is only 15 mm, at high heat fluxes significant interaction takes place between the stream generated in the microchannels and the inlet subcooled liquid. The dominant flow pattern is annular flow that occurs simultaneously at all the channels. This flow regime has a high heat transfer rate. Vapour occupies most of the channel core and then the dryout and periodic wetting phenomena follow. When large vapour slugs are formed at higher mass fluxes and move through the channel, thin liquid film walls are formed which cause both the bubble size and generation frequency to increase at the wall nucleation sites. These nucleate boiling heat transfer characteristics are exhibited over a wide range of conditions in small channels to produce higher heat transfer coefficients than found in large channels. The aspect ratio increased the area of the bubbles increased. Absence of churn flow at very small hydraulic diameters, is noted. Liquid-vapour mixture compressibility and the parallel channels flow enhanced flow instabilities in microchannel heat sinks. As reported from the literature there are two kinds of instabilities identified:

4.6 Summary

This chapter presents experimental results for different aspect ratio silicon multi-microchannel heat sinks using deionised water. Flow boiling experiments were performed in microchannel heat sinks with aspect ratios (α) of 0.33, 0.5, 0.67, 1, 1.5, 2, and 3.and hydraulic diameters from 50 to 150 μm. The effect of aspect ratio on two-phase flow boiling pressure drop

and heat transfer in the rectangular microchannel heat sinks was investigated for the heat fluxes of 151, 183, 271 and 363 kW m^{-2} and varying mass fluxes. Local heat transfer coefficients are presented at five locations and simultaneous high speed images reveal the local flow patterns.

Chapter 5 High spatial and temporal resolution wall temperature measurements with IR thermography

5.1 Introduction

To this chapter, the local two-phase heat transfer coefficients in a rectangular high-aspect-ratio ($a = \frac{W_{ch}}{H_{ch}} = 22$) polydimethylsiloxane (PDMS) microchannel with a hydraulic diameter of 192 μm were obtained using temperature measurements and saturation temperatures obtained from interpolating inlet and the outlet pressure measurements, the latter from integrated silicon ceramic-based pressure sensors located near the inlet and outlet of the microchannel. The experiments used FC-72 liquid with a mass flux of 7.37 kg $m^{-2}s^{-1}$ with associated heat fluxes ranging between 3.34 and 61.95 kW m^{-2}. The hydrodynamic and flow boiling characteristics of the microchannel were characterised using high frequency and high spatial resolution (15 μm/pixel and 200 fps) infrared thermography, with heat transfer coefficients obtained as function of axial position, lateral position and time at the inlet, middle and outlet sections of the microchannel base. This enabled the effect of heat flux on local temperature variation, flow boiling heat transfer coefficient distribution and the two-phase pressure drop to be studied. Heat transfer data represented as well as bubble dynamics and pressure drop starting with the heat transfer data, space averaged, with time. The local spatio-temporal evolution of the heat transfer coefficient was investigated using imposed heat flux as a parameter, whilst paying special attention to the maximum limit in heat transfer, referred to as critical heat flux (CHF). The local heat transfer coefficients data provided evidence that the two-phase heat transfer coefficient does not increase monotonically with the heat flux, and actually reduces under certain conditions. This decreasing trend of the heat transfer coefficient is shown to depend on the heat flux range and is correlated with vapour-liquid dynamics and dryout, observed simultaneously with the temperature measurements. This application of high speed thermography simultaneously with flow visualisation additionally enabled more detailed information to be obtained on two- phase flow and bubble dynamics. The local two-phase heat transfer data are correlated with simultaneous flow visualizations, as well as bubble dynamics and pressure drop.

5.2 Experimental setup and procedure

Flow boiling experiments were performed using the flow loop presented in chapter 3. The schematic of the experimental setup is shown in Figure 3.1. The liquid temperature prior to entry to the channel via the inlet was maintained at 21 ± 1 ºC. In this chapter, a high aspect-ratio ($\alpha > 20$), rectangular cross-section (width (W_{ch}) = 2.26 mm, height (H_{ch}) = 100 µm and length = 20 mm) polydimethylsiloxane (PDMS)-based microchannel, with a hydraulic diameter (D_h) of 192 µm, formed the test section. FC-72 (Tsat = 56 ºC at P = 1 atm) was pumped at a constant flow rate through the PDMS microchannel. The test section fabrication process is discussed in section 3.3 of chapter 3. During heating of the liquid in the channel, a spatial map of the wall-temperature was recorded from the glass side of the device. Simultaneous pressure measurements were acquired from the silicon pressure sensors integrated near the inlet and the outlet of the channel. Details about microprocessing and calibration of pressure sensors can be found in chapter 3.

High temporal and spatial resolution measurements were achieved using infrared (IR) thermography and simultaneous high-speed imaging from the glass side of the microchannel base. The spatial resolution determines how much detail can be resolved in each individual still image or "frame" and the temporal resolution which is the sampling rate in *time (*200 samples per second) determines the fastest change we can track between successive images. The FLYR IR camera was used with the lens type of MW G1WD 30 3.0 with a resolution of 640 × 512. The spatial resolution of the measurements was found to be 15.39 µm/pixel. This number was derived from the correlation of channel width with the pixels. In this study, the microchannel of 2.26 cm width and 20 mm length was divided in three equal parts which were studied separately in order to achieve high spatial resolution of the measurements alogn the channel. The frame rate was set to 200 Hz which is a high temporal resolution compared to previous studies that were performed using IR thermography technique in microchannels flow boiling experiments[24], [25], [111], [112], [116]–[119]. As already mentioned in Chapter2, only Krebs *et* al. [119] provided high spatial resolution of 10 µm /pixel wall temperature measurements at a temporal resolution of 120 frames per second. The other studies used higher spatial resolution than 50 µm /pixel. The integration time was set to 0.4050 ms and the temperature range for the measurements was adjusted in the range of 20 to 130.2 ˚C in order to. The surrounding temperature was set to 20 ˚C in the Research IR software. For every microchannel device, emissivity calibration was carried out as described in section 3.3 of chapter 3 before the device was used for the experiments. Firstly, the background of the measurements was set. The conductivity layer was used under a copper painted black layer, which was used for a heater.

The IR camera (x6580sc FLIR) was turned on. The waiting time of 10 min required before using the camera. The camera was set to 30 cm from the focus channel surface.

5. 3 Data reduction

The analysis of IR data in single-phase flow showed uniform heating of the microchannel as the temperature gradient was constant, without local temporal variations in excess of 0.2 ˚C. The transverse temperature profile showed a slight dip in temperature (~1˚C) at the channel centre. The conversion factor for the IR images was 15.39 μm/pixel and was calibrated to the width of the microchannel.

The Biot number that indicates the temperature uniformity within the channel by comparing the conduction resistance to the convection resistance was calculated as:

$$\mathrm{Bi} = \frac{\mathrm{h_{conv}}\tau_{\mathrm{w}}}{\mathrm{k_{ch}}} \tag{5.1}$$

where τ_w is the channel wall thickness, k_{ch} is the thermal conductivity of the glass and $\mathrm{h_{conv}}$ is the convective heat transfer coefficient calculated from Newton's cooling law:

$$\mathrm{Q} = \mathrm{h_{conv}A(T_w - T_f)}, \tag{5.2}$$

where $\mathrm{T_w}$ is the outer wall temperature of the channel and T_f is the fluid temperature, A is the outer channel surface and Q is the input power to the channel. Bi was found to range between 0.060 and 0.180. Since $Bi \ll 1$ the difference between the inner and outer wall temperature could be neglected. The value of $\mathrm{h_{conv}}$was found to vary from 452.6 to 13,000 W $\mathrm{m^{-2}}$ $\mathrm{K^{-1}}$ with 11.4 % uncertainty. The local microchannel pressure was interpolated assuming a linear profile of pressure from inlet to outlet [25, 29, 123].

The input power (Q) provided at the ITO glass was determined using Joule's first law. The heat transfer losses for single and two-phase flow conditions were estimated from the energy balance:

$$\mathrm{Q_{loss}} = \mathrm{Q} - (\mathrm{Q_{eff}}) \tag{5.3}$$

The effective heat transferred to the liquid during single-phase flow was estimated from:

$$\mathrm{Q_{eff}} = \dot{\mathrm{m}}\mathrm{c_{p,l}}\left(\mathrm{T_{l,out}}\text{-}\mathrm{T_{l,in}}\right) \tag{5.4}$$

where $T_{l,in}$ and $T_{l,out}$ are the inlet and outlet liquid temperatures, ṁ, 0the liquid mass flow rate (kg s^{-1}) and $c_{p,l}$, the liquid specific heat capacity, calculated at the mean temperature of the liquid. The maximum heat transfer losses for single-phase were calculated to be 2.5 %.

For two-phase flow conditions, the heat transfer losses from the channel surface to the surroundings were evaluated from:

$$Q_{loss}(x,y) = Q_{conv}(x,y) + Q_{rad}(x,y) \quad (5.5)$$

considering both convection (Q_{conv}) and radiation (Q_{rad}) losses. Then Q_{eff} was estimated from equation (2). The width of the microhannels was aligned with the y axis and the channel length with the x axis.

The convective losses were estimated from:

$$Q_{conv}(x,y) = h_{conv}A\left(T_{w,IR}(x,y) - T_{amb}\right) \quad (5.6)$$

where h_{conv} is the convective heat transfer coefficient of air estimated from empirical correlations for natural convection [124] and A, the microchannel heated surface area, $T_{w,IR}(x,y)$, the temperature distribution of the microchannel surface obtained using the IR camera and T_{amb} the ambient temperature close to the surface.

The radiative losses were estimated from :

$$Q_{rad}(x,y) = \varepsilon\omega A\left(T^4_{w,IR}(x,y) - T^4_{amb}\right) \quad (5.7)$$

where ε, the surface emissivity of the microchannel and $\omega = 5.67 \times 10^{-8}\ Wm^{-2}K^{-4}$, the Stefan–Boltzmann constant. The values obtained for Q_{conv} (uncertainty of 2.35 %) ranged between 0.003 W to 0.005 W and the values for Q_{rad} ranged between $2.15*10^{-7}$ to 0.00047 W (uncertainty of 0.15 %).

The average heat flux at the wall was calculated from:

$$q(x,y) = \frac{Q_{eff}}{A} \quad (5.8)$$

The local liquid temperature was calculated using:

$$T_l(x,y) = \frac{(q(x,y)\cdot P_h \cdot z)}{c_{p,l}\cdot \dot{m}} + T_{inlet,} \tag{5.9}$$

where P_h is the channel heated perimeter, z, the distance from the channel inlet, $T_{l,in}$ is the inlet temperature of the liquid and $T_{sat}(x)$, the local saturation temperature calculated from local pressure along the microchannel. The value of T_{sat} is dependent on local pressure and this dependence was implemented in the calculations of the heat transfer coefficient for precision (many previous studies have used a fixed value for T_{sat} ignoring the pressure drop in the microchannel).

The local heat transfer coefficient for single-phase flow was calculated using:

$$h_{sp}(x,y) = \frac{q(x,y)}{\left(T_{w,IR}(x,y) - T_l(x,y)\right)} \tag{5.10}$$

The local two-phase heat transfer coefficient for subcooled ($x_e < 0$) flow was determined as:

$$h_{tp}(x,y) = \frac{q(x,y)}{\left(T_{w,IR}(x,y) - T_l(x,y)\right)} \tag{5.11}$$

where $x_e$is the vapour quality.

The local two-phase heat transfer coefficient for saturated ($x_e > 0$) flow was determined as:

$$h_{tp}(x,y) = \frac{q(x,y)}{\left(T_{w,IR}(x,y) - T_{sat}(x)\right)} \tag{5.12}$$

The vapour quality at the saturated region was defined as:

$$x_e(x) = \frac{Q_{eff}\cdot (z - z_{sat})\cdot P_h}{\left(A_c \cdot m \cdot h_{fg}\right)} \tag{5.13}$$

where A_{cr} is the microchannel cross sectional area, h_{fg} is the latent heat of vaporisation, z is the stream-wise distance from channel inlet and z_{sat} is the position along the microchannel where vapour quality is zero ($x_e = 0$). For $z < z_{sat}$ liquid is under subcooled condition, and vapour quality $x_e = 0$.

Figure 5.1a presents the experimental and theoretical single-phase pressure drop as a function of the mass flux. The theoretical friction factor (f_{FD}) for fully developed laminar flow in a rectangular microchannel can be calculated from the correlation of Shah and London [125]. The comparison of the measured and predicted single-phase heat transfer coefficient is shown in Figure 5.1b. The theoretical correlation of Wang and Peng [126] was used to predict the single-phase heat transfer coefficient. Good agreement with the predictions has been achieved. It is found that the deviations among the pressure drop are higher than the predicted from correlation values at low mass fluxes. The large error of single-phase pressure drop at low mass fluxes can be possibly attributed to the use of flow rates lower than the flow rates usually used for the aforementioned equation [6]. For the experiments presented in this chapter, the main uncertainties are identified in Table 5.1.

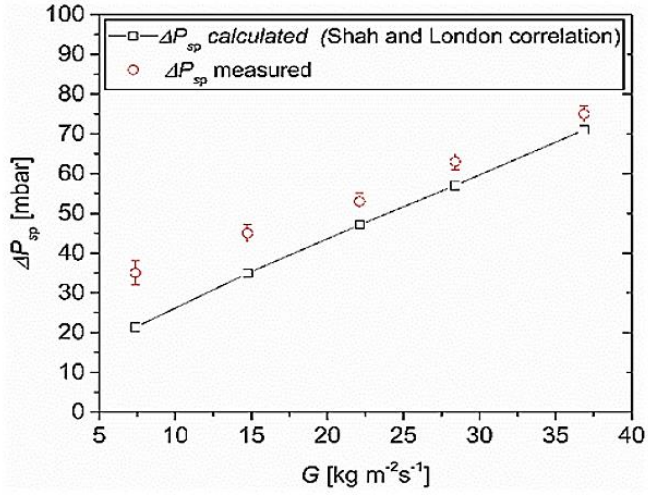

(a)

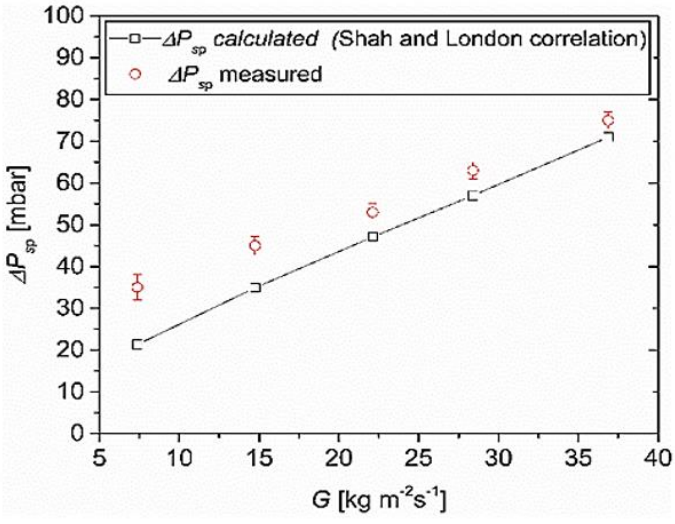

(b)

Figure 5. 1*(a) Experimental and theoretical single-phase pressure drop in function of the mass flux. (b) Experimental and theoretical single-phase heat transfer coefficient in function of the heat flux.*

Table 5. 1 *Summary of measurements uncertainties.*

Parameter	Maximum Uncertainty
Standard K-type thermocouple	± 0.5 °C
Pressure sensors	0.18 % (0.14 % minimum)
DC power supply	±1 % of reading
IR camera measured temperature	±1 ˚C from 20 ˚C to 120 °C
Pump volumetric velocity	0.5 %
Mass flux	9%
Heat flux	6 %
Heat transfer coefficient	11%
Vapour quality	3.2 %
Local liquid temperature	2.3°C (0.9 °C minimum)

5. 4 Results and discussion

5.4.1 Two-phase heat transfer coefficients during flow boiling

5.4.1.1 Spatially averaged two-phase heat transfer coefficients

The spatial average temperatures along the centreline for each of three sections (inlet, middle and outlet) were evaluated and from these and the calculated local saturation temperature and the average heat transfer coefficients were calculated ($h_{1}avg(t)$, $h_{2}avg(t)$, $h_{3}avg(t)$ respectively). The data shown is for fixed mass flux and varying heat flux. The wall temperature data are presented in Figures 5.2a, c and e and the heat transfer coefficient data in Figures 5.2 b, d and f.

Figures 5.2a, c and e show the variation of wall temperatures ($T_{w1,IR}avg(t)$, $T_{w2,IR}avg(t)$, $T_{w3,IR}avg(t)$) in the two-phase region with time, for increasing heat fluxes ranging from 13.9 to 61.95 kW m^{-2} at constant mass flux of G = 7.37 kg m^{-2}s^{-1}. The general trend observed in Figures 5.2a, c and e is that the channel wall temperature increased with heat flux and heated length. From visual observations synchronized with thermal images, bubble nucleation was observed

to start at q = 17.28 kW m^{-2}. This bubble nucleation appeared to be caused by superheating close to the sidewall near the outlet of the channel, where the temperature value was highest). This generated low amplitude temperature oscillations, induced as a result of bubble growth. The oscillation amplitude of$T_{w1,}g(t)$, $T_{w2,IR}avg(t)$ and $T_{w3,IR}avg(t)$ increased from 0.3 to 2 °C with increasing heat fluxes from 13.9 to 30.97 kW m^2. Between q = 13.9 kW m^{-2} and 30.97 kW m^{-2}, the temperature fluctuations with time where relatively low (< 2 °C) which we describe as a stable two-phase flow boiling mode in the microchannel. The stable flow boiling mode corresponds to a stable flow pattern (where bubbly-slug flow exists, as described by Cheng *et* al. [33]) at low vapour qualities 0 < x_e < 0.2. Figure 5.2e shows that during the stable flow boiling mode, the maximum wall temperature $T_{w3,IR}avg(t)$ was measured to be 93.5 ºC at the channel outlet for q = 30.97 kW m^{-2}. Flow instabilities, characterised by flow reversal were observed when q exceeded 30.97 kW m^{-2}, which also caused dryout at the channel outlet (unstable flow mode). Figures 4.2a, c and e show that for heat fluxes ranging between 47.78 and 61.95 kW m^{-2} the wall temperature fluctuations exceeded 4.5 ºC and displayed chaotic behaviour, particularly at the middle and outlet of the channel. The amplitude of the oscillations of $T_{w2,}g(t)$ and $T_{w3,IR}avg(t)$ reached occasionally a maximum and of 10 ºC as a result of local dryout at the channel outlet sidewalls. At q = 61.95 kW m^{-2}, $T_{w3,}g(t)$ reached 120 ºC (Figure 5.2e). The observed flow regimes were bubbly-slug flow, annular flow, wavy annular flow and annular-dryout. Annular flow was observed for q > 30.97 kW m^{-2} where the flow patterns were characterised by instability for which we observe flow reversal, dryout and rewetting. We refer to this as cycles of dryout. The actual flow patterns were set by a sequence of images. Figure 5.3 shows the typical flow patterns observed at the investigated microchannel for q = 30.97 kW m^{-2} and 42.78 kW m^{-2}. Fast abrupt bubble expansion was observed at the channel inlet for q = 42.78 kW m^{-2} which induced flow reversal and early dryout.

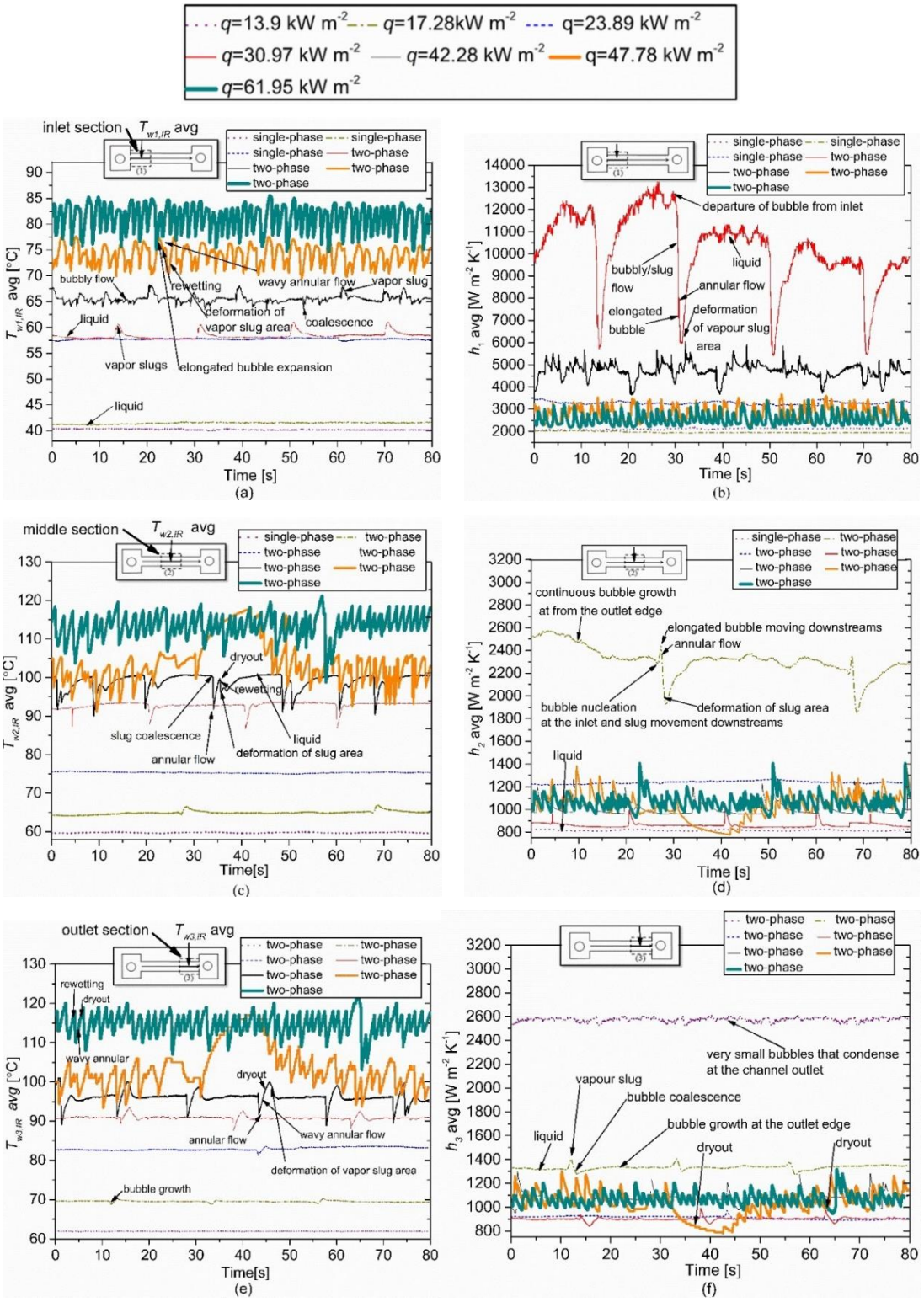

Figure 5. 2 *Temporal variation in wall temperature along the centreline as recorded for 80 s using infrared imaging from the inlet (a), middle (c) and outlet (e) of the microchannel for G =7.37 kg m^{-2} s^{-1} and from q =13.9 to 62.95 kW m^{-2}. The wall temperature was averaged along the centreline in the stream-wise direction. The associated averaged heat transfer coefficients are presented in (b), (d), (f), respectively and show the different heat transfer trends during two-phase flow boiling modes at the inlet, middle and outlet sections of the microchannel.*

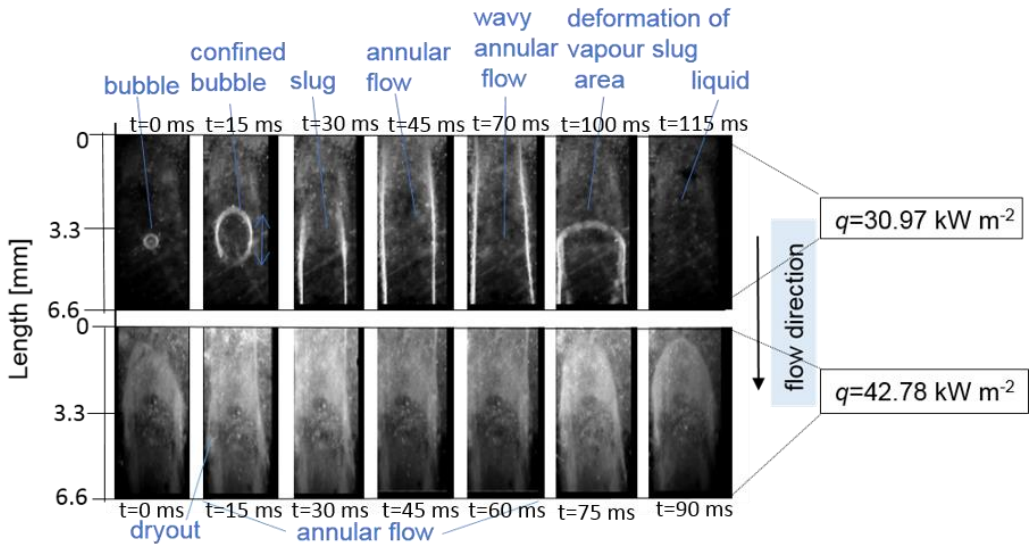

Figure 5. 3 *Typical flow regimes at the inlet of the investigated high aspect ratio rectangular microchannel. Sequence of optical images from the heater side of the inlet for G =7.37 kg m^{-2}s^{1} and q =30.97 kW m^{-2} and 42.78 kW m^{-2}. The images were cropped to show the section where the temperature measurements were carried out.*

Generally, the geometry of the channel plays an important role in the magnitude of the heat transfer rate. Wang and Sefiane [55] used FC-72 at G = 11.7 kg m^{-2} s^{-1}, in a single rectangular, high aspect ratio microchannel (with curved rather than sharp corners) with D_h = 548 μm and heat fluxes from 2.92 to 16 kW m^{-2}. They reported two-phase heat transfer coefficients lower than 1,000 W m^{-2} K^{-1}. In our case, using a rectangular cross section microchannel of high aspect ratio (a = 22) with higher cross section area (A_{cr} = 0.226 mm^2) resulted in higher average two-phase heat transfer coefficient values. The lowest two-phase HTC values were calculated between 900 and 2,000 W m^{-2} K^{-1} for the highest heat flux of q = 61.95 kW m^{-2}. Probably there is an enhancement because if the capillary effect that allows liquid rewetting at the channel corners.

This section has shown spatially averaged heat transfer coefficients as a function of time for separate sections (inlet, middle, outlet) of the microchannel averaged along the centreline at stream-wise direction. In the following section, a higher spatial resolution evolution of the heat transfer coefficient is presented for the whole channel. Figure 5.4 shows the heat transfer coefficient as a function of time and microchannel length.

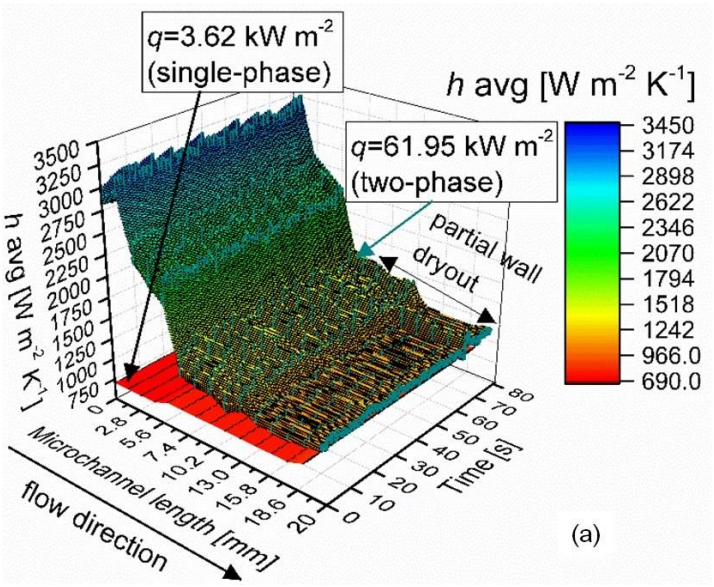
q=3.62 kW m-2
(single-phase)
h avg [W m-2 K-1]
q=61.95 kW m-2
(two-phase)
partial wall
dryout
3450
3174
2898
2622
2346
2070
1794
1518
1242
966.0
690.0
h avg [W m-2 K-1]
Microchannel length [mm]
flow direction
Time [s]
(a)

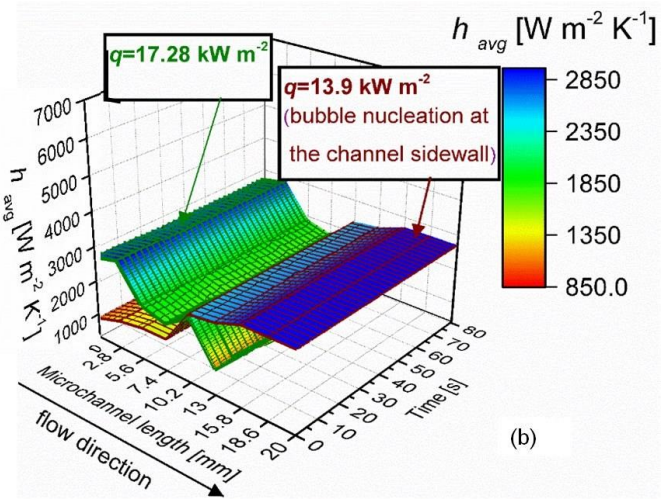
h avg [W m-2 K-1]
q=17.28 kW m-2
q=13.9 kW m-2
(bubble nucleation at
the channel sidewall)
2850
2350
1850
1350
850.0
h avg [W m-2 K-1]
Microchannel length [mm]
flow direction
Time [s]
(b)

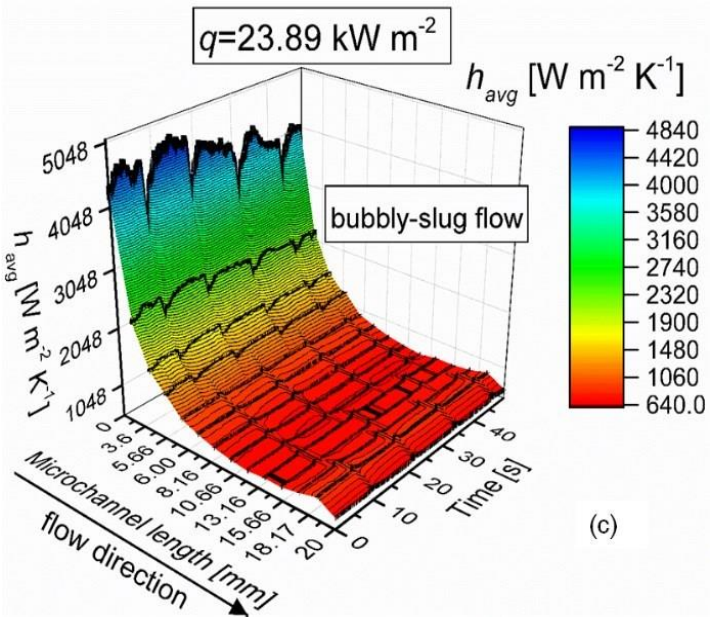
q=23.89 kW m-2
h avg [W m-2 K-1]
bubbly-slug flow
4840
4420
4000
3580
3160
2740
2320
1900
1480
1060
640.0
h avg [W m-2 K-1]
Microchannel length [mm]
flow direction
Time [s]
(c)

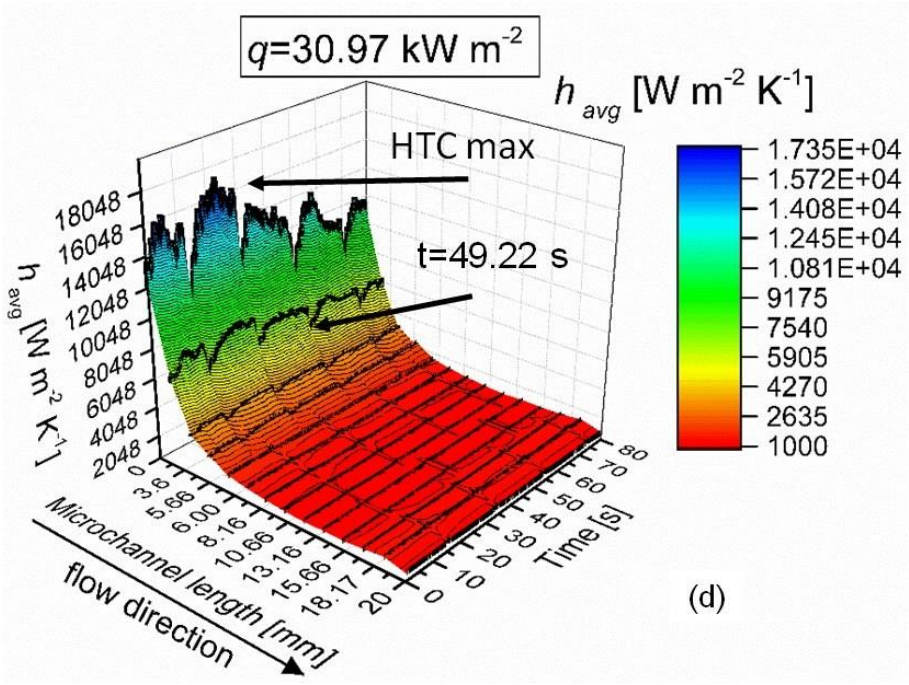
q=30.97 kW m-2
h avg [W m-2 K-1]
HTC max
t=49.22 s
1.735E+04
1.572E+04
1.408E+04
1.245E+04
1.081E+04
9175
7540
5905
4270
2635
1000
h avg [W m-2 K-1]
Microchannel length [mm]
flow direction
Time [s]
(d)

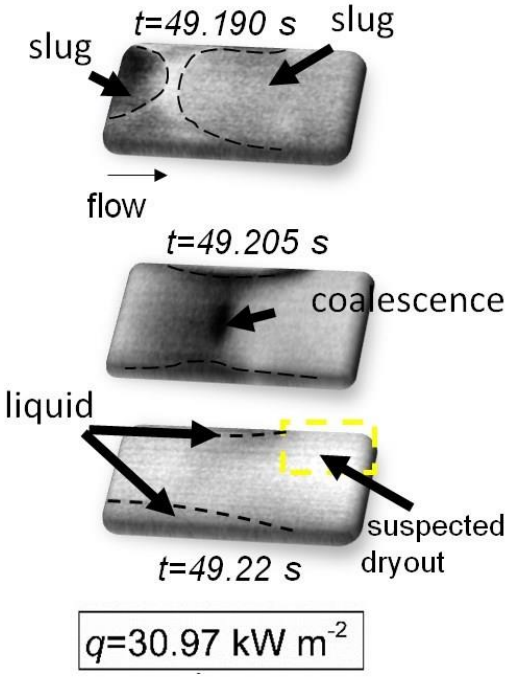
t=49.190 s
slug
slug
flow
t=49.205 s
coalescence
liquid
suspected
dryout
t=49.22 s
q=30.97 kW m-2

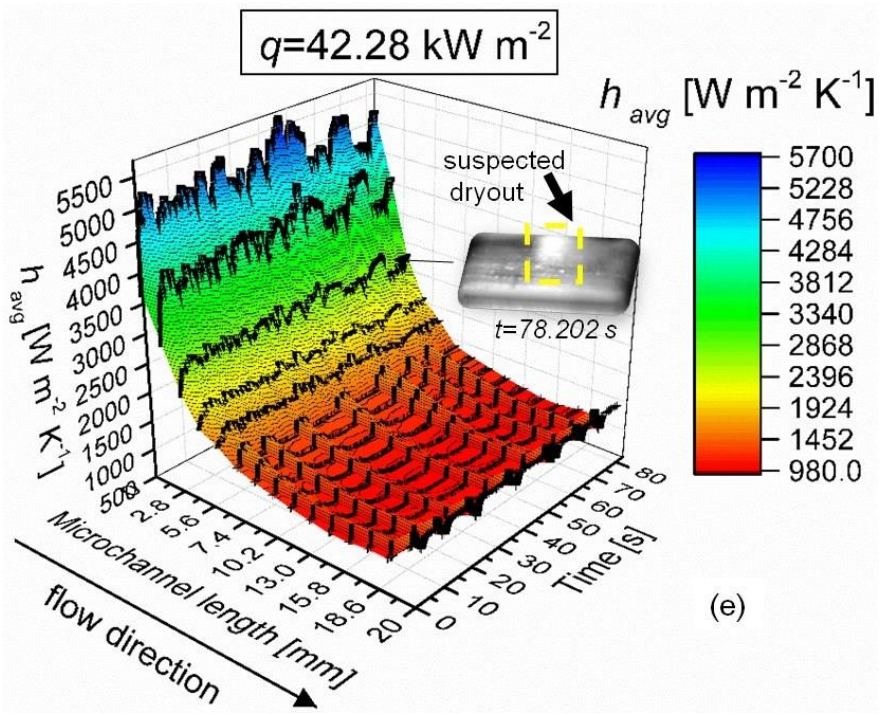
q=42.28 kW m-2
h avg [W m-2 K-1]
suspected
dryout
t=78.202 s
5700
5228
4756
4284
3812
3340
2868
2396
1924
1452
980.0
h avg [W m-2 K-1]
Microchannel length [mm]
flow direction
Time [s]
(e)

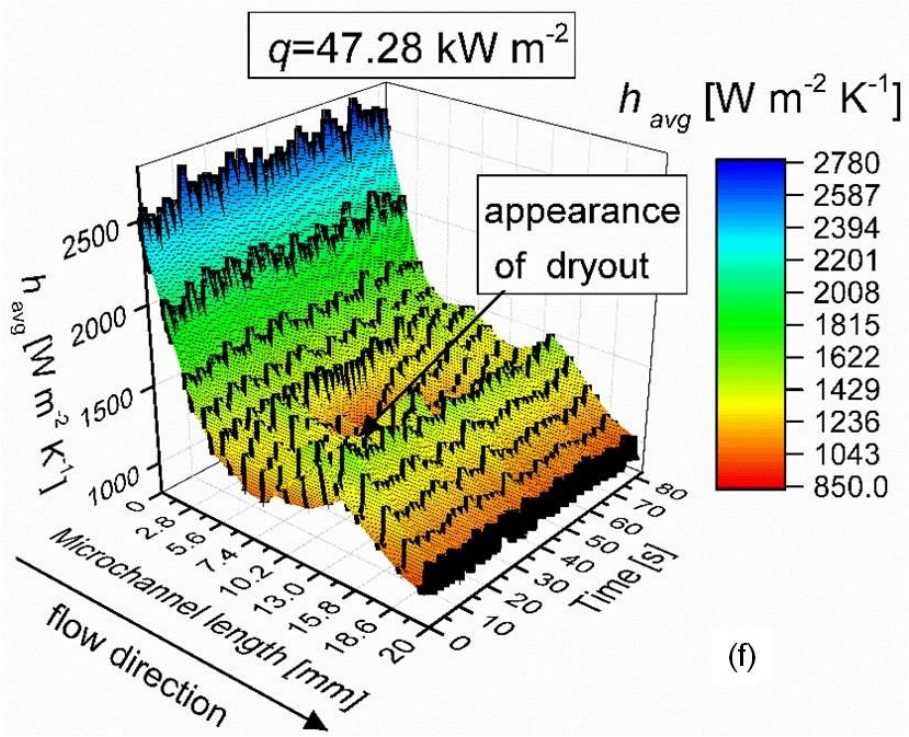
q=47.28 kW m-2
h avg [W m-2 K-1]
appearance
of dryout
2780
2587
2394
2201
2008
1815
1622
1429
1236
1043
850.0
h avg [W m-2 K-1]
Microchannel length [mm]
flow direction
Time [s]
(f)

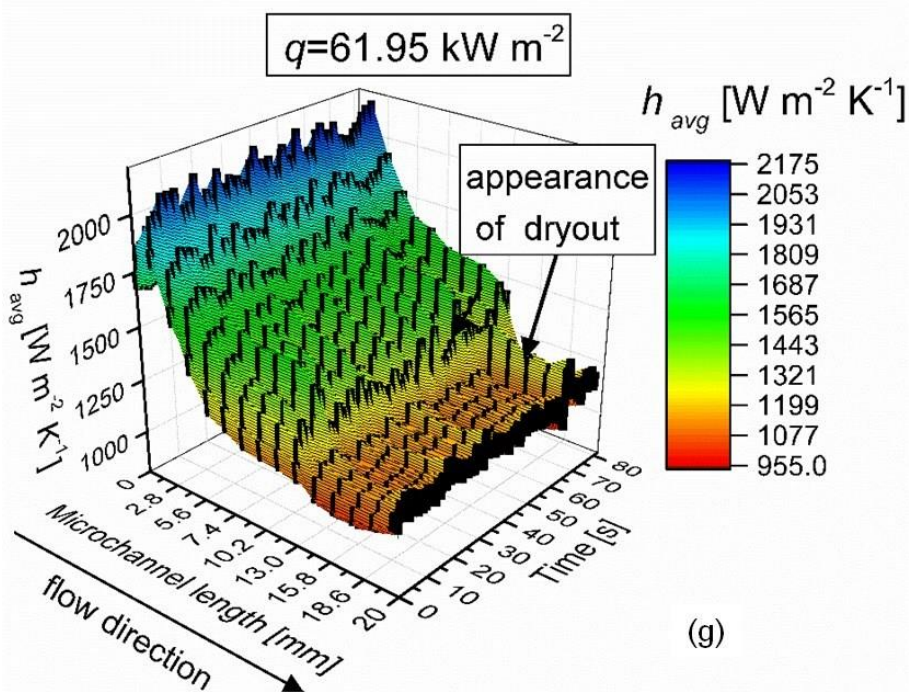

Figure 5. 4 *3D plots of the heat transfer coefficient as a function of time and whole channel length (a) for q = 3.62 18 kW m^{-2} (single-phase) and q = 61.92 kW m^{-2} (two-phase) (b) for q =13.9 kW m^{-2} and q =17.28 kW m^{-2} (two-phase), (c) for q = 23.89 kW m^{-2} (two-phase), (d) for q = 30.97 kW m^{-2} , (e) for q = 42.28 kW m^{-2} (two-phase), (f) for q = 47.28 kW m^{-2} and (g) for q = 61.95 kW m^{-2} (two-phase).*

Figure 5.4a compares average heat transfer coefficients for single-phase (for q = 3.62 kW m^{-2}) and two-phase at the highest heat flux (q = 61.95 kW m^{-2}). The single-phase heat transfer coefficient did not exceed 900 W m^{-2}K^{-1}. Even at the highest heat flux of 61.95 kW m^2 (Figure 5.4g), the average two-phase heat transfer coefficient at the channel outlet was calculated to be higher (fluctuated between 955 to 1321 W m^{-2} K^{-1}) than the single-phase flow. Figures 5.4b to g present average two-phase heat transfer coefficients as a function of time. Figure 5.4b shows that the two-phase heat transfer coefficient for q =13.90 kW m^{-2} ranged between 1,350 to 2,500 kW m^{-2} from inlet to outlet. For q = 17.28 kW m^{-2} the two-phase heat transfer coefficient ranged between 2,500 and 2,850 kW m^{-2}. For low heat fluxes, HTC was almost constant with time as negligible fluctuations occurred as indicated in Figure 5.4b. This was because at this heat fluxes there were alternations between liquid and bubbly flow regime. The elongated bubbles were observed to be flushed out of the channel and no flow reversal because of bubble growth was observed to occur. Different flow regimes occurring along the microchannel (bubbly-slug flow) resulting in important wall temperature differences along the channel length. Further increases of the heat flux resulted in suspected dryout of the wall at the outlet. Figure 5.4c shows that for

q = 23.89 kW m^{-2} K^{-1} when periodic fluctuations started, the highest two-phase average heat transfer coefficient was measured at the entrance of the channel, with a maximum value of 4,840 $Wm^{-2}K^{-1}$. The flow visualizations revealed alternation between liquid and bubbly-slug flow regimes. Figure 5.4d shows that the maximum value of heat transfer coefficient was measured for q = 30.97 kW m^{-2} K^{-1} at the channel entrance (bubbly-slug flow regime. The inlet two-phase heat transfer coefficient appeared to oscillate, peaking with an average period of 15 s and an average amplitude of 2,400 kWm^{-2} K^{-1}. As the bubble diameter reached that of the channel, annular flow was established at the outlet with partial dryout of the wall. As a result, this affected the uniformity of the two-phase heat transfer coefficient. At q = 42.28 kW m^{-2} (Figure 5.4e) annular flow was established along the whole microchannel length (see flow visualisation in previous Figure 5.3). Figures 5.4f and g show data for the highest heat fluxes (q = 42.28 kW m^{-2}). For q = 47.78 kW m^{-2} (Figure 5.4e) the two-phase average heat transfer coefficients ranged between 850 and 2,780 W m^{-2} K^{-1} and oscillated periodically with an amplitude of 250 kW m^{-2}. For q = 61.95 kW m^{-2}, the HTC ranged between 955 and 2,195 W $m^{-2}K^{-1}$ and oscillated periodically with an amplitude of 1,000 W 19 m^{-2} K^{-1}. The two-phase average heat transfer coefficients for q = 47.78 kW m^{-2} and 61.95 kW m^{-2} showed the same decreasing trends with channel length with almost the same range of HTC. Therefore, this relationship was observed to be almost independent of the heat flux. Hence, it can be concluded from the trends presented in Figure 5.4 that, even when suspected dryout occurs at the outlet during two-phase flow boiling, the average heat transfer coefficient for single-phase flow is always less than that for two-phase heat transfer. Furthermore, at increasing heat flux, suspected dryout, which is present mostly at the outlet of the channel for longer time (1.5-2 s), leads to a degradation of heat transfer and lower heat transfer coefficients. This deterioration occurred as a result of the axial bubble expansion, which controlled the heat transfer phenomena. The intermittency of the flow was accompanied by heat transfer coefficient fluctuations over time (Figures 5.4c, d, e, e, g. Suspected dryout of the wall occurred when the elongated bubble occupied the entire channel cross section at the channel outlet. The highest two-phase heat transfer coefficient values (up to 17,350 W m^{-2} K^{-1}) were recorded at the inlet section (entrance) for q = 30.97 kW m^{-2} where bubbly-slug flow regime was dominant at the inlet and middle and annular flow with suspected dryout at the sidewalls was dominant at the outlet. This alternation of flow regimes resulted in a high variation of the local heat transfer coefficient along the channel centreline.

5.4.1.2 Local two-phase heat transfer coefficients

In the previous section, the channel was divided into three regions and the heat transfer coefficient was then averaged within these domains. Such an approach enabled trends to be explored and orders of magnitude of the heat transfer to be derived. However, rapid local changes in heat transfer requires analysis of data with a much higher spatial resolution. To address this, heat transfer data with the highest spatial resolution achieved by the camera is presented in the following section.

Figure 5.5 shows the local, rather than averaged, two-phase heat transfer coefficients along the microchannel centerline plotted against time for three conditions: q = 30.97 kW m^{-2}, 42.2 kW m^{-2}and 61.95 kW m^{-2}. The local two-phase heat transfer coefficient was found to decrease with channel length for all heat fluxes except for the condition when q = 17.28 kW m^{2}. In this case, a minimum value was observed 15 mm from channel inlet. This result was attributed to the onset of boiling at this location in the microchannel. The general decreasing trend is consistent with observations reported in literature by Mirmanto [8] who attributed this to a decrease in the local fluid saturation temperature. The highest temporal variation of $h(x)$ was recorded at q = 30.97 kW m^{-2} as a result of bubble axial expansion in the channel. Bubble confinement resulted in high evaporation rates for this heat flux (Figure 5.5a). The extent of variation of $h_{tp}(x, t)$ along the channel length diminished with increasing heat flux because of the decrease of $h_{tp}(x, t)$ at the inlet during the unstable mode and suspected partial dryout at the wall downstream (Figure 5.5b, c). The $h(x, t)$values decreased with increasing heat flux, as is shown in Figure 5.5. Clear access to high temporal and spatial resolution local heat transfer data is very important during unstable modes of two- phase flows as will give a better understanding of what causes the instabilities. The high frequency oscillations of the local heat transfer coefficient along the channel, as measured in this work, underline the need to collect such data.

The two-phase heat transfer coefficient for q = 30.97 kW m^{-2}, ranged between 900 and 13,900 W m^{-2} K^{-1}, see Figure 5.5a. For this heat flux, Figure 5.5a shows that the highest heat transfer coefficient was measured at the channel inlet due to entrance effects. Figure 5.5i shows that the flow regime observed from the flow visualizations at the channel inlet, was bubbly-slug flow where liquid surrounded the elongated bubbles. The coalescence between bubbles-slugs resulted in a full confined (widthwise) vapour slug. Figure 5.5ii shows that during the vapour slug axial growth to the entrance of the channel, a decrease of 2,872 W m^{-2} K^{-1} of HTC occurred (at the channel entrance). The minimum value of HTC was measured (Figure 5.5iii) when the slug moved with direction to the channel exit while forming a flat meniscus.

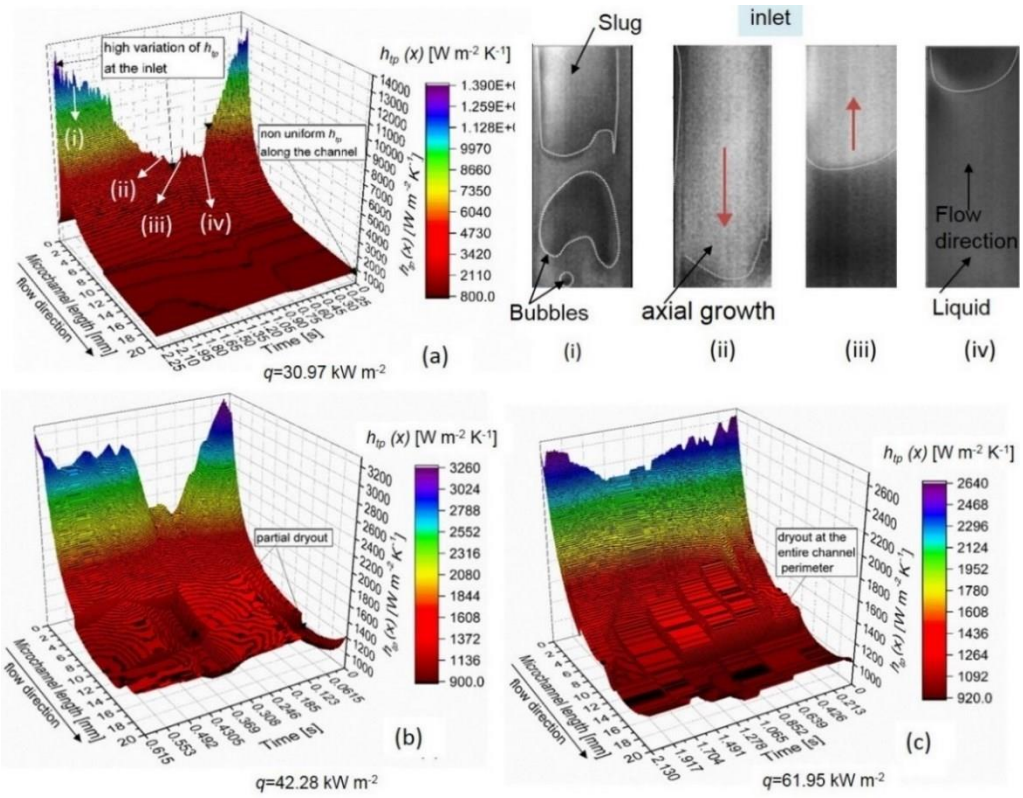

Figure 5. 5 *3D plots of local two-phase heat transfer coefficients $h(x)$ along the whole length at the centre of the microchannel centreline in the stream-wise direction with time intervals of 0.015 s for one cycle of dryout. The local values of $h_{tp}(x,t)$ were plotted for the heat fluxes of (a) q = 30.97 kW m^{-2} , (b) q = 42.28 kW m^{-2}, and (c) q = 61.95 kW m^{-2} and simultaneous flow visualisation results are shown for q = 30.97 kW m^{-2}.*

Figure 5.5iv shows the wetting of the channel surface. Increasing the heat flux to 42.28 kW m^{-2} resulted in lower values of $h(x)$ ranging from 1,136 to 3,260 W m^{-2} K^{-1}, (Figure 5.5b). Figure 5.5b shows that at the highest heat flux of q = 61.95 kW m^{-2}, $h_{tp}(x)$ varied less (1,000 to 2,800 W m^{-2}K^{-1}) due to suspected dryout at the outlet (Figure 5.9b). The frequency of $h(x)$ oscillations increased as suspected dryout lasted for longer periods as the vapour stayed in contact with the channel walls for a longer time. Figure 5.6 shows in detail the oscillations in $h(x)$ with time in the outlet section for q = 30.97 and 61.95 kW m^{-2}. The main difference between the two heat fluxes is that the t period of suspected dryout increased for the higher heat flux of q = 61.95 kW m^{-2} (where suspected dryout of the liquid film occurred as shown later in Figure 5.9). The $h(x, t)$ increase with length for q = 30.97 kW m^{-2} suggests that there is still a liquid film evaporating at the channel outlet. In contrast, for q = 61.95 kW m^{-2}, $h(x)$ showed a local decrease with microchannel length which is consistent with suspected dryout at the outlet (below the bubble).

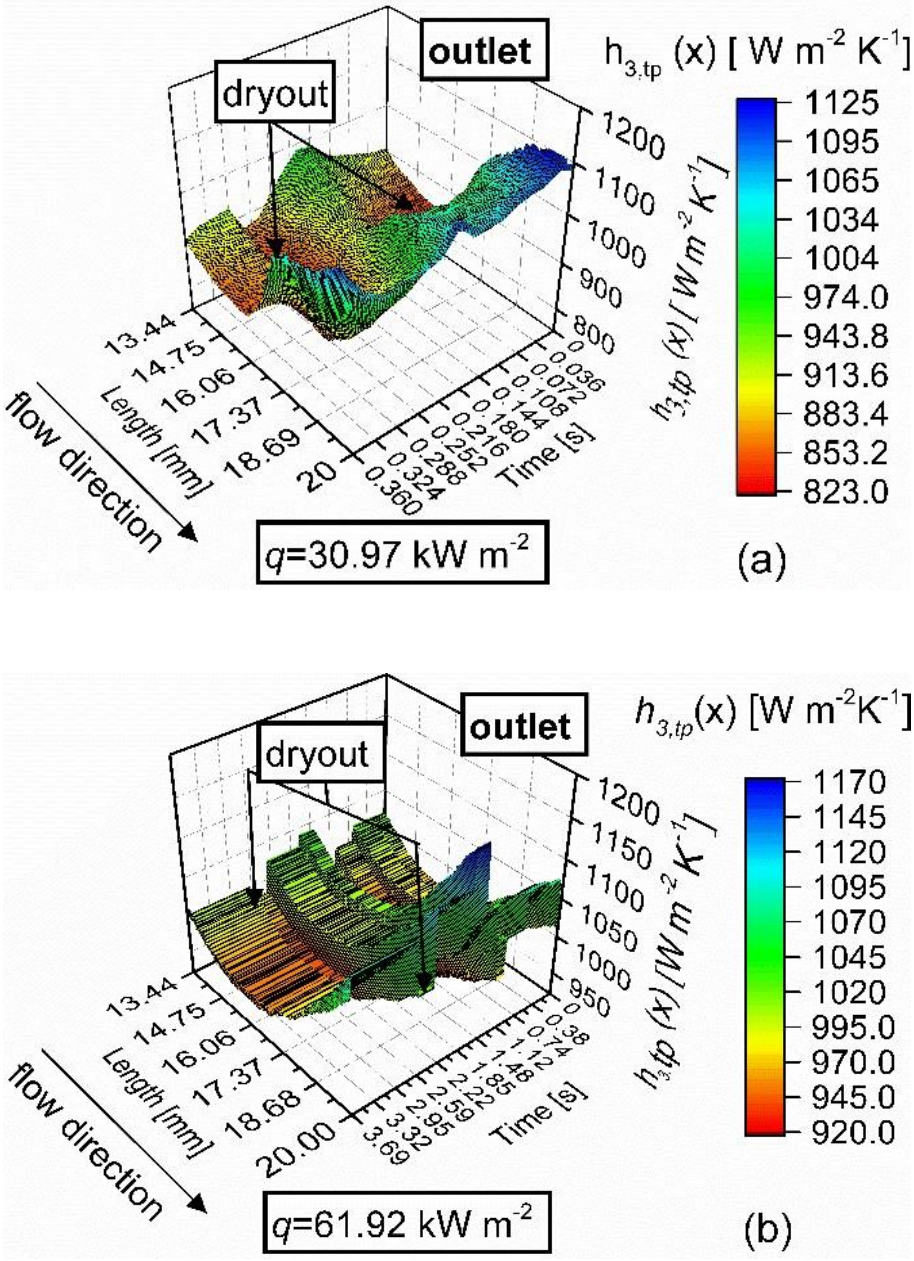

Figure 5. 6 *Local two-phase heat transfer coefficient $h_{tp}(x, t)$ along the microchannel centreline in the stream-wise direction with a time interval of 0.015 s for the outlet of the microchannel for (a) q = 30.97 kW m^{-2} and q = 61.95 kW m^{-2} (b).*

5.4.1.3 Maximum heat transfer rate (CHF)

An important limitation of heat transfer is the maximum achieved heat transfer rate, also referred to as critical heat flux (CHF). This maximum heat transfer rate also determines the trends in heat transfer dependence on heat flux condition. Although the critical heat flux has been studied by other researchers, there is not much research regarding the distribution of wall

dryout along the channel during the two-phase flow patterns (bubbly, slug and annular flow) and associated local temperatures. CHF is a very important parameter required for the calculation of the maximum feasible heat dissipation in microchannel devices, but its value is difficult to predict because of the conflicting trends that have been presented so far in flow boiling in microchannels.

Figure 5.7a shows the effect of heat flux on the time averaged (over 80 s) two-phase heat transfer coefficients obtained from the channel centreline (h_1avg, h_2avg, h_3avg, shown in Figure 5.2). The time averaged heat transfer coefficients for all sections decreased after a set of certain conditions, such as intermittent dryout of the wall. Figure 5.7a shows that the maximum time averaged heat transfer coefficient (HTC max) was calculated at the channel inlet for q = 30.97 kW m^{-2}. For this heat flux, the middle and outlet heat transfer coefficients overlapped and did not exceed 2,000 W m^{-2}K^{-1} with increasing heat flux. In Figure 5.7b the trend of the time averaged heat transfer coefficient (of the channel inlet centreline, h_1avg) was compared with the results obtained by Wang and Sefiane [9] who found similar decreasing trend with increasing heat flux using FC-72 for a single rectangular cross-section microchannel with rounded rather than sharp corners.

Results from previous researchers [13] have shown that CHF depends on mass flux, heated microchannel length and diameter. Figure 5.8 shows the effect of mass flux on CHF. The square-edged microchannels used in this study differ from those with rounded corners reported by Wang and Sefiane [55]. In Figure 5.8 the calculated q_c value from our study was compared with the calculated value from the Katto [11] correlation used for CHF prediction.

The result shows a relatively satisfactory agreement of the correlation with our data as well as some others from literature. For this chapter, only one mass flux was tested, therefore there is only one point, rather than a trend line. The high value of critical heat flux at the very small mass flux tested could be attributed to the geometry of the microchannel, which provides good wettability because of the capillary effect at the microchannel corners promoting thin film evaporation (high heat transfer) at high heat flux.

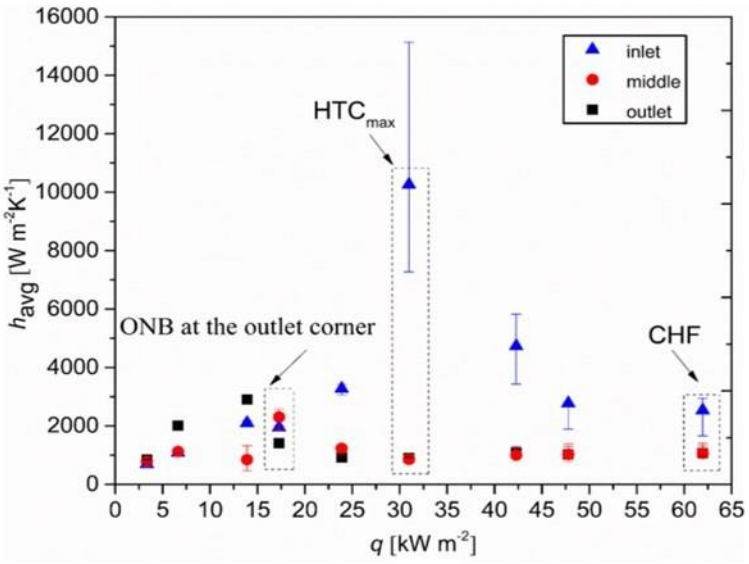

(a)

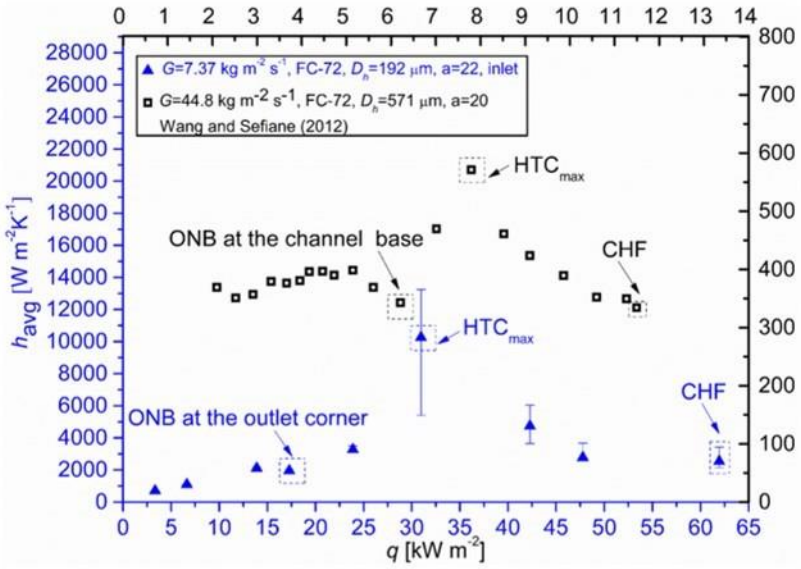

(b)

Figure 5. 7 *(a) Comparison between the time averaged, two-phase heat transfer coefficient for the PDMS microchannel inlet section with data from Wang and Sefiane [9] for* G *= 44.8 kg m^2 s^{-1} using FC-72 with* D_h *= 571 μm rectangular high aspect ratio (a = 20) microchannel for heat fluxes from 2 to12 kW m^{-2} and (b) Effect of heat flux on local heat transfer coefficient at the inlet, middle and outlet of the PDMS microchannel. The heat transfer coefficients were averaged over 80 s using the same data as that used for Figures 5.2b, d and f, for all the sections separately.*

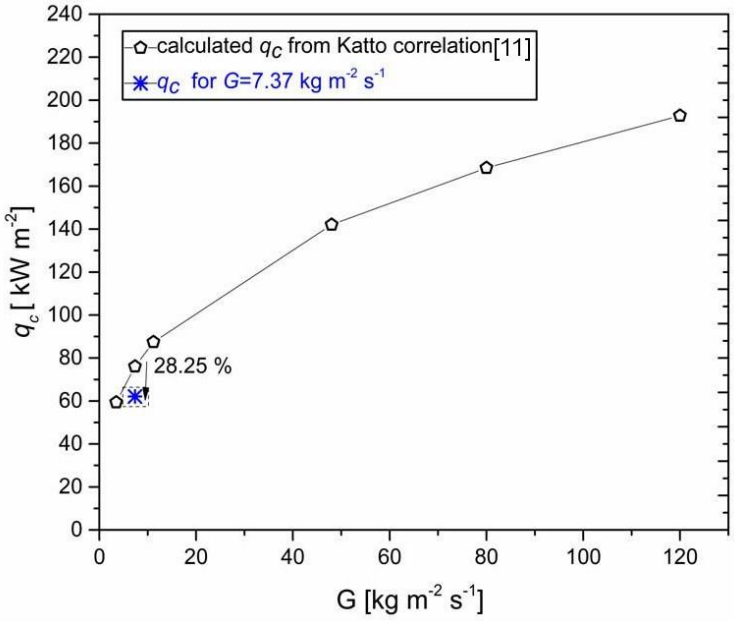

Figure 5. 8 *Comparison of the critical heat flux as a function of mass flux, from this study and previous experimental studies as well as the calculated critical heat flux obtained from Katto [11] correlation.*

The dryout mechanism depends on the heat transfer mechanism of the local flow regimes, as shown in Figure 5.9. From the literature [12], the critical heat flux results from a combination of the dryout of the liquid microlayer under growing bubbles, the dryout of the liquid thin film surrounding a slug and the total evaporation of the liquid thin film in annular flow.

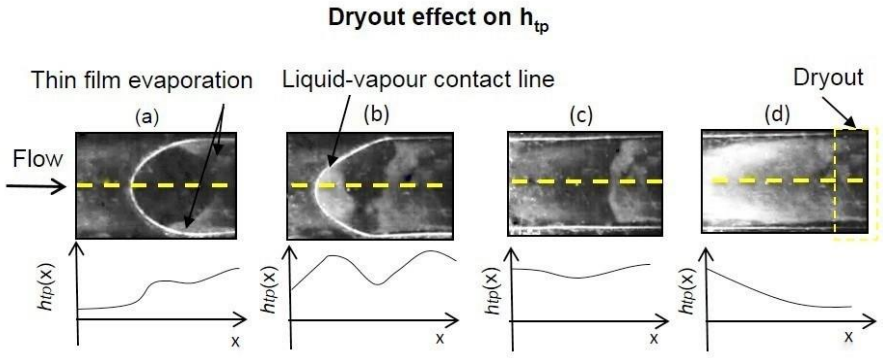

Figure 5. 9 *Sequence of optical images obtained with high-speed visualisation from the transparent ITO heater base. The two graphs below the images show the effect of partial thin film dryout on h_{tp}. The images were captured for G = 7.37 kg m^{-2}s^{-1} and q = 30.47 kW m^{-2}.*

Figure 5.9 shows a sequence of optical images obtained from the transparent ITO heater base for G = 7.37 kg m^{-2} s^{-1} and q = 30.47 kW m^{-2} at the channel outlet. These images show the axial growth of the fully confined bubble along the length of the microchannel. Because of the

transparency of the ITO heater the footprint of the bubble was visible as well as the liquidvapour contact line. The darker parts were related to liquid and the lighter areas to vapour. The evaporation occurred mainly at the confined bubble centre (a). During the bubble elongation, the vapour area increased and the meniscus elongated (b). The confined bubble growth caused reverse flow as the bubble growth occurred opposite of flow direction (c) and a vapour annulus covered the whole channel (d). Thin film evaporation caused suspected dryout at some parts of the channel outlet and heat transfer deterioration (d). The graphs below the images show the trends of $h_{tp}(x)$ as a function of channel length (x) and the effect of dryout on the heat transfer. The optical images have been correlated with IR images. Particularly, for the case (d) of local dryout on the channel surface, $h_{tp}(x)$ decreases with channel length.

5.4.1.4. Spatio-temporal two-phase heat transfer coefficients

All the heat transfer data presented are related to the centre of the microchannel cross section. This has been useful in identifying some of the important trends associated with heat transfer. From previous thermal imaging, there has been a suggestion that in certain circumstances there is a temperature variation across the channel and this prompted a full spatial heat transfer mapping of the microchannel surface.

This spatio-temporal 2D mapping of the heat transfer in terms of channel length and time combined with optical visualisation enables the elucidation of intricate two-phase behaviour. The main flow regimes observed were bubbly flow, slug flow and annular flow with flow reversal also occurring under certain circumstances.

Figures 5.10-5.13 display detailed 2D maps of the two-phase heat transfer coefficient $h_{tp}(x, y, t)$ of the heater base using values generated from thermal images of the channel surface. Figure 5.10a shows the uniformity of $h_{tp}(x, y)$ with time and high heat transfer coefficient rate variation at the channel inlet for q = 30.97 kW m^{-2}. Figure 5.10b reveals that after bubble coalescence and growth into an axially elongated bubble, oscillations occurred that locally enhanced the $h_{tp}(x, y)$ due to thin film evaporation and liquid agitation in the channel.

However, heat transfer deteriorated when partial dryout of the channel sidewalls occurred at the outlet of the channel. Figure 5.10b illustrates that the observed flow regimes at the channel outlet were slug flow (i), (ii), (iii), before slug coalescence (iv) slug coalescence led to the formation of an elongated bubble with a thin liquid film (v), followed by annular flow with droplets (vi), annular flow with partial dryout (vii) and finally almost full dryout of the channel sidewall (viii). During the axial growth of the elongated bubble (iv) the liquid film at the channel corners remained in contact with the wall for most of the channel length, ensuring a constant

coefficient from t = 0.54 s to 1.47 s. At t = 2.10 s complete dryout occurred, resulting in a deterioration of the two–phase local heat transfer coefficient across the entire heat transfer surface of the microchannel and consequently its cooling performance. The two-phase heat transfer coefficient at the sidewalls decreased to 721 W m^{-2} K^{-1}.

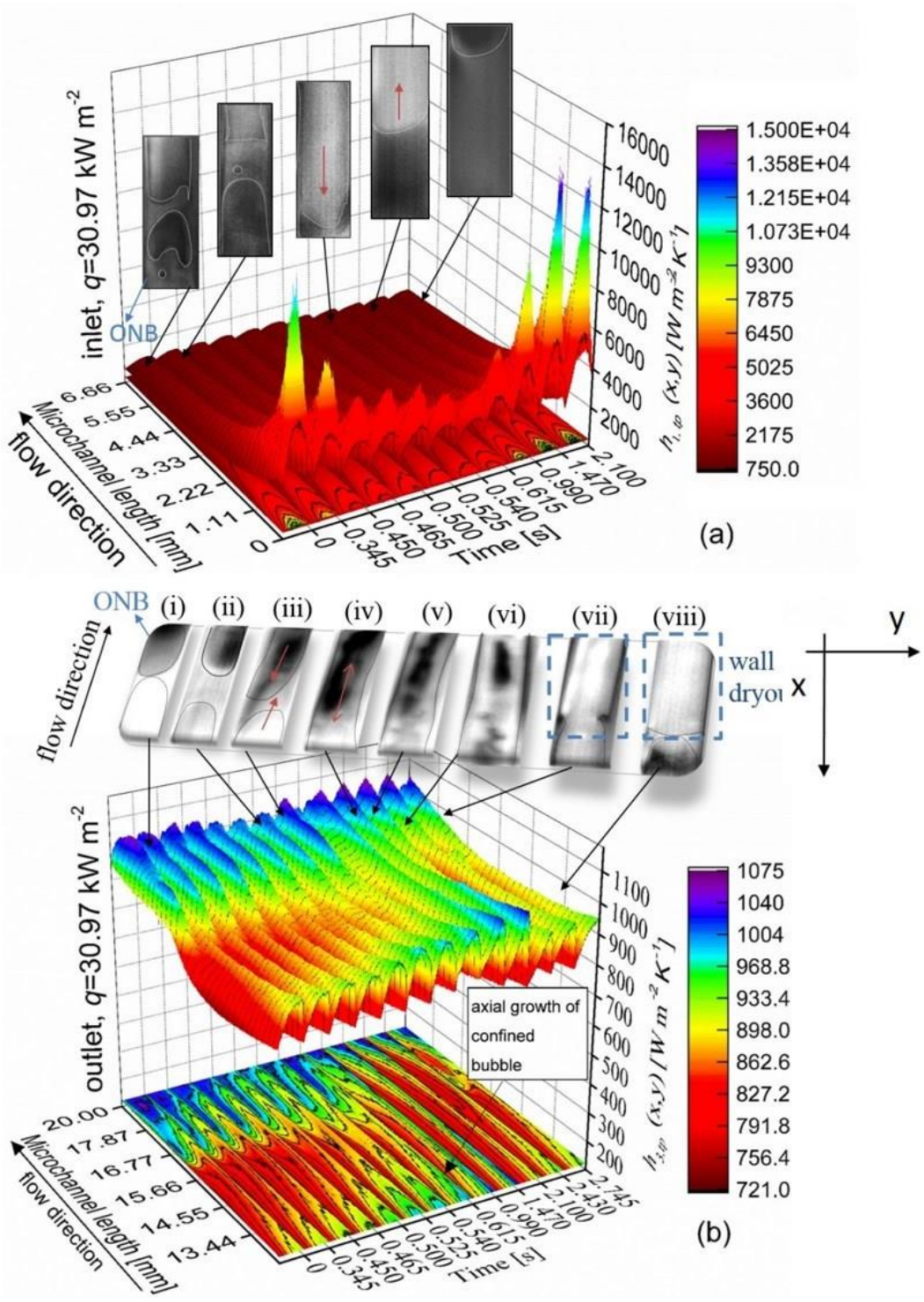

Figure 5. 10 *2D maps of the local two-phase heat transfer coefficient h_{tp} (x, y, t) with time for, the inlet (a) and the outlet (b) of the microchannel heat sink for q = 30.97 kW m^{-2}.*

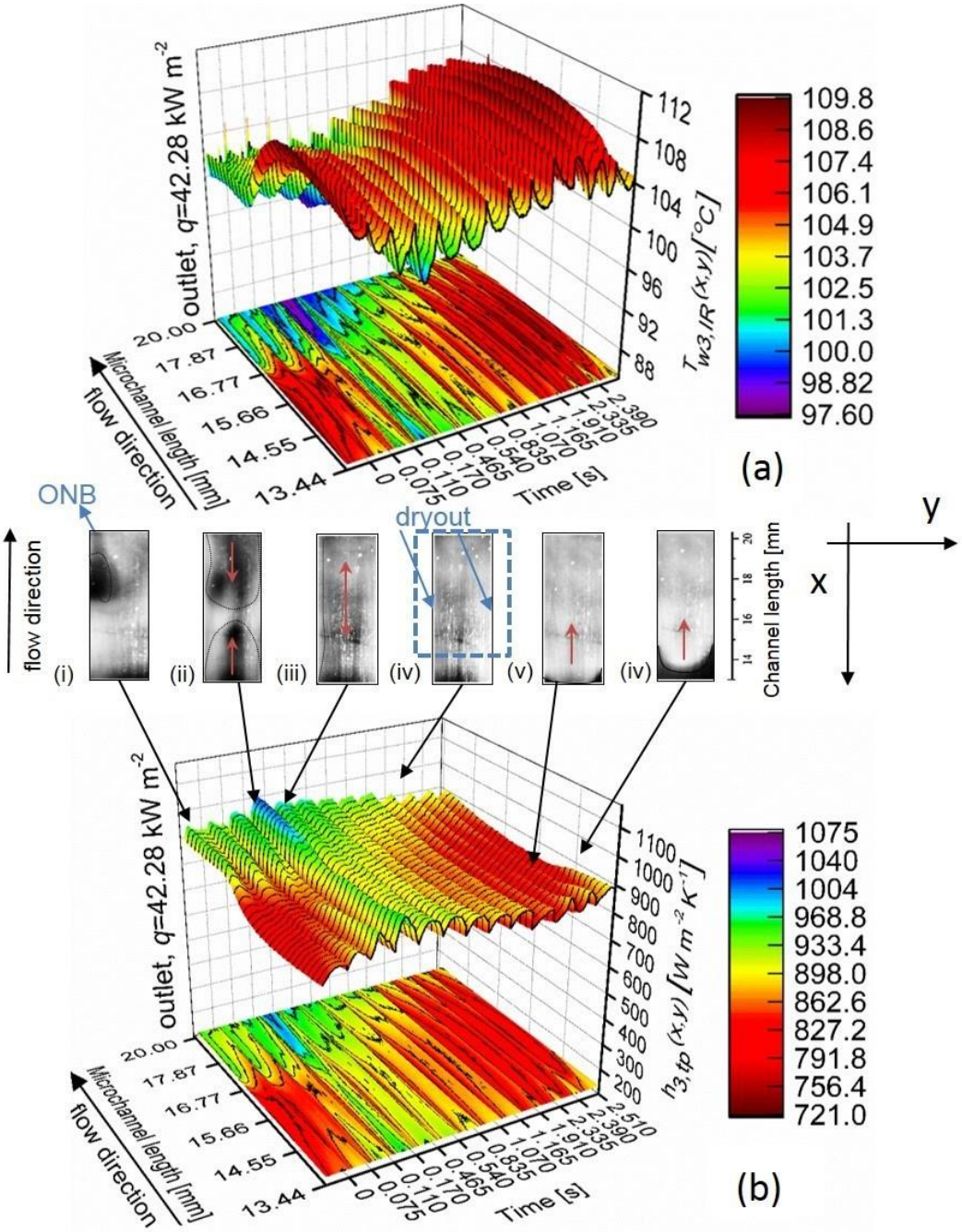

Figure 5. 11 *(a) $T_{w,}$ (x, y, t) (b) h_{tp} (x, y, t) during a cycle of dryout at q = 42.48 kW·m^{-2} at the channel outlet. The observed flow patterns were bubbly (i), slug (ii), annular (iii), annular dryout (iv), dryout (v) and liquid rewetting (vi).*

When the heat flux exceeded 30.97 kW m^{-2}, the heat transfer deteriorated because of the slugs that elongated axially, fully occupying the outlet cross section, inducing reversed flow.

The deterioration in heat transfer (due to partial dryout downstream) caused early CHF occurrence due to the aforementioned flow instabilities (cycles of dryout). Dryout cycles were the main flow phenomenon that characterized the two-phase heat transfer mechanism of the channel for heat fluxes higher than 42.28 kW m^{-2}.

Figures 5.11a and b present the variation of $T_{w,IR}$ (x, y, t) as a function of time for the higher heat flux of q = 42.28 kW m^{-2}. Initially, bubble nucleation (Figure 5.10i) occurred close to the superheated sidewall at the outlet of the channel and as the bubbles merged, they formed an elongated bubble. At t = 0.17 s, slug flow was observed as can be seen in Figure 5.11ii and h_{tp} (x, y, t) increased below the vapour slugs at the middle of the channel cross section presumably because of the existence of an evaporating liquid thin film (as suggested by the low temperature measured). Later, annular flow Figure 5.11iii developed and resulted in more uniform heat transfer coefficient across the microchannel. The heat transfer coefficient appeared to be uniform from the sidewalls to the channel centre because of the liquid film dryout at the vapour bubble base and the sidewalls, Figure 5.11iv. The dryout of the liquid film below the bubble and around the bubble (at the outlet) resulted in the lowest heat transfer coefficient values. Figure 5.11v and vi show that the heat transfer coefficient then increased at the areas where liquid rewetting occurred (around the slug).

The existence of a thin film underneath confined bubbles is revealed in some cases (in terms of low temperature values and black colour from observations) during high heat transfer rates. Figure 5.12 shows the local two-phase spatial heat transfer coefficients at a fixed time at the outlet for q = 42.49 kW m^{-2}. There is a strong correlation between the heat transfer data and the visual observations, which show the liquid-vapour distribution correlating with spatial variation of the heat transfer coefficients.

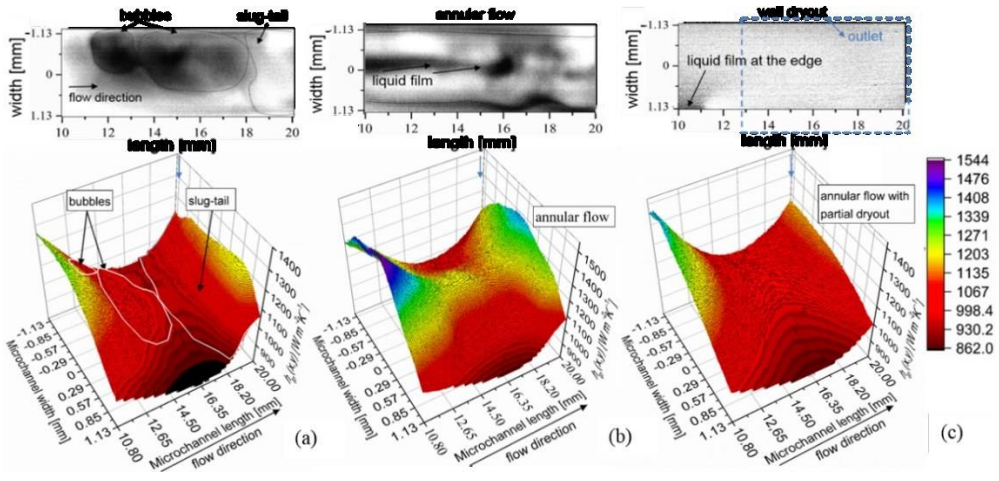

Figure 5. 12 *Local two–phase heat transfer coefficients (h_{tp} (x, y, t)) calculated for different flow regimes with q = 42.28 kW m^{-2} and G = 7.37 kg m^{-2}s^{-1}. The three snapshots were captured from positions an axial distance of 10 to 20 mm from the inlet, where h_{tp} (x, y, t) was measured between 862-1544 W m^{-2} K^{-1}. Bubbly-slug flow (a), annular flow (b) and annular flow with partial wall dryout (c) were the observed flow regimes.*

Figure 5.12b suggests that during annular flow there is liquid film at the centre of the channel in an axial direction, because there is local enhancement (900-1,400 W m^{-2} K^{-1}) of the heat transfer coefficient compared to the other regimes (Figures 5.13a and c).

Figure 5.13 shows the h_{tp} (x,y, t) at the highest heat flux (q = 61.95 kW m^{-2}). The surface map of the heat transfer combined with optical observations reveal some interesting mechanisms, such as boiling in the thin film as well as dryout cycles during the annular flow regime in the microchannel, which are correlated to the heat transfer coefficient variation. The observed flow regimes were annular flow at t = 0 s, partial dryout after 18mm for t = 0.125 s and complete dryout at t = 1.570 s. Film boiling occurred at the channel edges at t t = 1.570 s, and from t = 1.695 s to 1.840 s slug flow and thin film were established in the channel. From t = 1.995 s to 2.090 s annular flow was the main flow regime with simultaneous bubble nucleation from the sidewalls.

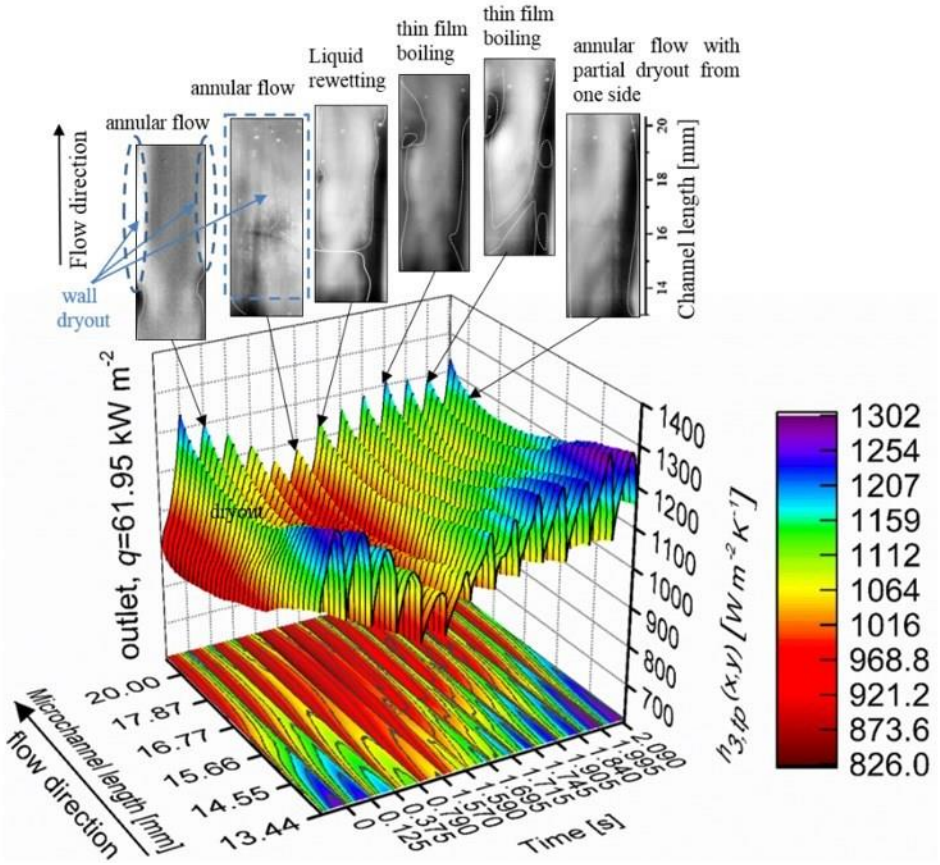

Figure 5. 13 *h_{tp} (x, y, t) during a cycle of dryout at q = 61.95 kW·m^{-2} at the channel outlet (3).*

At the highest heat flux of q = 61.95 kW m^{-2}, the visual images suggest that dryout occurs across the whole cross section of the microchannel outlet as the thin liquid film between the vapour slug and the wall evaporates (resulting in low values of h_{tp} values shown in Figure 5.13). The temperature at the highest heat flux (q = 61.95 kW m^{-2}) reached values up to 133 °C at the sidewalls, which is high enough to result in damage of devices as a direct result of local dryout at the heater surface (Figure 5.9b). It was observed that the evaporation of the liquid thin film surrounding bubbles occurred unevenly, first from the sidewall where initially bubble nucleation occurred and then from the other sidewall. The uneven distribution of the liquid was attributed the low surface tension of FC-72 ($\gamma_{FC-72} = 11\ \frac{mN}{m}$) and the low mass flux in these experiments. Inlet rewetting occurred unevenly mainly around the bubble (not at the heater base). It should be noted that dryout did not to occur uniformly on the microchannel perimeter.

Another very common presentation of the heat transfer data in the literature is the evolution of the heat transfer coefficient as a function of vapour quality *(x_e)*. To corroborate the collected data with data already published, the heat transfer data has been plotted as a function of vapour quality for three applied heat fluxes in Figure 5.14. This shows the relationship between the local two-phase heat transfer coefficient and local vapour quality for heat flux between 30.97 to 61.95 kW m^{-2}. The decrease of the two-phase heat transfer coefficient with increasing vapour quality has also been observed by many other researchers [3, 26], with the reduction in heat transfer with vapour quality usually being attributed to dryout.

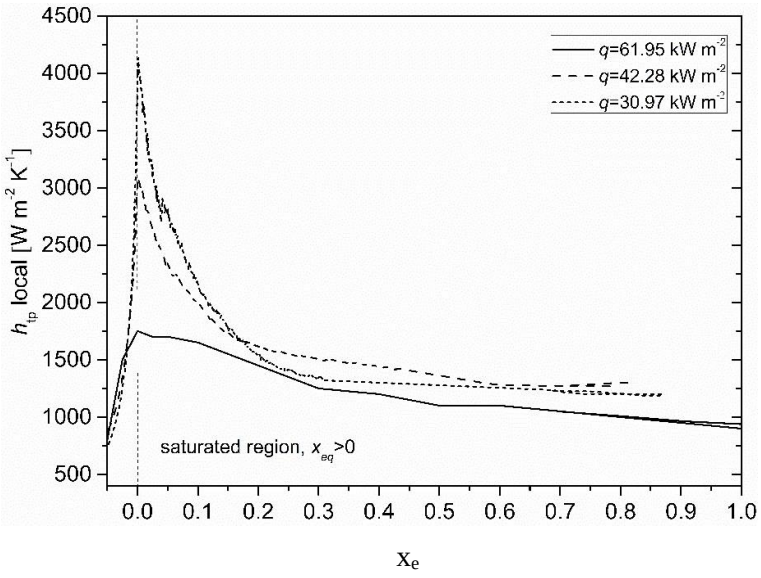

Figure 5. 14 *The relationship between local two-phase heat transfer coefficient and vapour quality for increasing heat fluxes at a constant mass flux of G = 7.37 kg m^{-2}s^{-1}.*

5.4.1.5 Bubble dynamics

The flow instabilities described in the previous section were related to bubble dynamics such as nucleation, growth and coalescence. Cycles of dryout and the heat transfer data were found to be closely correlated to these dynamics. The following, section takes a closer examination of these phenomena using IR imaging to reveal information which cannot be revealed using just optical observations. For example, IR imaging can assist in validating the existence (or otherwise) of very thin films on the wall of the microchannel via temperature changes, (a low temperature indicates the existence of a liquid film).

Bubble formation, growth, and axial growth was very fast because of the high aspect ratio of the microchannel. Figure 5.15a shows the temperature profile across the channel width (W_{ch}) at 0.95 mm from the channel outlet (black dashed line). The temperature variations across the channel base were captured by IR during bubble nucleation near the superheated sidewall and growth at a high frame rate and high spatial resolution. The IR thermal images next to the graph reveal the lower temperature distribution measured at the bubble base area (with d_1, d_2 ,$_3$, $d_4$the bubble area diameter for the different images). The wall temperature at the bubble base was observed to be lower than the temperature at the sidewall beyond the bubble and this was attributed to the thin film evaporation below the bubble. The superheat required for bubble nucleation was 15 °C on average and increased up to 60 °C for q = 61.95 kW m^{-2}. Figure 5.15b shows temperature profiles along the centreline in the stream-wise direction of the microchannel outlet region during the slug flow regime for q = 30.97 kW m^{-2}. The wall temperature increased with channel length until the onset of boiling at the channel inlet. Initially the snapshot at t = 0 s (1), shows the wall temperature profile at the outlet before the coalescence between a slug formed at the channel inlet and a bubble. At d_1 = 0.075 s the lowest temperature variation (88.5 – 91 °C) was observed where annular flow was established in the microchannel after the coalescence of the slugs took place.

Suspected dryout occurred at t= 1.890 s where the wall temperature increased to between 91 °C and 95 °C. The wall temperature then dropped again at t = 2.115 s which is the time where the bubble initially nucleated at the outlet corner. This ‘instability’ cycle was repeated again after 22.54 s. On average, the temperature profile follows a cyclic trend because of the alternating nature of the bubble dynamics (see blue and red arrows in Figure 5.15b).

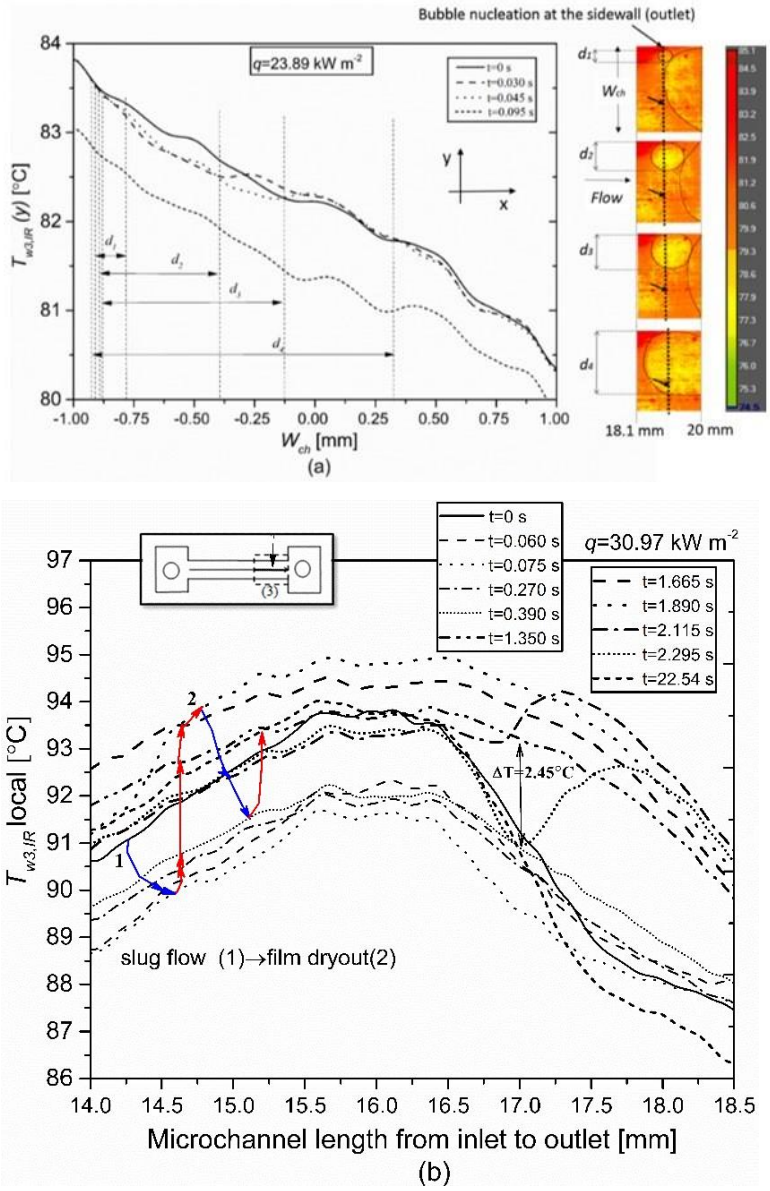

Figure 5. 15 *(a) Inset infrared images showing the clear differentiation of bubble boundaries during bubble growth near the corner at q = 23.89 kW m^{-2}. (b) Wall temperature profiles along the microchannel centreline of the outlet for q = 30.97 kW m^{-2}.*

5.4.1.6 Pressure fluctuations

A final element in this study is the examination of the correlation between pressure fluctuations and recorded heat transfer data. In previous sections, it has been demonstrated that heat transfer data are strongly related to the nature of multiphase flows and bubble dynamics. The multiphase flows and bubble dynamics induce fluctuations in pressure at the inlet and outlet

of the channel. Therefore, a correlation between pressure fluctuations and the heat transfer coefficient can be established, which is illustrated in Figure 5.16. It is worth noting that the oscillations in pressure and heat transfer coefficient are slightly out of phase with pressure oscillations being observed at both inlet and outlet. They were induced because of axial growth of the confined bubble, which caused flow reversal during slug /annular flow. For a wall temperature increase of 5 °C the averaged heat transfer coefficient dropped from 12,200 W m^{-2} K^{-1} to 6,000 W m^{-2} K^{-1} while the local pressure drop increased by 75 mbar. Pressure oscillations occurred because of bubble axial expansion that caused flow reversal in the channel. Flow reversal resulted in unstable flow mode with periodic pressure and wall temperature fluctuations. These temperature and pressure fluctuations resulted in periodic heat transfer coefficients fluctuations. Flow reversal occurred because of bubble expansion after bubble nucleation occurred at the channel entrance. Figure 16 shows that the pressure drop was periodically increased up to 75 mbar. This pressure drop increase was a result of the flow reversal induced by the axial expansion of the confined bubble along the microchannel. The two-phase heat transfer coefficient reached the maximum value of 12,000 W $m^{-2}K^{-1}$ initially when the bubble was confined at the channel entrance and then decreased down to 4,500 W $m^{-2}K^{-1}$ after bubble expansion that caused flow reversal [93]in the channel. Kandlikar [93] reported that the location of nucleation can affect the flow instabilities. When bubble nucleation is observed to occur at the channel inlet, the flow resistance in the backflow direction decreases and thus flow reversal occurs. During the high amplitude fluctuations at low mass fluxes bubble nucleation and confined growth occurred at the channel entrance inducing high pressure drop as a result of the blockage of liquid flow in the channel.

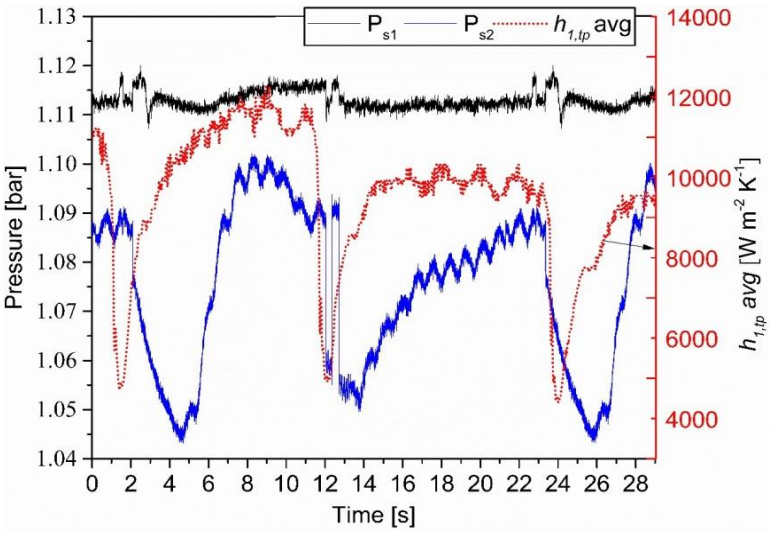

Figure 5. 16 *Two-phase pressure fluctuations at the inlet (Ps_1) and outlet (Ps_2) of the microchannel and the averaged locally two-phase hat transfer coefficient calculated at the channel inlet section for 29 s time interval at q = 30.97 kW m^{-2} and G = 7.37 kg m^{-2} s^{-1}.*

5.5 Conclusions

The study of two-phase flow boiling in a microchannel using FC-72 liquid has been conducted using high-resolution infrared thermography from the heater side of the channel with simultaneous optical observations and pressure measurements in the microchannel. The measurements enabled accurate high-speed recording of temperature distribution and the calculation spatio-temporal distribution of the two-phase local heat transfer coefficient. The use of the unique channel geometry and thin channel base coated with transparent heating allowed high-quality time and spatial resolution temperatures to be obtained and mapped at the channel wall. These, coupled with simultaneous visual images of the flow, have enabled us not only to identify fluctuations in heat transfer coefficient with high temporal and spatial resolution, but also to correlate these with the behaviour of bubbles within the flow.

High heat transfer coefficients were obtained due to the high aspect ratio of the microchannels, using a very small mass flow rate. This was achieved due to the confinement induced by the channel depth and the capillary effect that enhanced liquid flow at the channel corners. The highest heat transfer coefficient was measured on the centreline near the inlet of the channel were bubbly-slug flow was the main flow pattern observed from flow visualization. Probably the high rate of heat transfer coefficient at the channel inlet could be attributed to the thicker liquid film here compared to the outlet. Increasing further the heat flux, instability cycles occurred along the whole channel domain and the pressure drop increased, but the heat transfer coefficients were measured to be higher even in this case compared to single-phase flow, as the

dryout was only partial at the channel corners. Partial dryout occurred because of suppression of bubble nucleation observed at the channel outlet corners.

The wall temperature of single bubbles was captured as well as pressure oscillations with time. The two-phase spatially averaged heat transfer coefficient values were found to fluctuate in time. The plots of $h(x, y, t)$ suggested that only a portion of the heated cross section is completely dry at the channel outlet and uneven liquid distribution was observed at the channel base. The onset of dryout was followed by a significant drop in the local two-phase heat transfer coefficient along the microchannel.

At the ONB, an increase of the HTC at the channel middle occurred because of the bubble-slug coalescence during bubbly-slug flow regime which resulted in a local temperature decrease at the channel centre of the channel and therefore the HTC increased. The merging of bubbles induced higher local heat transfer coefficient at the centre of the channel cross section, but lower values along the channel edges. At heat fluxes higher than 42.28 kW m^{-2} annular flow was observed to become the dominant flow pattern along the whole channel domain.

The CHF was higher compared to results from larger hydraulic diameter channels using a similar mass flux and liquid, but with corners that were rounded in cross section. This was attributed to the capillary effects of a high aspect ratio rectangular cross section.
This enabled the effect of heat flux on local temperature variation, flow boiling heat transfer coefficient distribution and the two-phase pressure drop to be studied.

5.6 Summary

In this chapter, 2D two-phase heat transfer coefficients in a rectangular high-aspect-ratio polydimethylsiloxane (PDMS) microchannel were presented with simultaneous high speed images. High frequency and high spatial resolution infrared thermography images were correlated with heat transfer coefficients obtained as function of axial position, lateral position and time at the inlet, middle and outlet sections of the microchannel base. The of heat flux on local temperature variation, flow boiling heat transfer coefficient distribution and the two-phase pressure drop was studied. Heat transfer data represented as well as bubble dynamics and pressure drop starting with the heat transfer data, space averaged, with time. The local spatio-temporal evolution of the heat transfer coefficient was investigated using imposed heat flux as a parameter, whilst paying special attention to the maximum limit in heat transfer, referred to as critical heat flux (CHF). The local two-phase heat transfer data were correlated with simultaneous flow visualizations, as well as bubble dynamics and pressure drop.

Chapter 6 Dual inner wall temperature mapping with synchronised flow visualisation

6.1 Introduction

Two-phase flow boiling heat transfer in microchannels is linked to the liquid-vapour phase distribution on the channel base [47]. Early heat transfer deterioration that occurs in microchannels is associated with liquid film thinning that leads to local and temporal dryout. Therefore, it is necessary to investigate wall temperature distribution with experimental methods that provide high spatial (< 50μm/pixel, see Chapter 3) and temporal resolution (>120 fps, see Chapter3) results with microchannels that are optically accessible for simultaneous high-speed flow visualisation and infrared.

In this chapter, flow boiling heat transfer and associated flow patterns are experimentally investigated using dual wall temperature mapping with synchronised high-speed visualisation and pressure measurements from integrated pressure sensors. Flow boiling experiments are performed in a single high aspect ratio transparent microchannel of D_h = 192 μm using FC-72. The transient two-dimensional (2D) wall temperature maps recorded by the high-speed infrared camera are correlated with the simultaneous high-speed video optical images for constant mass flux and increasing heat fluxes. Local pressure is obtained from two integrated pressure sensors at the inlet and outlet of the microchannel and the generated two-dimensional wall temperature measurements $T_{w,in}(x, y)$ are used for the calculation of two-phase heat transfer coefficients, $h_{tp}(x, y)$. The 2D two-phase heat transfer coefficients $h_{tp}(x, y)$ are illustrated as a function of time in 3D high-resolution plots. The spatio-temporal resolution achieved in this study using IR thermography was 15.39 μm/pixel and 200 fps.

Sections 6.4.1 to 6.4.6 evaluate interfacial heat transfer coefficients and they are correlated with simultaneous high quality optical images obtained from flow visualisation using high-speed camera. The novelty of this work is that it enables high spatial and temporal resolution temperature measurements at the liquid-solid interface of the microchannel wall by using Polydimethylsiloxane (PDMS) which is transparent to midwave infrared (IR). Detailed interfacial heat transfer analysis with simultaneous flow visualisation at various mass fluxes and heat fluxes is presented. Two-phase interfacial heat transfer coefficient distribution is measured

at the bubble wall interface. Section 6.4.7 investigates heat transfer coefficient distribution using temperature maps obtained from the ITO/glass base, with synchronised high-speed visualizations from PDMS, which is optically transparent.

Particularly, the interfacial heat transfer analysis presents 3D plots of the interface heat transfer coefficients spatially averaged across the channel width as a function of channel length and time at three constant mass fluxes (G) of 36.87 kg $m^{-2}s^{-1}$, 73.74 kg $m^{-2}s^{-1}$ and 110.62 kg $m^{2}s^{-1}$ and increasing heat fluxes. Then, time averaged and spatially averaged heat transfer coefficients for the inlet, middle and outlet of the microchannel are illustrated in 2D plots as a function of heat flux for the three constant mass fluxes. Analytical 3D plots illustrate the spatially averaged across the channel width interfacial heat transfer coefficients as a function of channel length and time for the aforementioned mass fluxes. Particularly, 3D plots of the spatially averaged heat transfer coefficient are displayed as a function of time for the onset of boiling (ONB), maximum heat transfer coefficient (HTC_{max}) and maximum heat transfer rate. Critical heat flux (CHF) is also evaluated. Then heat transfer mechanisms are discussed during instability cycles. IR images provide 2D wall temperature patterns from the interface, during annular flow regime, which are correlated with high quality images from the channel base. Annular flow regime instabilities and their relation to local dryout is evaluated. The expression "suspected dryout" is used in the text because thin film thickness cannot be evaluated with the existing method. Local wall temperature fluctuations are analysed for G = 73.74 kg $m^{-2}s^{-1}$ and q = 38.52 kW m^{-2}. Local two-phase heat transfer coefficients spatially averaged along the channel centreline at flowstream direction are displayed with simultaneous pressure drop data from inside the microchannel as a function of time. 3D histograms are used to quantify the liquidvapour phase distribution of phases from the channel base using image-processing techniques. Liquid and vapour phases in the channel are highlighted using the contrast of the optical images. Liquid and vapour at the heater base are evaluated using optical images where the black colour is related to liquid and white colour to vapour. Film thinning because of liquid evaporation is correlated with the colour intensity scale. 3D plots of $T_{w,}(x, y)$ and $h_{tp}(x, y)$ as a function of channel width and length are illustrated during single-bubble growth and bubble confinement in the channel. Surface temperature and flow instabilities during the annular flow regime are evaluated by correlating images and IR images. The last section of this chapter illustrates high spatial and temporal resolution 3D and contour plots of 2D heat transfer coefficients $h_{tp}(x, y)$ as a function of time, during flow boiling on the microchannel surface from the ITO /glass channel base with simultaneous flow visualisations from PDMS.

The main objectives of this chapter are to present 3D plots of high-resolution two-dimensional two-phase heat transfer coefficients as a function of time, as there is a lack of spatially resolved data in this area. Additionally, to provide a detailed insight into flow boiling heat transfer mechanisms by using data from $h_{tp}(x, y)$ in conjunction with simultaneous optical images. These information can assist in improving prediction methods for flow boiling in microchannels and uncovering the role of specific flow features during flow boiling in microchannels that could enhance the local heat transfer during two-phase flow. These results aim to provide better insight into heat transfer mechanisms of flow boiling in microchannels and to provide a motivation for improving experimental approaches on interfacial heat transfer measurements with synchronised flow visualisation.

6.2 Experimental setup and procedure

The experimental method and test section used in this chapter is described in chapter 3. Infrared thermography is devised to measure the wall temperature distribution with high spatial and temporal resolution (15.39 μm/pixel and 200 fps) together with simultaneous synchronised flow visualisation. Because the microchannel is optically transparent, it allows flow visualisation from both sides. It is possible to achieve IR measurements from ITO/glass and PDMS with synchronized optical flow visualization. The advantage of measuring the wall temperature from PDMS side is the transparency to IR of the PDMS at midwave spectral range that allows wall temperature measurements from the channel side that is contact with the liquid.

6.3 Data reduction

The data reduction process of this chapter is described in section 4.3 of Chapter 4.

6.4 Results and discussion

6.4.1 Evaluation of method for interfacial wall temperature measurements

Figure 6.1b shows a high spatial resolution IR image obtained from the PDMS microchannel wall during flow boiling during bubbly flow regime. The interfacial wall temperature pattern is distinctly revealed due to the high spatial resolution method and transparency of PDMS to IR midwave range. The maximum temperature detected is 65.7 ˚C (red colour) and the minimum is 61.2 ˚C. The interfacial wall temperature appears to have non-uniform distribution at the bubble and surrounding bubble area, with the lowest values to exist at the bubble side close to the bulk liquid flow in flowstream direction. Figure 6.1a shows a photograph obtained using

liquid crystal thermography method by Kenning [106] during pool boiling. Liquid crystal thermography is one of the first methods used in order to obtain temperature patterns at wall interface level, between the wall and the liquid. The wall temperature in Figure 6.1a ranges from 108 °C, cold (red coloured areas) to 130 °C, hot (green patches). Cold spots and rings were observed on the channel base. The centre of the cold spots and the observed rings was related with the nucleation sites. The black regions around the channel indicated heating of the liquid crystal beyond its colour play limit of 132 °C. The spatial resolution of the liquid crystal thermography method is only 0.2 mm. The low response time and the possibility of interference of crystals with the local liquid flow in small diameters channels as well as the low spatial resolution of the temperature measurements requires methods to obtain higher-resolution data. Details of the wall temperature gradients at the interface can assist in a better understanding of the complex heat transfer phenomena during two-phase flow boiling in a microchannel.

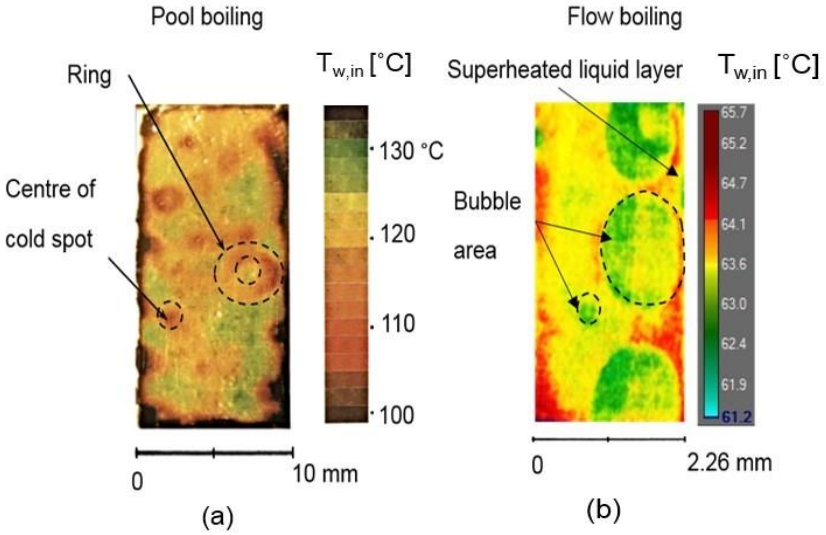

Figure 6. 1. (a) 2D wall temperature measurements obtained with liquid crystal thermography method by Kenning (1992) [106] for pool boiling. The photograph shows the crystal layer on the rear of the plate. The nucleation sites are related to the centres of cold spots and the rings.*(b) Two-dimensional IR image obtained during flow boiling from the transparent to infrared PDMS side of the microchannel using IR thermography with FC-72 dielectric coolant.*

6.4.2 Effect of heat flux on the spatially averaged interfacial heat transfer coefficient as a function of time for G = 36.87 kg $m^{-2}s^{-1}$, 73.74 kg $m^{-2}s^{-1}$and 110.62 kg $m^{-2}s^{-1}$

The interfacial heat transfer coefficients are important for accurate determination of the magnitude of the local fluctuations in the vicinity of the wall during flow boiling. However, it is difficult to determine the values of the heat transfer coefficient from experiments at the wall

solid-fluid interface due to lack of advanced methods. In this section, the interfacial wall temperature was measured using a PDMS microchannel, which is transparent to mid-wave IR. High spatial and temporal resolution temperature and pressure measurements from the integrated sensors near the inlet and outlet were used to determine the accurate interfacial heat transfer coefficient values. The heat transfer coefficient measurement s were also correlated with the synchronised optical images from the channel base. In this section the results show the spatially averaged two-dimensional heat transfer coefficients obtained at the inlet, middle and outlet of the microchannel for G = 36.87 kg $m^{-2}s^{-1}$, 73.74 kg $m^{-2}s^{-1}$and 110.62 kg $m^{-2}s^{-1}$ and increasing heat fluxes at the inlet liquid temperature of T_{inlet} = 21 °C.

6.4.2.1 2D plots that illustrate the effect of the heat flux on time averaged interfacial heat transfer coefficients for the inlet, middle and outlet of the channel for G = 36.87 kg $m^{-2}s^{-1}$, 73.74 kg $m^{-2}s^{-1}$and 110.62 kg $m^{-2}s^{-1}$

Figure 6.2 shows time averaged interfacial heat transfer coefficients and spatially averaged for the inlet, middle and outlet of the microchannel and the simultaneous time averaged pressure drop as a function of the increasing heat flux for the mass fluxes of 36.87 kg $m^{-2}s^{-1}$, 73.74 kg $m^{-2}s^{-1}$ and 110.62 kg $m^{-2}s^{-1}$. The interfacial wall temperature and local pressure drop measurements are averaged over the time of 60 s. Pressure drop was quantified across the whole microchannel domain while the wall temperature measurements were spatially averaged along each section. The error bars in Figure 6.2 show the maximum standard deviation and can provide details about the amplitude of the fluctuations during flow boiling. The analytical inlet pressure and outlet pressure measurements graphs are presented in Figure B.1 of Appendix B.

Time averaged interfacial heat transfer coefficient and spatially averaged for the inlet, middle and outlet of the microchannels showed increasing trend with increasing heat flux up to maximum after which it decreased with a further heat flux increase for all the tested mass fluxes. For low heat fluxes, the heat transfer coefficient increases almost linearly with heat flux. For the mass fluxes of 36.87 kg $m^{-2}s^{-1}$, 73.74 kg $m^{-2}s^{-1}$, at higher heat fluxes, the curve changes in slope before ONB and after HTC_{max} from where it decreases. For the highest mass flux of 110.62 kg $m^{-2}s^{-1}$ the slope changes just before ONB and after ONB maximum value.

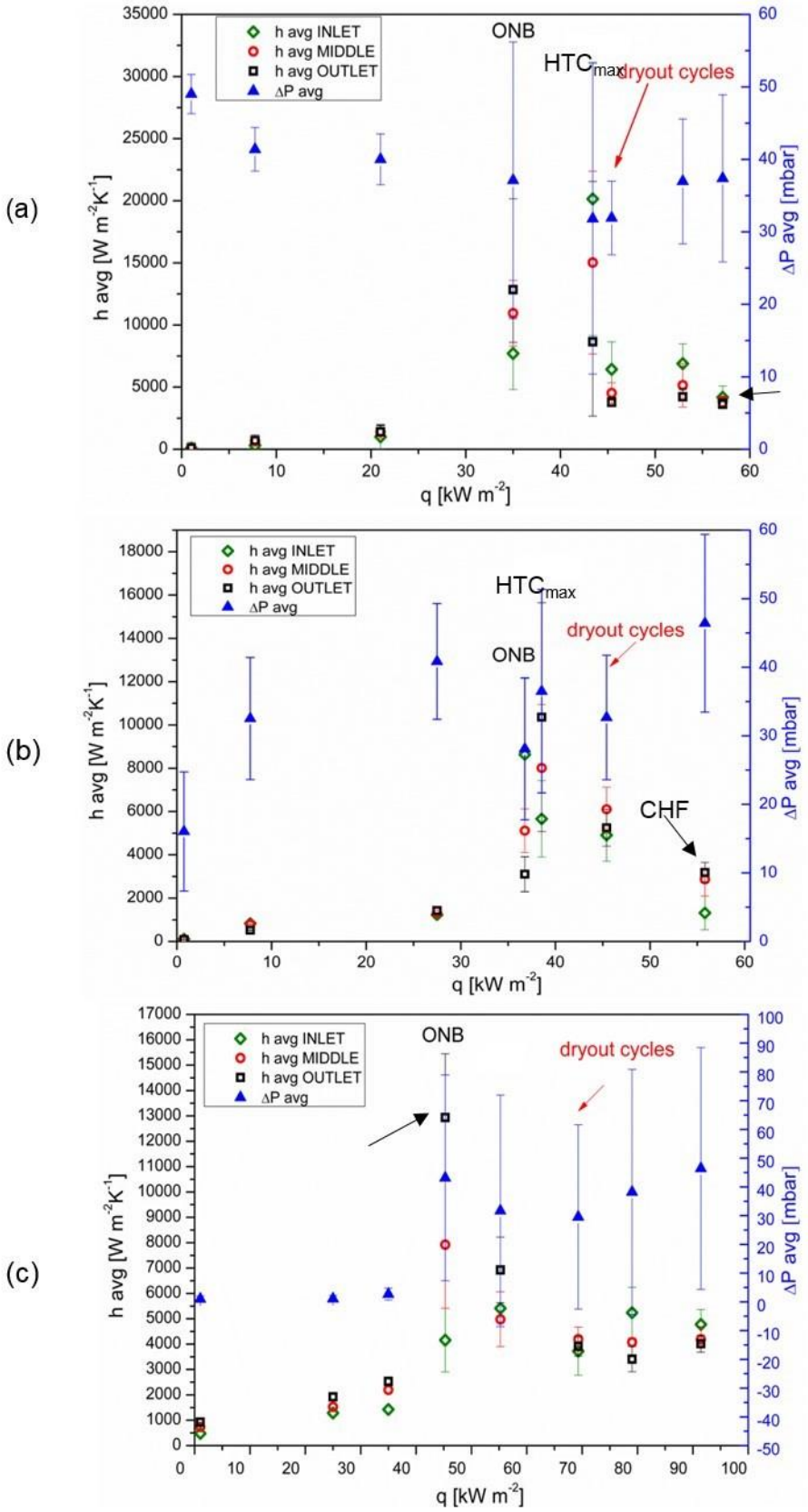

Figure 6. 2 *Time averaged interfacial heat transfer coefficients for inlet, middle and outlet with increasing heat flux and time averaged pressure drop for the mass fluxes of (a) 36.87 kg m^{-2} s^{-1}, (b) 73.74 kg m^{-2} s^{-1} and (c) 101.2 kg m^{-2} s^{-1}.*

The trends of the time averaged interfacial heat transfer coefficient for constant mass flux and increasing heat flux presented in Figure 6.2 are also observed by Wang *et* al. [55] and Chen and Garimella [19]. Figure 6.2a shows the effect of increasing heat flux on the averaged heat transfer coefficient h_{avg} and pressure drop ΔP_{avg} for the lowest tested mass flux of 36.87 kg $m^{-2}s^{-1}$. h_{avg} increases with increasing heat flux until it reaches a maximum value (HTC_{max}) simultaneously at all channel sections at the heat flux of 43.41 kW m^{-2}. Particularly, at q = 43.41 kW m^{-2}, h_{avg} increased up to the maximum of 22,000 W m^{-2} K^{-1} at the channel inlet, 15,000 W m^{-2} K^{-1} at the middle and 8,000 W m^{-2} K^{-1}at the outlet ΔP_{avg} starts from 50 mbar at single-phase flow conditions and decreases with increasing heat flux up to 43.41 kW m^{-2} (HTC_{max}) where it decreases down to 32 mbar. Onset of boiling (ONB) conditions occur at the heat flux just before HTC_{max} is reached, q = 35 kW m^{-2}. At ONB, h_{avg} is the highest at the outlet and reaches 13,250 W m^{-2} K^{-1}. h at the middle is measured to be lower, 1,120 W m^{-2} K^{-1} and at inlet has the lowest value of 7,000 W m^{-2} K^{-1}. After the HTC_{max} is reached, h_{avg} decreases with increasing heat flux at all sections while ΔP_{avg} at the two-phase flow region increases from 32 mbar to 38 mbar with increasing heat flux. h_{avg} at the middle and outlet is roughly 5,050 W m^{-2} K^{-1}, lower than the inlet, which has the highest value of 7,200 W m^{-2} K^{-1}. Deterioration of the heat transfer is related to periodic cycles of temporal suspected dryout during annular flow regime that occur on the channel surface. CHF is reached at q = 58 kW m^{-2} where all the sections have similar h_{avg} values in the range from 4,450 to 4,810 W m^{-2} K^{-1}.

The effect of heat flux on h_{avg} and ΔP_{avg} for the mass flux of 73.74 kg $m^{-2}s^{-1}$ is presented in Figure 6.2b. The trend of the h_{avg} is similar to the trend at lower mass flux shown in previous Figure 6.2a, however the trend of ΔP_{avg} differs from that at G = 36.87 kg $m^{-2}s^{-1}$ mainly for the single–phase region before ONB where it appears to increase with heat flux and to show high deviation. Particularly, Figure 6.2b shows that h_{avg} increases with increasing heat flux until it reaches a maximum value (HTC_{max}) at q = 38.6 kW m^{-2}. The two-phase heat transfer coefficient reaches its maximum value at all channel sections for q = 38.6 kW m^{-2}. The maximum value of h_{avg} is 11,200 W m^{-2} K^{-1} at the outlet, then decreases at 8,120 W m^{-2} K^{-1} in the middle and then decreases down to 5.051 W m^{-2} K^{-1}at the inlet. ΔP_{avg} starts from the value of 16 mbar at singlephase flow conditions and increases with increasing heat flux until the ONB where it presents a minimum of 28 mbar at q = 35.87 kW m^{-2} and then increases at HTC_{max} up to 37 mbar. After ONB, h_{avg} decreases with increasing heat flux at the middle and the outlet except the inlet where it reaches its maximum value of 6,200 W m^{-2} K^{-1} at q = 58 kW m^{-2} while ΔP_{avg} decreases to 37 mbar with increasing heat flux. All the two-phase heat transfer coefficients for heat fluxes higher than 58 kW m^{-2} decrease with increasing heat flux at 5,080 W m^{-2} K^{-1} for the

inlet and outlet, lower compared to the middle which increases to 6,133 W m^{-2} K^{-1} with increasing the heat flux up to 46 kW m^{-2}. The minimum of ΔP_{avg} is reached with the initiation of periodic dryout cycles and decrease of the two-phase heat transfer coefficient. The deterioration of the heat transfer starts at q = 46 kW m^{-2} because of periodic dryout cycles that occur on the channel surface. CHF is reached at q = 56 kW m^{-2} where the middle and the outlet of the channel have similar h_{avg} values in the range from 3,221 to 3,510 W m^{-2} K^{-1} while the lower value of 1,150 W m^{-2} K^{-1} is measured at the inlet.

Figure 6.2c shows the effect of heat flux on h_{avg} and ΔP_{avg} for the highest mass flux of G = 101.2 kg $m^{-2}s^{-1}$. The trend of h_{avg} with increasing heat flux is similar to the trend of the other two mass fluxes shown in previous Figures 6.2a and b, however the pressure drop trend differs from that at G = 36.87 kg $m^{-2}s^{-1}$ mainly for the single–phase region and it is similar to the single-phase pressure drop trend at G = 73.74 kg $m^{-2}s^{-1}$. Figure 6.2c shows that h_{avg} increases with increasing heat flux up to a maximum value which in this case is at the same heat flux that ONB occurs, q = 45.26 kW m^{-2}. Particularly, the two-phase heat transfer coefficient reaches its maximum value at the middle and the outlet for q = 45.26 kW m^{-2}. During ONB, the maximum value of 13.040 W m^{-2} K^{-1} is measured at the outlet, 8,032 W m^{-2} K^{-1} at the middle and 4.063 W m^{-2} K^{-1}at the inlet, which is the lowest. ΔP_{avg} starts from the value of 5 mbar at single-phase flow conditions and increases with increasing heat flux until the ONB where it reaches the maximum of 50 mbar at q = 46 kW m^{-2} and then decreases 34 mbar. The onset of boiling (ONB) occurs just before HTC_{max} is reached, at q = 36 kW m^{-2} where h_{avg} at inlet has the highest heat transfer coefficient which equals to 8,355 W m^{-2} K^{-1}. h_{avg} is measured to be 5,111 W m^{-2} K^{-1} at the middle and at the outlet 3,220 W m^{-2} K^{-1}.Increasing heat flux, h_{avg} decreases with increasing heat flux for all channel sections while ΔP_{avg} at the two-phase flow region increases from 37 mbar to 39 mbar with increasing heat flux. The two-phase heat transfer coefficients after the heat flux of HTC_{max} decrease down to 5,080 W m^{-2} K^{-1} for the inlet and outlet lower than the middle, which takes the average value of 6,133 W m^{-2} K^{-1} at 46 kW m^{-2}. The deterioration of the heat transfer starts at q = 46 kW m^{-2} because periodic cycles of suspected dryout are observed to occur on the channel surface. CHF is reached at q = 56 kW m^{-2} where the middle and the outlet have similar h_{avg} values that range from 3,221 to 3,510 W m^{-2} K^{-1}while the inlet lowest value of 1,150 W m^{-2} K^{-1} is measured at the channel inlet.

Single-phase pressure drop decreases with increasing heat flux because the density and viscosity of the liquid decreases with increasing temperature. At the mass flux of 101.2 kg $m^{-2}s^{1}$ which is the highest, the two-phase heat transfer coefficients appear to be independent of heat flux greater than q = 58 kW m^{-2} (Figure 6.2c). h_{avg} appears to be higher than the single-phase heat transfer coefficients for all the mass fluxes during two-phase flow boiling conditions. At

the tested mass fluxes, a slight decrease in pressure drop in the two-phase region is observed to occur with the initiation of the periodic dryout cycles.

Wang *et* al. [55] experimentally measured the time averaged heat transfer coefficient as a function of heat flux for the mass fluxes of 11.2, 22.4 and 44.8 kg $m^{-2}s^{-1}$ with FC-72 in a high aspect ratio microchannel with round corners and D_h = 550 μm. They found that the minimum of the time average two-phase heat transfer coefficient occurs at the heat flux where the onset of boiling occurs (ONB). They found that the heat flux of ONB increase with increasing mass flux from 2 to 6 kW m^{-2}. The heat transfer coefficients reached a maximum value after the ONB for all the mass fluxes but decreased with increase in the heat flux. The heat transfer coefficients increased with increasing mass flux. The maximum $h_{tp,in}$ was measured during two-phase flow boiling at the highest mass flux of 44.8 kg $m^{-2}s^{-1}$ and it decreased from the of 600 W $m^{-2}K^{-1}$ down to 330 W $m^{-2}K^{-1}$ with increasing heat flux from 6 to 11.8 kW m^{-2}.

6.4.2.2 3D plots of local interfacial heat transfer coefficient as a function of time at the onset of boiling (ONB)

In this section, the transient two-phase and single-phase interfacial heat transfer coefficients were deduced from wall temperature measurements obtained at the solid-fluid interface of the PDMS microchannel. The interfacial two-phase heat transfer coefficients presented in this section were locally averaged across the channel width at nine equally spaced locations along the channel domain. Because the wall temperature measurements were obtained from the PDMS side of the microchannel, the two-phase heat transfer coefficients were measured in the vicinity of the wall, from the liquid side, therefore they were related with the interfacial two-phase heat transfer. The interfacial heat transfer coefficients were calculated as a function of local pressure (t), assuming linear relation between the inlet and outlet pressure. 3D plots of local $h_{tp,}$ as a function of time and channel length are illustrated in the following figures of this section. Figure 6.3 illustrates the 3D plot of the local single-phase heat transfer coefficient spatially averaged across the microchannel width at 9 equally spaced locations along the microchannel domain, as a function of time for G = 73.74 kg $m^{-2}s^{-1}$ and q = 27.66 kW m^{-2}.Local $h_{sp,}$ slightly increased with channel length from 1,124 to 1,560 W m^{-2} K^{-1} and remained roughly constant with time.

Figure 6.4 presents 3D plots of the local interfacial two-phase heat transfer coefficient $h_{tp,in}$ as function of time and channel length at the onset of boiling (ONB) for the mass fluxes of 6.87 kg m^{-2} s^{-1}, 73.74 kg $m^{-2}s^{-1}$ and 110.62 kg $m^{-2}s^{-1}$. Figure 6.4a shows the fluctuations of the heat transfer coefficient along the channel length at ONB for the heat flux of 35 kWm^{-2} at the lowest mass flux of 36.87 kg m^{-2} s^{-1}. For the lowest mass flux, high amplitude local fluctuations occur

at the microchannel inlet and outlet. h_{avg} ranges from 4,800 to 20,300 W m^{-2} K^{-1}. Figure 6.4b shows the fluctuations of $h_{tp,}$ along the channel for G = 73.74 kg m^{-2} s^{-1}and q = 36.87 kW m^{-2}. $h_{tp,}$ Increases almost monotonically from inlet to outlet from 12,150 to 4,800 W m^{-2} K^{-1}. The 3D plot in Figure 6.4c illustrates the fluctuations of $h_{tp,}$ at the ONB for the highest mass flux of G = 101.2 kg m^{-2} s^{-1} which occurs at q = 45.26 kW m^{-2}. $h_{tp,}$ has the highest value at the outlet where fluctuations of high amplitude occur, as well as in the middle of the channel while $h_{tp,}$ has the lowest values at the inlet. $h_{tp,}$ ranges from 2,900 up to 15,450 W m^{-2} K^{1}during ONB at 101.2 kg m^{-2} s^{-1}.

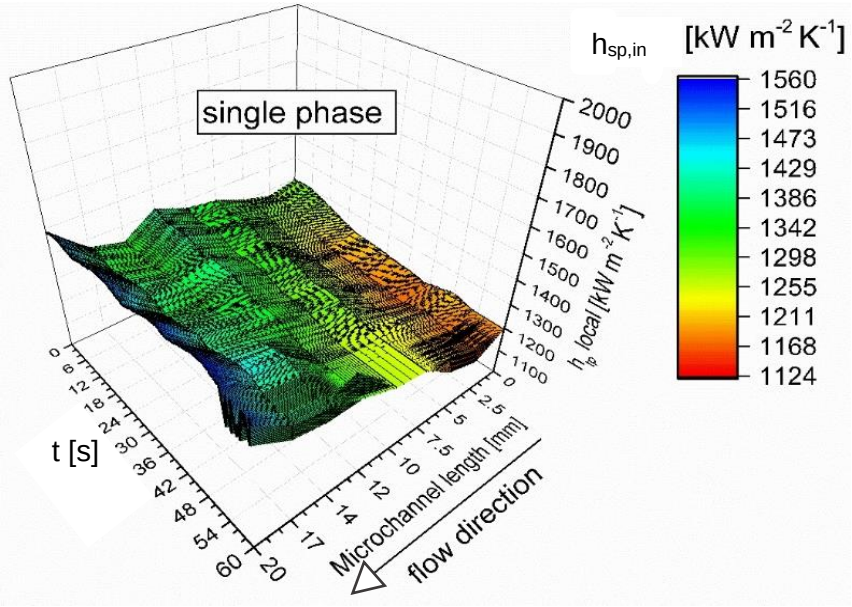

Figure 6. 3 *3D plot of the local single-phase heat transfer coefficient ($h_{sp,}$) spatially averaged across the channel with, as a function of time and channel length for G = 73.74 kg m^{-2}s^{-1} and q = 27.66 kW m^{-2}.*

Figure 6.5 displays optical images recorded at 200 Hz from the optically transparent ITO/glass channel base for the (a) inlet (b) middle and (c) outlet during onset of boiling for G = 101.2 kg m^{-2} s^{-1}and q = 45.26 kW m^{-2} (ONB). The arrow on the left, shows the liquid flow direction. The high-speed camera images reveal the bubble nucleation initiated at the superheated channel sidewall corners, then merging of the bubbles with bubbles growing at streamwise direction occurred as observed in the middle (b). Based on observations, liquid phase to liquid-vapour phase occurred during the bubbly flow regime. The bubbles grow at the sidewall as shown in Figure 6.5c. The small bubbles nucleate from the channel sidewall. ΔP_{avg} is measured to be 42.03 mbar at the inlet, 32.31 mbar at the middle and 43.16 mbar at the outlet. The inlet is occupied by liquid with small bubbles that condense as they move in the liquid and

are eventually flushed out of the channel. At the middle, the wall average value is 64.8 ˚C with a standard deviation of 4.24 ˚C.

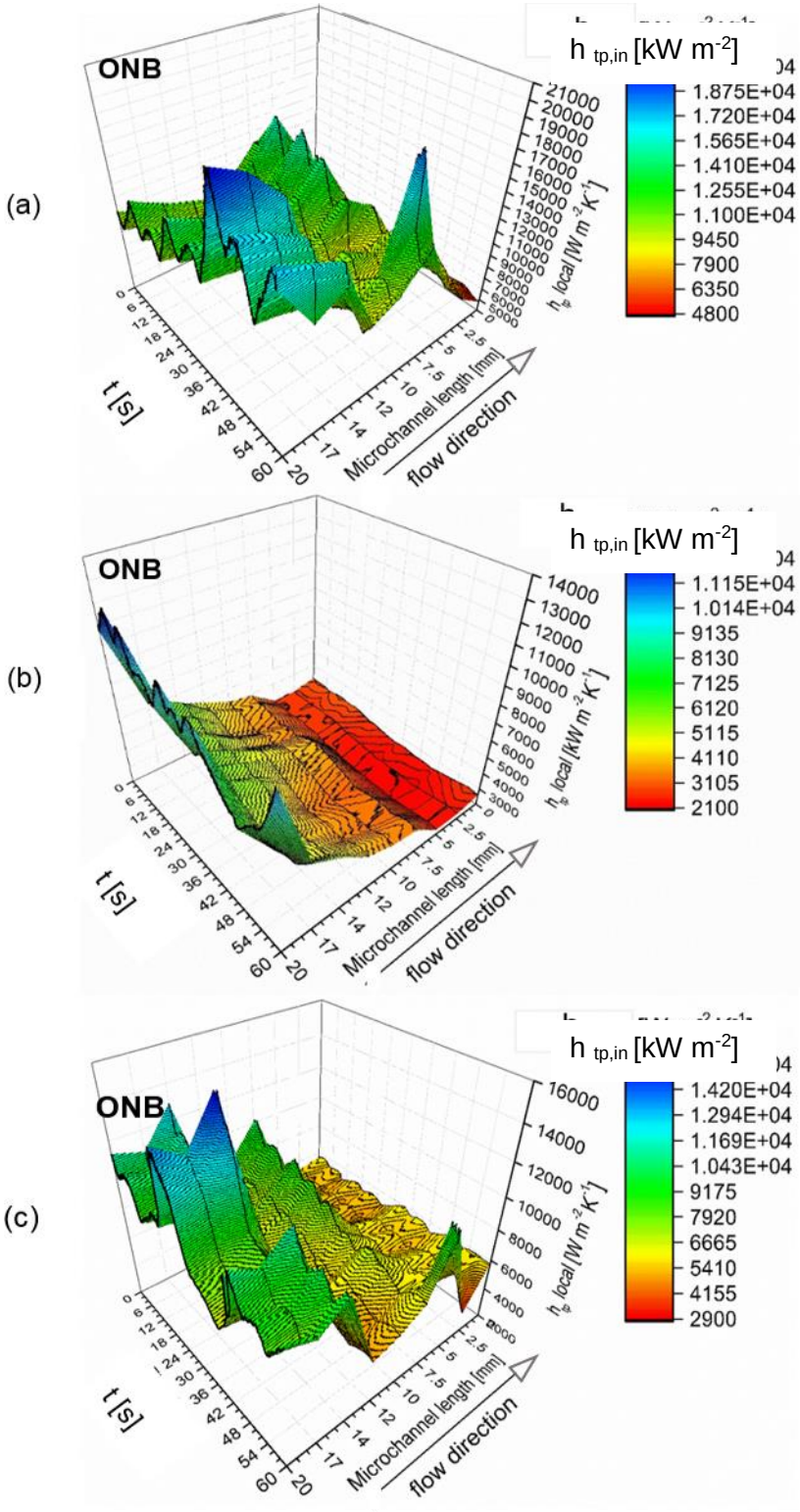

Figure 6. 4 *3D plots of the local $h_{tp,in}$ spatially averaged across the microchannel width at 9 equally spaced locations, as a function of time and channel length at ONB for (a) 36.87 kg m^{-2} s^{-1} and q = 35 kW m^{-2} (b) 73.74 kg m^{-2} s^{-1} and q=36.87 kW m^{-2} and (c) G = 101.2 kg m^{-2} s^{-1} and q = 45.26 kW m^{-2}.*

At the outlet, the average temperature is 60.33 ˚C with a deviation of 2.33 ˚C. The highest interfacial wall temperature value is measured at the channel middle.

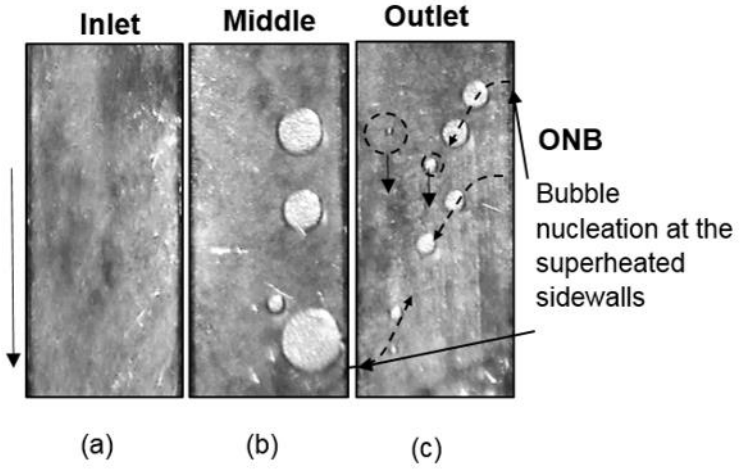

Figure 6. 5 *Optical images recorded at 200 Hz from the optically transparent ITO/glass channel base for the.(a) inlet (b) middle and (c)outlet for* $G = 101.2$ *kg* m^{-2} s^{-1} *and* $q = 45.26$ *kW* m^{-2} *(ONB). The arrow on the left shows the liquid flow direction.*

6.4.2.3 3D plots of maximum local interfacial heat transfer coefficient (HTC_{max}) as a function of time

Figure 6.6a illustrates the 3D plot of $h_{tp,in}$ as a function of time and channel length for the mass flux of 36.87 kg m^{-2} s^{-1} and q = 43.41 kW m^{-2}, where the heat transfer coefficient reaches maximum at all channel sections (HTC_{max}). Figure 6.6b shows that bubble nucleation and slug flow from thermal images at the inlet where the heat transfer appears to be enhanced at the inlet. The two-phase transfer coefficient increase is shown in the 3D plot of Figure 6.6a inlet. The thermal image sequence obtained with the high-speed IR camera from PDMS illustrates 2D interfacial wall temperature during alternation between liquid-bubbly-slug-annular- flow regimes. The IR snapshots show high spatial and temporal resolution inner wall temperature distributions during bubbly, slug and annular flow regime at the inlet of the microchannel. Based on observations, the alternation between liquid and liquid-vapour phase at the channel inlet assists in locally enhanced heat transfer. Following the observations in Figure 6.6b, bubble dynamics are analysed. Initially the liquid-phase in the channel, then bubble nucleates at a nucleation site near the superheated layer adjacent to the sidewall. The superheated layer reached maximum wall temperature of 62.9 ˚C. Bubble growth occurs when the bubble detaches from the surface and grows as it moves on the centreline of the channel in streamwise direction. The temperature gradient between the elongated bubble base and the superheated layer between the bubble and the channel sidewall can reach locally 2.5 ˚C. Bubble coalescence is observed to

occur near the superheated layers adjacent to the channel sidewalls and induce temperature gradient at the wall interface. Big vapour bubbles coalescence and result in elongated bubbles, which occupy almost the entire channel cross section. The vapour slug starts growing axially after it fully occupies the channel cross section. Finally, the vapour slug is flushed downstream and small bubbles follow the slug downstream. Flow reversal is not very evident because the vapour slug does not grow to occupy the whole microchannel length. In addition, the time duration of the vapour slug is not enough in order to induce local dryout or lead to decrease of $h_{tp,}$. For bubbles with diameter smaller than 0.3 mm, the interfacial wall temperature at the bubbles interface is lower than the surrounding temperature, between 59.6 ˚C and 60 ˚C, almost uniform temperature. However, when the bubble diameter is greater than 1.2 mm, the wall temperature distribution of the bubble becomes non-uniform. Low wall temperature values are measured at the periphery of the bubble while the interfacial wall temperature in the centre of the channel increased by 0.8 ˚C.

In Figure 6.7a the 3D plot of the two-phase heat transfer coefficient is shown as a function of microchannel length and time for the highest mass flux of G = 73.74 kg $m^{-2}s^{-1}$ at the heat flux of 38.54 kW m^{-2} where the maximum heat transfer coefficient. High amplitude fluctuations occur mainly at the channel inlet where h_{tp} is measured to be the highest and ranges from 3,900 to 15,650 W $m^{-2}K^{-1}$. Figure 6.7b presents the observed interfacial wall temperatures during the maximum heat transfer coefficient at q = 38.54 kW m^{-2} and G = 73.74 kg m^{-2} s^{-1}. Figure 6.7c shows the synchronised high quality optical images captured with a high-speed camera at the same frame rate of 200 Hz. During bubbly flow regime, the bubble grows in stream-wise direction along the channel centreline as shown to occur at t_{18} (Figure 6.7b). Then because of bubble coalescence between the small vapour bubbles, elongated bubbles are formed for t_7, t_{14}, t_{16} and slug flow regime exists with simultaneous bubbly flow regime. Slug flow is establishes at t_4, t_{20} (Figure 6.7b). Slug flow with boiling inside the liquid film at the sidewalls is observed to occur as well and is the main flow regime that occurs at these conditions in the channel as it has been observed for most of the IR images for t_1, t_5, t_{26}, t_6, t_4, t_{10}, t_{11}, t_{12}, t_2, t_{19}, presented in Figure 6.7b. Slugs with convex back liquid-vapour interface are observed for t_{21} (Figure 6.7c). Annular flow ring is formed after slug coalescence with simultaneous film boiling from the superheated channel sidewalls, for t_{22} (Figure 6.7b). Annular flow regime is finally established at t_3, t_{13} and t_{15}. (Figure 6.7b) The liquid-vapour distributions below the bubbles can be determined from the high quality optical images presented in Figure 6.7c. For q = 38.54 kW m^{-2} the interfacial wall temperature ranges between 63 °C and 67 °C at the channel inlet (Figure 6.7b).

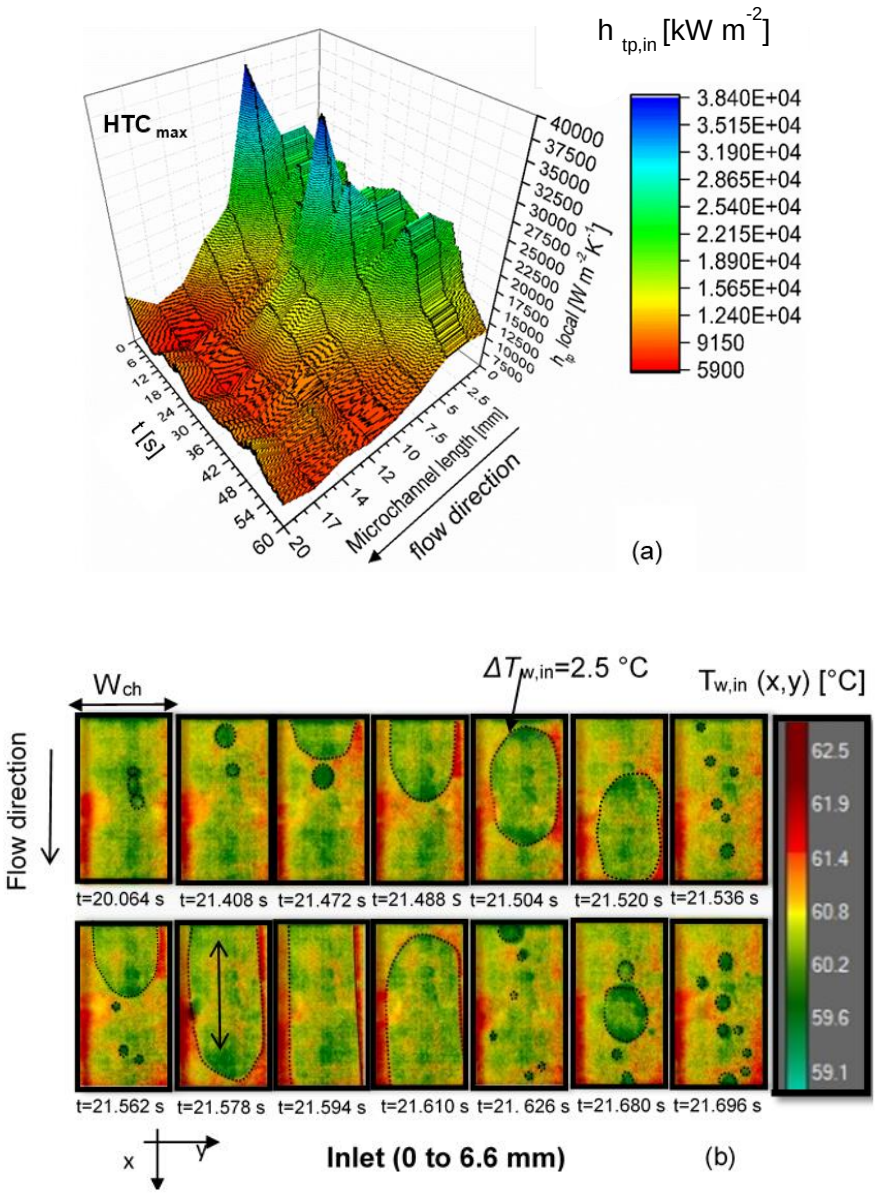

Figure 6. 6 *(a) 3D plot of the local two-phase interfacial heat transfer coefficient ($h_{tp,in}$) as a function of time at q = 43.41 kW m^{-2} where the maximum heat transfer coefficient occurs for G = 36.87 kg m^{-2} s^{-1} and (b) thermal image sequences obtained with high- speed IR camera from PDMS. The thermal images show interfacial wall temperature distribution of high spatial and temporal resolution of 15 µm/pixel and 200 fps during bubbly flow, confinement, slug and annular flow regime at the inlet of the microchannel with a time interval of 0.016 s.*

From the IR snapshots in Figure 6.8b the lowest $T_{w,}$ is measured at the bubbles, from 63.6 °C to 64.7 °C. Around the periphery of the bubble $T_{w,}$ is around 65.1 °C, higher compared to the bubble temperature. During slug flow the interfacial wall temperature of the slug core ranges from 65.1 °C to 65.6 °C, higher compared to the temperature of the small bubbles. Approaching the triple point line (solid-liquid-vapour) of the slug with direction from the vapour core to the liquid, $T_{w,}$ decreases. From the above observations it is concluded that the heat transfer

mechanism is a combination of thin film evaporation and bubble nucleation at the superheated channel sidewalls. The interfacial wall temperature at the channel sidewalls ranges from 65.6 °C to 67 °C while the elongated bubbles passes. Based on the observations, the main flow regime is slug flow with nucleation at sidewalls. High heat transfer coefficients are obtained during liquid to bubbly to slug flow alternation. Annular flow is established after slug coalescence and occurs only for a short time because the slug is flushed out downstream.

For the highest mass flux of G = 110.62 kg m^{-2} s^{-1}, the highest heat transfer coefficients are reached during the onset of boiling. Figure 6.9 shows the 3D plot of the two-phase h_{avg} as a function of time and length at increased heat flux after ONB at a heat flux of q = 55.23 kW m^{-2} and G = 110.62 kg m^{-2} s^{-1}. h_{avg} in Figure 6.7a is spatially averaged across the microchannel width at 9 equally spaced positions along the microchannel domain, as a function of time. $h_{tp,}$ decreases with direction from inlet to outlet and ranges from 8,200 to 3,900 W m^{-2} K^{-1}. Figure 6.8b shows a sequence of IR thermal images that show the interfacial wall temperature distribution during phase alternations between liquid flows and vapour bubbles and slug flow in the stream-wise direction. Based on observations slug flow causes flow reversal at the inlet from 0 to 6 mm. Bubbles are observed to nucleate adjacent to the superheated sidewall corner. The bubbles then depart in small from the sidewalls and grow in size in stream-wise direction. Initially the bubbles coalesce at the channel outlet. As the bubble grows bigger, it departs and moves opposite of flow direction. For this heat flux the difference compared to Figure 6.7a, the difference is that there is slug flow and bubble coalescence. The superheated layers at the sidewall corners appear to occupy more space of the interface. The heat transfer coefficients in this case appear to have lower values compared to Figure 6.7a.

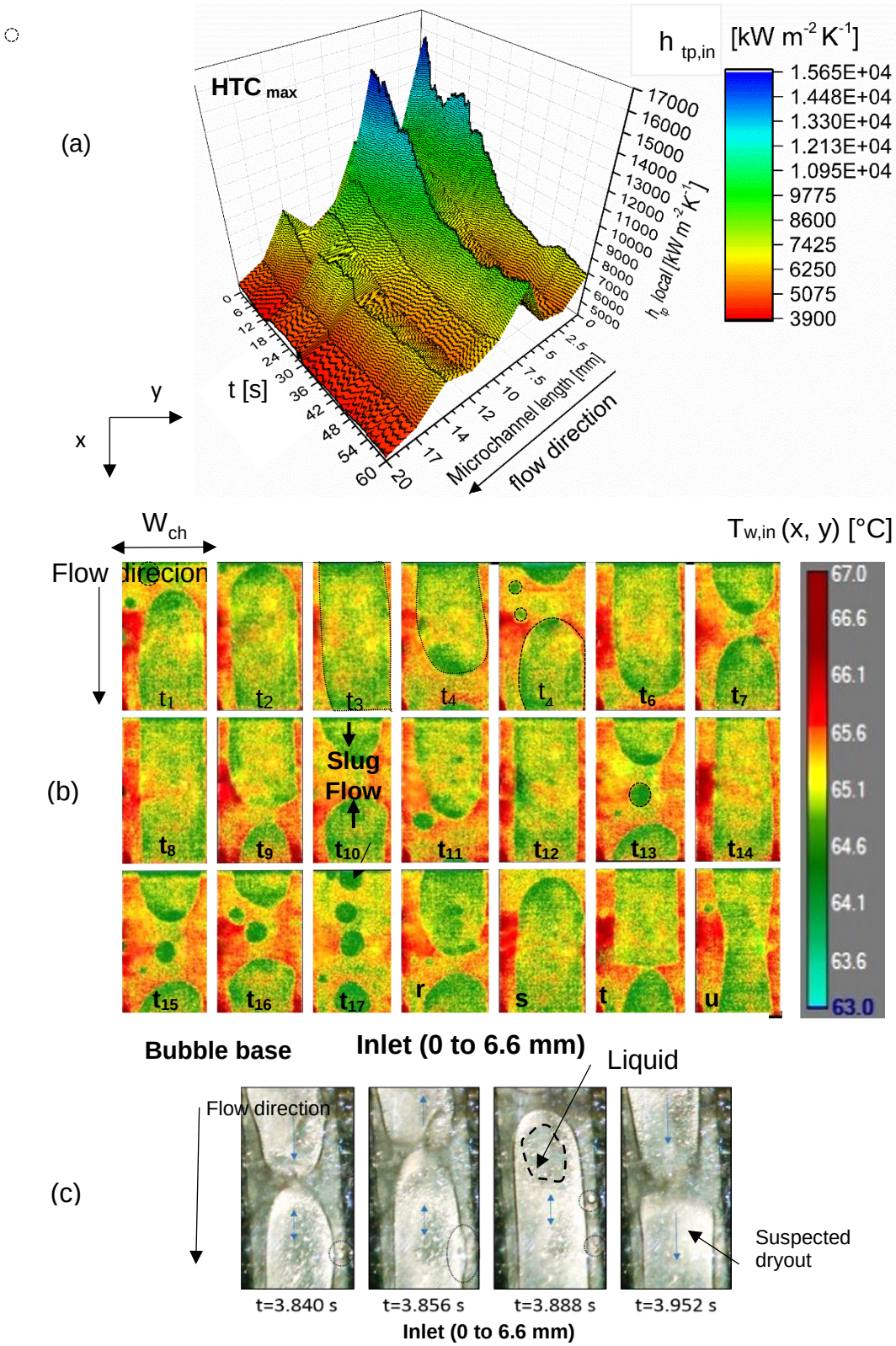

Figure 6. 7 *(a) 3D plot of the spatially averaged two-phase $h_{tp,in}$ across the microchannel width at 9 equally spaced positions along the microchannel domain, as a function of time and length at increased heat flux after ONB at the heat flux of q = 55.23 kW m^{-2} and G = 110.62 kg m^{-2} s^{-1}.*

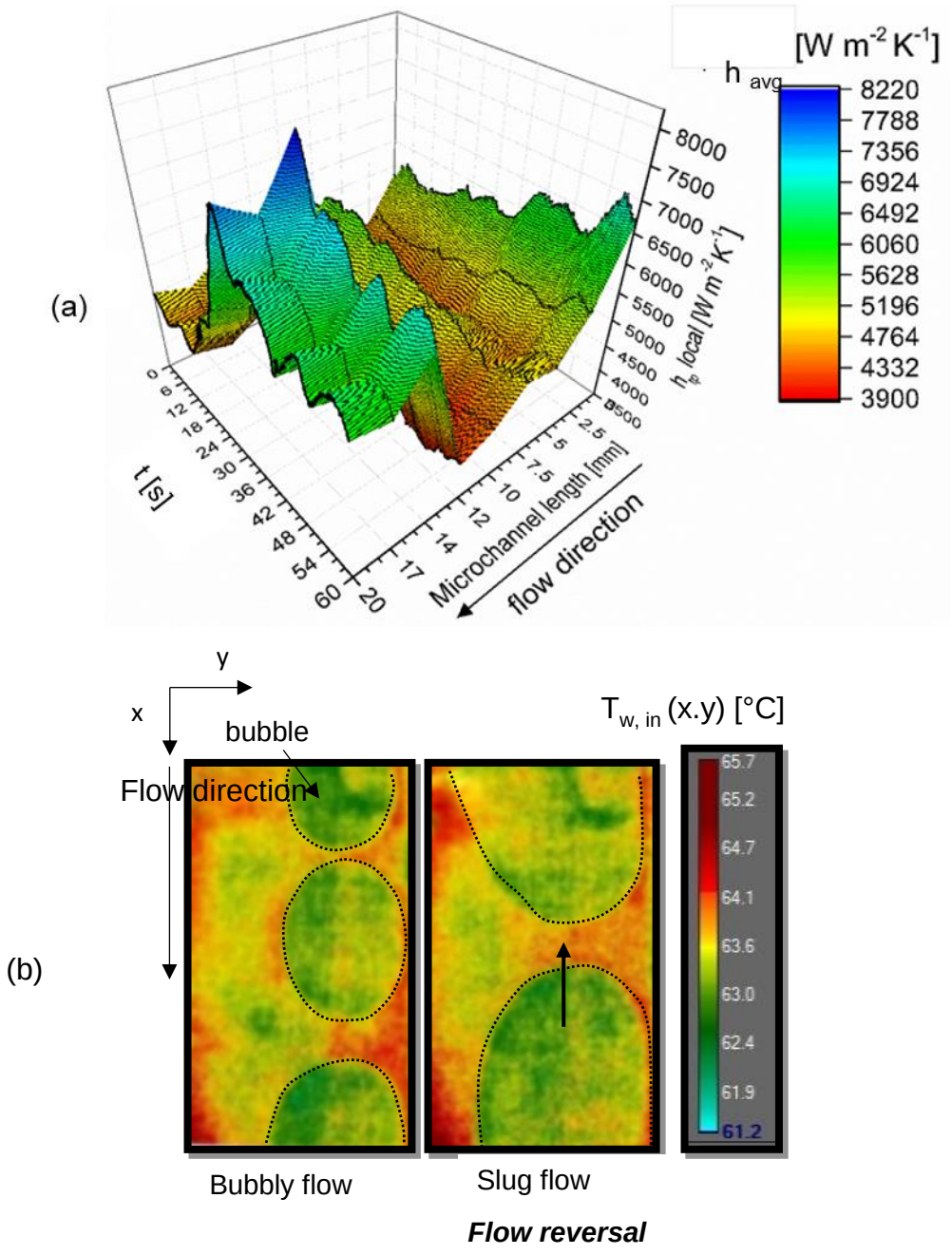

Figure 6. 8 *(a) 3D plot of the spatially averaged interfacial heat transfer ($h_{tp,in}$) across the microchannel width at 9 equally spaced positions along the microchannel domain, as a function of time at the heat flux of q = 55.23 kW m^{-2} after ONB at G = 110.62 kg m^{-2} s^{-1}and (b) a sequence of IR images that show the alternation between liquid flow with bubbles at the stream-wise direction and slug flow for the channel inlet from 0 to 6 mm length (inlet).*

6.4.2.4 3D plots of local interfacial HTC at the maximum heat flux

Figure 6.9 shows high speed visualizations obtained for Figure 6.10b to show from ITO channel base for q = 55.23 kW m^{-2} where after *ONB* at G = 110.62 kg m^{-2} s^{-1}.

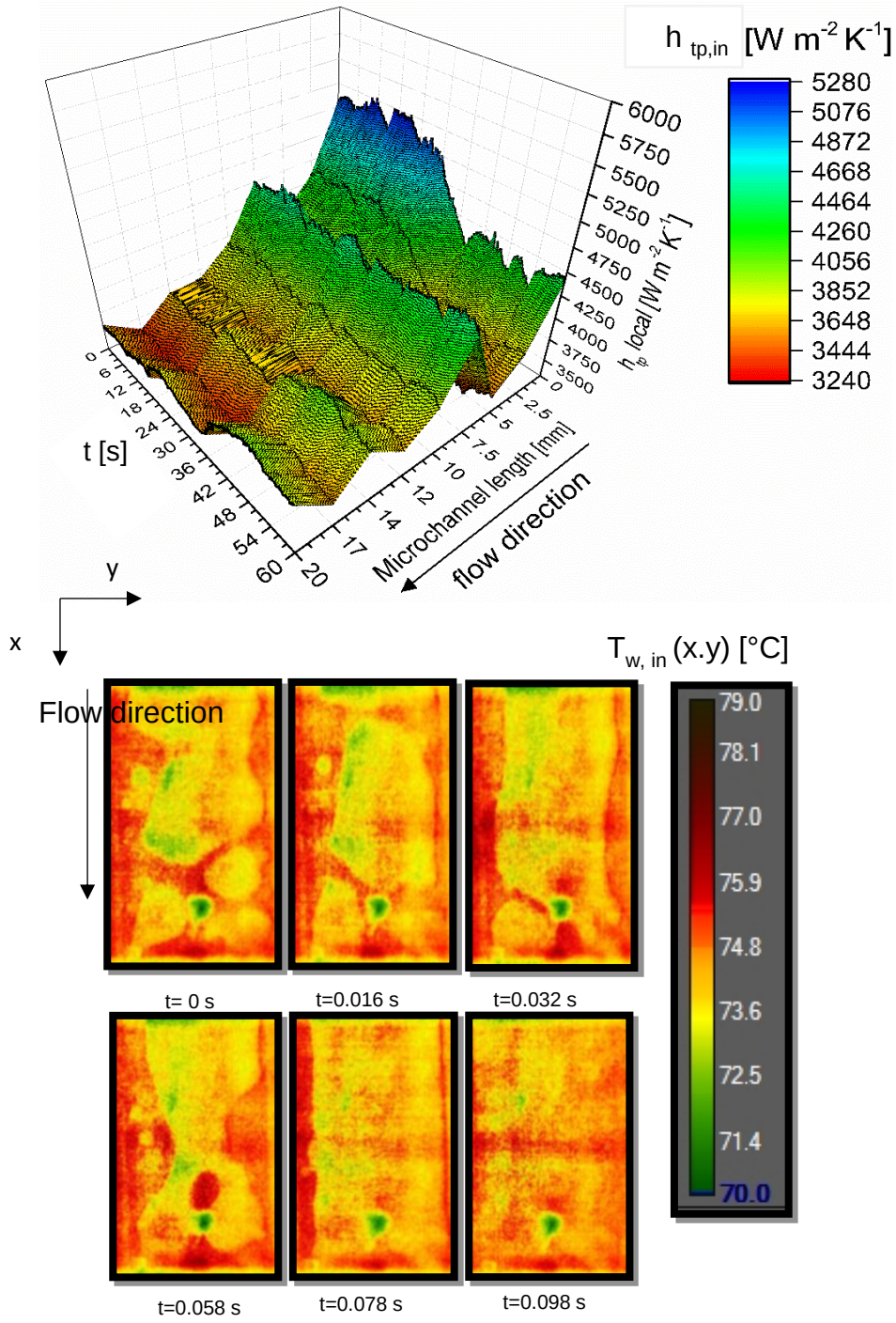

Figure 6. 9 *(a) 3D plot of the spatially averaged $h_{tp,in}$ across the microchannel width at 9 equally spaced positions along the microchannel domain, as a function of time for q = 57.13 kW m^{-2} and G = 36.87 kg m^{-2} s^{-1}. (b) Sequence of IR images that show the*

alternation between liquid flow with bubbles at the stream-wise direction and slug flow for the channel inlet from 13 to 20 mm length (outlet).

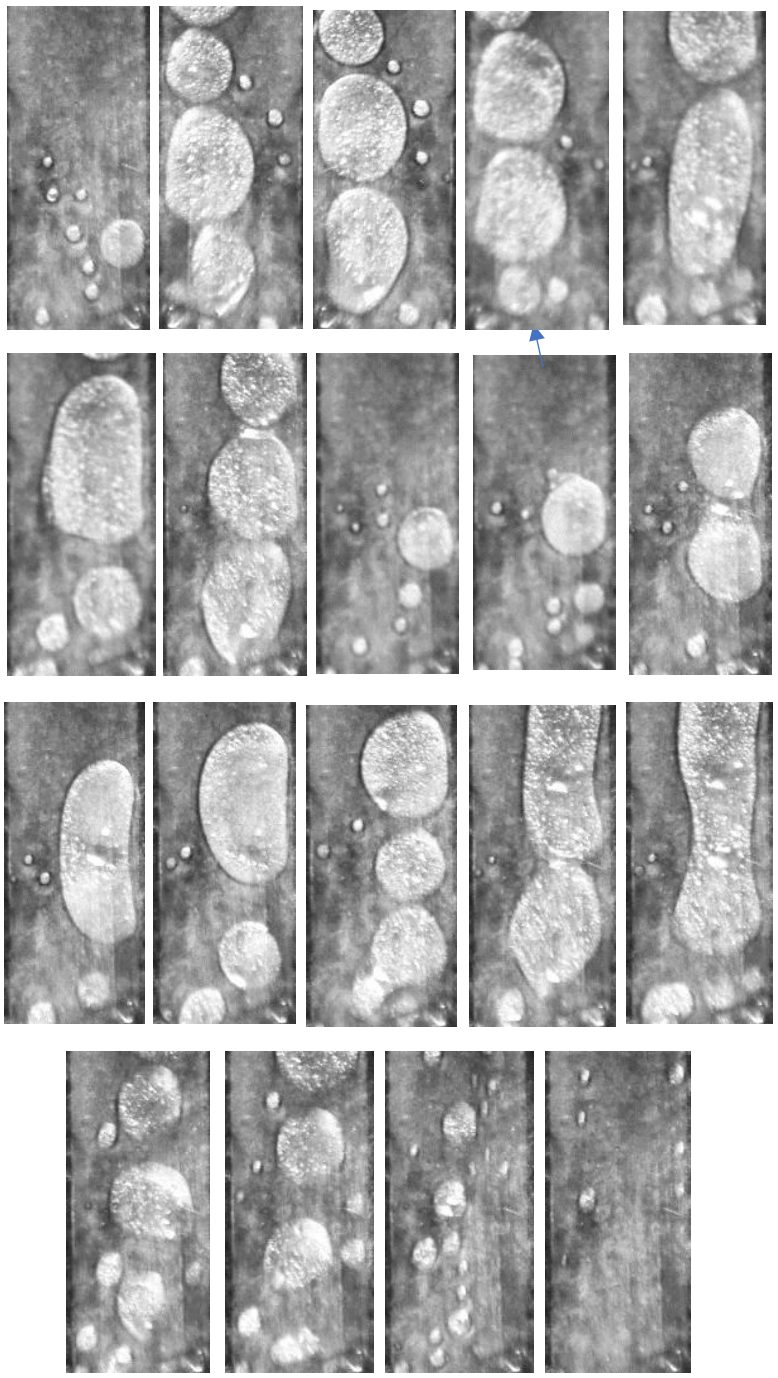

Figure 6. 10 *Image sequence of high- speed visualisations obtained from ITO/glass channel base for q = 55.23 kW m^{-2} after ONB at G = 110.62 kg m^{-2} s^{-1}.*

Figure 6.11a illustrates a 3D plot of local interfacial HTC which is spatially averaged across the microchannel width at nine equally spaced positions along the microchannel domain,

as a function of time at a heat flux of q = 55.52 kW m^{-2} and at a mass flux of G = 73.74 kg m^{-2} s^{-1}. Figure 6. 11b shows IR image sequence from which the alternation between liquid flows with bubbles in the stream-wise direction and slug flow for the channel inlet from 13 to 20 mm length (outlet).

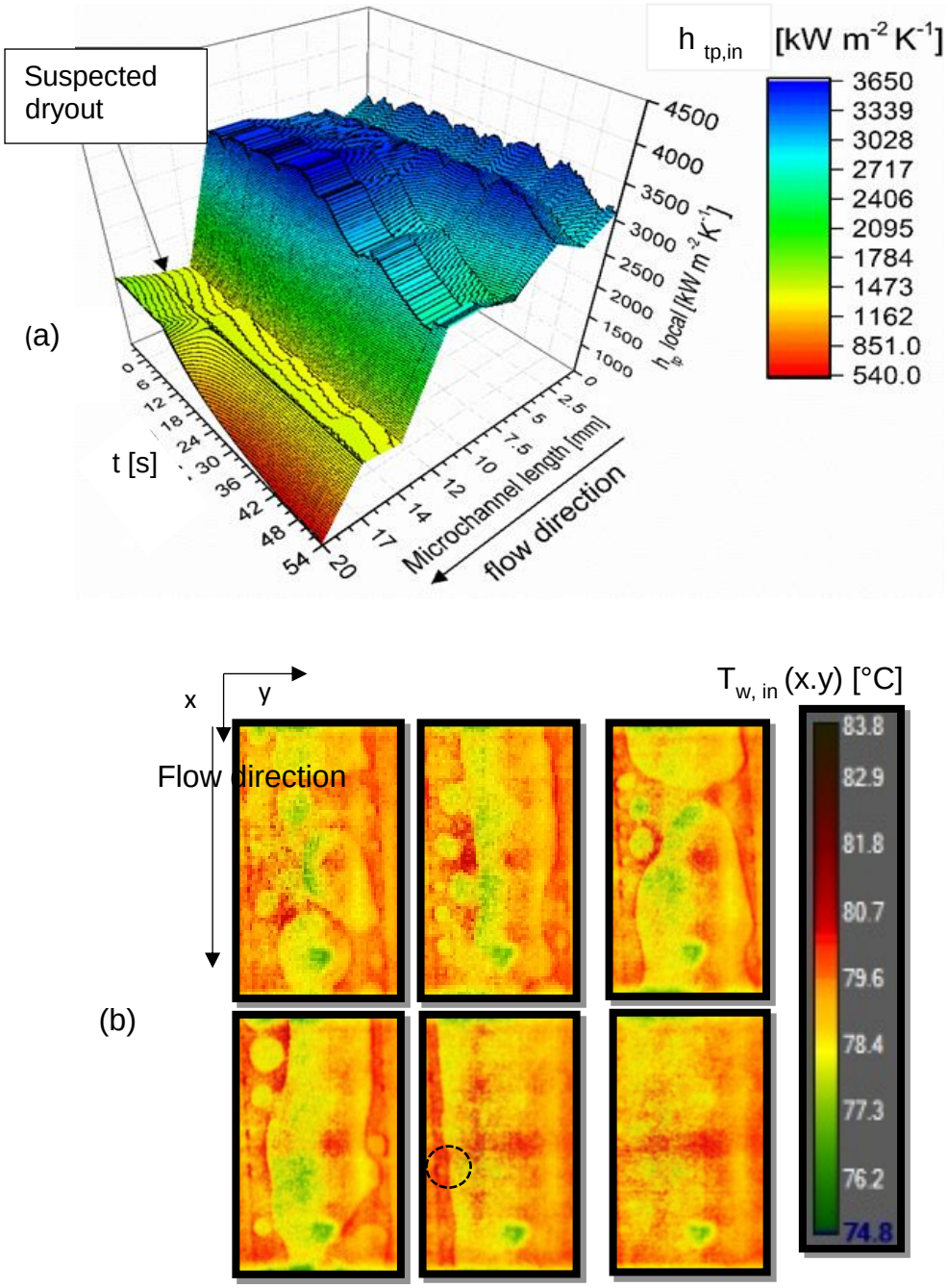

Figure 6. 11 *(a) 3D plot of local interfacial $h_{tp,}$ spatially averaged across the microchannel width at 9 equally spaced positions, as a function of time and channel length at q = 55.52 kW m^{-2} and G = 73.74 kg m^{-2} s^{-1} and (b) Sequence of IR images that show the alternation between liquid flow with bubbles in the streamwise direction and slug flow for the channel inlet from 13 to 20 mm length (outlet).*

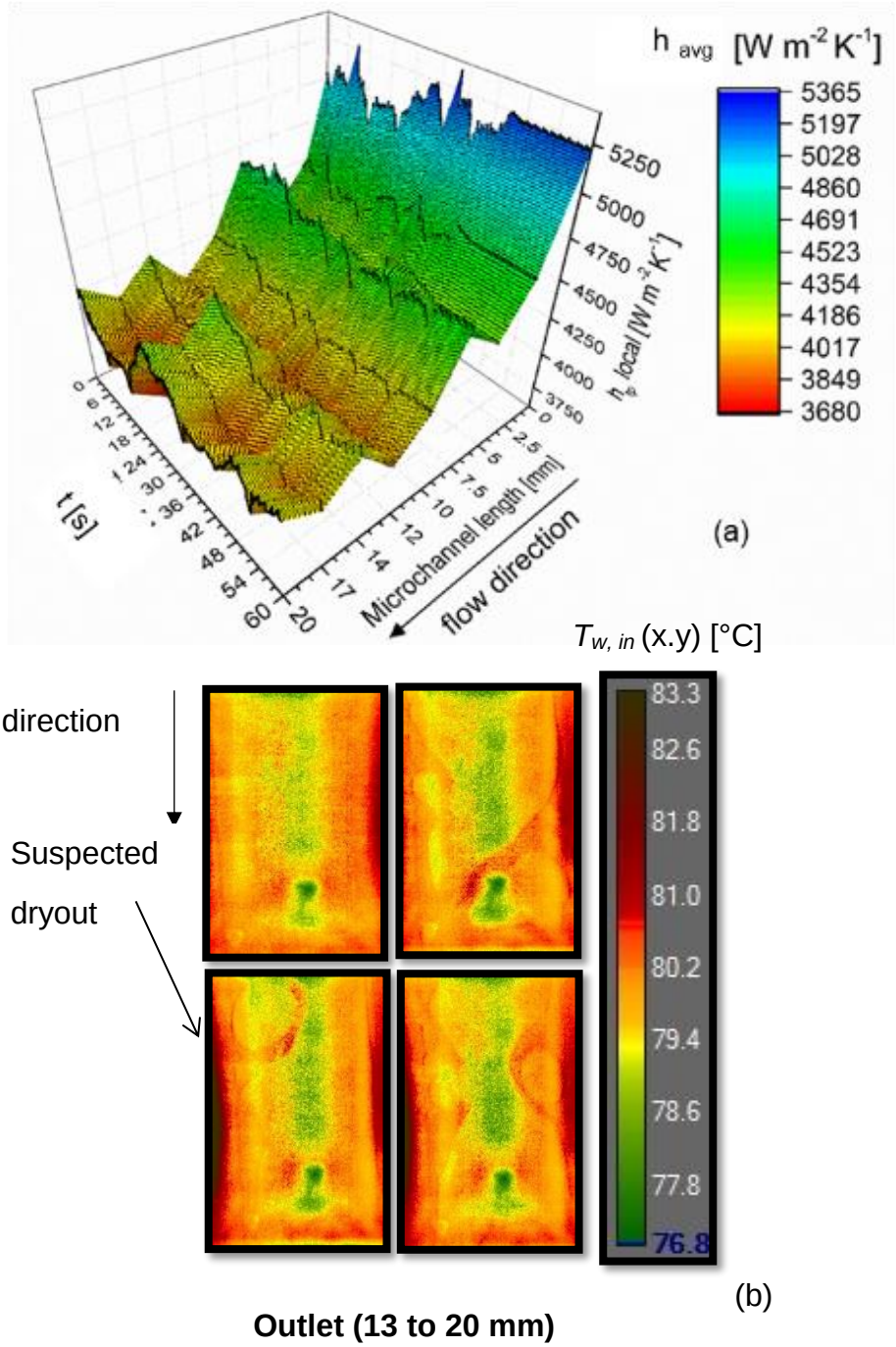

Figure 6. 12 *(a) 3D plot of local interfacial $h_{tp,in}$ spatially averaged across the microchannel width at 9 equally spaced positions, as a function of time and channel length at q = 91.46 kW m^{-2} and G = 101.62 kg m^{-2} s^{-1} and (b) sequence of IR images that show the alternation between liquid flow with bubbles in the stream-wise direction and slug flow for the channel inlet from 13 to 20 mm length (outlet).*

The 3D plot in Figure 6.12a illustrates the local interfacial $h_{tp,in}$ as a function of time for q = 91.46 kW m^{-2} and G = 101.62 kg m^{-2} s^{-1}. Figure 6.12b presents IR image sequence with interfacial wall temperature distribution of liquid flow with bubbles in the stream-wise direction and slug flow for the channel inlet from 13 to 20 mm length (outlet).

Table 6.1 summarises the two phase heat transfer coefficients for the whole channel as a function of time at the ONB, HTC_{max} and CHF conditions for the *mass fluxes of* 36.86, 73.74 and 101.92 kg m^{-2}s^{-1}. The HTC_{max} at the lowest mass flux of 36.86 kg m^{-2}s^{-1} was found to reach the highest value of 38,000 W m^{-2}K^{-1} where annular flow was found to be the dominant flow pattern. HTC_{max} occurred at the heat flux of 43.41 kW m^{-2}where the fluctuations from the inlet to the outlet of the channel were found to be very high, resulting in a range from 5,900 minimum to 38,000 W m^{-2}K^{-1} maximum two-phase heat transfer coefficient .

Table 6. 1*Minimum to maximum two-phase heat transfer coefficients for the whole channel as a function of time at the ONB, HCT_{max} and CHF conditions for the mass fluxes of 36.86, 73.74 and 101.9kg m^{-2}s^{-1}.*

G =36.87 kg m^{-2}s^{-1}		
Heat flux [kW m^{-2}]	**Two phase heat transfer coefficient [W m^{-2}K]**	
35.00	**ONB**	4,800-20,300
43.41	**HTC max**	5,900-38,000
57.13	**CHF**	3,240-5,280
G =73.74 kg m^{-2}s^{-1}		
Heat flux [kW m^{-2}]	**Two phase heat transfer coefficient [W m^{-2}K]**	
36.87	**ONB**	2,100-12,100
36.87	**HTC max**	2,100-12,100
55.52	**CHF**	540-3,650
G =101.92 kg m^{-2}s^{-1}		
Heat flux [kW m^{-2}]	**Two phase heat transfer coefficient [W m^{-2}K]**	
45.26	**ONB**	2,900-15,400
55.23	**HTC max**	3,900-15,600
91.62	**CHF**	3,680-5,365

6.4.2.5 Investigation of two-phase heat transfer during annular flow regime

6.4.2.5.1 Instability cycles

Two-dimensional interfacial two-phase heat transfer coefficient $h_{tp,in}(x, y)$ is presented as a function of time in 3D plot illustrated in Figure 6.13 for G = 36.8 kg m^{-2}s^{-1} and q = 57.13 kW m^{-2}. Based on observations from simultaneous optical images, the instability cycles during annular flow regime are presented in Figure 6.24. At t = 4.122 s bubble nucleation at channel sidewalls corners is suppressed. At t = 4.384 s evaporation of the liquid starts from the sidewall the opposite side of the channel. At t = 5.664 s evaporation occurs with direction from the right to the left. At t =5.856 s the lowest $h_{tp,in}(x, y)$ occurs because of suspected dryout at the channel sidewall corners because the slug occupied the entire channel cross section. At t = 5.872 s the vapour slug is flushed out due to inlet rewetting. At t = 5.888 s liquid occupies the channel and $h_{tp,in}(x, y)$ increases in flowstream direction. The IR images shown in Figure 6.14 were recorded from the PDMS side of the microchannel at the channel inlet. They reveal that the high temperature was observed after 3-4 mm from channel inlet. The high amplitude instabilities were observed in two cases. During the temperature decrease, the main flow patterns were bubbly and slug flow, which caused instant temperature increase resulting in the low amplitude fluctuations with high frequency. High amplitude fluctuations with low frequency occurred during annular flow as liquid evaporated from the sidewalls. Figure 6.24 shows the wall temperature patterns in IR image sequence obtained using IR thermography from PDMS during instability cycles. Local suspected dryout appears at the channel sidewall corners of the outlet.

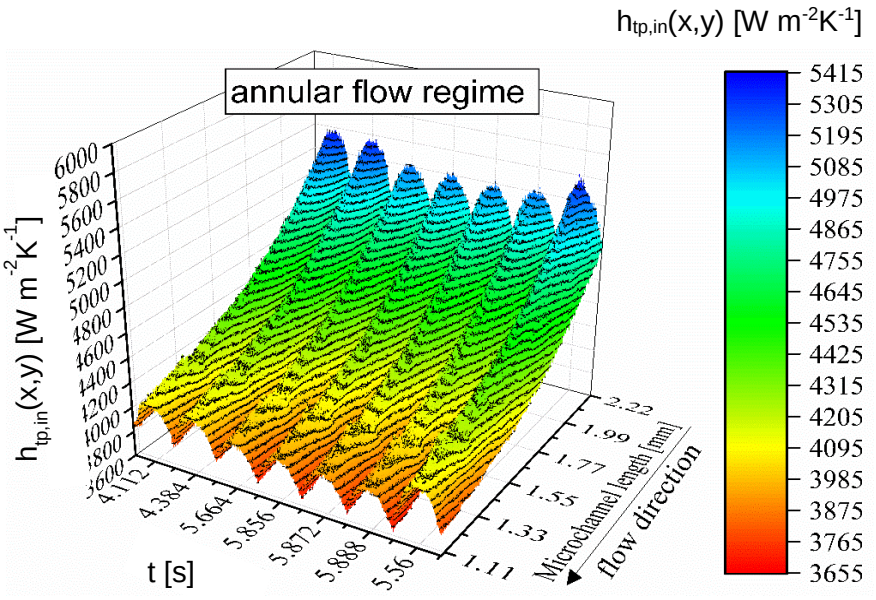

Figure 6. 13 *3D plot of interfacial $h_{tp,in}(x, y)$ as a function of time for G = 36.8 kg m^{-2}s^{-1}and q = 57.13 kW m^{-2}.*

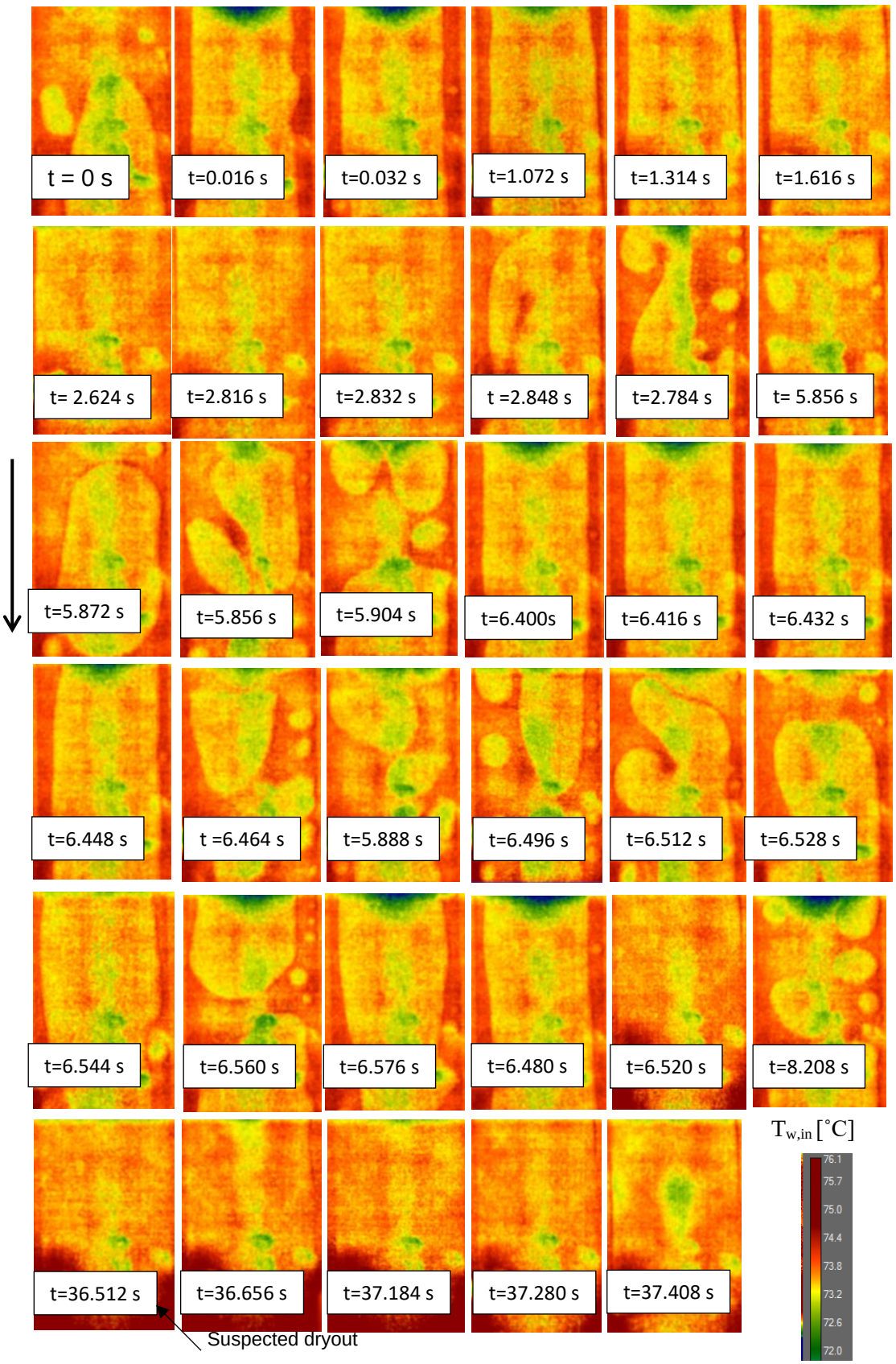

Figure 6. 14 *Image sequence that shows local flow patterns and temperature variation at the outlet, for G = 36.8 kg $m^{-2}s^{-1}$ and q = 57.13 kW m^{-2}.The IR images were recorded at 200 Hz.*

6.4.2.5.2 Correlation of IR thermography and optical images obtained with high-speed camera for the annular flow regime

Correlation from synchronised IR thermal videos from the PDMS side and high-speed visualisation images from the ITO transparent heater base allowed us to have a better understanding of the hotspot (suspected dryout) positions. Figure 6.15 shows correlation between simultaneous thermal images and optical images for annular flow and slug-bubby flow patterns. Firstly, the temperature measurements with IR camera were analysed for the middle of the microchannel. The main flow regime based on observations is the annular flow regime. Instabilities are caused by bubble nucleation adjacent to the channel sidewalls in the liquid. It is observed that the large amount of vapour in the channel supressed nucleate boiling at the channel corners of the sidewall, therefore forced convection boiling was mainly dominant. Figure 6.15 shows correlated thermal and optical images in the annular flow regime at G = 147.2 kg m^{-2} s^{-1} at q = 99.7 kW m^{-2}.

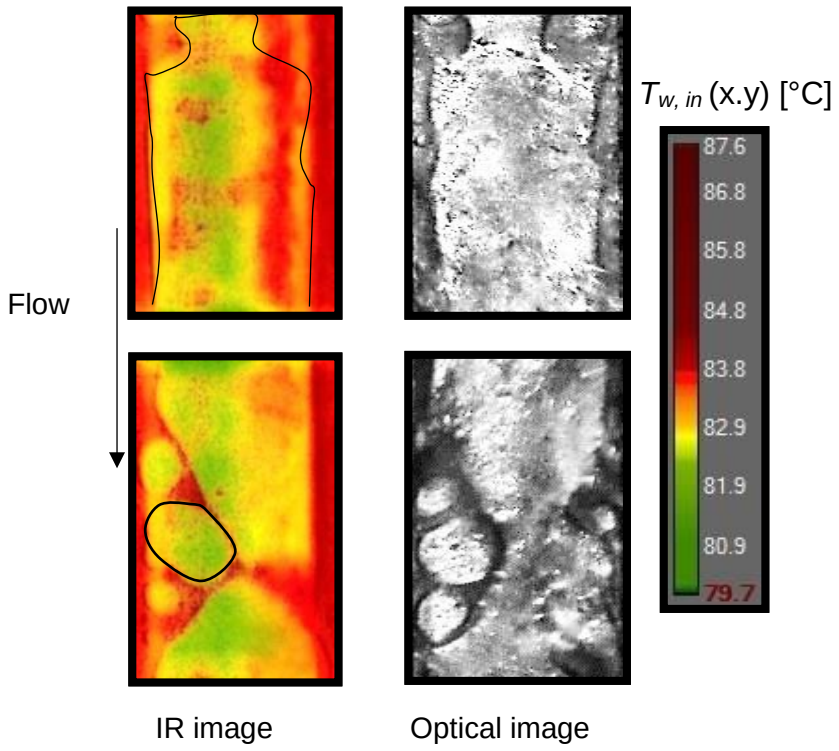

Figure 6. 15 *Correlation of simultaneous thermal images obtained from the transparent to infrared PDMS top with optical images obtained from the transparent ITO heater during slug-annular flow regime at G =147.2 kg m^{-2} s^{-1} and q = 99.7 kW m^{-2} at 200Hz .*

Figure 6. 16 correlates the (a) thermal image recorded with IR camera from the PDMS side with (b) a simultaneous optical image recorded from the transparent ITO/glass heater base during annular flow regime for G = 147.2 kg m^{-2} s^{-1} and q = 99.7 kW m^{-2}. The images illustrate

annular flow regime with a local hotspot induced with bubble burst mechanism. Interfacial wall temperature at the dispersed liquid drop is measured at 84 ˚C. Figure 6.16 shows the entrainment mass transfer with bubble burst mechanism that occurs during annular flow regime and causes instabilities in the film because hotspots appear on the interface.

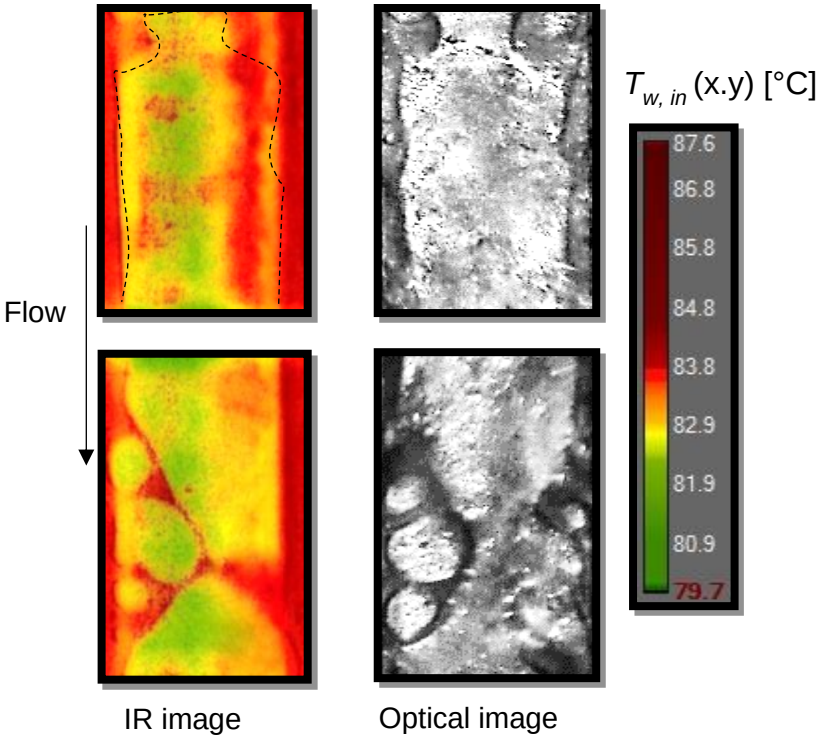

Figure 6. 16 *(a)Thermal image recorded with IR camera from PDMS side and (b)simultaneous optical image recorded from the transparent ITO/glass heater base during annular flow regime for G = 147.2 kg m^{-2} s^{-1} and q = 99.7 kW m^{-2}. Annular flow regime with local instability induced by bubble burst mechanism. $T_{w,}$ > 84 ˚C under the dispersed drop.*

The optical image, in Figure 6.16 shows that there is a liquid drop in the vapour annulus with a wall temperature of 84 ˚C. The drop appears as a red hot spot in the vapour core as shown in Figure 6.16. This observation results to the conclusion that liquid drops are formed because of bubbles burst in the vapour annulus.

Bubbles burst is one of the four basic entrainment mechanisms observed from experiments according to Isi and Grolmes [82]. Bubble burst occurs when the bubble reaches the interface and a thin liquid film forms at the top of the bubble, which separates it from the vapour flow. When the amount of entrained drops that exist in the vapour core increases, the vapour core expands periodically and covers a greater area in the channel cross section. Figure 6.17 shows the bubble burst mechanism from flow visualisation and Figure 6.18 the movement

of the resulting drop in the annulus. The observations from Figure 6.18 shows waves induced at the liquid-vapour interface when: bubbles nucleate in the liquid film because of bubble wall nucleation at the channel corners. Then drops are formed in the vapour core. The big sized drops are formed after the bursting of big vapour bubbles into the vapour core. The small droplets are results of smaller bubbles.

Figure 6.17 shows with an image sequence the bubble burst mechanism. Based on observations the bubbles burst in the vapour core and forms a big liquid drop that remains in the vapour. The drop remains in the vapour and evaporates as the vapour film goes back to its initial position. According to Isi and Grolmes [82] much larger drops can be formed on the bursting of bubbles by the motion of the surrounding liquid film filling on the crater left by the bubble. From theory, it is believed that the periodic movement of the liquid-vapour interface is attributed to the bubble nucleation at the channel sidewall, which is wetting by liquid. As the liquid is drained from the film, it can eventually rupture in several places resulting in entrained fine droplets. In our case, the droplets have a big size, with a diameter that can reach 0.7 ± 0.05 µm.

In annular flow regime, entrainment mass transfer occurs due to the effects of interfacial waves formed between liquid film and vapour core [82]. In other word, as the interfacial stress exceeds the surface tension, liquid droplets start to transfer into the vapour core. One of the entrainment mass transfer by bursting of bubbles at the interface and impingement of existing droplets of vapour core to the surface of liquid film. Entrainment mass transfer can affect heat transfer and fluid flow behaviour [83-85].

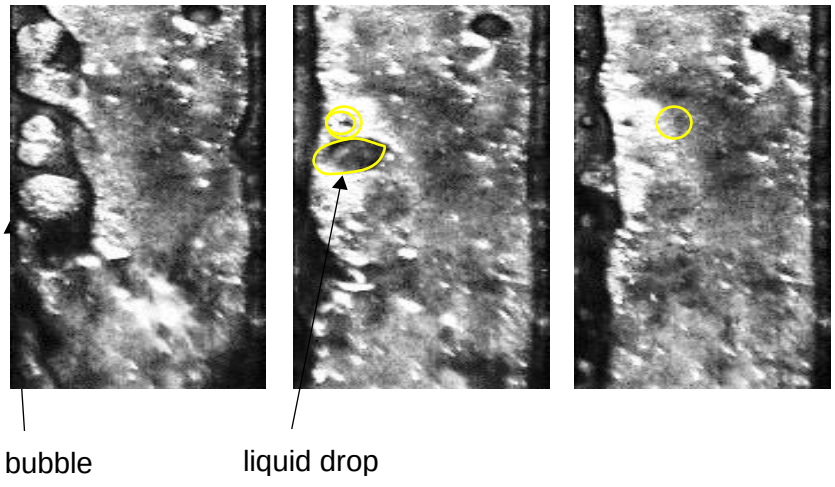

Figure 6. 17 Bubble burst mechanism for G = 147.2 kg m^{-2} s^{-1} and q = 99.7 kW m^{-2}.

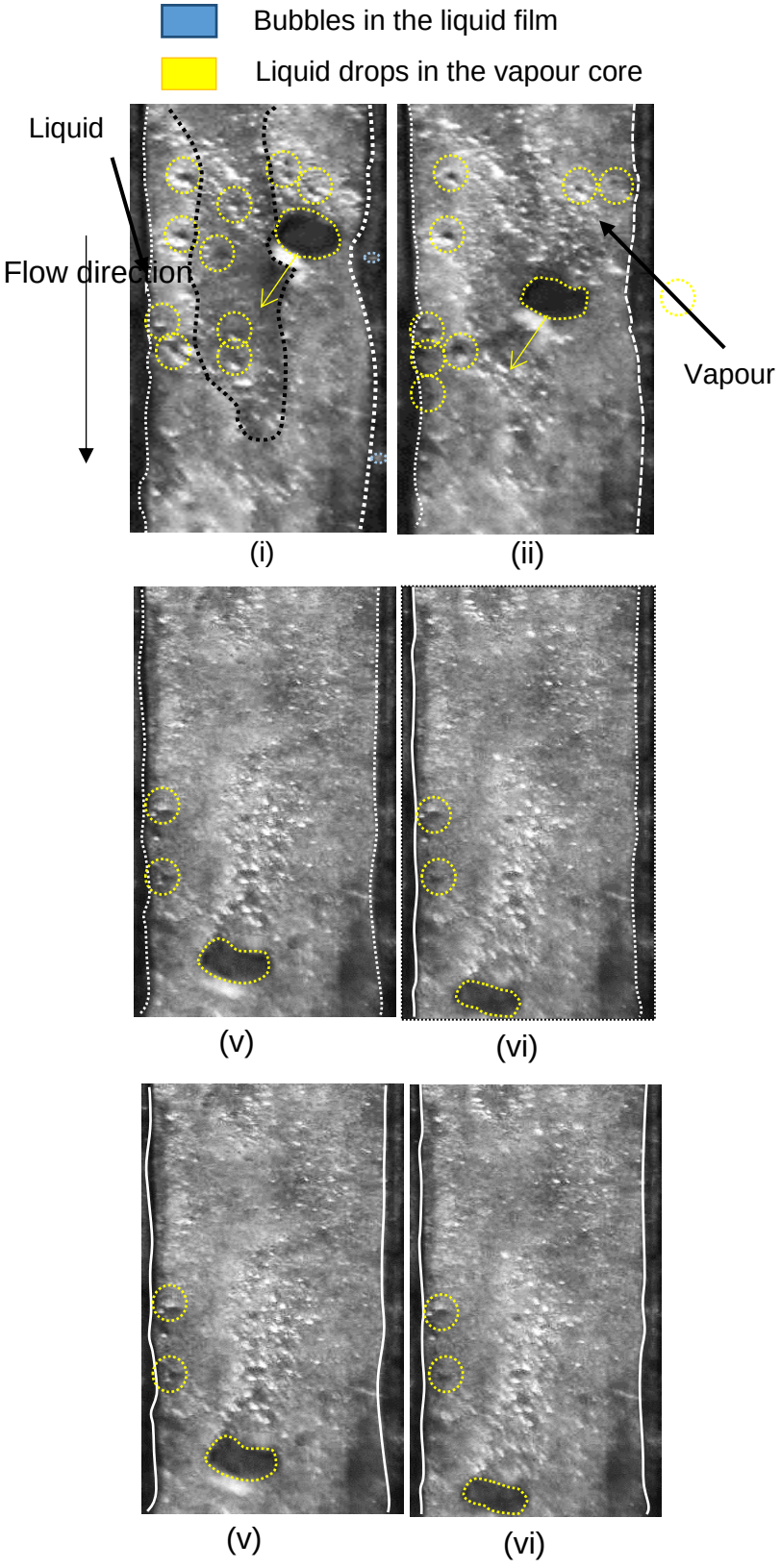

Figure 6. 18 *Annular flow regime with dispersed droplet for G = 147.2 kg m^{-2} s^{-1} and q = 99.7 kW m^{-2}.*

It is found that low values of entrainment result in lower probability of dryout occurrence [86]. Entrainment of mass transfer is in similar or at some situations higher order than evaporation contribution. This issue signifies the necessity of considering entrainment in simulations of fluid flow and heat transfer of annular two-phase flows. Most of the available correlations of entrainment are empirical and often derived for a specific fluid of special conditions and cannot be applied in other situations.

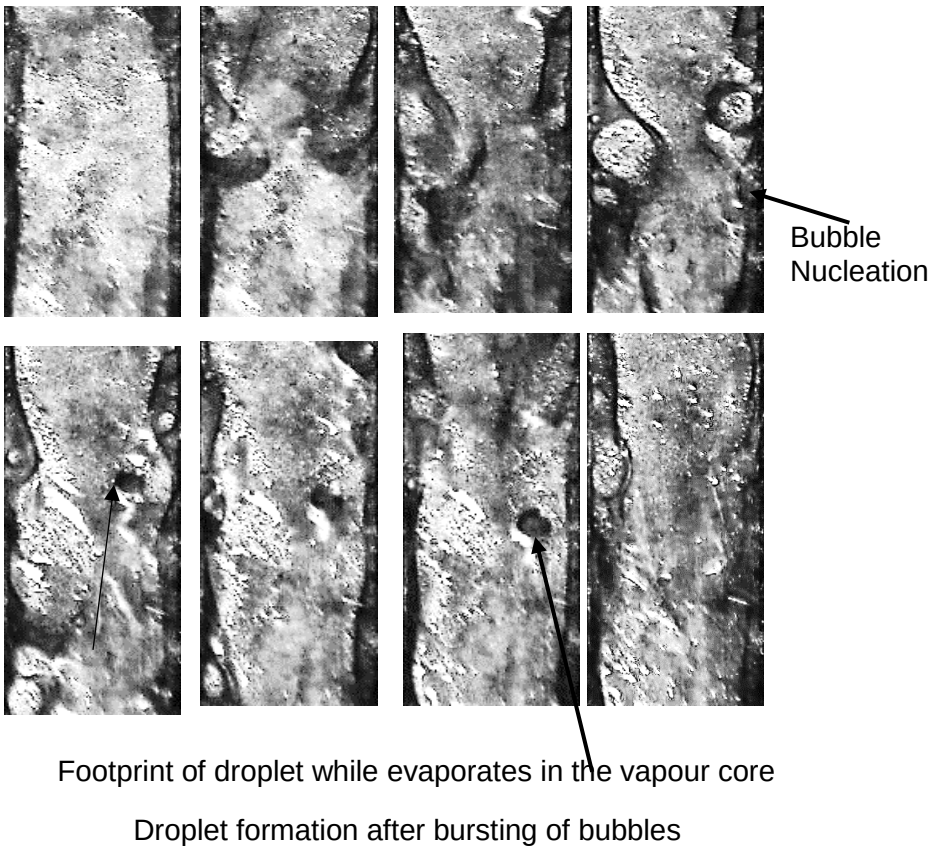

Figure 6. 19 *Churn-annular regime with boiling at the sidewalls and liquid droplets in the vapour core for* $G = 147.2\ kg\ m^{-2}\ s^{-1}$ *and* $q = 99.7\ kW\ m^{-2}$.

.

6.4.2.5.3 Correlation of interfacial wall temperature fluctuations with IR images during annular flow regime.

Vapour phase over the liquid phase in the annular flow regime commonly results in formation of some waves at their interface. These waves play an important role in occurrence of entrainment mass transfer. When a light fluid flows over a layer of a heavier one, their interface becomes unstable when the relative velocity exceeds a critical speed. This instability, known as Kelvin- Helmholtz instability, may occur at the interface of miscible or immiscible

fluids, or within a single fluid in the region of a strong density gradient [126]. The Kelvin Helmholtz instability is of great importance in annular flow heat and mass transfer behaviour.

For an unstable annular flow, interfacial waves grow/ decay exponentially in their amplitude as time spends. While on the contrary, experimental observations found interfacial waves of relatively steady amplitudes in typical annular flows. This issue demonstrates that the interfacial waves of common annular flow regimes are of stable condition and can be assumed to have constant amplitude and wavelength. Interfacial waves are assumed sinusoidal.

Figure 6.20 shows local interfacial wall temperature at the channel and the synchronised pressure drop fluctuations at the centre of the channel as a function of time for G = 147.2 kg m^2 s^{-1} and q = 99.7 kW m^{-2} during one instability cycle (a). The wall temperature fluctuations are produced from the thermal images of Figure 6.21-6.23, recorded with the IR camera from PDMS. Figure 6.21 shows the interfacial wall temperature patterns from t= 19.3423 s to 19.4473 s (duration of 0.105 s) of Figure 6.20.

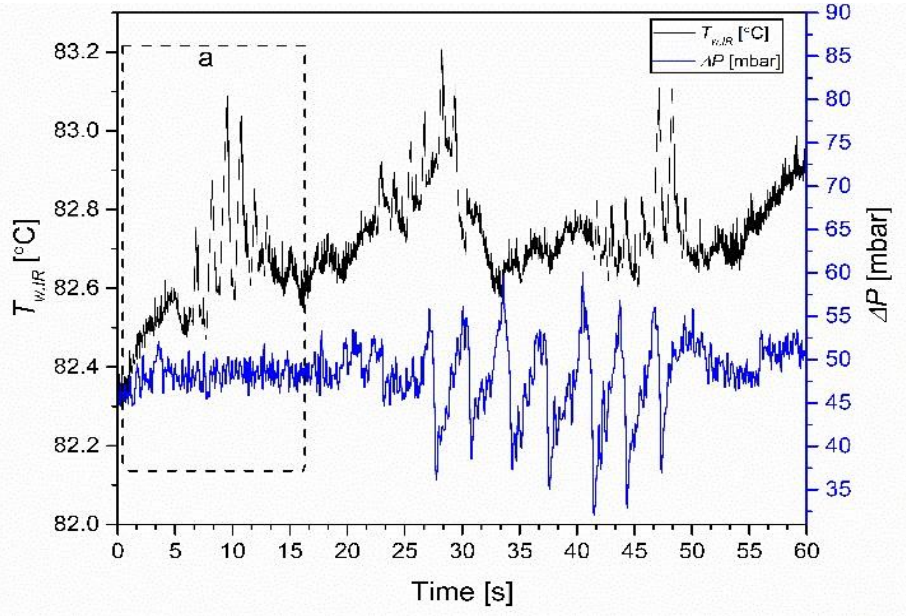

Figure 6. 20 *Local interfacial wall temperature at the channel centre and pressure drop as a function of time for G = 147.2 kg m^{-2} s^{-1} and q = 99.7 kW m^{-2}.*

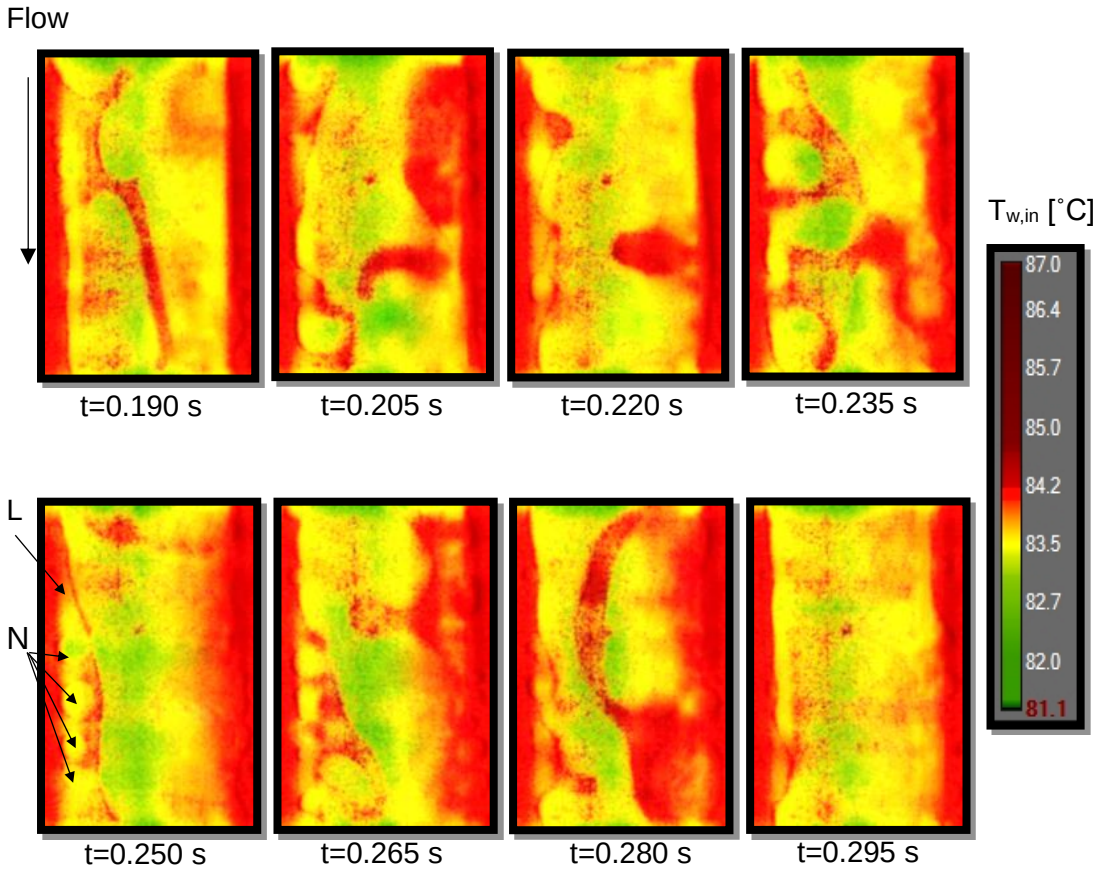

L: liquid **V:** vapour **N:** nucleation of bubbles **D:** dryout **C:**Collision

Figure 6. 21*Image sequence obtained with IR thermal camera from PDMS top of microchannel. The features in the image were identified by simultaneously obtained high speed images. From t = 19.3423 s to 19.4473 s (duration of 0.105 s) related to temperature fluctuations in Figure 6.20 .The above thermal images were captured on the heater base before the initiation of temporal dryout cycles for G = 147.2 kg m^{-2} s^{-1} and q = 99.7 kW m^{-2}.*

.

$T_{w,\,in}$ ranges between 81.1 and 87 °C. The side of the bubble near to the liquid film has lower temperature of 82 ˚C. The flow patterns alternated because of the interactions between slugs and bubbles. Bubbles nucleated from the hot sidewalls (channel corners). The bubbles grow in the liquid film between the sidewall where bubbles were nucleating and growing later in; the liquid appeared to have lower temperature distribution than the right side where little bubbles were nucleating in the thin liquid film. Some areas of channel that were covered with liquid appeared to have very high temperature and this was better clarified form the high-speed images. Higher amplitude temperature oscillations with pressure oscillations. Figure 6.22 shows the temperature during bubble dryout cycles. It it's interesting that annular flow is initially the pattern that provides the highest heat transfer rate as the temperature is uniformly distributed at the channels surface because the liquid (thin) film is evenly distributed.

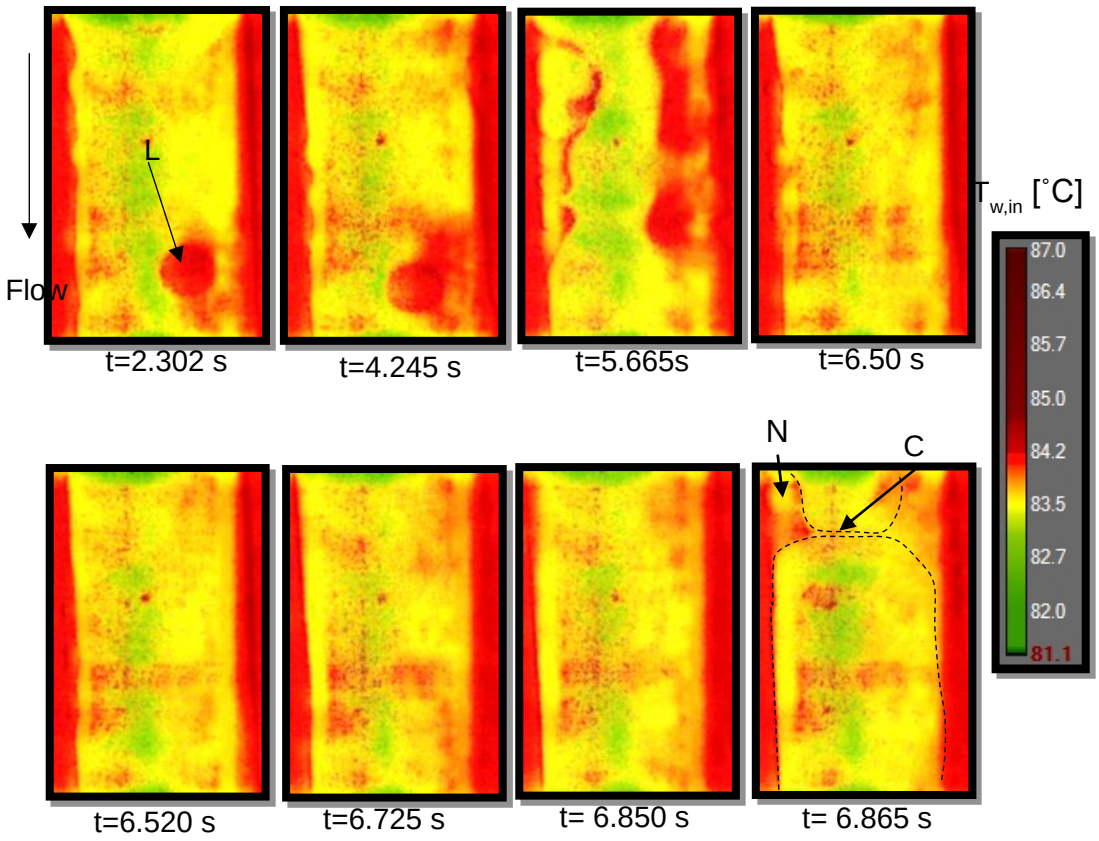

L: liquid **V:** vapour **N:** nucleation of bubbles **D:** dryout **C:**Collision

Figure 6. 22 *Image sequence obtained with IR thermal camera from PDMS top of microchannel. The features in the image were identified by simultaneously obtained high-speed images. From t =21.644 s to t = 26.207 s (duration of 4.563 s) related to temperature fluctuations in Figure 6.20 .The above thermal images were captured on the heater base during instability cycles for G = 147.2 kg m^{-2} s^{-1} and q = 99.7 kW m^{-2}.*

The conclusions from the above thermal IR images is that high local interfacial wall differences were induced during growth of big size bubbles. Based on observations, the superheated film adjacent to the channel sidewalls was identified. However, this liquid film appears to be where the highest temperature has been measured at the heater base. Therefore this means that the IR thermal images reveal that there is better heat removal under slugs were a very thin liquid layer probably evaporates. The hot areas show suspected dryout because of complete liquid evaporation at these locations.

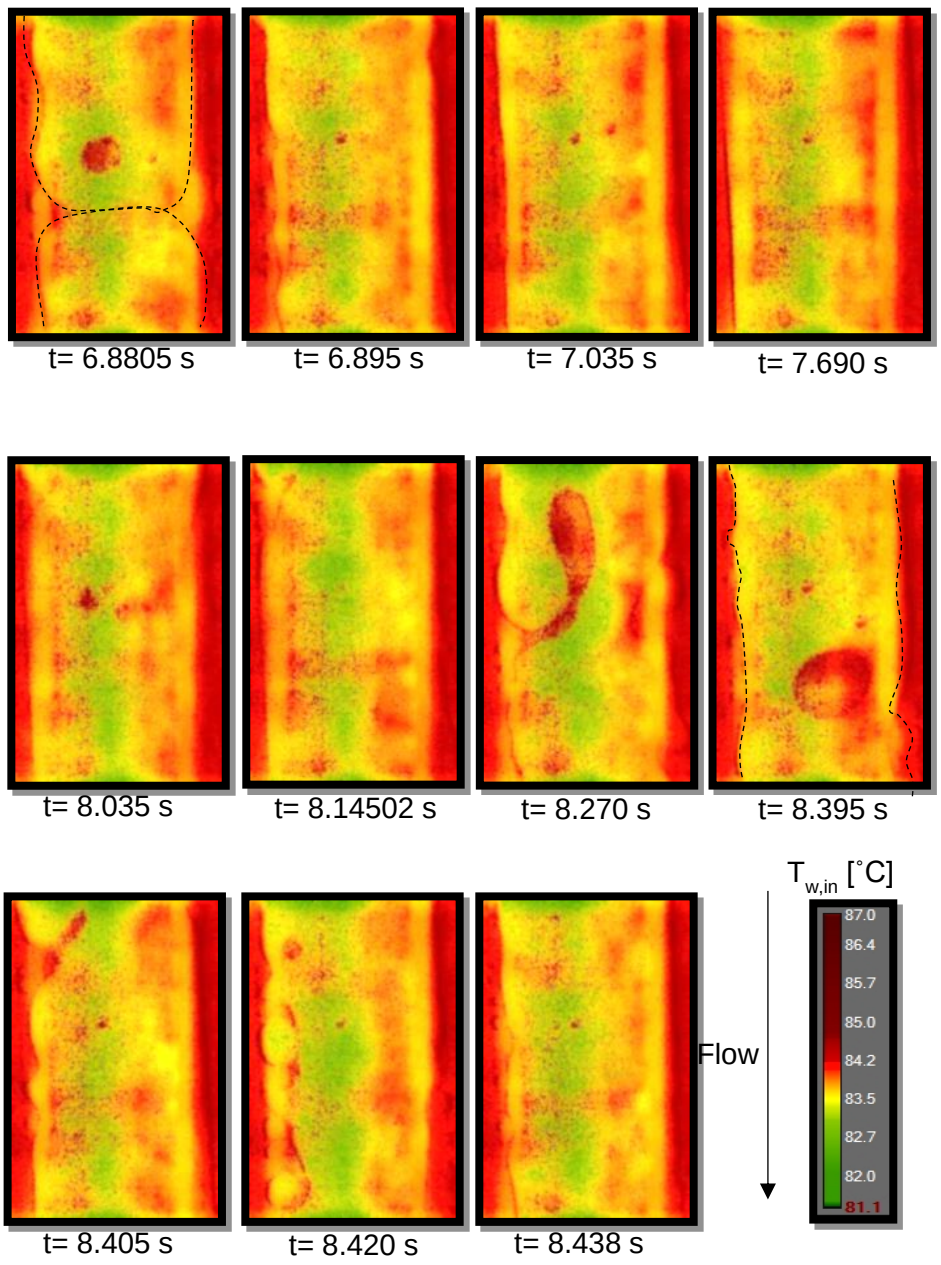

Figure 6. 23 *Image sequence obtained with IR thermal camera from PDMS top of microchannel. The features in the image were identified by simultaneously obtained high-speed images. From t =26.220 s to t = 27.538 s (duration of 1.318 s) related to temperature fluctuations in Figure 6.20 .The above thermal images were captured on the heater base during instability cycles for G = 147.2 kg m^{-2} s^{-1} and q = 99.7 kW m^{-2}.*

Optical image sequences shown in Figure 6.24 illustrate the instability cycle presented in previous thermal images (Figures 6.21 to 6.24) now in optical images from the ITO /glass. Suspected dryout was found to occur on the channel surface. The liquid-vapour distribution on the heater surface was evaluated by the contrast of the images where liquid is black colour and complete vapour is white colour. The scale is represents with numbers from 0 to 255 and show

the intensity. First, the profile across the channel appears to have a slight dip at the middle of the channel. The channel surface first starts to dryout from the centre of the channel.

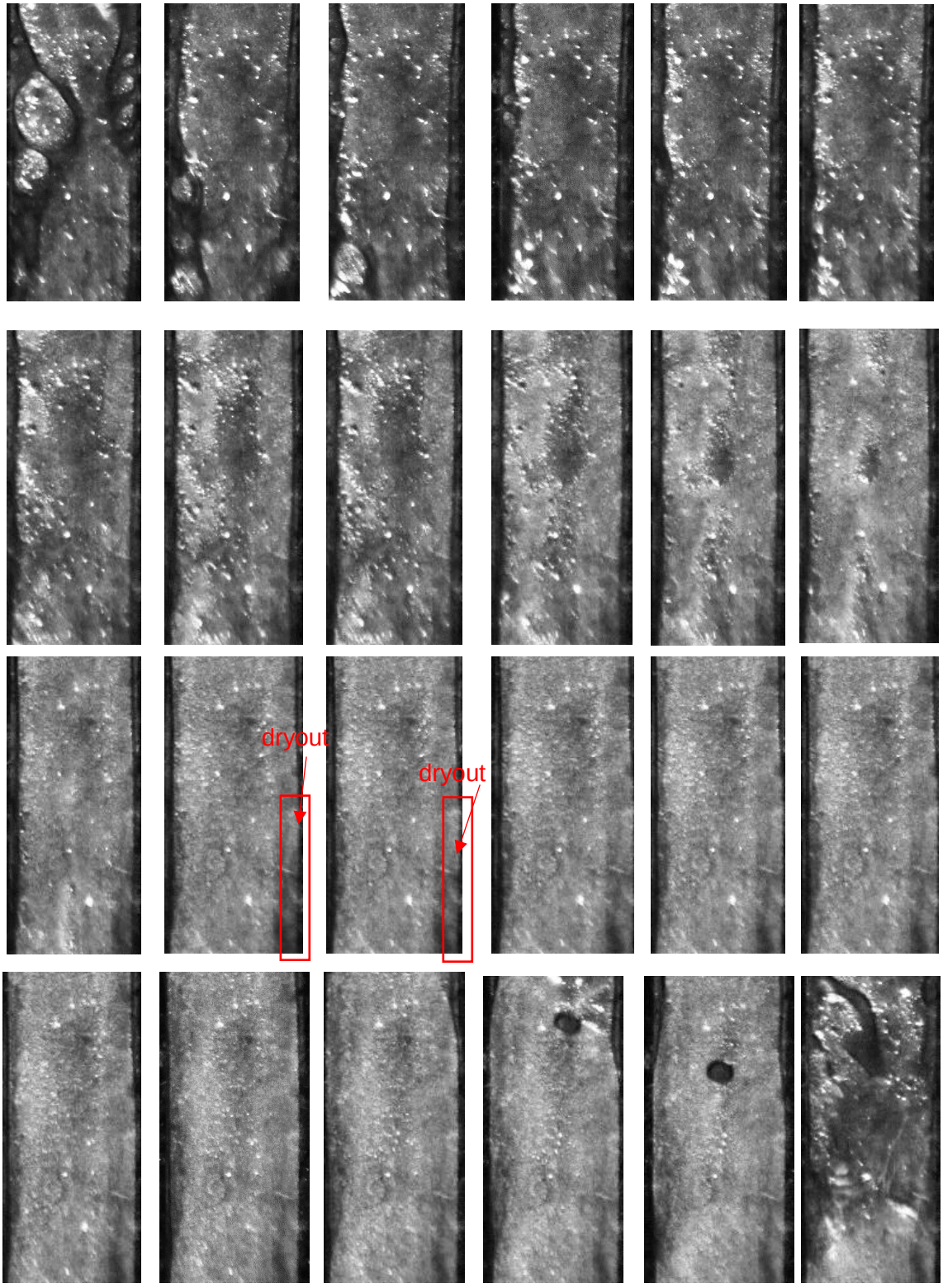

Figure 6. 24 *Image sequence obtained with high-speed camera from the transparent ITO heater at 200 Hz, simultaneously with the thermal images shown in Figures 6.24 to 6.26.*

Therefore, the dryout appears to start along the centreline of the channel and then to the sidewalls. Then rewetting occurs mainly at the channel sidewalls. Wall nucleation starts after channel wall rewetting in the thin liquid film.

6.4.2.6 Critical heat flux

Figures 6.25 shows the critical heat flux (q_c) with increasing mass flux for the inlet, middle and outlet section of the microchannel. From literature [13], the critical heat flux increases with increasing mass flux. In this case, the critical heat flux for each section increases linear with increasing mass flux.

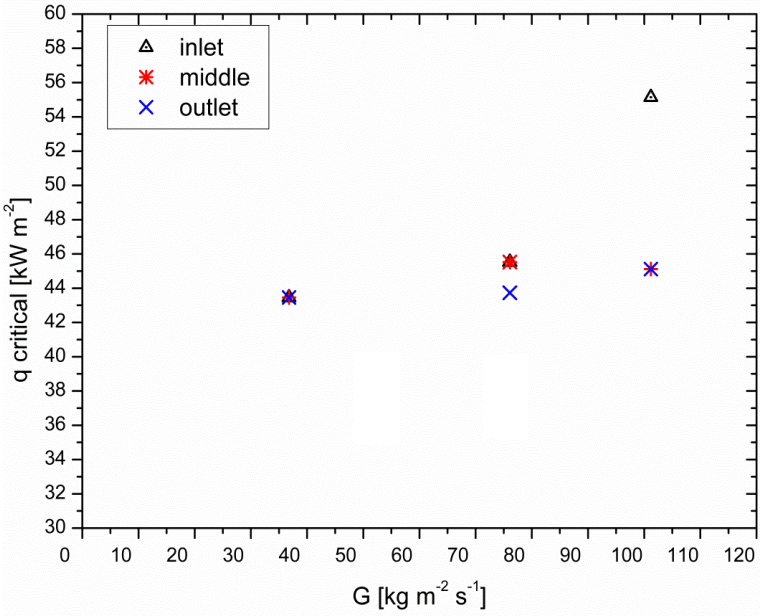

Figure 6. 25 *Critical heat flux (q_c) with increasing mass flux for the inlet, middle and outlet section of the microchannel.*

6.4.3 Interfacial wall temperature fluctuations at inlet, middle and outlet of the microchannel for G = 73.74 kg m^{-2} s^{-1} and q = 38.52 kW m^{-2}

This section presents inner wall temperature ($T_{w,}$) measurements spatially averaged across the channel width. Figure 6.26a shows the temporal $T_{w,}$ profiles at the inlet of the microchannel for G = 73.73 kg m^{-2}s^{-1} and q = 38.54 kW m^{-2}. $T_{w,in}$ is spatially averaged across the microchannel width at three locations of x = 0 mm, 3.3 mm and 6.6 mm. Figure 6.26a also shows the interface wall temperature averaged along the channel centreline of the inlet at flowstream direction. $T_{w,}$ Varied from 61.5 ˚C to 64.6 ˚C across the channel width of the inlet. The average temperature

along the centreline at flowstream direction roughly coincides with the averaged wall temperature across the channel at position of x = 3 mm. The amplitude and frequency of the fluctuations is equal for all the locations. The maximum value of $T_{w,}$ was measured across the microchannel width at 6.6 mm from the entrance and ranged between 62.7 °C to 66.3 °C. $T_{w,}$ fluctuations have the same amplitude across the width and length of the inlet. Figure 6.26b displays $T_{w,}$ fluctuations for smaller time scales of 5 s, 7 s, from Figure6.26a.

Figure 6.27a presents $T_{w,}$ fluctuations at the middle of the microchannel for the same for G = 73.73 kg m^{-2}s^{-1} and q =38.54 kW m^{-2}. $T_{w, \text{in}}$ measurements are averaged across the channel at locations of x = 6.6 mm, x = 9.9 mm and x = 13.2 mm from the channel entrance and along the channel centreline. The lowest averaged temperature values are measured across the entrance of the channel at x = 6.6 mm and they range between 62 to 64 °C. $T_{w,}$ takes the highest values across the microchannel width at 13.2 mm from the entrance and ranges between 63.8 °C to 66. 6 °C. The amplitude of $T_{w,}$ fluctuations across the width of the middle is higher, compared to inlet. Figure 6.27b shows temperature fluctuations from 32 to 40 s. The lowest averaged $T_{w,}$oscillation amplitude was measured along the channel centreline. Figure 6.28a presents $T_{w,}$ fluctuations at the outlet of the microchannel for G = 73.73 kg m^{-2}s^{-1} and q = 38.54 kW m^{-2}. The spatially averaged $T_{w, \text{in}}$ measurements are obtained across the microchannel width at x = 13.2, 16.2 and 20 mm from the channel entrance and they are compared with $T_{w,}$ spatially averaged along the centreline of the outlet. The lowest value of the average temperature is measured across the width at x = 13.2 mm from the channel entrance and ranges between 62.8 to 64.2 °C. The highest value of $T_{w,}$ is measured across the microchannel width at 13.2 mm from the entrance and ranges from 63.8 °C to 66.6 °C. $T_{w,}$ fluctuations at the outlet occur at higher frequencies compared to the inlet and the middle. The amplitude of the oscillations is higher across the microchannel width compared to the length. $T_{w,}$ along the channel centreline oscillated less compared to the fluctuations at the cross section. Figure 6.28b shows $T_{w,}$ fluctuations from 25 to 35 s.

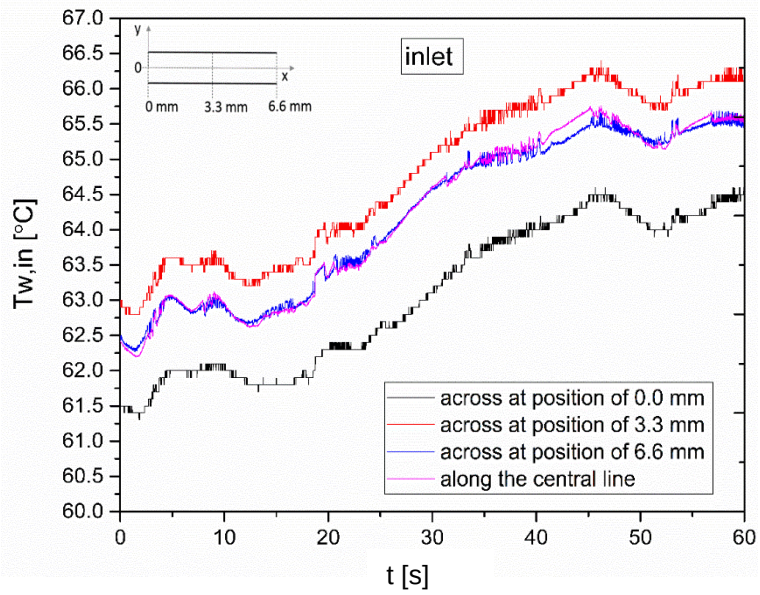

(a)

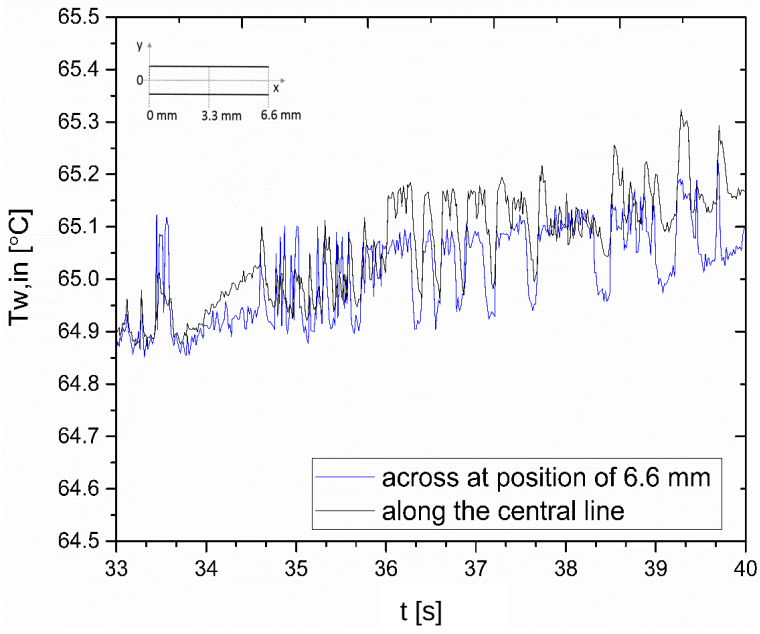

(b)

Figure 6. 26 *(a)Inner wall temperature fluctuations spatially averaged across the channel width at x= 0 mm, 3.3 mm and 6.6 mm from the channel entrance and along the channel centreline at flowstream direction of the inlet for G = 73.74 kg m^{-2} s^{-1}and q = 38.54 kW m^{-2} and (b) zoom in inner wall temperature fluctuations from 33 to 40 s.*

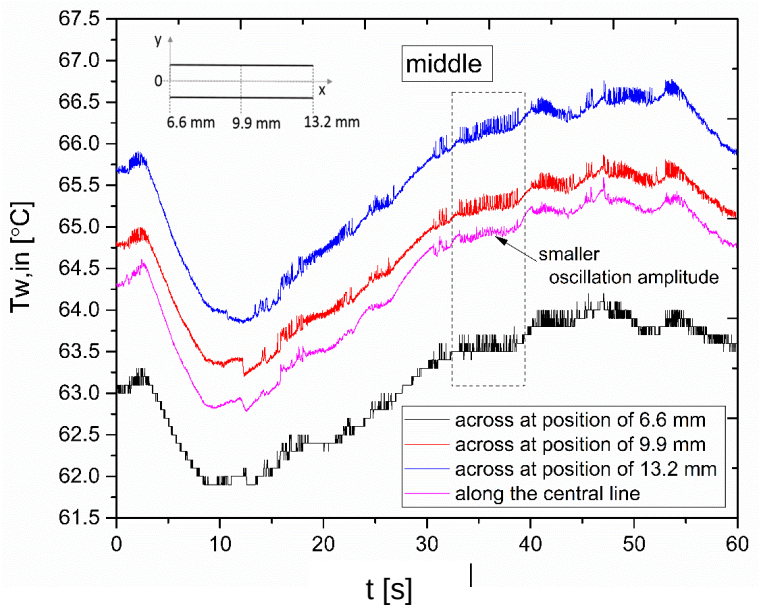

(a)

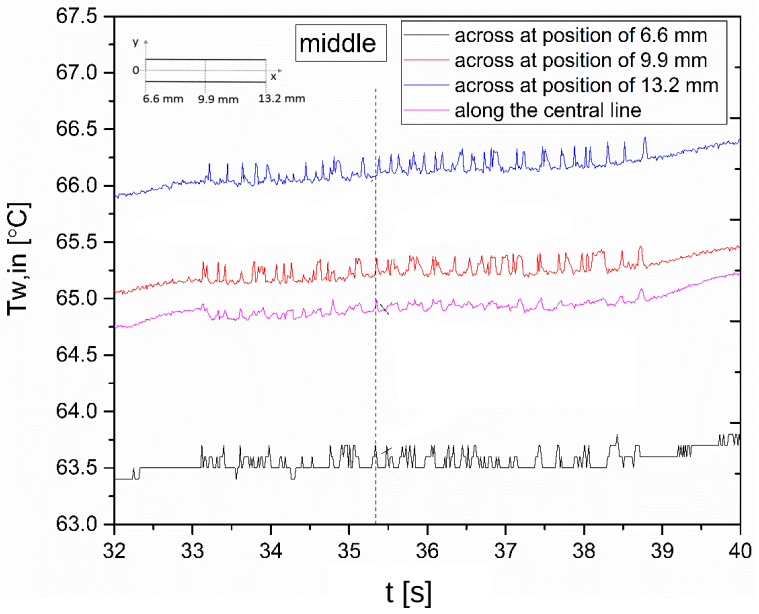

(b)

Figure 6. 27 *(a) Interfacial wall temperature fluctuations measured at x = 6.6 mm, 9.9 mm and 13.2 mm from the channel entrance. Spatially averaged across the microchannel and along the channel centreline for the middle of the microchannel for G = 73.74 kg m^{-2} s^{-1} and q = 38.54 kW m^{-2} for the time interval of 60 s and (b) zoom in the interfacial wall temperature fluctuations from 32 to 40 s.*

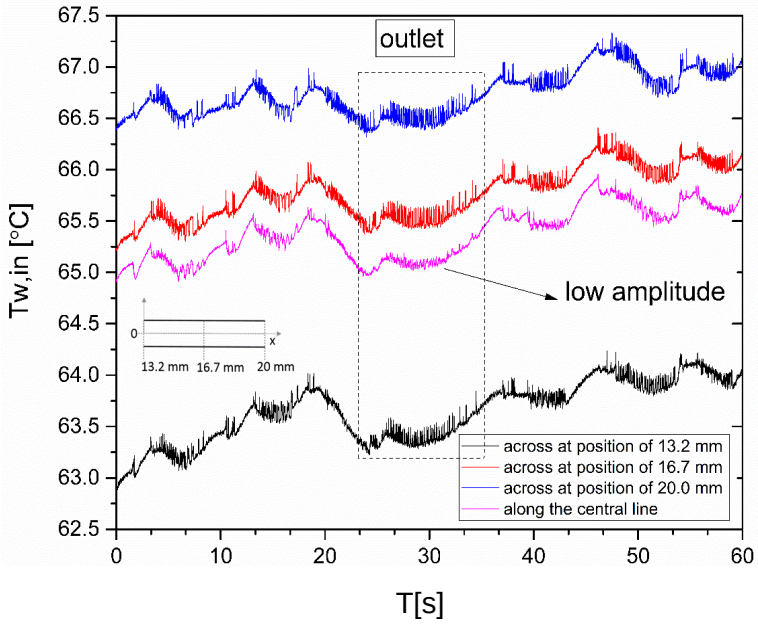

(a)

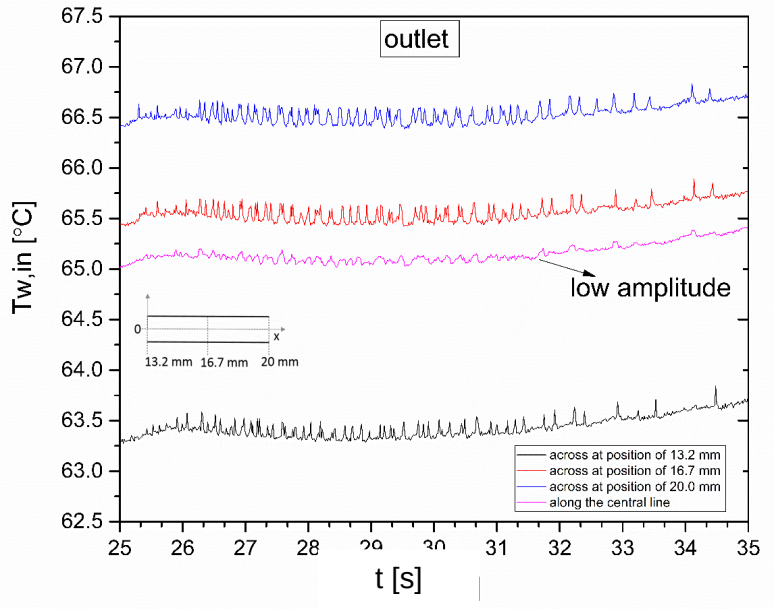

(b)

Figure 6. 28 *(a) Inner wall temperature fluctuations measured at three positions (13.2 mm, 16.2 mm and 20 mm) across the microchannel and along the channel central line for the outlet of the microchannel for G =73.74 kg m^{-2} s^{-1}and q=38.52 kW m^{-2} for a time interval of 60 s (b) interfacial wall temperature fluctuations from 25 to 35 s .*

Figure 6.29a presents $T_{w,}$ fluctuations at the outlet of the microchannel for G = 73.73 kg m^{-2}s^{-1} and q = 38.54 kW m^{-2} with $T_{w,}$was averaged spatially along the lines of outlet obtained at

three locations (y = -1.13, 0 and 1.13 mm). The temperature values at the channel corners (y = -1.13, 1.13 mm) are higher than the channel centre (y = 0 mm). $T_{w,in}$ at the sidewall corners approaches the $T_{w,in}$ values at the channel centre when they are at their maximum values but they deviate when from $T_{w,in}$ at the channel centre when they decrease with time. Figure 6.29b shows $T_{w,}$fluctuations from 30 to 50 s.

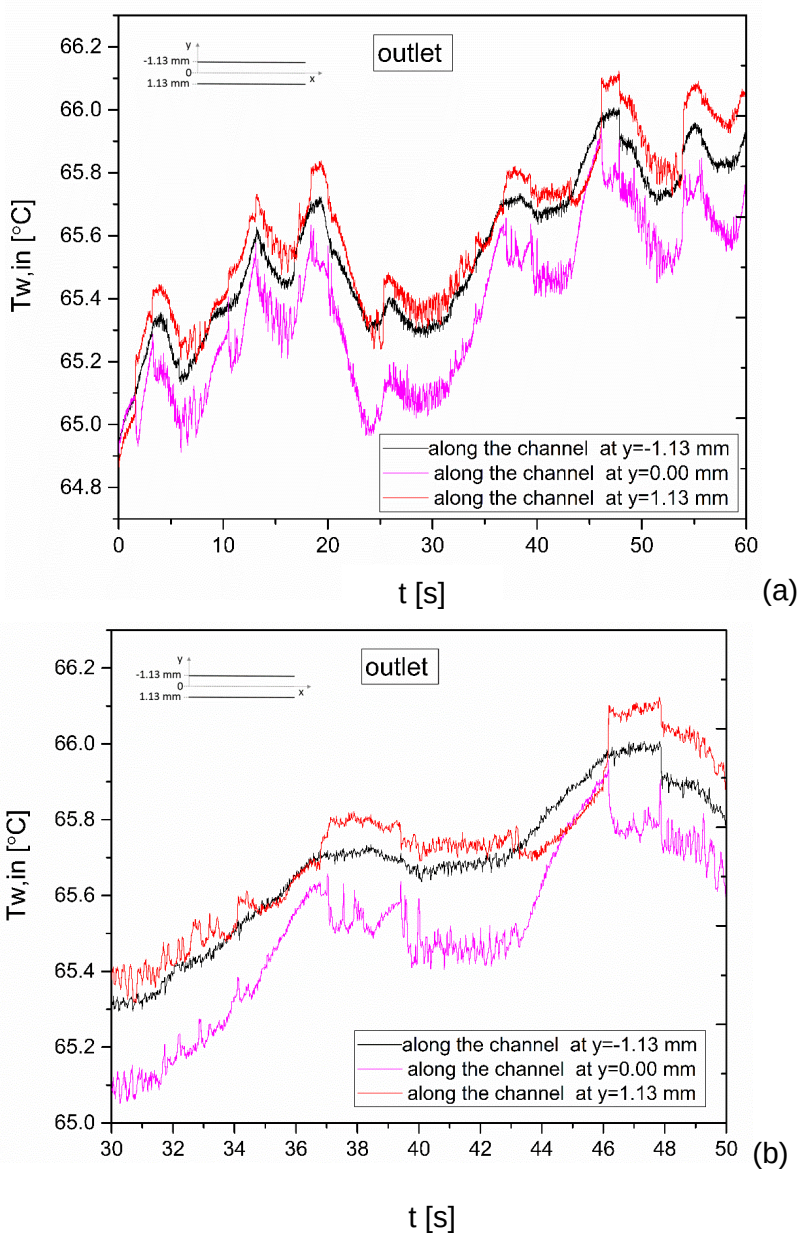

Figure 6. 29 *(a) Inner wall temperature fluctuations measured at three positions (at the corners: -1.13 mm, 1.13 mm and 0 mm centre) across the microchannel of the outlet for* G *= 73.74 kg* m^{-2} s^{-1} *and* q *= 38.52 kW* m^{-2} *and (b) fluctuations of* $T_{w,in}$ *from 30 to 50 s.*

6.4.4 Interfacial two-phase heat transfer coefficient and simultaneous pressure drop fluctuations

3D plots of spatially averaged $h_{tp,in}$ along the centreline of the channel for the inlet, middle and outlet for G = 73.74 kg m^{-2} s^{-1}and q = 38.52 kW m^{-2} are shown in Figure 6.30.

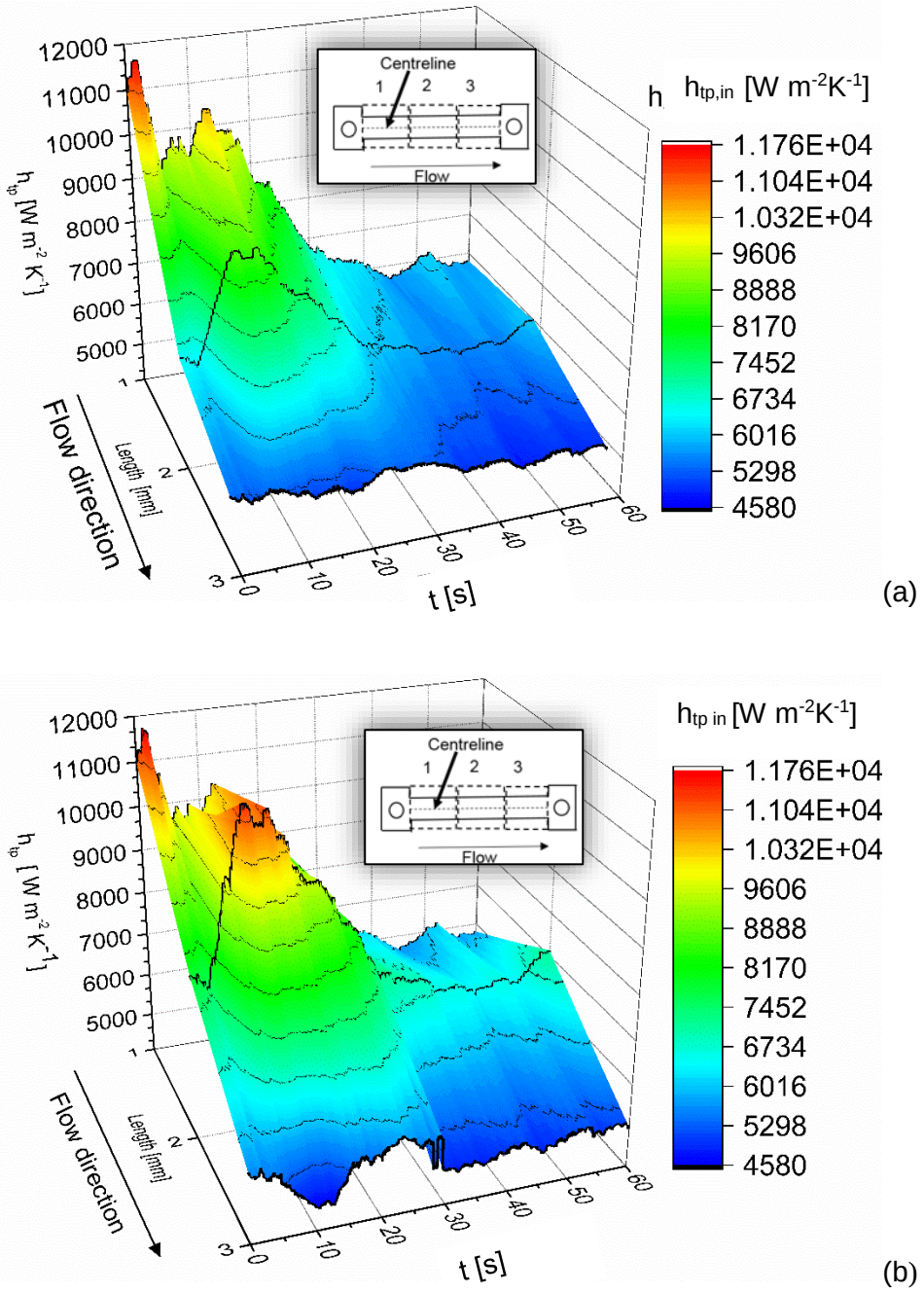

Figure 6. 30 *(a) 3D plot of spatially averaged h_{avg} along the centreline for the inlet, middle and outlet for G = 73.74 kg m^{-2} s^{-1}and q = 38.52 kW m^{-2}, $h_{tp,in}$ was obtained from time averaged pressure and (b) 3D plot of spatially averaged $h_{tp,in}$ along the centreline for the inlet, middle and outlet for G = 73.74 kg m^{-2} s^{-1}and q = 38.52 kW m^{-2}. $h_{tp,in}$ was obtained from local pressure as a function of time.*

In Figure, 6.30a $h_{tp,}$ is obtained from time-averaged pressure. In contrast, in Figure 6.30b the $h_{tp,}$ is obtained along the centreline for the inlet, middle and outlet for G = 73.74 kg m^{-2} s^{-1} and q = 38.52 kW m$^{-.2}$. $h_{tp,}$ *is* obtained from local pressure as a function of time. Figure 6.31 shows h_{tp} as function of time for 60 s time interval at the constant mass flux of G = 36.87 kg m^{-2}s^{-1} and heat fluxes of q = 45.50 kW m^{-2} (Figure 6.31a), q = 52.92 kW m^{-2} (Figure 6.31b) and q = 57.13 kW m^{-2} (Figure 6.31c).

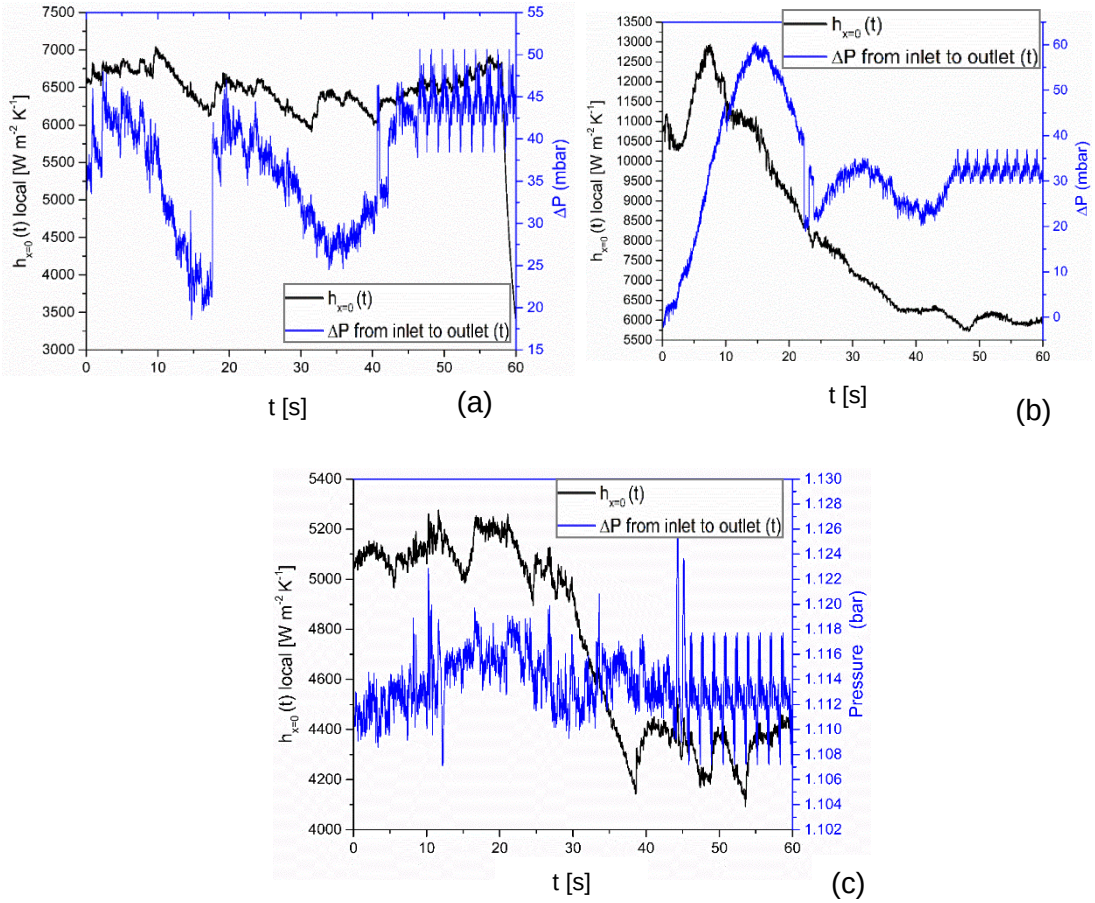

Figure 6. 31 *Local heat transfer coefficient fluctuations obtained at entrance (x =0 mm and y =0 mm) of the microchannel and simultaneous pressure drop fluctuations for (a) G = 36.87 kg m^{-2} s^{-1}and q = 45.50 kW m$^{-.2}$, (b) G = 36.87 kg m^{-2} s^{-1}and (c) q = 52.92 kW m$^{-.2}$.*

Figure 6.32 shows in smaller time scale from 5 to 15 s the results of Figure 6.31c. Figure 6.33 presents local heat transfer coefficient measured at x = 0 mm with simultaneous pressure drop for higher mass flux of 73.74 kg m^{-2} s^{-1}and q = 38.52 kW m$^{-.2}$.

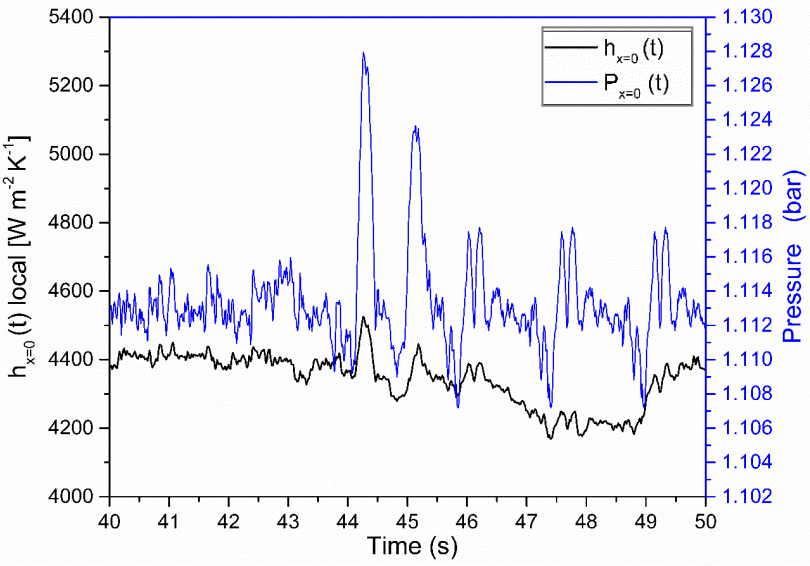

Figure 6. 32 *Local heat transfer coefficient with simultaneous local pressure fluctuations from 5 to 15 s of Figure 6.31c.*

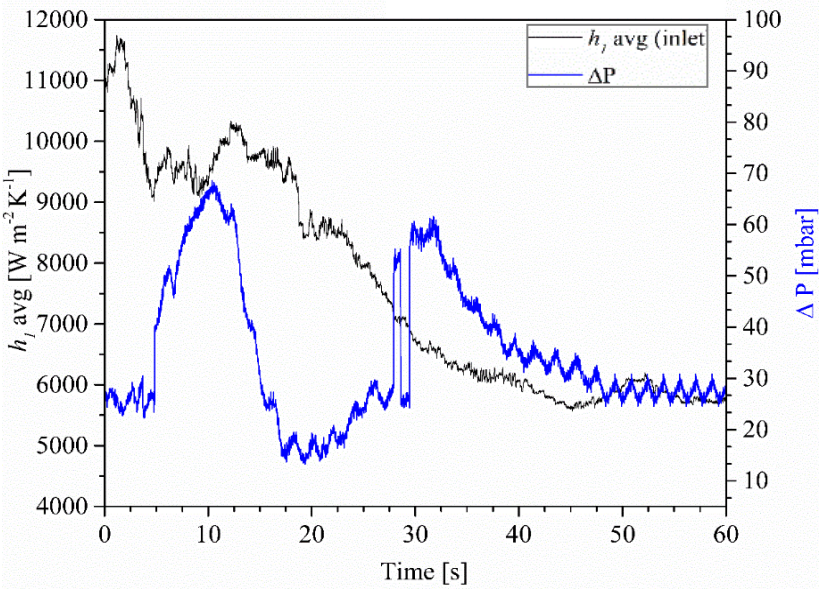

Figure 6. 33 *Local heat transfer coefficient measured at x= 0 mm with simultaneous pressure drop for G = 73.74 kg m^{-2} s^{-1}and q = 38.52 kW m^{-2}.*

6.4.5 Determination of the liquid-vapour distribution on the channel surface

High-speed visualisation is used from the transparent *ITO/glas*s channel base in order to produce high quality optical images and evaluate the liquid distribution on the channel base.

The snapshots of the observed flow patterns are recorded at 200 Hz. The high quality optical images are further processed using a *Matlab* code presented in the end of Appendix A, which extracts the noise from the image. The histograms of the images are produced and are shown below in 2D plots.

Figure 6.34 shows the distribution of the liquid and vapour phases on the channel inlet section surface by the number of pixels of the image as a function of intensity. The existence of liquid, vapour phase or both phases is represented with the intensity$I$, which has a scale from 0 to 256. The minimum of the scale, 0 is represented with the black colour in the 2D plots and is related with the liquid phase. The maximum of the scale is the number 256, represented with white colour in the 3D plots and is related with the vapour phase. The grey colour is related with liquid film thinning and existence of both phases on the channel surface. The high- speed images are captured at the channel inlet.

For the observed flow patterns, both liquid and vapour phase are found to exist at the channel inlet surface. The colour intensity changes from black to white when the liquid on the channel surface evaporates temporally and only vapour exists. At t = 0 s, the snapshot in correlation with Figure 6.35 shows that there is uniform distribution because there is liquid on the surface. However, the parts under the bubbles show no-uniformity and values I ranges between 140 and 180. Figure 6.35 high-speed images are recorded from ITO coated transparent heater presented in Figure 6.36. Figure 6. 36 shows the optical image sequence contained simultaneously from the ITO / glass transparent channel base at the heat flux of q = 38.54 kW m^{-2} where the maximum heat transfer coefficient occurs at G = 73.74 kg m^{-2} s^{-1}.

For the 3D plots presented in Figure 6.36 is used indexing syntax to view only 1 out of 8 pixels in each direction. Otherwise, the surface plot would be too dense. In the surface display, [0, 0] represents the origin, or upper-left corner of the image. This method was used with the histograms in order to identify the suspected dryout locations on the channel base. Temporal dryout is identified only at the outlet channel section of the microchannel at the highest power of q = 45 kW m^{-2}. Observed during slug flow only at annular flow regime. Figure 6.37a shows the liquid-vapour distribution on the heater during bubbly flow. The liquid-vapour distribution is different in each flow pattern therefore is non-uniform. The bubbles grow adjacent to the channel side at flow direction. Liquid is identified below the bubbles because of uniform pixel density (Figure 6.37c). At this position, a peak occurs when the slug occupies the entire cross section (Figure 6.37f). Then annular flow regime is establishes in the channel.

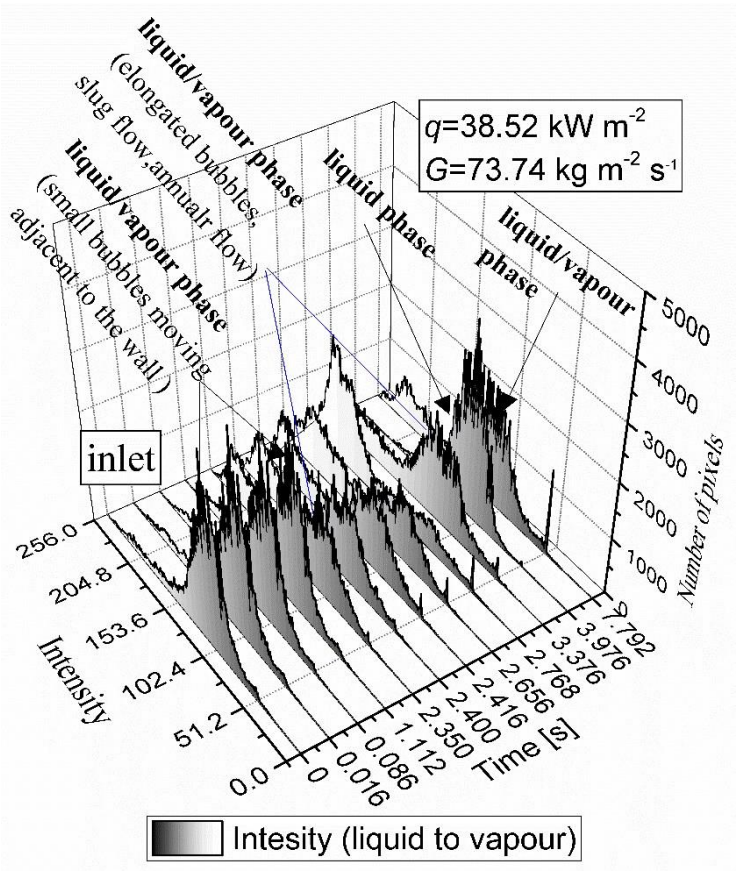

(a)

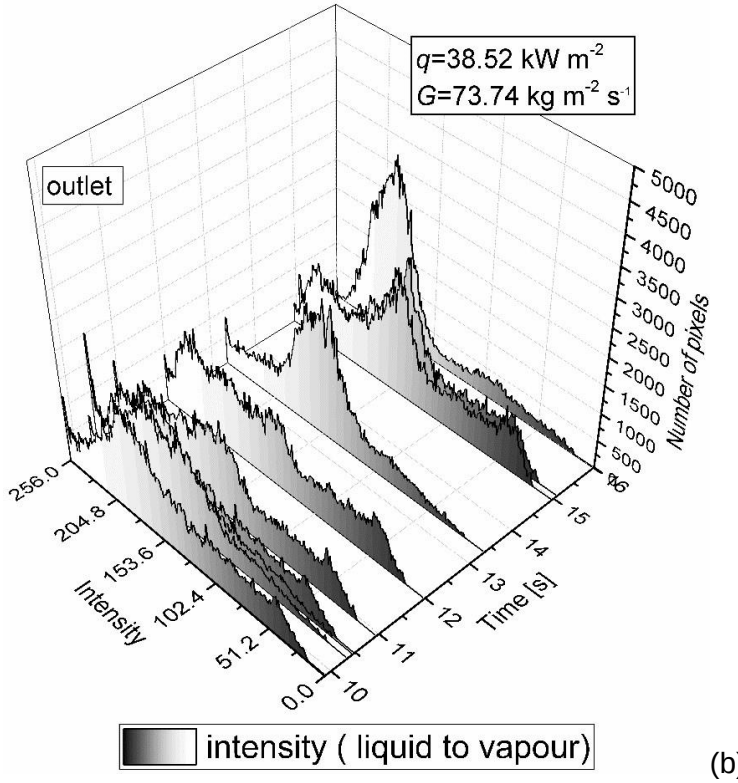

(b)

Figure 6. 34 *Number of image pixels as a function of time and intensity.*

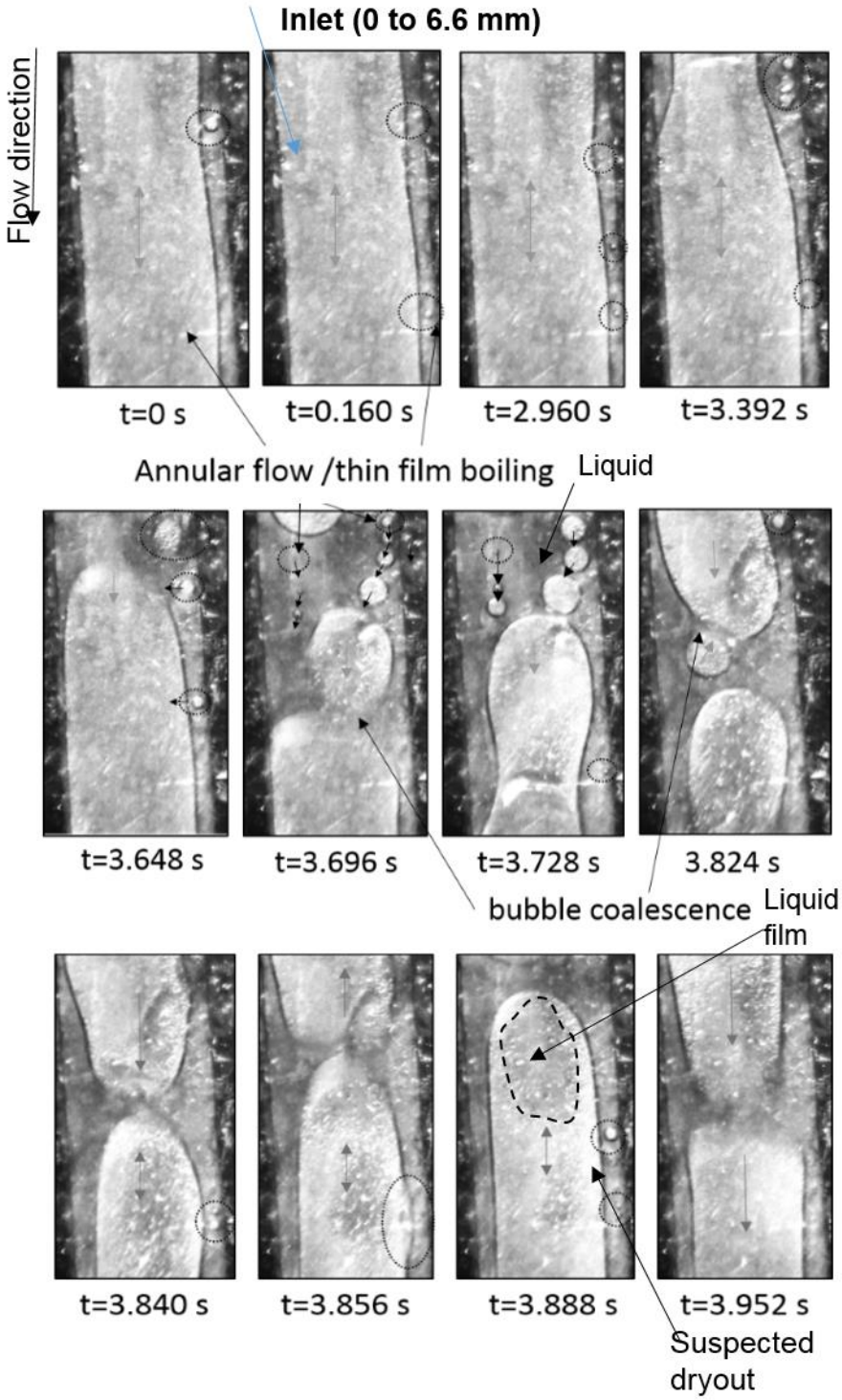

Figure 6. 35 *High-speed image sequences obtained from the transparent ITO heater base with for q = 38.54 kW m^{-2} where the maximum heat transfer coefficient occurs at G = 73.74 kg m^{-2} S-1.*

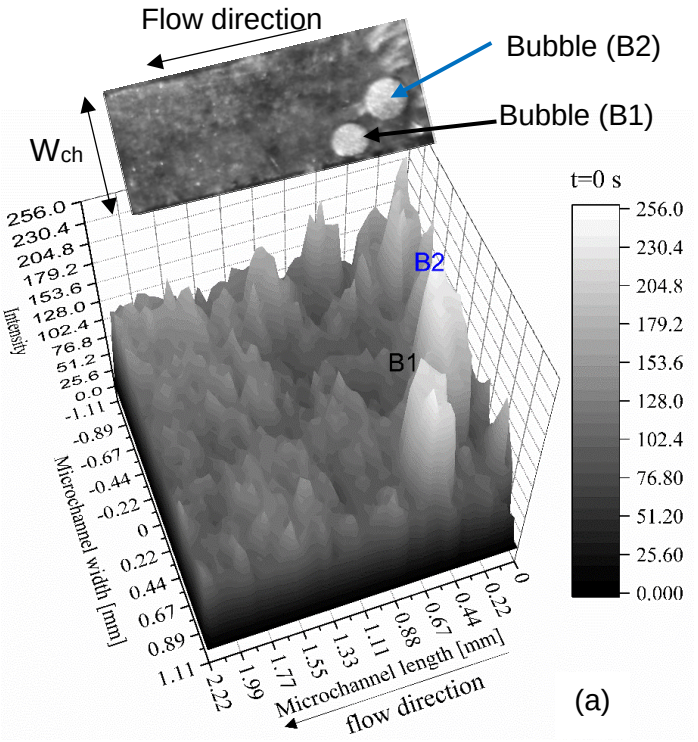

(a) 3D plot of pixel intensity as a function of channel width and length for the inlet during bubble growth near the sidewall corner. Flow direction is from the right to the left.

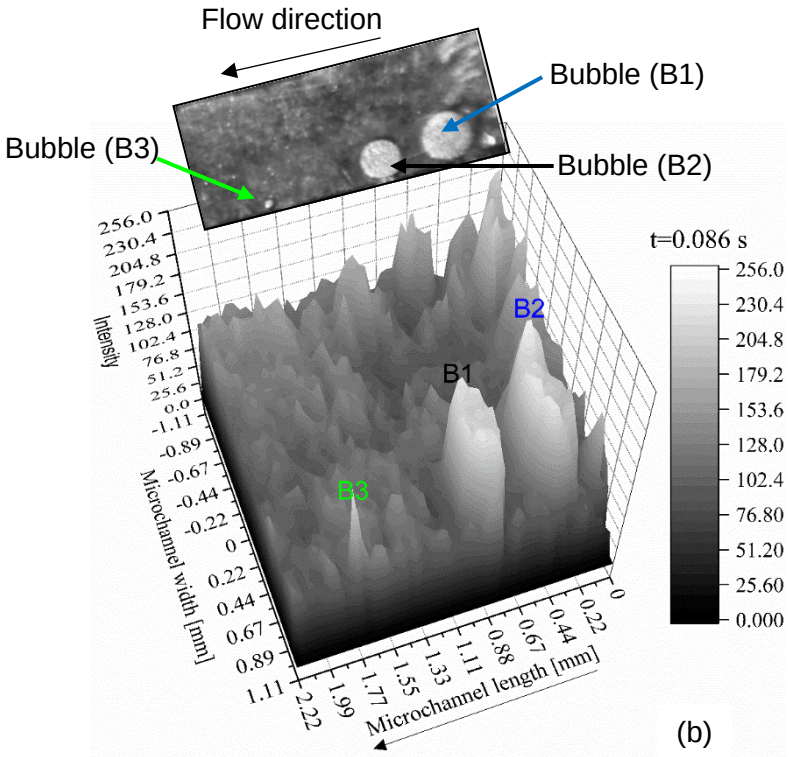

(b) 3D plot of pixel intensity as a function of channel width and length for the inlet after merging of the vapour bubbles near the sidewall corner. Flow direction is from the right to the left.

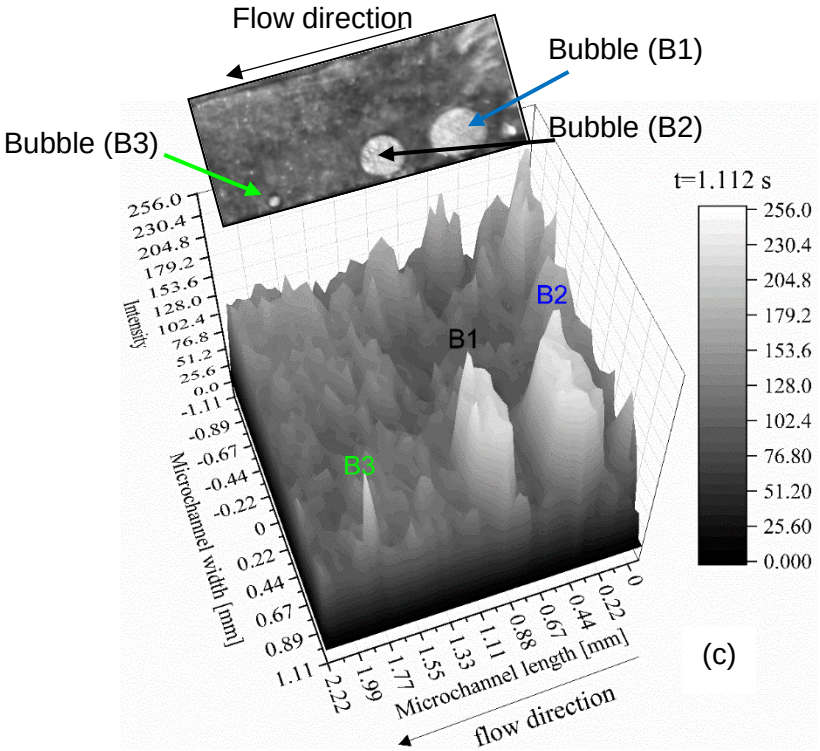

(c) 3D plot of pixel intensity as a function of channel width and length for the inlet during bubble growth near the sidewall corner. Flow direction is from the right to the left.

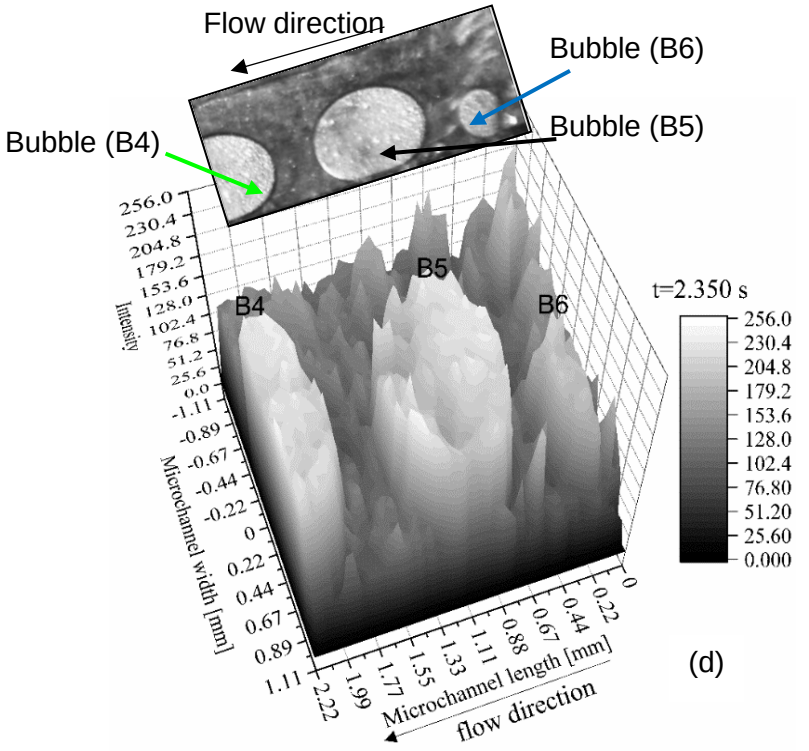

(d) 3D plot of pixel intensity as a function of channel width and length for the inlet during bubble growth near the sidewall corner. Flow direction is from the right to the left.

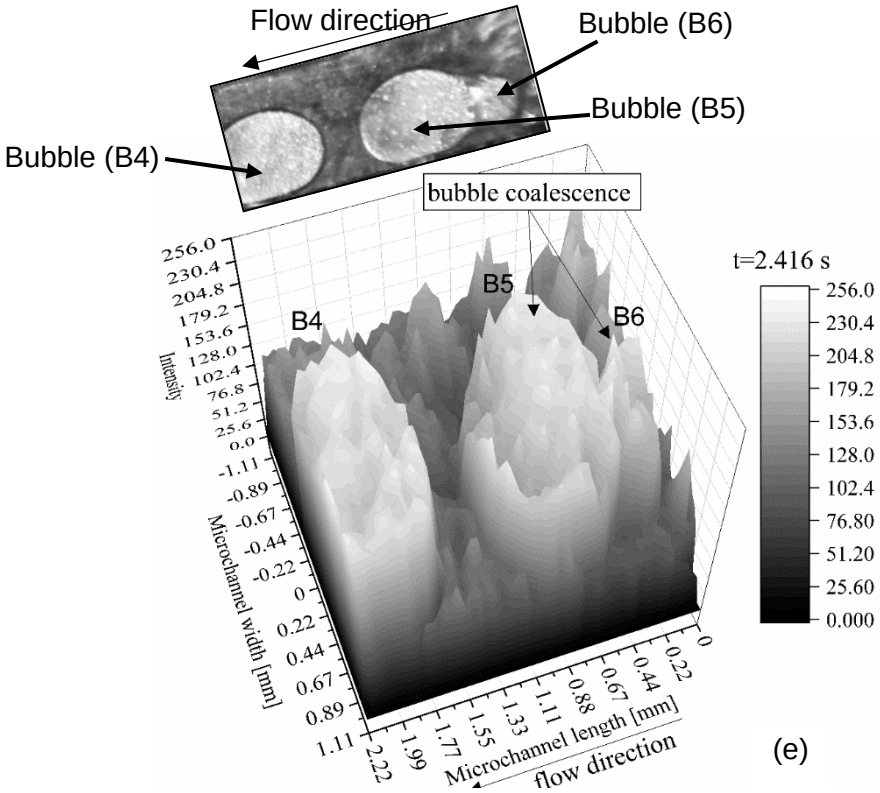

(e) 3D plot of pixel intensity as a function of channel width and length for the inlet during bubble growth coalescence. Flow direction is from the right to the left.

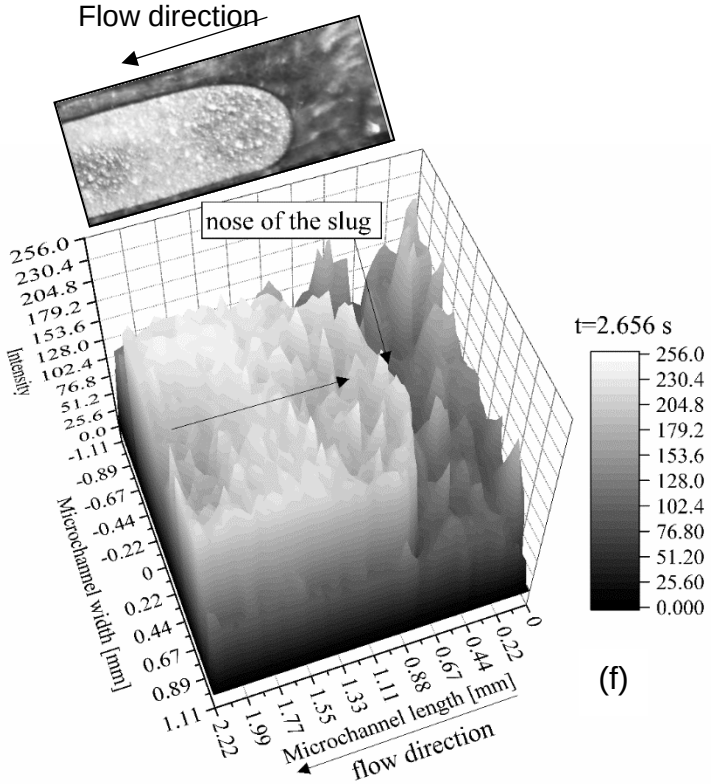

(f) 3D plot of pixel intensity as a function of channel width and length for the inlet during confined bubble axial growth opposite to flow direction. Flow direction is from the right to the left.

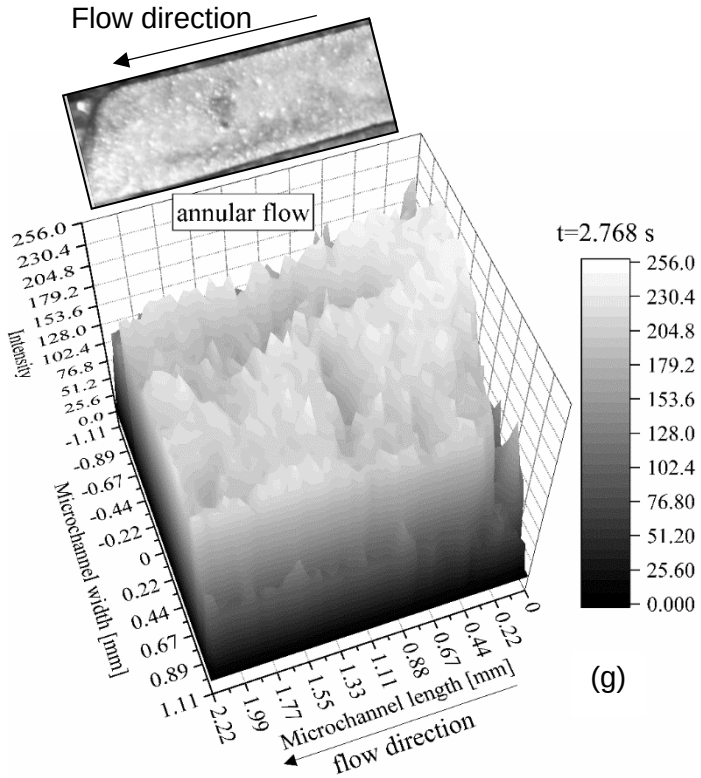

(g) 3D plot of pixel intensity as a function of channel width and length for the inlet during annular flow regime. Flow direction is from the right to the left.

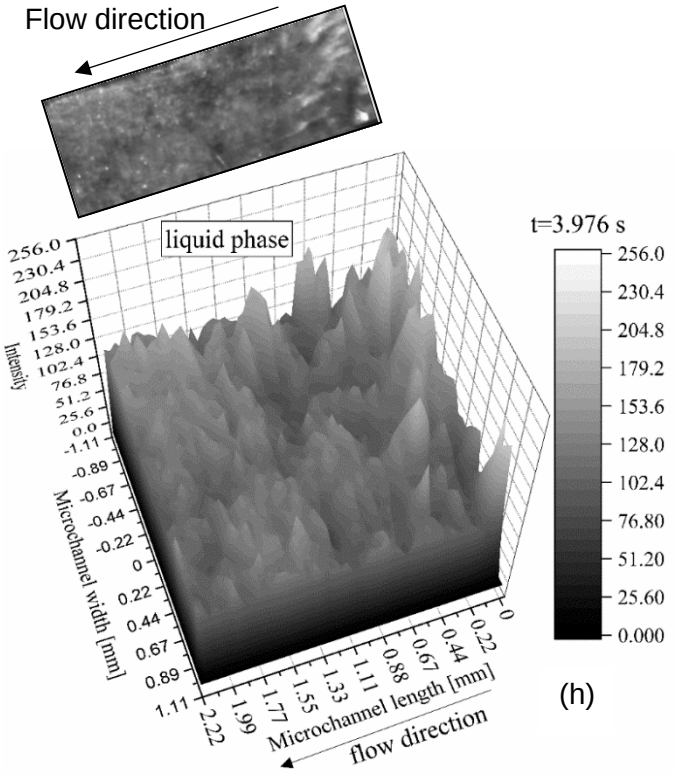

(h) 3D plot of pixel intensity as a function of channel width and length for the inlet during liquid single-phase flow. Flow direction is from the right to the left.

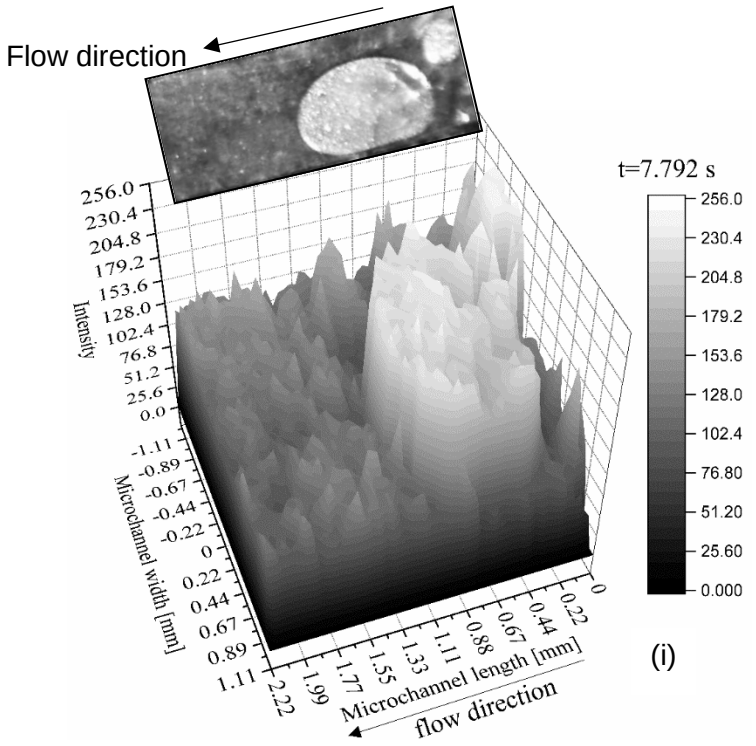

(i) 3D plot of pixel intensity as a function of channel width and length for the inlet during new periodic cycle of bubble growth adjacent to the sidewall corner. Flow direction is from the right to the left.

Figure 6. 36 *3D histograms (a), (b),(c),(d),(e),(f),(g),(h),(i))with flow visualisations from the heater base that verify dry areas. Colour intensity is plotted in function of inlet channel width and length for* q *= 38.54 kW m*$^{-2}$ *where the maximum heat transfer coefficient occurs at* G *= 73.74 kg m*$^{-2}$ *s*$^{-1}$.

6.4.6 Inner wall temperature distribution of the bubble during single bubble growth

Wall temperature patterns at the evaporating liquid-vapour interface of the channel wall during single bubble growth is revealed in Figure 6.37. The selected IR images of Figure 6.38 show the interfacial wall temperature patterns of the basic single bubble growth stages from nucleation to full confinement by depth and width of the microchannel. The presented high spatial and temporal resolution interfacial wall temperature maps of single bubble growth were captured at 200 Hz from the transparent to midwave infrared PDMS side at the channel outlet. Single bubble growth during flow boiling of *FC-72* is examined at the low G = 24.26 kg m^{-2} s^{-1} and q = 16.88 kW m^{-2} at T_{in} = 21 ± 1 °C.

The ability of the qualified method to detect temperature changes within high sensitivity of 0.2 ˚C is confirmed from the details and flow features revealed in the IR images presented in Figure 6.37. The infrared images are correlated with high-speed visualisation images from the

channel base and the bubble growth stages are discussed below. The high spatial resolution IR images reveal non-uniform interfacial wall temperature at the bubble base. The inner wall temperature at the bubble base shown in Figures 6.37a to e is measured lower than the surrounding temperature, in the range between 53.8 to 57.4 ˚C. The temperature range appears to be lower than the saturation temperature of FC-72. Bubble nucleation occurred from the channel sidewall where a superheated liquid layer with temperature in the range of 60 to 60.7 ˚C is observed in Figure 6.37a. Initially bubble grows symmetrically up to Figure 6.37g and maintains a spherical shape. The symmetrical growth of the bubble continuous up to Figure 6.37i with non-spherical shape because of the surrounding liquid evaporation at width-wise direction. Asymmetrical bubble growth commences in Figure 6.37j where the bubble width is approaching the channel cross section width and reaches the centreline of the channel, where drag force is more evident on the bubble. The drag force from the surrounding liquid is responsible for the deformation of the bubble liquid-vapour interface at flow direction (side a). In contrast, the interface of the bubble that is in contact with the liquid at side b (opposite to flow) appears to grow faster at opposite to flow direction. The deformation of the interface from the side opposite to flow direction is more rapid and it occurs due to evaporation of the surrounding liquid (yellow colour layer) that is thicker from this side and ranges from 58 to 58.4 ˚C. The bubble stops growing asymmetrically when it reaches the size of the channel cross section as shown in Figure 6.38o and starts to grow rapidly in axial direction. Figure 6.37o shows that the effect of drag force on bubble growth is no longer significant when the bubble occupies the entire channel cross section.

The *IR* snapshots reveal details of the single bubble growth stages. The frame rate of the *IR* camera was 200 Hz and the experiment was carried out for G = 23.59 kg m^{-2} s^{-1} and q = 16.88 kW m^{-2} using FC-72 in a high aspect PDMS microchannel. Important features are revealed from the high spatial resolution *IR* images in Figure 6.37. The appearance of a superheated liquid layer (red colour) between the bubble and the sidewall with initial maximum thickness of is important feature and has not been experimentally investigated in previous flow boiling experimental studies. Mukherjee and Kandlikar [82] predicted the existence of a thermal layer with uniform thickness which decreases from inlet to outlet and is greater than 0.2 mm. At this point, the superheated layer diminishes because of the occupation of the channel cross section by the vapour slug, which pushes the liquid-vapour interface of the bubble towards the sidewall. The superheated liquid layer between the vapour bubble and the channel sidewall is observed from Figure 6.37a to Figure 6.38g to increase with time as the bubble grows. The temperature of the superheated liquid ranges from 60 to 60.7 ˚C. Figure 6.37 s shows that the superheated liquid layer (red colour) around the vapour slug diminishes almost completely when the slug covers the microchannel cross section. After the slug is flushed out (Figure 6.38u), the superheated layer

reappeared adjacent to the channel sidewall from where a new bubble will nucleate and the cycle of bubble growth will start again.

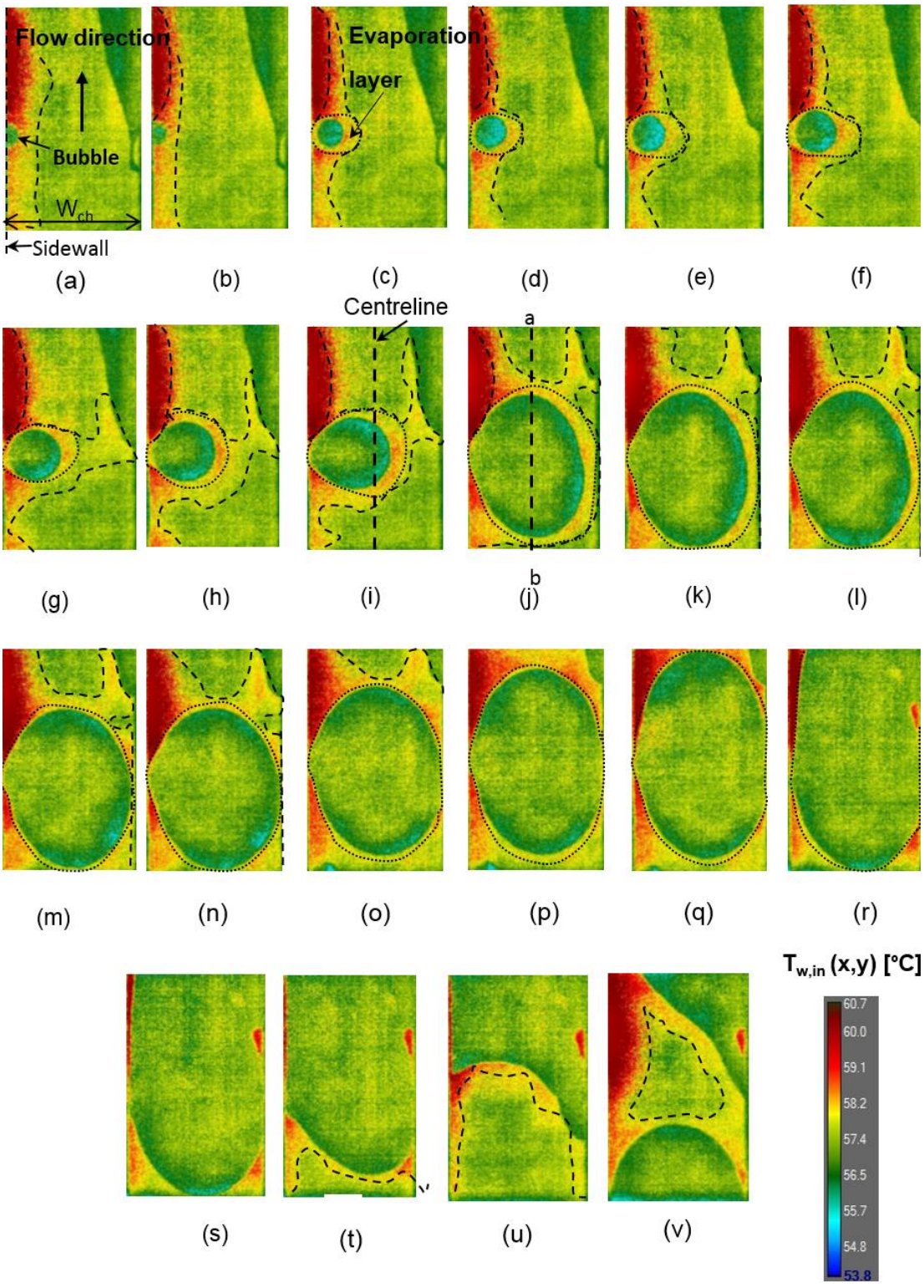

Figure 6. 37 *IR images selected from an image sequence that show inner wall temperature ($T_{w,in}$) patterns at the channel outlet from bubble wall nucleation to bubble confinement.*

The reason that leads to an isothermal, adiabatic shift of the liquid from a saturated to a superheated state in the absence of phase change is the decrease in pressure, according to Reinke [133]. This state is known as a metastable state as it is stable for a certain time and then becomes unstable just after a strong disturbance initiates the phase change. In the experimental results presented in Figure 6.38 during nucleate boiling, the liquid becomes locally superheated adjacent to the channel sidewalls and when it is sufficiently superheated, it allows nucleation that results in generation of vapour more vigorously at various nucleation sites inside or at the boundary of the liquid volume. Reinke [133] from his study on surface boiling of a superheated liquid results in the conclusions that bubble nucleation requires always the fluid to be at least locally metastable in contrast with evaporation of a stagnant liquid that is possible to occur even without superheat.. During the symmetrical growth of the spherical bubble, a spherical thermal layer was observed to surround the bubble (Figure 6.37c). The thermal layer around the bubble is formed because of evaporation of the surrounding liquid with a temperature range from 57.7 ˚C to 58.5 ˚C. Many researchers [13, 43, 53, 70, 100] concluded that the evaporation around the bubble controls the CHF mechanism. Therefore, it is important to be able to identify whether the evaporation layer exists or not and how it affects the heat transfer. The spherical shape of the bubble is possibly a result of the high evaporation around the bubble. During the spherical bubble growth, the thickness of the evaporation layer appears to be the highest. The temperature of the bubble base is lower than the surrounding layer. In Figure 6.37g, the bubble thermal layer between the bubble and the sidewall reduces in thickness and the temperature at this position starts to increase. Suspected dryout at the bubble base starts from this point. There is no much liquid to evaporate. Therefore, suspected dryout starts from the channel sidewall where the bubble is closer. When the bubble size reaches the channel cross section and the bubble touches the other side of the sidewall the evaporation layer between the vapour bubble and the sidewall diminishes and dryout occurs from the other side.

Figure 6.38 shows inner wall temperature $T_{w,}$ and simultaneous pressure obtained from the inlet (P_{in}) and outlet (P_{out}) of the microchannel as a function of time during bubble growth shown previously in Figure 6.38. $T_{w,}$ is the inner wall temperature spatially averaged along the line that crosses the bubble centre in parallel with channel length. The pressure measurements are obtained from the integrated pressure sensors inside the microchannel. The confined bubble growth results in pressure increase at the channel outletP_{out}, which causes instant decrease of pressure drop at 4.13 mbar. The pressure drop instantly increases 2.29 mbar when the bubble starts moving opposite to flow direction and then decreases again. The pressure drop fluctuations occur mainly at the channel outlet. The sharp increase in pressure is caused from the vapour slug, which

occupies almost entirely the channel cross section and therefore blocks the incoming liquid flow in the channel.

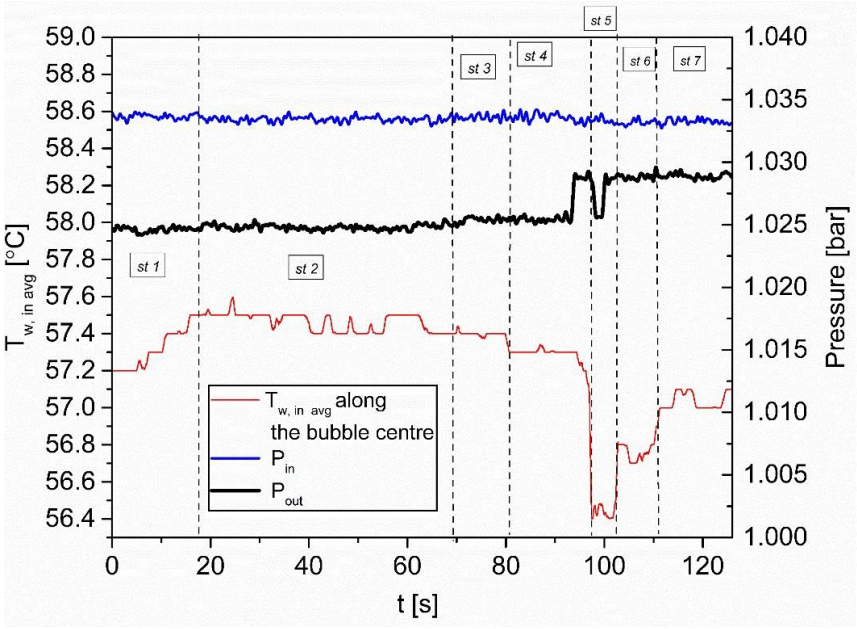

Figure 6. 38 *T_w, and pressure from the inlet (P_{in}) and outlet (P_{out}) of the microchannel as function of time during bubble growth shown in Figure 6.18. T_w, is spatially averaged along the line that crosses the bubble centre. The inner wall temperature measurements are obtained with the simultaneous pressure from the integrated pressure sensors inside the microchannel.*

Figure 6.39 shows the interfacial wall temperature profiles along the channel section from bubble wall nucleation to slug flow.

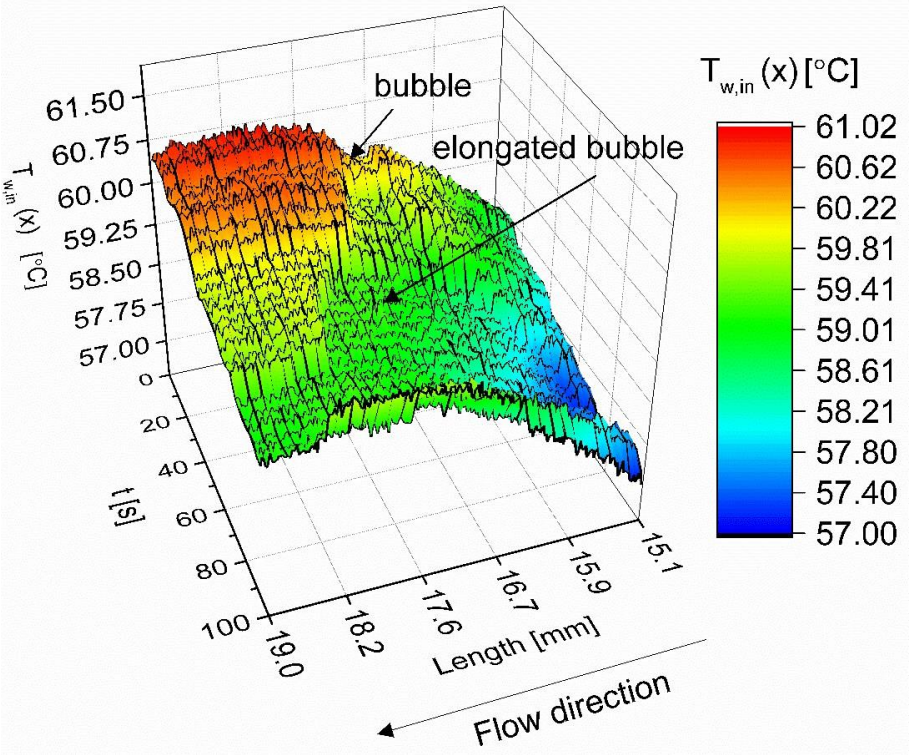

Figure 6. 39 *3D plot of local inner wall temperature profile along microchannel during bubble growth vs time for G = 23.59 kg m^{-2} s^{-1} and q =16.88 kW m^{-2} using FC-72 in a PDMS*

microchannel. Inner wall temperature $T_{w,}$ along the at flow direction the bubble from after wall nucleation to annular flow. High sensitivity of temperature measurements.

Next, the inner wall temperature patterns of transient annular flow regime are shown and reveal specific features that induce instabilities in the annular flow regime were studied, which was found to be the dominant flow regime for flow boiling. Figure 6.40 shows 3D plot of local $T_{w,}$ as a function of the length and time during the bubble growth to a slug as a result of the channel full confinement effect. The temperature was measured along the centre of the bubble. The bubble finally grows into a slug that occupies the channel cross section, where $T_{w,}$ at the centre of the channel was measured to be the lowest. The temperature gradient along the channel centreline was initially measured at 1.89 ˚C and then increased to 2.41 ˚C for the case of bubble full confinement to channel width. During partial confinement of the bubble due to channel depth, the temperature difference at the direction from the wall to the main flow was higher $\Delta T_{w,}(y) > \Delta T_{w,in}(x)$. The symmetric growth of the bubble was affected by the channel cross section confinement. When the bubble reached the channel cross section the temperature differences along the axis of symmetry where roughly the same $\Delta T_{w,}(y) = \Delta T_{w,in}(x)$.

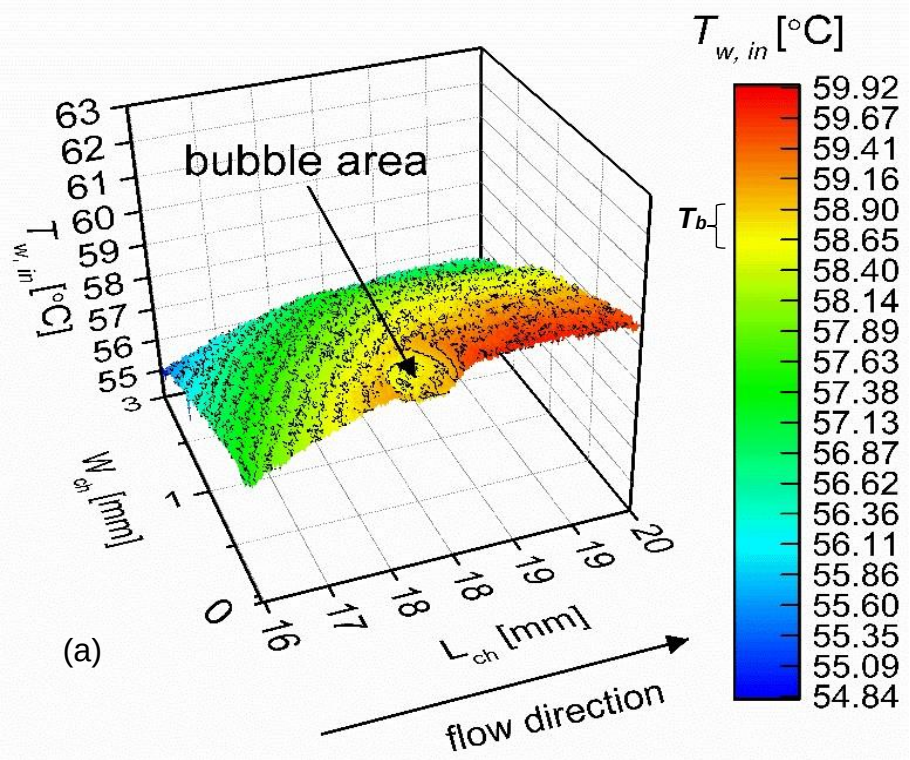

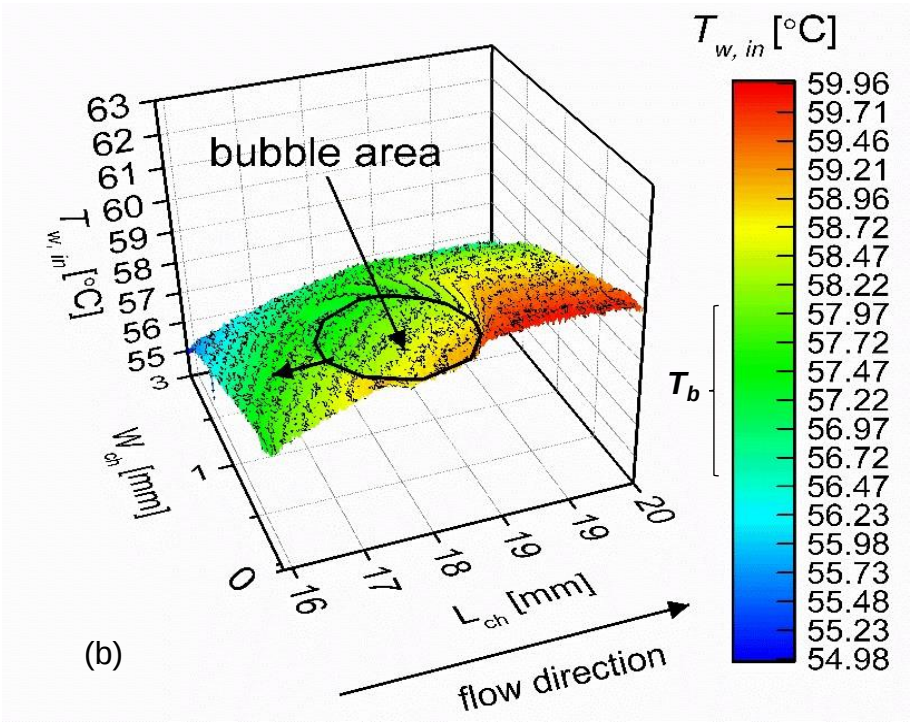
$T_{w,in}$ [°C]
59.96
59.71
59.46
59.21
58.96
58.72
58.47
58.22
57.97
57.72
57.47
57.22
56.97
56.72
56.47
56.23
55.98
55.73
55.48
55.23
54.98
T_b
bubble area
$T_{w,in}$ [°C]
63
62
61
60
59
58
57
56
55
W_{ch} [mm]
3
1
0
16
17
18
19
19
20
L_{ch} [mm]
flow direction
(b)

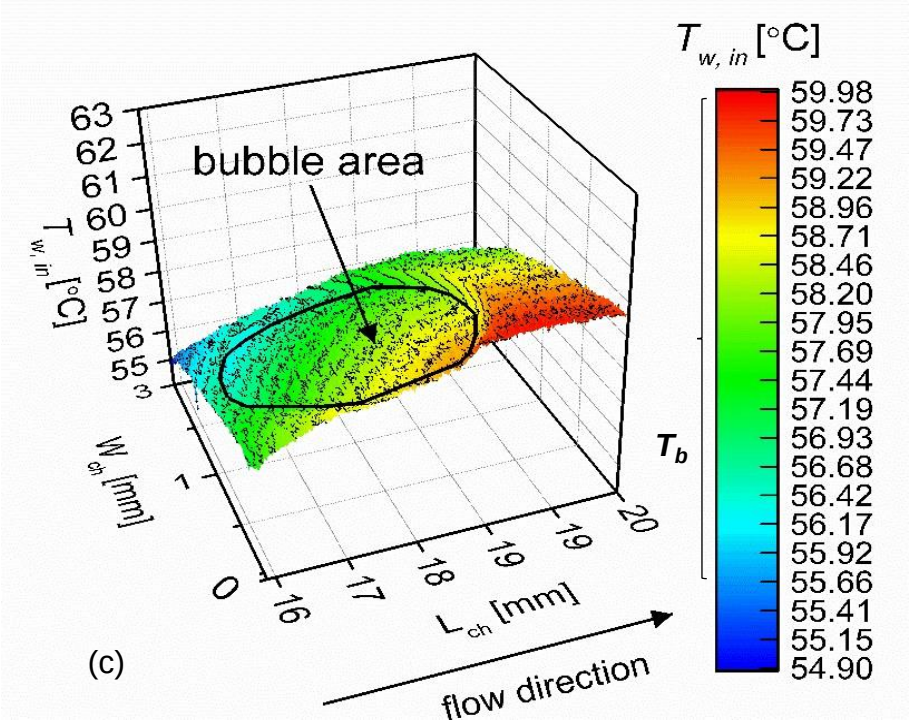
$T_{w,in}$ [°C]
59.98
59.73
59.47
59.22
58.96
58.71
58.46
58.20
57.95
57.69
57.44
57.19
56.93
56.68
56.42
56.17
55.92
55.66
55.41
55.15
54.90
T_b
bubble area
$T_{w,in}$ [°C]
63
62
61
60
59
58
57
56
55
W_{ch} [mm]
3
1
0
16
17
18
19
19
20
L_{ch} [mm]
flow direction
(c)

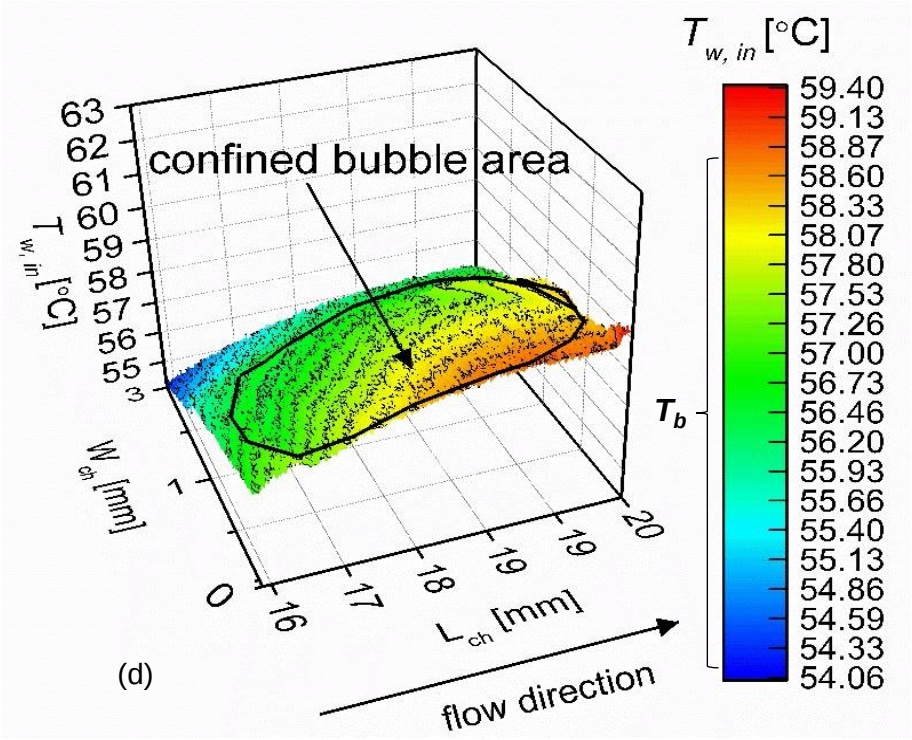

Figure 6. 40 *(a),(b),(c),(d) show 3D plots of inner wall temperature ($T_{w,}$) distribution across the channel during single bubble growth. Wall temperature is presented as a function of channel width and channel length. The range of the temperature of the bubble (T_b) is noted on the scale of each graph. The bubble was fully confined by the channel width in (d) where the highest temperature drop was measured to occur along the channel length.*

Table 6.1 presents interfacial wall temperature measurements for the bubble growth stages presented in Figure 6.40. T_b is the inner wall temperature distribution at the bubble area. For the case where the bubble is still small, presented in Figure 6.40a, the two-dimensional inner wall temperature ranges from 58.40 ˚C to 58.90 ˚C with a spatially averaged value of 58.65 ˚C ± 0.25 ˚C. The temperature gradient at the bubble base is measured at 0.5 ˚C. Figure 6.40b shows that when the bubble has non-spherical shape the temperature gradient is 1.99 ˚C. The temperature ranges from 57.22 ˚C to 59.21 ˚C with a spatially averaged value of 58.22 ˚C ± 1 ˚C. Figure 6.40 shows a temperature gradient of 2.54 ˚C at when the bubble covers the area of 7.645 mm^2. The wall temperature ranges from 56.42 to 58.96 ˚C with a spatially averaged value of 57.69 ˚C ± 1.27 ˚C. Figure 6.40 shows that the interfacial wall temperature gradient of the bubble increased to 3.2 ˚C during confinement by the channel width. This probably results from the thinning of the liquid film at the channel sidewalls. The spatially averaged wall temperature is measured at 57.5 ˚C ± 1.60 ˚C while the area of the bubble is 9.853 mm^2.

Table 6. 2 *Inner wall temperature of the bubble base T_b as a function of the bubble area shown in Figure 6.40. The bubble area was measured from high- speed, images using Image J. The high quality images were obtained from the transparent ITO/glass base of the microchannels.*

	Inner wall temperature at the bubble base, T_b [˚C]	Bubble area [mm^2]
a	58.40-58.90	0.785
b	57.22-59.21	6.0776
c	56-42-58.96	7.645
d	55.93-59.13	9.853

6.4.6.1 Spatial variation of the interfacial two-phase heat transfer coefficients during single bubble growth in a high aspect ratio microchannel illustrated in 3D plots

Figure 6.41 illustrates 3D plots of the two-dimensional two-phase interfacial heat transfer coefficient distributions $h(x, y)$ during single bubble growth at the channel outlet. The bubble expands and increases in size, therefore it occupies more surface. The limits of the heat transfer coefficient range remain the same over time but there are instant spatial variations with time. Initially, when the bubble occupies the area of 0.785 mm^2, $h_b(x, y)$ ranges between 1491 to 1,591 W m^{-2}K^{-1}(Figure 6.41a). In Figure 6.41b the bubble appears to occupy higher area of 6.006 mm^2 and the interfacial heat transfer coefficient range increases from 1484 to 1772 mm^2. In Figure 6.41c $h(x, y)$ ranges from 1,482 to 1,772 W m^{-2}K^{-1}. In Figure 6.41d after confinement of the bubble by the channel width the interfacial heat transfer coefficient ranges from 1405 to 1901 W m^{-2}K^{-1}. The bubble area occupied 7.645 mm^2.

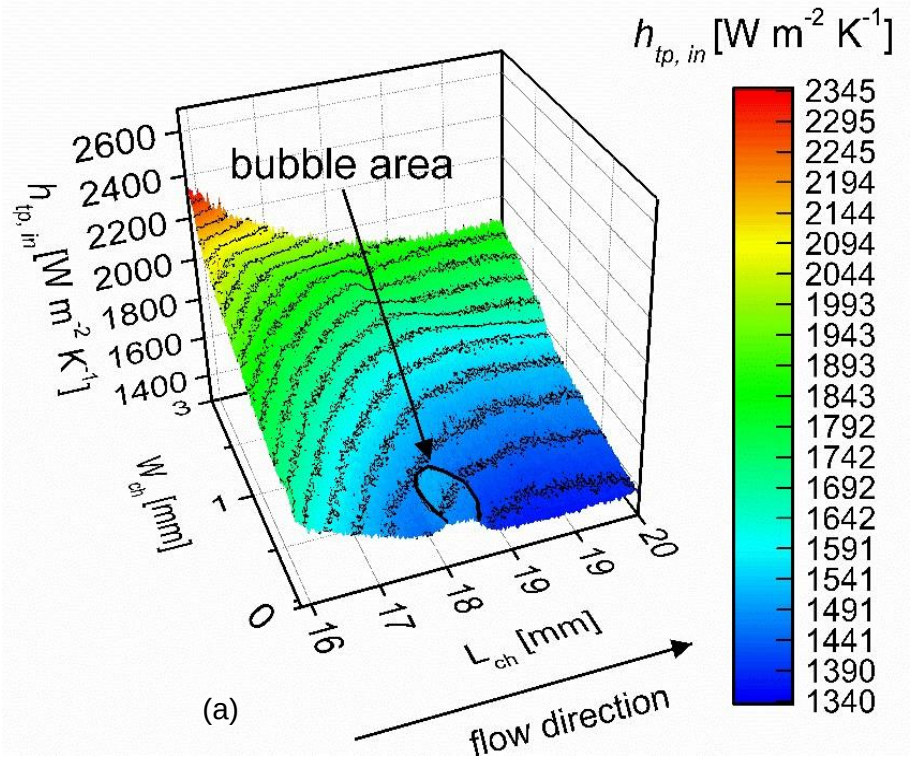
$h_{tp,\,in}$ [W m^{-2} K^{-1}]
2345
2295
2245
2194
2144
2094
2044
1993
1943
1893
1843
1792
1742
1692
1642
1591
1541
1491
1441
1390
1340
bubble area
$h_{tp,\,in}$ [W m^{-2} K^{-1}]
2600
2400
2200
2000
1800
1600
1400
W_{ch} [mm]
0
1
3
16
17
18
19
19
20
L_{ch} [mm]
flow direction
(a)

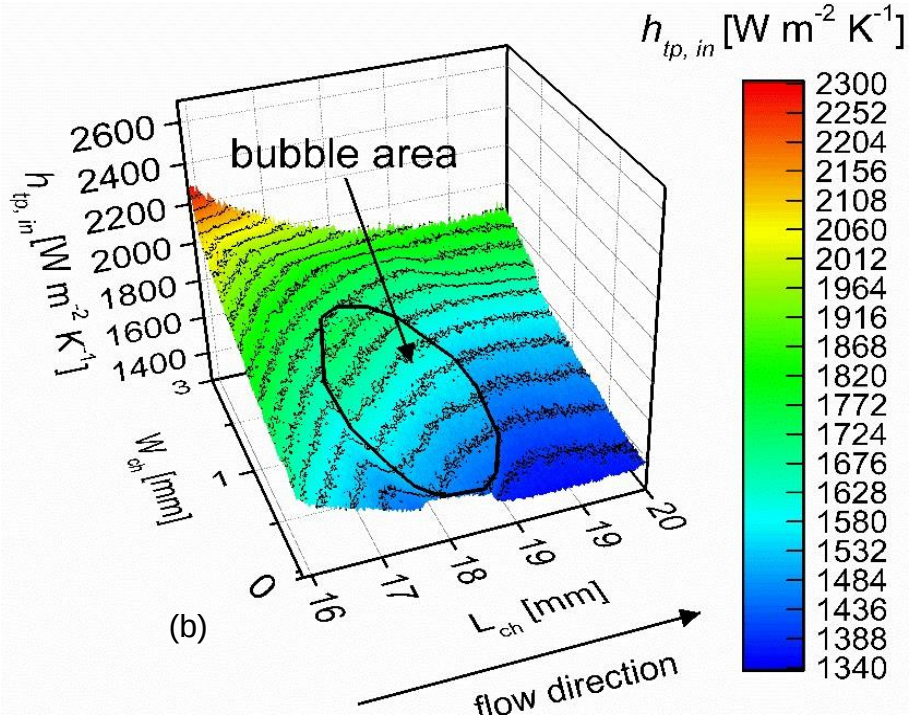
$h_{tp,\,in}$ [W m^{-2} K^{-1}]
2300
2252
2204
2156
2108
2060
2012
1964
1916
1868
1820
1772
1724
1676
1628
1580
1532
1484
1436
1388
1340
bubble area
$h_{tp,\,in}$ [W m^{-2} K^{-1}]
2600
2400
2200
2000
1800
1600
1400
W_{ch} [mm]
0
1
3
16
17
18
19
19
20
L_{ch} [mm]
flow direction
(b)

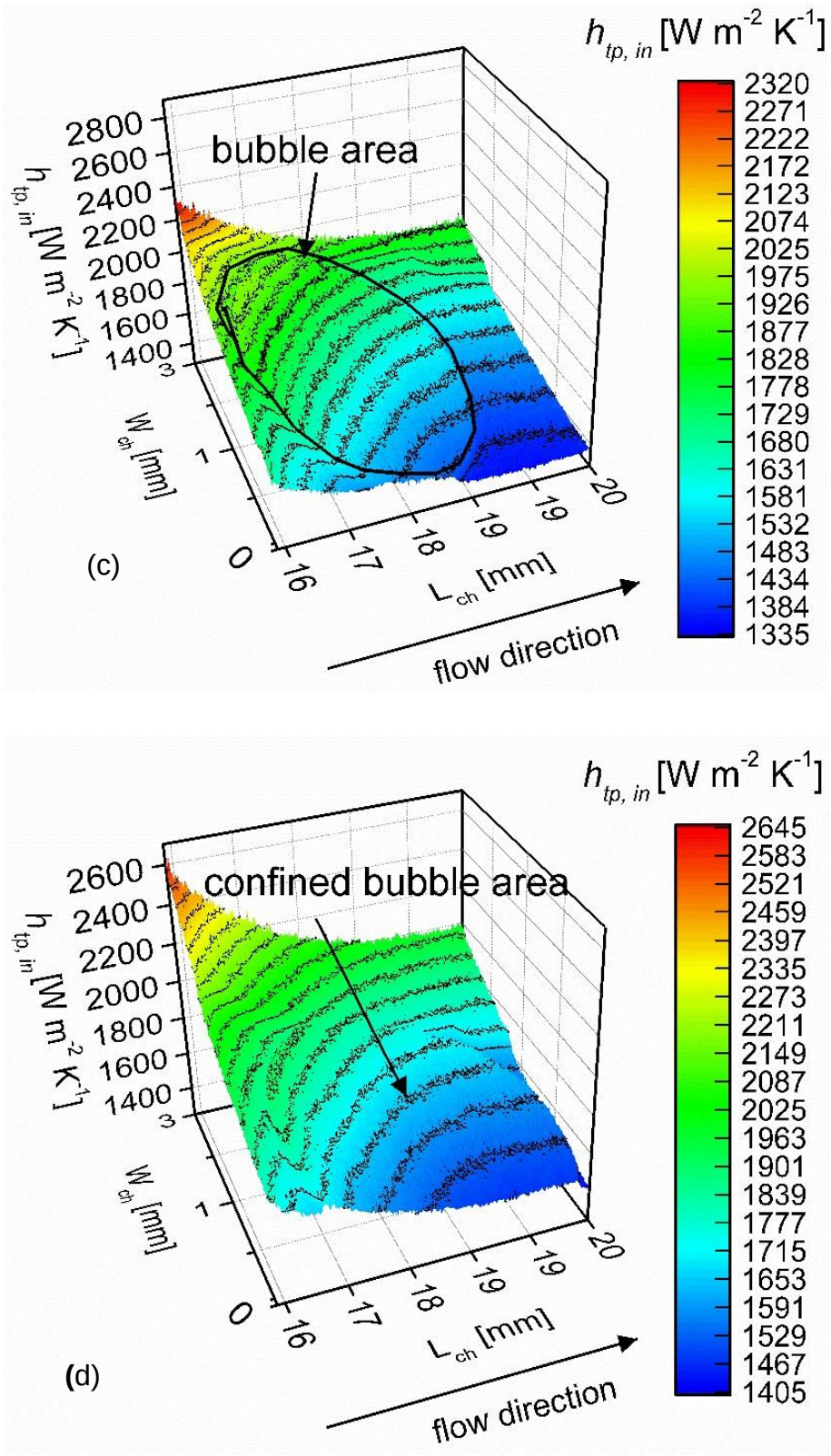

Figure 6. 41 *(a), (b),(c), (d) show patial variation of the interfacial two-phase heat transfer coefficients $h_{tp,}$ of the microchannels during single bubble growth.*

Table 6. 3 *Two-phase heat transfer coefficients of the bubble base $h_b(x, y)$, obtained from Figure 6.42. The letters a, b, c, d represent the graphs in Figure 6.41.*

	h_b(x,y) below bubble, T_b [˚C]	Bubble area [mm^2]
a	1491 -1591	0.785
b	1484-1772	6.0776
c	1482 -1975	7.645
d	1405-1901	9.8 53

6.4.6.2 2D Interfacial wall temperature measurements synchronised with pressure measurements for single bubble growth.

6.4.6.2.1 Bubble growth stages –correlation of infrared and optical high speed images

The schematic drawing in Figure 6.42 shows the location of the superheated layer in reference to the bubble during flow boiling in the microchannel. The width of the superheated layer is measured using Image J software.

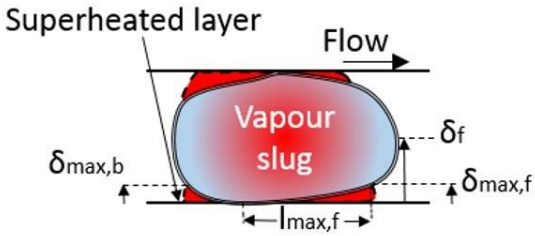

Figure 6. 42 *Schematic drawing of that shows the superheated layer measurements between the vapour bubble and the channel wall.*

The bubble growth stages are analysed using previous Figure 6.37-6.39. Figure 6.43 shows the measurements of the superheated layer width are obtained from the two-dimensional interfacial wall temperature patterns presented in previous Figure 6.38. Figure 6.44 shows the bubble growth rate in function of time. The bubble growth stages are obtained using the results in Figure 6.38. The typical bubble growth mode that was found in the literature consists of three stages of bubble growth. The main stages of bubble growth that are investigated from the study of Barber *et* al. [134] and Bogojevic *et* al. [18]. According to Barber *et* al. [134], firstly the bubble grows proportionally to the square root of time until t_{c1}. Then, as soon as the bubble diameter approaches the channel depth, the bubble immediately turns into linear growth. The linear growth

is then followed by a rapid exponential growth usually behaves as an elongation in the flow direction. Bubble elongation is promoted in channels with small hydraulic diameters as well as small channel depth. The time of bubble rapid elongation commencement is named as critical time (t_c): when bubble length growth rate greater of the bubble width growth rate. It is found that t_c is reduced by increasing heat flux and decreasing mass flux [134]. The non-linear accelerated motion of the bubble growth can be attributed to the microlayer evaporation. They observed that the bubble growth was defined by three stages. Firstly, unconfined bubble growth ($\leq D_{ch}$), partial bubble confinement ($D_b = D_{ch}$) and then full bubble confinement ($D_b \geq D_{ch}$).

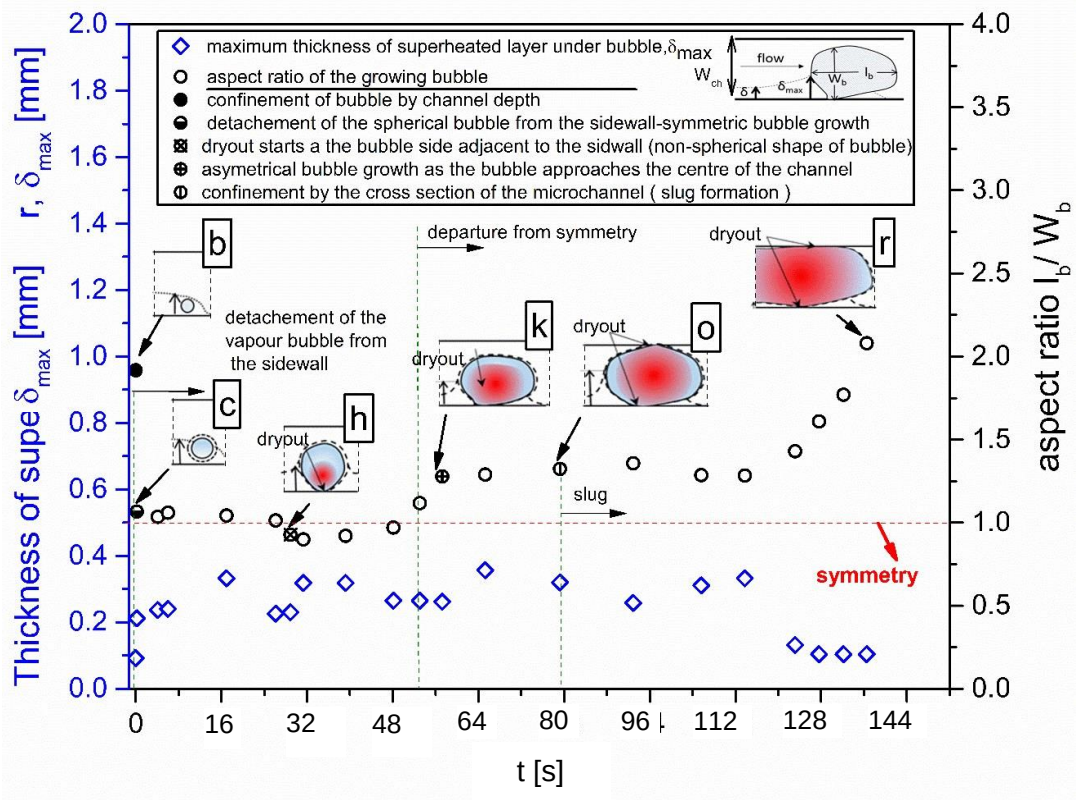

Figure 6. 43 *Aspect ratio of a single bubble growing in a microchannel during flow boiling conditions presented as a function of time (from high- speed images). In the same Figure, the superheated layer width (from IR images) observed to grow adjacent to the wall is plotted as a function of time.*

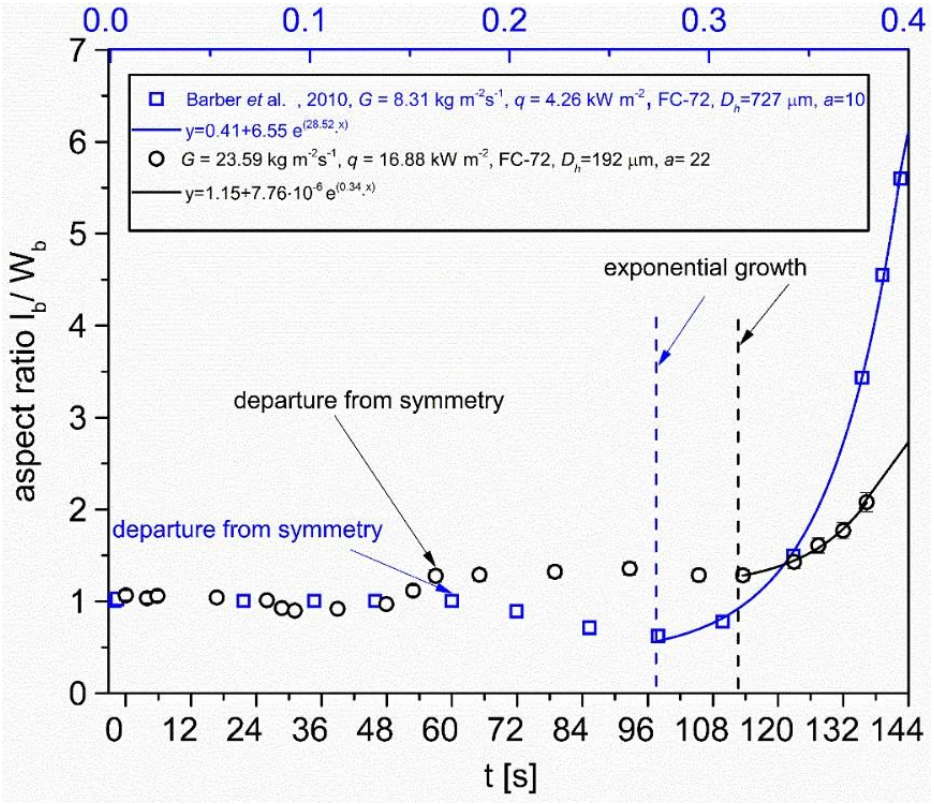

Figure 6. 44 *Aspect ratio of bubble as a function of time obtained with synchronised IR camera and high speed camera at 200 Hz and for G =23.59 kg m^{-2} s^{-1} and q = 16.88 kW m^{-2} using FC72 in the high aspect ratio (a = 22) PDMS microchannel (black colour) . The results were compared from the results from the study of Barber et al.*[134] *for a microchannel with curved corners and higher hydraulic diameter.*

Initially vapour grows in the superheated wall cavity at the channel sidewall as it is observed from the top view. A superheated layer surrounded the bubble. The thermal thickness of this layer decreased with channel length in the direction of the flow. During this phase, the averaged inner wall temperature of all the snapshots increased with time. The apparent hemispherical shape of vapour (on the sidewall) increased (very slow) mainly in width-wise direction. The inner wall temperature below the bubble is maintained almost constant with time. The inner wall temperature below the bubble was lower than the surroundings. After 68.97 s, a sudden decrease of temperature is measured at the bubble centre. This was probably an indication that the bubble reached the channel top where there is liquid. At 69 s total detachment of the spherical bubble occurred from the sidewall. This phase lasted t = 54 s. The bubble grew longitudinally at the early growth period.

Phase three starts from Figure 6.37 (d) and ends at Figure 6.37 (h). Rapid bubble growth starts when the temperature in the centre of the bubble takes suddenly a low value (not uniform temperature distribution in the base of the bubble, temperature drop of ΔT_3 = 0 .11 ºC). The bubble grows and detaches from the wall. The bubble then starts to grow symmetrically in both

directions (spherical bubble shape). As the bubble continues to grow it moves closer to the channel sidewall and it starts taking a non-uniform shape as it increases mainly width wise (t_3 = 25.15 s). When bubble departs from the wall, a thin layer is observed between the bubble and the wall. This phase lasts 13 s. Symmetric bubble growth. Lower temperature at the bubble interface is observed. The lower bubble interfacial temperature exists at the bubble side, which is closer to the lower temperature bulk liquid. The initial symmetric bubble growth could be attributed to the superheated layer surrounding almost uniformly the bubble at the initial growth stage. The main growth direction was across the channel.

Phase 4 starts at t = 16 s. The bubbles starts growing along the channel direction. Averaged wall temperature decreases with time as the bubble grows asymmetrically as it started growing in longitudinal direction. The asymmetrical bubble growth starts at 57 s, Figure 6.38. As a high temperature layer is formed around the half side of the bubble. Suddenly the superheated layer will occupy more space close to the wall as the bubble blocks the flow. The bubble will start growing from the side where higher temperature gradient exists. Therefore, the bubble grows in stream-wise direction. As the bubble growths, the apparent layer between the vapour bubble and the wall evaporates and the bubble looks as it is attached to the wall. The bubble keeps growing at stream-wise direction asymmetrically, from the side where high temperature gradient exists between the channel-superheated layer adjacent to the wall and the lower temperature of the bubble. The temperature at the centre of the bubble increases as the evaporation occurs mainly around the bubble contact line. At figure n, a liquid layer has been formed at the bubble surroundings while the inside and outside of the bubble are in higher temperature. After this liquid layer was formed then the bubble starts growing again width wise. The microchannel locally averaged temperature shows a temperature drop ($\Delta T4$ = 0.88 ºC) as the bubble diameter approaches the channel cross section (t_4= 16.938 s). The bubble is now growing mainly in longitudinal direction. Rapid temperature drop has been measured during the slug growth. Thin film boiling attributed in high heat flux dissipation as a large area of the channel occupied by a thin film liquid layer was evaporating as slug was growing in opposite of flow direction. Temperature drops due to microlayer evaporation were observed.

In phase 5, wall temperature drops sharply at the minimum value of 54.59 ºC and fluctuations of maximum 0.1 ºC start occurring for t_5 = 5.322 s as the bubble tail stays almost in constant position and the bubble front moves opposite to flow direction forming an elongated bubble.

Figure 6.45 shows that bubble with lowest contact angle resulted in the highest heat transfer coefficient. The liquid- solid contact angle or the heated surface wettability plays an important role in the formation of the liquid microlayer. Therefore, several studies have used

various types of liquids and solid surfaces in different operational conditions to determine their effect on the microlayer thickness.

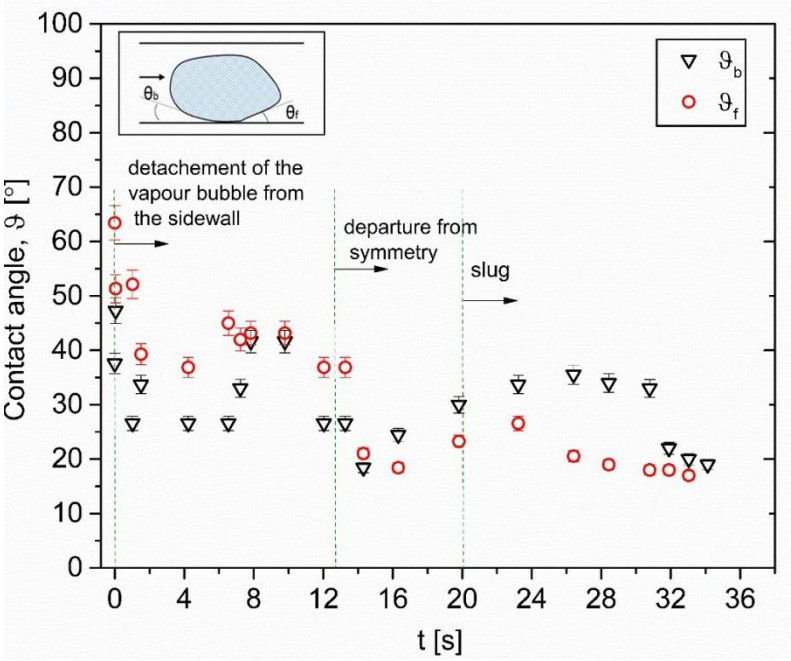

Figure 6. 45 *The advancing and receding contract angle between the bubble and the channel sidewall during single bubble growth observed to occur near a superheated layer adjacent to the sidewall of the microchannel. The contact angles were measured using Image J software from the high- speed images.*

6.4.6.3 Local liquid film evaporation during bubble confinement

Figure 6.46 shows that during the bubble growth on the channel surface, the percentage of wall dryout increases with time. This could be attributed to the evaporation of the liquid layer below the bubble. The IR images of Figure 6.37k and Figure 6.38d can confirm that. The layer between the sidewall and the bubble probably evaporated almost completely compared to Figure 6.37d. As the bubble expands in axial direction, the contact line of the bubble is directly attached to the channel sidewall and the total evaporation of the liquid layer causes the dryout. The difference between the side bubbles and the bubbles that grow on the main bottom of the microchannel. Figure 6.46 shows that after elongated bubble formation, the suspected dryout of the slug affects the heat transfer in the microchannels. The slug initially grows opposite to the flow from the back tip as the front tip of the slug remains almost in constant position.

Figure 6.47 presents the superheated layer width measured from the IR images as a function of the local velocity of the bubble front which was measured from high-speed visualisation results.

Then axial growth starts and the superheated layer form the backside is decreasing very fast resulting in annular flow and high evaporation rates.

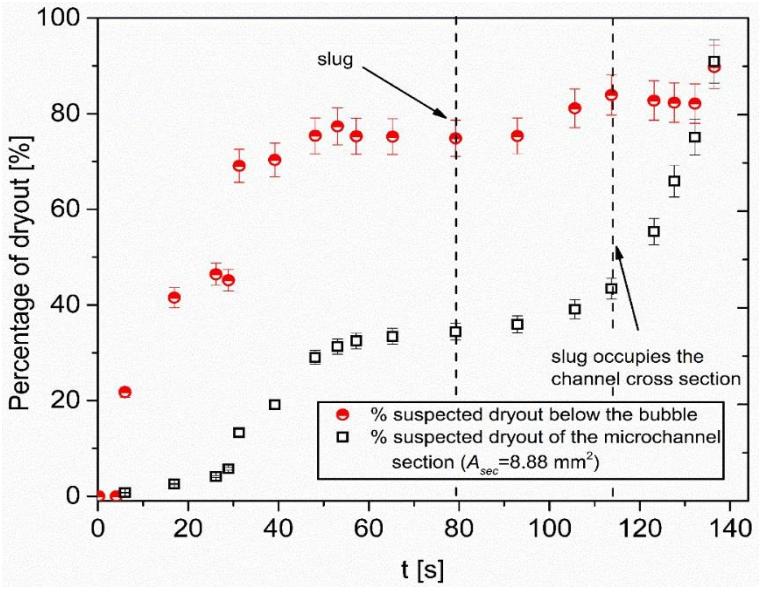

Figure 6. 46 *Dryout area percentage measured below the bubble and dryout are percentage of the channel as a function of time. The dryout area is confirmed by IR and flow visualisation images and was measure with Image J software.*

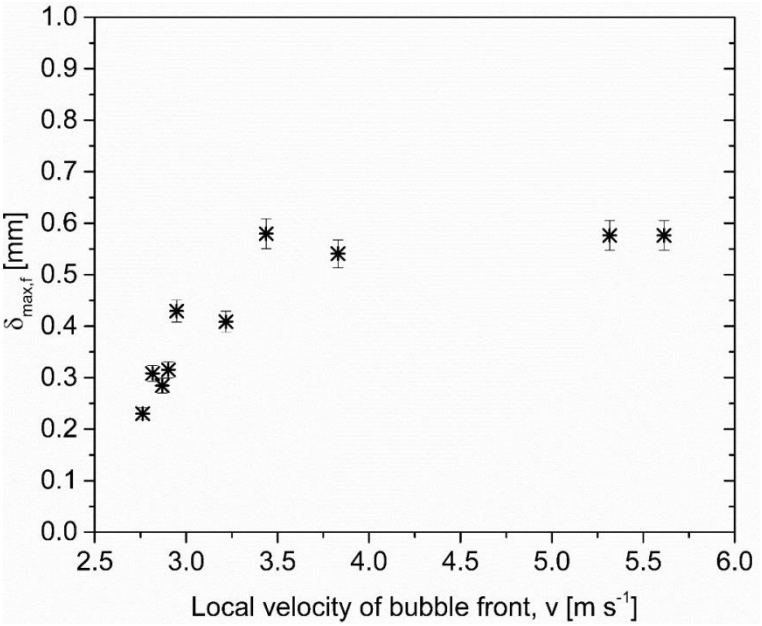

Figure 6. 47 *Thickness of the superheated layer measured from the IR images as a function of the local velocity of the bubble front which was measured from high-speed visualisation.*

The thickness of the front side superheated layer of the bubble was found to decrease in time but did not completely evaporated. Figure 6.48 shows the superheated layer width measurements from the IR images as a function of time.

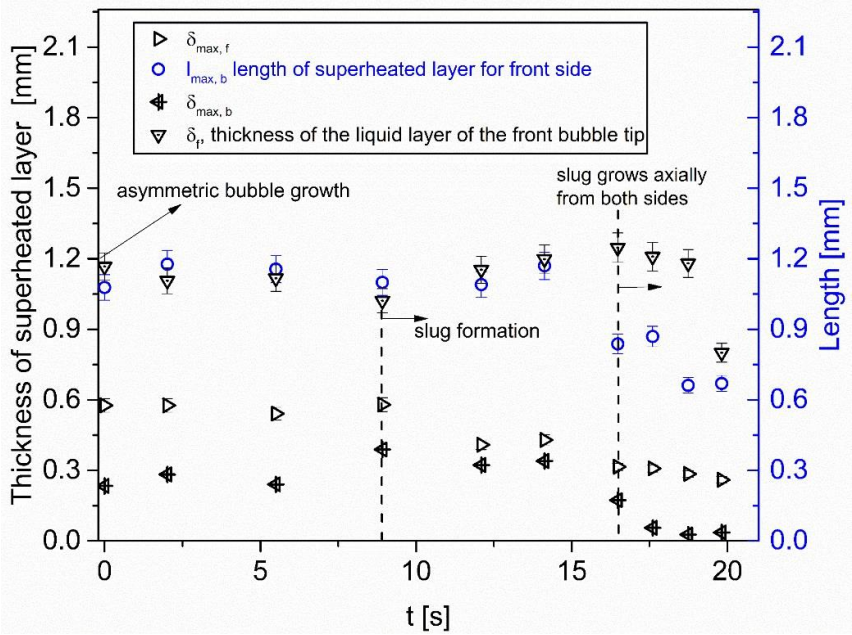

Figure 6. 48 *Thickness of the superheated layer measured from the IR images as a function of time.*

6.4.7 Wall temperature mapping from the ITO/glass channel base with synchronised high-speed imaging visualisation

Infrared thermography was combined with flow visualisation and pressure measurements from integrated pressure sensors inside the microchannel, in order to produce high spatial and temporal resolution two-phase heat transfer coefficient (*HTC*) maps across the full domain of a polydimethylsiloxane (*PDMS*) high aspect ratio microchannel (D_h = 192 μm). The local temperature and pressure data were obtained for a range of mass fluxes (G = 7.37-195.43 kg m^2 s^{-1}) and heat fluxes (q =13.64 to 185 kW m^{-2}) using FC-72 as the working liquid. The 3D plots of *HTC* provided fine details of local variations (during bubble nucleation, confinement, slug flow and annular flow). The local flow regimes were confirmed after correlation of the thermal images with the optical images obtained from flow visualization. The 3D plots of the two-dimensional two-phase heat transfer coefficient with time were correlated with vapour-liquid dynamics and liquid film thinning (from the contrast of the optical images) which resulted in suspected dryout. The correlation between the simultaneously obtained high-resolution thermal and optical images will assist in a better understanding of the heat transfer mechanisms during two-phase flow boiling

in microchannels. The 3D plots of *HTC* provided fine details of local variations during flow instability cycles and were correlated with the simultaneous optical images. This section presents local two-phase heat transfer data as well as bubble dynamics. The local spatio-temporal evolution of the heat transfer coefficient was examined for imposed mass fluxes (G = 7.37-195.43 kg m^{-2} s^{-1}) and heat fluxes (q = 13.64 to 185 kW m^{-2}).

6.4.7.1 Local wall temperature measurements as a function of time

Figure 6.50 shows wall temperature measurements which were obtained from IR video recordings of 60 s at three locations across the channel entrance (x_1= 0 mm) width for G =14.78 kg m^{-2}s^{-1} and q = 43.80 kW m^{-2}.$T_{w,a1}$ *is* obtained at the left channel edge (a), $T_{w,b1}$ at the centre (b) of the channel and $T_{w,c1}$ at the right channel edge (c).

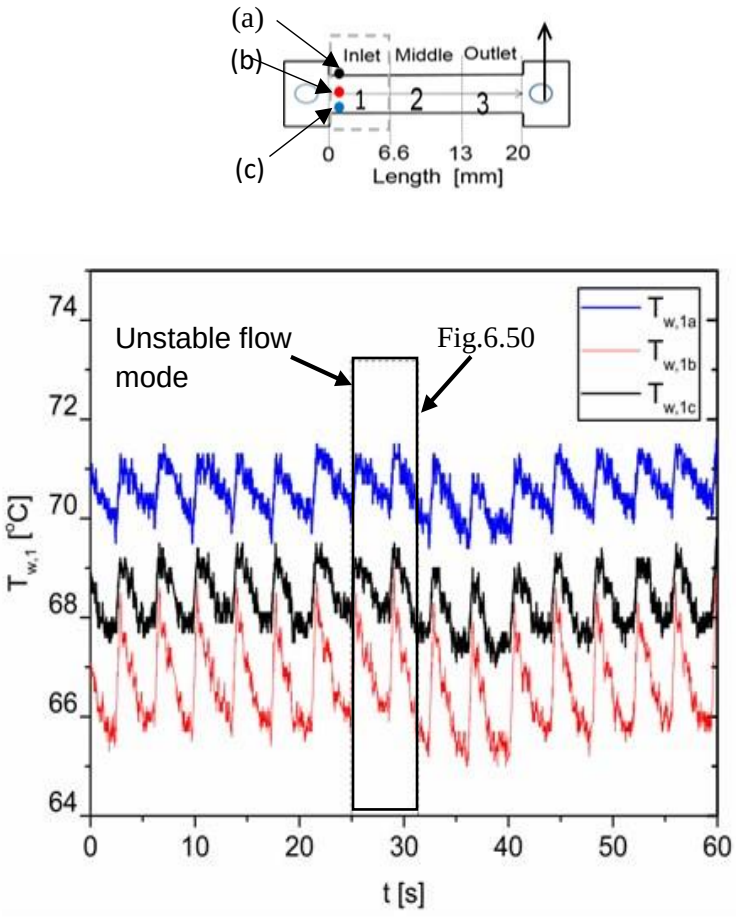

Figure 6. 49 *Local wall temperature measurements were obtained at the channel entrance as a function of time during two-phase flow boiling for G =14.78 kg m^{-2}s^{-1} and q = 43.80 kW m^{-2}. The measurements were obtained at three locations across the channel width ($T_{w,1}$: left channel edge, $T_{w,b1}$: centre, $T_{w,c1}$: other channel edge) at the channel entrance (position 1).*

Figure 6.49 shows that at the location x_1 = 0 mm (channel entrance) the cross sectional temperature is axisymmetric and uniform. At this location, the average temperature over time of the channel centre (b) presented a dip with temperature value of 71.57 ± 2.27 ˚C while the channel corners had high and similar temperature values of 76.90 ± 1.40˚C and 77.44 ± 1.23˚C.

The average temperature difference between the channel centre and the channel corners was 5.33 ± 1.87˚C for one corner (a) and 5.87 ± 1.04 ˚C for the opposite channel corner (c) very close to the high temperature values of the channel corners. This occurs only at periodic temperature peaks, which were related with bubble confinement in the channel. Further downstream at x_3 = 6.63 mm the channel cross section profile appeared suddenly to change. It was found to be non-axisymmetric with respect to the channel centre. The highest temperature values of 85.38 ± 0.58 ˚C were measured only on one corner of the channel (a) while the temperature values at b and c were very close, with temperature at the channel centre to be the lowest (79.36 ± 1.98 ˚C) compared to the corner (a). The cross section temperature profile was non-uniform and non-axis symmetric for all the rest of the channel length. All the wall temperature values across the channel width increased significantly after x_5 =16.30 mm. The temperatures at the channel corner (c) and the channel centre (b) was very close to the temperature at the corner (a) which was the highest (89.31 ± 1.39 ˚C).The following graph shows the averaged in time local temperatures at the three positions (a, b, c) across the channel width for the 6 positions (x_1 to x_6) along the channel. The temperature increases with the channel length up to 11.47 mm from the channel entrance where the highest temperature was measured to occur at the channel corner (a). After 22.47 mm the average temperatures across the channel decreased at 16.31 mm and increased slightly at 19.80 mm. The reason that the temperature decrease occurred was the existence of a nucleation site close to 16.31 mm at the upper corner (a) of the channel wall. The growth of bubble near the channel walls allowed the effective cooling of the channel at the position a not further temperature increase (> 92.69 ˚C) occurred that could lead to system failure. Figure 6.50 shows local wall temperature fluctuations along the microchannel for G = 14.38 kg m^{-2}s^{-1} and q = 47.78 kW m^{-2}.

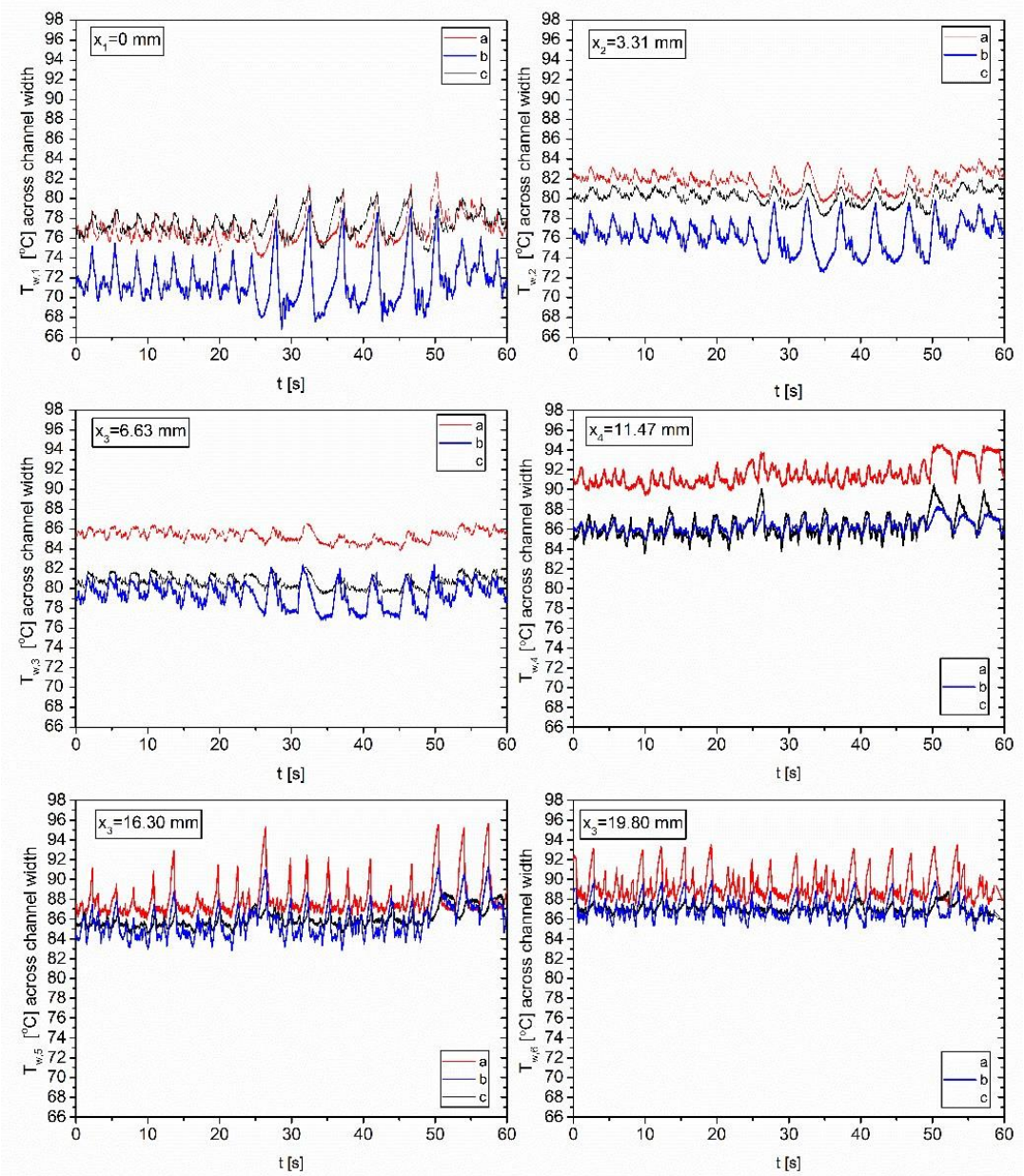

Figure 6. 50 *Wall temperature fluctuations measured at three positions (channel upper corner: centre of the channel width and other channel corner) across the channel width for* $G = 14.38$ *kg* $m^{-2}s^{-1}$ *and* $q = 47.78$ *kW* m^{-2}.

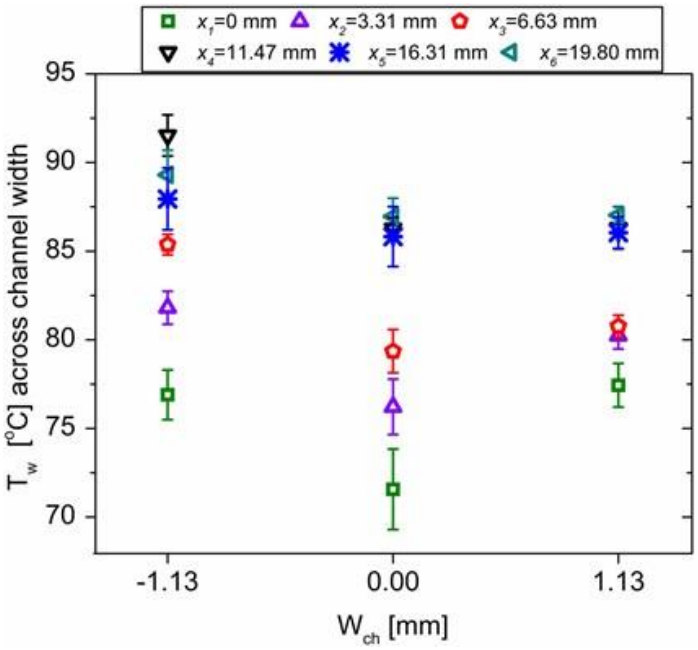

Figure 6. 51 *Averaged over time (with deviation) local temperatures at the three positions (a, b, c) across the channel for each positions from 1 to 6 along the channel length. Bubble nucleation started at x = 16.31mm, at the channel corner (a).*

FFT analysis is applied to the temperature fluctuations at three positions across the channel (a, c) in order to obtain the dominant frequency of fluctuations along the channel. In all positions, the highest amplitude was found at the channel middle, except the location of 11.47 mm and 19.80 mm from the channel entrance. For the case of 11.47 mm, the highest amplitude was identified at corner c and for 19.80 mm at the corner (a). We could consider that the high amplitude temperature fluctuations are related to the liquid film evaporation of the channel surface. According to Figure 6.51, the fluctuations have the highest amplitude at the channel entrance, which decreases with length up to 11.47 mm from the channel entrance. The fluctuation frequency of the temperature at corner (a) is measured to deviate from the others and start to increase after 6.31 mm, because of bubble nucleation.

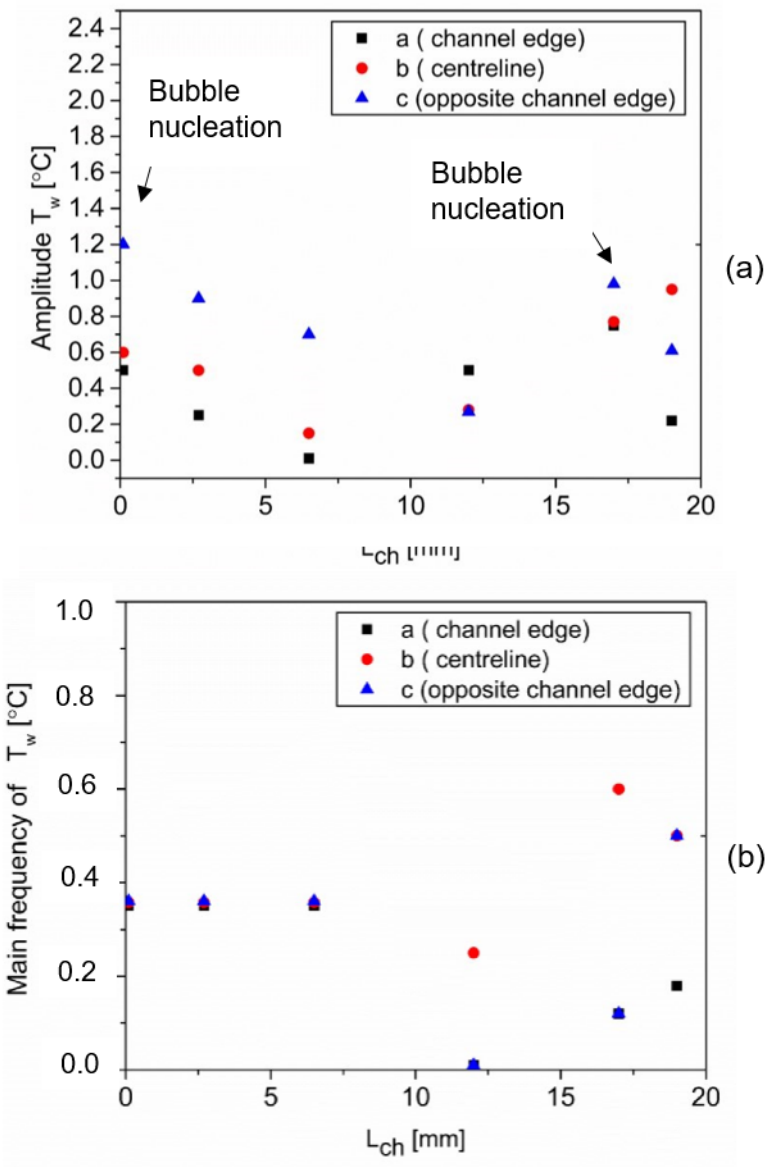

Figure 6. 52 **(***a) Amplitude and (b) main frequency of the wall temperature fluctuations at 6 positions from channel entrance to the outlet.*

Figure 6.51b shows that that the main frequency of fluctuations deviates (across the channel width) as approaching the outlet. The highest frequency (0.006 Hz) of the fluctuations occurred at the entrance and at 16.31 mm from the channel entrance at the location of the channel edge corner (a) due to bubble nucleation. At x_5 = 16.31 mm from the channel entrance, the average temperature decreased, a fact that confirms the bubble nucleation and growth at this positions that cooled down this part of the channel. Before the bubble nucleation, at x_4 = 11.47 mm from the channel inlet, the highest temperature was measured to occur at the channel corner (a).

Table 6. 4 *Main frequency and amplitude of fluctuation deduced using FFT analysis.*

	x (mm)	Amplitude	Main frequency
axial growth of the fully confined bubble	0	0.83-1.15	0.00346 (a, b, c)
bubble nucleation at the channel corner	16.31	0.67-1.05	0.00534 (only for (a)) 0.00053 for b and c

The main frequency of the temperature fluctuation and the amplitude were derived from FFT signal processing and they are presented in the above table for the positions along the channel where the amplitude was the highest High amplitude temperature fluctuations: due to bubble confinement effects that resulted in bubble axial growth at the channel entrance due to bubble nucleation at the channel corner (a) at the channel outlet. The main frequency of the temperature fluctuations was not the same for the temperature fluctuations along the whole channel cross section. The highest amplitude fluctuation occurs at the channel corner (a) where the bubble nucleation initiated. The measured temperature at the centre and the other corner of the channel were fluctuating at lower frequencies and high amplitudes. This possibly occurs due to the position of bubble nucleation.

6.4.7.2 2D & 3D plots of $h(x, y)$ for q < 45 kW m^{-2}

Figure 6.52 shows the local heat transfer coefficients as a function of time for the channel entrance (position 1). The local two-phase heat transfer coefficients in time were correlated with optical images (Figure 6.53) from t = 25 s to 31 s, in order to relate the observed flow patterns with the measured periodic temperature fluctuations. The values of h_{tp}(x, y) are produced using the wall temperature temporal profiles of Figure 6.49. Figure 6.53 shows the flow patterns recorded simultaneously along the microchannel from 0 to 10 mm (from channel entrance). According to Figure 6.53 the main flow patterns observed during flow boiling for G = 14.78 kg m^{-2}s^{-1} and q = 43.80 kW m^{-2}. Bubbly, slug and annular flow were the main flow regimes. The slug was formed from a single isolated bubble and not because of bubble coalescence. From the flow visualizations in Figure 6.53, bubble nucleation was observed to occur adjacent to the superheated edge (c) of the channel entrance. Bubble nucleation was also observed to occur simultaneously at the other upper channel edge (a) close to the outlet. Therefore, two nucleation sites where observed to cause bubble nucleation under certain conditions along the whole channel length. The correlation between Figure 6.52 and 6.53 reveals that the low amplitude temperature fluctuations

started when bubble nucleation occurred at the channel entrance, adjacent to the superheated channel sidewall (t = 26.180 s).

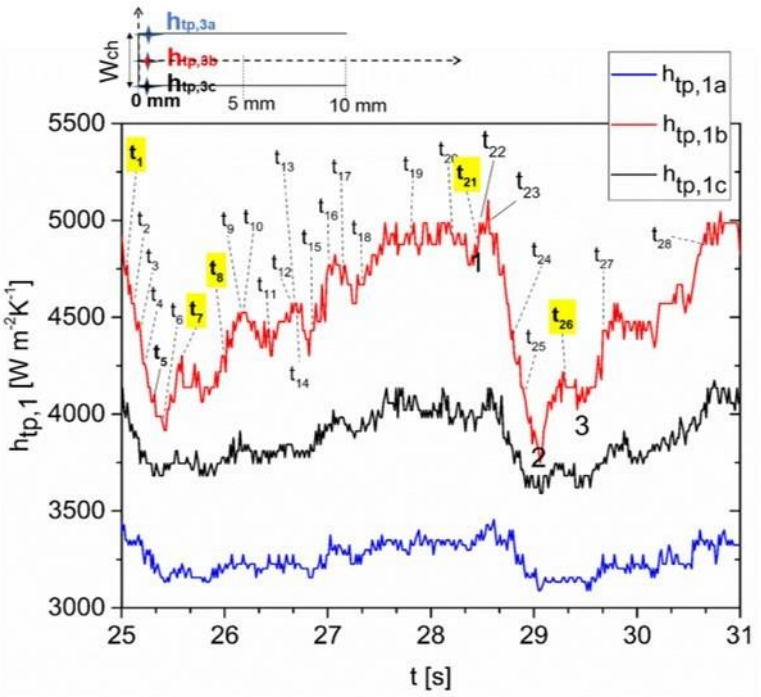

***Figure 6.* 53** *Local two-phase heat transfer coefficients were obtained at the channel entrance. The locations where $h_{tp,1a}$, $h_{tp,1b}$, and $h_{tp,1c}$ were calculated, are presented in the schematic on the top of the graph.*

The spherical bubble started growing while moving adjacent to the wall. The spherical bubble then moved to the centre of the channel when it started growing faster (t = 26.445 s). Confinement of the bubble by the channel height resulted in growing in widthwise direction. As soon as the bubble occupied the whole channel width (t = 26.652 s), axial growth of the bubble nose (end of bubble moving streamwise) occurred. This resulted in the formation of a bullet shape bubble (t = 26.691 s).

Bullet-shape bubble was formed when the nose of the bubble started growing axially while the bubble fully occupied the channel cross section at a position (close to the tail of the bubble) which was emphasized with a red arrow, in parallel to the width of the channel (t = 26.673 s). Then, the elongated bubble was flushed out from the channel because of the incoming liquid flow. This flow instability was accompanied by a low amplitude temperature fluctuation, which resulted in the drop of the local heat transfer coefficient in time. The two-phase heat transfer coefficient dropped by the maximum value of 250 W m^{-2} K^{-1} (Figure 6.52).

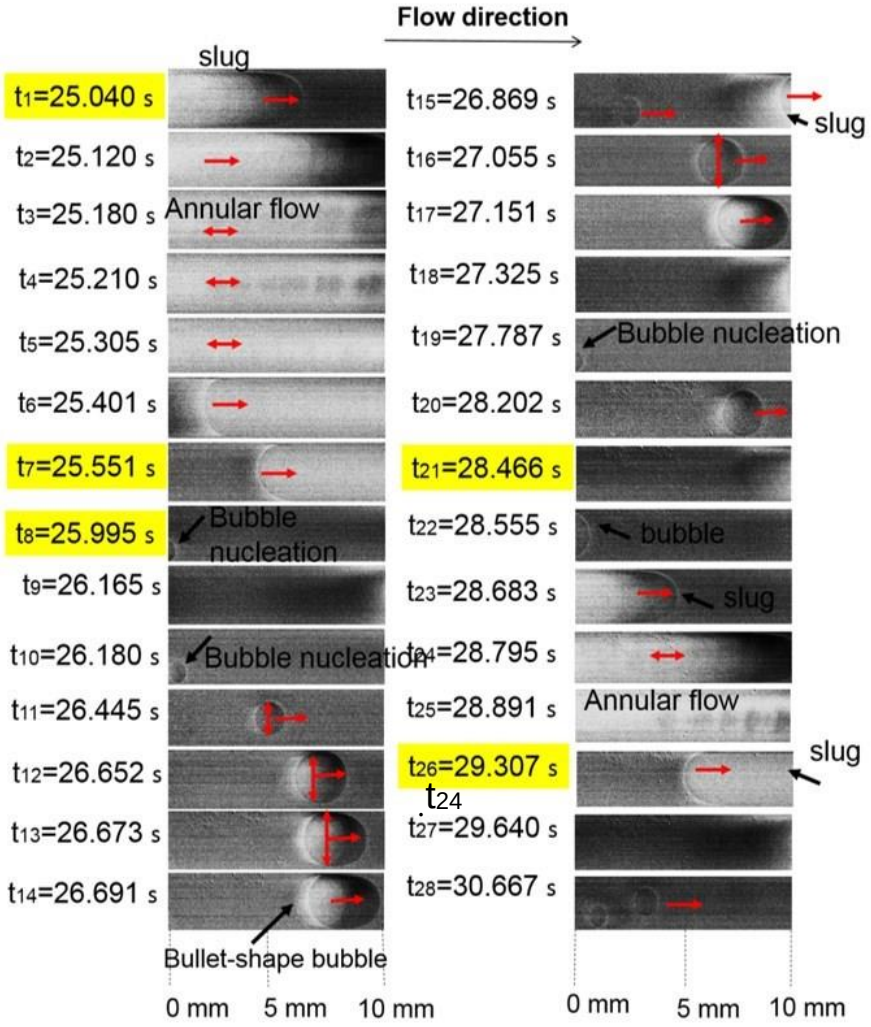

Figure 6. 54 Flow patterns observed during flow boiling from PDMS in the test section from 0 to 10 mm. The optical images were correlated with the heat transfer coefficient presented in Figure 6.54 at the channel entrance for q = 43.8 kW m^{-2}.

The correlation between the heat transfer coefficient fluctuations shown in Figure 6.52 and the simultaneous recorded low visualisation images shown in Figure 6.53 showed that the high amplitude temperature fluctuations started when the vapour bubble was observed to occupy the width of the channel entrance (t = 28.555 s). After the bubble occupied the channel width, a slug was formed because of the abrupt axial expansion of the bubble along the channel. The moving slug at the channel inlet (t = 25.040 s), was found to enhance locally the heat transfer coefficient (t_{23}, Figure 6.54a). The slug started growing axially in both directions, resulting in the establishment of annular flow regime (t = 25.180 s) along the whole channel length. The slug was then flushed out by the incoming liquid flow and a new cycle of low amplitude temperature fluctuation started when the bubble nucleated at the channel entrance (t = 25.995 s). This flow instability was accompanied by a high amplitude temperature fluctuation, which resulted in local

decrease of the local heat transfer coefficient by 1,250 W m^{-2} K^{-1} (Figures 6.52 and 6.53). The high amplitude fluctuations were further analysed by correlating the local heat transfer coefficient profiles, which are obtained along the channel centreline with time (Figure 6.54) with the observed thermal patterns from the IR thermal images (Figure 6.55).

Figure 6.54a presents the local two-phase heat transfer coefficient profiles along the channel centreline from 0 to 10 mm, as a function of time for G = 14.78 kg $m^{-2}s^{-1}$ and q = 43.80 kW m^{-2}. The high amplitude heat transfer coefficient fluctuation during a periodic instability cycle is depicted in Figure 6.54b using arrows and numbers from 1 to 3 that show the sequence of events. The local heat transfer coefficient profiles that of Figure 6.54 are obtained from the thermal images shown in Figure 6.55a. From Figure 6.55a and Figure 6.55b it is observed that the axial growth of the slug at t = 170 s results in increase of the local heat transfer coefficient up to 125 W m^{-2} K^{-1} from 4.2 to 6.8 mm along the centreline. However, when the slug is further elongated, it eventually occupies the whole channel cross section and results in annular flow after the complete occupation of the channel cross section with vapour and results in decrease of the heat transfer coefficient because of suspected local dryout at certain locations. At t = 580 s the heat transfer coefficient is observed to decrease along the sidewall possibly due to evaporation of the liquid film at the channel centre.

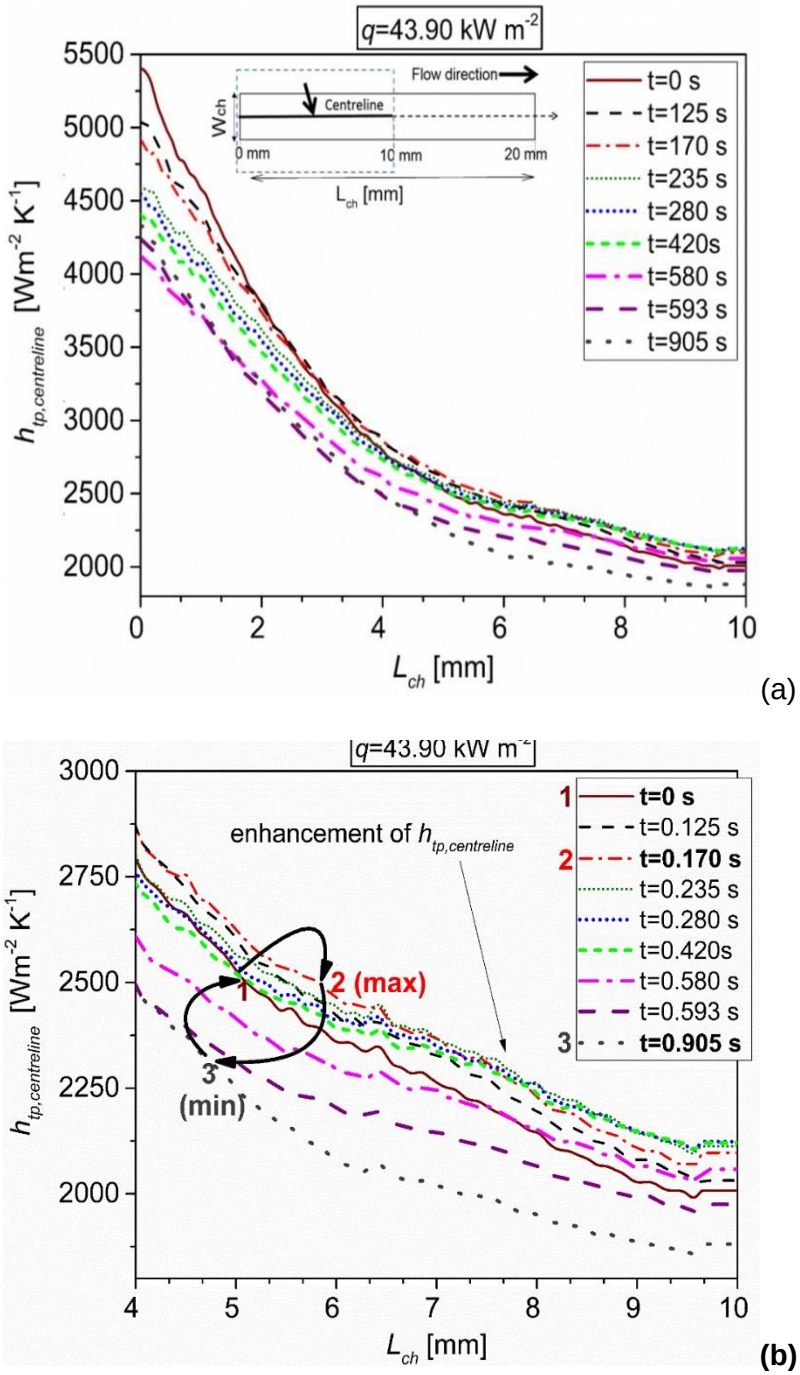

Figure 6. 55 *Local two-phase heat transfer coefficient profiles as a function of time along the channel centreline (from 0 to 10 mm) for G = 14.78 kg m^{-2}s^{-1} and q = 43.80 kW m^{-2}and (b) for the channel length from 4 to 10 mm. The cycle of the high amplitude fluctuation was represented with arrows related also to Figure 6.69.*

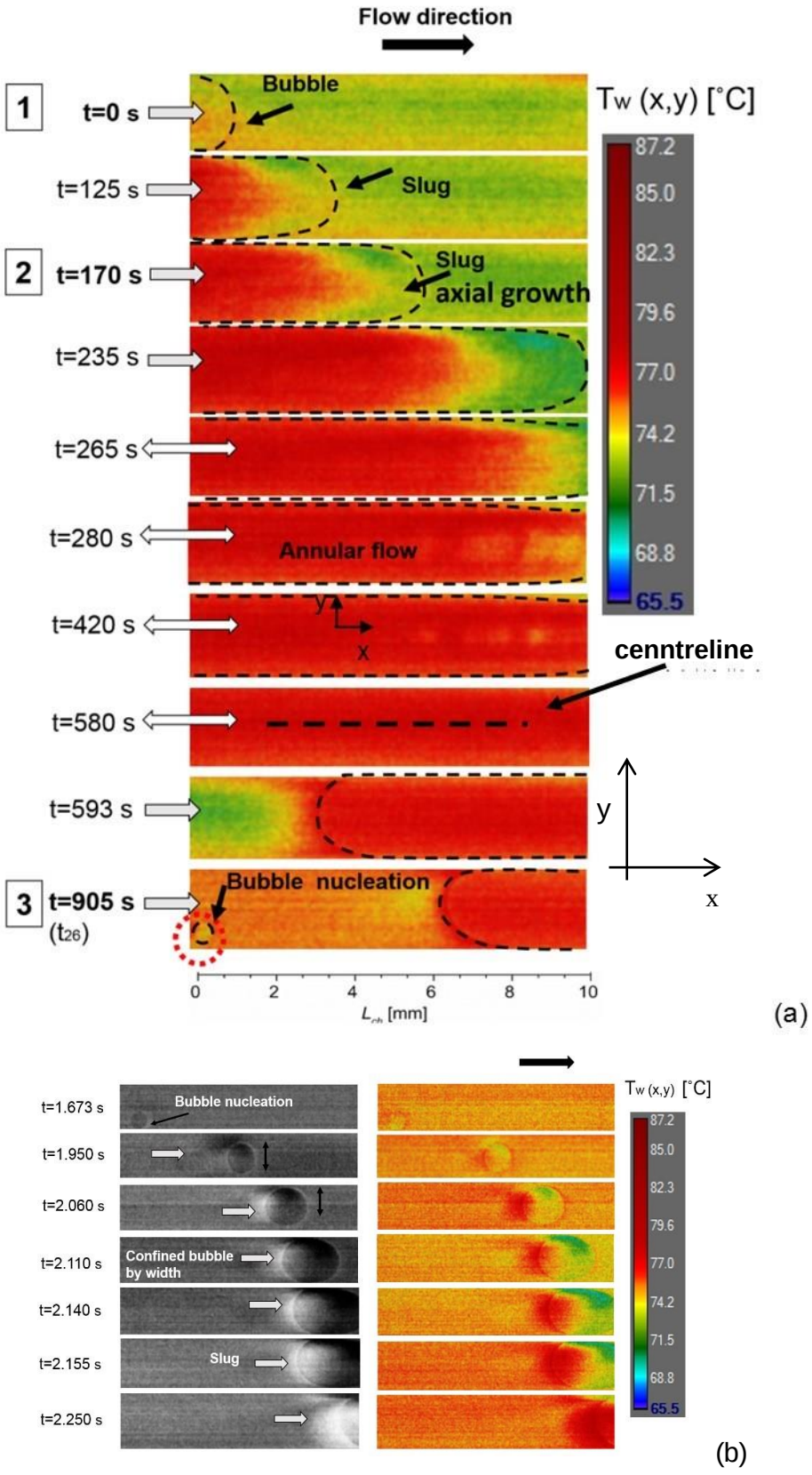

Figure 6. 56 *Two-dimensional wall temperature measured with the IR camera from the ITO/glass base of the microchannel and reveals the occurrence of (a) high amplitude and (b)*

low amplitude temperature fluctuations for G = 14.78 kg m^{-2}s^{-1} and q = 43.80 kW m^{-2}from 0 to 10 mm. The numbers 1, 2, 3 were related with the fluctuation cycle shown in Figure 6.54. High amplitude low frequency fluctuations are shown in (a) and low frequency fluctuations.

Figure 6.56 illustrates the 3D plot of the two-dimensional two-phase heat transfer coefficient along 10 mm from the entrance for G = 14.78 kg m^{-2}s^{-1} and q = 43.80 kW m^{-2} as a function of time. The flow boiling two-phase heat transfer coefficients decrease from the inlet to the outlet. The gradient is constant, without appearance of dips and peaks. The maximum heat transfer coefficient is measured at the channel centre and ranges from 4,371 to 4,860 W m^{-2}K^{-1} width during axial growth of the confined bubble at the inlet. h_{tp} (x, y) *v*aries significantly from 2,413 to 4, 860 W m^{-2}K^{-1} across the channel width, from the entrance to the location of 4.5 mm. The cross section profile from 4.5 to 10 mm shows less variation, from 1,190 to 2,413 W m^{-2}K^{1} possibly because of liquid film thinning or suspected dryout at the channel surface.

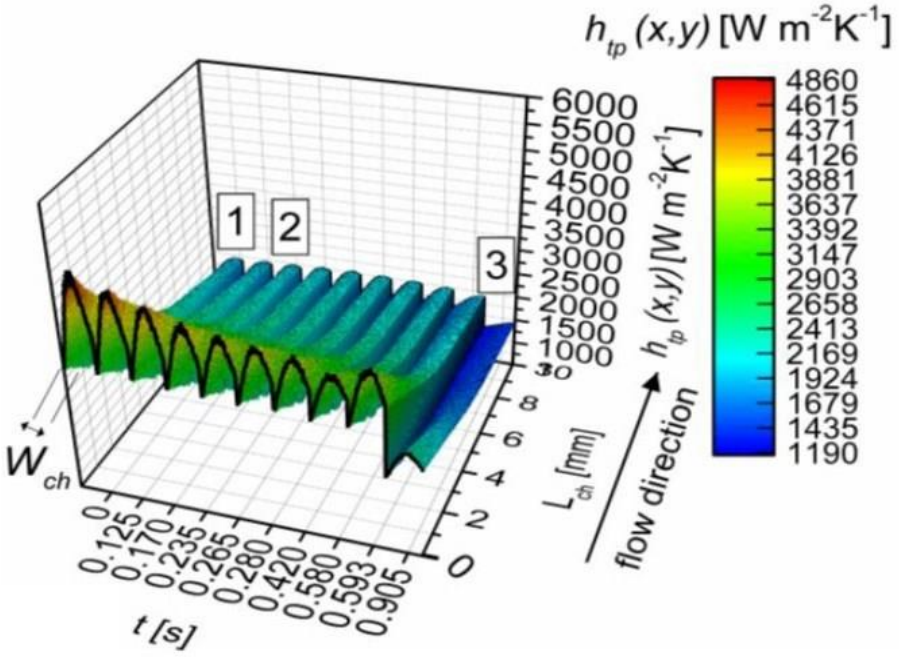

Figure 6. 57 *3D plot of the two-dimensional two-phase flow boiling heat transfer distribution across microchannel for G = 14.78 kg m^{-2}s^{-1} and q = 43.80 kW m^{-2} from 0 to 10 mm. The numbers 1, 2, 3 are related to the fluctuation cycle shown in Figure 6.64a.*

6.4.7.3 2D & 3D plots of $h(x, y)$ for q > 45 kW m^{-2}

At constant mass flux, for heat flux greater than 45 kW m^{-2}, deterioration of the two-phase heat transfer occurs at the outlet because of the suspected intermittent dryout. Figure 6.57 illustrates 3D plots of the high spatial and temporal resolution $h_{tp}(x, y)$ as a function of time for the whole domain and from 0 to 16 mm from the entrance for G = 14.78 kg m^{-2}s^{-1} and

q = 47.78 kW m^{-2} $h_{tp}(x, y, t)$ ranges from 1,220 to 4,180 W m^{-2}K^{-1}. The values of the two-phase heat transfer coefficients are lower compared to the heat flux of 43.80 kW m^{-2} shown in Figure 6.57. The maximum $h(x, y, t)$ is measured at the channel entrance.

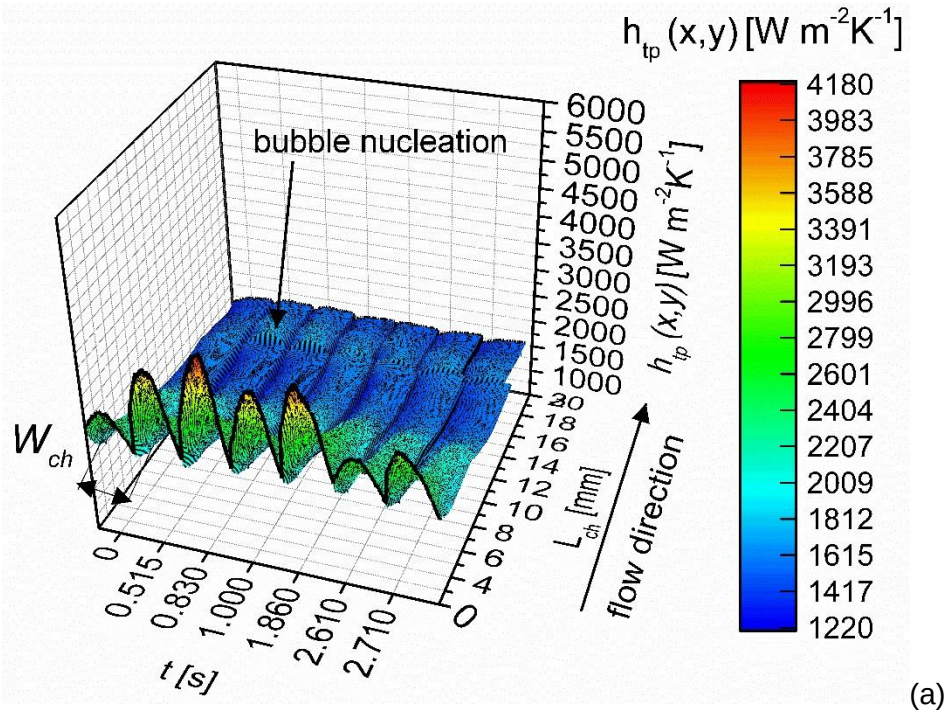

(a)

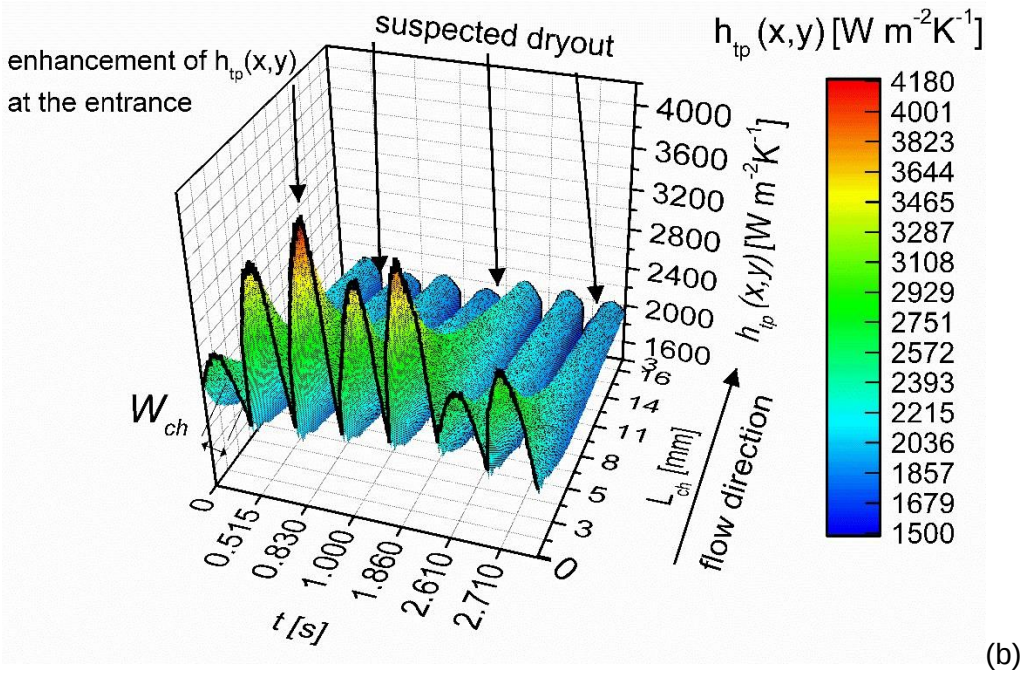

(b)

Figure 6. 58 *High spatial and temporal resolution 3D plots of the two-dimensional two-phase heat transfer coefficient $h(x, y)$, (a) across the whole domain of the microchannel and (b) for the length of 0 to 16 mm for G = 14.78 kg m^{-2}s^{-1} and q = 47.78 kW m^{-2}.*

Figure 6.58a shows $h(x, y, t)$ results for the same mass flux of *for* G = *14.78 kg* $^{-2}s^{-1}$and higher heat flux of q = *92.3 kW* m^{-2}. The 3D plot of the two-phase heat transfer coefficient distribution as a function of time for G = 14.78 kg $m^{-2}s^{-1}$ and q = 92.3 kW m^{-2} reveals a considerable difference of $h(x, y)$ values front the centre to the corners.

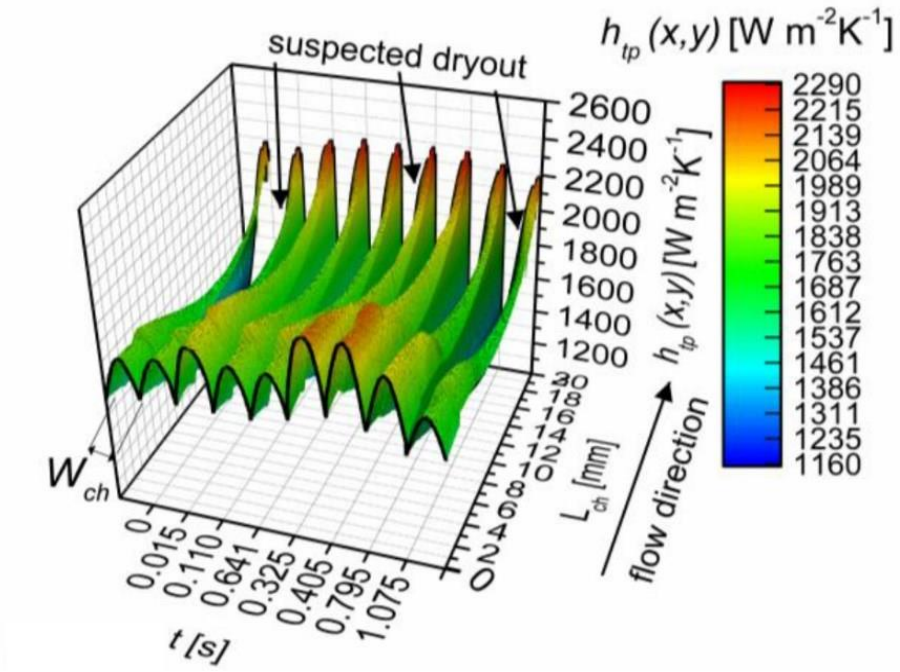

(a)

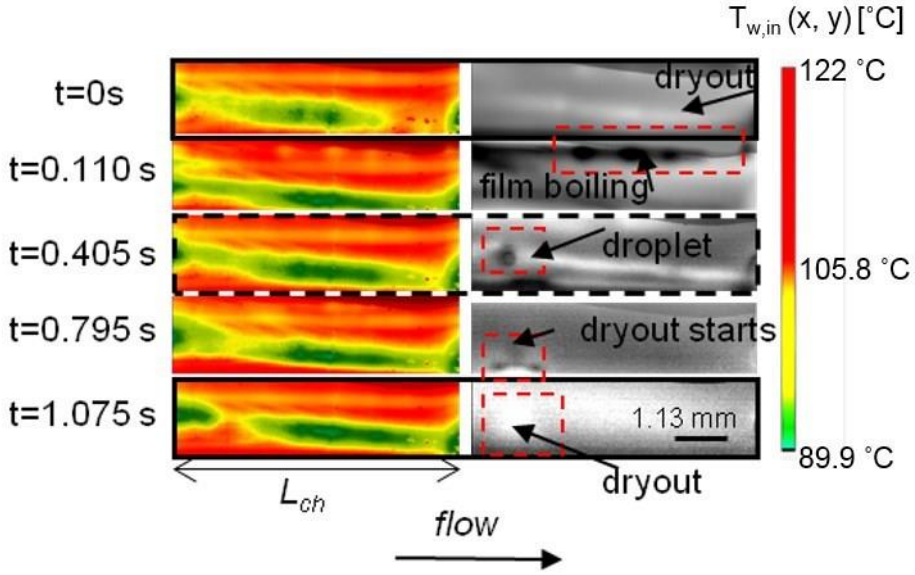

(b)

Figure 6. 59 *(a) 3D plot of the two-dimensional $h_{tp}(x, y)$ as a function of time and channel length for G = 14.78 kg* $^{-2}s^{-1}$ *and q = 92.3 kW* m^{-2}*and (b) correlation between thermal images obtained from the IR camera and optical images from the high- speed camera at the outlet.*

The 3D plot in Figure 6.58a shows non-uniform distribution of the heat transfer coefficient at the outlet (L_{ch}: 14-20 mm). The highest variation of the HTC across the channel width is measured after 12 mm and ranges from 1,160 to 2,290 W m^{-2} K^{-1}. The difference in the cross sectional profile of $h(x, y)$ at the outlet (10 to 20 mm) compared to the inlet, shows no maximum at the centre of the channel cross section. The position of maximum $h(x, y)$ occurs at one corner of the channel and not at the centre. The variation of the cross sectional $h(x, y)$ is higher at the outlet compared to the inlet section (from 0 to 10 mm). The flow patterns depicted in Figure 6.59b are observed from optical images recorded simultaneously with the IR images from the channel base. Based on the contrast of the flow visualisations, the light regions are correlated to suspected dryout of the channel wall. At high heat fluxes (q > 45 kW m^{-2}), the heat transfer coefficient decreases periodically. During the instability cycles, some areas around the centreline of the channel are observed to be white, colour related to suspected dryout during annular flow regime. Suspected dryout occurs only at one side of the outlet for a short time. The side of the wall where suspected dryout occurs is probably the location where bubble nucleation is suppressed. This is concluded from the simultaneous flow visualisations (Figure 6.58b). Correlation of the two-phase heat transfer coefficients (Figure 6.58a) with the simultaneous images of Figure 6.58b shows that directly after suspected dryout at the channel wall near the corner, rewetting of the channel walls occurs mainly at the corners due to the capillary wicking effect and rigorous film boiling commences adjacent to the corners of the channel.

Table 6. 5 summarises the 2D two-phase eat transfer coefficients (from minimum to maxim) along the microchannel as a function of time for G =14.78 kg $m^{-2}s^{-1}$ and increasing heat fluxes. The heat transfer coefficient decreases with increase of the heat flux.

Table 6. 6 *Range of 2D two-phase eat transfer coefficients (from minimum to maxim) along the microchannel as a function of time for three heat fluxes and G=14.78 kg $m^{-2}s^{-1}$..*

G =14.78 kg $m^{-2}s^{-1}$	
Heat flux [kW m^{-2}]	**Two phase heat transfer coefficient [W $m^{-2}K$]**
43.80	1,190-4,860
47.78	1,220-4,180
92.30	1,160-2,290

6.4.7.3 2D & 3D plots of $h_{tp}(x, y)$ for high mass flux

Figure 6.59 shows results from the local two-phase heat transfer coefficient profiles calculated along the channel centreline as a function of time from 0 to 10 mm, for G = 36.87 kg m^{-2}s^{-1} and q = 119.47 kW m^{-2}. The maximum $h_{tp,treline}$ is measured at the channel entrance (x_1 = 0 mm). In general, $h_{tp,treline}$ decreases from 0 to 6.2 mm. however, it increases again from 6.2 mm to 8 mm and drops again from 8 mm to 10 mm. The variation of $h_{tp,\ centreline}$ with the channel length is characterised by local dips and peaks that probably depended on the liquid distribution on the channel based. Figure 6.59 shows that $h_{tp,\ centerline}$ is enhanced at t = 0 s, from 6.2 mm (3,265 W m^{-2} K^{-1}) to 7.84 mm. particularly, it peaks at 7.84 mm with a value of 3,444 W m^{-2} K^{-1}. $h_{tp,treline}$ fluctuates because of local wall temperature and pressure fluctuations. The numbers 1, 2, 3 used in Figure 6.59 show the sequence of events during one cycle of fluctuation. $h_{tp,centreline}$ for x_1 = 0 mm (entrance) fluctuates from 3,700 to 3100 W m^{-2} K^{-1} during a cycle of wall temperature and pressure fluctuation, from t = 0 s to t = 0.395 s. At higher mass flux of G = 36.87 kg m^{-2}s^{-1} and high heat flux of q = 119.47 kW m^{-2} the high amplitude low frequency temperature fluctuations occurred with lower amplitude compared to lower mass fluxes of G = 14.78 kg m^{-2}s^{-1} and q = 92.3 kW m^{-2}.

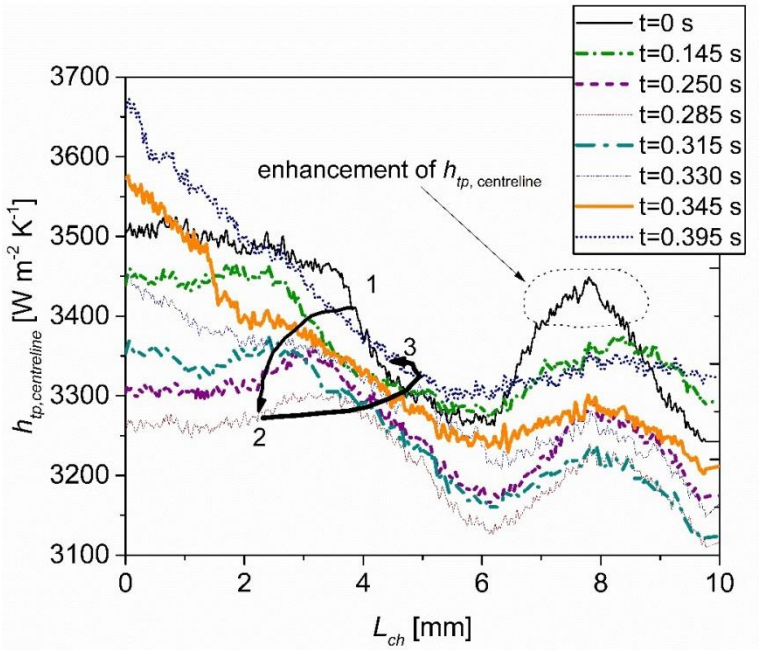

Figure 6. 60 *$h(x)$ along the centreline for the inlet and middle of the microchannel as a function of time for a periodic instability for G = 36.87 kg m^{-2}s^{-1}and q = 119.9 kW m^{-2}.*

Figure 6.60a, b and c show the 3D plot of $h_{tp}(x, y, t)$, synchronised optical images that show the flow patterns and simultaneous wall temperature capture with IR camera for G = 36.87 kg m^{-}

$^{2}s^{-1}$ and q = 119.47 kW m^{-2}. The wall temperature measurements in Figure 6.60c reveals the wall temperature distribution at the channel base during a cycle of instability. The periodic cycle of fluctuation is characterized with the numbers 1, 2, 3 that show the sequence of the events. The numbers are also related to the local two-phase heat transfer coefficient profiles along the centreline shown in Figure 6.60. The flow direction is from the left to the right. Figure 6.60c shows that the wall temperature ranges from 86.4 ^{o}C to 120.3 ^{o}C. The high wall temperature values between 105.1 ˚C and 120.3 ˚C are measured adjacent to the channel upper right corner (red colour). This probably occurs as a result of the suspected dryout of the liquid film near the upper corner during evaporation in the annular flow regime at t = 0.285 s. The white areas on the upper right corner show the possibility of suspected dryout in Figure 6.68b for t = 0.285 s. Bubble nucleation was observed to occur at the channel corners near the entrance. The bubbles grow adjacent to the wall. Coalescence between bubbles resulted in the formation of large agglomerates (t_1 = 0 s). Dimpled liquid areas are observed at the vapour base during the annular flow regime. The dimpled liquid areas appeared to decrease in size from t_2 to t_4. The dashed lines show the location where liquid film (at the right of the dashed line) exists between the vapour and the corner. At the left side of the dashed line suspected dryout of the liquid film was observed.

Table 6. 7 *Abbreviations used for flow patterns.*

Flow regimes	Abbreviation
Bubbly Flow	[B/F]
Bubble wall nucleation	[BWN]
Single bubble flow	[S-B/F]
Bubble Coalescence	[BC]
Slug Flow	[S/F]
Bullet-shape bubble	[B-S B]
Slug-Annular Flow	[S-A /F]
Annular Flow	[A/F]
Annular Dispersed Flow	[A-D/F]
Churn Flow	[CH/F]
Film Boiling	FB]
Suspected liquid film dryout	[S-DRY]
Drops	[DRO]

Figure 6.61a shows the evolution of $h(x, y, t)$ for G = 298 kg m^{-2} s^{-1} and q = 179.2 kW m^{-2}. The maximum value of $h(x, y, t)$ is measured at the centre of the channel entrance. The flow visualisations from the high–speed camera reveal the flow pattern presented in Figure 6.61b for t = 0.288 s. The flow regime from 0 to 7 mm is bubbly flow. Small bubbles appear to grow adjacent to the sidewall corners. The shape of the bubbles is non-spherical; possibly, due to the effect of drag force on the bubble is higher because of the high mass flux used. At the entrance, the heat transfer coefficient varied from 5,700 to 15,000 W m^{-2} K^{-1}. The bubbles grow in size as they move near the superheated sidewalls.

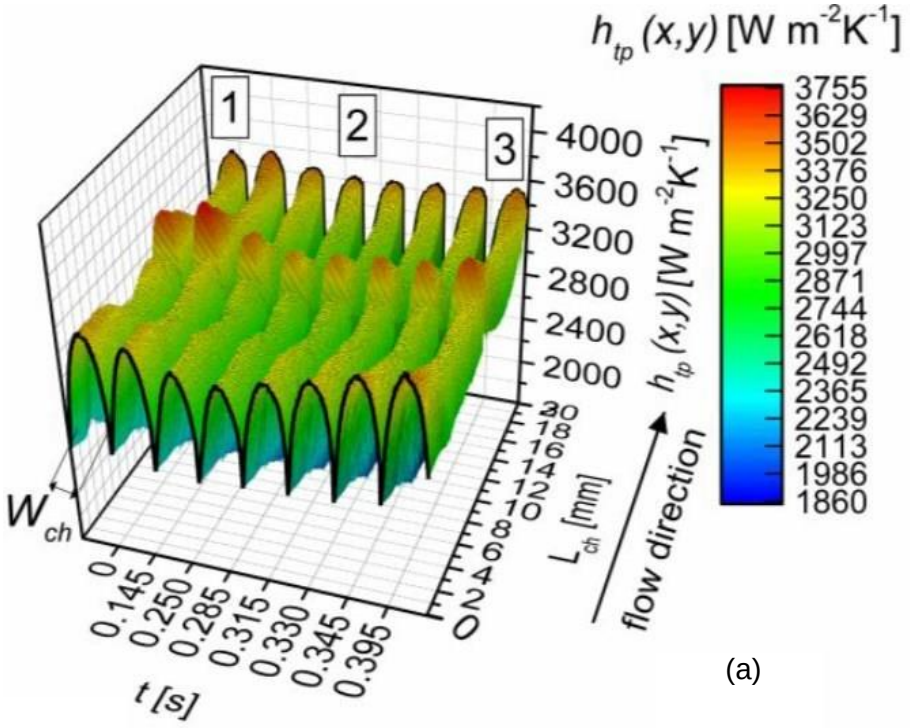

(a)

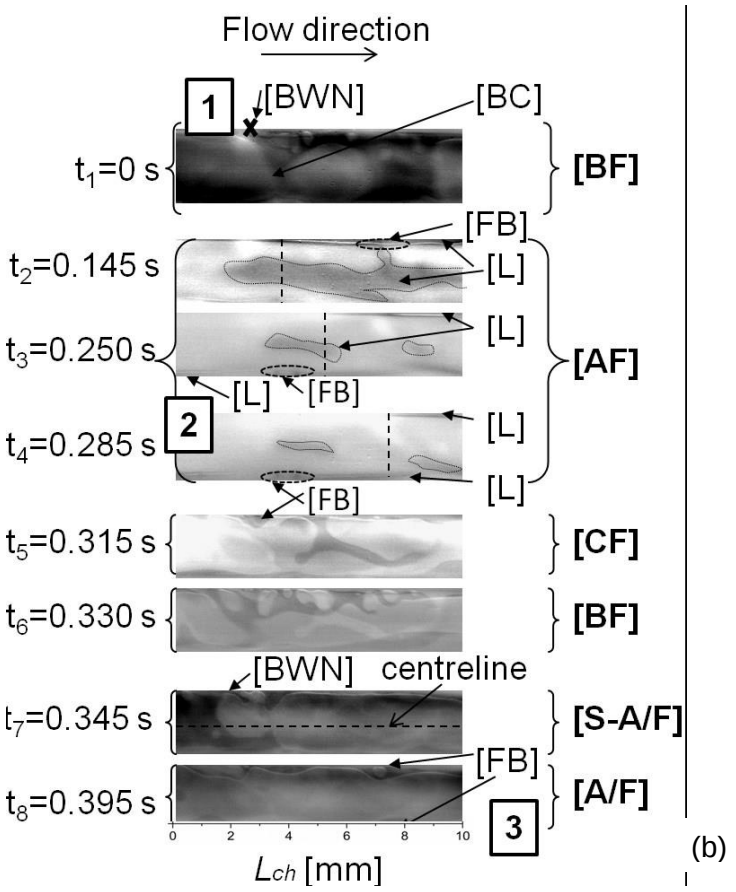

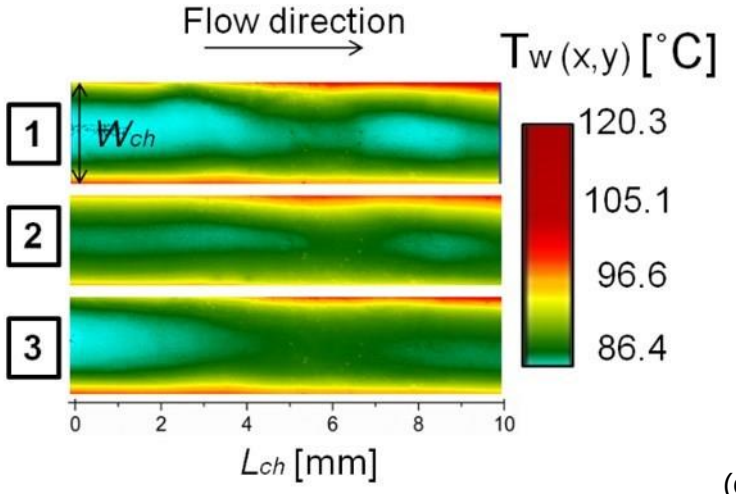

Figure 6. 61 *(a) 3D plot of high spatial and temporal resolution two-dimensional h_{tp} (x,y) as a function of time for a periodic cycle of instability for G = 36.87 kgm^{-2}s^{-1} and q = 119.9 kW m^{-2} and (b) flow patterns observed with high-speed imaging (200 Hz) from t = 0 s to t = 0.395 s simultaneously with (c) the thermal images, for G=36.87 kg m^{-2}s^{-1} and q = 119.47 kW m^{-2}.*

Then, from 9 to 14 mm the bubbles depart from the walls and coalescence, forming cap bubbles (curved tail) in different sizes that later form slugs as they grow due to evaporation of the liquid on their surface. An annular flow regime is dominant at the outlet (4 to 20 mm). Bubble growth in the superheated layer between the vapour core and the walls results in the formation of

large droplets in the vapour annulus (Figure 6.62b). The two-phase heat transfer coefficients are the highest at the entrance of the channel.

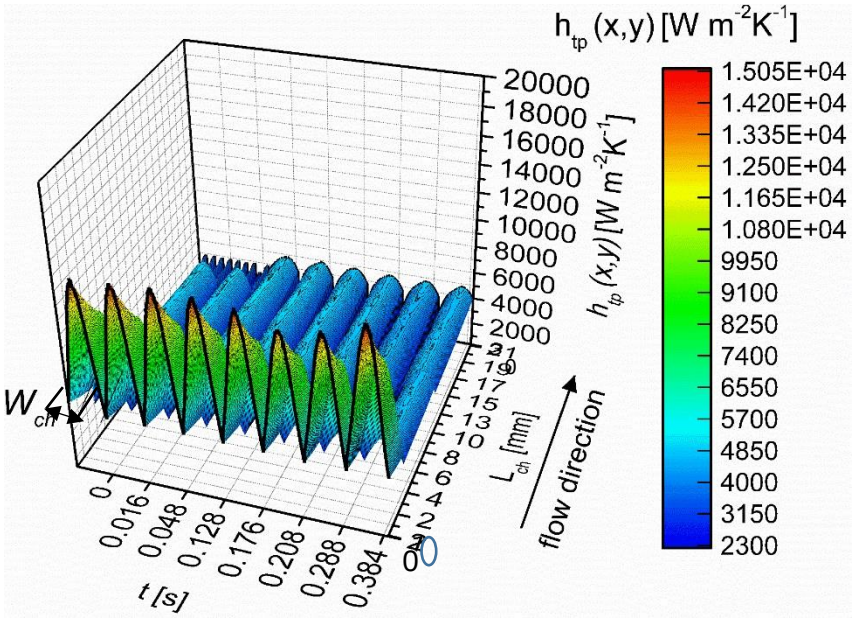

(a)

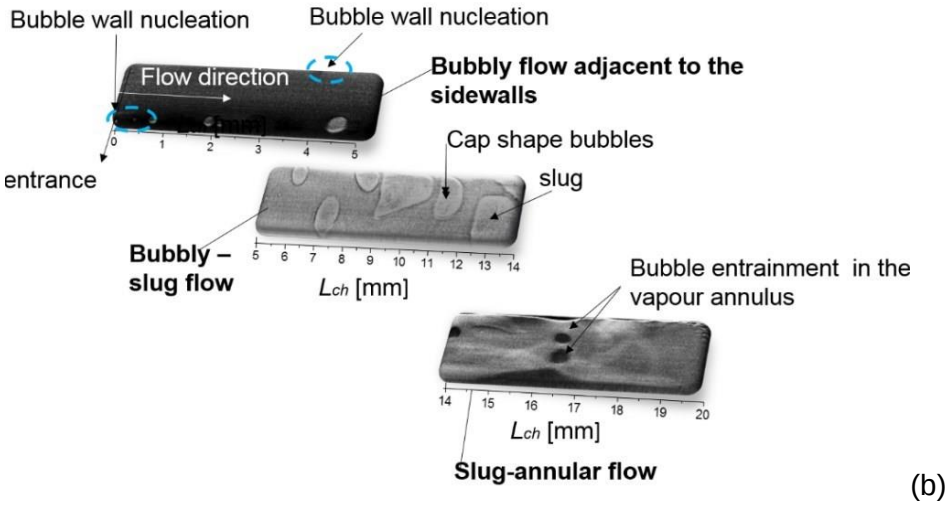

(b)

Figure 6. 62 *High spatial and temporal resolution 2D plot of $h(x, y, t)$ as a function of time for G = 298 kg m^{-2} s^{-1} and q =179.2 kW m^{-2} and (b) flow visualisation from high –speed camera results for the inlet, middle and outlet of the microchannel at t = 0.288 s.*

6.4.7.4 Bubble dynamics

The two-phase heat transfer coefficient in contour plot of Figure 6.62 reveal high heat transfer coefficients at the centre of the entrance of the channel.

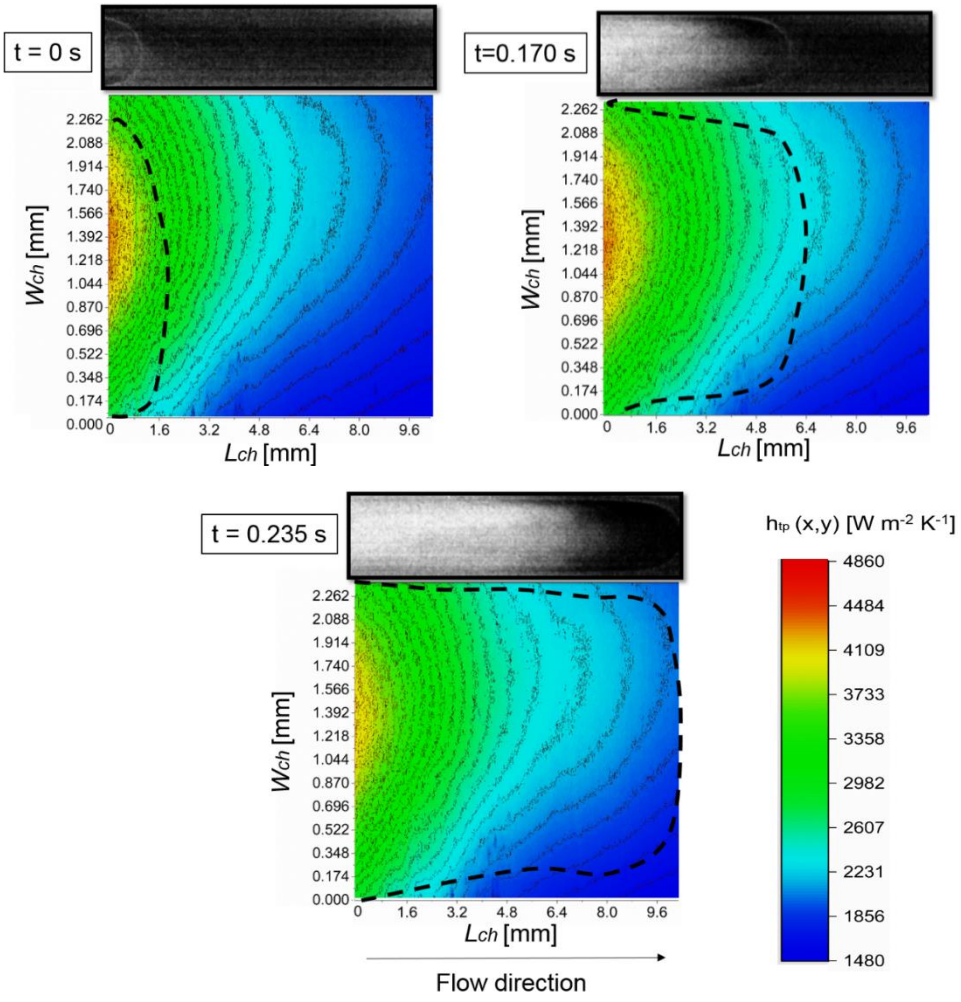

Figure 6. 63 *Contour plot of the heat transfer distribution at the channel inlet during bubble axial growth for G = 14.78 kg $m^{-2}s^{-1}$ and q = 42.80 kWm^{-2}.*

From flow visualisations, from t = 0 s to t = 0.170 s the confined bubble (from channel width) at the entrance of the channel was found to increase in length, axially, along the channel, by forming a slug. The reason why the heat transfer coefficient was higher below the bubble centre, could be explained based on the possible existence of liquid film. The enhancement of $h_{tp}(x,y)$ occurred possibly due to film evaporation at the bubble base during the growth of the bubble along the channel axial direction. The liquid film thickness profiles along the channel cross section peaked. At the centre of the bubble and increased with the bubble length (gas plugs).

Figure 6.63 demonstrates the effect of the confined bubble axial growth to the heat transfer coefficient at the channel entrance. The optical images are correlated with the contour plots of the heat transfer coefficient distribution $h(x, y)$. The heat transfer coefficient maximum value 4,860 W m^{-2} K^{-1}, measured at the centre of the bubble decreased with the axial growth of the bubble as

more liquid possibly evaporates under bubble. Instability in the curves was induced due to evaporation at the channel corners where the heat transfer coefficient is found to decrease around 2,231 W m^{-2} K^{-1}.

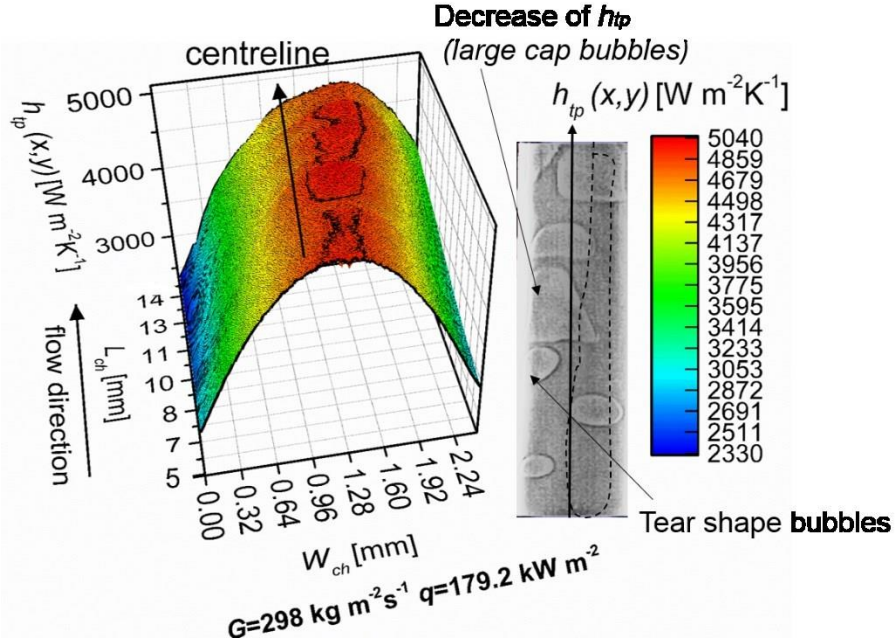

Figure 6. 64 *3D plot of two-phase heat transfer coefficient h(x, y) during bubbly flow from 5 to 14 mm along the channel. Correlation with simultaneous flow visualisation the same length.*

6.5 Conclusions

High spatial and temporal resolution thermal images were recorded using high-speed IR thermal imaging and synchronised optical imaging during flow boiling in a PDMS based microchannel. Local pressure measurements from the integrated pressure sensors near the inlet and outlet of the microchannel assisted in the calculation of accurate heat transfer coefficients. Local heat transfer coefficients were correlated with the contrast of the high quality optical images. The effect of the local flow patterns on the two dimensional two-phase heat transfer coefficient were studied with special attention on flow instability cycles. The 3D plots of the two-dimensional two-phase heat transfer coefficients as a function of time, revealed local enhancement of the heat transfer coefficient at the centre of the channel entrance. The maximum heat transfer coefficient occurred before axial expansion of the fully confined bubble at the channel entrance for

low mass fluxes and heat fluxes (q < 45 kW m^{-2}). However when axial expansion of the elongated confined bubble occurred along the whole channel domain resulted in flow reversal which caused suspected dryout at the channel edges and high amplitude and as a result, temperature and pressure fluctuations were induced in the channel. The wall temperature appeared non-uniform during boiling across the channel surface. The 3D two-phase heat transfer coefficient plots revealed details about the location of heat transfer enhancement and deterioration. The high spatial resolution of the heat transfer coefficient data revealed dips and peaks at the centre of the channel for high mass fluxes and where correlated with optical images that reveal the local flow regimes. The $h_{tp(x, y)}$ varied significantly across the channel width. The heat transfer coefficient profile across the channel section peaked at the centre of the entrance in all the examined cases. This occurred mainly at the entrance of the channel just before the axial expansion of a confined bubble for low mass fluxes. The heat transfer coefficient profile at the channel cross section was found non-uniform along the whole channel domain. The contrast of the optical images revealed the vapour-liquid interface during bubble confinement, slug and annular flow regime. Annular flow was the main flow regime observed to occur at high heat fluxes (q > 45 kW m^{-2}), with film boiling and entrainment of liquid drops in the vapour annulus that caused suspected dryout at the base. The effect of the confined bubble axial growth to the two-phase heat transfer coefficient distribution at the channel entrance was also studied at low mass fluxes and low heat fluxes. The high amplitude fluctuations of the local heat transfer coefficient were related with the axial growth of the confined to channel bubble along the whole length of the channel.

6.6 Summary

In this chapter, flow boiling heat transfer and associated flow patterns were experimentally investigated using infrared thermography to measure inner wall temperature from the PDMS side of the microchannel with synchronised high-speed visualisation and pressure measurements from integrated pressure sensors. Sections 6.4.1 to 6.4.6 evaluate interfacial heat transfer coefficients, which are correlated with simultaneous high quality optical images, obtained from flow visualisation using high- speed camera. Interfacial heat transfer analysis with simultaneous flow visualisation at various mass fluxes and heat fluxes was presented. Section 6.4.7 presents results of the heat transfer coefficient distribution using temperature maps obtained from the ITO/glass base, with synchronised high-speed visualizations from PDMS, which is optically transparent.

3D plots were presented with the interfacial heat transfer coefficients spatially averaged across the channel width as a function of channel length and time at three constant mass fluxes (G) of 36.87 kg $m^{-2}s^{-1}$, 73.74 kg $m^{-2}s^{-1}$ and 110.62 kg $m^{2}s^{-1}$ and increasing heat fluxes. Then, time averaged and spatially averaged heat transfer coefficients for the inlet, middle and outlet of the microchannel were illustrated in 2D plots as a function of heat flux for the three constant mass fluxes. Analytical 3D plots presented spatially averaged across the channel width interfacial heat transfer coefficients as a function of channel length and time for the aforementioned mass fluxes. The 3D plots of the spatially averaged heat transfer coefficient were presented as a function of time for the onset of boiling (ONB), maximum heat transfer coefficient (HTC_{max}) and maximum heat transfer rate as well as the critical heat flux (CHF). Heat transfer mechanisms were discussed using the trends of the heat transfer coefficients during instability cycles. IR images provided 2D wall temperature patterns from the interface, during annular flow regime, which were then correlated with high quality images from the channel base. Annular flow regime instabilities were then correlated with thin film thinning and temporal dryout. Local two-phase heat transfer coefficients spatially averaged along the channel centreline at flowstream direction were displayed with simultaneous pressure drop data from inside the microchannel as a function of time. Liquid and vapour distribution at the heater base was evaluated using optical images where the black colour was related to liquid and white colour to vapour. Liquid and vapour phases in the channel were highlighted using the contrast of the optical images and 3D histograms were used to quantify the liquid-vapour phase distribution of phases from the channel base using image-processing techniques. The thinning of the liquid film during annular flow because of liquid evaporation was correlated with the colour intensity scale. 3D plots of $T_{w,}(x, y)$ and $h_{tp}(x, y)$ as a function of channel width and length are illustrated during single-bubble growth and bubble confinement in the channel. The last section of this chapter illustrates high spatial and temporal resolution 3D and contour plots of 2D heat transfer coefficients $h_{tp}(x, y)$ as a function of time, during flow boiling on the microchannel surface from the ITO /glass channel base with simultaneous flow visualisations from PDMS.

Chapter 7 Overall Conclusions and summary of future work

7.1 General Conclusions

One- and two- dimensional two-phase heat transfer coefficients were obtained during flow boiling in silicon parallel multi-microchannels and at a PDMS-based high aspect ratio microchannel under uniform heating. The calculated two – dimensional heat transfer coefficients have shown that the use of Polydimethylsiloxane microchannel provided plenty of advantages such as ease of microchannel fabrication, optical accessibility as well as transparency to infrared radiation and optically accessibility.

Flow boiling of deionised water in nine different cross section aspect ratio silicon microchannels heat sinks under uniform heating has been investigated with particular attention to the effects of microchannels channels aspect ratio on the local two-phase heat transfer phenomena. An experimental system was designed and constructed to carry out the experimental investigations using nine microchannels heat sinks with aspect ratios that range from 0.33 to 3 with respective hydraulic diameters that range from 50 to 150 μm. The present study focused on the influence of increasing aspect ratio on flow boiling heat transfer performance during flow boiling in microchannels. Comparing heat transfer coefficients between the different aspect ratios and hydraulic diameters showed that silicon microchannels heat sink of α = 1.5 and D_h = 120 μm provided the maximum heat transfer coefficients with modest pressure drop values during two-phase flow. The microchannels were wide but not very shallow. Wall temperature at locations of *T2, T3, and T4* shows little variation between locations, but high amplitude fluctuations. High-speed imaging, performed simultaneously with pressure and temperature measurements, showed that inlet/outlet pressure and temperature fluctuations existed due to alternation between liquid/two-phase/vapour flows. For α = 1.5, bubble nucleation was observed at low mass fluxes. The bubble grows very fast but does not occupy the whole channel in order to cause backflow. At high aspect ratios, nucleation was observed to occupy very fast. The elongated bubble grows rapidly at the upstream and downstream end of the microchannels resulting in flow reversal and temporal dryout. Is it observed that when this happens at the high aspect ratio parallel channels of this study, the rest of the microchannels are affected by the excess flow as the microchannel is blocked and cause

parallel channel instabilities. Periodic phenomena of wetting, rewetting were observed for high aspect ratio channels. Since the heated length is only 15 mm, at high heat fluxes significant interaction takes place between the stream generated in the microchannels and the inlet subcooled liquid. At high heat fluxes, after venting of the microchannel the region of liquid droplets proved the onset of dryout.

During flow boiling in high aspect ratio microchannels (α = 3, 2) bubbles were observed to grow at sidewalls at the inlet (T1). For high aspect ratio channels, parallel instabilities result in temporal dryout simultaneously at all parallel microchannels (high amplitude instabilities). Elongated bubbles were proved a limited factor for heat transfer in microchannels because they resulted in pressure drop increase. Increasing the width of the microchannels for a constant depth, results in a decrease of pressure drop. In contrast, the use of small width channels results in parallel microchannel instabilities because of increase of the microchannels number and can induce temperature oscillations and dryout on the surface of the microchannels. High-speed camera imaging, performed simultaneously with pressure and temperature measurements, showed that bubble nucleation can be observed at high heat fluxes at small time-scales. Alternation between isolated bubble, confined bubble (plug /slug flow), annular flow and mist flow existed during flow boiling instabilities in parallel silicon microchannels.

The general trend identified for all channel designs for the saturated region at position 5 downstream is that the local heat transfer coefficient decreases after a maximum value with increasing heat flux. When large vapour slugs are formed at higher mass fluxes and move through the channel, thin liquid film near causes both the bubble size and generation frequency to increase at the wall nucleation sites. These nucleate boiling heat transfer characteristics are exhibited over high heat transfer coefficients.

Comparing microchannel heat sinks at constant W_{ch} of 150 μm and changing height from 50 μm (D_h = 75 μm, α = 3, A_{cr} = 7500 μm^2) to 100 μm (D_h =120 μm, α = 1.5, A_{cr} =15,000 μm^2) we conclude that the heat transfer coefficients with higher for values of height which are higher and the pressure drop is lower. There is an important effect of the microchannel height on the heat transfer and pressure drop because it can affect bubble nucleation and growth in the microchannels. At low mass fluxes and high heat fluxes nucleation was observed to occur the thin liquid film at the sides of the channels. Increasing the inlet subcooling temperature resulted in higher values of heat transfer coefficients with the penalty of high-pressure drop. For the microchannel heat sinks with the maximum height, the average pressure drop values were the lowest. After boiling occurrence, pressure drop increases significantly with increasing heat flux for the high aspect ratio microchannels. As the hydraulic diameter decreased, the magnitude of the pressure drop increased.

The second part study of the study investigated two-phase flow boiling in a microchannel using FC-72 liquid, using dual wall temperature mapping, which uses high spatial and temporal resolution infrared thermography met with simultaneous optical observations and pressure measurements in the microchannel. The use of the unique channel geometry and thin channel base coated with transparent heating allowed high-quality time and spatial resolution temperatures to be obtained and mapped at the channel wall. . Flow boiling experiments were carried out using FC-72 for the mass fluxes of 36.87 kg $m^{-2}s^{-1}$, 73.74 kg $m^{-2}s^{-1}$ and 110.62 kg $m^{-2}s^{-1}$ and increasing heat flux. Time averaged interfacial heat transfer coefficient and spatially averaged for the inlet, middle and outlet of the microchannels showed increasing trend with increasing heat flux up to a maximum after which it decreased with a further heat flux increase for all the tested mass fluxes. For low heat fluxes, the heat transfer coefficient increased almost linearly with heat flux. For the mass fluxes of 36.87 kg $m^{-2}s^{-1}$, 73.74 kg $m^{-2}s^{-1}$, at higher heat fluxes, the curve changes in slope before ONB and after HTC_{max} from where it decreases. For the highest mass flux of 110.62 kg $m^{-2}s^{-1}$ the slope changes just before ONB and after ONB. There is high fluctuation of pressure drop and wall temperature at ONB and CHF.

High rate of heat transfer coefficient was obtained due to the high aspect ratio of the microchannels by using a very small mass flow rate. This had an impact on two-phase heat transfer mechanism, which was dictated by periodic behaviour of the flow patterns in microchannels. Two-phase heat transfer coefficient was found to first increase with increasing exit vapour quality and then decreased at higher vapour quality. This was achieved due to the confinement induced by the channel depth and the capillary effect that enhanced liquid flow at the channel corners. The highest heat transfer coefficient was measured on the centreline near the inlet of the channel were bubbly-slug flow was the main flow pattern observed from flow visualisation. Probably the high rate of heat transfer coefficient at the channel inlet could be attributed to the thicker liquid film here compared to the outlet. Increasing further the heat flux, instability cycles occurred along the whole channel domain and the pressure drop increased, but the heat transfer coefficients were measured to be higher even in this case compared to single-phase flow, as the dryout was only partial at the channel corners. Partial dryout occurred because of suppression of bubble nucleation observed at the channel outlet corners.

The interfacial wall temperature of single bubbles was captured as well as pressure oscillations with time. The two-phase spatially averaged heat transfer coefficient values were found to fluctuate in time and the fluctuations were correlated with flow visualisations in order to obtain a better insight. The 3D plots of $h(x, y)$ assisted in a better understanding of the flow instability cycles and suggested that only a portion of the heated cross section is completely dry at the channel outlet and uneven liquid distribution was observed at the channel base. Highest

heat transfer coefficients values were obtained near the exit and near the entrance of the microchannels were nucleate boiling occurred. he onset of dryout was followed by a significant drop in the local two-phase heat transfer coefficient along the microchannel.

It was found that a superheated liquid layer near channel walls plays a significant role in bubble dynamics during boiling in microchannels. This superheated film results in acceleration in the bubble growth as the bubble comes closer to the channels sidewalls. The bubble dynamics determined the frequency of alternation between phases, and consequently the frequency of the pressure and temperature oscillations.

At the ONB, an increase of the HTC at the channel middle occurred because of the bubble slug coalescence during bubbly-slug flow regime which resulted in a local temperature decrease at the channel centre of the channel and therefore the HTC increased. The merging of bubbles induced higher local heat transfer coefficient at the centre of the channel cross section, but lower values along the channel edges. At heat fluxes higher than 42.28 kW m^{-2} annular flow was observed to become the dominant flow pattern along the whole channel domain.

The CHF was higher compared to results from larger hydraulic diameter channels using a similar mass flux and liquid, but with corners that were rounded in cross section. This was attributed to the capillary effects of a high aspect ratio rectangular cross section. This enabled the effect of heat flux on local temperature variation, flow boiling heat transfer coefficient distribution and the two-phase pressure drop to be studied.

The wall temperature distribution at the bubble wall interface was presented from bubble nucleation to bubble confinement and 3D plots of the interfacial $h_{tp}(x, y)$ as a function of channel length and width were produced. During partially confined flow: the evaporation between the bubble liquid-vapour contact line and the superheated liquid layer adjacent to the sidewall controlled the heat transfer under the bubble. The spherical shape of the bubble deformed when partial dryout occurred, as there was no liquid for evaporation, the bubble started evaporating from the contact line that was closer to the flowstream centreline. The temperature at the interface of the bubble and the wall was non-uniform. Wall temperature was found to decrease from the sidewall to the centre of the channel .The temperature was found to be lower inside of the bubble contact line. Around the bubble, the temperature was higher than the bubble temperature. The interfacial wall temperature of the confined bubble was non-uniform. Initially the bubble grows width- wise, as the temperature difference between the bubble contact lines that is closer to the bulk liquid is higher on that side. The IR images during bubble growth revealed the relation between the temperature difference and the radius of the bubble. When the bubble grows symmetrically in widthwise direction, the wall temperature distribution at the bubble base was measured close to the boiling point at the unconfined stage, where the bubble

size was very small and there was temperature uniformity at the bubble base. It is worth noting that the nucleation of the bubble appeared in the superheated thermal boundary layer adjacent to the sidewall of the channel. The temperature of this liquid superheated layer (confirmed from high-speed images) was higher than the boiling point of the liquid. The thickness of the superheated layer decreased from the inlet to the outlet. When the bubble occupied the channel depth then it got detached from the sidewall and started growing inside the superheated layer, which was adjacent to the sidewall. During bubble partial confinement (only by channel height), the wall temperature at the interface of the bubble appeared to be lower than the boiling point of the liquid which possibly proves the existence of the liquid microlayer which evaporates as the bubble base grows in diameter. As the spherical bubble increases in size in the superheated layer, the liquid between the bubble and the sidewall evaporates too. Dryout was suspected to occur at the side of the bubble that is closer to the sidewall. This could be possibly attributed to the fast evaporation of a very thin layer between the bubble and the wall. The other side of the bubble was surrounded by liquid; therefore, the temperature at the bubble base adjacent to the vapour-liquid contact line was lower. During full confinement of the bubble by the channel width, the superheated layer appears at both sidewalls. When the bubble is fully confined by the channel width, the highest temperature drop is measured along the bubble length (along the channel length). Then dryout is suspected to occur from the other side of the sidewall as the liquid between the bubble contact line and the sidewall almost completely evaporates.

In the single-phase region, pressure drop decreases slightly with increase of heat flux and then increases with heat flux at the two-phase region. In single –phase pressure decreases as result of the fluid viscosity decrease with increasing temperature of the fluid and in two-phase it increases as a result in the increase of vapour in the channel. 3D plots of $h_{tp}(x, y)$ as a function of time were presented for different mass flux and heat flux conditions. The 3D plots of $h_{tp}(x, y)$ were correlated with simultaneous obtained optical images. For low mass flux and high heat flux conditions cross section heat transfer coefficient was non-uniform as a result of local suspected dryout and at high mass fluxes peaks and dips of the two-phase heat transfer coefficient profiles were measured along the channel that can be related with interfacial waves. The contrast of the optical images revealed the vapour-liquid interface during bubble confinement, slug and annular flow regime. Annular flow was the main flow regime observed to occur at high heat fluxes, with droplet entrainment and suspected dryout.

The correlation of the contour plots of $h_{tp}(x, y)$ as a function of channel length and width with optical images assisted in a better understanding of the causes of liquid film dryout on the microchannel surface. Local heat transfer coefficients from the ITO/glass were correlated with optical images. The results revealed local enhancement of the heat transfer coefficient directly

at the confinement of the bubble at the channel entrance. Bubble nucleation was observed to occur at the high aspect ratio channel superheated sidewalls corners at higher flow rates. The bubbles we observed to grow in the superheated liquid layer at higher mass flux and heat flux. When bubble nucleation was suppressed at the channel sidewalls, vapour covered the channel section and local dryout occurred.

The main for conclusions for this study are summarised below:

- High heat fluxes can be achieved using very low flow rates with FC-72 in a PDMS microchannel; device of only 192 μm hydraulic diameter. Using low flow rates of coolant results in lower energy consumption of the pump and the entire cooling system.

- Improvement on the existing experimental methods on flow boiling was carried out by sign PDMS, transparent to infrared radiation, microchannels. Synchronized IR thermography from PDMS microchannels leads to the measurements of temperature at the vicinity of the wall. These results assisted in the determination of the inner wall two-phase heat transfer coefficient distributions which have not been measured experimentally before. These results are expected to be very useful for numerical simulations.

- The measured microchannel temperatures PDMS shows non-uniform behaviour. The spatial variation distributions are high at the channel across section particularly near the channel inlet. This occurs due to the liquid and vapour that pass through the channel base. The entrance region has high amplitude fluctuations due to bubble nucleation.

- Silicon microchannels with aspect ratios close to 1.5 (D_h=120 μm) result in good heat transfer with heat transfer coefficients up to 200 kW m^{-2} K and pressure drop values lower than 100 mbar.

.

7.2 Future recommendations

This work presented results of 1D and 2D two–phase spatial heat transfer coefficients as a function of time as well as averaged over time during flow boiling in microchannels. The results were obtained from synchronised wall temperature and pressure drop measurements and were correlated with the flow patterns obtained from high-speed optical imaging of the microchannels top or base. Five thin nickel film high-response time temperature sensors were used to measure

wall temperature locally in five positions in parallel silicon microchannels heat sinks of different microchannel aspect ratios in order to evaluate the different heat transfer performance of the heat sinks. There is a need for fast –response devices for high spatial resolution wall temperature measurements that are not flow intrusive and allow for simultaneous high quality optical images from the channel base. A novel high aspect ratio Polydimethylsiloxane (PDMS) microchannel device was fabricated and was used with infrared thermography. High spatial and temporal resolution measurements were provided in the vicinity of the wall due to the transparency of PDMS to mid-wave infrared. Two-dimensional interfacial heat transfer coefficients were measured at the wall during liquid evaporation. The PDMS microchannel was bonded on transparent indium tin oxide (ITO) coated glass. The optical accessibility of the ITO heater in combination with the optically accessible PDMS top resulted in a transparent microchannel device. PDMS is cheaper than glass and the fabrication of the channel is a simple and less cost effective technique. High–speed imaging synchronised flow visualisation could be simultaneously achieved from the microchannel base. Two–phase flow boiling experiments require both high-speed infrared thermography and flow visualisations in order to be able to evaluate the results. Liquid-vapour phase's variate with the flow pattern therefore can affect the heat transfer coefficient. 3D plots of the interfacial two–phase heat transfer coefficients during bubble growth confinement assisted in a better understanding of the two-phase enhancement mechanisms that occur in a single microchannel. Two-dimensional high spatial and temporal resolution two –phase heat transfer coefficients were plotted with time during flow boiling instabilities such as elongated bubble axial growth. The flow boiling experiments were carried out under uniform heating. Polydimethylsiloxane was the ideal material for implementation of miniature pressure sensors in the microchannel that allow for accurate high response time pressure fluctuations that occurred during the bubble growth. It is worth considering the roughness of the material and its effect on the heat transfer.

For parallel silicon microchannel heat sinks more experiments are required with different cooling liquids in order to assess the effect of different surface tensions on the bubble dynamics, flow instabilities and heat transfer characteristics of a microchannel heat sink with flow boiling. Safe and efficient operation of CPUs requires a junction temperature below 85 °C, therefore a cooling liquid with a saturation temperature close to a junction temperature should be considered. A cooling liquid with high dielectric constant is preferable, as it will not damage electronic equipment in the event of a leak or other failure.

The effect of microchannel aspect ratio on flow boiling heat transfer can be studied with PDMS microchannels of different aspect ratios and constant hydraulic diameter. Two dimensional wall temperature measurements at the liquid-solid interface can be used to study in

detail the effect of aspect ratio of a PDMS microchannel on the heat transfer and bubble dynamics. However, it was found that boiling significantly affects flow distribution in the present heat sink due to flow instabilities, causing the significant temperature non-uniformity in transverse direction. Additionally, multichannel microchips from PDMS and the interfacial heat transfer coefficients can be assessed with infrared thermography and high-speed imaging.

Microchannels with micro and nanostructured surfaces can be tested in order to observe enhancement of the heat transfer. Heat transfer enhancement can be achieved with using nanostructure surfaces that improve wettability. The nanostructured surfaces have a great advantage to be able to decrease the interfacial thermal resistance and therefore to expect significant heat transfer coefficient enhancement at the hydrophobic surfaces. These experiments are required in order to provide knowledge on the i.e. physics of surface structures interactions with microscale heat transfer and mass transfer process, which is lacking from this field. Smaller hydraulic diameters should also be investigated as higher heat transfer coefficients are expected at D_h < 50μm and aspect ratios in the range of 1 to 10 (Investigation of degree of confinement effects on pressure drop).

Infrared thermography technique and high-speed imaging can be combined with μ-PIV using a transparent microchannels form PDMS could be combined with resolution PIV flow measurements. Flow filed measurements could be achieved using a can be achieved during flow boiling in PDMS microchannels with synchronized IR thermography and high-speed imaging. Synchronised IR thermography and premeasurement s from inside the channel will assist in giving a very good insight into the flow boiling instabilities and heat transfer mechanisms.

PIV can be used for the measurements of bubble size and shape versus time, bubble departure frequency, wait and growth times bubble departure diameter. Data for nucleation site density, frequency, wait and growth times, 2D temperature history of the heater surface and velocity distribution within the liquid surrounding the bubbles. PIV can be also used to measure thickness of the liquid film, which is trapped between the heated wall and the elongated bubbles.

7.3 Summary

In this chapter, firstly section 7.1 provides the general conclusions of the research study and section 7.2 provides recommendations for future work.

References

[1] "International Technology Roadmap for Semiconductors (ITRS)," 2011.

[2] T. G. Karayiannis and M. M. Mahmoud, "Flow boiling in microchannels: Fundamentals and applications," *Appl. Therm. Eng.*, vol. 115, pp. 1372–1397, 2017.

[3] J. F. Tullius, R. Vajtai, and Y. Bayazitoglu, "A review of cooling in microchannels," in *Heat Transfer Engineering*, 2011, vol. 32, no. 7–8, pp. 527–541.

[4] I. Mudawar, "Assessment of high-heat-flux thermal management schemes," *IEEE Trans. Components Packag. Technol.*, vol. 24, no. 2, pp. 122–141, 2001.

[5] W. Qu and I. Mudawar, "Experimental and numerical study of pressure drop and heat transfer in a single-phase micro-channel heat sink," *Int. J. Heat Mass Transf.*, vol. 45, no. 12, pp. 2549–2565, 2002.

[6] D. B. Tuckerman and R. F. W. Pease, "High-performance heat sinking for VLSI," *IEEE Electron Device Lett.*, vol. 2, no. 5, pp. 126–129, 1981.

[7] X. Yin and H. H. Bau, "Uniform Channel Micro Heat Exchangers," *J. Electron. Packag.*, vol. 119, no. 2, pp. 89–94, Jun. 1997.

[8] J. C. Sturgis and I. Mudawar, "Assessment of CHF Enhancement Mechanisms in a Curved, Rectangular Channel Subjected to Concave Heating," *J. Heat Transfer*, vol. 121, no. 2, p. 394, 1999.

[9] A. Malik, "inNEMI Roadmap Identifies Trends Impacting Electronics Thermal Management.," 2016.

[10] T. Alam, P. S. Lee, C. R. Yap, and L. Jin, "A comparative study of flow boiling heat transfer and pressure drop characteristics in microgap and microchannel heat sink and an evaluation of microgap heat sink for hotspot mitigation," *Int. J. Heat Mass Transf.*, vol. 58, no. 1–2, pp. 335–347, 2013.

[11] T. Harirchian and S. V. Garimella, "Boiling Heat Transfer and Flow Regimes in Microchannels—A Comprehensive Understanding," *J. Electron. Packag.*, vol. 133, no. 1, p. 11001, 2011.

[12] I. Mudawar, "Recent Advances in High-Flux, Two-Phase Thermal Management," *J. Therm. Sci. Eng. Appl.*, vol. 5, no. 2, p. 21012, 2013.

[13] J. R. Thome, "State-of-the-art overview of boiling and two-phase flows in microchannels," *Heat Transf. Eng.*, vol. 27, no. 9, pp. 4–19, 2006.

[14] Z. Li, Y.-L. He, G.-H. Tang, and W.-Q. Tao, "Experimental and numerical studies of liquid flow and heat transfer in microtubes," *Int. J. Heat Mass Transf.*, vol. 50, no. 17–18, pp. 3447–3460, 2007.

[15] S. G. Kandlikar, "Fundamental issues related to flow boiling in minichannels and

microchannels," *Exp. Therm. Fluid Sci.*, vol. 26, no. 2–4, pp. 389–407, 2002.

[16] J. Lee and I. Mudawar, "Two-phase flow in high-heat-flux micro-channel heat sink for refrigeration cooling applications: Part II - Heat transfer characteristics," *Int. J. Heat Mass Transf.*, vol. 48, no. 5, pp. 941–955, 2005.

[17] W. Qu and I. Mudawar, "Flow boiling heat transfer in two-phase micro-channel heat sinks — I . Experimental investigation and assessment of correlation methods," vol. 46, pp. 2755–2771, 2003.

[18] D. Bogojevic, K. Sefiane, G. Duursma, and A. J. Walton, "Bubble dynamics and flow boiling instabilities in microchannels," *Int. J. Heat Mass Transf.*, vol. 58, no. 1–2, pp. 663–675, 2013.

[19] T. Chen and S. V. Garimella, "A Study of Critical Heat Flux During Flow Boiling in Microchannel Heat Sinks," *J. Heat Transfer*, vol. 134, no. 1, p. 11504, 2012.

[20] L. Jiang, M. Wong, and Y. Zohar, "Forced convection boiling in a microchannel heat sink," *J. Microelectromechanical Syst.*, vol. 10, no. 1, pp. 80–87, 2001.

[21] M. Lee, Y. K. Lee, and Y. Zohar, "Design, fabrication and characterization of a thermal microsystem integrated with heaters, pressure and temperature microsensors," *J. Micromechanics Microengineering*, vol. 21, no. 12, 2011.

[22] L. Zhang, E. N. Wang, K. E. Goodson, and T. W. Kenny, "Phase change phenomena in silicon microchannels," *Int. J. Heat Mass Transf.*, vol. 48, no. 8, pp. 1572–1582, 2005.

[23] M. Lee, Y. Y. Wong, M. Wong, and Y. Zohar, "Size and shape effects on two-phase flow patterns in microchannel forced convection boiling," *J. Micromechanics Microengineering*, vol. 13, no. 1, pp. 155–164, 2003.

[24] J. Barber, D. Brutin, K. Sefiane, J. L. Gardarein, and L. Tadrist, "Unsteady-state fluctuations analysis during bubble growth in a 'rectangular' microchannel," *Int. J. Heat Mass Transf.*, vol. 54, no. 23–24, pp. 4784–4795, 2011.

[25] J. Barber, K. Sefiane, D. Brutin, and L. Tadrist, "Hydrodynamics and heat transfer during flow boiling instabilities in a single microchannel," *Appl. Therm. Eng.*, vol. 29, no. 7, pp. 1299–1308, 2009.

[26] M. Mirmanto, "Local pressure measurements and heat transfer coefficients of flow boiling in a rectangular microchannel," *Heat Mass Transf. und Stoffuebertragung*, vol. 52, no. 1, pp. 73–83, 2016.

[27] M. Piasecka, "Heat transfer mechanism, pressure drop and flow patterns during FC-72 flow boiling in horizontal and vertical minichannels with enhanced walls," *Int. J. Heat Mass Transf.*, vol. 66, pp. 472–488, 2013.

[28] J. Xu, S. Shen, Y. Gan, Y. Li, W. Zhang, and Q. Su, "Transient flow pattern based microscale boiling heat transfer mechanisms," *Journal of Micromechanics and*

Microengineering, vol. 15, no. 6. pp. 1344–1361, 2005.

[29] C. Huh and M. H. Kim, "Pressure Drop, Boiling Heat Transfer and Flow Patterns during Flow Boiling in a Single Microchannel," *Heat Transf. Eng.*, vol. 28, no. 8–9, pp. 730–737, 2007.

[30] M. J. Kohl, S. I. Abdel-Khalik, S. M. Jeter, and D. L. Sadowski, "A microfluidic experimental platform with internal pressure measurements," *Sensors Actuators, A Phys.*, vol. 118, no. 2, pp. 212–221, 2005.

[31] C. L. Ong and J. R. Thome, "Macro-to-microchannel transition in two-phase flow: Part 2 - Flow boiling heat transfer and critical heat flux," *Exp. Therm. Fluid Sci.*, vol. 35, no. 6, pp. 873–886, 2011.

[32] D. B. R. Kenning and Y. Yan, "Pool boiling heat transfer on a thin plate : Features revealed by liquid crystal thermography," *Int. J. Heat Mass Transf.*, vol. 39, no. 15, pp. 3117–3137, 1996.

[33] Y. Wang and K. Sefiane, "Effects of heat flux, vapour quality, channel hydraulic diameter on flow boiling heat transfer in variable aspect ratio micro-channels using transparent heating," *Int. J. Heat Mass Transf.*, vol. 55, no. 9–10, pp. 2235–2243, 2012.

[34] D. Bogojevic, "Flow boiling and two-phase flow instabilities in silicon microchannel heat sinks for microsystems cooling.," University of Edinburgh, 2010.

[35] T. G. Karayiannis and M. M. Mahmoud, "Flow boiling in microchannels: Fundamentals and applications," *Appl. Therm. Eng.*, vol. 115, pp. 1372–1397, Mar. 2017.

[36] P. Cheng, G. Wang, and X. Quan, "Recent Work on Boiling and Condensation in Microchannels," *J. Heat Transfer*, vol. 131, no. 4, p. 43211, 2009.

[37] C. B. Tibiriçá and G. Ribatski, "Flow boiling in micro-scale channels-Synthesized literature review," in *International Journal of Refrigeration*, 2013, vol. 36, no. 2, pp. 301–324.

[38] S. G. Kandlikar, "Heat Transfer Mechanisms During Flow Boiling in Microchannels," *J. Heat Transfer*, vol. 126, no. 1, p. 8, 2004.

[39] J. R. Thome, "No Title," in *Two-Phase Flow and Flow Boiling in Microchannels. Wolverine Heat Transfer Engineering Data book III, Chapter 20*, Switzerland.

[40] C. B. Tibirica and G. Ribatski, "Flow boiling phenomenological differences between micro-and macroscale channels," in *Heat Transfer Engineering*, 2015, vol. 36, no. 11, pp. 937–942.

[41] S. G. Kandlikar and W. J. Grande, "Evolution of microchannel flow passages-thermohydraulic performance and fabrication technology," *Heat Transf. Eng.*, vol. 24, no. 1, pp. 3–17, 2003.

[42] M. Suo and P. Griffith, "Two-Phase Flow in Capillary Tubes," *J. Basic Eng.*, vol. 86, no.

3, p. 576, 1964.

[43] P. A. Kew and K. Cornwell, “Correlations for the prediction of boiling heat transfer in small-diameter channels,” *Appl. Therm. Eng.*, vol. 17, no. 8–10, pp. 705–715, 1997.

[44] T. Harirchian and S. V. Garimella, “Microchannel size effects on local flow boiling heat transfer to a dielectric fluid,” *Int. J. Heat Mass Transf.*, vol. 51, no. 15–16, pp. 3724–3735, 2008.

[45] N. Brauner and D. M. Maron, “Identification of the range of ‘small diameters’ conduits, regarding two-phase flow pattern transitions,” *Int. Commun. Heat Mass Transf.*, vol. 19, no. 1, pp. 29–39, 1992.

[46] C. L. Ong and J. R. Thome, “Macro-to-microchannel transition in two-phase flow: Part 1 - Two-phase flow patterns and film thickness measurements,” *Exp. Therm. Fluid Sci.*, vol. 35, no. 1, pp. 37–47, 2011.

[47] K. Cornwell and P. A. Kew, “Boiling in Small Parallel Channels,” in *Energy Efficiency in Process Technology*, P. A. Pilavachi, Ed. Dordrecht: Springer Netherlands, 1993, pp. 624–638.

[48] D. Steiner and J. Taborek, “Flow boiling heat transfer in vertical tubes correlated by an asymptotic model,” *Heat Transf. Eng.*, vol. 13, no. 2, pp. 43–69, 1992.

[49] J. Lee and I. Mudawar, “Low-temperature two-phase microchannel cooling for high-heat-flux thermal management of defense electronics,” *IEEE Trans. Components Packag. Technol.*, vol. 32, no. 2, pp. 453–465, 2009.

[50] B. Agostini, J. R. Thome, M. Fabbri, B. Michel, D. Calmi, and U. Kloter, “High heat flux flow boiling in silicon multi-microchannels - Part I: Heat transfer characteristics of refrigerant R236fa,” *Int. J. Heat Mass Transf.*, vol. 51, no. 21–22, pp. 5400–5414, 2008.

[51] S. M. Kim and I. Mudawar, “Review of databases and predictive methods for heat transfer in condensing and boiling mini/micro-channel flows,” *International Journal of Heat and Mass Transfer*, vol. 77. pp. 627–652, 2014.

[52] S. Kandlikar, “Effect of liquid-vapor phase distribution on the heat transfer mechanisms during flow boiling in minichannels and microchannels,” *Heat Transf. Eng.*, vol. 27, no. 1, pp. 4–13, 2006.

[53] S. Gedupudi, Y. Q. Zu, T. G. Karayiannis, D. B. R. Kenning, and Y. Y. Yan, “Confined bubble growth during flow boiling in a mini/micro-channel of rectangular cross-section Part I: Experiments and 1-D modelling,” *Int. J. Therm. Sci.*, vol. 50, no. 3, pp. 250–266, Mar. 2011.

[54] Y. Q. Zu, Y. Y. Yan, S. Gedupudi, T. G. Karayiannis, and D. B. R. Kenning, “Confined bubble growth during flow boiling in a mini-/micro-channel of rectangular cross-section part II: Approximate 3-D numerical simulation,” *Int. J. Therm. Sci.*, vol. 50, no. 3, pp.

267–273, Mar. 2011.

[55] K. J. L. Geisler and A. Bar-Cohen, “Confinement effects on nucleate boiling and critical heat flux in buoyancy-driven microchannels,” *Int. J. Heat Mass Transf.*, vol. 52, no. 11–12, pp. 2427–2436, 2009.

[56] M. Blomquist, A. Khalighi, and A. Mukherjee, “Numerical Study of Bubble Instability During Microchannel Flow Boiling,” no. 56871. p. V001T07A015, 2015.

[57] A. Mukherjee and S. G. Kandlikar, “Numerical simulation of growth of a vapor bubble during flow boiling of water in a microchannel,” *Microfluid. Nanofluidics*, vol. 1, no. 2, pp. 137–145, 2005.

[58] S. V. Garimella, V. Singhal, and D. Liu, “On-chip thermal management with microchannel heat sinks and integrated micropumps,” *Proc. IEEE*, vol. 94, no. 8, pp. 1534–1548, 2006.

[59] S. S. Bertsch, E. A. Groll, and S. V. Garimella, “Review and comparative analysis of studies on saturated flow boiling in small channels,” *Nanoscale Microscale Thermophys. Eng.*, vol. 12, no. 3, pp. 187–227, 2008.

[60] S. Saitoh, H. Daiguji, and E. Hihara, “Effect of tube diameter on boiling heat transfer of R-134a in horizontal small-diameter tubes,” *Int. J. Heat Mass Transf.*, vol. 48, no. 23–24, pp. 4973–4984, 2005.

[61] M. Lee, L. S. L. Cheung, Y. K. Lee, and Y. Zohar, “Height effect on nucleation-site activity and size-dependent bubble dynamics in microchannel convective boiling,” *J. Micromechanics Microengineering*, vol. 15, no. 11, pp. 2121–2129, 2005.

[62] V. Talimi, Y. S. Muzychka, and S. Kocabiyik, “A review on numerical studies of slug flow hydrodynamics and heat transfer in microtubes and microchannels,” *International Journal of Multiphase Flow*, vol. 39. pp. 88–104, 2012.

[63] J. Lee and I. Mudawar, “Fluid flow and heat transfer characteristics of low temperature two-phase micro-channel heat sinks - Part 1: Experimental methods and flow visualization results,” *Int. J. Heat Mass Transf.*, vol. 51, no. 17–18, pp. 4315–4326, 2008.

[64] T. N. Tran, M. W. Wambsganss, and D. M. France, “Small circular- and rectangular-channel boiling with two refrigerants,” *Int. J. Multiph. Flow*, vol. 22, no. 3, pp. 485–498, 1996.

[65] T.-H. Yen, N. Kasagi, and Y. Suzuki, “Forced convective boiling heat transfer in microtubes at low mass and heat fluxes,” *Int. J. Multiph. Flow*, vol. 29, no. 12, pp. 1771–1792, 2003.

[66] T. H. Yen, M. Shoji, F. Takemura, Y. Suzuki, and N. Kasagi, “Visualization of convective boiling heat transfer in single microchannels with different shaped cross-sections,” *Int. J. Heat Mass Transf.*, vol. 49, no. 21–22, pp. 3884–3894, 2006.

[67] H. S. Wang and J. W. Rose, “Film condensation in horizontal microchannels: Effect of channel shape,” *Int. J. Therm. Sci.*, vol. 45, no. 12, pp. 1205–1212, 2006.

[68] S. Lin, P. A. Kew, and K. Cornwell, “Flow boiling of refrigerant R141B in small tubes,” *Chem. Eng. Res. Des.*, vol. 79, no. 4, pp. 417–424, 2001.

[69] S. S. Bertsch, E. A. Groll, and S. V. Garimella, “Refrigerant flow boiling heat transfer in parallel microchannels as a function of local vapor quality,” *Int. J. Heat Mass Transf.*, vol. 51, no. 19–20, pp. 4775–4787, 2008.

[70] T. Chen and S. V. Garimella, “Measurements and high-speed visualizations of flow boiling of a dielectric fluid in a silicon microchannel heat sink,” *Int. J. Multiph. Flow*, vol. 32, no. 8, pp. 957–971, 2006.

[71] T. Harirchian and S. V. Garimella, “The critical role of channel cross-sectional area in microchannel flow boiling heat transfer,” *Int. J. Multiph. Flow*, vol. 35, no. 10, pp. 904–913, 2009.

[72] V. Dupont and J. R. Thome, “Evaporation in microchannels: Influence of the channel diameter on heat transfer,” *Microfluid. Nanofluidics*, vol. 1, no. 2, pp. 119–127, 2005.

[73] R. Revellin and J. R. Thome, “A theoretical model for the prediction of the critical heat flux in heated microchannels,” *Int. J. Heat Mass Transf.*, vol. 51, no. 5–6, pp. 1216–1225, 2008.

[74] Y. Wang, K. Sefiane, and S. Harmand, “Flow boiling in high-aspect ratio mini- and micro-channels with FC-72 and ethanol: Experimental results and heat transfer correlation assessments,” *Exp. Therm. Fluid Sci.*, vol. 36, pp. 93–106, 2012.

[75] O. Mokrani, B. Bourouga, C. Castelain, and H. Peerhossaini, “Fluid flow and convective heat transfer in flat microchannels,” *Int. J. Heat Mass Transf.*, vol. 52, no. 5–6, pp. 1337–1352, 2009.

[76] U. Soupremanien, S. Le Person, M. Favre-Marinet, and Y. Bultel, “Influence of the aspect ratio on boiling flows in rectangular mini-channels,” *Exp. Therm. Fluid Sci.*, vol. 35, no. 5, pp. 797–809, 2011.

[77] C. Amador, A. Gavriilidis, and P. Angeli, “Flow distribution in different microreactor scale-out geometries and the effect of manufacturing tolerances and channel blockage,” *Chem. Eng. J.*, vol. 101, no. 1–3, pp. 379–390, 2004.

[78] S. G. Singh, A. Kulkarni, S. P. Duttagupta, B. P. Puranik, and A. Agrawal, “Impact of aspect ratio on flow boiling of water in rectangular microchannels,” *Exp. Therm. Fluid Sci.*, vol. 33, no. 1, pp. 153–160, 2008.

[79] B. Markal, O. Aydin, and M. Avci, “Effect of aspect ratio on saturated flow boiling in microchannels,” *Int. J. Heat Mass Transf.*, vol. 93, pp. 130–143, 2016.

[80] O. Tonomura, S. Tanaka, M. Noda, M. Kano, S. Hasebe, and I. Hashimoto, “CFD-based

optimal design of manifold in plate-fin microdevices," *Chem. Eng. J.*, vol. 101, no. 1–3, pp. 397–402, 2004.

[81] R. Revellin and J. R. Thome, "A theoretical model for the prediction of the critical heat flux in heated microchannels," *Int. J. Heat Mass Transf.*, vol. 51, no. 5–6, pp. 1216–1225, Mar. 2008.

[82] A. Mukherjee, S. G. Kandlikar, and Z. J. Edel, "Numerical study of bubble growth and wall heat transfer during flow boiling in a microchannel," *Int. J. Heat Mass Transf.*, vol. 54, no. 15–16, pp. 3702–3718, 2011.

[83] S. G. Kandlikar, V. K. Dhir, and M. Shoji, *Handbook of Phase Change: Boiling and Condensation*, vol. 53. 1999.

[84] A. E. Bergles and W. M. Rohsenow, "The Determination of Forced-Convection Surface-Boiling Heat Transfer," *J. Heat Transfer*, vol. 86, no. 3, pp. 365–372, 1964.

[85] T. Sato and H. Matusmura, "On the Conditions of Incipient Subcooled-Boiling with Forced Convection," *Bull. JSME*, vol. 7, no. 26, pp. 392–398, 1964.

[86] S. G. Kandlikar, "Nucleation characteristics and stability considerations during flow boiling in microchannels," *Exp. Therm. Fluid Sci.*, vol. 30, no. 5, pp. 441–447, 2006.

[87] J. N. Chung, T. Chen, and S. C. Maroo, "A review of recent progress on nano/micro scale nucleate boiling fundamentals," *Front. Heat Mass Transf.*, vol. 2, no. 2, 2011.

[88] L. R. C. Sharp, R. R., *The nature of liquid film evaporation during nucleate boiling.* Washington, D.C: National Aeronautics and Space Administration., 1964.

[89] D. K. E. N.W. Snyder, "Post conference comments, Summary of Conference on Bubble Dynamics and Boiling Heat Transfer Held at the Jet Propulsion Laboratory," *JPL Memo No. 20–137*.

[90] R. B. M. Franklin D.Moore, "NoThe measurement of rapid surface temperature fluctuations during nucleate boiling of water," *AIChe*, vol. 7, no. 4, pp. 620–624.

[91] M. Ishii and M. A. Grolmes, "Inception criteria for droplet entrainment in two-phase concurrent film flow," *AIChE J.*, vol. 21, no. 2, pp. 308–318, 1975.

[92] J. R. Barbosa, A. H. Govan, and G. F. Hewitt, "Visualisation and modelling studies of churn flow in a vertical pipe," *Int. J. Multiph. Flow*, vol. 27, no. 12, pp. 2105–2127, 2001.

[93] L. Pan and T. J. Hanratty, "Correlation of entrainment for annular flow in horizontal pipes," *Int. J. Multiph. Flow*, vol. 28, no. 3, pp. 385–408, 2002.

[94] P. Sawant, M. Ishii, and M. Mori, "Prediction of amount of entrained droplets in vertical annular two-phase flow," *Int. J. Heat Fluid Flow*, vol. 30, no. 4, pp. 715–728, 2009.

[95] Z. Baniamerian, R. Mehdippour, and C. Aghanajafi, "Entrainment mass transfer in annular flow regime of two-phase carbon dioxide," *Sci. Res. Essays*, vol. 7, no. 49, pp. 4186–4195, 2012.

[96] G. Wang, P. Cheng, and H. Wu, “Unstable and stable flow boiling in parallel microchannels and in a single microchannel,” *Int. J. Heat Mass Transf.*, vol. 50, no. 21–22, pp. 4297–4310, 2007.

[97] X. Fu, S. L. Qi, P. Zhang, and R. Z. Wang, “Visualization of flow boiling of liquid nitrogen in a vertical mini-tube,” *Int. J. Multiph. Flow*, vol. 34, no. 4, pp. 333–351, 2008.

[98] D. Bogojevic, K. Sefiane, A. J. Walton, H. Lin, and G. Cummins, “Two-phase flow instabilities in a silicon microchannels heat sink,” *Int. J. Heat Fluid Flow*, vol. 30, no. 5, pp. 854–867, 2009.

[99] M. B. Bowers and I. Mudawar, “High flux boiling in low flow rate, low pressure drop mini-channel and micro-channel heat sinks,” *Int. J. Heat Mass Transf.*, vol. 37, no. 2, pp. 321–332, 1994.

[100] G. Wang, P. Cheng, and A. E. Bergles, “Effects of inlet/outlet configurations on flow boiling instability in parallel microchannels,” *Int. J. Heat Mass Transf.*, vol. 51, no. 9–10, pp. 2267–2281, May 2008.

[101] B. R. Fu, M. S. Tsou, and C. Pan, “Boiling heat transfer and critical heat flux of ethanol-water mixtures flowing through a diverging microchannel with artificial cavities,” *Int. J. Heat Mass Transf.*, vol. 55, no. 5–6, pp. 1807–1814, 2012.

[102] H. Lee, I. Park, I. Mudawar, and M. M. Hasan, “Micro-channel evaporator for space applications – 1. Experimental pressure drop and heat transfer results for different orientations in earth gravity,” *Int. J. Heat Mass Transf.*, vol. 77, pp. 1213–1230, Oct. 2014.

[103] T. G. Theofanous, J. P. Tu, A. T. Dinh, and T. N. Dinh, “The boiling crisis phenomenon part I: Nucleation and nucleate boiling heat transfer,” *Exp. Therm. Fluid Sci.*, vol. 26, no. 6–7, pp. 775–792, 2002.

[104] T. G. Theofanous, T. N. Dinh, J. P. Tu, and A. T. Dinh, “The boiling crisis phenomenon part II: Dryout dynamics and burnout,” *Exp. Therm. Fluid Sci.*, vol. 26, no. 6–7, pp. 793–810, 2002.

[105] N. Borhani and J. R. Thome, “Intermittent dewetting and dryout of annular flows,” *Int. J. Multiph. Flow*, vol. 67, no. S, pp. 144–152, 2014.

[106] Y. Katto and H. Ohno, “An improved version of the generalized correlation of critical heat flux for the forced convective boiling in uniformly heated vertical tubes,” *Int. J. Heat Mass Transf.*, vol. 27, no. 9, pp. 1641–1648, 1984.

[107] Y. Katto, “An analysis of the effect of inlet subcooling on critical heat flux of forced convection boiling in vertical uniformly heated tubes,” *Int. J. Heat Mass Transf.*, vol. 22, no. 11, pp. 1567–1575, 1979.

[108] J. Lee and I. Mudawar, “Two-phase flow in high-heat-flux micro-channel heat sink for

refrigeration cooling applications: Part I - Pressure drop characteristics," *Int. J. Heat Mass Transf.*, vol. 48, no. 5, pp. 928–940, 2005.

[109] F. T. Kanizawa, C. B. Tibiriçá, and G. Ribatski, "Heat transfer during convective boiling inside microchannels," *Int. J. Heat Mass Transf.*, vol. 93, pp. 566–583, 2016.

[110] S.-C. Yao and Y. Chang, "Pool boiling heat transfer in a confined space," *Int. J. Heat Mass Transf.*, vol. 26, no. 6, pp. 841–848, 1983.

[111] T. H. Kim, E. Kommer, S. Dessiatoun, and J. Kim, "Measurement of two-phase flow and heat transfer parameters using infrared thermometry," *Int. J. Multiph. Flow*, vol. 40, pp. 56–67, 2012.

[112] T. L. Liu and C. Pan, "Infrared thermography measurement of two-phase boiling flow heat transfer in a microchannel," *Appl. Therm. Eng.*, vol. 94, pp. 568–578, 2016.

[113] D. B. R. Kenning, "Wall temperature patterns in nucleate boiling," *Int. J. Heat Mass Transf.*, vol. 35, no. 1, pp. 73–86, 1992.

[114] J. Yoo, C. E. Estrada-Perez, and Y. A. Hassan, "An accurate wall temperature measurement using infrared thermometry with enhanced two-phase flow visualization in a convective boiling system," *Int. J. Therm. Sci.*, vol. 90, pp. 248–266, 2015.

[115] J. Xu, Y. Gan, D. Zhang, and X. Li, "Microscale boiling heat transfer in a micro-timescale at high heat fluxes," *J. Micromechanics Microengineering*, vol. 15, no. 2, pp. 362–376, 2005.

[116] I. Hapke, H. Boye, and J. Schmidt, "Flow bolling of water and n-heptane in micro channels," *Microscale Thermophys. Eng.*, vol. 6, no. 2, pp. 99–115, 2002.

[117] G. Hetsroni, A. Mosyak, Z. Segal, and E. Pogrebnyak, "Two-phase flow patterns in parallel micro-channels," *Int. J. Multiph. Flow*, vol. 29, no. 3, pp. 341–360, 2003.

[118] G. Hetsroni and R. Rozenblit, "Thermal patterns on a heated wall in vertical air-water flow," *Int. J. Multiph. Flow*, vol. 26, no. 2, pp. 147–167, 2000.

[119] D. Krebs, V. Narayanan, J. Liburdy, and D. Pence, "Spatially resolved wall temperature measurements during flow boiling in microchannels," *Exp. Therm. Fluid Sci.*, vol. 34, no. 4, pp. 434–445, 2010.

[120] M. Piasecka, K. Str??k, and B. Maciejewska, "Calculations of Flow Boiling Heat Transfer in a Minichannel Based on Liquid Crystal and Infrared Thermography Data," *Heat Transf. Eng.*, vol. 38, no. 3, pp. 332–346, 2017.

[121] Y. Lu, F. Wang, and H. Wang, "Boiling regimes in uncoated polydimethylsiloxane microchannels with a fine wire heater," *Heat Mass Transf. und Stoffuebertragung*, vol. 46, no. 11–12, pp. 1253–1260, 2010.

[122] D. C. Paine, T. Whitson, D. Janiac, R. Beresford, C. O. Yang, and B. Lewis, "A study of low temperature crystallization of amorphous thin film indium-tin-oxide," *J. Appl. Phys.*,

vol. 85, no. 12, pp. 8445–8450, 1999.

[123] O. Tuna, Y. Selamet, G. Aygun, and L. Ozyuzer, “High quality ITO thin films grown by dc and RF sputtering without oxygen,” *J. Phys. D. Appl. Phys.*, vol. 43, no. 5, 2010.

[124] T. Murakami, S. ichi Kuroda, and Z. Osawa, “Dynamics of polymeric solid surfaces treated with oxygen plasma: Effect of aging media after plasma treatment,” *J. Colloid Interface Sci.*, vol. 202, no. 1, pp. 37–44, 1998.

[125] J. Friend and L. Yeo, “Fabrication of microfluidic devices using polydimethylsiloxane,” *Biomicrofluidics*, vol. 4, no. 2, 2010.

[126] C.P. Cummins, “Fabrication of microchannels for use in micro-boiling experiments.,” The University of Edinburgh, 2011.

[127] T. Ashida *et al.*, “Thermal transport properties of polycrystalline tin-doped indium oxide films,” *J. Appl. Phys.*, vol. 105, no. 7, p. 73709, Apr. 2009.

[128] A. K. Kulkarni, K. H. Schulz, T. S. Lim, and M. Khan, “Dependence of the sheet resistance of indium-tin-oxide thin films on grain size and grain orientation determined from X-ray diffraction techniques,” *Thin Solid Films*, vol. 345, no. 2, pp. 273–277, May 1999.

[129] R. P. Madding, “Emissivity measurement and temperature correction accuracy considerations,” *Spie Conf. Thermosense XXI*, vol. 3700, pp. 393–401, 1999.

[130] D. Brutin, B. Sobac, F. Rigollet, and C. Le Niliot, “Infrared visualization of thermal motion inside a sessile drop deposited onto a heated surface,” *Exp. Therm. Fluid Sci.*, vol. 35, no. 3, pp. 521–530, 2011.

[131] R.Remsburgh, *Thermal design of Electronic Equipment*. .

[132] R. K. Shah and A. L. (Alexander L. London, *Laminar flow forced convection in ducts : a source book for compact heat exchanger analytical data*. Academic Press, 1978.

[133] R. P., *Surface boiling of superheated liquid*, 1997th ed. PSI-97-01, Switzerland.

[134] J. Barber, D. Brutin, K. Sefiane, and L. Tadrist, “Bubble confinement in flow boiling of FC-72 in a ‘rectangular’ microchannel of high aspect ratio,” *Exp. Therm. Fluid Sci.*, vol. 34, no. 8, pp. 1375–1388, Nov. 2010.

Appendix A

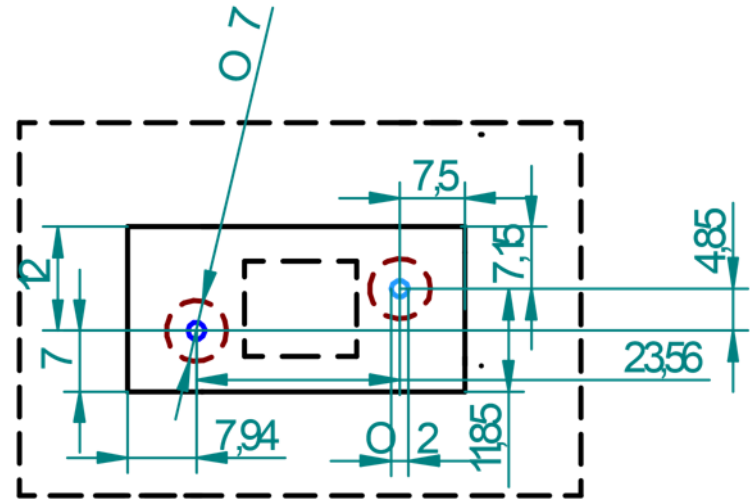

(a)

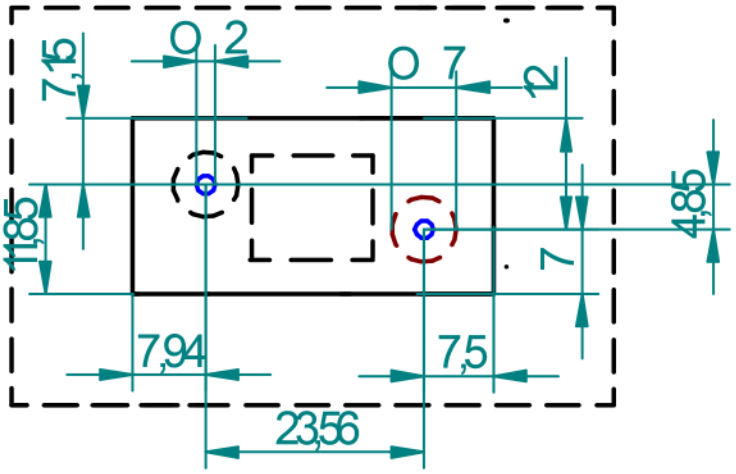

(b)

Figure A. 1 *Drawings of the transparent Plexiglas cover top case of the test module.*

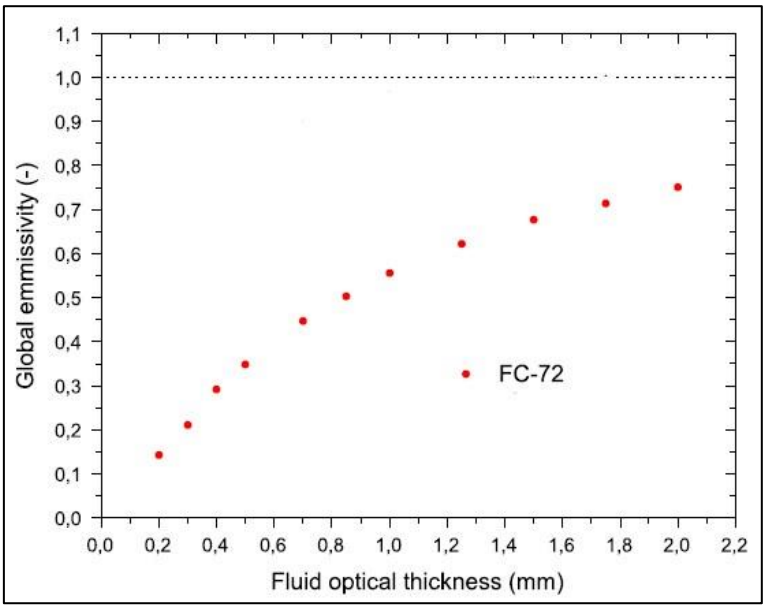

Figure A. 2 *Emissivity of FC-72 as a function of the thickness from Brutin et al. [121]*

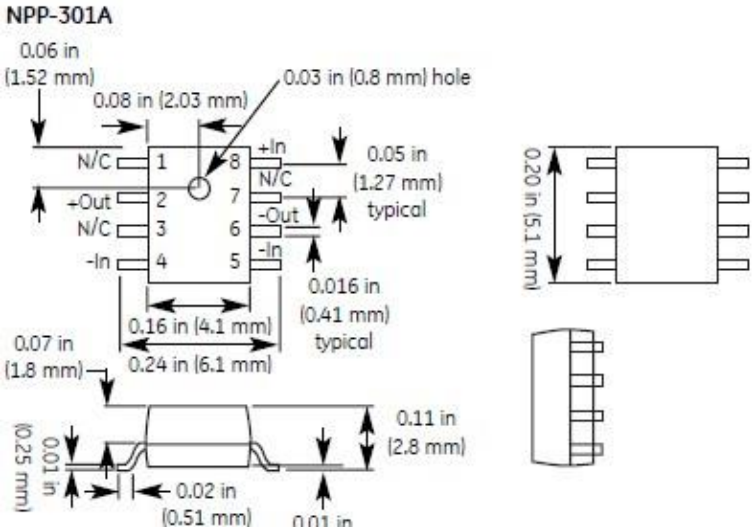

Figure A. 3 *Schematic drawing of the miniature pressure sensors.*

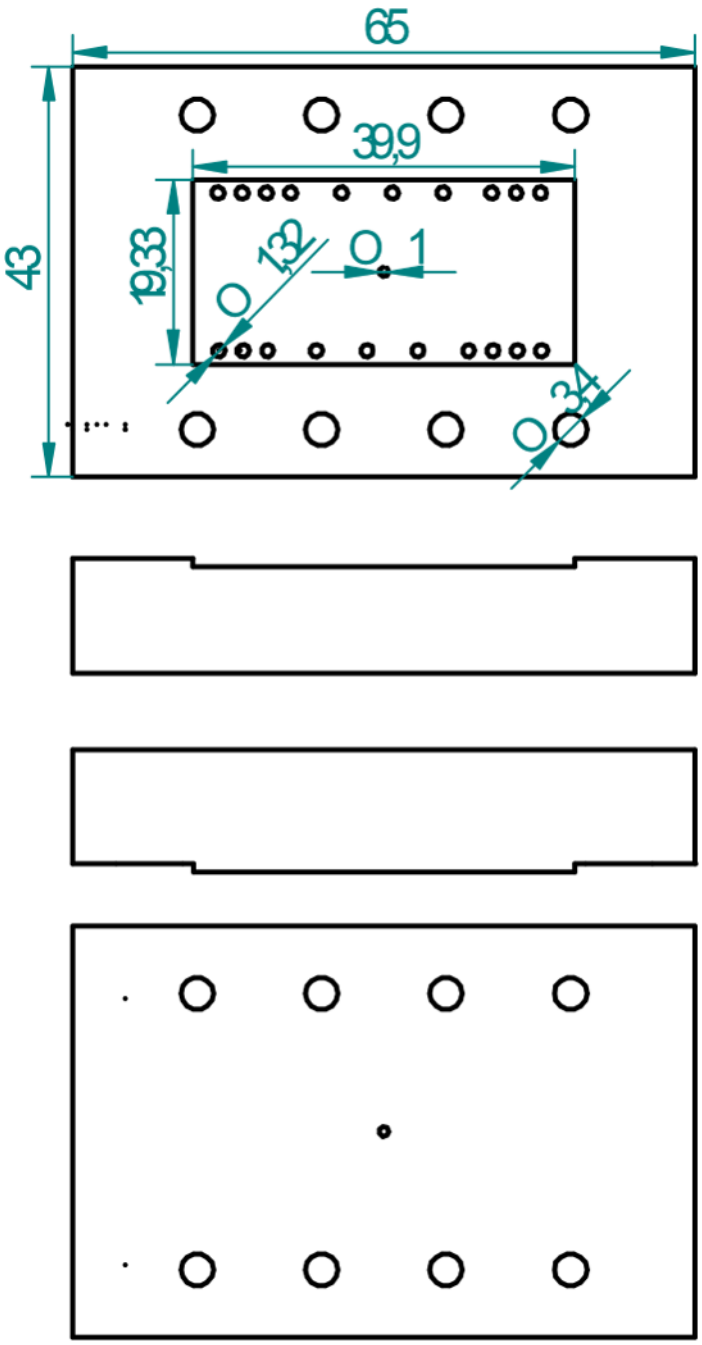

Figure A. 4 *Case for oven calibration from polycarbonate.*

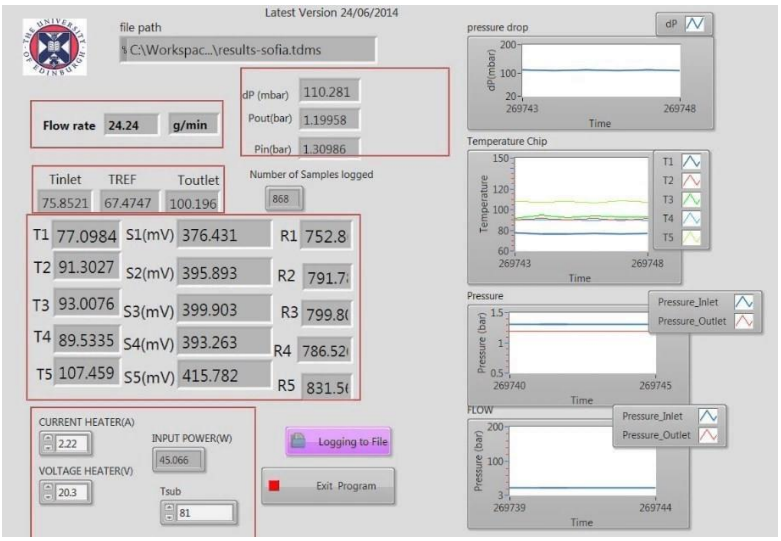

Figure A. 5 *LabVIEW programme interface used for the acquisition of pressure and temperature from the silicon microchannel heat sinks.*

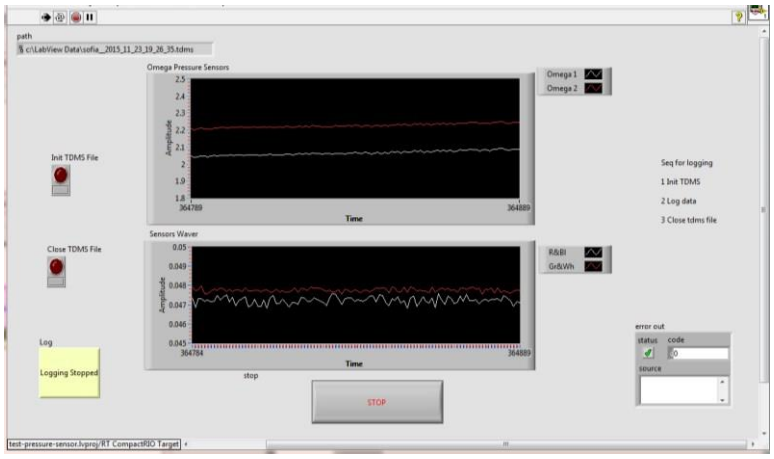

Figure A. 6 *LABVIEW code front panel for the acquisition of the pressure during calibration of the pressure sensors.*

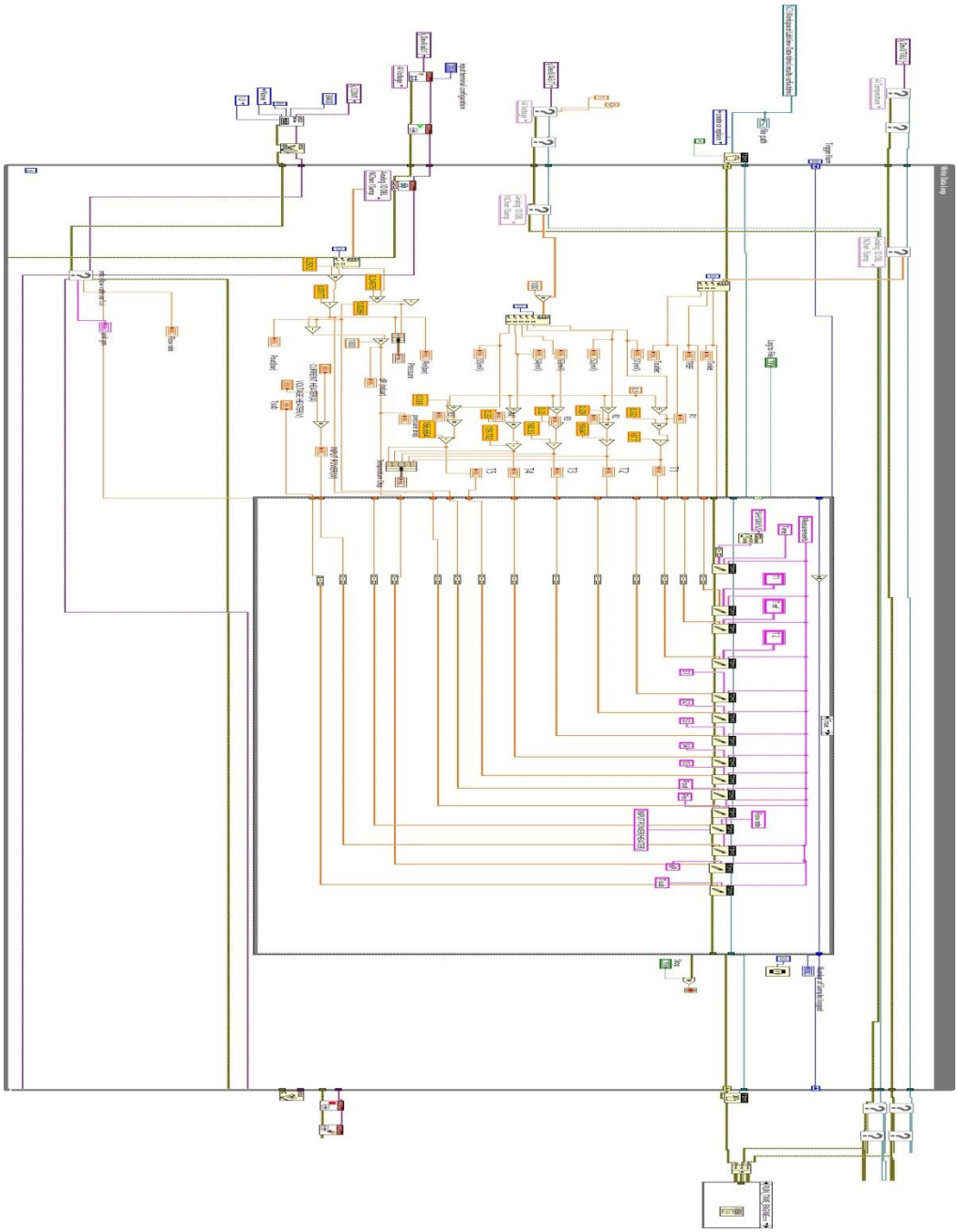

Figure A. 7 *LabVIEW code used for the temperature, pressure, and flow rate acquisition during experiments with silicon microchannel heat sinks.*

Matlab code for processing of high –speed images

```
%sol& histogram resuts
im=imread('1mlmlinannealed2.07win1Tboilingfr445_29.67s.png');      % imported
image

I=rgb2gray (im); % image converted to grayscale
Figure, imshow (I)
K = medfilt2 (I); % filtered image
Figure
Imshow (K)
Figure
Surf (double (K (1:8: end, 1:8: end))), zlim ([0 255]);
Colormap gray
Set (gca,'ydir','reverse');
Percentageas
= imopen(K,strel('disk',3)); figure,
imshow(background)
%View the background approximation image as a surface to see where illumination
varies.
%The surf command creates colored parametric surfaces that enable you to view
mathematical functions over a rectangular region.Because the surf function
requires data of class double,you first need to convert background using the
double command.The example uses indexing syntax to view only 1 out of 8 pixels
in each direction otherwise, the surface plot would be too dense. The example
also sets the scale of the plot to better match the range of the uint8 data
and reversesthe y-axis of the display to provide a better view of the data
(The pixels at the bottom of the image appear at the front of the surface
plot).In the surface display, [0, 0] represents the origin, or upper-left
corner of the image. The highest part of the curve indicates that the highest
pixel values f background occur nearthe middle rows of the image.%The lowest
pixel values occur at the bottom of the image.
for i=1:425     for
j=1:274 if
background(i,j)>260;
background(i,j)=50; end
end end
solution=double(background(1:8:end,1:8:end)); figure
surf(double(background(1:8:end,1:8:end))),zlim([0 255]);
set(gca,'ydir','reverse'); colormap gray

I2 = I - background; % for liquid the intensity must be 0 ( dark) where most
     of the pixels are concentrated
   figure
imshow(I2)
figure
surf(double(I2(1:8:end,1:8:end))),zlim([0 255]);
set(gca,'ydir','reverse'); colormap gray


I3 = imadjust(I2); imshow(I3);

level = graythresh(I3); bw = im2bw(I3,level); bw =
bwareaopen(bw, 50); imshow(bw)

%Histogrammes  imhist(I);figure;

histogram=imhist(background); figure;
imhist(background);

figure;
imhist(K);
```

Appendix B

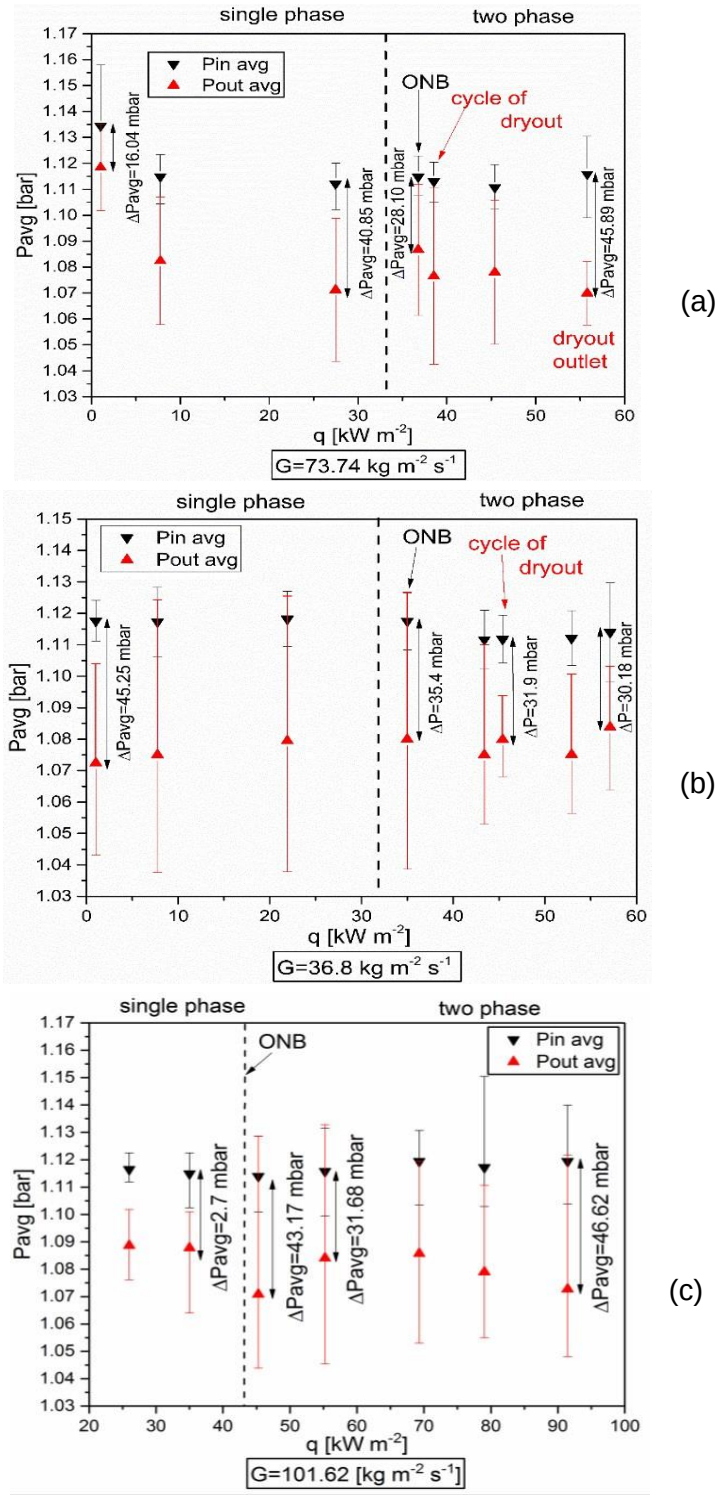

Figure B. 1 *Averaged pressures over time (60 s), obtained near the inlet and the outlet of the microchannel from single to two-phase flow boiling by increasing the heat flux.*

Publications and presentations

The following publications and presentation have been made during the course of the present investigation:

- **Journal Publications**

Korniliou S., Mackenzie Dover C.M., Harmand S., Sefiane K, Walton A. Two-dimensional heat transfer coefficients with simultaneous flow visualizations during two-phase flow boiling in a *PDMS* microchannel. *Accepted for publication in Applied Thermal Engineering (ATE), September 13, 2017.*

Mackenzie Dover C.M., Li Y., Korniliou S., Sefiane K., Terry J., Walton. Polydimethylsiloxane (PDMS)-based microfluidic channel with integrated commercial pressure sensors. *Publiced in IEEE Sensors Journal, September 2017.*

Korniliou S., Mackenzie Dover C.M., Harmand S., Duursma G., Christy J.R.E, Terry J.G., Walton A.J., Sefiane K. Wall temperature mapping with high resolution IR thermography during flow boiling in a *PDMS* microchannel with integrated pressure sensors. *Submitted to the International Journal of Thermal Sciences, May 2017.*

- **Conference publications and presentations**

Korniliou S., Mackenzie Dover C.M., Harmand S., Sefiane K, Walton A.J. Wall temperature mapping with high resolution IR thermography during flow boiling in a *PDMS* microchannel with integrated pressure sensors. Paper presented at: *Proceedings of the International Conference on Materials & Energy; 2017 July 06-09; Tianjin, China. (Received best poster award).*

Korniliou S., Mackenzie Dover C.M., Harmand S., Duursma G., Christy J.R.E, Terry J.G., Walton A.J., Sefiane K. Dual wall temperature mapping with high resolution IR thermography during flow boiling in a *PDMS* microchannel with integrated pressure sensors. Paper presented at *Proceedings at the International Heat Transfer Symposium and Heat Powered Cycles Conference; 2016 June 26-30; Nottingham, UK. (Received best paper award).*